ICASE
International Conference on AEROSPACE SCIENCE & ENGINEERING

SEVENTH INTERNATIONAL CONFERENCE ON

AEROSPACE SCIENCE & ENGINEERING

Emerging Technologies in Aerospace Engineering & Geographic Information Science

NATIONAL CENTER OF GIS & SPACE APPLICATIONS

Institute of Space Technology

Islamabad, Pakistan

ICASE Proceedings



Institute of Space Technology

PROCEEDINGS

Seventh International Conference on Aerospace Science and Engineering

December 14 – 16, 2021

Institute of Space Technology

Islamabad, Pakistan

Organized by

National Center of GIS and Space Applications (NCGSA)

Editorial Board

Dr. Najam Abbas Naqvi
Conference Secretary
Institute of Space Technology,
Islamabad, Pakistan

Mr. Usama Ahmed
Technical Program Manager
Institute of Space Technology,
Islamabad, Pakistan

Mr. Faaiz Ahmed Jeelani
Business Development Manager
National Center of GIS & Space Applications
Islamabad, Pakistan

Ms. Aqsa Zouq
Manager Research Content
National Center of GIS & Space Applications
Islamabad, Pakistan

Ms. Mahnoor Ajmal
Manager Proceedings
Institute of Space Technology,
Islamabad, Pakistan

International Standard Book Number

E-Copy: 978-969-9448-05-8
Hard Copy: 978-969-9448-06-5

Copyright © 2022

This document is subject to the copy right. All rights are reserved with Institute of Space Technology (IST), Islamabad, Pakistan. IST can use, publish or reproduce this document in any form under the copyright law and no part of this document can be reproduced by anyone without the prior written permission of IST.

Institute of Space Technology (IST), Islamabad, Pakistan.

Preface

Institute of Space Technology (IST), one of the premier institutes in Pakistan, is a federally chartered, degree awarding Institute offering graduate and baccalaureate programs in Aerospace, Avionics, Electrical, Mechanical, Materials Science & Engineering, Space Science, Physics, Mathematics, Remote Sensing & GISc, Astronomy & Astrophysics, Global Navigation Satellite Systems (GNSS) and Applied Mathematics & Statistics.

National Center of GIS and Space Applications (NCGSA), a project of the Higher Education Commission (HEC) of Pakistan, led by the Institute of Space Technology is a consortium of seven research laboratories in seven Higher Education Institutions of Pakistan. NCGSA encompasses endeavors that strive to achieve and sustain human, technological, research, and entrepreneurial capacities in the areas of space science, technology, and its applications.

Institute of Space Technology, being the pioneer institute in Aerospace Science & Engineering envisioned an international forum wherein scientists, researchers, engineers, academicians, private and public industry professionals, entrepreneurs, and students from all across the globe could interact and share the latest research trends related with Space Science, Technology and its Applications. Consequently, the first International Conference on Aerospace Science and Engineering (ICASE) was organized in 2009.

Since its inception ICASE is a regular biennial event of IST which provides a platform to share research experiences, foster academia-industry linkages, and evaluate the latest findings in the emerging disciplines of Space Science and Technology.

ICASE 2021 featured a diverse blend of ten thematic areas including Aeronautics and Astronautics, Satellite Technology, Information & Communication Technologies, Positioning, Navigation & Timing, Geographic Information Science, Remote Sensing & Photogrammetry, Environment & Climate Science, Applied Physics & Mathematics, Astronomy, Astrophysics, & Astrobiology, Space Law, Management & Outreach.

A wide variety of sessions including Technical Sessions, Plenary Sessions, Leaders' Session, Panel Discussions, Workshops & Trainings, Meet the Scientists Forum, Forum 360: STEM Education, STEP Stakeholders' Forum, Scientific Networking Session, Science at Glance Session, Emerging Technologies Summit, Product & Poster Exhibition, Symposiums, GSA Summit and Star Gazing engaged students and professionals from all domains of 'Emerging Technologies in Aerospace Science and Geographic Information Science' in the mesmerizing three day conference.

ICASE 2021 hosted more than 45 International and National keynote speakers from up to 18 different countries namely France, Spain, Netherlands, Belgium, Italy, Turkey, Croatia, New Zealand, China, Japan, Indonesia, Philippines, Saudi Arabia, Egypt, Jordan, Morocco, Latvia and Niger.

Owing to COVID 19 and subsequent travel restrictions around the world, ICASE 2021 was executed seamlessly in hybrid mode. To ensure that the platforms remain inclusive at all levels and maximum engagement from around the world is ensured, a number of talks by invited keynote speakers and guests were delivered virtually.

Conference Secretary

January 2022

Table of Contents

1	Conference Organization	VII
2	List of Papers Published in IEEE Xplore	XX
3	List of Posters	XXIV
4	Research Papers	1
4.1	Application of Lotus Root Bionic Structure for Increment in Impact Load Bearing Capability of a Satellite's Return Capsule *Obaid Ur Rehman, Shahzad Hameed, Zuhaib Hassan*	2
4.2	Recent Advancements in Thermal Barrier Coatings (TBC) for High-Temperature Gas Turbines *Zahid Mehmood, Prof. Dr. Ali Sarosh, Osama Ali Ahmed Awan*	6
4.3	Design & Development of Static-Thrust Test-Bench for Aviation Based Piston Engines *Syed Muhmmad Basit Ali, Usama Saleem, Irtiza Ali*	15
4.4	Nose Landing Gear Conceptual Design and Analysis for M.A.L.E U.C.A.V *Asim Mehmood, Gohar Majeed, Kashif Mehmood, Usama Rehman, Muhammad Adeel Khan*	19
4.5	Design and Analysis of an Effective Ventilation System to Reduce COVID-19 Spread in A Confined Room *Salem Mohammed Alohani, Muzaffar Habib, Muhammad Anas*	26
4.6	Development of Low Cost Wind Tunnel for Measuring Lift & Drag *Hira Aftab, Beenish Batul*	42
4.7	Resolution Improvement in GNSS Based Synthetic Aperture Radar Using GPS L1 Signals from Different Look Angles *Muhammad Shoaib Ul Hassan, Hassan Sadiq, Najam Abbas Naqvi, Mohammad Usman*	48
4.8	Evaluation of Flight Mechanics Performance of a Fighter Aircraft Using Computational Fluid Dynamics *Asra Imtiaz, Hussna Zainab, Dr. Hossein Raza Hamdani*	52
4.9	CFD Analysis of Multi-Element Natural Laminar Flow Air Foil NLF (1)-0115 for A Fixed-Wing UAV *Absar Ahmed Khan*	56
4.10	An Overview of Passive Flow Control Techniques in Supersonic Flows *Zukhruf Liaqat, Aamer Shahzad*	66
4.11	Possible Seismo-Ionospheric Anomalies Associated with the Earthquakes Occurred in 2018 Using GNSS TEC: A Statistical Analysis *Muhammad Arqim Adil, Munawar Shah, Asim Khan, Ejaz Nazir, Mohamed Freeshah, Hamza Bin Babar*	71

4.12	Analysis of The Atmospheric Anomalies Associated with Mw>6.0 Continental Earthquake in The Afghanistan and Tajikistan *Daboor Sultana, Dr. Munawar Shah*	76
4.13	Analysis and Comparison of Maximum Power Point Tracking Algorithms for Electrical Power System of the CubeSat's *Usman Azeem, Dr. Rehan Mahmood*	79
4.14	Formation Flying Strategy for Attitude Determination and Control of CubeSat *Muhammad Abubakar Arshad, Dr. Rehan Mahmood, Dr. Mohammad Tahir*	86
4.15	Overview of ICUBE-N: National CubeSat of Pakistan *Usman Imran, Muhammad Asfandyaar Arshad, Arooj Shafique, Rehan Mahmood, Rizwan Mughal, Hayat Muhammad Khan*	91
4.16	Design and Development of a Portable Dish Antenna for SATCOM Man-Pack Terminal *Shujaat Hussain, Awais Munawar Qureshi, Rizwana Kausar, Mohsin Javaid*	96
4.17	Design and Simulation of Cost-Efficient Reaction Wheel for 1U CubeSat *Pawan Kumar, Oscar Lionel*	104
4.18	Comparative Study of Image to Image Translation Models for Abnormal Weather Effects Removal *Maria Siddiqua, Naeem Akhter, Javaid Khurshid*	112
4.19	Pick and Place Hand-Gestured-Robot for Physically Challenged People *Muhammad Ihtisham Babar, Muhammad Ibtisam Babar, Azeema Azhar*	117
4.20	A Review of Vulnerabilities and Cyber-Security Threats Associated with Overseas Telecom Companies' Operations *M Naveed Tahir, Areeba Azhar, Adnan Maqsood*	124
4.21	Sentiment Analysis of Social Media Text For Selective World Events And Geographical Segregation *Muhmmad Ahsan khan*	132
4.22	Autonomous Drone Navigation using Deep Convolutional Neural Network *Muhammad Arif Arshad, Saddam Hussain Khan, Muhammad Waleed Khan, Suleman Qamar, Asifullah Khan*	140
4.23	Parameter Identification and Optimization of Permanent Magnet DC Motor using Nonlinear Least Square Error Method *Raja Muhammad Sohail Khan, Hamza Malik, Hammad Munawar*	146
4.24	Threats to the Navigation of Drone Based Delivery Services *Imtiaz Nabi, Salma Zainab Farooq, Sunnyaha Saeed*	151
4.25	Investigation of Pre-Seismic Ionospheric and Atmospheric Anomalies before Mw 6.1 El Salvador Earthquake on October 28, 2018 *Abdur Rafeh Abbasi, Abdul Hanan Hamid, Muhammad Arqim Adil, Daboor Sultana, Saqib Mehdi, Erman Senturk*	156
4.26	Uplifting Agriculture through Information and Communication Technology and Geospatial Applications: A Review of Potential Tools and Techniques *Muhammad Adnan Shahid, Saif Ullah Khan, Subhe Seeme, Muhammad Danish Majeed, Muhammad Saqlain*	163
4.27	Atmospheric Monitoring Using Artificial Intelligence Models & Applications *Muhammad Mubeen, Dr. Shahid Mahmood, Moosa Bin Saif*	168

4.28	Unsupervised Classification of Hyperspectral Images using PCA and K-Means *Ayesha Malik, Mamoona Waheed*	173
4.29	Implementation Of The Maximum Cross Correlation (MCC) Method In Python For Ocean Current Estimation Over The Arabian Sea *Sheeza Khalid, Waqas A. Qazi*	177
4.30	Landslide Hazard Assessment And Monitoring In Azad Kashmir Using Sentinel-1 InSAR Data *Labeeqa Zaheer, Waqas A.Qazi*	181
4.31	Modeling and Simulation of BSAR (Bi Static Synthetic Aperture Radar) System Using Reflected BeiDou B1I Signals *Hassan Sadiq, Muhammad Shoaib ul Hassan, Muhammad Usman*	187
4.32	Flood Mapping and Crop Damage Assessment using Sentinel-1 SAR GRD and Optical Data through Google Earth Engine *Tariq Abbas, Waqas A. Qazi*	191
4.33	Prototype of an Autonomous Farming Robot: A Smart Farming System *Moaz Rao, Muhammad Shaarif Younas, Nauman Latif, Ahmad Hammad, Sadia, Ilyas Mahmood Qureshi*	197
4.34	Design and CFD Analysis of Outer Aerodynamics of 10kw Horizontal-Axis Wind Turbine *Noman Ahsan, Saqlain Abbas, Muhammad Ahmad, Ijaz Ali, Zulkarnain Abbas, Muhammad Umair Shahid*	202
4.35	Autonomous Unmanned Aerial Vehicle for Agricultural, Security, Emergency and Other Uses *Dr. Amir Rashid Chaudhry, Javid Rashid Ch, Dr. Imran Tahir, Tayyaba Shafaq, Imaan Shahid Raja, Salman Amir, Zohair Anjum, Nabeel Uddin Sheikh*	206
4.36	Simulations for Boundary Layer Flows and Heat Transfer of Cross Fluid over Moving Flat Plate *Mazhar Shehzad, Ammar Mushtaq*	213
4.37	Design, Analysis and Fabrication of Composite Curing Compressive Mold for Aerospace Applications *Muhammad Ayaz Ahmad, Sabih Ahmad Khan, Syed Irtiza Ali Shah, Hamza Akbar Khan, Taimur Ali Shams*	220
4.38	Libration Points of Space *Ms. Hadia Batool, Ms. Sumaira Abbasi*	228
4.39	Deinococcus Radiodurans as A Chassis for Synthetic Biology Experiments in Space Biology *Muneef U. Rehman, Khudeja Salim, Faisal F. Khan*	232
4.40	Event Rate of Extreme Mass Ratio Inspiral Systems in M32 Galaxy *Muhammad Waqas, Asad Ali, Rafia Sarwar*	241
4.41	Strategizing Pakistan's Space Policy for Defensive Discourse: A Case Study of Pulwama-Balakot Crisis *Noor Ul Huda Atif*	248
4.42	Multip-GNSS Navigation Performance Assessment and Improvement Quantification *Arif Hussain, Syed Hadi Hussain Shah, Hina Magsi, Arslan Ahmed, Faheem Akhtar Chachar*	252

4.43	GNSS TEC based Ionosphere Anomalies Related to the 2019 M_w 6.2 Thailan Earthquake *Shireen Mushtaq, Rimsha Ashraf, Dr. Munawar Shah, Punyawi Jamjareegulgran*	259
4.44	Investigation of Seismo Ionospheric Anomalies Associated with the M_w 6.7 Mongolia Earthquake *Shireen Mushtaq, Rimsha Ashraf*	265
4.45	Estimation of Drag Reduction of a Cargo Tractor-trailer using CFD Analysis in Different Configurations *Muhammad Rashid Liaqat, Ahmad Hammad, Dr. Mohsin Khalil Ahmad*	273
4.46	Simulations of Thin Gray Fluid Over a Moving Flat Plate *Sadia Maryam, Mazhar Shehzad, Ammar Mushtaq*	277
5	Author Index	283

Conference Executive Committee

Name	Designation	Conference Role
Maj. Gen. Rehan Abdul Baqi (H.I) (Retd.)	Vice Chancellor, IST	Conference Chair
Dr. Najam Abbas Naqvi	Chairman NCGSA	Conference Secretary
Dr. Suhail Akhtar	Dean, IST	Technical Committee Chair
Mr. Mirza Kashif Begg	CFO, IST	Treasurer
Wg Cdr Ishaat Saboor Khan (Retd.)	Registrar, IST	Coordination Chair
Engr. Amer Azam Qazi	Director Administration, IST	Administration Chair
Brig. Zia Ahmed (Retd.)	Director Human Resource, IST	Human Resource Chair
Mr. Rehan Rasheed	Director Civil Works	Conference Facilities Chair
Col Amir Najam Riaz (Retd.)	Addl. Director Audit, IST	Conference Audit Chair
Mr. Zulfiqar Ahmed	Head of Department, IT	IT Facilities Chair
Dr. Muhammad Uzair Khan	Chairman IEEE Islamabad Section	Technical Sponsor Chair

Technical Committee

Name	Designation & Affiliation	Conference Track
Dr. Suhail Akhtar	Dean Institute of Space Technology	Technical Committee Chair
Dr. Syed Hossein Raza Hamdani	Head of Department Aeronautics and Astronautics, IST	Aeronautics & Astronautics
Dr. Iqbal Rasool Memon	Professor Dept. of Aeronautics and Astronautics, IST	
Dr. Abdul Waheed	Head of Department Avionics Engineering, IST	
Dr. Asif Israr	Head of Department Mechanical Engineering, IST	Mechanical Engineering for Aerospace Applications (Aero-Astro)
Dr. Muhammad Zubair	Professor Dept. of Mechanical Engineering, IST	
Dr. Ibrahim Qazi	Head of Department Material Science & Engineering, IST	Aerospace Materials Design and Engineering (Aero-Astro)
Dr. Wilayat Hussain	Professor Dept. of Material Science & Engineering, IST	
Dr. Abdul Basit Saim	Assistant Professor Dept. of Material Science & Engineering, IST	
Dr. Qamar-ul-Islam	Professor Dept. of Electrical Engineering, IST	Satellite Technology
Dr. Rehan Mahmood	Principal Investigator/ Lab Director Small Satellite Technology & Research Lab, NCGSA	
Dr. Khurram Khursheed	Head of Department Electrical Engineering, IST	Information & Communication Technologies
Dr. Altaf Hussain	Head of Department Computer Science, KICSIT	
Dr. Jamshed Riaz	Professor Dept. of Aeronautics and Astronautics, IST	Positioning, Navigation & Timing
Dr. S. Zaineb Farooq	Assistant Professor	

	Dept. of Electrical Engineering, IST	
Dr. Farooq Hayder	Assistant Professor Dept. of Aeronautics and Astronautics, IST	
Dr. Bakhtiar K. Kasi	Dean Faculty of Information and Communication Technology, BUITEMS	Geographic Information Science
Dr. Muhammad Shafique	Associate Professor National Center of Excellence in Geology, UoP	
Dr. Zahir Ali	Head of Department National Center for Remote Sensing & Geo Informatics	Remote Sensing & Photogrammetry
Dr. Waqas Ahmed Qazi	Chief Technology Officer Offshore Monitoring Ltd, Cyprus	
Dr. Saleem Ullah	Associate Professor Dept. of Space Science, IST	
Dr. Zia ul Haq	Principal Investigator Remote Sensing, GIS and Climatic Research Lab, NCGSA	Environment & Climate Science
Dr. Shahid Iqbal	Assistant Professor Dept. of Space Science, IST	
Dr. Salman Ahmad	Head of Department Applied Mathematics and Statistics, IST	Applied Physics & Mathematics
Dr. Fazeel Mehmood Khan	Associate Professor Dept. of Space Science, IST	
Dr. Saeeda Sajjad	Principal Investigator Space & Astrophysics Research Lab, NCGSA	Astronomy, Astrophysics & Astrobiology
Dr. Imran Khan	Assistant Professor Dept. of Space Science, IST	
Ms. Ayesha Jagirani	Asia Pacific Space Cooperation Organization, China	Space Law, Management & Outreach
Dr. Ausima Sultan Malik	Head of Department Humanities Department, IST	
Dr. Ayesha Bukhari	Assistant Professor Dept. of Humanities, IST	

International Scientific Committee

Name	Designation	Affiliation
Dr. Abdulrahman H. Bajodah	Professor	King Abdulaziz University, Saudi Arabia
Dr. Tamer Mekky Ahmed Habib	Research Associate Professor	The National Authority of Remote Sensing and Space Sciences (NARSS), Egypt
Dr. Alim Rustem Aslan	Professor	Istanbul Technical University (ITU), Turkey
Dr. Christine, Marie, Eugenie Amory	Senior Scientist	Sorbonne Université, Ecole polytechnique,Institut Polytechnique de Paris, Université Paris Saclay, Observatoire de Paris, CNRS, Laboratoire de Physique des Plasmas (LPP), France
Dr. Andres Calabia Aibar	Associate Professor / Visiting Professor	Nanjing University of Information Science and Technology (NUIST), China Universidad Politécnica de Madrid (UPM), Spain
Dr. Jean L. Rasson	Advisor of Geophysics research	Department of Geophysics Services & Research, M/s Royal Institute of Meteorology, B5670, Dourbes, Belgium
Dr. Mark Van Der Meijde	Professor	University of Twente, Netherlands
Dr. Relly Margiono	Researcher and Lecturer	Geophysics, Sekolah Tinggi Meteorologi Klimatologi dan Geofisika (STMKG), Indonesia
Dr. Ali Nouh Ali Ma'bdeh	Head of GIS & RS Section	Al - Bayt University, Jordan
Dr. Fadia W. Al-Azawi	Assistant Professor	Al-Karkh University of Science, Iraq
Dr. Mounkaila Mohamed	Lecturer	University Abdou Moumouni Niamey, Niger
Dr. Andris Slavinskis	Associate Professor	UT Tartu Observatory, Estonia
Mr. Hamza Hameed	Team Lead - Legal	Space Generation Advisory Council (SGAC), Italy
Dr. Muhammad Sharif	Advisor Science & Technology	Islamic World Educational, Scientific and Cultural Organization (ICESCO), Morocco

Dr. Chen Jie	Associate Professor	Northwestern Polytechnical University (NPU), China
Dr. Gustavo Alonso Rodrigo	Professor	Technical University of Madrid, Spain
Dr. LIU Cun-liang	Professor	Northwestern Polytechnical University, China
Dr. Shufan Wu	Professor	Shanghai Jiao Tong University, China
Dr. Zhigang Gao	Associate Professor	Northwestern Polytechnical University, China
Dr. Huiqing Fan	Professor	Northwestern Polytechnical University (NPU), China
Dr. Renato Filjar	Professor	University of Rijeka & Krapina University of Applied Sciences, Croatia
Dr. Dinesh Manandhar	Associate Professor	The University of Tokyo, Japan
Dr. Xiaoliang Wang	Associate Research Fellow	Shanghai Jiaotong University, China
Dr. Eng. Ariel C. Blanco	Director	Philippines Space Agency, Philippines
Dr. Salman Ashraf	Remote Sensing Scientist	GNS Science, New Zealand

National Scientific Committee

Name	Designation	Affiliation
Dr. Adnan Maqsood	Associate Professor	National University of Sciences and Technology, Islamabad, Pakistan
Dr. Ali Sarosh	Associate Professor	Institute of Avionics and Aeronautics (IAA), Air University, Islamabad
Dr. Ali Javed Hashmi	Assistant Professor	Air University, Islamabad, Pakistan
Dr. Muhammad Kamran Saleem	Associate Professor	University of Central Punjab Lahore, Pakistan
Dr. Nosherwan Shoaib	Associate Professor	Research Institute for Microwave and Millimeter-Wave Studies (RIMMS) National University of Sciences and Technology (NUST), Islamabad, Pakistan
Dr. Syed Ali Hassan	Associate Professor	School of Electrical Engineering and Computer Science (SEECS)
Dr. M. Uzair Khan	Associate Professor	FAST - National University of Computer and Emerging Sciences
Dr. Abdul Malik Khan	Director	embedINN Pvt. Ltd., Islamabad, TecSoB LLP, Islamabad
Dr. Arslan Ahmed	Assistant Professor	Sukkur IBA University, Sukkur, Pakistan
Dr. Muhammad Ayyaz Ameen	General Manager	Pakistan Space & Upper Atmosphere Research Commission (SUPARCO)
Ms. Maria Zubair	GIS Specialist	Punjab Information Technology Board, Lahore, Pakistan
Dr. Dostdar Hussain	Associate Professor	Department of Computer Sciences, Karakoram International University
Prof. Dr. M. Farooq Ahmed	Professor/Chairman	Department of Geological Engineering, UET, Lahore
Dr. Nadia Imtiaz	Principal Scientist	Theoretical Physics Division, PINSTECH (PAEC), Pakistan
Dr. Salar Ali	Head of Environmental Science Department	University of Baltistan, Skardu
Dr. Shafqat Ali	Assistant Professor	GIK Institute, Topi, Swabi, Pakistan

Prof. Dr. Muhammad Ali Ismail	Professor	Department of Computer and Information Systems Engineering, NED University of Engineering and Technology
Dr. Muhammad Jawed Iqbal	Professor	University of Karachi, Karachi, Pakistan
Dr. Rubina Waseem	Assistant Professor	Department of Strategic Studies National Defence University, Islamabad, Pakistan

Technical Review Committee

Sr. No.	Reviewer Name	Designation	Affiliation / Institution
1	Dr. Abdul Faheem Khan	Associate Professor	Institute of Space Technology, Pakistan
2	Dr. Abdul Kabir	Assistant Professor	Institute of Space Technology, Pakistan
3	Dr. Abdul Waheed	Head of Department and Principal Investigator	GNSS & Space Education Research Lab, Institute of Space Technology, Pakistan
4	Dr. Abrar-Ul-Haq Baluch	Associate Professor	Institute of Space Technology, Pakistan
5	Dr. Adnan Maqsood	Tenured Associate Professor	National University of Sciences and Technology, Pakistan
6	Dr. Adnan Shahid	Head of Department and Principal Investigator	Agricultural Remote Sensing Lab, University of Agriculture Faisalabad, Pakistan
7	Dr. Ali Saroosh	Associate Professor	Air University, Islamabad, Pakistan
8	Dr. Amir Gilani	Associate Professor	Institute of Space Technology, Pakistan
9	Dr. Anjum Tauqir	Professor	Institute of Space Technology, Pakistan
10	Dr. Asad Ali	Associate Professor	Institute of Space Technology, Pakistan
11	Dr. Bakhtiar K. Kasi	Dean and Principal Investigator	Spatial Decision Support System Lab, Balochistan University of Information Technology, Engineering and Management Sciences, Baluchistan, Pakistan
12	Dr. Ch. Bilal Ahmad	Assistant Professor	Institute of Space Technology, Pakistan
13	Dr. Danish Ali Sunny	Assistant Professor	Institute of Space Technology, Pakistan
14	Dr. Farrukh Aziz Bhatti	Assistant Professor	Institute of Space Technology, Pakistan
15	Dr. Fazeel Mahmood Khan	Associate Professor	Institute of Space Technology, Pakistan
16	Dr. Hayat Muhammad Khan	Assistant Professor	Institute of Space Technology, Pakistan

17	Dr. Ihtzaz Qamar	Professor	Institute of Space Technology, Pakistan
18	Dr. Imran Ali Khan	Assistant Professor	Institute of Space Technology, Pakistan
19	Dr. Iqbal Rasool Memon	Professor	Institute of Space Technology, Pakistan
20	Dr. Irfan Majid	Assistant Professor	Institute of Space Technology, Pakistan
21	Dr. Jamshed Riaz	Professor (Adjunct Faculty)	Institute of Space Technology, Pakistan
22	Dr. Khalid Mehmood	Assistant Professor / Co-Principal Investigator	Remote Sensing GIS & Climate Research Lab, University of Punjab, Lahore, Pakistan
23	Dr. Khurram Khurshid	Head of Department and Co-Principal Investigator	Small Satellite Technology & Research Lab, Institute of Space Technology, Pakistan
24	Dr. Komal Nain Sukhia	Assistant Professor	Institute of Space Technology, Pakistan
25	Dr. Madiha Tahir	Assistant Professor	Institute of Space Technology, Pakistan
26	Dr. Maryiam Javed	Associate Professor	Institute of Space Technology, Pakistan
27	Dr. Moazam Maqsood	Assistant Professor	Institute of Space Technology, Pakistan
28	Dr. Muhammad Abdul Basit	Assistant Professor	Institute of Space Technology, Pakistan
29	Dr. Muhammad Farooq Haydar	Assistant Professor	Institute of Space Technology, Pakistan
30	Dr. Muhammad Naeem	Professor	Institute of Space Technology, Pakistan
31	Dr. Muhammad Nawaz	Associate Professor	Institute of Space Technology, Pakistan
32	Dr. Muhammad Shafique	Associate Professor / Principal Investigator	GIS & Space Applications in Geosciences Lab, University of Peshawar, Pakistan
33	Dr. Muhammad Shakir	Assistant Professor	Institute of Space Technology, Pakistan
34	Dr. Muhammad Umer	Assistant Professor	Institute of Space Technology, Pakistan
35	Dr. Muhammad Usman	Assistant Professor	Institute of Space Technology, Pakistan

36	Dr. Muhsan Ehsan	Senior Assistant Professor & Program Coordinator	Bahria University, Pakistan
37	Dr. Munawar Shah	Assistant Professor	Institute of Space Technology, Pakistan
38	Dr. Nadia Imtiaz	Principal Scientist	Pakistan Institute of Nuclear Science & Technology, Pakistan
39	Dr. Najam Abbas Naqvi	Head of Department / Chairman	National Center of GIS & Space Applications, Institute of Space Technology, Pakistan
40	Dr. Naseem Ahmad	Assistant Professor	Institute of Space Technology, Pakistan
41	Dr. Nazia Khatoon	Assistant Professor / Head of Department	Prime Institute of Health Sciences, Islamabad, Pakistan
42	Dr. Nosherwan Shoaib	Associate Professor	National University of Sciences and Technology, Pakistan
43	Dr. Qamar ul Islam	Professor	Institute of Space Technology, Pakistan
44	Dr. Rabia Zafar	Director ORIC & Co-Principal Investigator	Spatial Decision Support System Lab, Sardar Bahadur Khan Women's University, Quetta, Pakistan
45	Dr. Raees Fida Swati	Assistant Professor	Institute of Space Technology, Pakistan
46	Dr. Rahila Naz	Associate Professor	Institute of Space Technology, Pakistan
47	Dr. Rehan Mahmood	Assistant Professor & Principal Investigator	Small Satellite Technology & Research Lab, Institute of Space Technology, Pakistan
48	Dr. Rizwan Mughal	Associate Professor	Institute of Space Technology, Pakistan
49	Dr. Sadia Saeed	Assistant Professor	Institute of Space Technology, Pakistan
50	Dr. Sadia Shakil	Assistant Professor	Institute of Space Technology, Pakistan
51	Dr. Saeeda Sajjad	Assistant Professor / Principal Investigator	Institute of Space Technology, Pakistan
52	Dr. Sajid Ghaffar	Assistant Professor	Institute of Space Technology, Pakistan
53	Dr. Saleem Ullah	Associate Professor	Institute of Space Technology, Pakistan

54	Dr. Salma Zainab Farooq	Assistant Professor	Institute of Space Technology, Pakistan
55	Dr. Salman Ahmad	Head of Department	Institute of Space Technology, Pakistan
56	Dr. Salman Atif	Assistant Professor	National University of Sciences and Technology, Pakistan
57	Dr. Sami Ullah Dawar	Head of Department / Co-Principal Investigator	GIS & Space Applications in Geosciences Lab, Shaheed BB University Sheringal, Dir Upper, Pakistan
58	Dr. Suhail Akhtar	Dean	Institute of Space Technology, Pakistan
59	Dr. Syed Ali Irteza	Assistant Professor	Institute of Space Technology, Pakistan
60	Dr. Syed Hossein Raza Hamdani	Head of Department	Institute of Space Technology, Pakistan
61	Dr. Syed Wilayat Husain	Professor	Institute of Space Technology, Pakistan
62	Dr. Talha Irfan Khan	Assistant Professor	Institute of Space Technology, Pakistan
63	Dr. Umair Ali	Assistant Professor	Institute of Space Technology, Pakistan
64	Dr. Umer Sohail	Assistant Professor	Institute of Space Technology, Pakistan
65	Dr. Waqas Ahmed Qazi	Associate Professor	Institute of Space Technology, Pakistan
66	Dr. Waqas Ashraf	Associate Professor	Institute of Space Technology, Pakistan
67	Dr. Zia ul Haq	Associate Professor / Principal Investigator	Remote Sensing GIS & Climate Research Lab, University of Punjab, Lahore, Pakistan
68	Dr. Arslan	Assistant Professor	Sukkur Institute of Business Administration, Pakistan
69	Mr. Danial Amin	Assistant Manager	National Engineering and Scientific Commission, Pakistan
70	Mr. Izhar Hussain Kazmi	Assistant Professor	Institute of Space Technology, Pakistan
71	Mr. Muhammad Nadeem Khan	Lecturer	Institute of Space Technology, Pakistan
72	Mr. Saad Rifhat Qureshi	Lecturer	Institute of Space Technology, Pakistan

73	Ms. Saima Siddiqui	Assistant Professor	Institute of Space Technology, Pakistan
74	Mr. Shakaib Ahmed	General Manager	National Engineering and Scientific Commission, Pakistan
75	Ms. Aneeqa Abrar	Lecturer	Institute of Space Technology, Pakistan
76	Ms. Maria Mehmood	PhD Scholar	National University of Sciences and Technology, Pakistan
77	Mr. Muhammad Aqib Khan	Research Associate / Team Lead	National Center of GIS & Space Applications, Institute of Space Technology, Pakistan

Conference Management Team

Sr. No.	Name	Conference Role
1.	Dr. Najam Abbas Naqvi	Secretary ICASE 2021
2.	Dr. Abdul Waheed	Manager Technical Review Committee
3.	Mr. Usama Ahmed	Technical Program Manager
4.	Mr. Faaiz Ahmed Jeelani	Public Relations Manager
5.	Mr. Nouman Sheikh	Procurement Manager
6.	Mr. Aqib Khan	Technical Sessions Manager
7.	Ms. Aqsa Zouq	Paper Review & Research Content Manager
8.	Mr. Faran Ali	Operations Manager
9.	Ms. Mahnoor Ajmal	Workshops Manager
10.	Ms. Faiza Badar	Graphics Manager
11.	Mr. Muhammad Afnan	Web Manager
12.	Mr. Sohaib Ahmed	Protocol Manager
13.	Mr. Oscar Lionel	Hospitality Manager
14.	Ms. Ayesha Malik	Registrations Manager
15.	Mr. Amir Faizan Malik	Content Writing Manager
16.	Mr. Danial Raza Kazmi	Forums Manager

List of Papers Published in IEEE Xplore

International Standard Book Number

Xplore Compliant: 978-1-6654-8319-3
Print: 978-1-6654-8318-6

Sr. No.	Author Name & Affiliation	Research Title
1	Dr. Sami Ullah *Shaheed Benazir Bhutto University, Pakistan*	Time Series Analysis of Bindi Dheraja Riverine Forest of Sukkar, Sindh, Pakistan using Remote Sensing
2	Khadeejah Motiwala *Institute of Space Technology, Pakistan*	Gamma-ray Burst High-latitude Emission: Simulating the Propagation Effect
3	Yusha Anis *Pakistan Space & Upper Atmosphere Research Commission, Pakistan*	Developing Heat Index for Heat Wave Hazard Mapping: A Case Study of Sindh Province, Pakistan
4	Ali Hanif *National University of Sciences and Technology*	Deep Learning Based Radar Target Classification Using Micro-Doppler Features
5	Syed Roshaan Ali Shah *Pakistan Space & Upper Atmosphere Research Commission, Pakistan*	Deep Learning on High Spatial and Temporal Cadence Satellite Imagery for Field Boundary Delineation
6	Muhammad Asim Mustafa *Institute of Space Technology, Pakistan*	Using Optical Remote Sensing and Radar Altimeter Data for Lake Volume Estimation of Manchar Lake, Pakistan
7	Muhammad Ihtisham Babar *Pakistan Aeronautical Complex, Pakistan*	Robust Non-Linear Dynamic Inversion Control System To Improve Stability Of Large Aircraft In Crosswind
8	Muhammad Ihtisham Babar *Pakistan Aeronautical Complex, Pakistan*	PanAir Study of Variation in Canard Location and Dihedral on Lift Characteristics of a Close-Coupled Wing-Canard Configuration
9	Afaq Ahmed	

	Bahria University Islamabad, Pakistan	Blockchain Based RFID Prototype For Medicine Traceability along the Healthcare Supply Chain
10	Asim Mehmood *Institute of Space Technology, Pakistan*	Main Landing Gear Conceptual Design and Analysis for M.A.L.E U.C.A.V
11	Dr. Awais Munawar Qureshi *National University of Sciences and Technology, Pakistan*	Design and Development of a Vivaldi Antenna Array for Airborne X-Band Applications
12	Hadiqa Khan *Pakistan Space & Upper Atmosphere Research Commission, Pakistan*	Probabilistic Assessment of Storm Surge Hazard along Coastal Regions of Sindh Province, Pakistan
13	Hina Magsi *Sukkur Institute of Business Administration University, Pakistan*	Investigation of Ionospheric Scintillation using BeiDou during Geomagnetic and Non-geomagnetic Storm Conditions Over Pakistan
14	Obeid Muhammad Usmani *Air University, Pakistan*	Mathematical Modelling and Analysis of Submarine Propeller Shaft
15	Zarrar Haider *National University of Sciences and Technology, Pakistan*	Control System Mathematical Model Design of Ornithopter Flapping Wing Unmanned Air Vehicle for Agile Performance
16	Muzamil Ali *Pakistan Institute of Engineering and Applied Sciences, Pakistan*	Design and Development of a High Precision Thrust Measurement System
17	Danial Ahmed Mir *Institute of Space Technology, Pakistan*	Modern and Classical Pitch Control for Yak54
18	Nadia Jabeen *Institute of Space Technology, Pakistan*	Detection of Thermal Fronts in the Arabian sea through SAR (Synthetic Aperture Radar) imagery
19	Muhammad Shahzad Anjum *Xiamen University, Malaysia*	The Spectral Parameters of Gamma-Ray Blazars
20	Zohaib Altaf	

	Air University, Pakistan	Aerodynamic Shape Optimization of Doubly Offset Serpentine Diffuser using Response Surface Methodology
21	Sadia Azhar *Air University, Pakistan*	Modeling and Analysis of a Vibratory Bowl Feeder
22	Sadia Maryam *National University of Sciences and Technology, Islamabad, Pakistan*	Simulations of Thin Gray Fluid Over a Moving Flat Plate
23	Fahad Sagheer *University of Engineering and Technology, Peshawar, Pakistan*	Investigations of mechanical properties of Sn-3.5Ag-0.5La lead-free solder alloy for green electronics
24	Muzaffar Habib *National University of Sciences and Technology, Pakistan*	Autonomous control of a Quadcopter using Machine Learning algorithm
25	Obaid-ur-Rehman *Pakistan Space & Upper Atmosphere Research Commission, Pakistan*	UAV Assessment of Crop Evapo-transpiration Dynamics in Winter Wheat and Barley under Varying Pressures of Fungal Diseases
26	Syed Saddam ul Hassan *Air University, Pakistan*	Generalised Modelling of Sound Signatures for Characterization of Multi-copter Unmanned Air Vehicles based on Aero-acoustics Measurements and CFD Analysis
27	Jabir Shabbir Malik *Beijing Institute of Technology, China*	Analysis and Estimation of Zenith Wet Delay and Zenith Tropospheric Total Delay at Earth's different Geographical Areas
28	Dr. Muhammad Shahid Iqbal *Institute of Space Technology, Pakistan*	Climate Change an Emerging Risk: A Case Study of Sutlej River Basin, Pakistan
29	Sheher Bano *Air University, Pakistan*	Design and implementation of dual-axis solar tracking system for maximizing the efficiency of solar cells
30	Muhammad Taimur Khan *Institute of Space Technology, Pakistan*	Storm time ionospheric variations from GNSS TEC and Swarm satellites
31	Amna Hafeez	

	Institute of Space Technology, Pakistan	Machine learning based thermal anomaly detection associated with three earthquakes in Pakistan using MODIS LST
32	Muhammad Aitessam Ahmed *Institute of Space Technology, Pakistan*	Design and Development of Audio Processing and Speech Recognition Algorithm
33	Hoor Bano *Institute of Space Technology, Pakistan*	Attitude Estimation & Control of a CubeSat Using Linear Quadratic Gaussian Approach
34	Syed Riaz un Nabi Jafri *NED University of Engineering and Technology, Pakistan*	Campus Terrain Surveying and Mapping using Low Range 2D Laser Scanners
35	Khizar Ahmad Baqai *Superior University, Pakistan*	Review on "ADVANCE SEAPLANE CONCEPTUAL DESIGN ADAPTING TRIMARAN BOAT HULL CONCEPT
36	Muhammad Asfandyar Arshad *Small Satellite Technology Research Lab, National Center of GIS & Space Applications, Pakistan*	Dynamic Analysis of 3U deployer (iPOD) Structure
37	Maria Mehmood *National University of Sciences and Technology, Pakistan*	Performance Analysis of global ionosphere/TEC models over Islamabad
38	Syeda Saleha Fatim Ali *Lahore University of Management Sciences, Pakistan*	Geospatial Application of Groundwater Quality Index for Lahore Metropolitan, Pakistan: A Retrospective Approach

List of Posters

Sr. No.	Author Name & Affiliation	Research Title
1	Jahanzeb Tariq Khan *National University of Sciences and Technology, Pakistan*	Impact of Sampling Delays and Communication Breakdown on the Stability of Spacecraft Formation
2	Asim Khan *Institute of Space Technology, Pakistan*	GPS TEC anomalies associated with Mw>7 earthquakes in Japan
3	Sana Asif *Institute of Space Technology, Pakistan*	Design of low cost AIS receiver for ICUBE-N
4	Dr. Azhar Imran Mudassir *Air University, Islamabad, Pakistan*	Rise of Educational Software and Impact of COVID-19 Outbreak in Pakistan
5	Masood Bari *University Of Karachi, Pakistan*	Find The Shortest Route With The Help Of Network Analysis
6	Muhammad Abdul Moiz *Institute of Space Technology, Pakistan*	Computational Study of Fe-Doped ZnO as a Photocatalyst to Reduce the Environmental Pollution from Textile Industry
7	Haniya Usmani *Generation's School, Pakistan*	The Perks Of Space Exploration
8	Quratulain Danish *CECOS University of IT & Emerging Sciences, Pakistan*	Network analysis of DEGs with putative roles in neuronal development under microgravity conditions

Research Papers

Application of Lotus Root Bionic Structure for Increment in Impact Load Bearing Capability Of a Satellite's Return Capsule

Obaid Ur Rehman
School of Astronautics,Beihang University
Beijing, China
libra_obaid@hotmail.com

Shahzad Hameed
School of Astronautics, Beihang University
Beijing, China
shahzadhameed817@outlook.com

Zuhaib Hassan
School of Astronautics,Beihang University
Beijing, China
zuhaibhassanbinkhalid@gmail.com

***Abstract*— Nature has been astonishingly inspired man to look around and learn in various fields since ages. Lotus root design, being one of the famous inspiring techniques in recent era has been studied and applied to the structure of a Satellite's Reentry capsule. The paper presents a study related to improvement in the impact stress bearing capability in structure that strikes and lands on earth with a relatively high velocity despite the use of parachute. For achieving better structural designs, bionics have been playing a significant role in almost every field. This paper presents a stress reduction of 10.18 % by the application of using a lotus root concept in the Return Capsule. Moreover the distribution of stresses in the cross-sectional area of Reentry vehicle was analyzed and presented**

Keywords--Bionic structure, Re-entry capsule, FEM Analysis

I. INTRODUCTION

Exploration of space has helped man to widen its horizon. Human exploration has now surpassed the earth's close space and progressively motivated researchers to look forward into the Deep Space. Exploration methods have slowly evolved from initial remote sensing explorations to landing expeditions. One of the major purposes is to approach the extra-terrestrial revolving bodies, collect sample and return them back for further deep advance researches. NASA and USSR's space programs have been working on their space explorations since back in 1950's and 1960's however many other countries have joined upon in 90's and second millennium like the Chinese CNSA and Japanese JAXA.

Light Reentry Vehicles have now become an indispensable part of deep space and celestial world exploration due to their imperative capabilities and characteristics. As a general process it can be summarized that a satellite is deployed in space to perform a landing on another planet or a designated comet and after the successful collection of sample it returns back to earth which itself is a complex, but vital procedure which can cause catastrophic failures if not planned and executed appropriately. An extensive in depth study and a broad range of knowledge of reentry technology deems necessary for carrying sample from the interplanetary space [1]. After the releasing of Space capsule till the time it lands back to earth, is just a few hours job generally termed as EDL (Entry Descent and Landing) procedure [2]. Figure 1 briefly explains the procedure of EDL procedure of Stardust Capsule. Despite bearing the high Reentry heat, during the EDL process the structure not only has to bear the ground or water impact load but also the high g loads. Reentry speed typically is higher than the First cosmic velocity of earth which is also termed as orbital velocity. Space return capsules generally are blunt-bodies without wings that re-enters the Earth's atmosphere. The primary difference between a Satellite and Reentry Capsules is the capability to survive reentry and return a payload to the Earth's surface from space. Return vehicles can broadly be classified under two different subheads that are manned and unmanned capsules. If viewed in a general perspective they both have several similarities and commonalities however they also differ in many sub-systems and technicalities. A crewed space capsule necessarily has to attain the ability to sustain life in the vacuum, often with a harsh and extremely demanding thermal and radiation environment. Many subsystems are required to accomplish this task including reaction control system, LSE (life saving and support equipment), weightlessness restraint seats for astronauts, Docking Mechanisms, Communication antennas, Launch and abort systems Parachute and the list goes on. However the unmanned capsule comparatively has a very less complex system as the life saving and much other equipment can be easily omitted from the unmanned one. Current examples of crewed capsules include Soyuz, Shenzhou, Orion, CST-100, and Dragon 2. The unmanned capsules are Hayabusa Muses-C, Stardust, Genesis and many others.

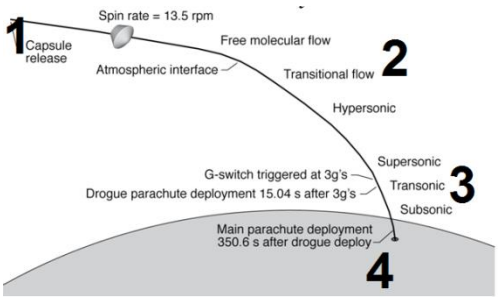


Fig. 1. Nominal Stardust capsule entry sequence

EDL process can be distributed into 4 major steps as

1. Separation and Spinning of capsule
2. Atmospheric Reentry
3. Descend
4. Landing

Un-manned Space capsules have typically been about 1 meters or lesser in diameter and the manned can be up to 5

meter or more. The unmanned Reentry capsule design has to be structurally strong as well as volumetrically efficient, so it is typically feasible to create small capsules having performance which is comparable to lifting body in all but lift-to-drag ratio for less cost. Space capsules are built in manner so they are well suited to reentries possessing high energy.

The entry velocities of space capsules have considerably high values. To reduce this high velocity, the schematic shape of capsules are designed such to generate drag which in turn slows the capsule. Table 1 shows the comparison of three famous return capsules Hayabusa, Genesis and Stardust [3].

TABLE I. DATA COMPARISION OF STARDUST,GENESIS AND HAYABUSA REENTRY CAPSULES

Description	Stardust	Genesis	Hayabusa
Reentry initial Velocity (km/s)	12.5	10.7	12.04
Reentry capsule mass (kg)	46	200	18
Reentry angle (degree)	-8.2	-10	-12.35
Spin velocity (rpm)	15	15	2
Parachute opening Mach No	1.4	1.8	0.8
Diameter big bottom (m)	0.811	1.52	0.4
Radius of curvature of spherical segment with large base (m)	0.22	0.44	0.2
Peak Reentry Heat flow (MW/m2)	11.9 to 12.6	7.5	11
Front end thermal protection material type	PICA	Outer layer C/C and inner is C/fiber	Carbon-Phenolic material
Thickness of Thermal Protective Layer (mm)	58.4	60	30
Type of decelerating parachute	Parachute with umbrella	Tapered umbrella	Nothing
Main parachute Umbrella type	Tapered umbrella	Parachute	Cross umbrella

Despite using the blunt shape and making use of parachutes the velocity of capsules remain still on the higher side at about 8m/s at the touch down [3]. The structure bears a shear impact load when it collides with the ground or splashes in water. To cater for this load, this paper presents a new innovative scheme by using the nature inspired structure of a lotus root.

Since life is estimated to have appeared on earth, nature has gone through extreme evolution over a huge span of 3.8 Gyr [4]. Nature has forced evolution of objects with high performance using commonly found materials functioning in both the macro and Nano-scale domains. Developing better understanding of the functions provided by matter and processes evolved in nature can help mankind to imitate and produce optimized structures, devices and processes. 'Bio-mimetic' is referred to a biologically inspired design derived from nature. During research, the author could not find any study in which the lotus roots bio-metric has been used in the field of return capsule's structure. Yiyuan Zu [5] has discussed Applications and Engineering Analysis of Lotus Roots and their advantages. The study verified that presence of oval holes in lotus roots causes the huge amount of compressive stresses available in cross sectional area occurred at the ends of major axis of the actual holes with in the lotus root. This was a very important conclusion because once the oval holes were re-simulated as circular ones the location of maximum compressive stress changed to the location where short axis of oval holes was present.

Architectural bionics improves the appearance of modern structures. It works on the basis of pristine specimens of flora and fauna, which are used to create innovative patterns. A few major trends in the structural evolution due to field of bionics are: bio based materials, biomechanics, semi-bionic architectures, bionic urbanism, green-architecture, bionic architectural ecology, architectural transplantism, and various others. They permeate and enhance one another [6].

II. METHODOLOGY

A. *Generic return capsule structure (Case-1)*

The main structure of a capsule contains a sample container, parachute bay, electronic bay and a heat ablative shield on the outer body. The aft end of a capsule enters first, interacting and impacting the atmosphere thus withstands the g-forces induced. The rounded shape typically used for aft end also known as the blunt body of a capsule forms a shock wave that keeps most of the heat away from the body, though a thermal protective system is still necessary thus ablative shields are used for it. Space capsule must reenter at a precise angle of attack to prevent a skip off the surface of the atmosphere of destructively high accelerations. While Descend phase, as shown in step 3 of Figure 1, the ablative shield separates from the structure after its desired results within Reentry phase (step 2 of figure 1), thus the remaining structure impacts on the ground. Remaining structure contains the parachute attached to a sample container having a structural layer that strikes the ground.

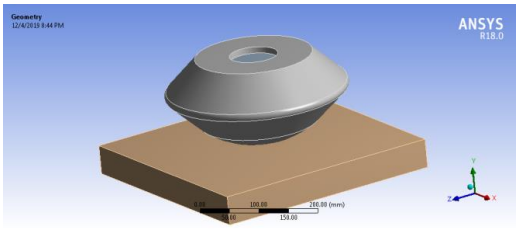


Fig. 2. Re-entry capsule model

Taking leads from the three aforementioned Return Capsules namely Stardust, Genesis and Hayabusa MUSES-C, a generic structure of a capsule was modeled in ANSYS [7]. The model was of the dimension 200mm by 200 mm and weighs 6.382 kgs. Figure 2 shows a model in ANSYS software which wherein an entry capsule is visible before the impact onto the ground. The surface beneath the capsule has been modeled as sand for realistic approach.

Since by the time the capsule reaches the earth's surface the ablative material has already been utilized and detached from the capsule, hence the material used for simulation was considered Aluminum AL 2024-T4 and the ground was modeled as SAND. The material selected for the

capsule i.e. AL 2024-T4 has density of 2785 kg/m^3, its shear modulus is 2.86x10^{10} Pa and the Poisson ratio is 0.33.

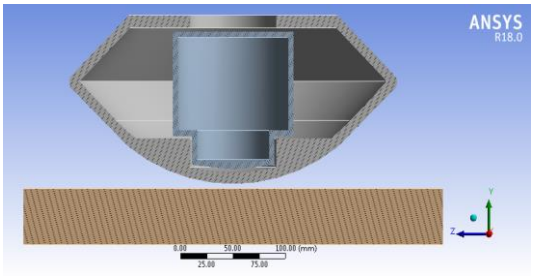


Fig. 3. Reentry Model Y-Z plane cut section (Case-1)

Figure 3 depicts an inside view of the reentry model by cutting a section in Y-Z plane. This section shows an internal closed chamber which contains the extra-terrestrial materials hence the basic aim of our research is to make sure that this inside chamber remains safe even after the impact.

B. *Structure of a lotus root*

Lightening holes have been purposefully used in aerospace industry since ages to lighten the structure yet maintain its structural integrity. Lotus root can be seen to have the same principle applied in it. Understanding the internal oval holes containing structure of a lotus root helps us to design a better structure. Figure 4(a) demonstrates a fresh lotus root sliced carefully to visualize the holes.

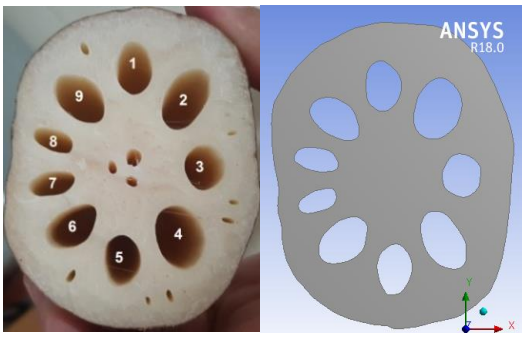


Fig. 4. (a) Lotus root internal structure (b) Lotus root points translated in Ansys software

Structure of lotus root is quite complex as evidently visible in the figure above, the sliced lotus root had 9 larger oval holes that were translated in ANSYS software as shown in Figure 4(b). To guarantee an acceptable degree of consistency between the model and actual structure and effectively improve the efficiency of FEM analysis, the model of lotus root was simplified.

The smaller holes were deliberately disregarded as the manufacturing process of smaller ones would be difficult. These holes were then translated on the base of space capsule already modeled in Section 2.1. The lotus root structure has already been studied in detail by Yiyuan Zhu [5] and its 2D structural analysis also proved that shape of holes in the lotus root causes significant changes in the stress states thus inspiring creation of new structures and materials.

C. *Lotus root bionic structure application in Return Capsule structure (Case-2)*

As a new scheme the lotus root sketch was duplicated by the extraction of points and the scaled down into ANSYS on the model of Reentry capsule as shown below in Figure 5.

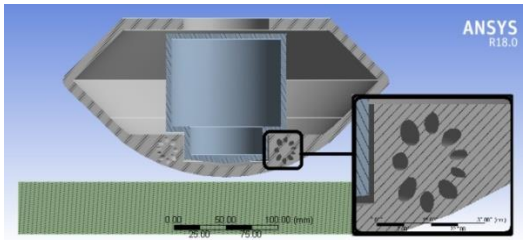


Fig. 5. Re-entry capsule with Lotus root base(Case-2)

The reduction of this mass in a bionic pattern causes the weight reduction in capsule. The weight is reduced by 2.522% and the final capsule weighs 6.221 kgs.

D. *Von Mises Stress*

Conservation of momentum and energy is an inevitable part of the physics of impact. The force which tends to decelerate a mass of a moving object when it strikes another structure, the force satisfies conservation of momentum. The impacting body's kinetic energy will be partially converted to strain energy inside the target and will partly be dissipated through friction and local plastic deformation however the strain energy is radiated away as stress waves. To verify that the model sustains the impact load of structure and ground the Von-Mises stress criterion will be used. This criterion is also termed as maximum distortion energy criterion is associated with the change in shape of the material and is normally applied to ductile materials like metals.

$$\sigma_v^2 = \sqrt{\frac{(\sigma_{11}-\sigma_{22})^2-(\sigma_{22}-\sigma_{33})^2-(\sigma_{33}-\sigma_{11})^2+6(\sigma_{12}^2+\sigma_{23}^2+\sigma_{31}^2)}{2}} \quad (1)$$

Where σ_v is the Von-Mises stress as $\sigma_{11}, \sigma_{22}, \sigma_{33}, \sigma_{12}, \sigma_{23}$ and σ_{31} are the six components of stress tensor. Yielding occurs when the equivalent stress reaches the yield strength of the material.

III. Results and Discussions

A. *Impact Analysis setting*

A short time duration impulse event was generated. The analysis was carried for 0.01 second where in the capsule hit the ground. Finite element model cut in plane to view the cross-sectional area of the capsule and the meshes are shown in Figure 6. An automatic generated mesh was used by means of ANSYS Workbench meshing tool. Areas where high precision was a requirement, the meshing tool automatically adjusted the mesh density so that a high quality based mesh is guaranteed [8]. The structure of Case 1 and Case 2 had different numbers of mesh and nodes due to their different requirements and are shown in figure 6(a) and figure 6(b) respectively. The minimum size of auto generated mesh is relatively smaller vis a vis the overall size of the capsule thus the requirement of calculation accuracy is met. ANSYS Explicit is used to solve the impact of Reentry capsule.

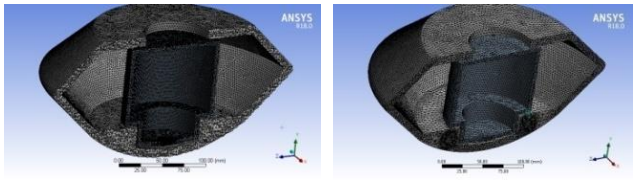
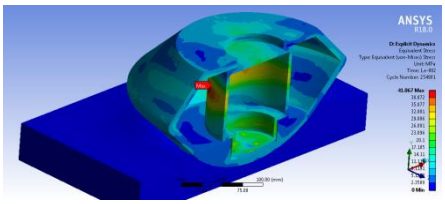


Fig. 6. (a)Mesh Case-1 (b) Mesh Case-2

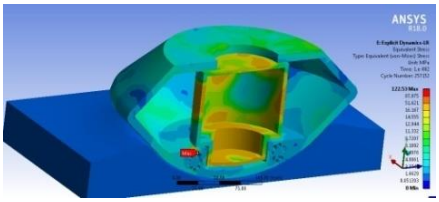
For the boundary conditions the gravity was applied in –Z direction i.e. directing towards the ground. A velocity of 8000mm/s (8m/s) was imparted to the Return capsule. The sand block was fixed from remaining 5 surfaces so as to simulate an area in which the capsule lands.

B. Von-Mises Stress comparison

The solution for equivalent Von-Mises stress as per ANSYS solver was analyzed and the values were compared to verify that model of reentry vehicle will be able to sustain the impact loads. The von-Mises maximum value was found to be 41.067 MPa for case-1 and 122.53 MPa for case 2. Both values were lesser than the yielding stress value of Aluminum AL 2024-T4 which is 255 MPa thus conforming that the structure remains safe in both cases.



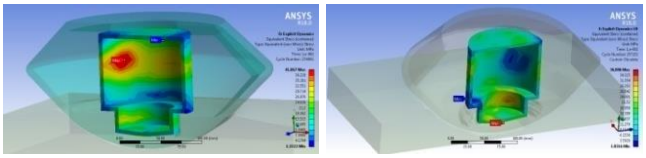
(a) Nephogram:Case-1(generic structure)



(b) Nephogram:Case-2 (lotus root bionic structure)

Fig. 7. (a) & (b) Von-Mises stress Nephograms

The basic aim of this paper is to reduce the stress on the sample container by application of Lotus root bionic structure application. Comparing both capsule containers in case 1 and 2 a maximum value of 41.067 MPa and 36.886 MPa were calculated respectively which makes a significant stress reduction of 10.18%.



Container:Case-1 (b) Container:Case-2

Fig. 8. Stress Nephograms of Re-entry vehicle's container

The basic reason of this stress management can be explained by closely examining the lotus root section in Figure 8 as elaborated in Figure 9. This special region distributes the stress vectors in such a way that the stress values are higher towards the lotus root holes thus reducing the stress concentration in container containing extra-terrestrial material.

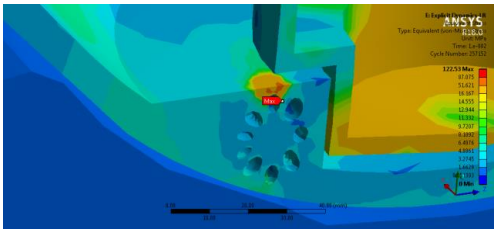


Fig. 9. Lotus root section on base of Return capsule

IV. CONCLUSIONS

By analyzing the FEM results of the model, it can be concluded that the structural design of the capsule meets the essential requirements of strength, no structural damage will occur because the high stress zones are focused on the lotus root edges. Because of the oval holes of lotus root, the largest stress in the cross-sectional area of structure occurred near the lotus root hole as evident in Figure 9. Major conclusions are as follows:

a) In both cases, the maximum stress value remained lesser than the yielding stress value.

b) A 10.18 % stress reduction was observed in Case-2 due to the bionic lotus root structure.

V. REFERENCES

[1] Yoshifumi Inatani, "Reentry Capsule for Sample Return from Asteroids in the Planetary Exploration Missions" J. Phys.: Conf. Ser. 1005 012049(2018)

[2] Prasun N. Desai, Dan T. Lyons, "Entry, Descent, and Landing Operations Analysis for the Stardust Re-Entry Capsule", NASA Langley Research Center, Hampton, VA, 23681-2199, Jet Propulsion Laboratory, Pasadena, CA 91109-8099

[3] GENG Yunfei, GAOJie, LUYadong, LiQi "Demostration of Light Reentry Vehicle Development" Journal Spacecraft Engineering, Vol 23 No 6, Page 99 (2014)

[4] B. Bhushan, "Bio-mimetics: Lessons from nature an overview," Philosophical Transactions of the Royal Society A: Mathematical, Physical and Engineering Sciences, vol. 367, no. 1893, pp. 1445–1486, (2009).

[5] Yiyun Zhu, Chang Jiang Wang and Diane Mynors, "Applications and Engineering Analysis of Lotus Roots under External Water Pressure", Hindawi Publishing Corporation, Applied Bionics and Biomechanics, Article ID 2386982 (2016)

[6] Irina Mayatskaya, Victor Eremin, "Bionics and the choice of rational structural form" Volume 110, 2019, International Science Conference SPbWOSCE-2018, E3S Web of Conferences, Article No 01042 (2019)

[7] ANSYS Software, ANSYS Academic Research Release 18.0. ANSYS Inc., USA.

[8] Mou WJ, Yang JZ, Chen JY, et al. Finite element analysis for power car skeleton based on ANSYS Workbench[J]. Science Technology and Engineering, 22:5592-5594 (2010)

Recent Advancements in Thermal Barrier Coatings (TBC) for High-Temperature Gas Turbines

Zahid Mehmood
Department of Aerospace Engineering
CAE, NUST
H-9 Islamabad, Pakistan
Zahid_mehmood@cae.nust.edu.pk

Prof. Dr. Ali Sarosh
Department of Mechanical and Aerospace engineering
Air University
E-9 Islamabad, Pakistan
ali.sarosh@mail.au.edu.pk

Osama Ali Ahmed Awan
Department of Mechanical and Aerospace engineering
Air University
E-9 Islamabad, Pakistan
osamaaliahmadwan@outlook.com

***Abstract*— Gas turbines can produce a tremendous amount of energy and have wide industrial applications due to their small size and lower weight. Their efficiency depends on two factors i.e., turbine inlet temperature and thermodynamic efficiencies. By increasing the turbine inlet temperature (TIT), turbine blades face high-temperature hot corrosion (850 ℃ to 950 ℃) that limits the life of the turbine blade. During hot corrosion, molten sodium salts and vanadium oxide condense over the surface of turbine blades, consume protective oxide layers, and diffuse into the microstructure of superalloy. As a result, fatigue, and creep phenomena get accelerated leading to fracture. A survey of past few years shows that the use of thermal barrier coatings (TBC) has proven to be an effective strategy to avoid premature failure. In this paper, an extended survey has been presented about the improvement of hot corrosion resistance by TBCs by reinforcement with Nanoparticles, rare earth elements, gradient aluminum layers, and metallic bond coatings. The performance parameters of different reinforcements have been evaluated by XRD techniques, SEM spectroscopy, and corrosion kinetics curves.**

Keywords*— *High-temperature hot corrosion, low-temperature hot corrosion, fatigue life, creep rate, thermal barrier coatings, nanostructured coatings, rare earth elements, gradient coatings

I. INTRODUCTION

A gas turbine is used to produce a tremendous amount of energy and has many useful applications due to their smaller size and weight. Its efficiency depends on two factors: i.e., higher turbine inlet temperature and efficiency of compressor and turbine. The increase in inlet temperature is driven by improvement in turbine blade metallurgy, coatings, and cooling techniques. Turbine efficiency and blade life are enhanced by hot corrosion, erosion, thermo-mechanical creep, and fatigue properties of turbine blades. Hot corrosion is accelerated due to molten deposits which harm the blade surface [1]. Mainly, hot corrosion has two types which are discussed in this research work:

A) Type-1: HTHC (high-temperature hot corrosion)

The first type is where the hot corrosion is observed from 850 to 950℃. The chemical reaction starts due to molten metal on the TBCs (Thermal Barrier Coatings) and sweeps down to substrate material [2, 3]. HTHC is due to Na_2SO_4 (sodium sulfate), NaCl (sodium chloride), and V_2O_4 (Vanadium Oxide). The impurities in fuel can lower the melting point of Na_2SO_4, moreover, during combustion NaCl can form Na_2SO_4 by reacting with SO_2 (sulfur dioxide) and oxygen as shown by the following reaction [4]. Presence of Vanadium accelerates the solubility of turbine blade protective oxide in Na_2SO_4 [5]. It starts by breaking the oxide layer, followed by depletion of chromium content of substrate material, substrate oxidation loss of material integrity, which finally leads to blade failure along with material strength.

$$2NaCl\,(l) + SO_2\,(g) + O_2\,(g) \rightarrow Na_2SO_4\,(l) + Cl_2\,(g)$$

B) Type-2: LTHC (low temperature hot corrosion)

In the subsequent type, hot corrosion is studied for the temperature limit from 650 to 800 ℃ [6]. A high partial pressure SO3 (sulfur trioxide) formed as a byproduct of combustion leads to LTHC Reaction.

Research has shown that HTHC effects the life of the turbine blade. This paper presents a survey of the performance of Nano-structured TBCs, rare earth elements, and multilayer TBCs against HTHC. It has been found in recent research that the additions of Nano-structured TBCs, rare earth elements, and multilayer TBCs provide better performance as compared to the conventional coatings. This study has employed XRD, SEM, and corrosion kinetic curves to evaluate several types of coatings.

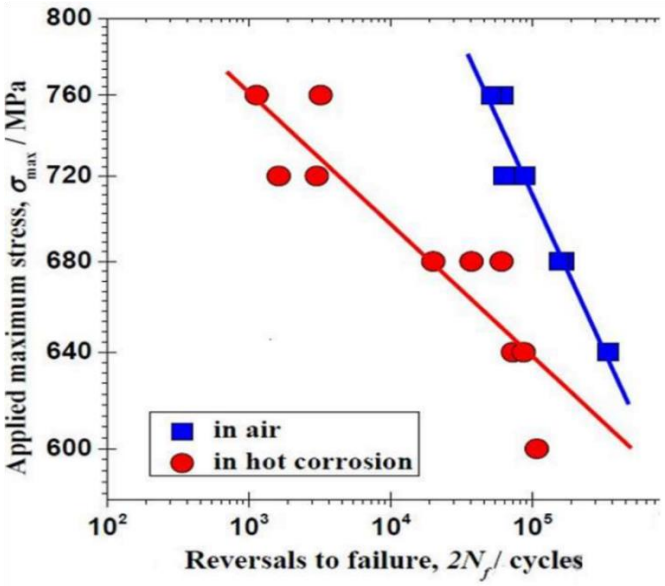


Figure 1 Basquin curve representing the number of cycles to failure for superalloy DZ125 in air and the presence of hot corrosive environment [7].

II. Influence of Hot Corrosion on Turbine Blade Life

With exceptional strength properties at elevated temperature, Ni (Nickel) based super-alloys are usually used as a substrate material for turbine blades. chemical composition of refractory elements effects the mechanical properties of the substrate. Cr (chromium) and Ti (Titanium) are necessary for resistance against hot corrosion [8]. Cr restricts the Na_2SO_4 molten deposits by forming Cr_2O_3 (chromium oxide). Other materials like Nb (Niobium) and Mo (Molybdenum) serves up to 1200 °C and 1300°C, in uncooled systems, respectively. However, hot corrosion challenges the turbine blades and disks as they reduce their fatigue life [9-11]. The fatigue testing of Ni superalloy DZ125 also indicates lower fatigue strength in the presence of a corrosive environment [12]. The Basquin curve presented in Fig. 1 presents a lower fatigue life of DZ125 superalloy in a hot corrosive environment.

Furthermore, hot corrosion experiments done on Ni superalloy 617 has shown that hot corrosion accelerates the creep rate in corrosive environments [13]. During hot corrosion, $M_{23}C_6$ carbides are precipitated at grain boundaries, which depletes Cr and cause inter-granular corrosion. These carbides enhance the fatigue and creep rate of turbine blades due to which, grain boundaries are weakened by the cyclic loadings and lead to fracture. Therefore, to enhance the turbine blade life, resistance against corrosion is essential. Thermal barrier coatings (TBCs) are utilized as resistance against hot corrosion [14].

III. Hot Corrosion Resistant TBCs

TBCs protect the turbine blade against hot corrosion and thermal stresses, thus enhancing the efficiency and the operating temperature of the gas turbine [15]. They protect turbine blades against thermal shock, hot corrosion, and erosion degradation [16-18]. A TBC consists of a low thermal conductivity topcoat, which protects the substrate against hot corrosion, and the metallic bond coat, which provides adhesion between the topcoat and substrate. The common methods for TBCs applications are EB-PVD (electron beam-physical vapor deposition), HVOFC (high-velocity oxygen fuel coating), and APS (atmospheric plasma spraying) [7, 19, 20]. APS is a widely used deposition because of cost-effectiveness and higher efficiency [21, 22].

Yttria-Stabilized Zirconia (YSZ) is the most widely used TBC [23, 24]. However, its performance degrades at the temperature above 1200℃ in the presence of corrosive environment and fuel impurities. These conditions deteriorate TBCs by thermal cycling and spallation by hot corrosion [25-28]. Before the occurrence of hot corrosion reaction, ZrO_2 (Zirconia) is stabilized in the tetragonal phase and stabilized by Y_2O_3 (Yttria) [29, 30]. During hot corrosion, the acidic salts deplete the Y_2O_3 which lead to phase transformation of tetragonal to monoclinic phase for Zirconia. Additional stresses and cracks are added in the coatings due to this phase transformation. Corrosion products induce stresses in TBCs, by reducing their thermal contraction upon cooling [31]. Wide-scale research has been done to improve the effectiveness of TBCs. These research works have focused on Nanostructured TBCs and rare earth metals and compounds.

A) Nanostructured TBCs

Nanostructured YSZ coatings have shown an increase in thermal fatigue, bonding strength, and decreased the thermal conductivity of TBCs in comparison to conventional coatings [32-34]. Hot corrosion experiments of Nanostructured YSZ TBCs have revealed better resistance in the presence of a corrosive environment.

Accelerated corrosion is performed on conventional and nanostructured coating specimens in the presence of 55 wt. % V_2O_5 and 45 wt. % Na_2SO_4. The specimens are heated at 1000°C for 30 hours to capture the hot corrosion effects. The process can be explained by following reactions in the existence of molten salts [35].

$NaVO_3$ formed during the experiments has a low melting point and it easily penetrates the coatings. Where it reacts with Y_2O_3 to transform ZrO_2 from tetragonal to the monoclinic form of YVO_4.

$$ZrO_2.Y_2O_3\ (s) + 2NaVO_3\ (I) \rightarrow m\text{-}ZrO_2\ (l) + 2YVO_4\ (s) + Na_2O\ (I)$$

In addition to the above reaction, V_2O_5 also reacts readily with Y_2O_3 at a temperature above 800ºC to transform tetragonal Zirconia to monoclinic form.

$$ZrO_2.Y_2O_3\ (s) + V_2O_5\ (I) \rightarrow m\text{-}ZrO_2\ (l) + 2YVO_4\ (s)$$

The stresses and cracking developed by hot corrosion are more pronounced in conventional coatings while nanostructured coatings resist transformation as shown in Fig. 2. High surface roughness and porous zones are formed in nanostructured coatings, which prolong reaction with molten salts and resist ZrO_2 transformation. In conventional coatings, cracking starts earlier after 12 hours of disclosure to hot corrosion and delamination occurs after 24 hours. However, nanostructured coatings demonstrated resistance to hot corrosion as the growth of crack is delayed to 24 hours.

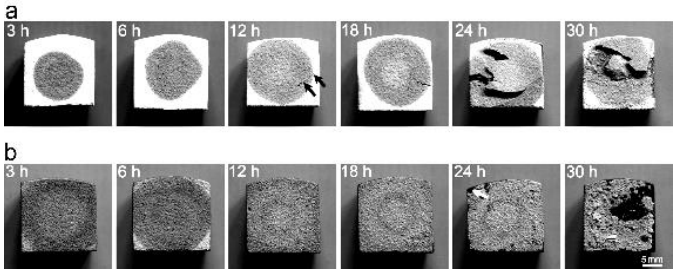


Figure 2 Hot carrion test on Nano-structured and conventional coatings [36].

In recent study, a layer gradient nanostructured $Sc_2O_3_Y_2O_3$ co-stabilized Zr_2O_3 (ScYSZ) was compared with conventional coatings to improve performance of thermal barrier coatings. The thermal cycling life of conventional coatings is less than that of ScYSZ. Also the average insulation temperature of ScYSZ is higher than that of conventional coatings [37].

B) Effect of Rare Earth Elements and Compounds

The addition of rare earth elements or compounds stabilizes YSZ and offers better corrosion resistance than conventional YSZ coatings [38-42]. In experiments, it was found that Scandia and Yttria co-stabilized Zirconia (ScYSZ) offer improved corrosion resistance in comparison with Nanostructured YSZ and Scandia [43, 44]. ScYSZ has different hot corrosion behavior from YSZ coatings [45]. In the matter of YSZ coatings, spallation occurs in topcoat while in ScYSZ coatings spallation occurs in bond coat. ScYSZ delays the phase transformation of zirconia [43]. Also, in ScYSZ, spallation occurs in the bond coat while in YSZ coatings it occurs in the topcoat. Research has shown that Nanostructured Ceria and Yttria co-stabilized Zirconia (CYSZ) exhibits better corrosion resistance than conventional coatings[46]. CeO_2 resists the reaction with the molten salts and obstructs diffusion [47, 48].

The hot corrosion resistance is enhanced for Ceria stabilized zirconia (CSZ) coatings due to the overlay of alumina (Al_2O_3), as it reduces the penetration of molten salts and decreases the depletion of Zirconia stabilizers [49]. Higher porosity and lower γ-phase in nano Al_2O_3 resist chemical reaction, which gives it an advantage over micro Al_2O_3. After the hot corrosion test, thermal stresses and cracking occur in CSZ with the transformation of ZrO_2 and formation of irregular shape products of YVO_4, $CeVO_4$, and CeO_3. The extent of degradation in CSZ/ micro Al_2O_3 is lower than CSZ due to the lesser transformation of zirconia. However, no damage and hot corrosion products are found in layered composite CSZ/nano Al_2O_3 coatings.

It is found in research that corrosion resistance is improved due to less transformation of ZrO_2 in gadolinia (Gd_2O_3), ytterbia (Yb_2O_3) and yttria co-stabilized ZrO_2 (GdYb-YSZ). Yb_2O_3 limits the intensity of GdYb-YSZ to react with molten salts [50]. It acts as a stabilizer for tetragonal ZrO_2 while Y_2O_3 and Gd_2O_3 react with molten salts. After the hot corrosion test, the monoclinic phase content of ZrO_2 in GdYb-YSZ coatings is also less than YSZ coatings. Similarly, $Gd_2Zr_2O_5$ + YSZ and $Gd_2Zr_2O_5$ coatings offer higher corrosion resistance than YSZ coatings, because of less depletion of Y_2O_3. Moreover, development in thermal stresses and cracking in $Gd_2Zr_2O_5$ + YSZ and $Gd_2Zr_2O_5$ coatings takes a longer time in the corrosive environment than YSZ coatings [51].

The hot corrosion test of titania stabilized zirconia (TiSZ) has revealed the superior performance of TiSZ in comparison with YSZ and CSZ [52]. XRD Peaks of coatings obtained after the hot corrosion test indicate no monoclinic phase of ZrO_2 in the matter of TiSZ as shown in Fig. 3.

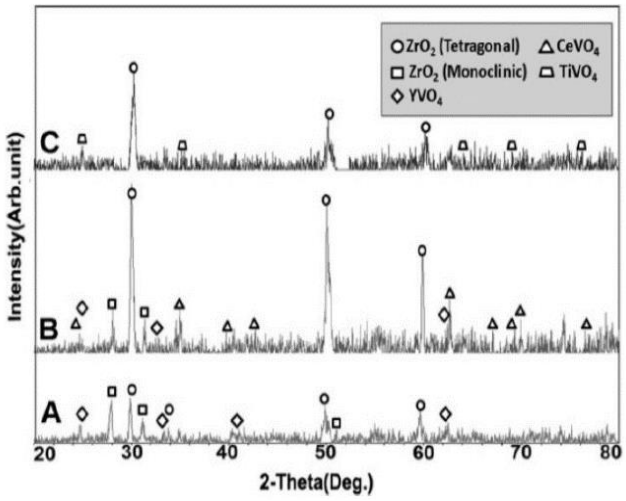


Figure 3 XRD patterns after exposure to hot corrosive environments (a) convention YSZ coatings (b) CSZ coating and (c) TiSZ coatings [52].

Tantalum (Ta) doping on YSZ lowers thermal conductivity and stabilizes YSZ up to 1500 °C due to strong interaction between Y^{3+} and Ta^{5+} ions. The hot corrosion resistance of Y_2 O_3 and tantalum oxide (Ta_2O_5) co-doped zirconia coating (TaYSZ) is found superior to YSZ coatings. The reaction of a molten mixture of Na_2SO_4 and V_2O_5 with TaYSZ coating is weak and reaction products are Na_2TO_3, $TaVO_5$, and Ta_9VO_{25}.

In contrast to YSZ coatings, the TaYSZ coating resist phase transformation and the corrosion products are small. Therefore, thermal cracking and stresses in TaYSZ coatings are not induced due to their higher corrosion resistance. The Scanning Electron Microscope (SEM) images of both coatings, developed following the hot corrosion test, are shown in Fig. 4.

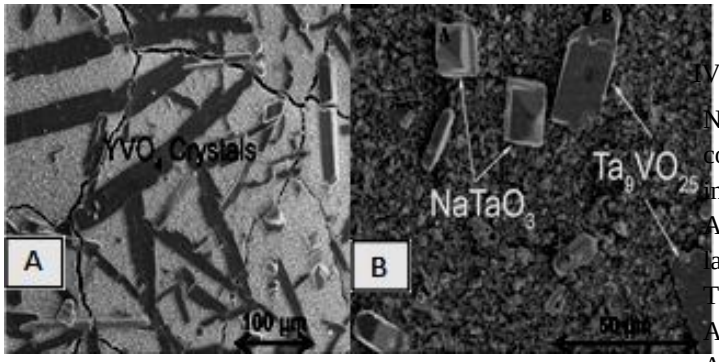


Figure 4 SEM images of (a) conventional YSZ coating and (b) TaYSZ coating developed after hot corrosion tests are presented [53].

C) Hot Corrosion Comparison of Base Metal, Bond Coating, and Multiple Layered TBCs

In one study, the hot corrosion performance of a five-layered coated specimen with LZ as top layer (LZ+YSZ/YSZ/YSZ+BC), duplex YSZ (YSZ/BC), base metal Inconel 738(BM), NiCrAlY bond coat (BC), , and duplex Lanthanum Zirconate (LZ/BC) is compared [54]. The hot corrosion resistance of coated specimens is in the following order.

Five Layered coating> YSZ> LZ> BC> BM

The exposure of BM to a molten mixture of Na_2SO_4 and V_2O_5 forms Na_2VO_3 which acts as a catalyst in the oxidation of metallic ions and forms Al_2O_3, Cr_2O_3, NiO . The spinels $NiAl_2O_4$ and $NiCr_2O_4$ formed lead to mass gain, severe strains, and spallation of oxide layers. The BC offers superior corrosion resistance than the BM due to the development of Al_2O_3 and Cr_2O_3 layers, which prohibits the diffusion of oxidizing agents. The spallation of these oxide layers occurs due to thermal stresses and chemical reaction with molten salts.

Due to hot corrosion in BC, the Al and Ni oxide layers are dissociated because of the fluxing mechanism.

YSZ shows improved hot corrosion resistance than the BC and worse than LZ. However, LZ has low hot corrosion resistance at a higher number of cycles than YSZ, due to propagation of cracks and low fracture toughness. The five-layered coating exhibits better hot corrosion resistance than YSZ and LZ coatings. The top layer reacts with the molten salts and protects the YSZ coatings, thus it has better corrosion resistance than the YSZ and LZ coatings.

The parabolic corrosion rate constant 'K_p' measures the hot corrosion performance of coatings. Lower 'K_p' indicates better performance of coatings against hot corrosion performance. It is given by the following relation

$$K_p=((\Delta W/A)^2)/t$$

Where, 't' is the hot corrosion time. and ΔW/A is the weight gain per unit surface area.

V. Hot Corrosion Resistant Metallic Bond Coatings

NiCoCrAlY and NiCrAlYSi coatings are renowned as hot corrosion and oxidation resistant coatings and are also used in bond coats of Thermal Barrier Coatings (TBC) [55]. Al_2O_3 is formed due to the depletion of bond coatings. Al_2O_3 layer is a protective layer, but it is not continuous [56]. Thus, it causes spallation.

Al_2O_3 reacts with Na_2O to form AlO_2^-, reprecipitating the Al_2O_3 and releasing the O^{2-}. O^{2-} accelerates the formation of Al_2O_3 thus consuming more Al from the coating. In the presence of NaCl, Al_2O_3 is additionally dissolved by the oxychlorination process. To avoid deterioration in mechanical properties, Al content is kept lower than 5 wt. %. The application of nanostructured reinforced coatings, doping in rare earth metals and composite/gradient coating is also investigated.

$$Al_2O_3 + 1/2O_2 + NaCl \rightarrow 2NaAlO_2 + Cl_2$$

A) Nanostructured Reinforced Coatings

The addition of nano Al_2O_3, nano SiO_2, and nano CeO_2 exhibits better corrosion resistance in comparison to normal coatings. The mass change of these nano-particle coatings gauges the corrosion performance of such coatings. Mass change is defined as the difference of mass gained from scale formation to mass loss by spallation of oxide scales. Mathematically it is written as

$$M_c = (m_1-m_0 *A_0/A)/ A_1$$

Here, M_c is the mass change of coating; m_1, mass change of coated sample; A_1, superficial area of the coated part of the sample; m_0, mass change of uncoated sample; *A*, superficial area of the uncoated sample; A_0, superficial area of the uncoated part of the test sample. In the presence of salt (75 *wt* % Na_2SO_4/ 25 *wt* %K_2SO_4) at 1050 °C, the mass change (corrosion kinetics) curves of coatings with and without nanoparticles are exhibited in Fig. 5.

Fig. 6. depicts that nanoparticle coatings have better corrosion resistance with enhanced thermal fatigue. Whereas CeO_2 has the superior hot corrosion resistance. The addition of nanoparticles serves as the nucleus for heterogeneous nucleation and results in microstructure refinement.

Nanoparticles also enhance corrosion resistance and improve thermal fatigue. Coatings without nanoparticles are affected by spallation and deformation of a surface while no

spallation is observed for coatings reinforced by nanoparticles as shown in Fig. 5.

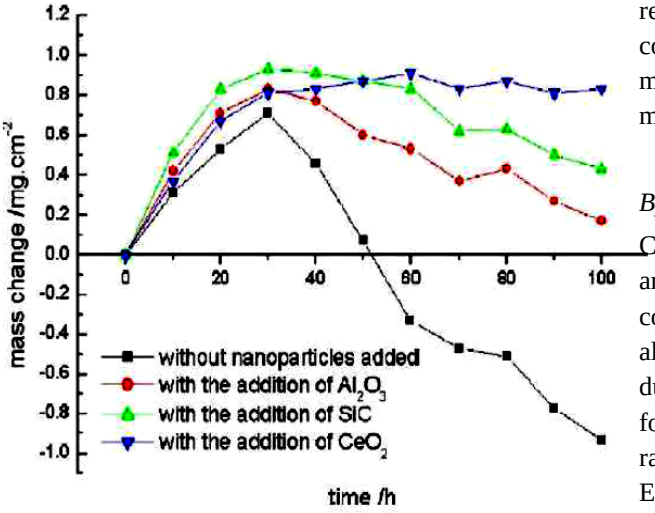


Figure 5 The corrosion kinetics (mass change) curves of NiCoCrAlY coatings [57].

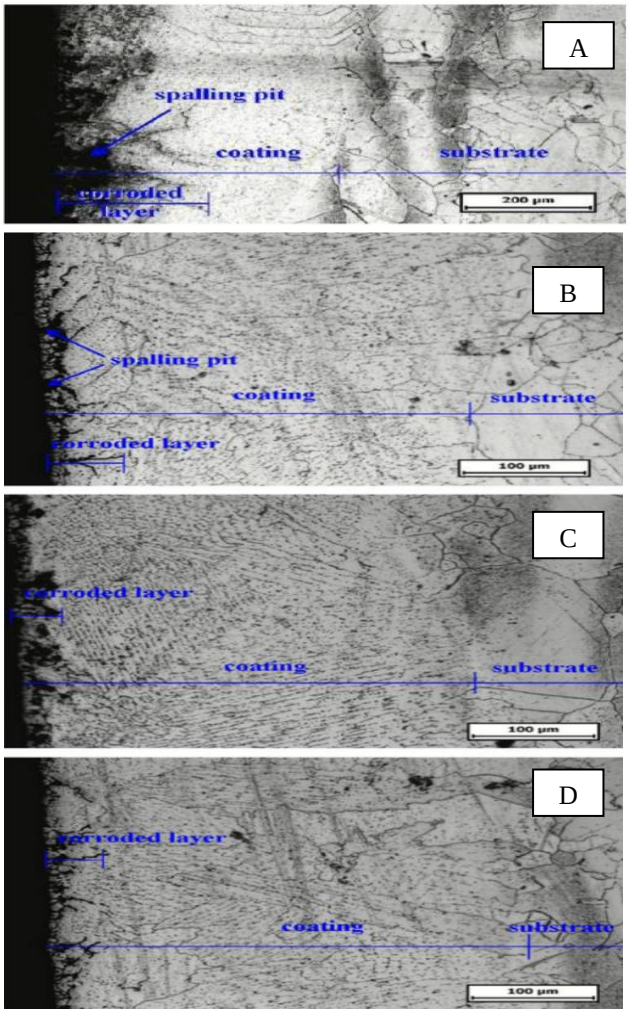


Figure 6 SEM images of (A) NiCoCrAlY coating without nanoparticles, (B) with nano Al2O3, (C) nano SiC and (D) nano CeO2 are displayed [57].

In recent study, APS technique was applied to deposited nano-$Gd_2Zr_2O_7$ (nano-GZ) powder after synthesizing by co-precipitation method on the nickel-based substrate. The hot corrosion resistance of conventional coatings was compared with nano-GZ coatings. It was found that the hot corrosion resistance of conventional coatings is less that of GZ coatings. As nano GZ coatings acts as a barrier to pores and micro-cracks which play a major role in infiltration of molten salts to the TBCs [58].

B) Doping with Rare Earth Elements

Co-Al-Y-Ce coated samples have better corrosion resistance and lesser mass gain as compared to Co-Al and Co-Al-Y coated specimens [59]. Co accelerates to the outer layer, and also a synergetic effect is produced to resist hot corrosion due to the doping of Y and Ce [60]. Co enhances the formation of Al_2O_3 in NiAl coatings and lowers the diffusion rate of sulfur [61].

Experiments have also revealed that Co-Al-Si coatings have better corrosion resistance and lower mass gain than the Co-Al coatings [59, 62]. The reason being is the formation of β-NiAl which has higher Al content and it facilitates the formation of Al_2O_3 [63].

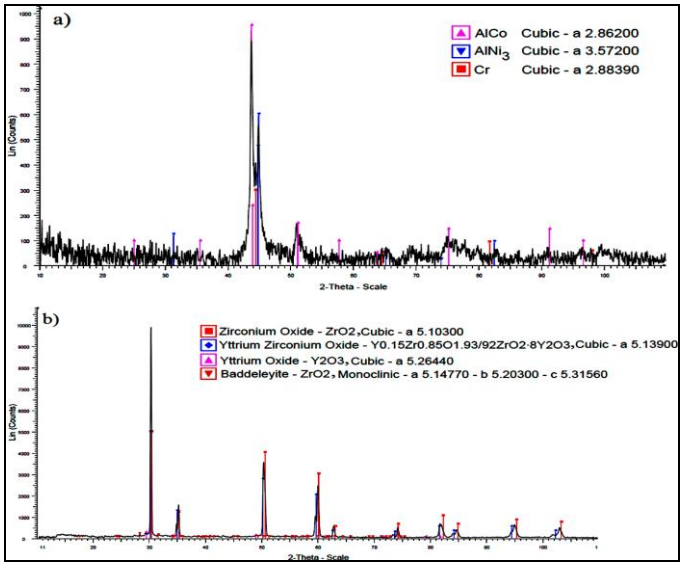


Figure 8 XRD pattern (a) single coating on γ-TiAl (b) double coating on γ-TiAl [67].

$$[Si] + \gamma'[Ni_3Al] \rightarrow \delta[Ni_2Si] + \beta[NiAl]$$

Moreover, SiO_2 is formed as a byproduct and is resistant to molten salts. Si restricts inter diffusion of an element between the substrate and the coating. Also, it improves the oxidation resistance of NiAlHf coatings [64].

Pt modified coatings also exhibit better corrosion resistance and lower mass gain due to the transformation of θ- Al_2O_3 to α- Al_2O_3 at initial stages of hot corrosion and formation of Cr_2O_3 which hinders oxygen, sulfur, and chlorine [65].

C) Composite / Gradient NiCoCrAlYSi Coatings

The composite coatings**,** inner NiCoCrAlYSi layer, and outer AlSiY layer exhibit better corrosion resistance[66]. The gradient NiCoCrAlYSi coatings are

prepared by depositing NiCoCrAlYSi target first for forty microns and then Al target for ten microns. Normal NiCoCrAlYSi coatings have a thickness of forty microns. During hot corrosion, Al is consumed rapidly from the normal coating as it offers less resistance to Al diffusion. In composite and gradient coatings, more β-NiAl phase is formed which is corrosion resistant. It also serves as an Al reservoir in reaction with corrosive salts thus increasing resistance of composite and gradient coatings. Experiments have shown that gradient coatings have lower mass gain and higher corrosion resistance. In a recent study, an alloy with chemical composition of Ti-48Al-2Nb-2Cr known as γ-TiAl is employed as substrate. One sample contain one layer and second contains two layers. The experiment was conducted to investigate the microstructure and isothermal oxidation resistance at 1050℃ [67]. It was found that due to presence of oxide layers of ZrO2 and Y2O3, better high isothermal oxidation resistant TBCs are formed. Fig. 8. shows XRD experimental results of the single and double layered coatings on γ-TiAl substrate [67].

V. Conclusion

Hot corrosion occurs from 650 °C to 950 °C and in the existence of molten sodium salts and vanadium oxide. Resistance against hot corrosion is essential for avoiding premature failures in turbine blades. Nanostructured, rare-earth element co-doped, and multiple layered TBCs have improved hot corrosion resistance. These coatings avoid the phase transformation of zirconia to monoclinic phase from tetragonal phase and the formation of large crystalline corrosion products. However, conventional YSZ fails in resisting these two phenomena. Hot corrosion also degrades metallic bond coatings by spallation of protective alumina layer and depletion of aluminum. The addition of Nano reinforced particles, rare earth elements, and gradient coatings improve the hot corrosion resistance of metallic bond coats. These additions increase aluminum content, stabilize the protective layer, and prohibit penetration of elements between coating and substrate. XRD, SEM, and corrosion kinetic curves are used to evaluate diverse types of coatings.

VI. Future Work

In the view of the above discussion, it is possible that the hot corrosion resistance of turbine blades can be enhanced by the addition of nanoparticles, rare-earth metals, and gradient coatings. However, there is a need to analyze their effects on the properties of coatings, the cost-effectiveness of modifications, and the comparison of coating techniques like EB-PVD, HVOFC, APS, etc.

VII. Recommendations

A standard hot corrosion testing procedure can be derived as the parameters vary between research works. Fatigue and creep testing of modified coatings may also incorporate in hot corrosive environments, as they are the most affected.

VIII. References

[1] L. Zheng, Z. Maicang, and D. Jianxin, "Hot corrosion behavior of powder metallurgy Rene95 nickel-based superalloy in molten NaCl–Na2SO4 salts," *Materials & Design*, vol. 32, no. 4, pp. 1981-1989, 2011.

[2] M. Siba, W. Wanmahmood, M. Z. Nuawi, R. Rasani, and M. Nassir, "Flow-induced vibration in pipes: Challenges and solutions—A review," *Journal of Engineering Science and Technology*, vol. 11, no. 3, pp. 362-382, 2016.

[3] S. Li, X. Yang, and H. Qi, "High-temperature hot-corrosion effects on the creep–fatigue behavior of a directionally solidified nickel-based superalloy: Mechanism and lifetime prediction," *International Journal of Damage Mechanics*, vol. 29, no. 5, pp. 798-809, 2020.

[4] J. Sahu, B. R. Kumar, S. Das, N. Paulose, and S. Mannan, "Isothermal high temperature low cycle fatigue behavior of Nimonic-263: Influence of type I and type II hot corrosion," *Materials Science and Engineering: A*, vol. 622, pp. 131-138, 2015.

[5] F. Pettit, "Hot corrosion of metals and alloys," *Oxidation of Metals*, vol. 76, no. 1-2, pp. 1-21, 2011.

[6] V. Mannava, A. S. Rao, N. Paulose, M. Kamaraj, and R. S. Kottada, "Hot corrosion studies on Ni-base superalloy at 650 C under marine-like environment conditions using three salt mixture (Na2SO4+ NaCl+ NaVO3)," *Corrosion Science*, vol. 105, pp. 109-119, 2016.

[7] R. Steinbrech, V. Postolenko, J. Mönch, J. Malzbender, and L. Singheiser, "Testing method to assess lifetime of EB-PVD thermal barrier coatings on tubular specimens in static and cyclic oxidation tests," *Ceramics International*, vol. 37, no. 1, pp. 363-368, 2011.

[8] J. Chang, D. Wang, T. Liu, G. Zhang, L. Lou, and J. Zhang, "Role of tantalum in the hot corrosion of a Ni-base single crystal superalloy," *Corrosion Science*, vol. 98, pp. 585-591, 2015.

[9] S. Li, X. Yang, H. Qi, J. Song, and D. Shi, "Low-temperature hot corrosion effects on the low-cycle fatigue lifetime and cracking behaviors of a powder metallurgy Ni-based superalloy," *International Journal of Fatigue*, vol. 116, pp. 334-343, 2018.

[10] P. Jena, R. Singh, L. Mahanta, S. Paswan, and J. Sahu, "Low cycle fatigue behaviour of nickel base superalloy IN 740H at 760° C: Influence of fireside corrosion atmosphere," *International Journal of Fatigue*, vol. 116, pp. 623-633, 2018.

[11] S. Kargarnejad and F. Djavanroodi, "Failure assessment of Nimonic 80A gas turbine blade,"

Engineering Failure Analysis, vol. 26, pp. 211-219, 2012.

[12] X. Yang, S. Li, and H. Qi, "Effect of high-temperature hot corrosion on the low cycle fatigue behavior of a directionally solidified nickel-base superalloy," *International journal of fatigue*, vol. 70, pp. 106-113, 2015.

[13] A. Homaeian and M. Alizadeh, "Interaction of hot corrosion and creep in Alloy 617," *Engineering Failure Analysis*, vol. 66, pp. 373-384, 2016.

[14] R. Synnott, Y. Panchenko, and A. Paczoski, "Turbine blade with hot-corrosion-resistant coating," ed: Google Patents, 2020.

[15] R. Ahmadi-Pidani, R. Shoja-Razavi, R. Mozafarinia, and H. Jamali, "Laser surface modification of plasma sprayed CYSZ thermal barrier coatings," *Ceramics International*, vol. 39, no. 3, pp. 2473-2480, 2013.

[16] N. P. Padture, "Advanced structural ceramics in aerospace propulsion," *Nature materials*, vol. 15, no. 8, p. 804, 2016.

[17] C. Ramachandran, V. Balasubramanian, and P. Ananthapadmanabhan, "Thermal cycling behaviour of plasma sprayed lanthanum zirconate based coatings under concurrent infiltration by a molten glass concoction," *Ceramics International*, vol. 39, no. 2, pp. 1413-1431, 2013.

[18] R. Ahmadi-Pidani, R. Shoja-Razavi, R. Mozafarinia, and H. Jamali, "Improving the thermal shock resistance of plasma sprayed CYSZ thermal barrier coatings by laser surface modification," *Optics and Lasers in Engineering*, vol. 50, no. 5, pp. 780-786, 2012.

[19] L. Gao, L. Wei, H. Guo, S. Gong, and H. Xu, "Deposition mechanisms of yttria-stabilized zirconia coatings during plasma spray physical vapor deposition," *Ceramics International*, vol. 42, no. 4, pp. 5530-5536, 2016.

[20] Y. Li, Y. Xie, X. Liu, and X. Zheng, "Effect of physical vapor deposited Al2O3 film on TGO growth in YSZ/CoNiCrAlY coatings," *Ceramics international*, vol. 38, no. 6, pp. 5113-5121, 2012.

[21] P. R. AHMADI, R. Razavi, R. Mozafarinia, and H. Jamali, "characterization of ceria and yttria stabilized zirconia thermal barrier coatings on in 738 superalloy," 2012.

[22] X. Chen *et al.*, "Thermal cycling failure of new LaMgAl11O19/YSZ double ceramic top coat thermal barrier coating systems," *Surface and Coatings Technology*, vol. 205, no. 10, pp. 3293-3300, 2011.

[23] S. Bose, *High temperature coatings*. Butterworth-Heinemann, 2017.

[24] C. Roy, M. Noor-A-Alam, A. Choudhuri, and C. Ramana, "Synthesis and microstructure of Gd2O3-doped HfO2 ceramics," *Ceramics International*, vol. 38, no. 3, pp. 1801-1806, 2012.

[25] L. Guo, M. Li, and F. Ye, "Comparison of hot corrosion resistance of Sm2Zr2O7 and (Sm0. 5Sc0. 5) 2Zr2O7 ceramics in Na2SO4+ V2O5 molten salt," *Ceramics International*, vol. 42, no. 12, pp. 13849-13854, 2016.

[26] I. N. Qureshi, M. Shahid, and A. N. Khan, "Hot corrosion of yttria-stabilized zirconia coating, in a mixture of sodium sulfate and vanadium oxide at 950 C," *Journal of Thermal Spray Technology*, vol. 25, no. 3, pp. 567-579, 2016.

[27] L. Gao, H. Guo, L. Wei, C. Li, S. Gong, and H. Xu, "Microstructure and mechanical properties of yttria stabilized zirconia coatings prepared by plasma spray physical vapor deposition," *Ceramics International*, vol. 41, no. 7, pp. 8305-8311, 2015.

[28] Y. Yin *et al.*, "Hot corrosion behavior of the La2 (Zr0. 7Ce0. 3) 2O7 ceramic in molten V2O5 and a Na2SO4+ V2O5 salt mixture," *Journal of Alloys and Compounds*, vol. 689, pp. 123-129, 2016.

[29] Y. Hui *et al.*, "High-temperature corrosion behavior of zirconia ceramic in molten Na2SO4+ NaVO3 salt mixture," *Ceramics International*, vol. 42, no. 1, pp. 341-350, 2016.

[30] H. Huang, C. Liu, L. Ni, and C. Zhou, "Evaluation of microstructural evolution of thermal barrier coatings exposed to Na2SO4 using impedance spectroscopy," *Corrosion Science*, vol. 53, no. 4, pp. 1369-1374, 2011.

[31] M. Saremi and M. Habibi, "An Investigation on Hot Corrosion Resistance of Plasma Sprayed YSZ - Ceria TBC in Na2SO4+ V2O5 at 1050° C," *Supplemental Proceedings: Materials Processing and Energy Materials*, vol. 1, pp. 429-437, 2011.

[32] A. Keyvani, M. Saremi, M. H. Sohi, Z. Valefi, M. Yeganeh, and A. Kobayashi, "Microstructural stability of nanostructured YSZ–alumina composite TBC compared to conventional YSZ coatings by means of oxidation and hot corrosion tests," *Journal of alloys and compounds*, vol. 600, pp. 151-158, 2014.

[33] H. Jamali, R. Mozafarinia, R. Shoja Razavi, R. Ahmadi-Pidani, and M. Reza Loghman-Estarki, "Fabrication and evaluation of plasma-sprayed nanostructured and conventional YSZ thermal barrier coatings," *Current nanoscience*, vol. 8, no. 3, pp. 402-409, 2012.

[34] H. Jamali, R. Mozafarinia, R. S. Razavi, and R. Ahmadi-Pidani, "Comparison of thermal shock resistances of plasma-sprayed nanostructured and conventional yttria stabilized zirconia thermal barrier coatings," *Ceramics International*, vol. 38, no. 8, pp. 6705-6712, 2012.

[35] S. Yugeswaran, A. Kobayashi, and P. Ananthapadmanabhan, "Initial phase hot corrosion mechanism of gas tunnel type plasma sprayed thermal barrier coatings," *Materials Science and Engineering: B*, vol. 177, no. 7, pp. 536-542, 2012.

[36] H. Jamali, R. Mozafarinia, R. Shoja-Razavi, and R. Ahmadi-Pidani, "Comparison of hot corrosion behaviors of plasma-sprayed nanostructured and conventional YSZ thermal barrier coatings exposure to molten vanadium pentoxide and sodium sulfate," *Journal of the European Ceramic Society*, vol. 34, no. 2, pp. 485-492, 2014.

[37] W. Fan *et al.*, "Microstructural design and thermal cycling performance of a novel layer-gradient nanostructured Sc2O3–Y2O3 co-stabilized ZrO2

thermal barrier coating," *Journal of Alloys and Compounds*, p. 154525, 2020.

[38] L. Guo *et al.*, "Calcium-magnesium-alumina-silicate (CMAS) resistance property of BaLn2Ti3O10 (Ln= La, Nd) for thermal barrier coating applications," *Ceramics International*, vol. 43, no. 13, pp. 10521-10527, 2017.

[39] F. Wang, L. Guo, C. Wang, and F. Ye, "Calcium-magnesium-alumina-silicate (CMAS) resistance characteristics of LnPO4 (Ln= Nd, Sm, Gd) thermal barrier oxides," *Journal of the European Ceramic Society*, vol. 37, no. 1, pp. 289-296, 2017.

[40] X. Xiaoyun, G. Hongbo, G. Shengkai, and X. Huibin, "Hot corrosion behavior of double-ceramic-layer LaTi2Al9O19/YSZ thermal barrier coatings," *Chinese Journal of Aeronautics*, vol. 25, no. 1, pp. 137-142, 2012.

[41] A. Bhattachaya, V. Shklover, K. Kunze, and W. Steurer, "Effect of 7YSZ on the long-term stability of YTaO4 doped ZrO2 system," *Journal of the European Ceramic Society*, vol. 31, no. 15, pp. 2897-2901, 2011.

[42] S. Li, Z.-G. Liu, and J.-H. Ouyang, "Study on hot corrosion reactions between SmYbZr2O7 ceramic and vanadium pentoxide at temperatures of 600–1000° C in air," *Materials Chemistry and Physics*, vol. 130, no. 3, pp. 1134-1138, 2011.

[43] M. Loghman-Estarki, R. S. Razavi, H. Edris, S. Bakhshi, M. Nejati, and H. Jamali, "Comparison of hot corrosion behavior of nanostructured ScYSZ and YSZ thermal barrier coatings," *Ceramics international*, vol. 42, no. 6, pp. 7432-7439, 2016.

[44] H.-f. Liu, X. Xiong, X.-b. Li, and Y.-l. Wang, "Hot corrosion behavior of Sc2O3–Y2O3–ZrO2 thermal barrier coatings in presence of Na2SO4+ V2O5 molten salt," *Corrosion science*, vol. 85, pp. 87-93, 2014.

[45] M. R. Loghman-Estarki, M. Nejati, H. Edris, R. S. Razavi, H. Jamali, and A. H. Pakseresht, "Evaluation of hot corrosion behavior of plasma sprayed scandia and yttria co-stabilized nanostructured thermal barrier coatings in the presence of molten sulfate and vanadate salt," *Journal of the European Ceramic Society*, vol. 35, no. 2, pp. 693-702, 2015.

[46] M. Hajizadeh-Oghaz, R. S. Razavi, A. Ghasemi, and Z. Valefi, "Na2SO4 and V2O5 molten salts corrosion resistance of plasma-sprayed nanostructured ceria and yttria co-stabilized zirconia thermal barrier coatings," *Ceramics International*, vol. 42, no. 4, pp. 5433-5446, 2016.

[47] J. Kärger, D. M. Ruthven, and D. N. Theodorou, *Diffusion in nanoporous materials*. John Wiley & Sons, 2012.

[48] M. Saremi, A. Keyvani, and M. Heydarzadeh Sohi, "Hot corrosion resistance and mechanical behavior of atmospheric plasma sprayed conventional and nanostructured zirconia coatings," in *International Journal of Modern Physics: Conference Series*, 2012, vol. 5: World Scientific, pp. 720-727.

[49] M. Nejati, M. Rahimipour, and I. Mobasherpour, "Evaluation of hot corrosion behavior of CSZ, CSZ/micro Al2O3 and CSZ/nano Al2O3 plasma sprayed thermal barrier coatings," *Ceramics International*, vol. 40, no. 3, pp. 4579-4590, 2014.

[50] L. Guo, C. Zhang, M. Li, W. Sun, Z. Zhang, and F. Ye, "Hot corrosion evaluation of Gd2O3-Yb2O3 co-doped Y2O3 stabilized ZrO2 thermal barrier oxides exposed to Na2SO4+ V2O5 molten salt," *Ceramics International*, vol. 43, no. 2, pp. 2780-2785, 2017.

[51] M. Habibi, L. Wang, and S. Guo, "Evolution of hot corrosion resistance of YSZ, Gd2Zr2O7, and Gd2Zr2O7+ YSZ composite thermal barrier coatings in Na2SO4+ V2O5 at 1050° C," *Journal of the European Ceramic Society*, vol. 32, no. 8, pp. 1635-1642, 2012.

[52] M. Habibi and S. Guo, "The hot corrosion behavior of plasma sprayed zirconia coatings stabilized with yttria, ceria, and titania in sodium sulfate and vanadium oxide," *Materials and Corrosion*, vol. 66, no. 3, pp. 270-277, 2015.

[53] M. Habibi, L. Wang, J. Liang, and S. Guo, "An investigation on hot corrosion behavior of YSZ-Ta2O5 in Na2SO4+ V2O5 salt at 1100° C," *Corrosion science*, vol. 75, pp. 409-414, 2013.

[54] C. Ramachandran, V. Balasubramanian, and P. Ananthapadmanabhan, "On the cyclic hot corrosion behaviour of atmospheric plasma sprayed Lanthanum Zirconate based coatings in contact with a mixture of sodium sulphate and vanadate salts: A comparison with the traditional Ysz duplex and NiCrAlY coated samples," *Vacuum*, vol. 97, pp. 81-95, 2013.

[55] L. Shi *et al.*, "Influences of MCrAlY coatings on oxidation resistance of single crystal superalloy DD98M and their inter-diffusion behaviors," *Journal of Alloys and Compounds*, vol. 649, pp. 515-530, 2015.

[56] K. Zhang, M. Liu, S. Liu, C. Sun, and F. Wang, "Hot corrosion behaviour of a cobalt-base super-alloy K40S with and without NiCrAlYSi coating," *Corrosion Science*, vol. 53, no. 5, pp. 1990-1998, 2011.

[57] H. Wang, D. Zuo, G. Chen, G. Sun, X. Li, and X. Cheng, "Hot corrosion behaviour of low Al NiCoCrAlY cladded coatings reinforced by nano-particles on a Ni-base super alloy," *Corrosion Science*, vol. 52, no. 10, pp. 3561-3567, 2010.

[58] M. Bahamirian, S. Hadavi, M. Farvizi, M. Rahimipour, and A. Keyvani, "Enhancement of hot corrosion resistance of thermal barrier coatings by using nanostructured Gd2Zr2O7 coating," *Surface and Coatings Technology*, vol. 360, pp. 1-12, 2019.

[59] Z. Liu, X. Zhao, and C. Zhou, "Improved hot corrosion resistance of Y–Ce–Co-modified aluminide coating on nickel base superalloys by pack cementation process," *Corrosion Science*, vol. 92, pp. 148-154, 2015.

[60] H. Guo, D. Li, L. Zheng, S. Gong, and H. Xu, "Effect of co-doping of two reactive elements on alumina scale growth of β-NiAl at 1200° C," *Corrosion science*, vol. 88, pp. 197-208, 2014.

[61] Q. Fan, S. Jiang, H. Yu, J. Gong, and C. Sun, "Microstructure and hot corrosion behaviors of two Co modified aluminide coatings on a Ni-based

superalloy at 700 C," *Applied surface science*, vol. 311, pp. 214-223, 2014.

[62] H. He, Z. Liu, W. Wang, and C. Zhou, "Microstructure and hot corrosion behavior of Co–Si modified aluminide coating on nickel based superalloys," *Corrosion Science*, vol. 100, pp. 466-473, 2015.

[63] C. Fu, W. Kong, and G. Cao, "Microstructure and oxidation behavior of Al+ Si co-deposited coatings on nickel-based superalloys," *Surface and Coatings Technology*, vol. 258, pp. 347-352, 2014.

[64] P. Dai, Q. Wu, Y. Ma, S. Li, and S. Gong, "The effect of silicon on the oxidation behavior of NiAlHf coating system," *Applied surface science*, vol. 271, pp. 311-316, 2013.

[65] R. Liu, S. Jiang, H. Yu, J. Gong, and C. Sun, "Preparation and hot corrosion behaviour of Pt modified AlSiY coating on a Ni-based superalloy," *Corrosion Science*, vol. 104, pp. 162-172, 2016.

[66] J. Ma, S. M. Jiang, J. Gong, and C. Sun, "Hot corrosion properties of composite coatings in the presence of NaCl at 700 and 900° C," *Corrosion science*, vol. 70, pp. 29-36, 2013.

[67] S. Nouri, S. Sahmani, M. Asayesh, and M. M. Aghdam, "Microstructural characterization of YSZ-CoNiCrAlY two-layered thermal barrier coating formed on γ-TiAl intermetallic alloy via APS process," *Intermetallics*, vol. 118, p. 106704, 2020.

Design & Development of Static-Thrust Test-Bench For Aviation Based Piston Engines

Syed Muhmmad Basit Ali
Institute of Aviation Studies
University of Management & Technology
Lahore, Pakistan
bux.basit@gmail.com

Usama Saleem
University of Management & Technology
Lahore, Pakistan
F2017206036@umt.edu.pk

Irtiza Ali
University of Management & Technology
Lahore, Pakistan
F2017206026@umt.edu.pk

***Abstract*— Internal combustion engines have been pioneers in the aviation industry, use of piston engines for aircraft propulsion, from propeller-driven bi-planes to turbo-prop, commercial and cargo airliners. To provide an adequate amount of thrust piston engine rotates the propeller at a specific rpm, allowing enough mass airflow. Thrust is the only forward-acting force of an aircraft that helps heavier than air bodies to fly. Depending on the mathematical model and variables included in that with correct measurement. Test-benches have been a bench-mark in the aerospace industry to analyze the results before a flight, having paramount significance in reliability and safety engineering. Depending on the mathematical model and variables included in that with correct measurement. Calculation of thrust from a piston engine also depends on environmental changes, the diameter of the propeller, and the density of air. The project would be centered on piston engines used in the aviation industry for light aircraft and UAVs. Static thrust tests are performed on the ground and safety concerns hold paramount importance. The execution of this study involves research, design, manufacturing, and results based on reverse engineering initiating from virtual design, analytical analysis, and simulations. The final evaluation of results gathered from various methods such as co-relation between conventional mass-spring and digital loadcell. On average we received 19kg of thrust (25+ engine run-ups – around 40 hours of engine run) only 10% deviation from analytically calculated thrust – providing 90%+ accuracy.**

Keywords—Aeronautics, Evaluation, Static-Thrust, Test-Bench, Piston Engine.

I. INTRODUCTION

Thrust, a force that acts on the reaction principle by Newton's 3rd law. When an object accelerates mass in a direction, there is a repulsive force in the opposite direction [1]. Measurement of thrust can be achieved by two methods, a direct way where the actual force produced by the propulsor to an instrument designed to respond to that particular stimulus or an inferential way where two or more characteristic of the system is measured than through a mathematical model thrust is calculated [2].

Ground tests are usually done on a test rig to evaluate the desired characteristics and structural integrity of the piston engine before installation. Static tests assist to ascertain the engine's actual parameters are the same as the design parameters specified in the datasheet [3]. As airborne aircraft's thrust measurement is based on several individual measurements. Only one possible method of measuring the actual thrust of a piston engine excluding the altitude and airspeed influences is a static test on the ground with the help of a load cell [4]. The test rig is a metallic structure, having the capability to withstand loads imposed by a piston engine, an electronic load cell to determine the amount of thrust, and a data acquisition system to obtain data from the test rig [5].

II. LITERATURE

A. EASA Certification Requirements

Every regulatory authority describes the generally accepted means of compliance and guidance material over both designing and maintenance of aircraft. Certain equipment must be certified by the regulatory authority to get into service. Having in mind these limits or factors which has to be considered to design a mount that is safe and operable. Engine mount should be fail-safe and have adequate strength to bear all those arose stresses during engine run. EASA publishes these requirements in its Certificate Specification – Engines, Annex VII to ED Decision 2020/006/R [6].
Some of the factors are as follows:

- Fire Proofing
- Vibration Isolation
- Corrosion Prevention
- Strength
- Fail-Safe

B. Existing Designs Study Leading to Design Parameters

After studying more than 25 patents and more than 60 research papers, the design parameters concluded involves these guidelines:

- The test-bench consists of three Basic Units:
    1. Fixed Holding Structure
    2. Movable Frame (Engine) or Aircraft
    3. Load Cell & Display Unit.
- The design should be robust to bear all kinds of loads (weight, thrust, and vibrational loads).
- Aim to develop a mobile test-bench – having fewer limitations to airflow and structural loads.
- Design should permit the forward/backward motion and restrict the sideways motion.
- The system developed should hold at least 90% accuracy.
- The material selected should resist fatigue cracks and corrosion.

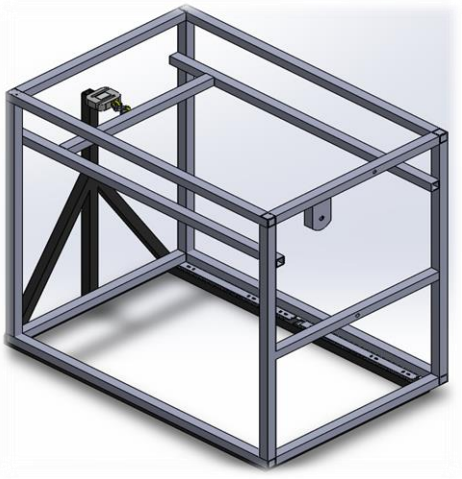
III. METHODOLOGY

Initiated from literature research considering the practices which are performed in the measurement of the static thrust of piston engines. With consulting some of the major key

industrial available prototypes, analyzing the outcomes and shortcomings of the respective model. A test-stand was virtually designed in the view of those parameters specified in literature and market study, with the help of Solidworks. The initial material consideration was stainless steel but due to some capabilities issues and cost analysis, mild steel was chosen as per the analysis. After design approval, the material considered was analyzed for structural loadings. The facilities such as machining, welding, and CNCs were used to manufacture an assembly. In the process of designing, four designs were proposed from which one is selected for the assembly, due to its robust nature and exceptional capabilities to resist buckling and other structural deformities.

A. Software Design

The preliminary conceptual and detailed designs were established using reverse engineering principles – dictating for a 3d software design as the initial step. All designs were made component by component then assembled through solidworks 3d. The final assembly is as follows:



1 Final assembly of test-bench (Virtual).

B. System Description

- Engine Attachment - The engine has three attachment points with the forward stand, having 4 fasteners securing the engine with three vibration isolators. As a safety redundancy of attachment, there are two titanium plated wires wound twice between the engine and the attachment stand. There are three vibration isolators two of the same size installed upstream at the upper attachments, bolted on each side with spring washers to have further vibrational damping characteristics. On the third attachment at the lower side, there is an iron plate having two bold attachments with the engine and a significantly larger vibration isolator connecting that mounting plate to the test stand. Due to uneven attachment points, the most reliable attachments points were considered neglecting the symmetry of attachments.
- Load Cell & Digital Scale - To avoid a significant amount of losses, the sensor placements are of paramount importance, in the following test bench we have established a way to install a load cell in line with the crankshaft. To get the thrust vector (force) in line with the load cell. The load cell is directly coupled with a digital scale to provide the real-time readings of thrust since the project utilizes an s-type load cell measuring both compression and tension forces – both kinds of propellers can be used (pusher/attractor). As in test and evaluation, we have installed both configurations with a three-blade propeller as well, and the strength and safety indicated were remarkable.
- The engine provided in the prior design is STHIL MS-070 engine. Originally, manufactured for a chainsaw, modified for MCC paraglider with a reduction drive to provide 1900 rpm reduced from around 7000 rpm. MS-070 is a two-stroke engine, single-cylinder piston engine. The throttle is coupled with a wire to the top-left of the forward stand. Engine specifications provided by the manufacturer are as follows:

TABLE 1: ENGINE SPECIFICATIONS

STHIL MS-070 Engine Specifications	
Power	4.8 kW
Crankshaft RPMs	6800
Weight	10.2 kg
Bore | Stroke	58 mm | 40mm
Ignition System	Flywheel magneto ignition system
Displacement	105.7 cm
Fuel Capacity	1.2 liters

- Vibration isolators are of industrial grade with two threaded ends, attached to separate plates and the whole assembly is reinforced by an elastomer material.

C. Analytical Analysis

The analytical analysis of the test-bench involves stress calculations, deflection calculations, load calculations, critical buckling loads, thrust loads and various yield limits – The beams selected for the test bench are constituents of mild steel AISI 1212, also referred ass low-carbon steel. Material's mechanical and physical properties as per analytics are listed below [7]:

TABLE 2: MATERIAL LIMITATIONS & ANALYTICAL RESULTS

Property	**Amount (Metric)**
Hardness	126
Tensile Strength, Ultimate	440 MPa
Tensile Strength, Yield	370 MPa
Maximum Elongation at Break	15%
Young's Modulus	205 GPa
Bulk Modulus	140 GPa
Poisons Ratio	0.290
Shear Modulus	80 GPa
Density	7.87 g/cc

$$\Psi = \frac{Wx}{48EI}(3l^2 - 4x^2) \quad (1)$$

$$S = \frac{Wx}{2Z} \quad (2)$$

$$F_{cr} = \frac{n\pi^2 EI}{L^2} \quad (3)$$

(1) represents the equation used to calculate stress among the beams, while (2) represents the mathematical model for calculating maximum deflection in the beam under respective load, and (3) represents the Euler's mathematical model to calculate critical buckling load of the beams. All results were analyzed and came under the limits of material and dimensional characteristics [8].

- E = Modulus of Elasticity
- I = Moment of Intertia
- W = Load

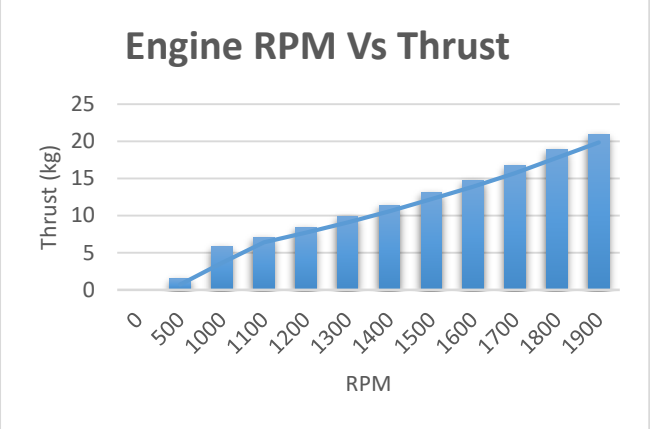


Fig. 1 Engine Vs RPM – Analytical Results

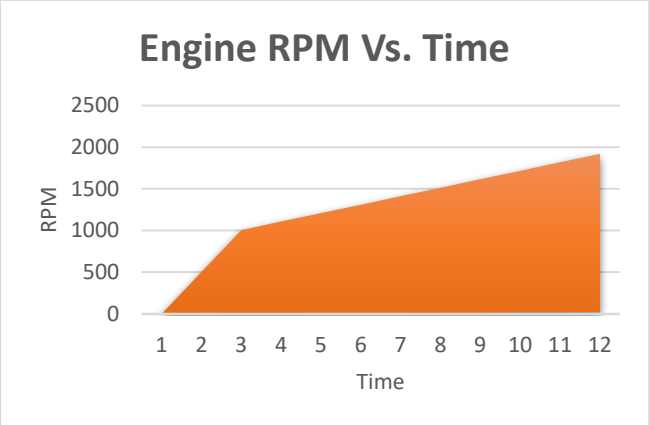


Fig. 2 RPM Vs Time – Real-Time values from RPM Sensors

D. *Finite Element Model Analysis*

Finite element model was built and static structural simulations resulted similar results as per analytical:

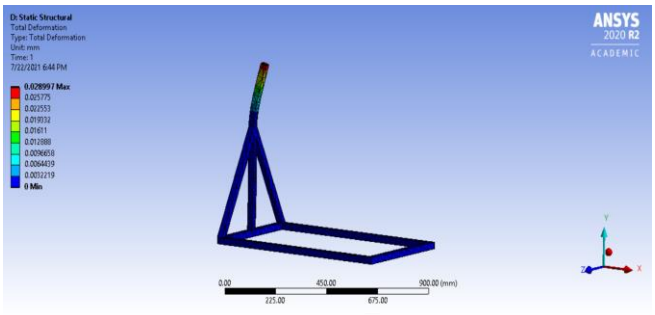


Fig. 2 Static Structural Simulation - Equivalent Stress

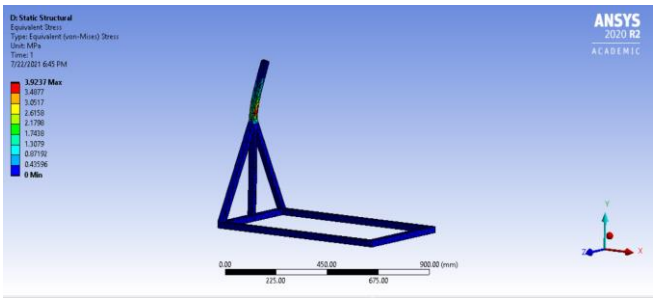


Fig. 3 Static Structural Simulation - Total Deformation

E. *Thrust Calculation*

The mathematical model used to analyse the thrust values of the engine is as follows:
Area of Propeller: $A = \pi D^2/4$ = 1809.55 in^2 => 1.17 m^2
Engine Power: P = 4.8 kW => 6.43691 hp => 489.66 kg-m/s
Air Density (ambient): ρ = 1.225 kg/m^3

$$\text{Static Thrust} = T = 1.225 \frac{\pi(0.0254 \,.\, d)^2}{4} \left[\left(RPM \,.\, 0.0254 \,.\, pitch \,.\, \frac{1min}{60sec} \right)^2 \right] \left(\frac{d}{3.29546 \,.\, pitch} \right)^{1.5}$$

$$T = 21.433 \text{ kg}$$

Legend:
0.0254 & 3.29546 = Conversion Factor
RPM = Propeller Speed
Pitch = Distance covered in one revolution.

F. *Belt Reduction Drive*

Ratio of Belt Diameters: $= \frac{D1}{D2} = \frac{8}{2.25} = 3.56$

Speed of Large Pulley (Propeller) $= \frac{Drive\ RPM}{Ratio} = \frac{6800}{3.56} = 1913.11\ RPM$

The real-time measurement of propeller rpm has been done which came across 1910 revolutions per minute, neglecting the instrumentation errors.

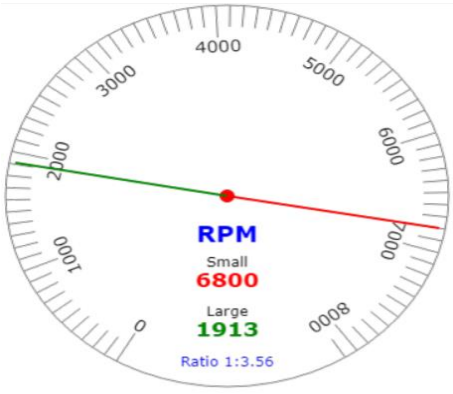


Fig. 5 RPM Reduction Gauge Illustration

IV. Work Techniques & Apparatus

The aspect having paramount importance to specify the work techniques is a suitable selection of material, a comprehensive study was done to select mild steel beams as structural members of test-bench due to its resistance for deformation, certain elasticity, and vibration resistance capabilities. After a suitable material is selected the work techniques to join them have paramount importance to avoid any kind of convenience of breakdown [9]. In order to achieve a structure that is capable of withstanding all the involved loads like weight, thrust, and structural friction strongest joints were made. Following are the work techniques involved:

- Grinding
- Machining (CNC/Milling/Lathe)
- Welding (SMAW)

A. Load Cell

To measure the static thrust of an engine on a test bench many sensors play a vital role. The sensors or modules that need to be configured in the thrust bench mechanism need to detect and read any slight changes in the environment. These sensors do not operate alone and require a mean of an electronic hub or board through which its physical or electrical signals can be interpreted and then displayed

A 500 kg load cell that uses an HX711 amplifier to operate. It is an S-type load cell that can bear up to 500kg of force. The load cell provides electrical signals to the amplifier, the amplifier measures the electrical resistance that changes in the load cell due to the force being applied. Through this, we can measure the exact change in force being applied by the engine of the thrust bench over time.

B. RPM Sensors

RPM sensors are internal electronic devices that play a major part in an engine's functionality. The sensors measure the number of cycles an engine crankshaft achieves per minute. This provides information about, where the cylinder heads are located and can be fired accordingly. Two rpm sensors would be integrated one for engine rpm and the other for propeller rpm.

The RPM sensor in our thrust bench mechanism is going to be an electronic spark sensor configured with a display.
For the project, we are going to use a Digital Tachometer using an optical sensor with a separate power source for measuring the RPM of the engine. Simply we have interfaced rpm sensor module with a battery and an integrated digital module for display. The optical sensor module consists of an optical receiver and transmitter signal (sunlight or separate) in a single pair that can work as a digital tachometer

V. CONCLUSTION & RESULTS

All the tests performed at different times of the day and at different environmental conditions, the team was able to synthesize a result of 19 kg of thrust on a digital scale. The results were co-related with another loadcell and a manual mass-spring system, we received the highest thrust of 20 kg (averaging all the results taken). Not a significant loss from the analytical calculation, which in terms of proving the capability and accuracy of the test-bench designed. The assembly was modified from wheels to linear couplings to avoid frictional losses – which are represented in the table below.

From the research to designing, to measure static-thrust of aviation-based piston engines, there are not many complexities. A basic consideration of sustainable design and testing methods should be decided. A material to withhold the weight and thrust loads of the engine. To achieve all these benchmarks every step involved in this project should be taken with extreme precision. From the data analysis, it is concluded that the project can be performed with extraordinary results.

TABLE 2: RESULTS

Sr. No.	System Results		
	Configuration	***Digital***	***Conventional***
1	With Wheels	14	15
2	Without Wheels	19	20

[a.] Final testing and evaluation results of the test-bench

ACKNOWLEDGMENT

First, all the gratitude to the most gracious and almighty Allah and, our sincere gratitude to Sir. Nadir Munir for an upbeat inspiration, healthy criticism which helped us along the way, and guidance throughout this project. And sincere gratitude towards Prof. Dr. Ahmed Aizaz, Associate Vice Principal, IAS for his valuable experience and guidance throughout this journey.

Utmost respect & gratitude towards Sir. Ahmed Rehan, TechnoCrafts for sponsoring this project, exceptional practical trainings, and for their technically advanced facility.

REFERENCES

[1] National Academy of Sciences, "Commercial Aircraft Propulsion & Engineering Research," National Academy of Engineering, vol. 6. 2016. National Academy of Sciences.

[2] J O. Babayomi, O. C. O, Low-cost ground test equipment for piston engines. 2013 IEEE International Conference on Emerging & Sustainable Technologies for Power & ICT... Imo State, Nigeria.

[3] Mingtai, C., Static Thrust Measurement for Propeller-driven Light Aircraft. Shanghai, Shanghai Institute of Aerospace Research – China, 2012.

[4] Ribeiro, A., Design and methodology of Thrust testing - Master Dissertation, 2013 Brazil: Sao Paulo University.

[5] Miguel, A., Development of a Test Bench for UAV Propulsion Systems Characterisation. 1st ed. Lisboa: Tecnico Lisboa, pp.22-47, 2017.

[6] EASA, Certification Specifications and Acceptable Means of Compliance (CS-E) - Annex VII to ED Decision 2020/006/R. 6th ed. 2020, Cologne: EASA.

[7] Lane, L., *UAV Engines Ltd., 2019*, United Kingdom: www.uavenginesltd.co.uk. [Online]

[8] ÇOBAN, S., Unmanned Aerial Vehicles (UAVs) According to Engine Type. *Journal of Aviation*, III(2), 2018, pp. e-ISSN: 2587-1676.

[9] H. Wittenberg, E. T., 2002. Flight Physics: Essentials of Aeronautical Disciplines and Technology, with Historical Notes, Springer: ISBN 978-1-4020-8664-9.

Nose Landing Gear Conceptual Design and Analysis for M.A.L.E U.C.A.V

Asim Mehmood
Institute of Space Technology
Islamabad,Pakistan.
asim831998@gmail.com

Gohar Majeed
Institute of Space Technology
Islamabad,Pakistan.
gohar.majeed@ist.edu.pk

Kashif Mehmood
National University of Science and Technology
Islamabad,Pakistan.
chkashif94@gmail.com

Usama Rehman
Institute of Space Technology
Islamabad Pakistan
usamarehman987@gmail.com

Muhammad Adeel Khan
Politecnico di Torino
Turin, Italy.
engr_adeel44@yahoo.com

***Abstract*— Among the major components for any Unmanned Combat Aerial Vehicle (UCAV) landing gear is of significant importance, as it performs the function of supporting weight, shock-absorbing structure, taxiing, and providing stable ground support during the nonoperational period, Takeoff and at the most critical phase of Landing. This study presents the Conceptual Design, Preliminary Structure Design, Sizing and Stress Analysis, Finite Element Analysis, Drag Strut design, and Design of Oleo Pneumatic Shock Absorber which is incorporated into Nose Landing Gear (NLG) strut for Medium Altitude Long Endurance Unmanned Combat Aerial Vehicle (MALE UCAV). The MALE UCAV design was carried out by different groups and this study is a part of that program. The conceptual design was carried out by fulfilling the preset constraints of Nose Landing Gear weight, its height, and location. Tri-cycle layout configuration was selected and geometric parameters such as Wheel track and Wheel base and other parameters were worked out. A detailed study of all the possible loading conditions was conducted and the most critical and maximum loads were selected for sizing and stress analysis. Two candidate materials were selected and based on the Normal stress and Shear stress criteria, simultaneously sizing and stress analysis was carried out leading to the desirable design of the Nose Landing Gear strut. The finalized design was modeled and FEA was carried out and results were obtained.**

Keywords—landing gear, Nose Landing Gear, landing gear conceptual design, strut sizing, sizing and stress analysis, landing loads, finite element analysis

I. INTRODUCTION

Unmanned Aerial Vehicle (UAV) serve dozen of purposes ranging from scientific, commercial to military applications. The majority of functions include transport, research and development, reconnaissance, and some form of remote sensing. This study deals with the preliminary design and static analysis of the main landing gear system for a MALE UCAV (Medium Altitude Long Endurance Unmanned Combat Aerial Vehicle) adhering to CS-23 Certificate Specification. The designed UCAV for which landing gear is designed in this study belongs to fixed-wing Combat UAVs mainly used for defense applications. The designed UAV is closely related in terms of design parameters to the Chinese CH-5 and American MQ-9 Reaper, and owing to this resemblance the design of landing gear will be closely in proximity of landing gear of these reference UCAVs in TABLE I.

UAVs are remotely controlled aircrafts which increase the risk of crash on landing several times, thus a reliable and strong landing gear system is of paramount importance. Like any gear system of a vehicle, landing gear provides a means for the UAV to perform its basic functions of Takeoff, Landing, and Taxiing of UAV. Stable ground support is provided by Landing gear during the non-operational period and at the most critical phase of landing. Landing Gear Strut acts as a mechanical shock absorbing structure and a channel to transfer loads to the airframe in the fuselage which is a stronger part as compared. It absorbs the impact energy and transmits it to stronger structural members of the airframe to dissipate this energy in order to avoid the failure of components. [1] A highly preferred landing gear strut comprises of high strength, low weight, low level of complexity, and economic feasibility. Thus a landing gear consisting of these qualities will result in increased efficiency of UAV [2].

TABLE I COMPARISON OF DESIGN PARAMETERS

Parameter	MQ-9 Reaper	Ch-5	Design UCAV
Length	36.1 ft.	36.75 ft.	35 ft.
Wingspan	65.7 ft.	68.8 ft.	62 ft.
Height	12.6 ft	12.47 ft	12.6 ft
MTOW	10,494 lb.	6724 lb.	6433 lb.
Range	1200 mi	6,214 mi	2486 mi
Endurance	14 hrs.	35 hrs.	20 hrs.
Service Ceiling	50,000 ft.	30,000 ft.	25,000 ft.

II. CONCEPTUAL DESIGN

Landing gear configurations under our consideration are a) Tail Wheel Type b) Tandem Type c) Tricycle Type. Tail Wheel type configuration has the Main or Front landing gear positioned a little ahead of the Center of Gravity (C.G) of UAV which creates the need for another gear for empennage. In Tandem type configuration the main landing gear and tail gear are arranged in a manner that both are aligned in a straight line along the longitudinal axis of the aircraft [2]. Based on the requirements and its use in similar types of UCAV such as CH-5 and time tested MQ-9 Reaper, our chosen configuration is the Tricycle- type of configuration, one wheel is placed at the nose of UAV and the other two main wheels are connected either to the wings or the fuselage of the UAV. This configuration prevents the UAV from nosing over as well as avoids the ground looping due to evenly distribution of weight and the well-balanced center of gravity. [2]

Landing gear design is carried out at the end of the design cycle for an aircraft the reason being the number of inputs required to carry out its design procedure. Moreover, aircraft center of gravity both the forward and aft positions must be available [3].The conceptual design is carried out based on predefined constraints which are tabulated in TABLE II.

TABLE II INITIAL DESIGN CONSTRAINTS

Parameter	Value
UCAV (**Fwd**) $X_{C.G}$	17.92 ft.
UCAV (**Aft**) $X_{C.G}$	18.11 ft.
Nose Landing gear length	**5 ft.**
Nose Landing gear total weight	**62.52 lb.**
Maximum Landing weight m_L	5870 lb.
(**N. L. G**) $X_{C.G}$	8.2 ft.
(**M. L. G**) $X_{C.G}$	18.5 ft.
Lateral Tip over angle Ψ	64.3 deg.

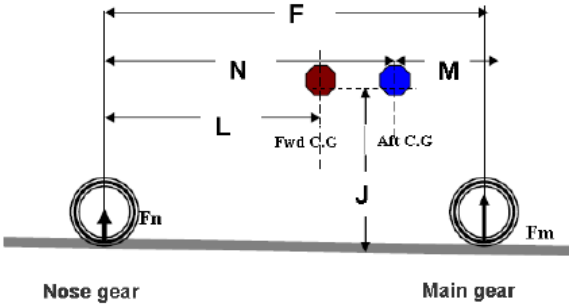


Fig. 1 Parameters for Landing gear configuration

Conceptual design parameters necessary to accurately configure the landing configuration were worked out following the literature for conceptual design provided in [1] [4]. F is the wheel base, L is the distance amid Forward C.G and NLG, and N is the distance amid Aft C.G i.e. (C.G corresponding to empty weight) and NLG. M is the distance between Aft C.G and MLG [4]. TABLE III contains the worked out design parameters

TABLE III DESIGN PARAMETERS

Parameter	Selected Value
Wheel Base (F)	10.8 ft.
Wheel Track	10.39 ft.
Parameter L	9.72 ft.
Parameter N	9.91 ft.
Turnover Angle (∅)	25.7 deg
Tip back Angle (α_c)	15 deg
Height (H_f)	4.47 ft.

III. LANDING LOADS

Subsection C - Structure of the CS-23 Certification Specifications postulates the use of Limit ground loads that can be used in the designing cycle of the landing gear. The limit ground loads indicated in the subsection are recognized as inertia forces and loads acting externally and which are born by the aircraft structure. Every external reaction and ground load condition should be in balance with the angular and linear forces of inertia in a balanced or conventional way. The requirements of ground load postulated in subsection C should be fulfilled at the max designing weight, excluding that sections CS 23.479, 23.481, and 23.483 may possibly be fulfilled with at the designed landing weight permitted under section CS 23.473 subsection (b). [5]

Taking into account the most relevant landing conditions for the main landing gear, landing loads were calculated for each condition fulfilling the requirements of each condition. Selection of relevant landing conditions and calculation of loads in each condition is in itself a detailed discussion and out of scope for the present discussion. Landing loads are tabulated in TABLE IV.

TABLE IV LANDING LOADS

No	Load Condition	Main Gear Reactions (N)		
		X	Y	Z
1	Level landing (three point contact)	2576.70	0	- 6054.28
2	Braked roll	0	0	-14291.64
3	Supplementary Nose Wheel (aft)	5448.85	0	-6811.06
4	Supplementary Nose Wheel (forward)	2724.42	0	-6811.06
5	Supplementary Nose Wheel (side)	0	-4767.74	-6811.06

IV. NOSE LANDING GEAR

The total weight of the aircraft is born by the landing gear system and approximately 5-10% of this total weight is taken by Nose Landing Gear. It is one of the most significant components, enables the steering and taxing of the aircraft. The nose landing gear comprises of main strut with incorporated oleo-pneumatic shock absorber and a drag strut as well. The main strut shock absorber absorbs the impact energy and dissipates it effectively whereas a drag strut takes on a part of the loading along with providing strength and fixes the position by restricting the sideways movement of the main strut. The nose landing gear strut is designed in accordance with the given set of constraints and also meeting the stability requirements in accordance with CS-23 certificate specification. Some constraints like lateral stability, Horizontal Stability, and Ground clearance have been satisfied in working of conceptual design parameters. The remaining constraints such as weight and length will be satisfied during sizing of N.L.G. The designing of the N.L.G focuses on the dimensional sizing of the main strut, the drag struts, and piston-cylinder assembly of the oleo-pneumatic shock absorber that absorbs the major portion of energy due to impact during the landing of aircraft. The design of single acting oleo-pneumatic shock absorber follows the detailed procedure as described by Norman S. Currey [4] . The procedure to achieve the strut design needs not just designing the strut to bear load but also to meet the weight (62.52 lb.) and length (5 ft.) constraints. The first step or sizing of the strut and cylinder for a shock absorber is carried out following methods of beam designing. The strut is designed to bear the respective normal and shear stresses whereas the cylinder also bears hoop stress. The working stresses are limited using a F.O.S (factor of Safety) = 2.3..

A. Landing Gear Schematic Layout and Axis System

The Nose Landing gear layout depicts the oleo-pneumatic shock absorber and a Drag strut at an angle of 33.44 attached to the main strut just above the starting point of the Cylinder. Positive X-axis starting from the nose towards the tail of UCAV. Positive Y-axis is taken along the right-wing chosen by keeping the same orientation. To complete the triad following the right-hand rule positive Z-axis points vertically

downward as depicted in Fig 2. All dimensions are taken in feet.

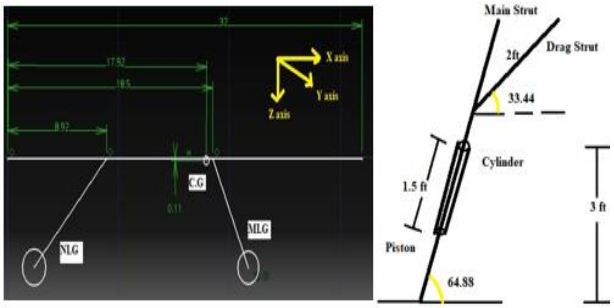


Fig. 2 Landing Gear Schematic with Axis System and NLG Layout

B. Shock Absorber

A shock absorber is a component with a mechanism to absorb and dissipate the impact energy thus protecting the aircraft structure from impulsive shock loads. The function of a shock absorber is to damp impulsive shock loads which arise due to the deceleration motion of the aircraft during landing or encountering a bump while taxing. [6]. There are several types of shock absorbers in a variety of aircraft depending upon the requirement. These include a) Leaf Spring b) Rubber spring c) Pneumatic Shock Absorber d) Liquid Spring e) Oleo-Pneumatic Shock Absorber. The leaf spring shock absorbers are the most common type used widely in general aviation aircraft. The strut is made up of spring steel and acts as a shock-absorbing structure and performs its usual function. Rubber spring shock absorber consists of a bearing, guide rod, and vulcanized rubber disks stacked. Contrary to these two types the pneumatic and liquid spring shock absorbers use fluids for the purpose of shock absorption. The pneumatic shock absorber uses only air as a working fluid whereas the liquid spring-type uses liquids such as oil for the purpose. A hybrid of both pneumatic and liquid spring is the oleo-pneumatic shock absorber. Its design simplicity, serviceability, and efficient mechanism make it an obvious choice for our application.

1) Design of Oleo-Pneumatic Shock Absorber

Oleo-Pneumatic shock absorber is the first choice for use in contemporary aircraft of the present age. It is the most reliable and efficient form of shock absorber with efficiency reaching as high as 90% and weighing seven-folds less than the earlier type of shock absorbers [6]. Shock loads accompanied resulting during landing are dissipated by forcing the liquid such as oil against the compartment of gas i.e. nitrogen. Both fluids are compressed and the kinetic energy is absorbed by the liquid which is forced out of the compartment through the orifice plate holes. The pressure of gas controls the rebound by pushing the liquid back through the recoil orifice to the liquid container, dissipating the energy in the process and preventing the shock loads to reach the aircraft structure.

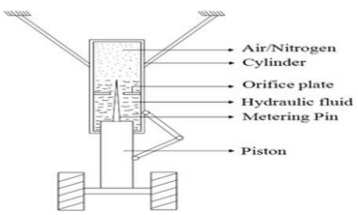


Fig. 3 Schematic Diagram of Oleo Pneumatic Shock Absorber

For the present study, a single-acting shock absorber is designed according to the procedure described by Norman S. Currey [4].

V1 is extended volume
V3 is compressed volume
P1 is extended pressure 60<P1<300 psi
P2 is Static pressure
P3 is compressed pressure

$$Stroke\ (S) = 0.32m = 12.6in$$

$$P_2 = 1200\ psi$$

$$Compression\ ratio = \frac{1.9}{1}\ \text{Compressed to Static}$$

Max vertical load picked from TABLE IV

$$Max\ static\ Load = 14291.06\ N = 3211.78\ lbf$$

$$P_3 = 1.9 * P_2 \quad (1)$$

$$P_3 = 2280\ psi$$

$$Piston\ Area\ (A) = \frac{Max\ static\ load}{static\ pressure} \quad (2)$$

$$A = \frac{3211.78\ lb}{1200\ psi} = 2.67\ in^2$$

$$Piston\ Diameter\ (D) = \sqrt{\frac{A*4}{\pi}} = \sqrt{\frac{2.67*4}{\pi}} \quad (3)$$

$$D = 1.87in$$

$$V_3 = 0.10 * Displacement \quad (4)$$

$$V_3 = 0.10 * (S * A)$$

$$V_3 = 0.10 * (12.6 * 2.67) = 3.36\ in^3$$

$$V_1 = V_3 + Displacement \quad (5)$$

$$V_1 = 3.36 + 33.64 = 37\ in^3$$

$$P_1 = \frac{P_3 * V_3}{V_1} \quad (6)$$

$$P_1 = \frac{2280*3.36}{37} = 207.04\ psi$$

$$Minimum\ Permissible\ Overlap\ (O) = 2.75 * D \quad (7)$$

$$O = 2.75 * 1.87 = 5.14\ in$$

$$Cylinder\ Length\ (L) = S + O \quad (8)$$

$$L = 12.6 + 5.14 + 1in\ (margin) = 18.4\ in$$

C. Critical Loads

For the sizing, we don't limit to a single landing condition rather we take a comprehensive approach and pick the most critical load in each direction from the TABLE IV. The loads are transferred to attachment of Landing gear i.e. point where maximum loading occurs, then transformed into local landing gear axis and identified as Axial, Bending, Shear, and Torsion Loads. TABLE V and VI contain the critical and transformed loads respectively.

TABLE V CRITICAL LOADS

LOADS (N)		
X	**Y**	**Z**
5448.85	4767.74	-14291.64

TABLE VI TRANSFORMED LOADS IN LANDING GEAR AXIS

Reactions	**Fx (N)**	**Fy (N)**	**Fz (N)**	**Mx (Nm)**	**My (Nm)**	**Mz (Nm)**
Main Strut	-10862	3034	1293	119.3	1176.4	-4758.1
Drag Strut	4071 Axial	1733.8 Shear	1858.4 Shear	-1114.2 Torsion	1200.1 Bending	-2612.8 Bending

D. Material Selection

Material for landing gear strut should be of adequate strength to withstand the loads and be easily machineable. Titanium Alloys have specific strength i.e. strength to weight ratio and resistant to corrosion. These properties make it suitable for components with high strength requirements such as landing gear. Aluminum Alloys constitute a major portion of material used in aircraft construction due to its low density and high strength making it a suitable candidate for consideration for our application. Steel is another material widely used in high-strength applications but its high density results in weight penalty which makes it unsuitable for our application. For our purpose we selected Al 7076-T61 having yield strength 572 MPa, Shear Strength 300 MPa [7] and Ti-6Al-6V-2Sn having yield strength 1210 MPa, Shear Strength 760 MPa [8]

E. Sizing and Stress Analysis

The strut is a hollow cylinder with a circular cross-section. The outer radius (Ro) is determined by varying the thickness as a percentage of the outer radius. The values of Ro which satisfy both the Design Bending Stress and Design Shear Stress are selected. The selection focused on finding Ro with thickness of 10% and 15% of Ro. The sizing is done using absolute values in order to size for maximum stresses.

1) Shock Absorber Cylinder

During the design of Oleo-pneumatic we already fix the piston diameter as 47.5mm thus the cylinder internal radius Ri is fixed as Ri= 24.24mm. We perform sizing and stress analysis to find the suitable cylinder size that not only withstands the axial, shear, torsion, and bending but also withstands hoop stress as well. The choice of material for the cylinder is Ti-6Al-6V-2Sn as we are in need of a cross-section that fulfills internal radius constraint and doesn't exceed the cross-sectional size of the main strut.

TABLE VII TRANSFORMED LOADS FOR CYLINDER SIZING

Reactions	Fx (N)	Fy (N)	Fz (N)	Mx (Nm)	My (Nm)	Mz (Nm)
Value	-15283 Axial	-4768 Shear	600 Shear	7.8 Torsion	521.5 Bending	-4340.9 Bending

TABLE VIII CYLINDER SIZING AND STRESS ANALYSIS

Ro (m)	Ri (m)	Axial Stress (MPa)	$\sigma_{B,My}$ (MPa)	$\sigma_{B,Mz}$ (MPa)	Hoop Stress (MPa)	Net Normal (Axial +Hoop $+\sigma_{B,My}$) (MPa)	Net Normal (Axial+ Hoop $+\sigma_{B,Mz}$) (MPa)
0.03	0.024	15.60	54.80	221.67	66.30	124.84	439.90

1) Main Strut and Drag Strut

a) Al7076-T61

We have limited the design stress by using a F.O.S 2.3 therefore the size of the strut should be such that the working stresses do not exceed the design stresses $\tau_{design} = 130.43\ MPa$ $\sigma_{design} = 248.7\ MPa$.

TABLE IX NLG SIZING, NORMAL STRESS AND SHEAR STRESS ANALYSIS AL-7076-T61

Strut	t	Ro (m)	Ri (m)	Axial Stress (MPa)	Net Normal Axial+ $\sigma_{B,My}$ (MPa)	Net Normal Axial+ $\sigma_{B,Mz}$ (MPa)	$\tau_{T,Mx}$ (MPa)	Net Shear $\tau_{Fy} + \tau_T$ (MPa)	Net Shear $\tau_{Fz} + \tau_T$ (MPa)
Main	10%	0.043	0.038	9.85	64.65	231.52	2.77	5.11	8.26
	15%	0.038	0.032	8.63	65.76	239.72	2.89	4.94	7.69
Drag	10%	0.035	0.031	5.57	109.25	231.30	48.13	53.20	52.86
	15%	0.031	0.0263	4.86	112.22	238.59	49.83	54.25	53.96

2) Ti-6Al-6V-2Sn

In a similar manner for Ti-6Al-6V-2Sn using F.O.S=2.3 $\tau_{design} = 330.43\ MPa$ $\sigma_{design} = 526.08\ MPa$.

TABLE X NLG SIZING, NORMAL STRESS AND SHEAR STRESS ANALYSIS TI-6AL-6V-2SN

Strut	t	Ro (m)	Ri (m)	Axial Stress (MPa)	Net Normal Axial+ $\sigma_{B,My}$ (MPa)	Net Normal Axial+ $\sigma_{B,Mz}$ (MPa)	$\tau_{T,Mx}$ (MPa)	Net Shear $\tau_{Fy} + \tau_T$ (MPa)	Net Shear $\tau_{Fz} + \tau_T$ (MPa)
Main	10%	0.033	0.0297	16.72	137.98	507.16	6.14	10.12	15.47
	15%	0.03	0.0255	13.85	129.97	483.5	5.88	9.17	13.59
Drag	10%	0.027	0.0204	9.36	239.47	511.82	104.84	114.77	114.3
	15%	0.024	0.0243	8.11	235.21	501.07	107.4	113.37	112.8

F. Final Selection

The Finally Selected Size is that of Ti-6Al-6V-2Sn for 15% of Ro thickness. The reason for selection is that Ti-6Al-6V-2Sn provides better strength to weight ratio as compared to Al7076-T61.The total Weight of the NLG struts is 13.789 kg i.e. 30.4 lb. thus satisfying the weight constraint as well.

TABLE XI FINAL SELECTED SIZE

Strut	t	Ro (mm)	Ri (mm)
Main	15%	30	25.5
Drag	15%	24	24.3
Cylinder	6 mm	30	24.25

G. Layout CAD and FEM Model

The layout consists of several parts however only essential components such as Upper mounting brackets for both main and drag strut, Fork Lug, Main strut, and Drag strut go into FEM Model for analysis. The drag strut is connected to the main strut as a welded connection to ensure proper load transfer and simplify the analysis.. The design of the upper mounting brackets, and fork lug are based on the principle of simplified lug analysis and it is an iterative process. The axial stress at the connection point is calculated, then depending upon the constraint of available space and weight a 3D space is drawn. Different layouts of the upper mounting bracket and fork lug used in similar UAVs are studied and a layout meeting the constraints is selected. Using different materials strength analysis is performed until an appropriate size lug fulfilling the constraints is obtained. FEM analysis is performed and if the results are within the required range, the design is finalized otherwise the whole process is repeated. FEM model components dimensions are tabulated in TABLE XII.The complete Nose Landing Gear consists of several parts as depicted in Fig 4.

1. Main Strut

2. Drag Strut
3. Oleo-Pneumatic Cylinder
4. Oleo-Pneumatic Piston
5. Fork
6. Fork-Piston connection
7. Torque Link
8. Upper mounting brackets for both struts
9. Drag strut lower mounting bracket
10. Female lug for drag strut connection

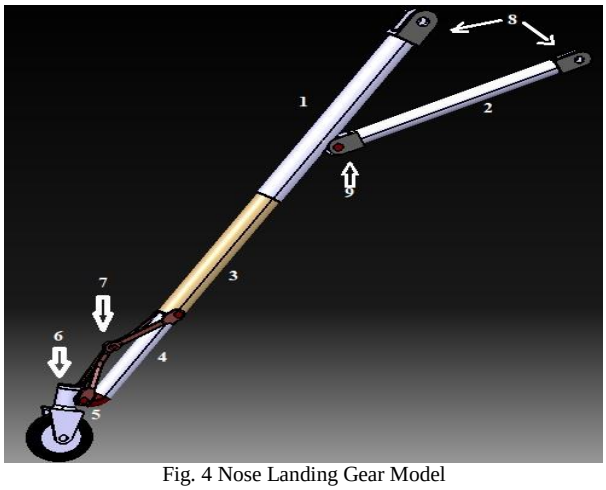


Fig. 4 Nose Landing Gear Model

TABLE XII FEM Model Component Dimensions

Parameter	Main Strut Upper Mounting Bracket	Drag Strut Upper Mounting Bracket	Fork Lug
Inner radius R_i (mm)	15	12	10.70
Outer radius R_o (mm)	40	30	22.19
Thickness t (mm)	17	12	6.1

V. Finite Elements Analysis

We utilize finite element analysis on the designed landing gear to verify and further enhance our worked-out design. The results obtained are more precise and give a better insight. For the purpose of FEA only the 15% thickness case of Ti-6Al-6V-2Sn i.e. Ro=30mm for main strut, Ro=24mm for drag strut is modeled and analysis is carried out. The FEA model consists of the main strut and drag strut with upper mounting brackets and the piston fork connection. Only static analysis is performed using boundary conditions as upper mounting brackets as fixed support, fork wheel connection takes the loads. For the Analysis different size mesh starting from 7mm to 5 mm element size is used for each model to obtain precise results and study the dependence of results on the mesh size. The design of the upper mounting brackets and the fork lug are based on the principle of simplified lug analysis and it is an iterative process. The axial stress at the connection point is calculated, then depending upon the constraint of available space and weight a 3D space is drawn. Different layouts of the upper mounting bracket and fork lug used in similar UAVs are studied and a layout meeting the constraints is selected. Using different materials strength analysis is performed until an appropriate size lug fulfilling the constraints is obtained. FEM analysis is performed and if the results are within the required range, the design is finalized otherwise the whole process is repeated again. The complete Main Landing Gear consists of several parts as depicted in the layout.

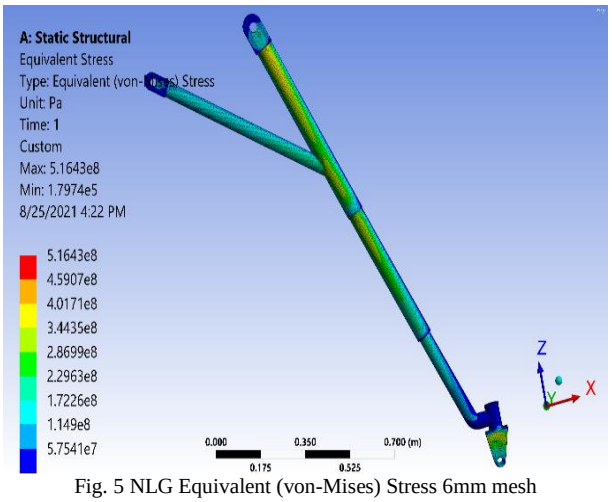


Fig. 5 NLG Equivalent (von-Mises) Stress 6mm mesh

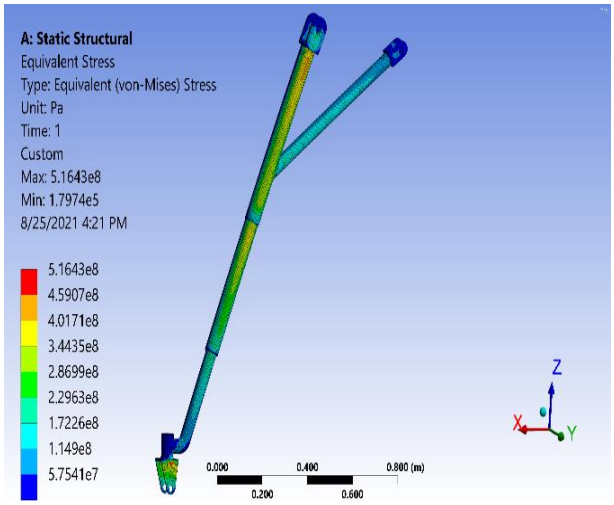


Fig. 6 NLG Equivalent (von-Mises) Strain 6mm mesh

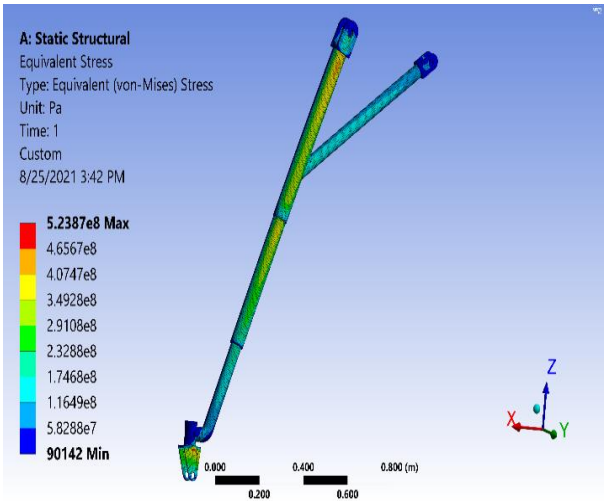


Fig. 7 NLG Equivalent (von-Mises) Stress 5mm mesh

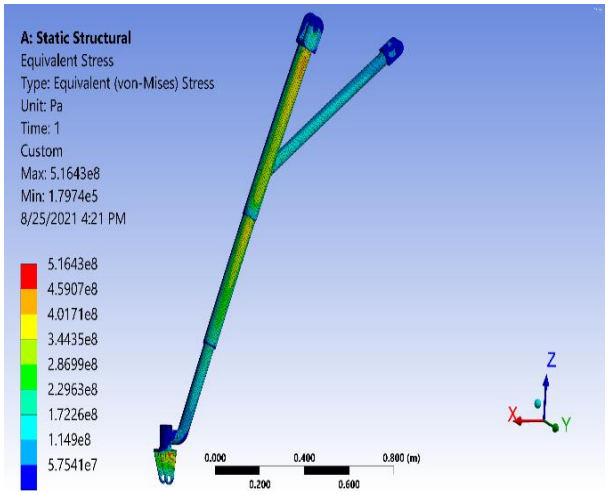


Fig. 8 NLG Equivalent (von-Mises) Strain 5mm mesh

FEM analysis shows that the main strut takes the majority of load which results in higher stresses born by the main strut whereas the drag strut takes a part of the load from the main stress thus reducing the level of stress on the main strut hence providing structural support to the landing gear.

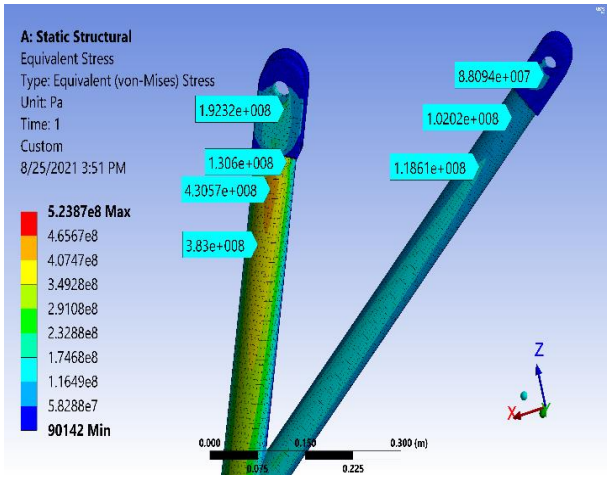


Fig. 9 Close-up view NLG Equivalent (von-Mises) Stress 5mm mesh

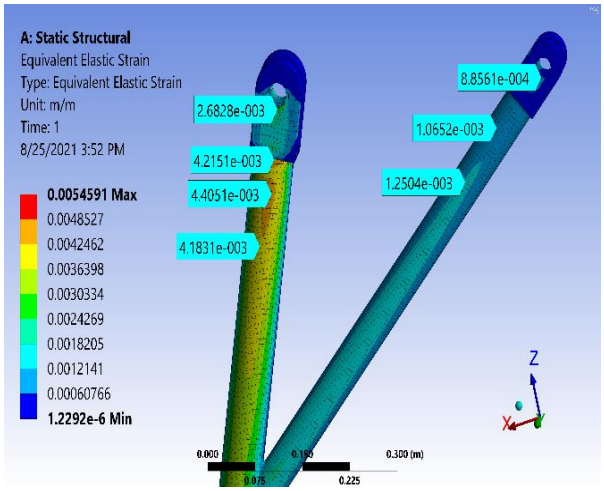


Fig. 10 Close-up view NLG Equivalent (von-Mises) Strain 5mm mesh

The area of interest for both the main strut and drag strut are near to the attachment of strut upper mounting brackets. Measuring the level of stress and strain at various points of interest confirms that stress and strain lie within the design values thus there is no risk of failure.

TABLE XIII FINITE ELEMENT ANALYSIS RESULTS

Model	Nodes	Elements	Skewness	Orthogonal Quality	Max Stress (MPa)	Max Strain
7mm	145165	43295	0.6080	0.5247	506	0.00527
6mm	185118	52520	0.5792	0.5600	516.43	0.00538
5mm	243751	65800	0.5162	0.6285	523.87	0.00545

Von-misses stresses arising in the structure should not exceed the yield stress of the material. The obtained strain values for different mesh sizes show that the deformation remains within the elastic limit when compared with the yield strain of Ti-6Al-6V-2Sn i.e. 0.010341mm/mm which means that linear elastic FEA is valid in our case. With different elements size mesh, the number of nodes and elements change but there is no significant change in stress which means it is insensitive to mesh size therefore it is concluded the FEM Analysis is valid. Results gathered for different mesh sizes in FEA show that both stress and strain remain within the limits of material thus satisfying the maximum loading cases for the landing gear, therefore our designed landing gear is safe.

VI. Conclusion

This study provides the simplest procedure to design Nose Landing gear for a UAV. A desirable design for Nose landing gear is achieved through parametric study utilizing Aluminum and Titanium alloy of adequate strengths. Simultaneous sizing and stress analysis for 10% and 15% of outer radius thickness cases result in different sizes of the main strut. The selected size for the main strut is Ro =30 mm and for drag strut Ro=24 mm for Ti-6Al-6V-2Sn. The simplified design of the oleo-pneumatic shock absorber leads to the sizing of cylinder Ro=30mm adopting the same method as main strut sizing and stress analysis. The total weight for the designed landing gear comes out to be 30.4 lb. thus satisfying the weight constraint of 62.52 lb. FEM analysis for the final model at 5 mm element size mesh shows that maximum equivalent stress is 523.87 MPa which is below the yield strength of Ti-6Al-6V-2Sn 1210MPa.

Landing gear should be as simple as possible because complexity increases the cost at a higher rate than the weight. Simpler design leads to fewer structural support members which in turn leads to a bigger cross-sectional area of the main strut of the landing gear. The addition of drag strut provides structural rigidity to the landing gear by dividing the load and providing resistance to structural deformation. However, if the design requirement prevents the use of additional structural components then a bigger cross-sectional main strut with approximately 10-20% of outer radius thickness will be adequate to bear the stresses and resist the deformation but a negative effect is a significant increase in the total weight.

References

[1] A. Jha, "Landing Gear Layout Design for Unmanned Aerial Vehicle," in 14th National Conference on Machines and Mechanisms (NaCoMM09), Durgapur, 2009.

[2] J. Parmar, V. Acharya and D. Challa, "SELECTION AND ANALYSIS OF THE LANDING GEAR," International Journal of Mechanical

Engineering and Technology (IJMET), ISSN 0976, vol. 6, no. 2, pp. 10-18, 2015.

[3] A. Dutta, "DESIGN AND ANALYSIS OF NOSE LANDING GEAR," International Research Journal of Engineering and Technology (IRJET), vol. 03, no. 10, 2016.

[4] N. S. Currey, Aircraft Landing Gear Design : Primciples and Practices, Washington, D.C.: American Institute of Aeronautics and Astronautics,Inc, 1988.

[5] E. A. S. A. (EASA), "Easy Access Rules for Normal, Utility, Aerobatic and Commuter Category Aeroplanes (CS-23) (Amendment 4)," European Aviation Saftey Agency (EASA), 2018.

[6] R. Ganugapenta, S. M. sudhan, M. D. Babu and B. S. R. Satheesh, "SYSTEM DESIGN AND ANALYSIS OF MAIN LANDING GEAR," INTERNATIONAL JOURNAL OF CURRENT ENGINEERING AND SCIENTIFIC RESEARCH (IJCESR), vol. 5, no. 2, 2018.

[7] "Aluminium 7076-T61," Matweb, [Online]. Available: http://www.matweb.com/search/datasheet_print.aspx?matguid=8916a21e7d604d3499f7637fde053930. [Accessed 08 2021].

[8] "Titanium Ti-6Al-6V-2Sn (Ti-6-6-2) STA 910 C/ 540 C," Aerospace Specification Metals Inc, [Online]. Available: http://asm.matweb.com/search/SpecificMaterial.asp?bassnum=MTP663. [Accessed 08 2021].

Design and Analysis of An Effective Ventilation System To Reduce Covid-19 Spread In a Confined Room

Salem Mohammed Alohani
Aerospace EngineeringDepartment
College of Aeronautical Engineering, NUST
Risalpur, Pakistan
s.mohammed.90eccae@cae.nust.edu.pk

Muzaffar Habib
Aerospace EngineeringDepartment
College of Aeronautical Engineering, NUST
Risalpur, Pakistan
muzaffar.habib@cae.nust.edu.pk

Muhammad Anas
Aerospace EngineeringDepartment
College of Aeronautical Engineering, NUST
Risalpur, Pakistan
manas.91eccae@cae.nust.edu.pk

***Abstract*— The purpose of this project is to design and analyze an efficient and effective ventilation system for a small room to remove maximum COVID germ particles in the shortest possible time. Al first, the spread of germs was modeled and simulated using ANSYS Fluent software to find the spread of germ particles inside the confined room. Later, nine different problem cases were made consisting of different exhaust locations and different outlet exhaust boundary conditions. Geometry for different locations of the ventilation sources was created, later CFD analysis was performed using the ANSYS Fluent software. The transient analysis was performed using the Discrete Phase Method (DPM) in ANSYS Fluent software. The Reynolds Averaged K – epsilon turbulence model was used to capture the spread of germ particles inside the room. The CFD results for all 9 cases were analyzed and it was observed that without a ventilation source, the cough particles slowly spread in the room and then were settled on the floor. With the ventilation source (exhaust fan), the cough particles merged with the airflow and exited the room through the outlet. As the velocity of the fan was increased, it was observed that the time required for cough particles to vacate the room, was reduced. The research was concluded with the selection of optimal exhaust velocity and the location of the exhaust system inside the room. The case with an exhaust source near to the ground was proved to be most effective in eliminating the germ particles, with an inflow condition of 10 m/s.**

Keywords*— Discrete Phase Method, COVID Ventilation, cough, RANS.

I. INTRODUCTION

Humankind has regularly encountered epidemics over the timespan of the last decade such as spinach flu, swine flu, etc. Recently the world has been affected by the COVID-19 pandemic, which has proved to be more powerful and deadly as compared to its predecessors. These diseases spread from

an infected person's mouth or nose in the form of small liquid droplets as they cough or sneeze. These droplets can

stay in the air or on surfaces for a long time can infect other persons coming in contact. Studies so far suggest that a confined room or classroom is one of the most favorable locations for the spread of COVID-19 germs. The importance of an effective ventilation system for removing exhaled aerosols and preventing cross infections cannot be denied [1][2][3][4].

Researchers have studied multiple techniques for stopping the spread of such pandemics by the use of sanitizers, masks, isolation, etc. [3][5][6]. Designing an effective ventilation system is also known to be an effective remedy in reducing the transmission rate of these viruses [7][8][9]. Ventilation can be described as a disturbance created by the natural or forced air into a steady flow of air. A good ventilation system is designed to remove infectious germs particles from the confined and congested areas to open air.

Fluid flow analysis is performed to track the motion of the infected particles and their probability of infecting others. Computational Fluid Dynamic (CFD) analysis is performed to effectively model the fluid motion inside the confined areas of rooms [10] [11] [12]. The distance traveled by the germs and the residence time are predicted using the CFD analysis. These distance and traveling times also depend on the factors like coughing velocity, airflow pattern, cough or sneeze droplet size, etc [13][14]. The movement of the fluid particles is dependent on the size of aerosols. Particles having a diameter of fewer than 10 microns are light enough to spend more time in the air and hence enhance the chances of virus spread [4]. On the other hand, particles having an aerosol diameter of greater than 10 microns settle to the ground relatively quickly [15].

This study is aimed at analyzing the transmission and propagation of aerosol particles emitted for respiratory events, like cough or sneeze in an indoor space such as an office or classroom. To study the spread of cough particles in the area, the CFD analysis was first performed inside an empty room without ventilation and later it was integrated by a ventilation source to simulate and visualize the particles getting out of the room. The first step of the project was to simulate a steady-state analysis of the cough inside a room just to learn how it spreads. The cough was simulated using a discrete phase method with transient modeling. This puts the simulation closer to the real-life scenario where one can visualize cough particles entering inside the room environment through the mouth and then exiting the room environment with the help of a ventilation system at a specific speed and under a certain time. The analysis has been done using ANSYS software and its different modules such as Fluent, ICEM, and design modular have been used to simulate the cough inside the room [16].

In this research, first, a room geometry of 15 by 15 ft. was generated and then a velocity inlet source was added to act as a cough source. The cough particles enter the room through this inlet source. Discrete phase modeling was used to track the movement of cough particles inside the room. The spread of the germs was observed using the velocity path lines. Our problem deals with liquid-gas phase interaction. Hence, we have to use both multiphase and models. The volume of the fluid method was used to capture the multiphase nature of the problem. The volume of the Fluid method is an advection

scheme that allows to track the shape and position of the interface. This scheme couples with the Navier-Stokes equation to operate properly. The volume of the fraction is a discontinuous volume fraction function that allocates the cell the value between 0 and 1.

Time taken by the cough particles to settle down and reach zero velocity was noted. After the initial simulation, a ventilation (velocity output) source was added. As an initial case, a rectangular exhaust fan was given a 5 m/s exit velocity and movement of germs outside the room was observed. Time taken to clean the room was noted. Later, different CFD cases were analyzed with different ventilation locations and fan exit velocities. The results were then compared to find an optimal ventilation system.

II. Literature Review

A. Governing equations

The basic technique used in Computational Fluid Dynamic (CFD) is to replace continuous fluid boundaries into discrete fluid boundaries. In a continuous domain, each flow variable is defined at every point in the domain. In discrete domain, each flow variable is defined only at the grid points or for 3 D at the cell nodes. In a conventional CFD problem, flow variables such as velocity, pressure, density, etc are solved for each grid point on the mesh. The governing equations and appropriate boundary conditions are defined as well. CFD software approximates these in the discrete domain in terms of the discrete variables. Most commercial CFD codes use finite volume or finite-element methods as it is better suited for modeling flow inside complex geometries [6]. The solution of the following equations is required for solving any flow problem.

- Continuity equation (conservation of mass)
- Momentum equation (conservation of momentum)
- Energy equation (conservation of energy)

For this research, a finite control volume solution strategy is considered to determine the properties of fluid inlet and outlet are calculated. The flow is considered incompressible. The problem is also amused to be adiabatic therefore energy equation is also simplified.

1) Continuity equation

The continuity equation works on the principle of conversation of mass i.e., the mass entering any control volume must be equal to mass going outside the control volume. The differential form of the continuity equation is as under,

$$\frac{D\,\rho}{D\,t} + \nabla.(\rho\,\bar{V}) = 0 \qquad (1)$$

In this particular problem, we have assumed our flow to be incompressible hence density variations are not taken into consideration therefore $\frac{D\,\rho}{D\,t}$ becomes zero, the used simplified version of the continuity equation is as under,

$$\nabla.(\rho\,\bar{V}) = 0 \qquad (2)$$

2) Momentum equation

The momentum equation works on the principle of conversation of momentum of the system i.e., the momentum of any closed and preserved system should be converted to pressure forces exerted on the boundaries without any losses. The differential form of the momentum equations are as under,

$$\rho\,\frac{D\,u}{D\,t} = -\frac{\partial\,p}{\partial\,x} + \frac{\partial\,\tau_{xx}}{\partial\,x} + \frac{\partial\,\tau_{yx}}{\partial\,y} + \frac{\partial\,\tau_{zx}}{\partial\,z} + \rho\,f_x \qquad (3)$$

$$\rho\,\frac{D\,v}{D\,t} = -\frac{\partial\,p}{\partial\,y} + \frac{\partial\,\tau_{xy}}{\partial\,x} + \frac{\partial\,\tau_{yy}}{\partial\,y} + \frac{\partial\,\tau_{zy}}{\partial\,z} + \rho\,f_y \qquad (4)$$

$$\rho\,\frac{D\,w}{D\,t} = -\frac{\partial\,p}{\partial\,z} + \frac{\partial\,\tau_{xz}}{\partial\,x} + \frac{\partial\,\tau_{yz}}{\partial\,y} + \frac{\partial\,\tau_{zz}}{\partial\,z} + \rho\,f_z \qquad (5)$$

B. Eulerian Multiphase Modeling Approaches

We are using the Eulerian multiphase approach to capture the phase interaction. The eulerian multiphase approach can be accounted in two categories,

- Dispersed continuous phase interaction
- Continuous-continuous phases interaction

In the dispersed continuous phase interaction, dispersed phases might be solid particles, liquid droplets, or gas bubbles. They are absorbed in the continuous phase. The dispersed phase is mostly very small and is in mm or even smaller. On the other hand, in the continuous phase's interaction, the two phases form a discrete interaction between them. In other words, they are immiscible. For example, the interaction of oil and water or interaction of water and air. It is mostly used when we are interested to examine this interaction. The full Eulerian model is divided into two sub-models. [7]

- Mixture models
- The volume of the fluid model

The mixture model is a simplified version of Dispersed continuous phase interaction and the Volume of fluid method is the simplified version of continuous-continuous phase interaction. In this research, the air was used as static fluid and water coming out of the injector and there is a discrete interaction. [7] Therefore, the volume of the fluid method was used in this research [8].

C. ANSYS Fluent Software.

Fluent solvers are based on the finite volume method. The domain is discretized into a finite set of control volumes or cells. FLUENT offers a wide array of physical models that can be applied to a wide array of industries. The general conservation (transport) equation for mass, momentum, energy is discretized into algebraic equations.

III. Methodology

The room consists of one inlet, out the outlet, and the ventilation source. The back wall was defined separately during meshing as the particles will strike on the wall. The volume of fluid method which is the Eulerian approach and a continuous phases interaction model is used for the continuous inlet flow. The Reynolds Averaged Navier Stokes (RANS) model k-epsilon was used to capture the turbulence and fluctuations of the system. The Discrete Phase model (DPM) is used to capture the germs. This project consists of two major parts, these parts are as follows, the first part is to make the room and put the cough and sneeze source without the ventilation source. And the second part is to see the spread of germs in the room. The project has been divided into different parts. In the first part, we have taken water as a working fluid and a continuous stream of fluid is taken as input. The continuous inlet will let the flow enter without any pause. But

the procedure will be cleared. After that, we will use the ventilation source with the continuous inlet source of a cough fluid. The spread will be noticed. The last step will be the use of the Discrete Phase Model (DPM). The Discrete Phase Model (DPM) is a utility of ANSYS Fluent which allows the users to define the discrete phases. It allows the users to enter the particles in the working domain for a defined timeline. For our cases, the cough and sneeze consist of small discrete particles which will act as germs and these particles will enter the domain for a small amount of time, this small-time will be the time that a person sneezes. The time was taken as 0.5 seconds as a normal person's cough time is almost 0.5 seconds. The discrete particles will enter from the inlet interact with the air that is present in the room and interacts with the air that is coming from the ventilation source and the germs are spread inside the room and concerning the time the particles will leave the room from the outlet and the room will be germ-free. The following steps were taken to complete this project,

- Geometry creation for all cases
- Mesh creation of all cases using ICEM CFD software.
- Numerical setup of all cases in ANSYS Fluent.
- Simulation for the steady-state analysis of cough without ventilation source
- Simulation for the steady-state analysis of cough with ventilation source at velocity 5 m/s
- Simulation for the steady-state analysis of cough with ventilation source at velocity 10 m/s
- Simulation for the transient flow analysis of cough with ventilation source at velocity 5 m/s using Discrete phase method (DPM)
- Simulation for the transient flow analysis of cough with ventilation source at velocity 10 m/s using Discrete phase method (DPM)
- Simulation for the transient flow analysis of cough with exhaust at velocity 10 m/s using Discrete phase method (DPM)
- Simulation for the transient flow analysis of cough with exhaust at velocity 5 m/s using Discrete phase method (DPM)
- Comparison of results in all cases
- Final design and conclusion.

IV. CFD Analysis

A. 3D Modeling

The geometry was created in ANSYS design modular. The general dimensions of the room were taken and the room was created. The inlet was taken as the source for the cough. The inlet was very small. The outlet was taken as the window which was placed on the opposite side of the inlet. The red area in the figure below shows the outlet and the yellow part shows the walls. The inlet is not visible in the figure below because it is very small. The outer wall is closed for better visualization. The geometry is shown as under.

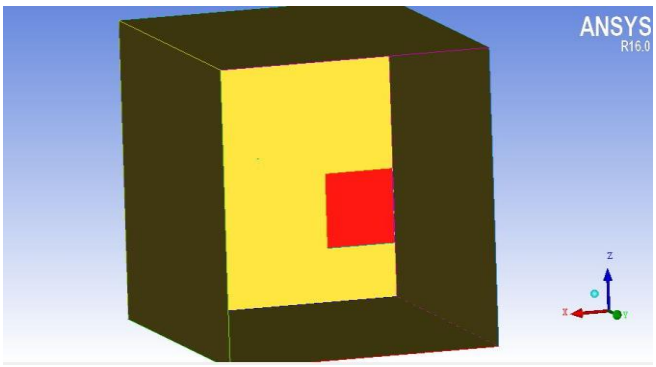


Figure 1. Room CAD Model

B. Meshing

The geometry was imported into ICEM CFD software. The mesh was created using the blocking technique. The mesh was refined at the inlet because the gradient of properties at that point was very high. The named selection was done. The quality, orthogonal quality, and other parameters of the mesh were up to standards. The general information of mesh is shown as under.

Mesh element	Information
Total elements	461164
Total nodes	450300
Orthogonal quality	Min 0.0270391-- Max 1
Method	Triangular

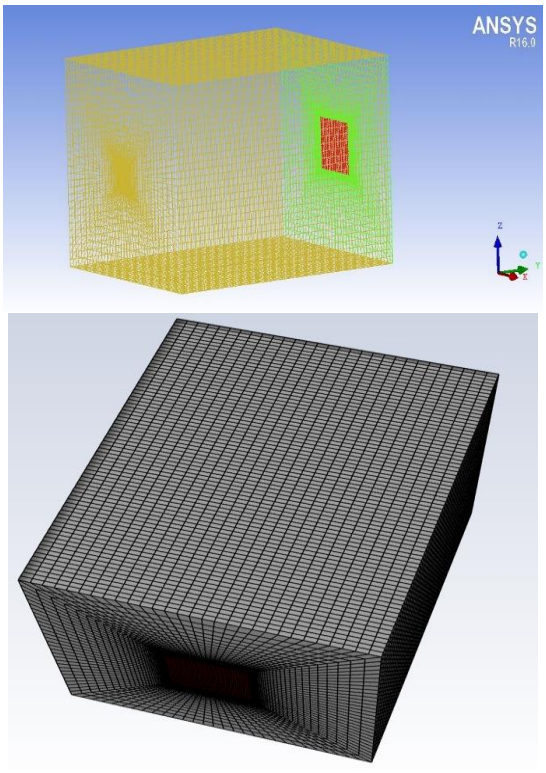


Figure 2. Geometry Meshing

C. Air and Water fraction

The phases of the fluids were defined. The air was defined as the primary phase and the water was defined as the secondary phase. The sneeze for simplicity was taken as water, as it contains the denser parts. The domain was initialized by air and water (cough source) was entering from the velocity inlet [17] [18].

D. Numerical Setup in Fluent

The numerical details of the simple case are described as under,

1) Time Step size

In this part, we have considered that there is no time dependency. It is a Steady-state solver for incompressible, turbulent flows. Hence to solve the problem, the time-dependent terms of the governing equations were neglected.

2) Compressible or incompressible

Our problem is incompressible, as described in the problem statement. Hence, the density was kept constant, and the compressibility effects were ignored.

3) Grid Independence Study

If any particular flow field variable doesnot change significantly with the change is grid size, we call the CFD problem to be grid independent. The purpose of the grid independence study is to find appropriate mesh size that is both acceptable computationally and also produce result with significant accuracy. In this research, a velocity value of any arbitrary point was chosen inside the grid, and then simulations were performed with different mesh sizes. Once the value became stable and no significant change was noeted in the velocity value, the grid size was finalized. This method of grid independence study is iterative and time-consuming and not suitbale for large CFD problems.

In grid Independence a certain parameter is analyzed for finer and finer mesh sizes till the change in its value becomes negligible or ignorable There are three methods usually used for grid independence

i. Global size reduction method

ii. Surface or Curve mesh reduction method

iii. iii. Y+ value matching method

4) Convergence Criteria

Convergence is said to be achieved when the force convergence value which is the square root sum of squares (SRSS) of the imbalance of the forces is greater than the criteria which are the product of SRSS and tolerance value were taken equal to 0.001.

5) Reynolds number

Reynolds number is the ratio of inertial to viscous forces. The formula of Reynolds number is,

$$Re = \frac{U * H * \rho}{u} \qquad (6)$$

where U is the free stream velocity in m/s. H is the height in meters. ρ is the density (kg/m^3) and μ is the kinematic viscosity $N.s/m^3$. The inlet velocity for both cases was set to 6.5 m/s. The Reynolds number was calculated to it was in turbulent regime. For, turbulence we used the k-epsilon RANS model. Reynold's Averaged Navier-Stroke model is based on averaging of fluctuating terms. The fluctuation of Reynold stresses in the Navier stokes equations causes instability in the CFD solution.

6) K-$\mathcal{E}$ Turbulence model

Initially the Spalart-Allmaras (SA) turbulence model was used. The SA turbulence model is a low Reynolds number model and does not require the use of wall functions as such. This allows use of less dense grid near-walls, which saves computational cost. The K-ε turbulence model is computationally expensive due to simultaneous solution of two equations for turbulence modeling. The results indicated at most 5 % variation in the results using both turbulence models and therefore all subsequent analysis was performed using the K-ε turbulence model.

V. CFD Simulation Results

The results obtained during CFD simulations of all 10 cases are described below,

*A. **Case 1:** This is the first case of our simulations. In this case, a simple cough source was placed and the Volume of Fluid (VOF) method was used to capture the interaction of sneeze with air inside the room. There was no ventilation source placed in the room. The results obtained are as under.*

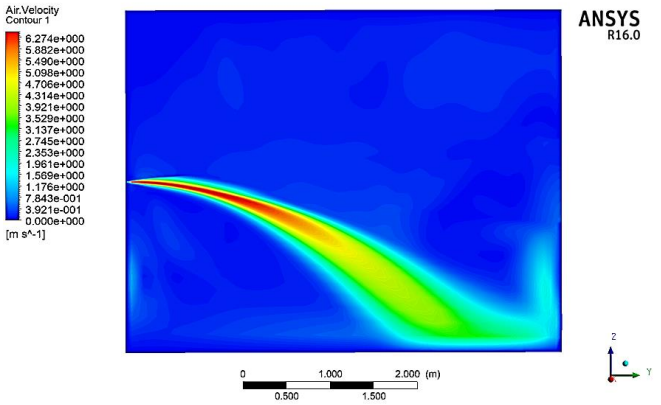


Figure 3 Air velocity in domain

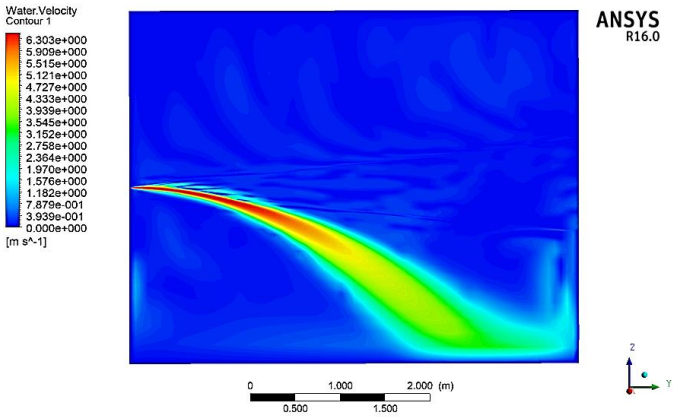


Figure 4 Water velocity in domain

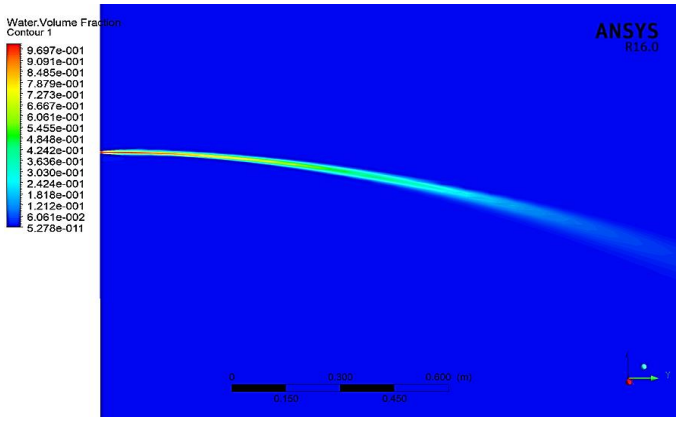


Figure 5 Water volume fraction

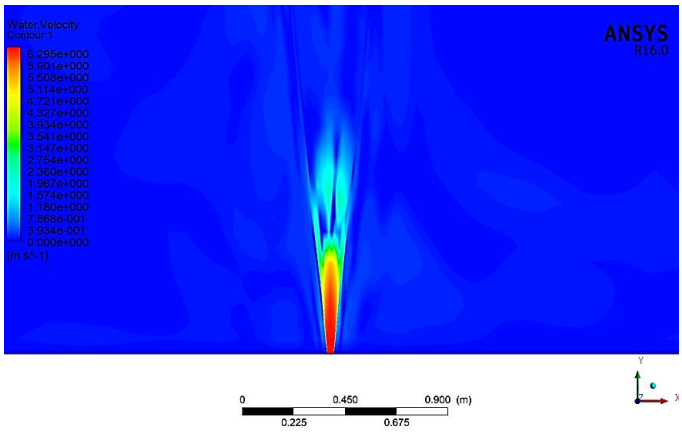


Figure 6 Water velocity cut plane

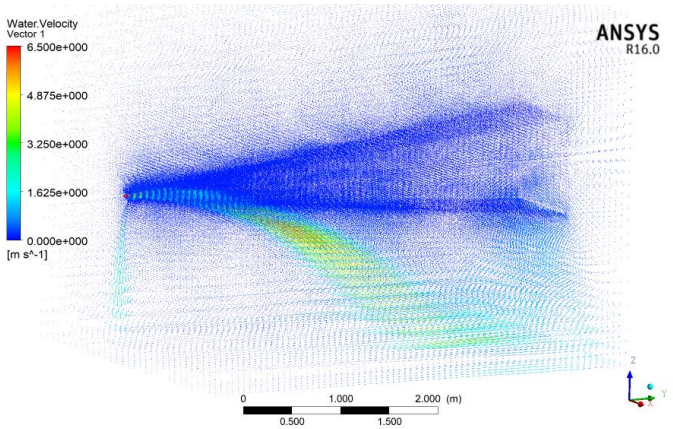


Figure 7 Water velocity vectors

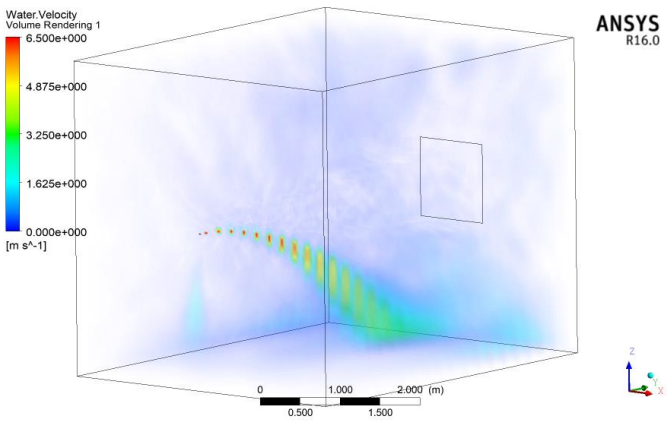


Figure 8 Water velocity volume rendering

B. *Case 2: In this case, a simple inlet was placed and we used the Volume of Fluid (VOF) method to capture the interaction of sneeze with air inside the room. In this case, the ventilation source was placed in form of the window. The flow entered the domain interacted with the air and came out due to the presence of a ventilation source*

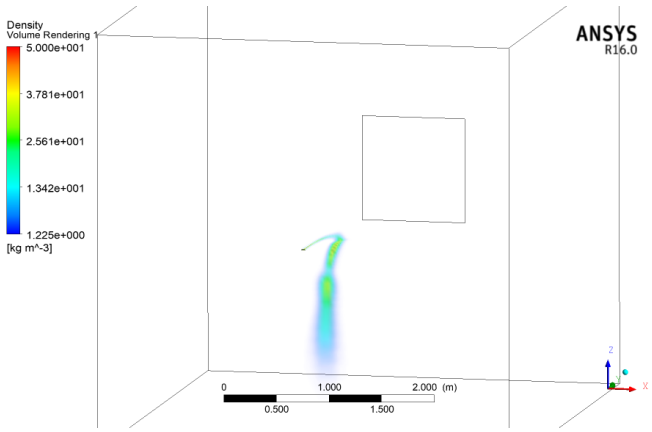


Figure 9. Density volume rendering

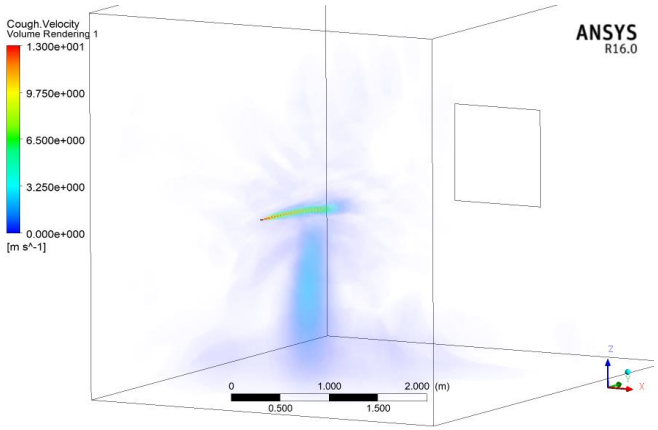
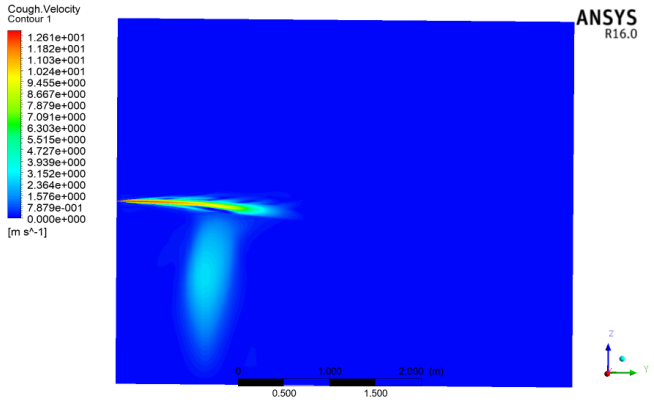


Figure 10 Volume rendering of cough velocity



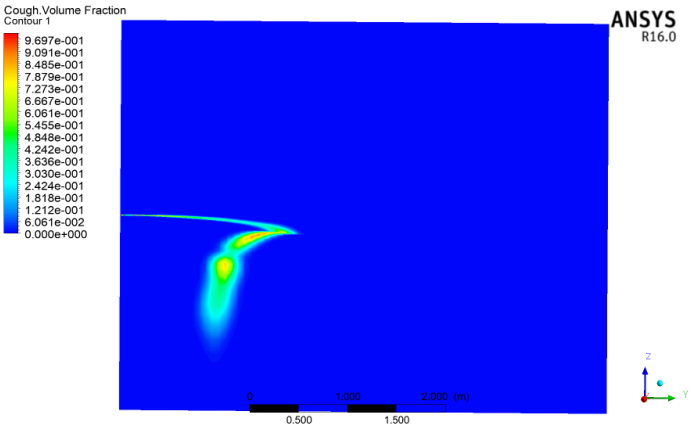


Figure 13 Volume fraction of cough

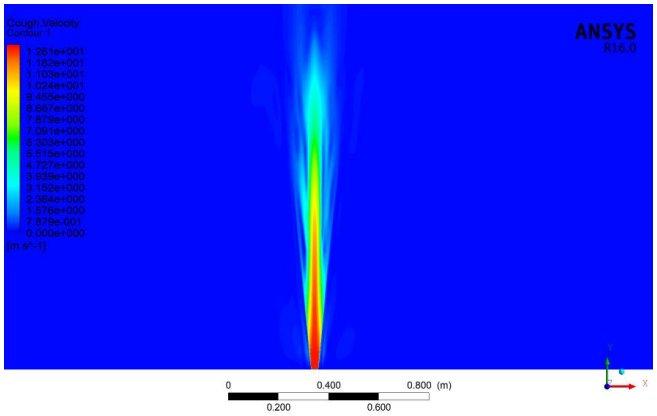


Figure 11 Contour of cough velocity top view

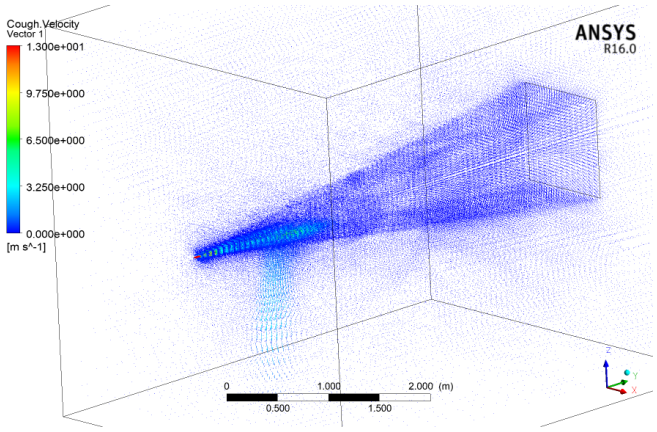


Figure 12 Vectors of cough velocity

C. Case 3

In this case, we used a fan as the ventilation source. The velocity was given to the fan. This case includes further two analyses. In the first analysis, the velocity of the fan was set as 5 m/s. In this case, the volume of fluid method is used to capture the phase interactions.

The results of both cases are presented in this section of the report.

1) Fan velocity 5 m/s

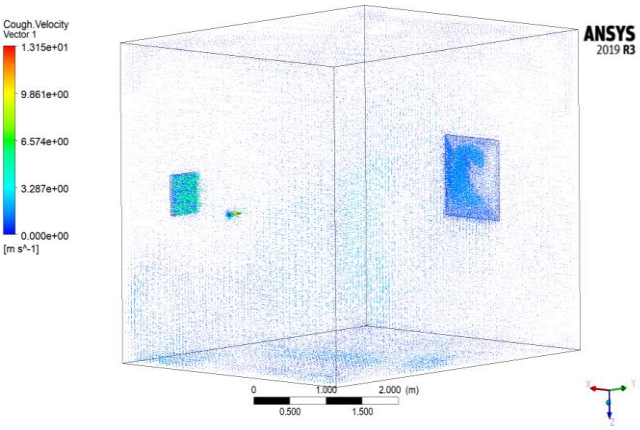


Figure 14 Vectors of cough velocity

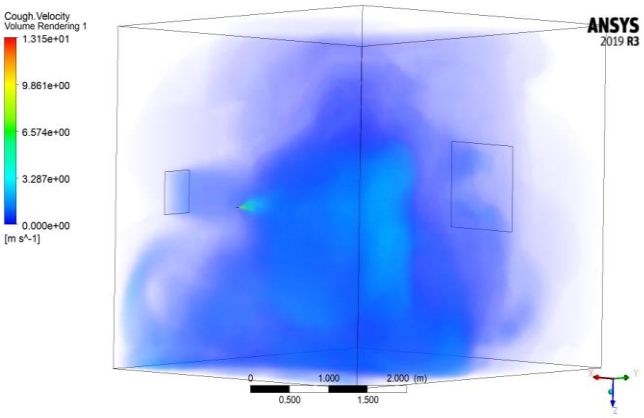


Figure 15 Volume rendering of cough velocity

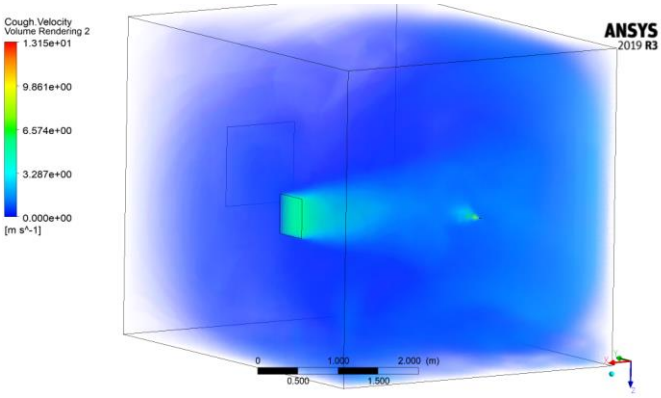


Figure 16 Volume rendering of cough velocity with air velocity

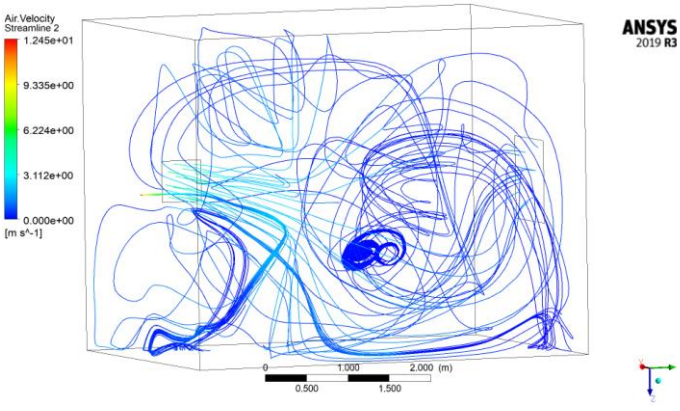


Figure 17 Velocity streamlines of cough and air flow

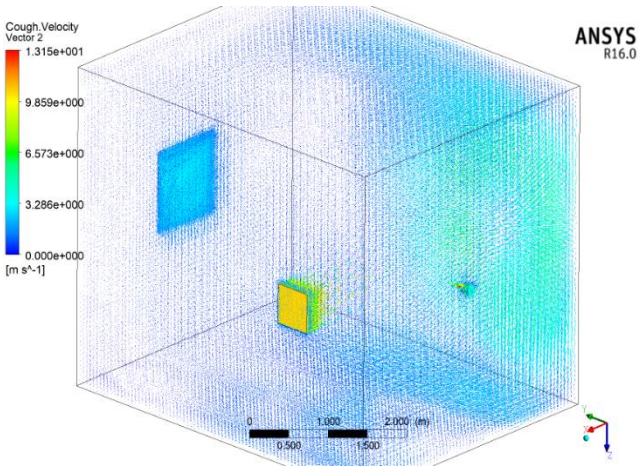


Figure 18 Vectors of cough and air velocity

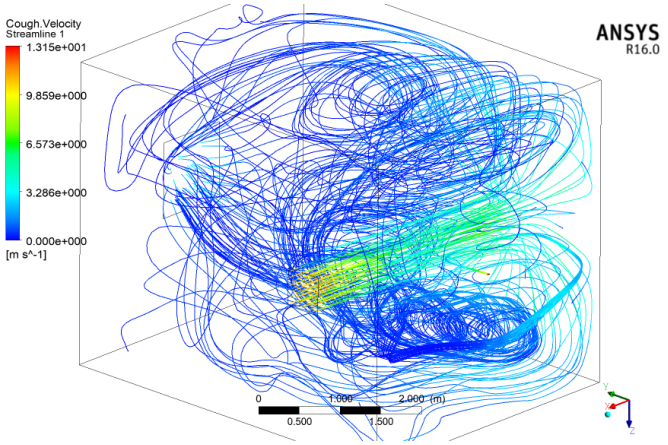


Figure 19 Velocity streamlines of cough and air velocity

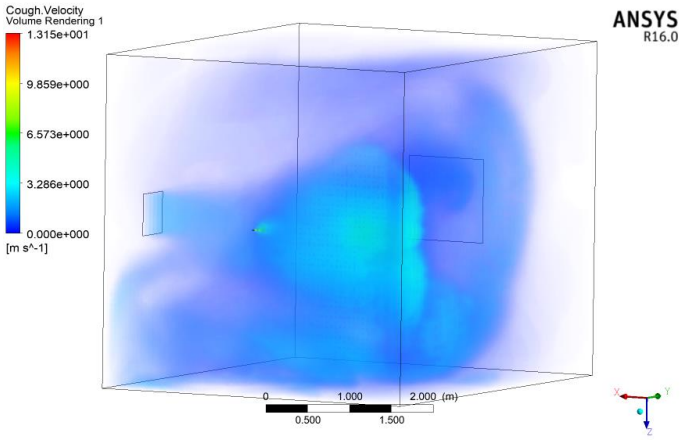


Figure 20 Volume rendering of cough velocity

D. Case 4

Fan velocity 10 m/s

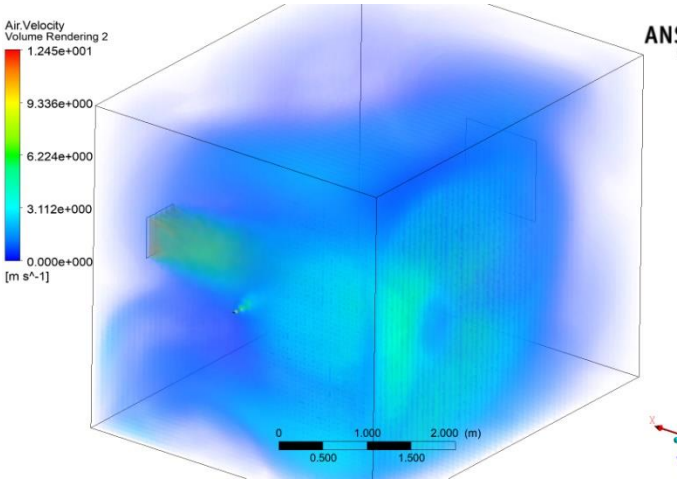


Figure 21 Volume rendering of air velocity

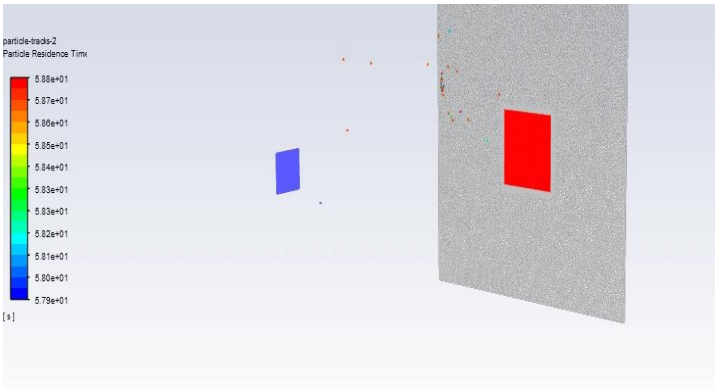


Figure 24 Screenshot at last time step

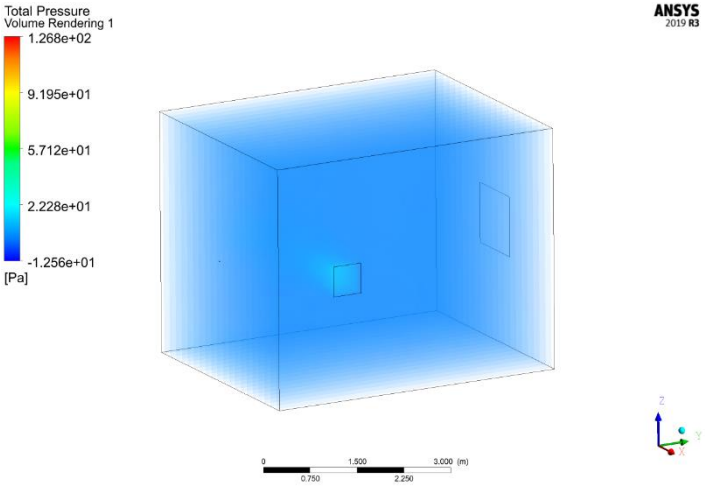


Figure 25 Total pressure-volume rendering

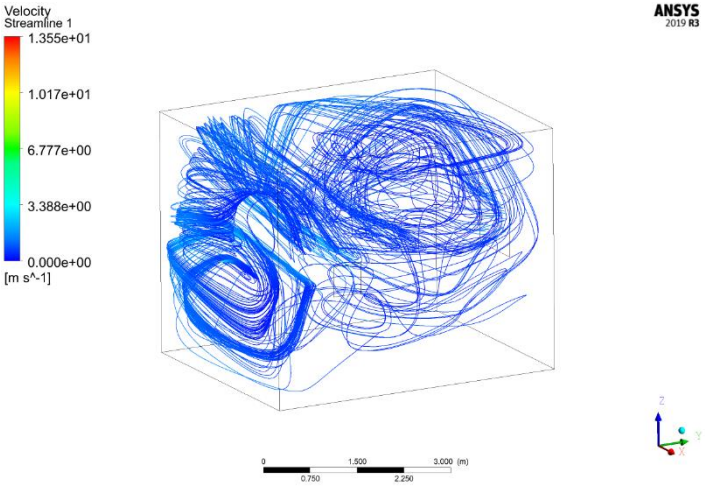


Figure 26 Velocity streamlines

E. Case-5

In this case, the fan has been working at 5m/s speed to carry the cough particles outside the room, below has been shown the particle at different time steps, this simulation is transient.

In the upcoming cases, the DPM technique is used to capture interactions. In this case, the fan has been working at 5m/s speed to carry the cough particles outside the room, below has been shown the particle at different time steps, this simulation is transient

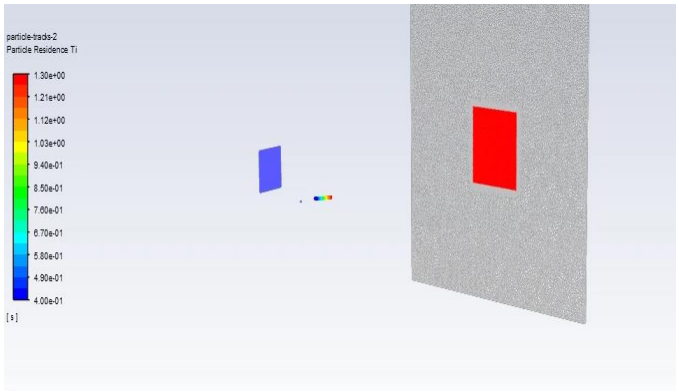


Figure 22 Screenshot at Initial time step

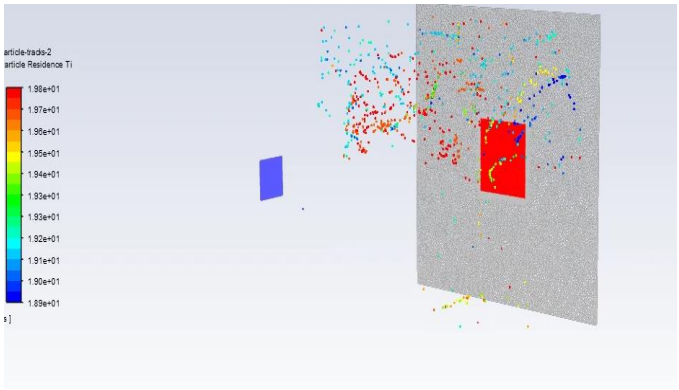


Figure 23 Screenshot at middle time step

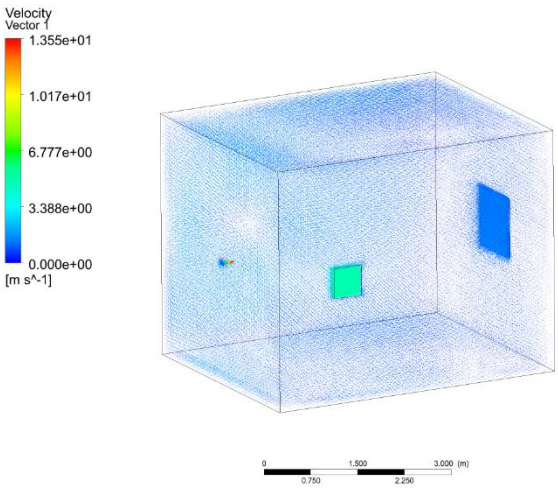


Figure 27 Velocity vectors

F. Case-6

In this case, the fan has been working at 10 m/s speed to carry the cough particles outside the room, below has been shown the particle at different time steps, this simulation is transient.

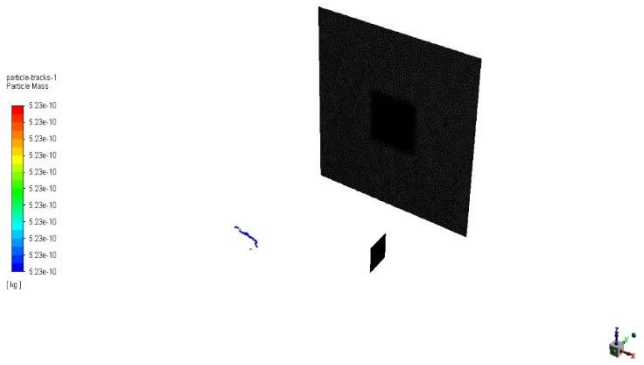


Figure 28 Screenshot at Initial time step

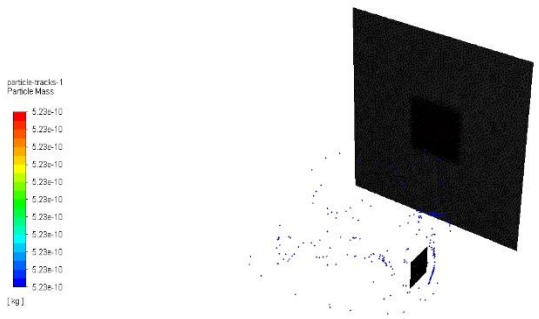


Figure 29 Screenshot at middle time step

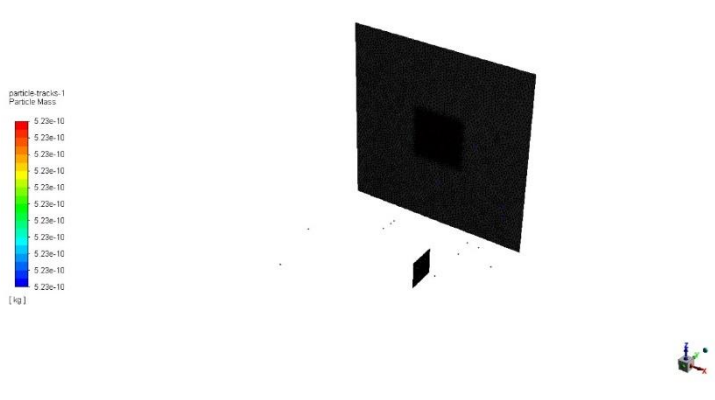


Figure 30 Screenshot at last time step

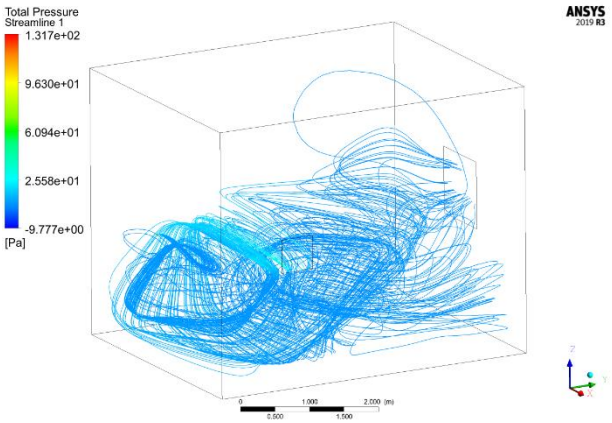


Figure 31 Total pressure Streamlines

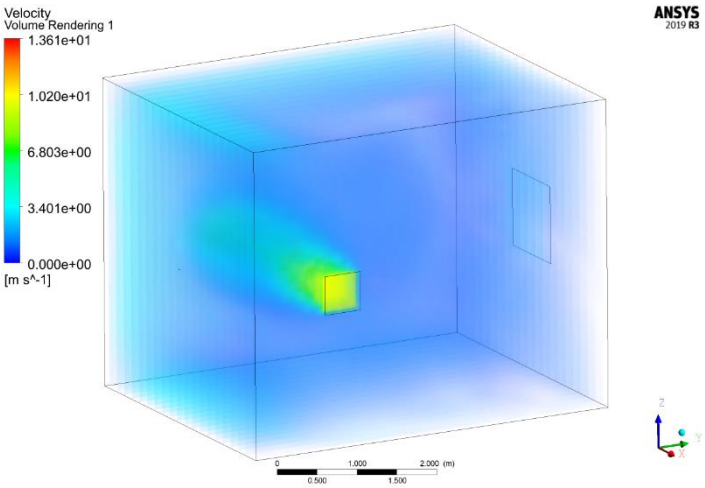


Figure 32 Velocity volume rendering

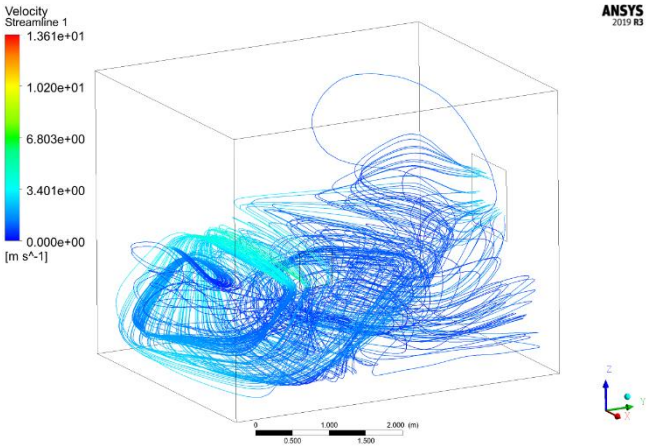


Figure 33 Velocity streamlines

G. Case-7

In this case, the exhaust has been working instead of a simple fan to carry the cough particles outside the room, below has been shown the particle at different timesteps, this simulation is transient. The speed of exhaust is high in this case 10 m/s)

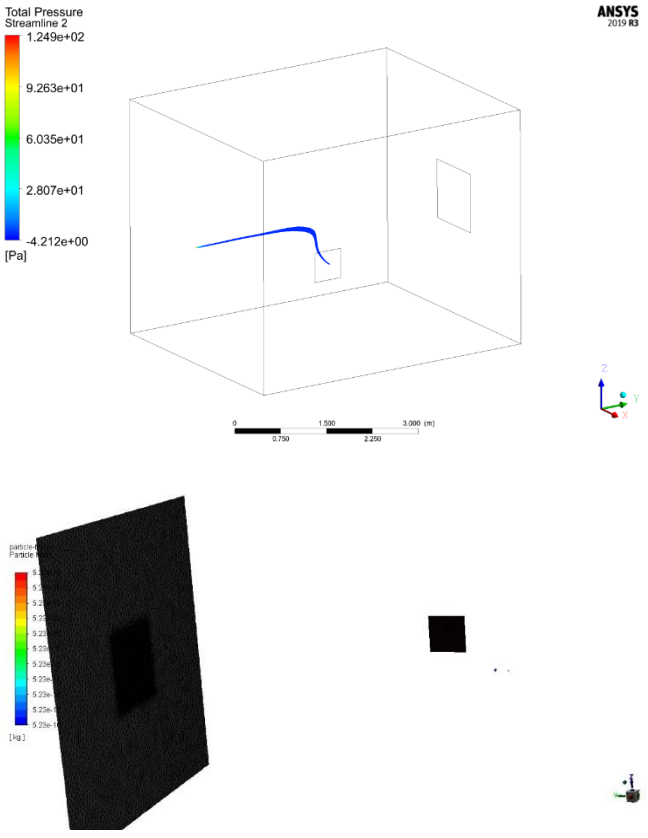


Figure 34 Screenshot at Initial time step

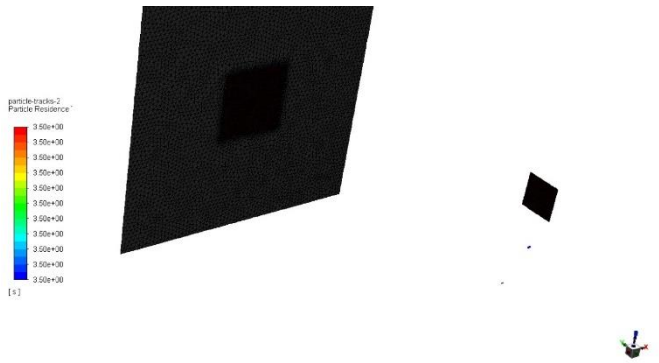


Figure 35 Screenshot at middle time step

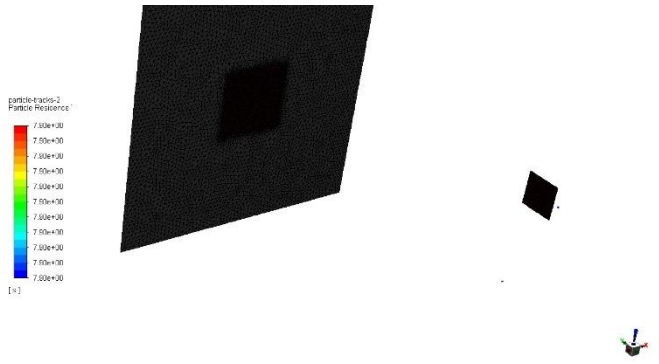


Figure 36 Screenshot at last time step

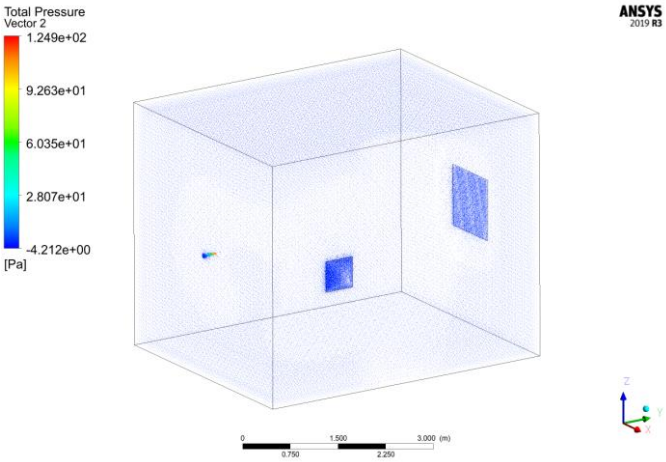


Figure 37 Total pressure vectors

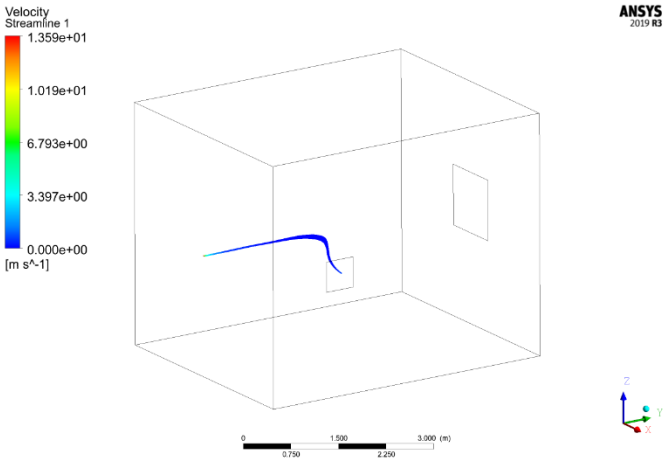


Figure 38 Velocity streamlines

H. Case-8

In this case, the exhaust has been working instead of a simple fan to carry the cough particles outside the room, below has been shown the particle at different timesteps, this simulation is transient.
The speed of exhaust is low in this case (approx. 5 m/s)

The speed of exhaust is low in this case (approx. 5 m/s)

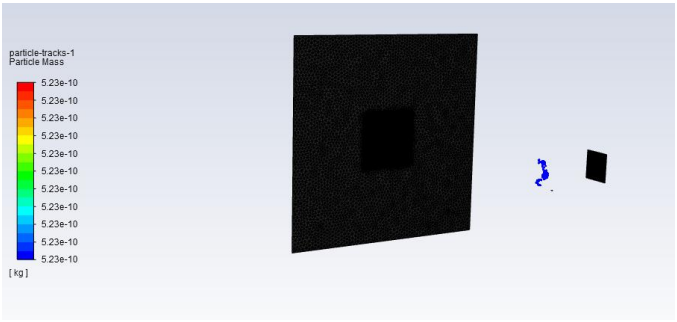


Figure 39 Screenshot at Initial time step

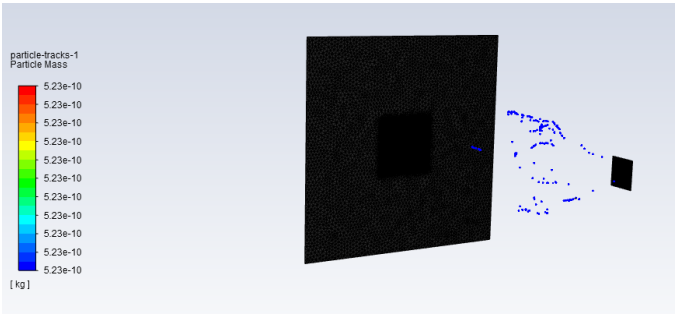


Figure 40 Screenshot at middle time step

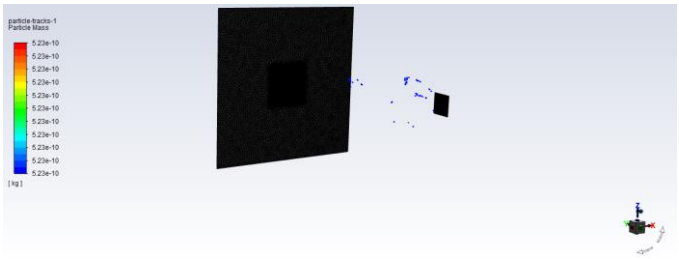


Figure 41 Screenshot at last time step

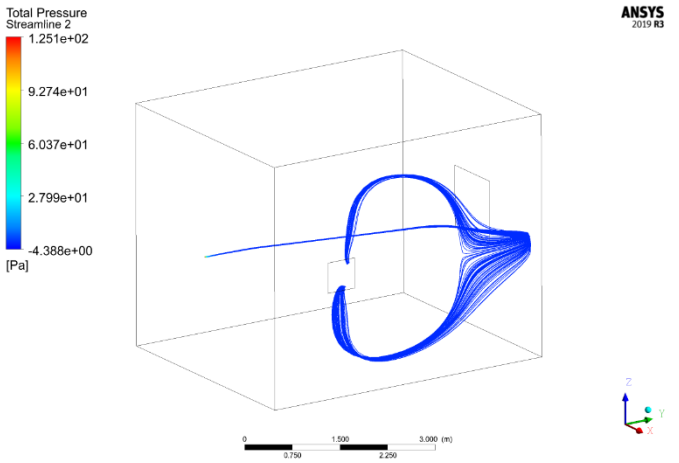


Figure 42 Total pressure Streamlines

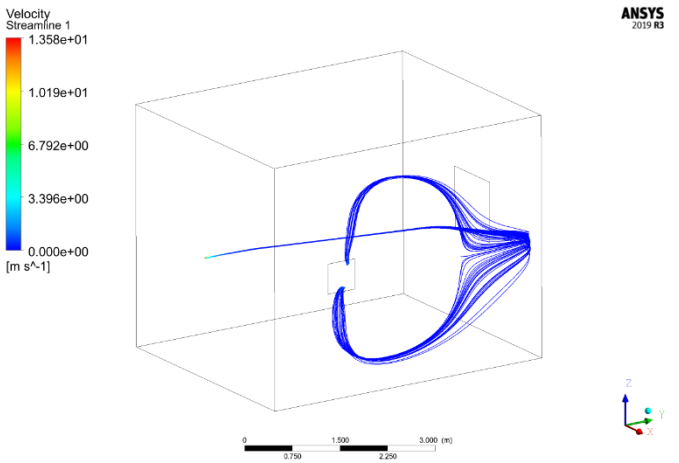


Figure 43 Velocity streamlines

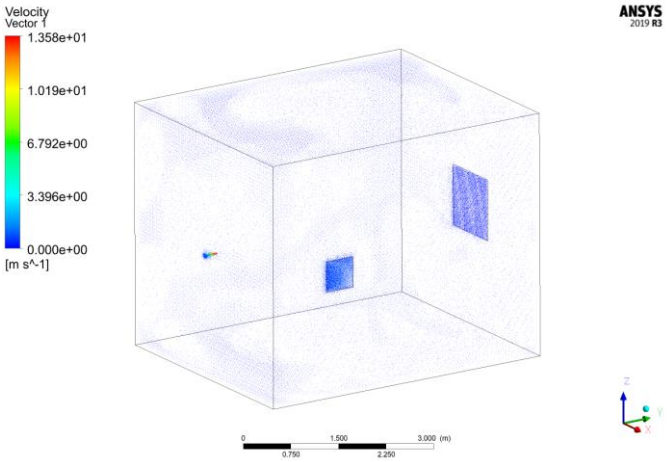


Figure 44 Velocity vectors

I. *Case-9*

In this case, a simple fan has been working to carry the cough particles outside the room, below has been shown the particle at different time steps, this simulation is transient.
The speed of exhaust is high in this case (approx. 10 m/s). The main change, in this case, is the location of the fan, which is now at the top of the room instead of on the wall.

The speed of exhaust is low in this case (approx. 10 m/s), in this case, the location of exhaust has been shifted from wall to bottom of the room.

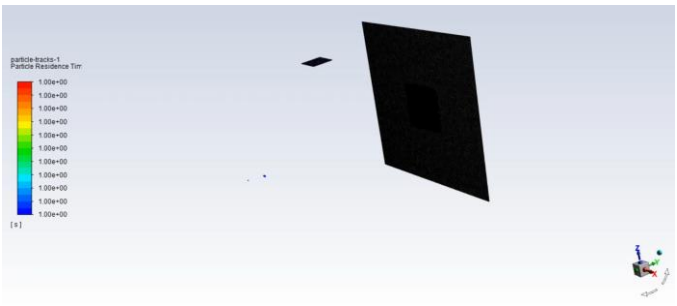


Figure 45 Screenshot at Initial time step

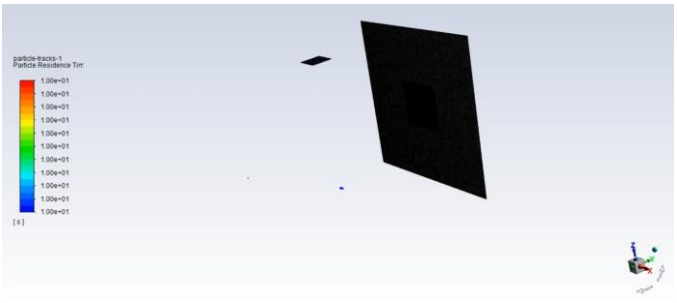


Figure 46 Screenshot at middle time step

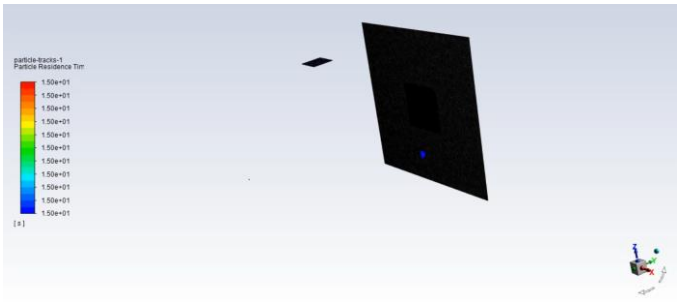


Figure 47 Screenshot at last time step

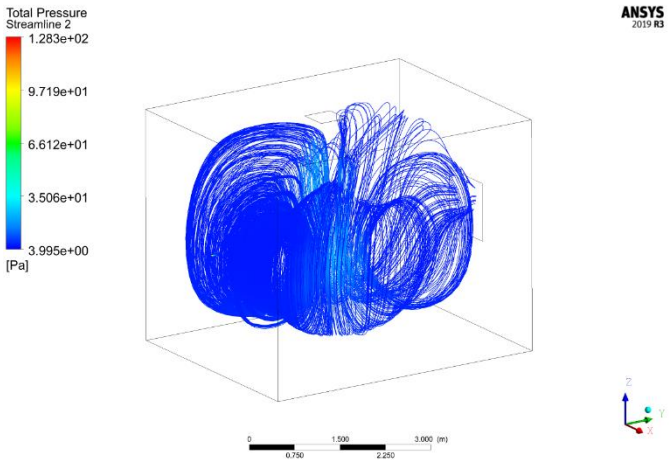


Figure 48 Total pressure Streamlines

vectors

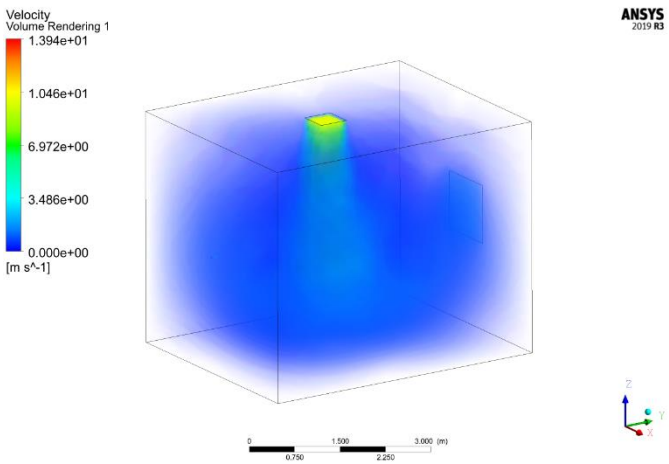


Figure 49 Velocity volume rendering

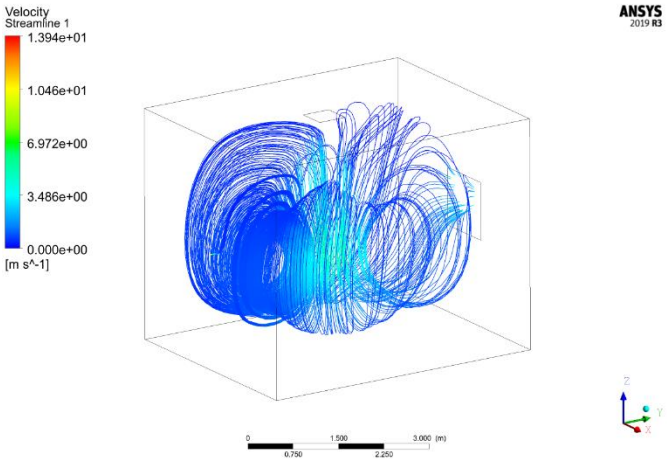


Figure 50 Velocity streamlines

J. *Case-10*

In this case, the exhaust has been working instead of a simple fan to carry the cough particles outside the room, below has been shown the particle at different time steps, this simulation is transient.

The speed of exhaust is low in this case (approx. 10 m/s), in this case, the location of exhaust has been shifted from wall to bottom of the room.



Figure 51 Screenshot at Initial time step

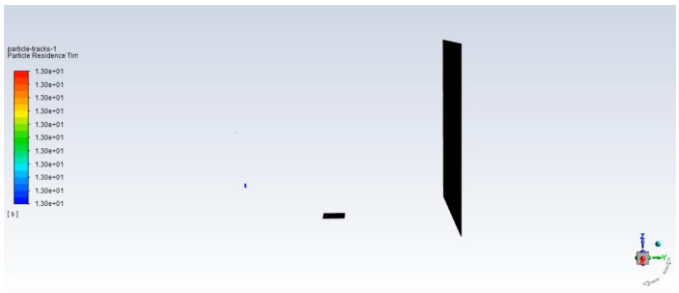


Figure 52 Screenshot at middle time step



Figure 53 Screenshot at last time step

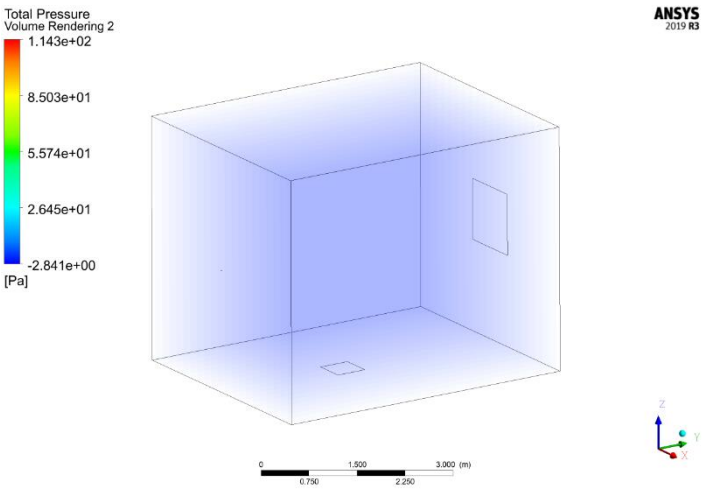


Figure 54 Total pressure-volume rendering

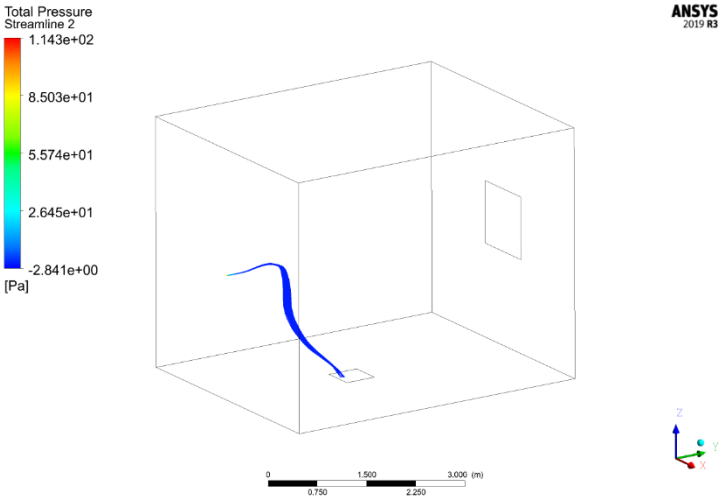


Figure 55 Total pressure Streamlines

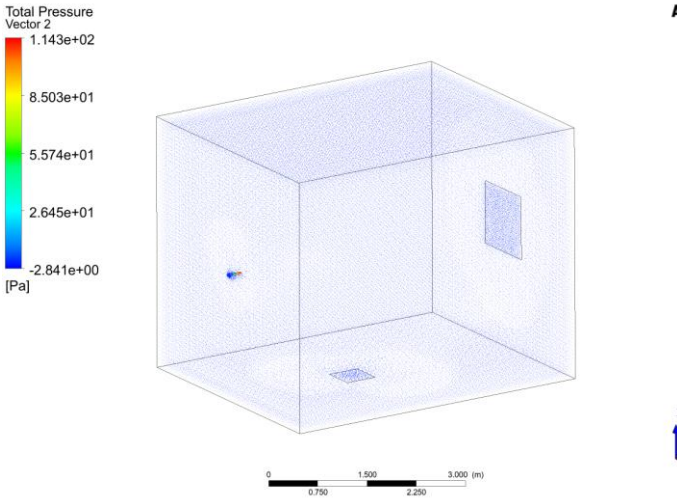


Figure 56 Total pressure vectors

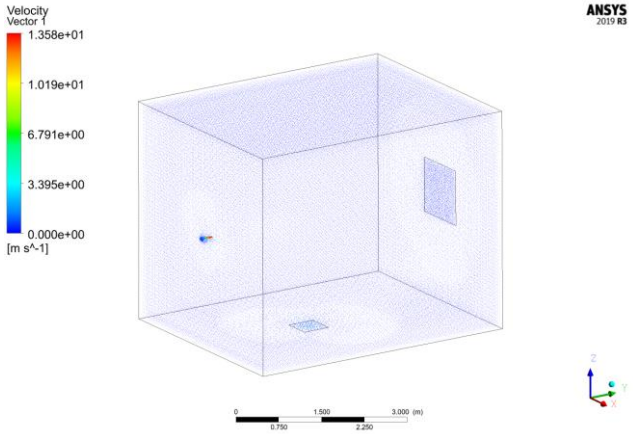


Figure 59Velocity vectors

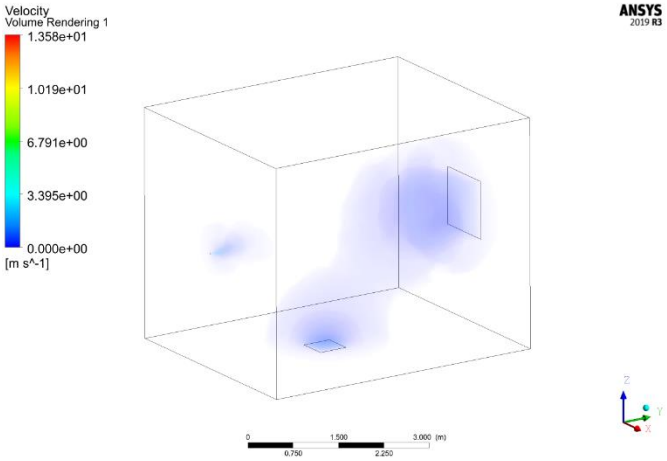


Figure 57 Velocity volume rendering

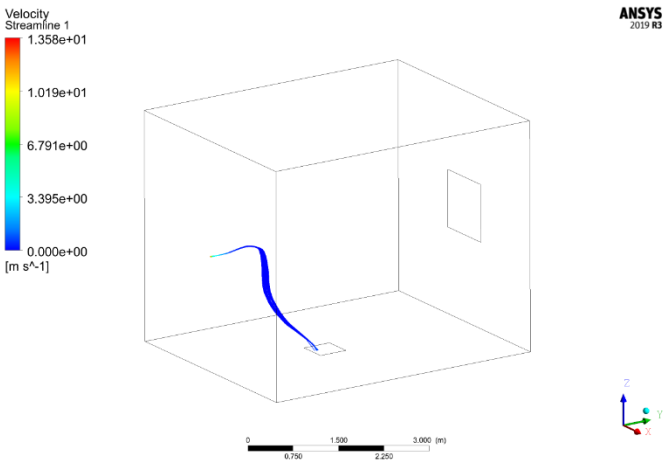


Figure 58 Velocity streamlines

VI. Discussion of Results

The above results show that different cases take different times to remove cough and sneeze particles from the room. An effective ventilation system takes minimum time to remove maximum germs from the room while the least efficient design will more time. Table 1 shows the summary of the result of all cases.

Results show that case 1 takes the most time to remove the germs from the room. Case 1 was the simple analysis of cough without ventilation source, without any ventilation system it takes a large amount of time to remove the germs particles. The 2nd and 3rd cases were the steady-state analysis of cough with ventilation source at velocity 5 m/s and 10 m/s respectively. It is shown that with an increase in the inflow velocity the time to remove the germs is decreasing. But in these cases, the ventilation source was a window only. The germs came out of the room through a window. Hence, a large amount of time is taken here too. In the 4th and 5th cases there is a presence of the fan. The trend is the same, as we increase the velocity of the fan the time is reducing from 75 to 55 seconds only. But in this case, the ventilation source was a fan. In the 6th and 7th cases we changed the ventilation source to an exhaust. They are the transient flow analysis of cough with exhaust at velocities using the Discrete Phase Method (DPM). The trend was the same again as we increase the velocity the time to remove the germs was reduced. The results till now showed that the best case was to use a ventilation source using the exhaust is the best-case scenario. The best thing to optimize was the location of the ventilation source. For this, two more cases were simulated, one with the ventilation source above the room and the other with a ventilation source below the room. The ventilation source, the exhaust were placed at the roof and flow of the room. Case 8th shows that the case in which the ventilation source is at the roof. The results showed the sneeze particles enter inside the room and due to ventilation at the top the particles spread inside the room. This is dangerous in the current situation of Covid, we must make the ventilation system such that the spread does not affect the people inside the room. Hence, the last case was created in which the ventilation source was at the bottom. The particles enter the room and leave the room from the ventilation source in 15 seconds. This was the most optimized design for the ventilation system which takes a small amount of time to remove the germs with the least spread. The results obtained were according to the literature.

TABLE 1: RESULT COMPARISON OF ALL 10 CASES OF CFD SIMULATIONS HAVING DIFFERENT VENTILATIONS VELOCITIES AND LOCATIONS

Variables	**Case 1**	**Case 2**	**Case 3**	**Case 4**	**Case 5**	**Case 6**	**Case 7**	**Case 8**	**Case 9**	**Case 10**
Ventilation	No	5 m/s with window only	5 m/s with window and fan	10 m/s with window and fan	5m/s with fan	10 m/s with fan	10 m/s with exhaust	5 m/s with exhaust	10 m/s with fan on roof	10 m/s with exhaust on bottom
Type of ventilation	None	Only window	Window and fan	Window and fan	Window and Fan	Window and Fan	Window and Exhaust	Window and Exhaust	Window and Fan	Window and Exhaust
Position of fan/exhaust	-	-	-	-	Wall	Wall	Wall	Wall	Roof	Floor
Time to get room clean (average)	Didn't get clean	250 seconds	200 seconds	200 seconds	75 seconds	55 seconds	20 seconds	35 seconds	40 seconds	15 seconds

VII. Conclusion

This research uses CFD simulation analysis to study the spatial spread of cough and sneeze droplets in a confined room. The project was aimed at designing and modeling an effective ventilation system for a small room. Different cases were selected based on different locations of exhausts and different exhaust velocities. It was observed that when there was no ventilation source, the cough spread in the room and then was settled on the ground in the room. But when a ventilation source (fan) was introduced, the cough particles merged with the airflow and exited the room through the outlet. As the velocity of the fan was increased, it was observed that the number of cough particles exiting the room through the outlet increased. The results obtained show that the cough comes out from the velocity inlet. The volume fractions show the actual path taken by the cough, the velocity vectors show that the germs in the cough come down due to gravity and gather at the lower surfaces. This is clearly shown in the volume rendering part. The velocity is high as it comes out of the mouth. It decreases over time and due to gravity, it settles down. The velocity vectors show the path taken by the cough. The showed that the case with the ventilation source exhaust with a velocity of 10 m/s and placed at the bottom is the most optimized ventilation system.

REFERENCES

[1] X. Gao, J. Wei, H. Lei, P. Xu, B. J. Cowling, and Y. Li, "Building ventilation as an effective disease intervention strategy in a dense indoor contact network in an Ideal City," *PLoS One*, vol. 11, no. 9, pp. 1–20, 2016, doi: 10.1371/journal.pone.0162481.

[2] Y. Li *et al.*, "Role of ventilation in airborne transmission of infectious agents in the built environment - A multidisciplinary systematic review," *Indoor Air*, vol. 17, no. 1, pp. 2–18, 2007, doi: 10.1111/j.1600-0668.2006.00445.x.

[3] T. Jefferson *et al.*, "Physical interventions to interrupt or reduce the spread of respiratory viruses: Systematic review," *BMJ*, vol. 339, no. 7724, p. 792, 2009, DOI: 10.1136/bmj.b3675.

[4] R. Tellier, "Review of aerosol transmission of influenza A virus," *Emerg. Infect. Dis.*, vol. 12, no. 11, pp. 1657–1662, 2006, DOI: 10.3201/eid1211.060426.

[5] B. J. Cowling, Y. Zhou, D. K. M. Ip, G. M. Leung, and A. E. Aiello, "Face masks to prevent transmission of influenza virus: a systematic review," *Epidemiol. Infect.*, vol. 138, no. 4, pp. 449–456, 2010, DOI: 10.1017/S0950268809991658.

[6] A. D. LANGMUIR, "Epidemiology of airborne infection.," *Bacteriol. Rev.*, vol. 25, pp. 173–181, 1961, DOI: 10.1128/mmbr.25.3.173-181.1961.

[7] R. L. Kitching, "Air-borne Infection," *Br. Med. J.*, vol. 2, no. 4485, pp. 965–966, 1946, DOI: 10.1136/bmj.2.4485.965-b.

[8] C. B. Beggs, S. J. Shepherd, and K. G. Kerr, "Potential for airborne transmission of infection in the waiting areas of healthcare premises: Stochastic analysis using a Monte Carlo model," *BMC Infect. Dis.*, vol. 10, pp. 1–8, 2010, DOI: 10.1186/1471-2334-10-247.

[9] C. J. Noakes and P. Andrew Sleigh, "Mathematical models for assessing the role of airflow on the risk of airborne infection in hospital wards," *J. R. Soc. Interface*, vol. 6, no. SUPPL. 6, 2009, DOI: 10.1098/rsif.2009.0305.focus.

[10] S. Bhattacharyya, K. Dey, A. R. Paul, and R. Biswas, "A novel CFD analysis to minimize the spread of COVID-19 virus in a hospital isolation room," *Chaos, Solitons and Fractals*, vol. 139, p. 110294, 2020, DOI: 10.1016/j.chaos.2020.110294.

[11] S. Peng, Q. Chen, and E. Liu, "The role of computational fluid dynamics tools on investigation of pathogen transmission: Prevention and control," *Sci. Total Environ.*, vol. 746, p. 142090, 2020, DOI: 10.1016/j.scitotenv.2020.142090.

[12] Mariam *et al.*, "CFD Simulation of the Airborne Transmission of COVID-19 Vectors Emitted during Respiratory Mechanisms: Revisiting the Concept of Safe Distance," *ACS Omega*, vol. 6, no. 26, pp. 16876–16889, 2021, DOI: 10.1021/acsomega.1c01489.

[13] L. Bourouiba, "The Fluid Dynamics of Disease Transmission," *Annu. Rev. Fluid Mech.*, vol. 53, pp. 473–508, 2021, DOI: 10.1146/annurev-fluid-060220-113712.

[14] L. Morawska and J. Cao, "Airborne transmission of SARS-CoV-2: The world should face the reality," *Environ. Int.*, vol. 139, no. April, p. 105730, 2020, DOI: 10.1016/j.envint.2020.105730.

[15] J. Gralton, E. Tovey, M. L. McLaws, and W. D. Rawlinson, "The role of particle size in aerosolised pathogen transmission: A review," *J. Infect.*, vol. 62, no. 1, pp. 1–13, 2011, DOI: 10.1016/j.jinf.2010.11.010.

[16] J. Redrow, S. Mao, I. Celik, J. A. Posada, and Z. gang Feng, "Modeling the evaporation and dispersion of airborne sputum droplets expelled from a human cough," *Build. Environ.*, vol. 46, no. 10, pp. 2042–2051, 2011, DOI: 10.1016/j.buildenv.2011.04.011.

[17] S. Shao *et al.*, "Risk assessment of airborne transmission of COVID-19 by asymptomatic individuals under different practical settings," *J. Aerosol Sci.*, vol. 151, no. September 2020, p. 105661, 2021, DOI: 10.1016/j.jaerosci.2020.105661.

[18] M. R. Pendar and J. C. Páscoa, "Numerical modeling of the distribution of virus carrying saliva droplets during sneeze and cough," *Phys. Fluids*, vol. 32, no. 8, 2020, doi: 10.1063/5.0018432.

Development Of Low Cost Wind Tunnel For Measuring Lift & Drag

Hira Aftab
Institute of Aviation studies
University of Management & Technology Lahore, Pakistan
hira.aftab97@gmail.com

Beenish Batul
Institute of Aviation Studies
University of Management & Technology Lahore, Pakistan
beenish.batul@umt.edu.pk

Abstract-- The wind tunnel helps in understanding of complex fluid flows. Although commercial wind tunnels are only limited to industries and exclusive institutions, this paper discusses the development of low cost subsonic open circuit wind tunnel for educational-purposes. The aim is to develop an open circuit wind tunnel with 0.03 Mach to meet the Reynold number of 6.4 × 10^4. For generating flow, nine electrical fans were used at the diffuser end, and honey comb structure was made by plastic straws at the contraction cone for creating laminar flow. For providing the visibility of the airflow, smoke system was introduced which comprises of fog machine and reservoir. Moreover, six copper tubes were attached ahead of test section for converting smoke into linear pattern. For experimentation, wooden airfoil of NACA 0012 was used with chord of 0.1092m and a wing span of 0.17m having pressure taps inside airfoil chord wise. For measuring data, digital manometer were attached to pressure ports on the airfoil, so the readings taken from sensors are used for calculating lift and drag. Then, quantitative measurements of lift and drag were compared with published literature.

Keywords— Wind tunnel, Reynolds number, airfoil, lift, drag, manometer, subsonic

I. INTRODUCTION

A wind tunnel (WT) is an instrument used for experimenting with the airflow stream over an object. It provides a cheaper way of airflow profile testing over different bodies including the calculation of the aerodynamic forces both in industries and also for research. The wind tunnel has three parts. The First part is the intake which is mostly like a divergent-convergent duct. This is accompanied by the straight tunnel that is the second part of it. Likewise, the third part is inverse of the first part made of a converging-diverging nozzle tunnel. Wind tunnels ease the testing of scale models of ships, aircraft, and vehicles in the basic understanding of fundamentals of aerodynamics. Moreover, wind testing is effective as it allows the improvement of scale models of changing the profile to reduce lift and drag coefficient and also reduce fuel consumption. Wind tunnel also helps in material testing specifically in the estimation of the fatigue life. Some wind tunnels are large enough that it allows the testing of the entire aircraft. Different wind tunnels have different in-built functions. Some are operable by digital sensors and some by load cells. The medium that provides forces and helps in testing is either air or fluid that passes over the object and sensor measured the required values.

The development of WTs gave researchers an practical idea of how flows perform. Wind tunnels are classified in different ways. Classification is based on operational flow regimes. The Reynolds number is used for the classification of incompressible flow. Mach number and Reynolds number are both used for the classification of compressible flow. Generally, there are two types of wind tunnel, that are OCWT (Open Chamber Wind Tunnel) and CCWT (Close Chamber Wind Tunnel). Further, they are categorized into four different types based on the speeds they can produce. These four WTs are named subsonic, transonic, supersonic, and hypersonic wind tunnels. The purpose of testing any model in the wind tunnel is the data validation of the results obtained from the relevant model and full scale. Practically wind tunnel is classified by its size. For a low-speed wind tunnel having Mach< 0.3 the test section dimensions must be less than 1m*1m. In the same way, WT is classified according to different applications, either used to checking forces or for checking ice formation. (Barlow, Rae, and Pope, 1999). Different calculations can be taken from the wind tunnel by using different methods. Calculations include finding forces acting on the wind tunnel. Checking the characteristics of boundary layer separation. Also different types of ice formulation and how ice formation can be prevented can be checked.

The wind tunnel (UMT wind tunnel) discussed in this paper is a low cost, open chamber wind tunnel that is used for educational purposes. The wind tunnel is developed for measuring aerodynamic forces. The wind tunnel is operable at a velocity that lies in the subsonic region. For the measurement of aerodynamic forces the test piece used is a small-scale rectangular wing made from the symmetrical airfoil. Different types of sensors are used on WT for taking measurements of air pressure and air velocity. The wind tunnel must be properly sealed for all these measurement. These include an anemometer, pressure sensors like manometer (Louis, 2010)

To measure aerodynamic forces like lift and drag we use a rectangular wing made from NACA 0012 airfoil. The wind tunnel is operable at Reynold number of 6.4*10^4. Nine fans are incorporated that provide the flow of air over the airfoil by suction. The test section is of glass and glass protector used on it for checking the angle of attack of the airfoil. Aerodynamic forces of lift and drag can be measured by using pressure tabs with a manometer The specific formulas of lift and drag are taken from the book of Anderson's Fundamentals of Aerodynamics. The values could be extracted by using the integration of the coefficient of pressure.

II. LITERATURE

Wind tunnel testing is predominant in aerodynamics and also aeromechanics. Wind tunnel experimental analysis of the lift, drag, boundary, velocity, moment and pressure distribution plays significant role in fluid mechanics theory. These factors have remarkable role in performance of the aircraft. All these factors are important in designing, for increasing the fuel economy of the automobile or of aircraft and also in the teaching basic aerodynamic principles. It also helps in

aerodynamic analysis of sting- mounted test models. Wind tunnel provides a way to demonstrate principles of the flight mechanics as well as the application of these in designing. Recent example of the wind tunnel testing is the measurement of the inviscid fluid flow and the mechanical energy losses to wind tunnel design that experiment is done by using instrument for the pressure distribution measurement. For finding values of Cl and Cd a set of equations needed that taken by literature. The work of Abbot et al. helps in the graph of co efficient of lift and the angle of attack. These are used for finding pressure distribution on the airfoil. Uncertainty analysis is done for finding the precision of the used method. The entire testing area is equipped with glass to allow the airflow observation over the entire object. This low speed wind tunnel is equipped with digital manometer that calculates the rate of pressure variation over the entire section. It was found that there is adverse pressure gradient in the direction of air due to the increase of the angle of attack. (Nan, L., 2013).

In 2020, research was done in the mechanical engineering department and technology workshop center of the University of Bagdad to design and construct a low-speed small model of a subsonic wind tunnel. The wind tunnel is designed on a specific set of standard dimensions that could be used for laboratory educational experimentation. It is designed for the calculation of lift, drag, and moment coefficient by using pressure distribution. The flow speed is measured by using a digital flow meter. Floe is generated by using five high-speed fans and these are regulated to control different fan speeds during experiments. Readings were taken after the calculation of the deciding factors. Validation of these results showed accuracy with the theatrical calculated values and it was approved for laboratory experimentation.

Modification to the test section of the wind tunnel is done to improve the visibility and to convert it into the converging duct flow. The wind tunnel is incorporated with the smoke rake and a low-cost lightning system (low power laser-based) for improving the visibility of the airflow over the object. The paper illustrated different ways of wind tunnel testing by using cheap materials along with the best airflow visibility through a smoke rake injection system. The smoke visualization helps in detecting inviscid streamline airflow and the boundary layer separation

III. Working Principle of WT

WT working principle is on the Bernoulli's principle and continuity equation.

A. *Continuity law:*

The principle of continuity or equation of continuity, the principle of the fluid procedure, in short, defines the flow in the time volume minus what the stream from the volume must accumulate in this volume. This principle is the result of the law of conservation of mass. This equation fully describes the behavior of fluid motion, plus the second equation based on Newton's law of motion, and the 3rd equation created on energy saving. Engineeringtoolbox.com. (2019) Aplusphysics.com. (2019).

Fluid flow rate = A*v
A1v1 = A2 v2

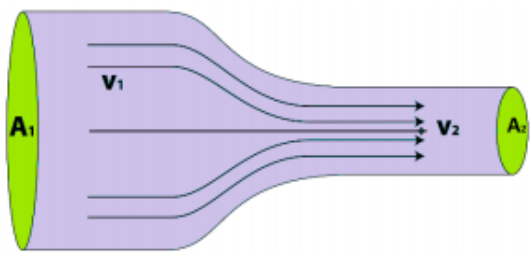


Fig. 1. Continuity for Fluids *Courtesy by nuclear-power.net*

B. *Bernoulli's law:*

Bernoulli's law (Fig. 2) can be seen as a declaration of the conservation of energy principle applicable for fluids flowing whose equation is shown below. Scienceworld.wolfram.com. (2019).

$P + ½ \rho v^2 + \rho g h = \text{constant}$
As $P_1 + ½ \rho v1^2 + \rho g h_1 = P_2 + ½ \rho v2^2 + \rho g h_2$

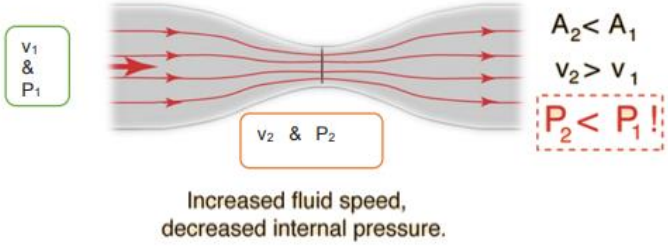


Fig. 2. Bernoulli's law *Courtesy by math.stackexchange.com*

IV. Wind Tunnel Design

In OCWT, there is an exhaust and intake. The open type of WT is the easiest and inexpensive to construct. In open-type WTs, the air is discharged directly into the workshop and is usually recycled in the workshop before investment, although some wind tunnels use compressed gas sources. There are two basic sorts of OCWTs. (i) Blower, (ii) Suck down. The easiest way to distinguish between the two basic types of WT is the position of the fan. The blower tunnel is most flexible because the fan is located at the entry to the WT; therefore, the test sector can be replaced. Blower type WTs are so tolerant that the outlet diffusers can usually not be there entirely to provide easier contact to test samples and devices, although, this omission usually leads to significant power outages. Suck-down WTs are generally further prone to low-frequency instability in the coming backflow than blowers, although it claims that the suction vortex is less problematical in these types of tunnels because it does not permit the fan section earlier incoming the test. (Iopscience.iop.org, 2020.)
The wind tunnel presented in this paper is OCWT, suction type as shown in Fig. 3.

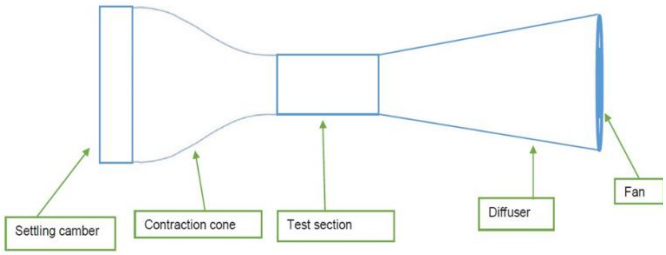


Fig. 3. 2D view of wind tunnel Courtesy by UMT wind tunnel

A. 2D WT measured dimensions

The dimensions of the WT are shown in Fig. 4. There is a curve in the inner side of the contraction cone but not in the diffuser. This is because high-velocity air is required in the test section. As the air is sucked at the honeycomb structure, it passes through the contraction cone before entering the test part. Because of the cure in the contraction cone, the velocity of air is increased and it enters the test section. There is no curve in the diffuser as this section is used as an outlet for the airflow.

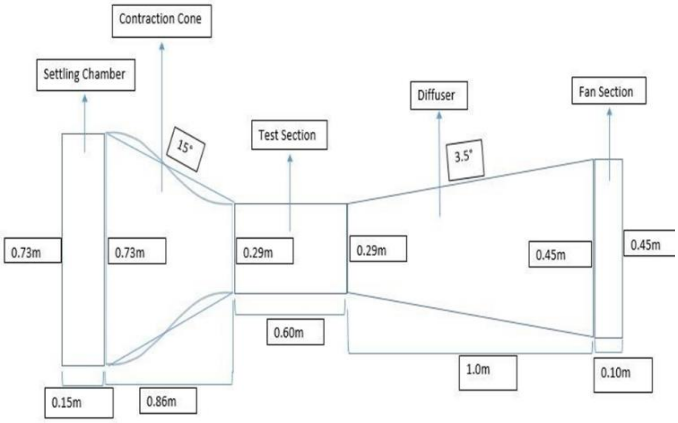


Fig. 4 2D view along the dimensions of wind tunnel Courtesy by UMT wind tunnel

V. Resources for Wind Tunnel Development

Different resources were used in the development of wind tunnel. Three types of wood are required to manufacture all the sections. A high strength wood is required to be used as a main border, a low weight wood is required to be used at the outer sides of border, and a smooth wood is required to be used on the inner sides of border for smooth airflow. For this purpose, different types of woods are analyzed which are discussed below.

A. Wood for main borders

Woods generally used for borders because of their hardness are Oak, Scottish Wood, Tower Burn Wood, and Partal Wood. All these woods are hard and suitable to use for the main borders of any project. However, they have high weight and are expensive as well as they are not easily available in the market except for Partal wood. It has a low weight as compared to others and is readily available in the market. For this reason, Partal wood was used as the main border in this wind tunnel

B. Wood for outer borders

For the outer borders of the wind tunnel, low-weight wood is required with efficient strength. For this purpose, different woods like pine wood, poplar wood, walnut, rosewood, and plywood can be used. However, among these woods, plywood is the basic wood used extensively in all woodworks. So in this project, plywood ash wood is used for the outer sides of the main border.

C. Wood for inner borders

For the inner side of the wind tunnel, smooth wood is required for smooth airflow. For this, different woods like pine boards, oak plywood and fiberboard (MDF) can be used. Pine is a softwood but expansive while the oak plywood becomes heavy for the inner border. Thus, MDF sheets are used for inner borders which are less expansive and commonly used in woodworks.

D. Air Supply by Fans

Air supply to wind tunnel is given by using suction phenomena with the help of using fans. These fans are usually available in size of 0.125m which is suitable to use as it produces enough flow and requires only nine fans to cover the whole area of the fan section (Fig. 5). These fans require low power which in turn create a high suction



Fig. 5. Fan used in Wind Tunnel Courtesy by UMT Wind Tunnel

E. Pipes for honey comb structure manufacturing

It is mandatory to provide a straight airflow inside the wind tunnel. This can only be possible by inserting large amount of round pipes in the honeycomb structure. For this purpose, different types of pipes are available from which Plastic Straws having 6.096mm diameter are selected due to their low weight (Fig. 6).

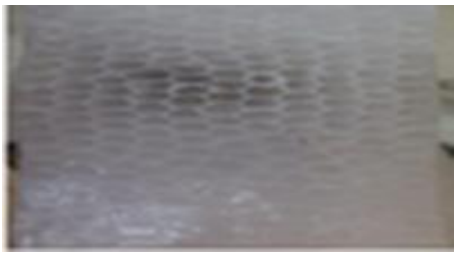


Fig. 6. Pipe straws used for honey comb structure Courtesy by UMT Wind Tunnel

VI. Manufacturing of Wind Tunnel

After all the sections of the wind tunnel are manufactured separately, they are integrated successfully. These sections

are joined with each other with the help of clamps, in such a way that the honeycomb structure is attached to the contraction cone. The contraction cone is attached to the test section, the test section is further joined with the diffuser, and finally, the fan section is fitted with the diffuser. The wind is finally painted to prevent them from changing the environment and then placed on the stand. In Fig. 7, the unpainted integrated WT is shown.



Fig. 7. Wind tunnel in integrated form Courtesy by UMT Wind Tunnel

VII. Modification of Wind tunnel

Further modifications were done in the wind tunnel to improve its performance and taking measurements. These include sealing of connecting joints, incorporating airflow visualization, sensors installation, and lift and drag measurement.

A. Sealing of open joints

Sealing is done to avoid pressure loss for the measurement of lift and drag. The wind tunnel has openings in the joints that cause air leakage due to which aerodynamic forces cannot be measured accurately. (Affix. 2019). BISON silicon-based sealant is used for WT joints sealing. It can seal air and maintain pressure inside the wind tunnel the sealant is applied on the joint openings with the help of a gun.

B. Airflow Visualization

Modification of wind tunnel test section is done by installation of smoke flow duct in the exit section of contraction section to visualize airflow over the airfoil. The smoke visualization duct can display inviscid flow over the object (airfoil) and separation of the boundary layer in the test section. A smoke duct is designed to see the smooth flow of air, the smoke collected in the reservoir, and ducts discharge a bunch of uniform smoke in the entry section of the test section, in the direction against the nozzle or diffuser model. The whole airflow in the test section brings out the boundary layer separation and the desire internal flow. A duct attached to the reservoir and smoke ducts; supplies smoke to the duct. The fans in the wind tunnel suck smoke from the duct and visualize the flow of air over the object.

Smoke system is designed for improving airflow visibility. The design of the system is shown in Fig. 8, smoke rake for flow visualization is shown in Fig. 9.

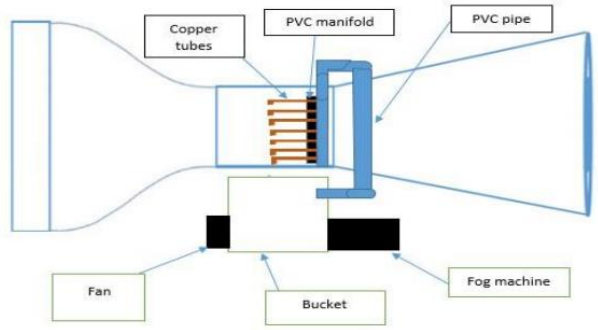


Fig. 8. Design of smoke system used in WT- Courtesy by UMT wind tunnel.



Fig. 9. Smoke Rake Courtesy by UMT wind tunnel



Fig. 10. Smoke system on wind tunnel Courtesy by UMT wind Tunnel

C. Sensors

For the measurement of aerodynamic forces dynamic pressure and speed is required. In today's aviation industry different type of pressure sensors are used to measure dynamic pressure, ambient pressure and static pressure of the air. The pressure of the air on airfoil can be determined by making pressure tapping along the top and bottom of the airfoil. These tapping are connected to the digital manometer for taking pressure measurements as shown in Fig. 11.



Fig. 11. Sensors used in wind tunnel (left) and sensors installed on WT (right)- Courtesy by UMT wind tunnel

VIII. Test piece (Airfoil NACA 0012)

The test piece used is rectangular wing for lift and drag calculation. The airfoil is NACA 0012 with span of 0.17m. It is a symmetrical airfoil. It is selected because it has simple geometry, is best demonstrator for low subsonic flows and is easily experimented airfoil. The dimension of airfoil was selected according to the dimensions of the test section of the wind tunnel. The chord of the selected airfoil is 0.1092m.
The airfoil is manufactured by using Cal wood and Eucalyptus tree wood and cut according to the selected dimensions of NACA 0012 airfoil. 8 holes chord wise are made and narrow plastic tubes are passed from these holes. The holes are made in such a way that four holes are above the chord and four holes below the chord. These are the points from where pressure readings are taken, 4 above and 4 below the chord whose location is shown below.

For the lift and drag determination, the value of coefficient of lift (Cl) and drag (Cd) is required respectively. This is obtained by using the pressure (P) values obtained from the WT experiment into the integration formulas shown below.

Cl (xi)= $\int_0^1 CPU - CPL\ (dx/c)$

Cd (xi) =$\frac{2}{c}\int_0^1 \sqrt{\frac{q1}{q0} - \frac{q2}{q0}(dy)}$

Where

CP = (P-P_{ref}) /(0.5*density*velocity^2)

Table 1 Pressure tapping on airfoil

Port #	Distance Along the Chord From Leading Edge (mm)
1	20
2	35
3	50
4	65

A. Experimental Grpahs of NACA 0012

The experimental graphs of NACA 0012 are taken from a research paper at a Reynold number of 4*10^4 (Fig. 12). This data is collected for the purpose of comparing the measurements taken from UMT wind tunnel, although errors are expected due to difference in Reynold number as for UMT wind tunnel its value is 6.4*10^4. collected for the purpose of comparing the measurements taken from UMT wind tunnel, although errors are expected due to difference in Reynold number as for UMT wind tunnel its value is 6.4*10^4.

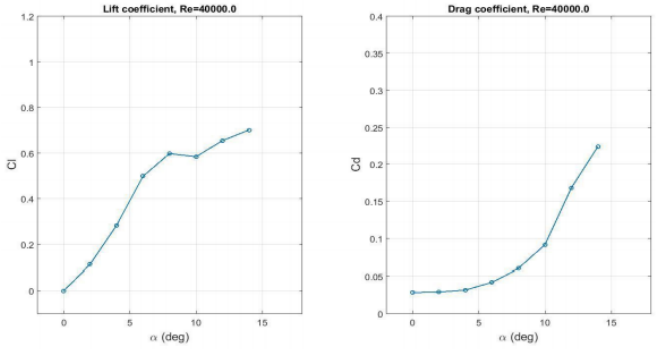


Fig. 12. Experimental graphs of NACA 0012- Courtesy by Sauvageat, 2016

IX. Results and Discussion

The conditions while running the test are as follows;

Temperature: 30℃
Density: 1.164 kg/m^3
Velocity: 9.5m/s
P_{ref}= 0.49 kpa

The WT test is run and pressure readings from digital manometers are noted. These reading are used as input to the formulas given in Section VIII along with the test conditions. The readings obtained are shown in the table below;

Table 2 Cl and Cd from WT measurements

Quantity	**UMT WT data**
Cl	0.071
Cd	0.037

The data obtained in Table 2 was compared with the experimental results available for NACA 0012 at Reynold number close to our WT. The results are shown in Table 3.

Table 3 Comparison of results

Quantity	**UMT WT data**	**Sauvageat et al. 2016 data**
Cl	0.071	0.44
Cd	0.037	0.026

The comparison of data shows variation in results which were further investigated. The first reason was that the Reynold number didn't match with the data used that led to difference in values for Cl and Cd obtained from the two sources. This being said, the wind tunnel being a low cost development, is a good representation of the more accurate WTs used for aerodynamic measurements from which the students can benefit and have practical insight into the wind tunnel measurements .

X. Conclusion

The wind tunnel developed can be used to calculate lift and drag for different airfoils and is a good practical representative of the procedure used to conduct wind tunnel tests in the aerospace industry. The wind tunnel has been developed at a low cost and can be effectively used for educational purpose. The work can be further extended to incorporate the setup that can take measurements at different

angle of attacks and by taking steps to improve the accuracy of coefficient of lift and drag values respectively.

REFERENCES

[1] Nan, L., 2013. The Methods Of Drag Force Measurement In Wind Tunnels. FACULTY OF ENGINEERING AND SUSTAINABLE DEVELOPMENT

[2] 2008. A Simple Educational Wind Tunnel Setup For Visualization Of Duct Flow Streamlines And Nozzle/Diffuser Boundary Layer Separation. [online] Available at [Accessed 18 January 2021].

[3] . Kalagobe, T., 2017. WindTunnel Testing Of A NACA0012Aerofoil. [online] Available at: [Accessed 18 January 2021].

[4] Mpoweruk.com. 2005. Aerodynamic Lift And Drag And The Theory Of Flight. [online] Available at: [Accessed 18 January 2021].

[5] Wikiwand. 2021. Aerodynamic Force | Wikiwand. [online] Available at: [Accessed 18 January 2021].

[6] (PDF) Low Subsonic Wind Tunnel – Design and Construction", *ResearchGate*, 2020. [Online]. Available: https://www.researchgate.net/publication/323408885_Low_Subsonic_Wind_Tunnel__Design_and_Construction. [Accessed: 18- Dec- 2019].

[7] Sauvageat, E., 2016. Prediction and Comparison of low-Reynolds Airfoil Performance. *MES Reoprt*, 1, p.1.

[8] 1991. *Fundamental Of Aerodynamics*. 3rd ed. [ebook] McGrwa Hill companies Inc., pp.283,284. Available at:<http://ftp.demec.ufpr.br/disciplinas/TM045/FUNDAMENTALS_OF_AERODYNAMICS.PDF> [Accessed 9 January 2021].

[9] Lyon,, C., 1997. *Summary Of Low Speed Airfoil Data*. [online] Mselig.ae.illinois.edu. Available at: <https://m-selig.ae.illinois.edu/uiuc (R mukesh, 2014)

Resolution Improvement in GNSS Based Synthetic Aperture Radar Using GPS L1 Signals from Different Look Angles

Muhammad Shoaib Ul Hassan
Department of Space Sciences
Institute of Space Technology
Islamabad, Pakistan
shoaibulhassan365@gmail.com

Hassan Sadiq
Department of Space Sciences
Institute of Space Technology
Islamabad, Pakistan
hassanniazi948@gmail.com

Najam Abbas Naqvi
National Center of GIS and Space Applications
Institute of Space Technology
Islamabad, Pakistan
najm_naqvi@yahoo.com

Mohammad Usman
ABM ASTUMA (PVT) LTD
Islamabad, Pakistan
musman751@hotmail.com

***Abstract*—The Global Positioning System (GPS) is used to calculate position of a user and navigation purposes around the globe. This paper describes a way to use reflected GPS signals to obtain images of the targeted area of interest with improved resolution. The GPS signals reflected from different objects on surface of earth could be used in different remote sensing applications because they provide valuable information about reflecting surface. Generally, the principle is based on a kind of synthetic aperture radar (SAR) which image reconstruction is performed by using a technique called matched filter. The process to generate GPS signal and reconstruction of image is simulated for different time periods on MATLAB. Different point target based scatter images of the interested area are obtained with the help of SAR signal processing techniques. Later on these obtained images are combined by image fusion using stationary wavelet transformation (SWT) technique to improve the resolution.**

Keywords—GPS, Bistatic synthetic aperture radar, SAR signal processing, Image Fusion

I. INTRODUCTION

GPS was developed by U.S Department of Defense (DOD) to come up with accurate estimation of position, velocity and time to U.S military [1]. We use direct GPS signals for positioning and navigation purposes while reflected GPS signals that are also called multipath signals can be used for different remote sensing applications [2]. Many innovative applications have been proposed in remote sensing field on the basis of reflected signals including soil moisture analysis [3], oil slicks detection, ocean altimetry and wind speed and direction estimation [4][5].

Bistatic synthetic aperture radar (BSAR) is one of the most developing areas based on GPS transmissions. A lot of work has been done in this field on both experimental and theoretical level. A single GPS receiver that is located near or on the ground could collect signals directly from satellites as well as reflected from the surface of earth. At any time of the day 4-8 GNSS satellite are consistently available at any position on Earth's surface over horizon of a single constellation with a chance of increasing this number with

fully operational constellations. A combination of GPS-based SAR images taken from a variety of satellites can improve image resolution by working on points such as targets. [6]. The key parameter in a remote sensing system is spatial resolution which is characterized by the analysis of point spread function (PSF) [7].

II. MATHEMATICAL MODELING

This research describes simulations for a BSAR imaging system that uses reflected GPS signals, reflected from area of interest on surface of the Earth. A BSAR system consists of GPS satellites, GPS receiver and its signal detection components. A GPS satellite that moves onto the orbit may act as the basis for synthetic aperture, even if the continual shift in satellite geometry is quite modest and results in a very long data acquisition period of several hours. The data acquisition time may be of order of seconds, in case a receiver is placed on a moving platform. Due to the continuous motion of GPS satellites, the signal received during integration time at receiver's position will be a frequency modulated (FM) signal. The basic concept of radar exhibits that range resolution is opposite of signals bandwidth which makes it possible for BSAR imaging system to get high resolution and enough range at the same time. This helps the BSAR system to obtain high quality images of the target area with low cost [8].

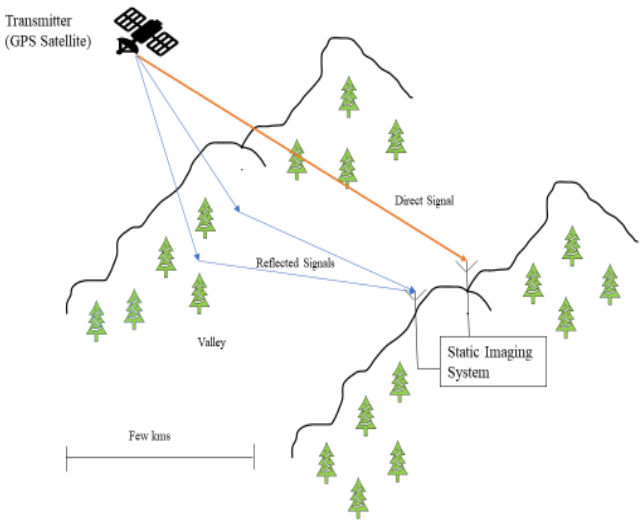


Fig.1 Imaging Scenario-Static Imaging System

The transmitter, targets and receiver geometry can be seen in Fig. 1. If we perform sampling for longer period for above mentioned scenario then there is a possibility of generating an image with stationary receiver. With a stationary receiver change in geometry is being provided with the help of moving GPS satellites. Although change in the geometry is relatively a low process and it takes data acquisition time in the order of hours. Monitoring landslides and seismic studies for long times are some of the applications that uses this type of systems. The possibility of applying this method for the purpose of imaging has been defined in many research papers [9].

As the signal reaches to a target on Earth, it is reflected back. The way of reflection totally depends on the irregularity of surface and insulating properties of the targeted surface. For imaging, non-specular reflected signals are considered as more useful. As a result of this kind of reflection signal will be dispersed in a wider angle and will be further attenuated according to travelled distance. We can consider that some point reflectors comprise the surface of the target.

To generate the synthetic aperture, moving GPS satellites completing one orbit in about 11 hours and 58 minutes will provide the change in geometry. GPS data is required in the order of hours to provide the requisite synthetic aperture by an orbiting GPS satellite which is not possible in practical scenario. Thus, there was a need to process the data with selected amount only during image reconstruction skipping other and modernizing phase, frequency and time of week (TOW) updates appropriately. This divides GPS data into portions known as skipping time (Ts) and dwell time (Tdw). The first is the time interval during which the information is not processed or omitted to effectively affect the geometry. Second one is the period, when GPS data for the correlation of direct and reflected signals to construct an image are processed by reconstruction algorithms. A distribution of satellites during observation time is shown in Fig. 2

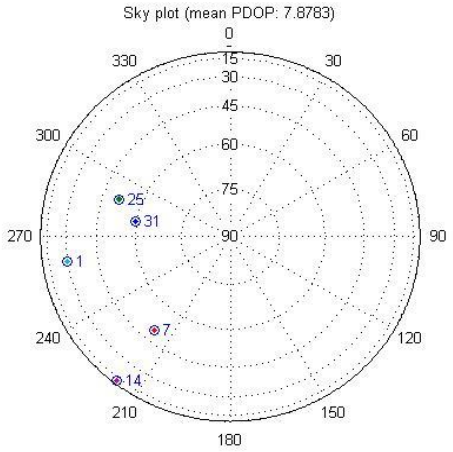


Fig. 2 Polar Plot-Showing Visible GPS Satellites

By using the above information, different images were generated for using different satellites that were providing different look angles. Each image is capable of pointing the target with different view. In MATLAB, a simple code based on SWT was used to combine these images in order to get more information. A basic concept about image fusion is shown in Fig. 3. The basic purpose of combining images is to extract un-necessary information from images and as an output it gives complete detailed image which we call as a fused image.

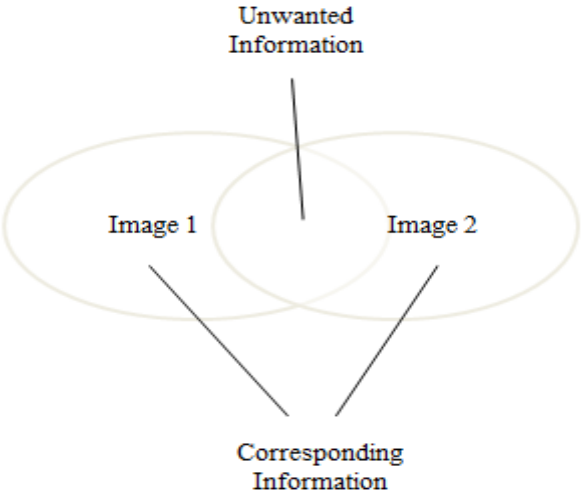


Fig. 3 Basic Concept of Image Fusion

There are different types of image fusion that are widely used for different applications. One of those types is wavelet transform that is specifically used for the fusion of images having same type of characteristics. Additionally, this technique has two types: one is discrete wavelet transform (DWT) and other is stationary wavelet transform (SWT).

The DWT obeys some defined rules of discrete set of wavelet scales and translations in order to implement wavelet transform. In these types of transformation, signal is mutually divided into orthogonal set of wavelets. On the other hand, SWT is almost very similar to DWT except the difference that the process of down sampling is suppressed due to which SWT is translation invariant.

The main purpose of this research is to improve the resolution of simulated images in a suitable software environment. In general, image fusion is a process in which two images are joined together into a solo image holding the significant structures and topographies from each of the original images. The significant uses of image fusion are: medical image processing for better diagnostics and interpretation of diseases, imaging to analyze microscopic details, remote sensing, engineering and robotics and computer sciences including computer vision. From many types of image fusion techniques, SWT technique was employed that was most suitable for our images.

III. Experiment

The simulation work was performed in MATLAB. The simulation work is intentionally divided into two parts, signal synthesizer and reconstruction engine. The signal

synthesizer helps to synthesize the signal that is coming from analog to digital converter (ADC) of GPS frontend while reconstruction engine helps to generate image. Care has been made to ensure that a digitized GPS signal was only available to the reconstruction engine along with satellite's ephemeris information and receiver's location.

The purpose of signal synthesizer is to determine the orbits of satellite together with the individual PRN code offsets. It incorporates direct signals from all satellites in view, and also signals reflected from the target, as well as receiver noise. The reconstruction engine divides the intended area into square bins and attempts to correlate the incoming signal in a coherent manner with a specific individual model chirp that is unique to each bin. Fig. 4 depicts a search area, where targets can be located. Two arrays of size 101 each were chosen to approximate the area where a target can be found, while the target has a pixel size of 20m resulting in an area of around 2000 m^2. The size of 20m was a random value during initial simulations and the target size was referred to as one element, square or pixel value in the box.

The position (0, 0, 6378050) in Earth Centered Earth Fixed (ECEF) coordinate system is specified at the center of area being searched, while target could be at any place in the matrix. Actually, these are the north-pole coordinates that were assigned to simplify the coordinate transformation. Two targets are settled down at (20, 0, 6378050) and (-20, 0, 6378050) respectively in the ECEF coordinate system. The starting position and velocity of receiver is specified to be at (0, 0, 6378050) and (0, 0, 0) respectively.

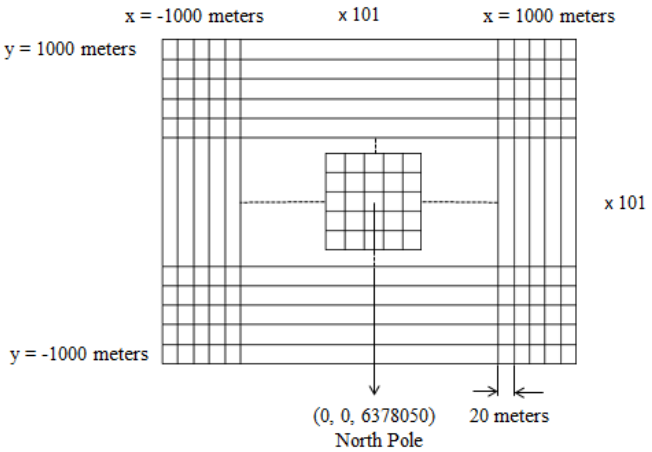


Fig. 4 Position of the Target

The processing of matched filters plays an important role in this simulation. It is done with the help of sample-by-sample multiplication of two signals in MATLAB, followed by accumulation. This procedure was carried out for each sample and data in two dimensional matrices were stored. Subsequently, the matrix was scanned over time for each sample, making the procedure equivalent to the matched filter processing and each instant of time yielded a new correlation value. A uniform maximum correlation value is expected for the target's location. The output of matched filter is given by:

$$S_{ij}(\tau) = \int_{-\frac{Ts}{2}}^{\frac{Ts}{2}-\tau} S_{Rij}(t+\tau)\, S_{Rij}{}^{*}(t)\, dt \qquad \textbf{(1)}$$

Where Ts represents the time of observation and (*) is the complex conjugate.

For the development of GPS scenario, a key consideration is to simulate various GPS errors. The errors such as satellite clock error, orbital error and atmospheric error behaves mostly in the same manner and thus produces error in the measurements of pseudorange and carrier phase [8]. During simulation, direct and reflected signals can be affected by these errors and they can prohibit the mechanism of generating correct images. In our instance, atmospheric effect errors, receiver clock and position errors can be more significant than in comparison to other problems. During MATLAB simulations, the results revealed that the errors due to atmosphere had a significant effect on our simulations. However, a receiver clock error is introduced as a result of the quartz clock utilized in the receiver, which causes drift into the clock and results in incorrect placement in a commercial receiver and loss of target in our simulation.

IV. Results and Discussions

According to simulations, a reasonable spatial resolution needs at least one hour of integration time to meet the requirements. Two hours of data, on the other hand, revealed a resolution of the sub-meter level. The quality of the image is directly related to the geometry variations of GPS satellites; hence the image resolution relies on the time of integration. Different images were constructed by using the above mentioned information that directly pin points the target at desired location with different satellite geometries.

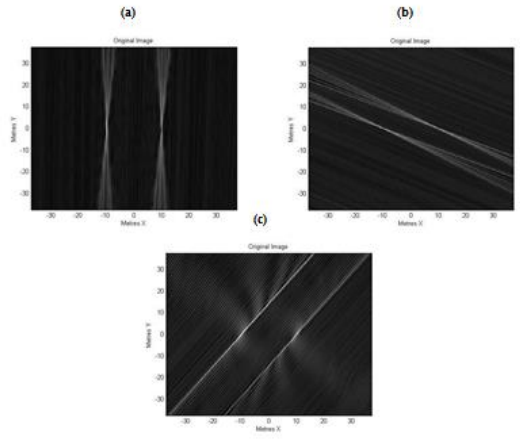


Fig. 5 Images obtained with integration time of 7000 seconds (a) SV-27 (b) SV-25 (c) SV-16

Fig. 5 show the results obtained by integrating over 7000 seconds for different satellites. The resolution of these simulated images can be improved by merging them with each other with the help of stationary wavelet transform image fusion.

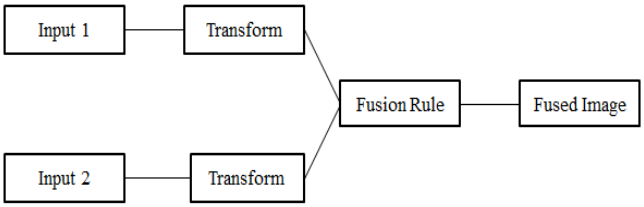


Fig. 6 Basic Block Diagram for Image Fusion

A block diagram for complete image fusion process is shown in fig. 6. Two images as input 1 and input 2 are combined together with stationary wavelet transformation technique in order to form a single image that has detailed information.

Table (1) shows that images obtained from SV 16, 25 and 27 are fused with each other with the following combination:

TABLE 1 IMAGE FUSION COMBINATION

Figure	Combination
7(a)	16,25
7(b)	16,27
7(c)	25,27

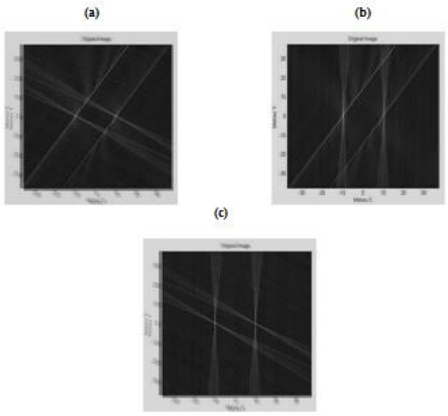


Fig. 7 Fused images obtained from (a) SV 16 & 25 (b) SV 16 & 27

The fusion results in Fig. 7 Shows that simulated images obtained from any two satellites having different viewing angles gives better resolution for pin pointing a target's position.

CONCLUSION

The entire process of generating GPS signals and reconstruction of images was simulated during the present research. The simulated images have been fused by means of stationary wavelet transformation. The results indicate that in high-resolution land and change monitoring applications, this method may be used to obtain detailed information at cheaper cost with fixed area images.

REFERENCES

[1] E. D. Kaplan and C. Hegarty, Understanding GPS/GNSS: principles and applications, Artech House 2017.

[2] M. Usman and D. W. Armitage, "Acquisition of reflected GPS signals for remote sensing applications," Proceedings of 2nd International Conference on Advances in Space Technologies, 2008, pp. 131–136.

[3] A. Egido, G. Ruffini, M. Caparrini, C. Martin, E. Farres, and X. Banque, "Soil Moisture Monitorization Using GNSS Reflected Signals" arXiv preprint arXiv:0805.1881 May, 2008.

[4] E. Valencia, A. Camps, H. Park, N. Rodriguez-Alvarez, X. Bosch-Lluis, and I. Ramos-Perez, "Oil slicks detection using GNSS-R," In 2011 IEEE International Geoscience and Remote Sensing Symposium, 2011, pp. 4383-4386.

[5] R. Notarpietro, S. De Mattia, M. Campanella, Y. Pei, and P. Savi, "Detection of buried objects using reflected GNSS signals," EURASIP Journal on Advances in Signal Processing, 2014(1), pp. 1-13.

[6] F. Santi, M. Bucciarelli, D. Pastina, M. Antoniou, and M. Cherniakov, "Spatial Resolution Improvement in GNSS-Based SAR Using Multistatic Acquisitions and Feature Extraction," IEEE Transactions on Geoscience and Remote Sensing 54, no. 10 (2016): pp. 6217-6231.

[7] M. Soumekh, Synthetic aperture radar signal processing Vol. 7, New York: Wiley, 1999.

[8] Y. Zhang, X. Qi, H. Li and H. Mu, "Bistatic Synthetic Aperture Radar Imaging With Multi-GNSS Transmiitters," IEEE International Geoscience and Remote Sensing Symposium, pp. 2909-2912, July, 2019.

[9] M. Usman, D. Armitage, "Initial Experiments for a Remote Imaging System based on Reflected GPS Signals" Journal of Space Technology, Vol 3, No. 1 July, 2013

Evaluation Of Flight Mechanics Performance Of A Fighter Aircraft Using Computational Fluid Dynamics

Asra Imtiaz
Institute of Space Technology (IST)
Islamabad, Pakistan
asraimtiaz22@gmail.com

Hussna Zainab
Institute of Space Technology (IST)
Islamabad, Pakistan.
hussnazainab@gmail.com

Dr. Hossein Raza Hamdani
Institute of Space Technology (IST)
Islamabad,Pakistan
hraza@hotmail.com

***Abstract*— F-104 Starfighter has always been considered as a marvel in the field of engineering because of its design and ability to sustain flights at higher speeds. The aim of this research is to examine the viscous, compressible and steady state flow over this vintage aircraft using modern computational techniques and validate the results using flight data and results from Advanced Aircraft Analysis (AAA). The second objective of the research is to carry out the analysis on the scaled down model and comparing the results to flight conditions thus defining the technique as a substitute for wind tunnel testing.**

Keywords— F-104, CFD, Mach number, CAD, FLUENT, AAA

I. INTRODUCTION

F-104 Starfighter, manufactured by Lockheed Martin, is a supersonic interceptor which was originally used as a bomber. F-104 had set many records and was considered a wonder in the field of engineering. Its design was considered phenomenal since it had a light airframe and the most technically advanced and powerful engine available. This aircraft became the first operational fighter to sustain flights at speeds greater than Mach 2. Furthermore, it became the first aircraft to hold world speed and altitude record simultaneously. The exterior of Starfighter was also a design marvel as it had an aerodynamic streamlined fuselage. All the weapons, avionics, undercarriage an engine were installed in a cramped internal layout. One of the best part of the F104 was the selection of General Electric J79 axial-flow turbojet engine.

The aerodynamic efficiency of any aircraft plays a very vital role in the design and performance. The Computational Fluid Dynamics (CFD) supports the performance analysis of these aircrafts. The CFD analysis, in the present time, is being used for optimization of problems in aeronautical engineering. CFD uses numerical scheme approaches and advanced solver techniques which have been a replacement of wind tunnels in accurate design and modelling of complex problems.

The main objective of this research is to study the flow analysis around the F-104 surface. This flow is subjected to different Mach conditions at different angle of attacks. This defined range of Mach numbers includes subsonic and transonic flow conditions. Clean geometry of the aircraft has been generated using CATIA V5 software.

One of the most critical steps of the analysis is finalization of boundary conditions. Correct choice of the conditions is the key for accurate numerical analysis. The conditions for engine inlet, exhaust, aircraft, inlet and outlet have been defined for each flight condition. Calculation of boundary conditions at the exhaust of engine is a complex procedure therefore mathematical modelling of the J79 engine has been carried out at different flow conditions.

After the analysis of this model the results are compared and validated with existing flight data. Another software, AAA, is used to generate these derivatives. The results obtained from this software at a specific flight condition are also used to validate the results.

The next step of the research includes the analysis of scaled down model of the Starfighter at the same flight conditions. This additional part of the research proves the working mechanism behind a wind tunnel. As we know that for wind tunnel testing a scaled down model of an aircraft is used and the analysis is carried out at required flight conditions. Its main goal is to predict the free flight conditions of an aircraft. This entire process of predicting the conditions is very complex and challenging since it is being done at sub-scale conditions. It is quite evident that using CFD instead of wind tunnel testing is very economical. The CFD method is also capable of producing results over an extensive data set enabling a thorough analysis of flow.

Finally, these results are compared and validated with the previously carried out analysis.

II. AIRCRAFT SPECIFICATIONS

A. Design Specifications

Before any analysis we need to study the design specifications. Using these design specifications the CATIA model has been developed. Following table shows the detailed design specifications.

TABLE I DESIGN SPECIFICATIONS *[1]*

Crew	1
Length	54 ft 8 in
Wingspan	21 ft 9 in
Height	13 ft 6 in
Wing area	196.1 sq ft
Empty weight	14,000 lb
Power plant	1×GE J79 turbojet

Airfoil	Biconvex 3.36% root and tip

B. Performance Specifications

TABLE II PERFORMANCE SPECIFICATIONS *[1]*

Maximum speed	1528 mph , Mach 2
Combat range	420 mi
Ferry range	1630 mi
Service ceiling	50,000 ft
Rate-of-climb	48,000 ft/min
Lift-to-drag	9.2
Wing loading	105 lb/sq ft
Thrust/weight	0.54

III. METHODOLOGY

A. CATIA Model

The first step of the analysis is CAD modeling of F-104 which is done using CATIA V5R20. The flow analysis is done over this solid model. While modeling we need to be careful that the parts of the geometry must not intersect or overlap each other because if the geometry is not perfect it would result in poor quality mesh. The geometry of F-104 used for analysis is shown in the Fig.1 below.

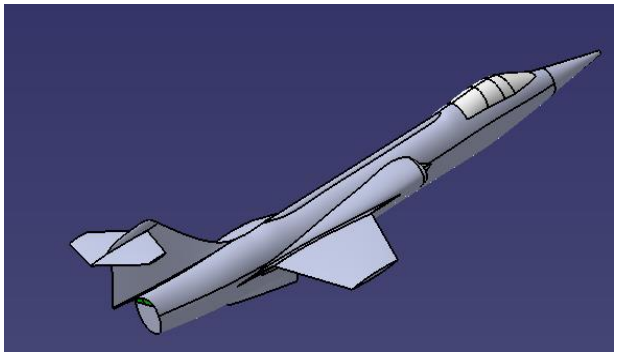


Fig. 1 F-104 Starfighter modeled using CATIA V5

B. Mesh Generation

This geometry is further imported for meshing in ANSYS ICEM 18. The size of the surface mesh is defined using curve setting parameters. A circular domain is defined around the body of the aircraft which is almost ten times greater than the length of the aircraft. The radius of the domain is 460 ft. For scaled down model the radius is 100ft. The volume occupied by the fluid in these bounds is divide into meshes. Octree method is used for volume meshing.

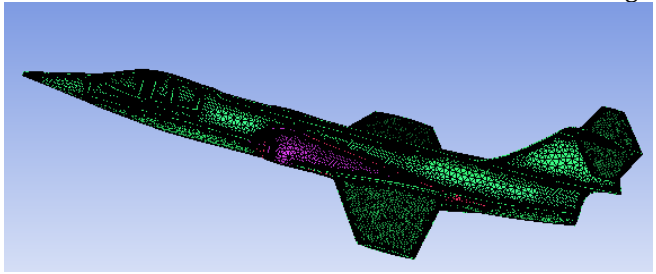


Fig. 2. Meshed Geometry of Aircraft

C. Grid Independence

Accuracy of results depends significantly on the size of grid. A fine grid might contain a lot of cells and thus give more accurate results but it will require greater computational power. However if a less dense grid with fewer number of cells is used it will not give accurate results. Therefore, it is important to wisely choose the grid size. For this purpose a grid independence study is carried out. Three different meshes were generated and the results for drag, lift and momentum were evaluated. After comparing the results it was observed that variation of results between grid 2 and 3 is quite negligible. On the other hand, grid 1 has less number of cells and could not provide accurate results. Finally grid 2 was selected for analysis.

TABLE III GRID INDEPENDENCE ANALYSIS

Grid	**Cells**
Grid 1	5.02 million
Grid 2	7.53 million
Grid 3	11.29 million

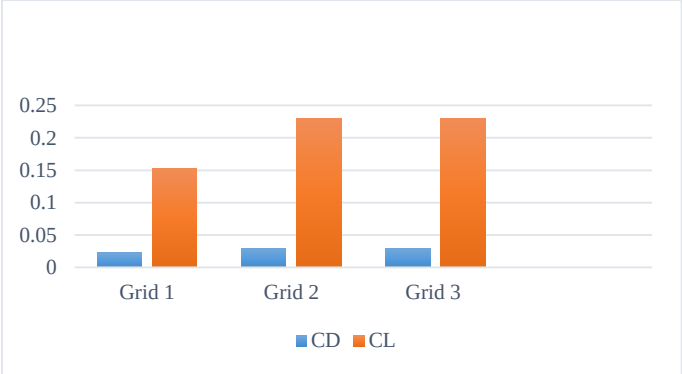


Fig. 3 Grid Independence study

D. Turbulence Model

Selection of turbulence model is yet another vital step to obtain an accurate solution. The turbulence models used for this analysis is K-ω SST and SA. The solver used is density-based because all the simulations are dealing with compressible flow. Energy equation was also selected.

E. Materials

The fluid used in these simulations is air with ideal gas properties. It was considered that F-104 was flying at sea level conditions. Moreover viscosity was solved using Sutherland equations.

F. Boundary Conditions

The surfaces of the aircraft were selected as wall so that no slip condition can be maintained. Inlet of the engine was selected as pressure outlet and the exhaust was selected as pressure inlet. For all Mach numbers the static pressure was calculated using isentropic equations. Mass flow rate for the engine was selected as 77 kg/s. Its analysis was carried out at Mach numbers 0.4, 0.7 and 0.9 respectively. The mass flow for the scaled down model was chosen as 1 kg/s.

G. Solver Setup

The solver with explicit algorithm was used. The courant number is set to 1. For flow discretization 2nd order upwind scheme was selected and 1st order upwind scheme for turbulent viscosity. Convergence of residuals and force coefficients are monitored for each case.

IV. ANALYSIS OF FLOW ON F-104

The flow over the aircraft has been analyzed at three different Mach numbers; 0.4, 0.7, 0.9 at four different angle of attacks; 0, 5, 10, 15. Following contours and plots show the flow over the aircraft.

A. Pressure Contours

The pressure contours at Mach number 0.4, 0.7 and 0.9 at zero angle of attack.

It is evident that the dynamic pressure is varying higher at certain portions and low at other portion. That is at sharp edges dynamic pressure is more. With the increase in Mach number the pressure also increases.

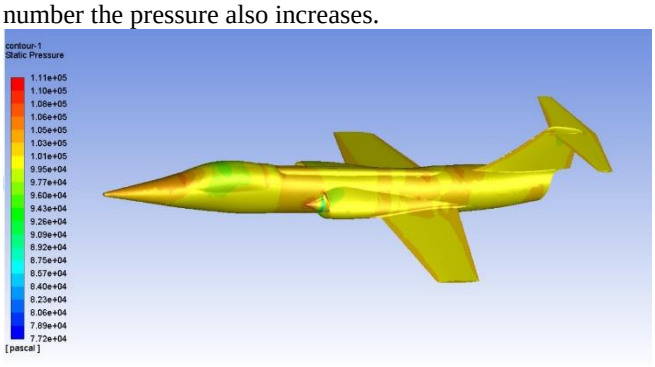


Fig. 4 Pressure Contours at Mach 0.4 & AoA 5

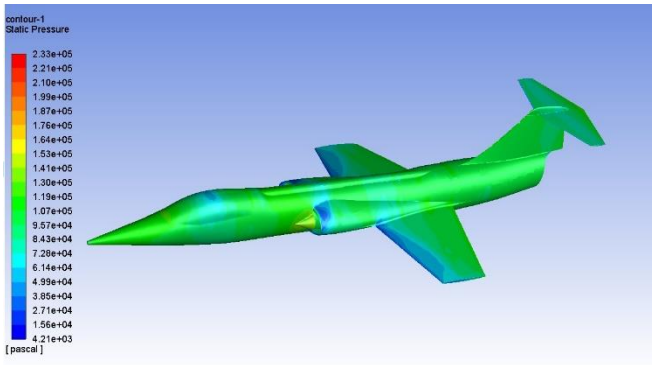


Fig. 5 Pressure Contours at Mach 0.9 & AoA 9

B. Velocity Contours

The variation of velocity is higher at curved and edge portions of the surface of the Starfighter. Velocity increases when Mach number increases.



Fig. 6 Velocity Contours at Mach 0.4 & AoA 5

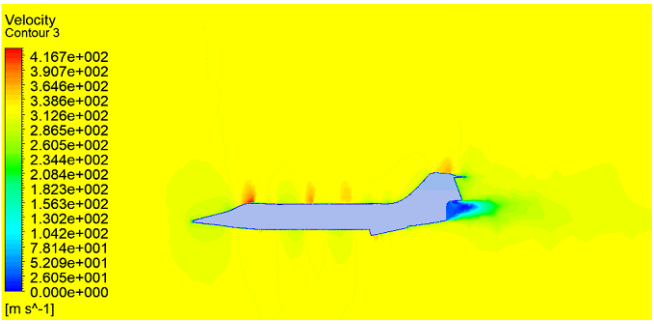


Fig. 7 Velocity contours at Mach 0.9 & AoA 5

V. ANALYSIS USING AAA

The first step of the analysis as defining the geometry of the entire aircraft. Using these defined parameters the software develops the geometry of the aircraft. The next step is to define the weights, center of gravity. Other parameters like propulsions systems are also provided. Using empirical formulae it defines the stability and control derivatives, aerodynamic forces and moments on the provided flight conditions. The results obtained from here are compared to the previous results obtained from CFD.

The accuracy of the results through any software depends majorly on the geometry of the aircraft. In CFD we import an accurate model that has been designed on CATIA on the other hand AAA accumulates the information provided and constructs a geometry which may or may not be very accurate. The figure below shows the front and side view of the aircraft created by AAA. It can be seen as compared to CFD this geometry is not very accurate.

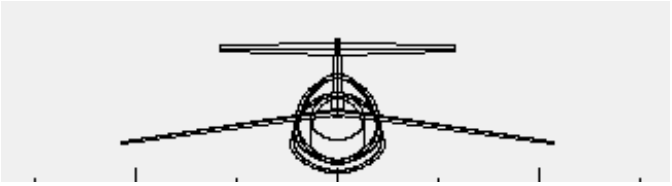


Fig. 8 Front view of Geometry

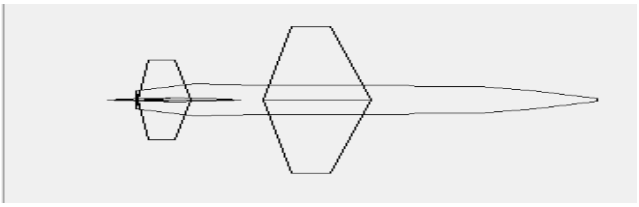


Fig. 9 Top view of Geometry

VI. ANALYSIS OF SCALED DOWN MODEL

The model of F104 has been scaled down in ICEM using geometric scaling by a factor of 4.4. A mesh is then generated on this scaled down model using the exact technique which was used earlier. The analysis was carried out on the exact same cases using the same boundary conditions and solver setup. Following contours at same conditions are plotted.

A. Pressure Contours

The pressure contours obtained here show the same behavior as the previous pressure contours.

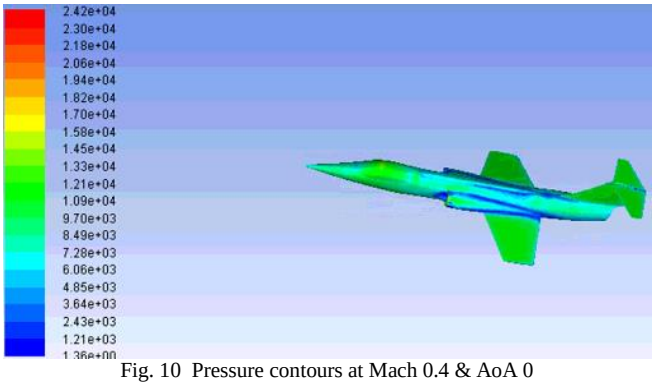


Fig. 10 Pressure contours at Mach 0.4 & AoA 0

B. *Velocity Contours*

The velocity contours show the patters as observed previously. The reasons for this behavior has been explained in the analysis of F-104.

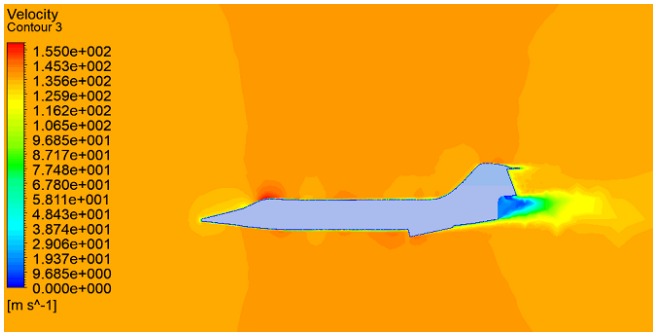


Fig. 11 Velocity Contours at Mach 0.4 & AoA 0

VII. RESULT AND DISCUSSION

After the simulations are carried out for each case the results are validated with existing data of F-104 obtained.

TABLE IV RESULTS

Parameter	**Flight Data**	**F-104**	**AAA**	**Scaled Down**
L/D [1]	9.2	9.42	10.42	9.40
C_{Do} [2]	0.0172	0.018	0.0205	0.0185
$C_{M\alpha}$ [2]	-1.5	-1.64	-1.66	-1.59
$C_{L\alpha}$ [2]	4.44	4.25	4.24	4.01

It is evident that the results obtained from CFD analysis of the aircraft are very much close to that obtained from the flight data. However the little difference we observe can be removed by using prism mesh instead of tetrahedral mesh. But in our analysis we had limited computational power.

The results obtained from AAA are also very close however the geometry in AAA is not very accurate this is the reason the drag here is a little more compared to original results.

It is also apparent that the results for scaled down model are also close to those obtained from flight and those obtained through analysis of the full scale model. These results can again be refined by using prism mesh.

Another way to get more refined is to take a model with the complete engine analysis. Since that is an entirely different task to model the engine we can still consider it as a future scope of this project.

From the CFD analysis it is evident from the contours that the flow properties obtained for both the models are quite comparable with each other.

VIII. CONCLUSION

In this research CFD analysis of the F-104 Starfighter is conducted, studied and then compared with reference values. The design and mesh size played a key role in the accuracy of results. This vintage aircraft which has been an engineering wonder was analyzed at different flow conditions and the results obtained were accurate to a great level. The model was then scaled down. Analysis over this scaled down model in ANSYS gave us almost the same results as the actual flight data. This ensures that the testing during design of an aircraft which is carried out using wind tunnels can be conducted using numerical equation using certain CFD tools like ANSYS. This method of testing is not only accurate but also gives the opportunity to carry out tests on wide range of conditions.

ACKNOWLEDGMENT

Several people played an important role in the completion of this research. First we will like to than our parents for their complete support. We would like to thank our project supervisor and all the seniors that have been always there for us.

REFERENCES

[1] J. L. K. Loftin, "NASA SP-468: Quest for Performance The evaluation of Modern Aircraft," NASA, Washington D.C., 2004 .

[2] R.K.Heffly, "Aircraft Handling Qualitiess Data," NASA, 1972.

[3] I. Arif, "Computational Analyis of Integrated Engine Exhaust Nozzel on a sSupersonic Fighter Aircraft," Jornal of Applied Fluid Mechanics , vol. 11, 2018.

[4] B. Kodavanla, "CFD Analysis of F-104 Falcon," Internation Journal of Mechanical and Production Engineering Research and Development , vol. 8, no. 2, 2018.

[5] M.R, "Role of Computational Fluid Dynamics and Wind Tunnel in Aeronautics R&D," 2012.

[6] M. Sharma, "Flow analysis over F-16 Aircraft wing using Computational Fluid Dynamics," International Journal of Emerging Technology and Advanced Engineering , 2013.

[7] P. Bulat, "Comparison of turbulence models in the calculation of Supersonic Separate flows," World Applied Siences Journal .

[8] H.S.Jr., "Flight Testing the F-104 Auomatic Flight Control System".

CFD Analysis of Multi-Element Natural Laminar Flow Airfoil NLF (1)-0115 for a Fixed-Wing UAV

Absar Ahmed Khan
Institute of Space Science and Technology (ISST), University of Karachi
Karachi, Pakistan
Absar.Ahmed.Khan@hotmail.com

***Abstract*—As the use of composite structures in the aerospace vehicles have significantly increased over the years, it has now become possible to acquire levels of surface smoothness and tolerances by using the laminar airfoil. Studies have shown that the use of Natural Laminar Airfoil (NLF) results in substantial gains in the performance of aerospace vehicle. On the other hand, the deployment of slats and flaps in NLF airfoils is a fairly novel concept allowing substantial enhancement in the aerodynamic performance as compare to a single-element NLF airfoil. Of late, various attempts have been made to exploit NLF airfoils, however many studies have shown that the harnessing of optimized results has not met notable success. For instance, as the laminar flow reaches the leading-edge (LE), it faces significant loss owing to the contamination at the LE that results in the reduction of the lift coefficient (C_l). This creates hazardous situation during the takeoff and landing. In this paper, the NLF(1)-0115 with max thickness 15% at 44.1% chord and max camber 1.8% at 30% chord is used to design a 2-D multi-element airfoil with slat and flap for an Unmanned Aerial Vehicle (UAV). The multi-element airfoil is designed and analysed on Ansys Fluent using Spalart-Allmaras (S-A) turbulence model for various Reynolds and Mach numbers where the loss of lift coefficient due to contamination is expected to be minimal, simultaneously the low drag coefficient is expected to occur. While the low-drag benefit as a result of the laminar flow could be achieved during the cruise flight, the use of NLF airfoil in a UAV shows rich potential for meeting mid and far-term objectives of lowering the UAV energy consumption, whether fossil or electric.**

Keywords— Natural Laminar Flow, Multi Element Airfoil, Ansys Fluent, Unmanned Aerial Vehicle, NLF(1)-0115, Aerodynamics, Energy

NOMENCLATURE

C_l = Lift coefficient

C_d = Drag coefficient

$C_{l,max}$= Maximum lift coefficient of airfoil

$\propto$ = Angle of Attack / Alpha / AoA

v = Fluid velocity

ρ = Density

μ = Kinematic viscosity

LE = Leading Edge

TE = Trailing Edge

UAV =Unmanned Aerial Vehicle

Ma = Mach Number

Re = Reynolds Number

NLF = Natural Laminar Flow

C_p = Pressure Coefficient

L/D = Lift-to-Drag Ratio / Aerodynamic Efficiency

I. INTRODUCTION

If the flow over the wings is laminar, fast-moving Unmanned Aerial Vehicle (UAV) may achieve significant gains in cruise efficiency. Active laminar flow control may avoid turbulent flow across the majority of the wing. However, the system has certain drawbacks as the take-off weight is increased, while also increasing the cost and making maintenance more difficult [1]. On the other hand, Natural laminar flow (NLF) is a potential alternative to active laminar flow control. NLF makes use of an airfoil design that promotes laminar flow to extend farther across the airfoil than other traditional forms. Over the majority of the chord, the airfoil form must maintain a favorable pressure gradient. While the benefits of laminar flow for increasing aerodynamic efficiency are well recognised, the issue of sustaining natural laminar flow at higher Reynolds numbers and Mach values associated with fast-moving UAVs has never been research in great details.

NASA has experienced the NLF for over five decades and the results suggest that the use of NLF airfoils reduce the viscous drag on the aircrafts [2]. While there have been classic concerns about the achievability and maintainability of NLF wings, the later studies conducted by NASA have suggested that the NLF airfoils have demonstrated satisfactory performance on modern metal and composite airframe surfaces [3, 4, 5, 6, 7, 8]. These experiments by NASA, more than 30 in total, were carried out using the varying freestream conditions with the maximum Mach number achieved was 0.7.

Unlike the difficulties encountered on older airframe surfaces during the second world war up to 1950s, NLF is now possible owing to the modern technology used in the fabrication and manufacturing of wings. While NLF has been tested to reduce drag by using the modern composites for wing surfaces and with the Mach up to 0.7, this study tests the aerodynamic performance of NLF(1)-0115 airfoil beyond Mach 0.7. While NLF has shown persistent and durable results at high-speed subsonic conditions, this study entails the use of supersonic conditions of Mach 1.18 to understand the aerodynamic behavior of the airfoil. While NLF airfoils have been tested by NASA for various chord Reynolds numbers as large as 30×10^6, this research has numerically tested the airfoil for Re 38.5×10^6 to identify the aerodynamic effects on the airfoil despite the presence of turbulent layer.

Other studies by NASA have shown that the usually low lift coefficients and consequently low generated drag, form drag generated on wings is the greatest contribution to overall aircraft drag under cruising conditions for most aircraft [9]. For cargo aircraft, wing profile drag accounts for approximately a third of overall drag. With the decrement in the size of the aircraft, from commercial airplanes to UAVs, the profile drag tends to increase, as shown in the Table 1.

Various approaches have been identified to reduce the form drag on the wings. One of the most known approaches is the deployment of high-lift system, such as slats and flaps, so the lift coefficient can be maximised [10]. When compared to a traditional turbulent-flow wing with no high-lift technology deployed on the wings, this strategy can cut form drag by nearly half. While the cost of manufacturing an aircraft rises as high-lift devices are deployed, the promised returns in terms of reaching maximum aerodynamic efficiency are more tempting. The employment of Multi Elements – Slats and Flaps – with the NLF airfoil results in pressure recovery that a single-element NLF airfoil cannot achieve [10]. Multi-Element NLF airfoils have been employed in a variety of aircraft types, including business jets [11] and rotorcraft applications [12], however most of their usage have been in subsonic conditions. This does not suggest that the NLF airfoils have never been used in supersonic conditions for optimum aerodynamic efficiency. The primary idea behind Multi-Element NLF airfoils is to take use of favorable pressure gradients to assist stabilize the boundary layer without causing turbulent separation [13].

Studies have shown that Multi-Element airfoils can attain a $C_{l,max} > 2$, allowing the potential benefit to reduce the wing planform area or enabling the use of light weight high-lift system. These benefits for Multi-Element NLF comes without any trade-offs and compromises, thus allowing the designer a greater degree of freedom [14].

This work focuses on the design and analyses of the multi-element NLF(1)-0115 airfoil with max thickness 15% at 44.1% chord and max camber 1.8% at 30% chord. Within our design, a 2-D multi-element airfoil for an Unmanned Aircraft System (UAV) is being hypothesised. Various studies on the NLF airfoils have been conducted [15, 16, 17, 18, 19], whereas no study has been found to have conducted analysis on NLF(1)-0115 by deploying high-lift multi-elements, viz., slats and flaps.

TABLE I. FORM DRAG ON VARIOUS AIRCRAFTS [9]

Type of Aircraft	Form Drag on Wings / Total Aircraft Drag
Sailplane	*> 1/2*
Unmanned Aerial Vehicle (UAV)	*1/3 to 1/2*
Transport	*~ 1/3*
Low-speed general aviation	*> 1/3*
Business jet	*~ 1/3*

II. GEOMETRY AND GRID GENERATION

The airfoil studied for this research is NLF(1)-0115 with max thickness 15% at 44.1% chord and max camber 1.8% at 30% chord (Fig. 1). The main element of the airfoil, as presented in the Fig. 1, has chord length of 1.4 meters. The airfoil is placed in a C-type domain while the whole geometry is processed on Ansys SpaceClaim.

To capture the fluid flow behavior as suggested in various research studies [20, 21, 22, 23, 24], we have used semicircle with the radius of 13.5m and the rectangular grid of 27m as shown in Fig. 2.20

The primary reason the C-grid is used for 2-D airfoils is for the fact that the curvature of the mesh grid has to correspond with the leading edge of the airfoil. Studies have shown that this allows to capture better separation of flow. Besides, the mesh does not need to be updated as alpha is changed [43].

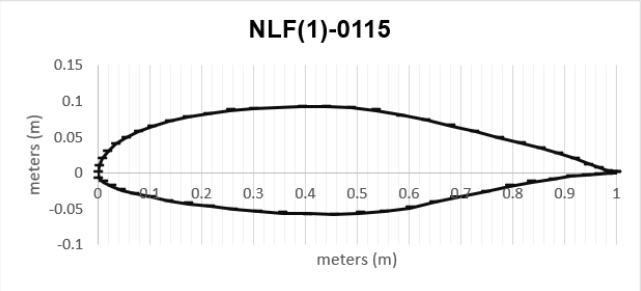


Fig. 1. NLF(1)-0115 Airfoil

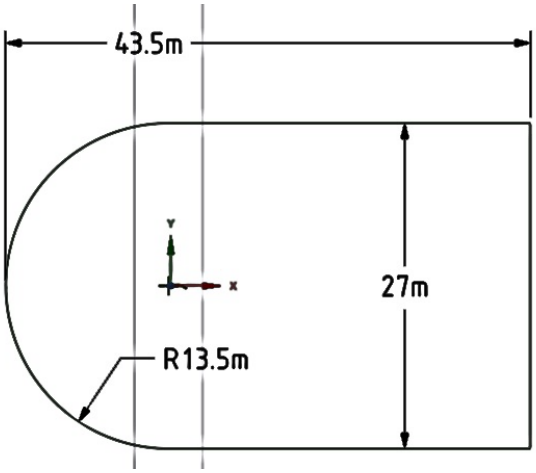


Fig. 2. C-grid with multi-element NLF(1)-0115 in center

The leading edge slat and trailing edge flap deployed on the NLF(1)-0115 airfoil are shown in the following Fig. 3.

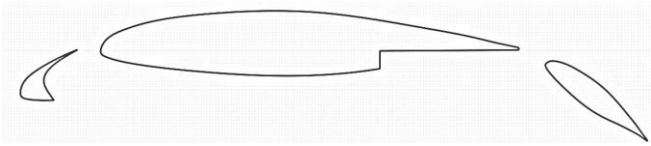


Fig. 3. Multi-element NLF(1)-0115 airfoil with leading edge slat and trailing edge flap

To investigate the effect of leading edge slat and trailing edge flap, the mesh is generated on Ansys Fluent. The triangular mesh was generated with varying number of inflation layers and first layer thickness based on the y+ values. The y+ value for various cases ranged between 1 and 30. Following Fig. 4a, b, c and d highlight the generated mesh on the c-domain. The number of elements generated at which $C_{l,max}$ was obtained were 101,724. The mesh was evaluated for skewness and orthogonal quality to ensure that the convergence and results do not falter. The mesh skewness ranged between 0.11 to 0.78 and show in Fig. 4e, whereas the mesh orthogonal quality remained between 0.37 to 0.95 as shown in Fig. 4f [32, 33]. The average wall y-plus value was 3.7 and shown in Fig. 4g.

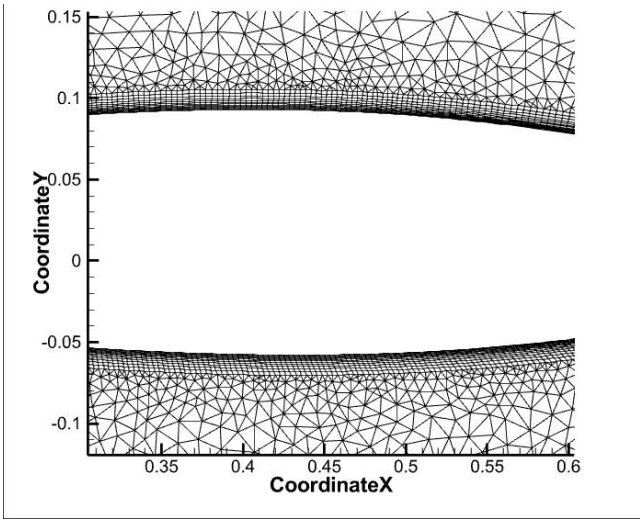


Fig. 4a. Mesh generation over main element airfoil

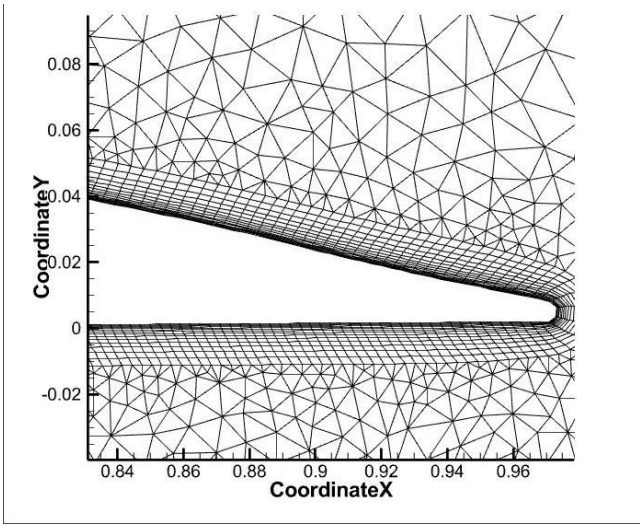


Fig. 4b. Mesh generation over the trailing edge

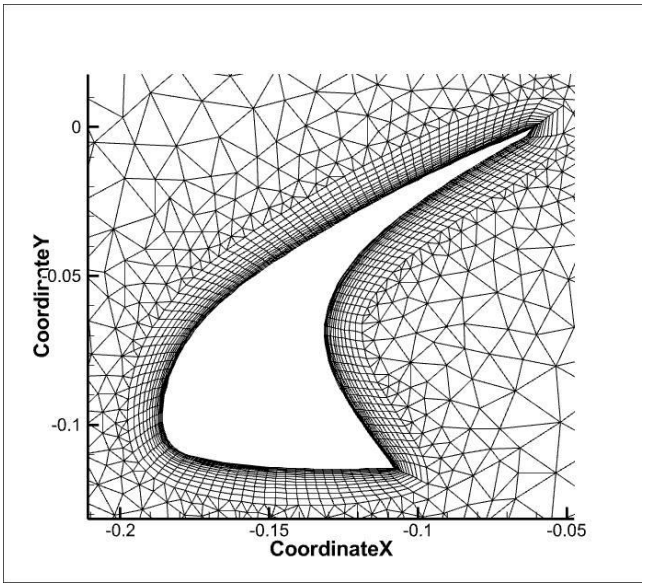


Fig. 4c. Mesh generation over leading edge slat

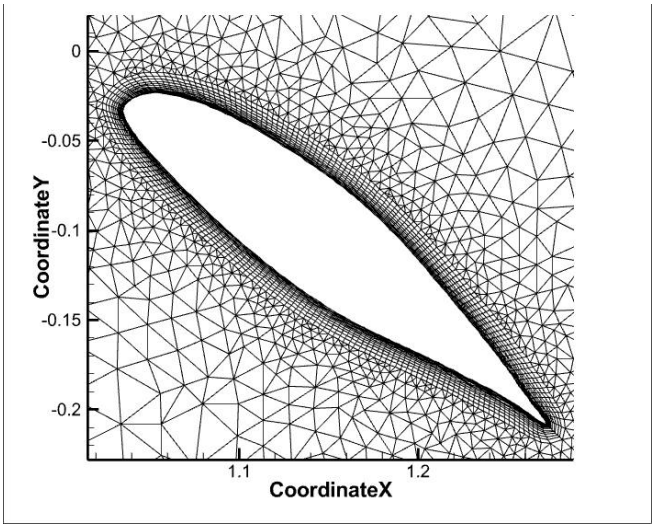


Fig. 4d. Mesh generation over trailing edge flap

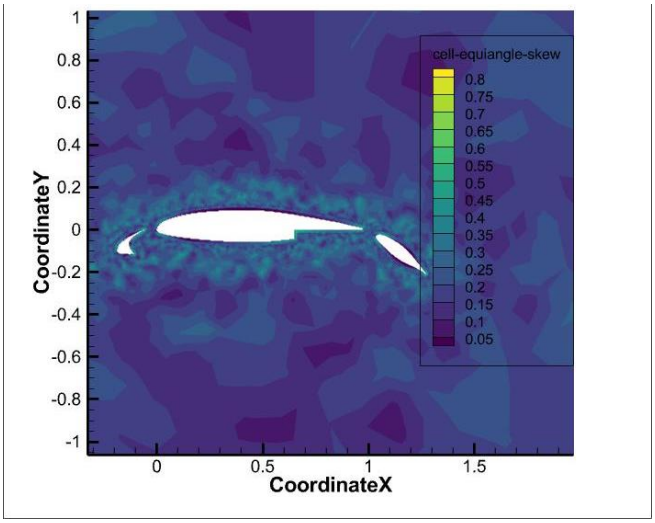


Fig. 4e. Mesh Skewness Quality

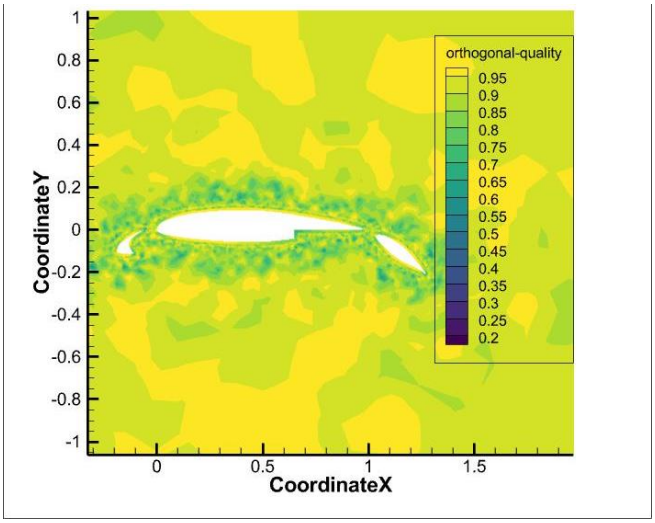


Fig. 4f. Mesh Orthogonal Quality

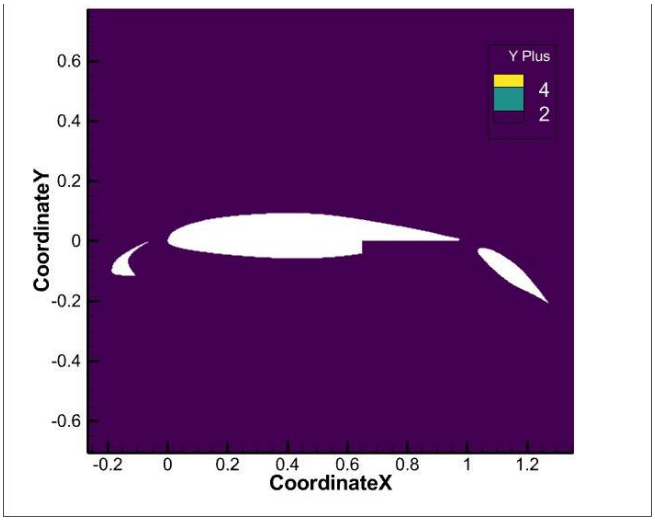


Fig. 4g. Wall Y-plus at Ma=0.71 at $\propto = 5^{\circ}$

III. COMPUTATIONAL METHODOLOGY

A. *Turbulence Modelling*

In order to study the effect of leading edge slat and trailing edge flap on the NLF airfoil and evaluate its aerodynamic performance, the Spalart-Allmaras (S-A) turbulence model was used. The Spalart-Allmaras is Reynolds Average Navier-Stokes (RANS) one-equation model used for a modified turbulence kinematic viscosity ($\tilde{v}$). S-A model allows the use of less computational effort as compared to other turbulence model. However, the S-A model has extensively been used within the CFD to study the external flow to study various aerospace problems and the results have also been validated with the experimental research over the decades [39, 40, 41, 42]. The standard model is given in the following transport equation (1).

$$\frac{D\tilde{v}}{Dt} = P - D + \frac{1}{\sigma}[\nabla.((v + \tilde{v}) + C_{b2}(\nabla\tilde{v})^2] \quad (1)$$

where,

d = distance between airfoil wall point and solid wall

$v = \frac{\mu}{\rho}$ = laminar kinematic viscosity

u = fluid velocity

B. *Test Cases*

The test cases studied are presented in the following Table II:

TABLE II. TEST CASES SUMMARY

Case No.	Mach No.	Reynolds No.	
1	0.19	6.47 x 10^6	Speed of Sound: 343m/s Length: 1.39m
2	0.42	1.37 x 10^7	
3	0.71	2.31 x 10^7	
4	1.18	3.85 x 10^7	

C. *Boundary Layer and Solver Settings*

The airfoil boundary is a solid wall and it was set for 'no-slip condition'. The Inlet was assigned was 'Velocity Inlet', Outlet was assigned as 'Pressure Outlet', whereas the Airfoil was set to 'Wall'. At the outset of the Fluent, the 'Double Precision' was selected. The use of Double Precision while raised the convergence time with more CPU usage, it is deemed necessary to resolve the pressure differences that drive the flow [27, 28, 29]. Convergence based on double precision is believed to be more accurate [30, 31]. Since four cases with varying Mach numbers were studied and the flow appeared compressible, therefore the "Pressure-based" solver was used. The standard sea-level density and dynamic viscosity of 1.225 kg/m3 and 1.7894e-5 kg/m-s was used respectively. The increased under-relaxation was applied by using the SIMPLE-Consistent or Semi-Implicit Method for Pressure-linked Equations: Consistent (SIMPLEC) that is a pressure-velocity coupling method. SIMPLEC may frequently find a converged solution more rapidly for very simple situations (laminar flows with no extra models active) when convergence is restricted by the pressure-velocity coupling [32, 33]. The pressure-correction under-relaxation factor in SIMPLEC is set to 1.0 to enhance the convergence process and get the solution in time. Increasing the pressure-correction under-relaxation to 1.0, on the other hand, may cause instability in certain situations owing to excessive mesh skewness [34, 35]. Using the SIMPLEC method was justified with the use of Mesh Adapt or Adaptive Meshing approach that was used to improve the mesh quality, specifically skewness and orthogonal quality [36, 37]. The convergence criteria is set to 1e-5 for all the residuals.

IV. COMPUTATIONAL RESULTS

A. *Section Characteristics*

Four different test cases with varying Mach and Reynolds Numbers were used to identify the fluidic and aerodynamic behavior of the NLF(1)-0115 multi-element airfoil. The section characteristics for the NLF(1)-0115 airfoil for various Mach and Reynolds numbers are presented in the Fig. 5 and 6. The lowest Mach and Reynolds number tested respectively is 0.19 and 6.47 x 10^6. The highest aerodynamic efficient (L/D) achieved in this low Mach and Reynolds number configuration and plotted in the Fig. 7 is 10.20 at $\propto = 10^{\circ}$, while the maximum lift coefficient ($C_{l,max}$) of 2.50 was achieved at $\propto = 17^{\circ}$ (Fig. 8). As the Mach and Reynolds number is increased to 0.42 and 1.37 x 10^7 respectively, it is identified that the maximum aerodynamic efficiency (L/D) reached to $\propto = 15^{\circ}$, while the maximum lift coefficient ($C_{l,max}$) of 2.63 was achieved at $\propto = 18^{\circ}$. When the Mach and Reynolds numbers are further increased to 0.71 and 2.31 x 10^7 respectively, the maximum aerodynamic efficiency (L/D) of 11.71 was obtained at $\propto = 15^{\circ}$ and plotted in the Fig. 11, whereas the maximum lift coefficient ($C_{l,max}$) of 2.68 was achieved at $\propto = 18^{\circ}$ (Fig. 12). Further introducing the Mach and Reynolds numbers to 1.18 and 3.85 x 10^7, it is noticed that the maximum aerodynamic efficiency (L/D) ratio as plotted in Fig. 13 has increased to 12.08 but has remained existent at $\propto = 15^{\circ}$, similar to the preceding Mach numbers tested; simultaneously, the maximum lift coefficient ($C_{l,max}$) of 2.72 has performed similarly. The C_l vs alpha for Ma=1.18 is plotted in Fig. 14.

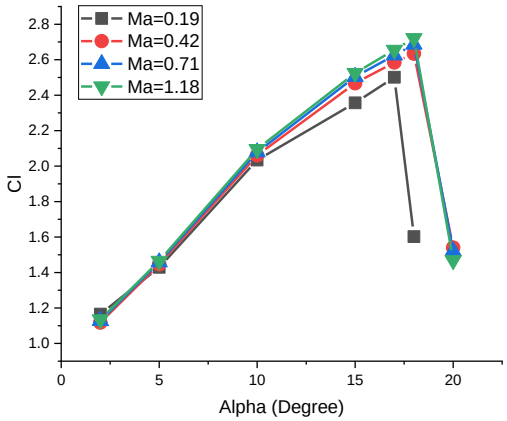


Fig. 5. Alpha vs Cl

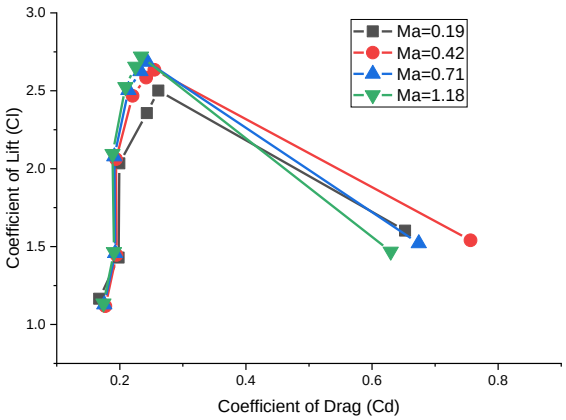


Fig. 6. Cd vs Cl

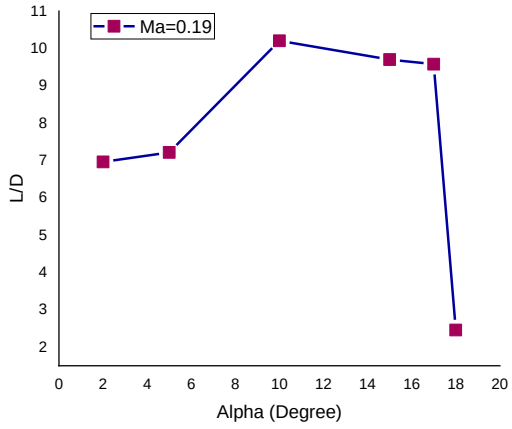


Fig. 7. Alpha vs L/D (Ma=0.19)

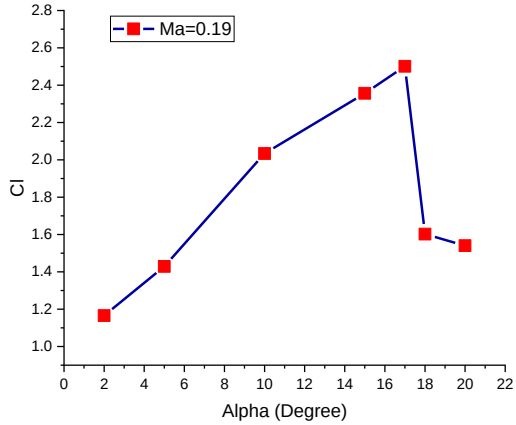


Fig. 8. Cl vs Alpha (Ma=0.18)

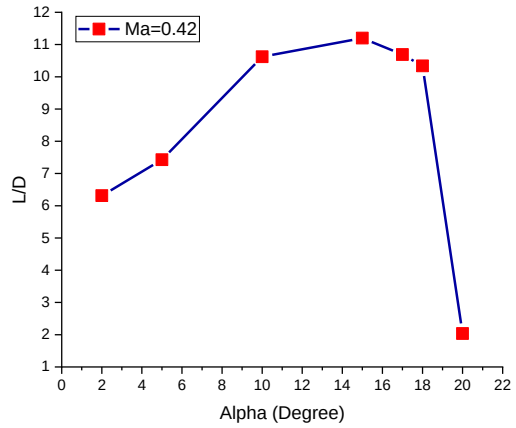


Fig. 9. Alpha vs L/D (Ma=0.42)

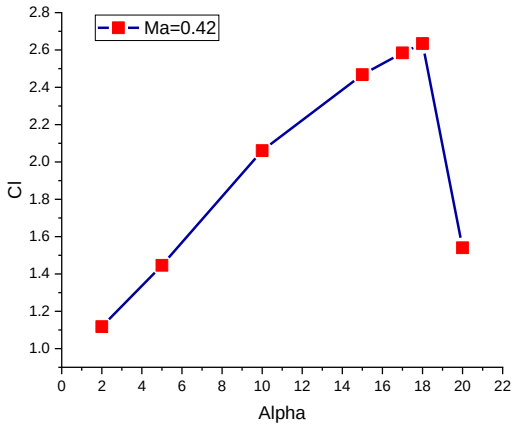


Fig. 10. Cl vs Alpha (Ma=0.42)

The performance improvements offered by the multi-element NLF airfoils may be quantified from the Breguet range equation (equation 2) that significantly influences the design of modern aircrafts, including engines.

$$Range = a_{\infty}\left(\frac{ML}{D}\right)\left(\frac{1}{TSFC}\right)ln\left(\frac{W_i}{W_f}\right) \quad (2)$$

For aircrafts using non-NLF airfoils, for instance, Boeing 747-400 at an altitude of 31,000 ft, there is an increase in L/D until the airfoil stalls and the decrement starts happening. At low Mach numbers, a non-NLF aircraft encounters boundary layer separation at the trailing edge, but at high Mach numbers, shock waves develop on the wing. For these aircrafts having non-NLF airfoil, the aerodynamic performance (ML/D) is maximum at lift coefficient (C_l) of 0.5. But then, the NLF airfoils exhibit a different phenomenon, as the numerical results obtained suggest. The maximum aerodynamic performance (ML/D) has consistently increased as the velocity reaches the speed of sound (343 m/s). It is identified that the maximum ML/D in the lowest calculated Ma=0.19 is 2.02. As the Mach number is increased to 0.42, the maximum ML/D reaches 4.70. When Ma=0.71, the ML/D gets as high as 11.71. However, at Ma=1.18, the maximum ML/D is 12.08. The aerodynamic Fig. of merit for the various tested Mach numbers is presented in the Fig. 15.

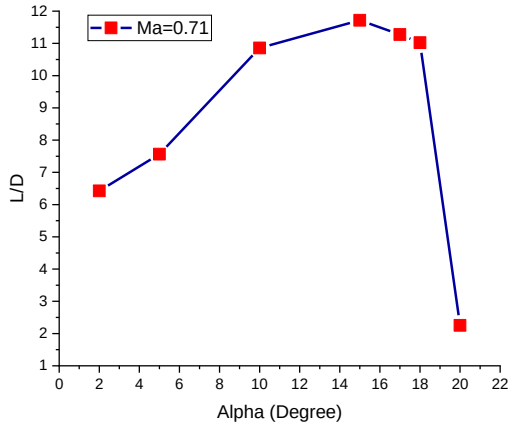


Fig. 11. Alpha vs L/D (Ma=0.71)

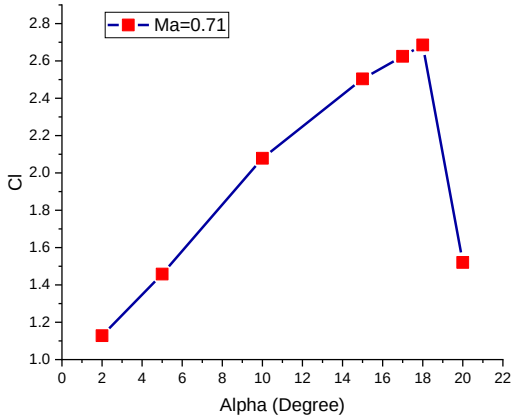


Fig. 12. Alpha vs Cl (Ma=0.71)

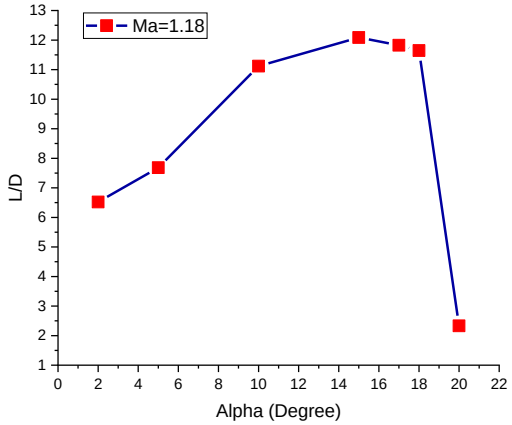


Fig. 13. Alpha vs L/D (Ma=1.18)

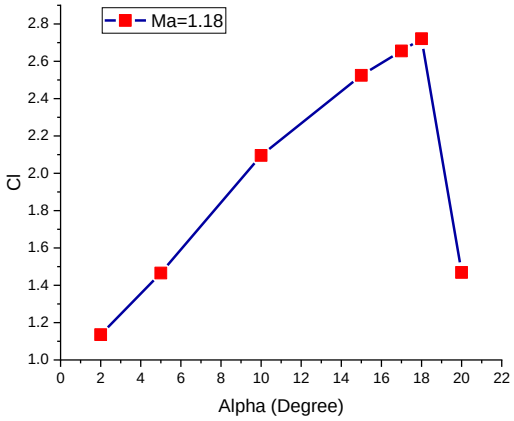


Fig. 14. Alpha vs Cl (Ma=1.18)

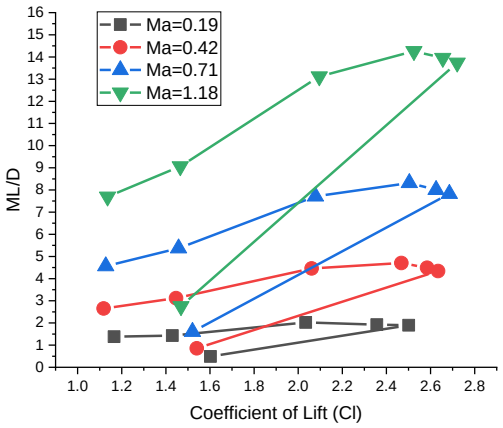


Fig. 15. Aerodynamic Fig. of Merit of Multi-Element NLF(1)-0115 Airfoil

The CFD results of boundary layer separation for various Mach numbers and alpha is presented in the Fig. 16.

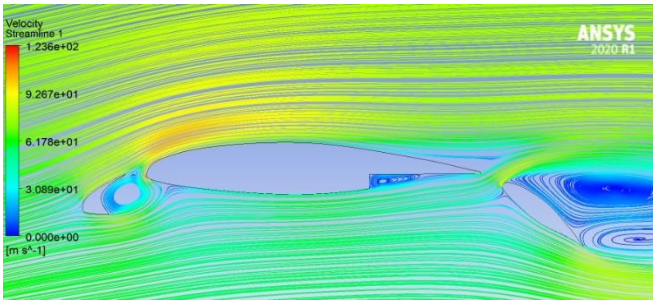


Fig. 16a. Boundary layer separation for Ma=0.18 at 5 Alpha

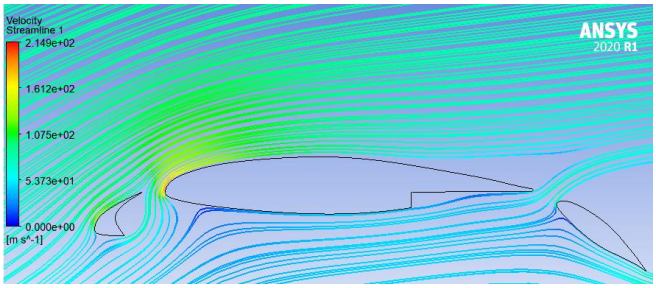


Fig. 16b. Boundary layer separation for Ma=0.18 at 15 Alpha

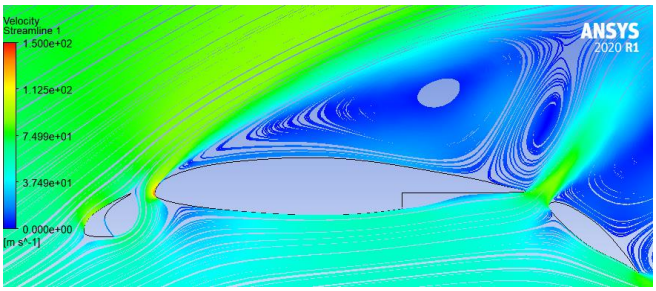


Fig. 16c. Boundary layer separation for Ma=0.18 at 18 Alpha

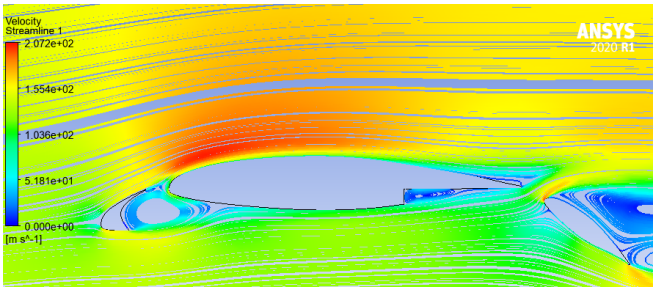


Fig. 16d. Boundary layer separation for Ma=0.42 at 2 Alpha

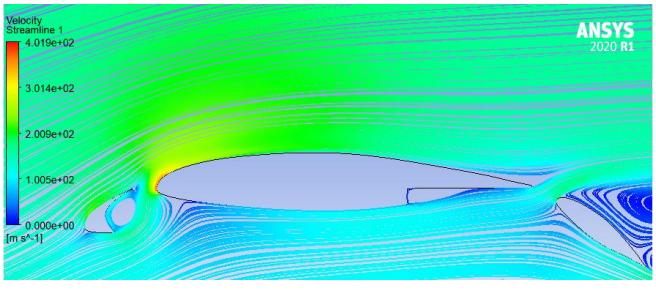


Fig. 16e. Boundary layer separation for Ma=0.42 at 10 Alpha

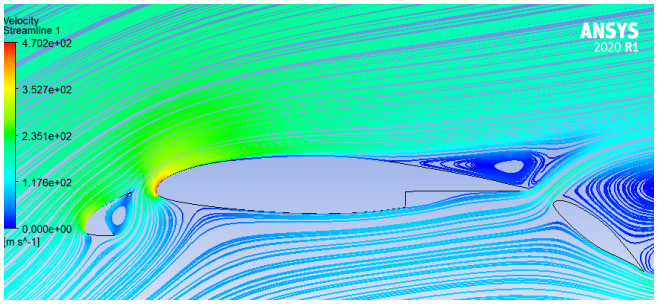


Fig. 16f. Boundary layer separation for Ma=0.42 at 18 Alpha

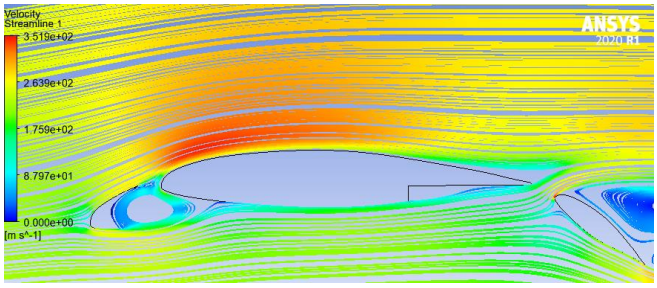


Fig. 16g. Boundary layer separation for Ma=0.71 at 2 Alpha

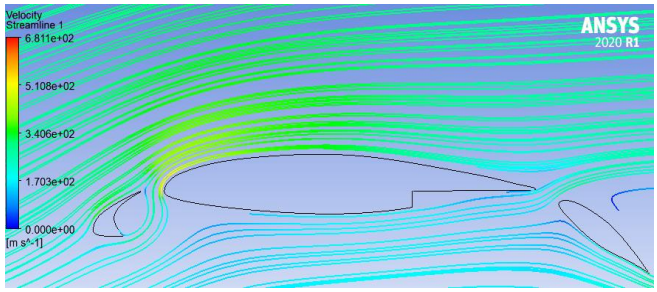


Fig. 16h. Boundary layer separation for Ma=0.71 at 10 Alpha

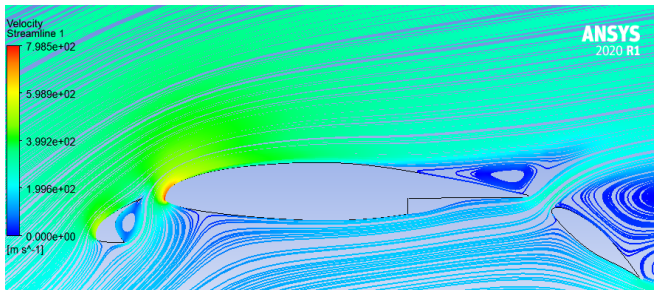


Fig. 16i. Boundary layer separation for Ma=0.71 at 18 Alpha

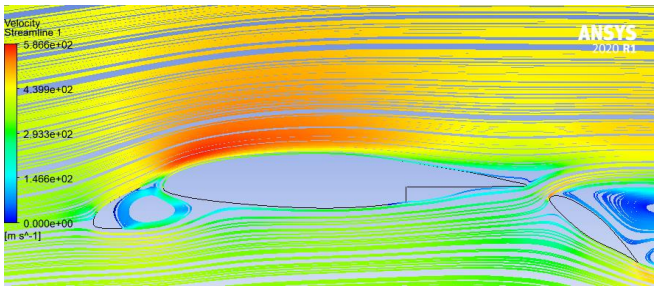


Fig. 16j. Boundary layer separation for Ma=1.18 at 2 Alpha

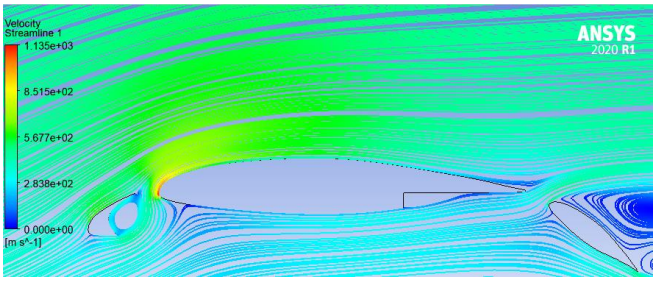


Fig. 16k. Boundary layer separation for Ma=1.18 at 10 Alpha

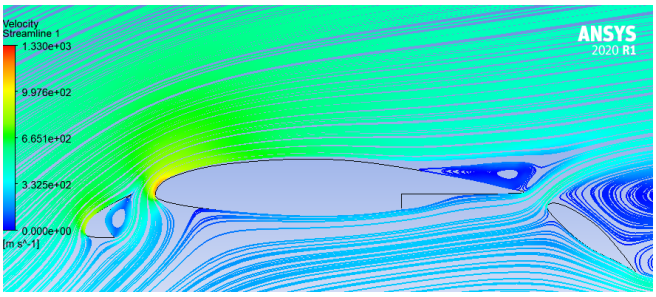


Fig. 16l. Boundary layer separation for Ma=1.18 at 18 Alpha

B. Pressure Distribution

The plotting for the pressure distribution on the multi-element airfoil is presented in the Fig. 17. The effects of increasing Mach number on the pressure distribution is rather prominent.

One particular observation of increasing Mach number on pressure distribution is the increase in lift coefficient (C_l). The origin of this behavior is seen in the Fig. 15 when the Mach number is increased from 0.19 to 0.42 and then to 0.71, ultimately reaching 1.18.

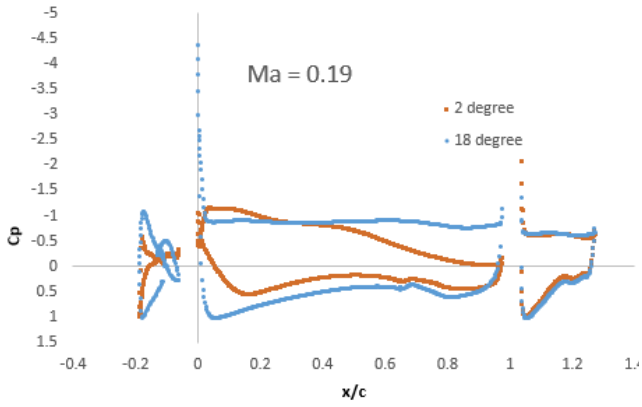


Fig. 17a. Distribution of Pressure at Ma=0.19 on various Alpha

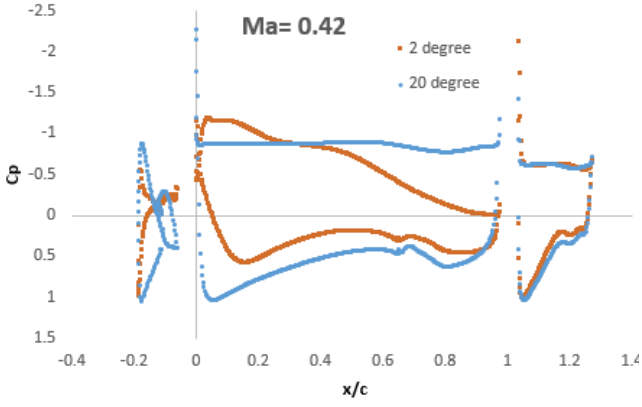


Fig. 17b. Effect of Ma=0.42 on various Alpha

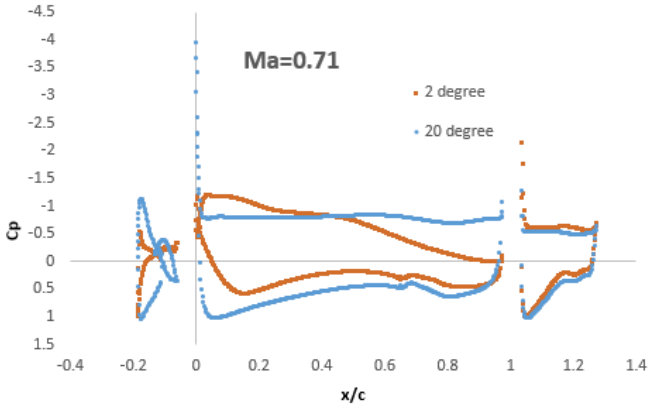


Fig. 17c. Effect of Ma=0.71 on various Alpha

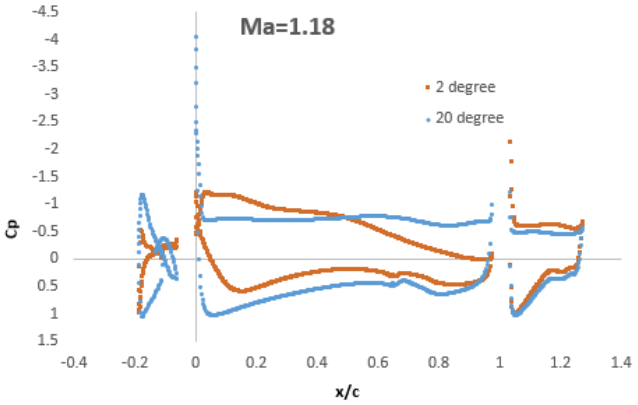


Fig. 17d. Effect of Ma=1.18 on various Alpha

In all the Mach number test cases, the increase in pressure coefficient (Cp) has gone up between $\alpha = 5^{\circ}$ and $\alpha = 10^{\circ}$. However, while the pressure has increased beyond up until the stall angle is achieved, what is critically important to note is that little influence of increase in Mach number at the slot between the slat and main element and flap and main element, except when the pressure distribution beyond $\alpha = 10^{\circ}$. It is also identified that the increase in freestream Mach number creates additional flow acceleration on the upper surface of the main element of airfoil. This phenomenon helps in stabilizing the boundary layer while it also promotes delaying transition [38].

From the pressure distributions plotted in the Fig. 17 for various alpha and corresponding Mach numbers, one critical observation is made. The pressure coefficient tends to increase at the aft element (flap) rather than the fore element (slat). This also suggests that the NLF may perform well only when the aft element is deployed and fore element is removed from the current configuration. This theory demands further investigation.

When the results of the NLF(1)-0115 multi-element airfoil are compared against the single element NLF(1)-0115 airfoil using the XFoil [44], the results suggest that at Ma=0.19 and Re=4.65x10^6, the C_l at $\propto = 5^{\circ}$is 0.77, which in comparison with the multi-element airfoil of similar Mach number but different Reynolds number of 6.47x10^6 is 100.529% less. Similarly, at Mach number of 0.4 and Reynolds number of 9.86x10^6, the C_l at $\propto = 10^{\circ}$is 1.23, whereas for similar Mach number but Reynolds number of 1.37x10^7, the C_l is 2.06. The results are plotted in the following Fig. 18 and 19.

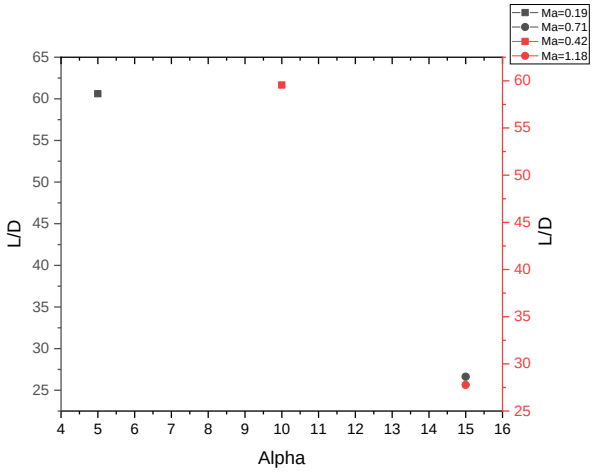


Fig. 18. Alpha vs L/D of NLF(1)-0115 [44]

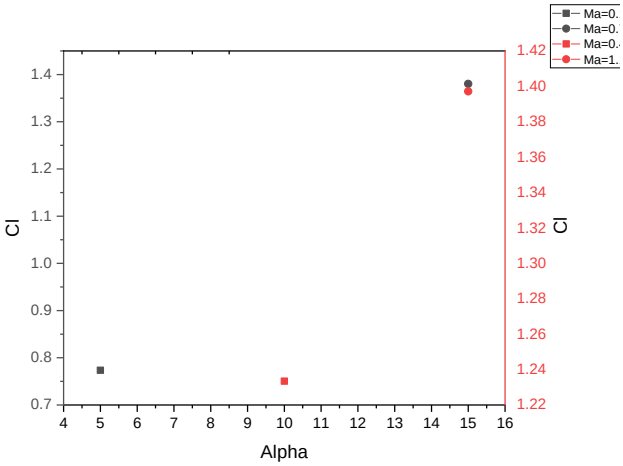


Fig. 19. Alpha vs Cl of NLF(1)-0115 [44]

V. Conclusion

The multi-element Natural Laminar Flow NLF(1)-0115 airfoil for a fast moving UAV was designed and computationally evaluated in this research. It has been identified that the deployment of multi-element – the leading edge slat and trailing edge flap – allows the improvement of aerodynamic efficiency (L/D) and the aerodynamic performance (ML/D) as the Mach number is increased from 0.19 to 1.18. The computational results also demonstrated that the trailing edge boundary layer separation at high Mach number has little turbulence, inherently owing to the aerodynamic characteristics of the natural laminar flow airfoil NLF(1)-0115. Through the deployment of the slat and flap, the separation of boundary layer that create turbulence is also improved. The multi-element configuration enables significant improvement in the NLF airfoil. The maximum aerodynamic performance (ML/D) from the Breguet range equation achieved was 14.26 at Mach number 1.18 and $\alpha = 15^{\circ}$ which when compared to the lowest tested Mach number at 0.19 where ML/D was highest at 2.02 at $\alpha = 10^{\circ}$. The results show high lift coefficients at relatively low value of drag coefficient. It was also identified that achieving significant laminar flow behavior on the lower surface of the multi-element airfoil is fundamentally challenging.

Results have confirmed that there is an increase in pressure on the lower surface of the aft element. This may be suggestive of the idea that the NLF airfoils may perform better only when the aft element is deployed and the fore element is removed from the configuration. Further studies may be required to computationally and experimentally investigate this hypothesis to not only obtain a boundary layer separation without turbulence at the trailing edge but also the aerodynamic optimization of the multi-element airfoil itself.

References

[1] L. Steers, "Natural Laminar Flow Flight Experiment", *NASA Dryden Flight Research Center*, 1981. [Online]. Available: https://ntrs.nasa.gov/api/citations/19810010484/downloads/19810010484.pdf. [Accessed: 03- Sep- 2021].

[2] B. Holmes, C. Croom, E. Hastings, C. Obara and C. Vandam, "Flight research on natural laminar flow", *NASA Langley Research Center*, 1986. [Online]. Available: https://ntrs.nasa.gov/api/citations/19880005568/downloads/19880005568.pdf?attachment=true. [Accessed: 15- Aug- 2021].

[3] B. Holmes, C. Obara, G. Gregorek, M. Hoffman and R. Freuhler, "Flight Investigation of Natural Laminar Flow on the Bellanca Skyrocket II", *SAE Technical Paper Series*, 1983. Available: 10.4271/830717 [Accessed 4 September 2021].

[4] B. Holmes and C. Obara, "Observations and implications of natural laminar flow on practical airplane surfaces", *Journal of Aircraft*, vol. 20, no. 12, pp. 993-1006, 1983. Available: 10.2514/3.48203 [Accessed 2 September 2021].

[5] B. Holmes, C. J. Obara and L. Yip, "Natural laminar flow experiments on modern airplane surfaces", *The Pennsylvania State University*, 1984. [Online]. Available: https://citeseerx.ist.psu.edu/viewdoc/download?doi=10.1.1.731.3131&rep=rep1&type=pdf. [Accessed: 18- Aug- 2021].

[6] C. J. Obara and B. Holmes, "Flight-measured laminar boundary-layer transition phenomena including stability theory analysis", *Stanford University*, 1985. [Online]. Available: https://searchworks.stanford.edu/view/5714059. [Accessed: 09- Jul- 2021].

[7] D. WARD and S. MILEY, "An evaluation of flight test measurement techniques for obtaining airfoil pressure distributions and boundary layer transition locations", *2nd Flight Testing Conference*, 1983. Available: 10.2514/6.1983-2689 [Accessed 4 August 2021].

[8] W. Wentz, A. Ahmed and R. Nyenhuis, "Further Results of Natural Laminar Flow Flight Test Experiments", *SAE Transactions*, vol. 94, pp. 508-521, 1985. [Accessed 4 September 2021].

[9] D. Somers, "Design of a Slotted, Natural-Laminar-Flow Airfoil for Business-Jet Applications", *Airfoils Incorporated, Port Matilda, Pennsylvania*, 2019. [Online]. Available: https://ntrs.nasa.gov/api/citations/20190031816/downloads/20190031816.pdf. [Accessed: 11- Jul- 2021].

[10] A. M. O. Smith, "High-Lift Aerodynamics", *Journal of Aircraft*, vol. 12, no. 6, pp. 501-530, 1975. Available: 10.2514/3.59830 [Accessed 2 June 2021].

[11] Y. Shi, C. Mader, S. He, G. Halila and J. Martins, "Natural Laminar-Flow Airfoil Optimization Design Using a Discrete Adjoint Approach", *AIAA Journal*, vol. 58, no. 11, pp. 4702-4722, 2020. Available: 10.2514/1.j058944 [Accessed 14 June 2021].

[12] J. Coder, M. Maughmer and D. Somers, "Theoretical and Experimental Results for the S414, Slotted, Natural-Laminar-Flow Airfoil", *Journal of Aircraft*, vol. 51, no. 6, pp. 1883-1890, 2014. Available: 10.2514/1.c032566 [Accessed 17 June 2021].

[13] R. T. Whitcomb and L. R. Clark, *An Airfoil Shape for Efficient Flight at Supercritical Mach Numbers*, 1st ed. NASA technical memorandum, 1965, pp. 1-57.

[14] . Coder and D. Somers, "Design of a slotted, natural-laminar-flow airfoil for commercial transport applications", *Aerospace Science and Technology*, vol. 106, p. 106217, 2020. Available: 10.1016/j.ast.2020.106217 [Accessed 16 June 2021].

[15] M. Fujino, Y. Yoshizaki and Y. Kawamura, "Natural-Laminar-Flow Airfoil Development for a Lightweight Business Jet", *Journal of Aircraft*, vol. 40, no. 4, pp. 609-615, 2003. Available: 10.2514/2.3145 [Accessed 4 September 2021].

[16] Y. Shi, C. Mader, S. He, G. Halila and J. Martins, "Natural Laminar-Flow Airfoil Optimization Design Using a Discrete Adjoint Approach", *AIAA Journal*, vol. 58, no. 11, pp. 4702-4722, 2020. Available: 10.2514/1.j058944 [Accessed 4 September 2021].

[17] Z. Han, J. Chen, K. Zhang, Z. Xu, Z. Zhu and W. Song, "Aerodynamic Shape Optimization of Natural-Laminar-Flow Wing Using Surrogate-Based Approach", *AIAA Journal*, vol. 56, no. 7, pp. 2579-2593, 2018. Available: 10.2514/1.j056661 [Accessed 4 September 2021].

[18] M. Selig, M. Maughmer and D. Somers, "Natural-laminar-flow airfoil for general-aviation applications", *Journal of Aircraft*, vol. 32, no. 4, pp. 710-715, 1995. Available: 10.2514/3.46781 [Accessed 4 September 2021].

[19] M. Selig, M. Maughmer and D. Somers, "Natural-laminar-flow airfoil for general-aviation applications", *Journal of Aircraft*, vol. 32, no. 4, pp. 710-715, 1995. Available: 10.2514/3.46781 [Accessed 18 August 2021].

[20] S. Xiao and Z. Chen, "Investigation of Flow over the Airfoil NACA 0010-35 with Various Angle of Attack", *MATEC Web of Conferences*, vol. 179, p. 03020, 2018. Available: 10.1051/matecconf/201817903020 [Accessed 24 June 2021].

[21] A. Diab, M. Alaa, A. Hossam El-Din, H. Salem and Z. Ghoneim, "Performance Degradation of Wind Turbine Airfoils due to Dust Contamination: A Comparative Numerical Study", *Volume 9: Oil and Gas Applications; Supercritical CO2 Power Cycles; Wind Energy*, 2015. Available: 10.1115/gt2015-44012 [Accessed 16 August 2021].

[22] M. Mohamed and R. Yadav, "Flow separation control using the cetacean species nose design", *European Journal of Mechanics - B/Fluids*, vol. 89, pp. 139-150, 2021. Available: 10.1016/j.euromechflu.2021.05.005 [Accessed 7 August 2021].

[23] I. F. Zidane, K. M. Saqr, G. Swadener, X. Ma and M. F. Shehadeh, "COMPUTATIONAL FLUID DYNAMICS STUDY OF DUSTY AIR FLOW OVER NACA 63415 AIRFOIL FOR WIND TURBINE APPLICATIONS", *Jurnal Teknologi*, vol. 79, no. 7-3, 2017. Available: 10.11113/jt.v79.11877 [Accessed 15 August 2021].

[24] A. Meana-Fernández, J. Fernández Oro, K. Argüelles Díaz and S. Velarde-Suárez, "Turbulence-Model Comparison for Aerodynamic-Performance Prediction of a Typical Vertical-Axis Wind-Turbine Airfoil", *Energies*, vol. 12, no. 3, p. 488, 2019. Available: 10.3390/en12030488 [Accessed 4 September 2021].

[25] N. Sorensen et al., "CFD code comparison for 2D airfoil flows", *Journal of Physics: Conference Series*, vol. 753, p. 082019, 2016. Available: 10.1088/1742-6596/753/8/082019 [Accessed 14 September 2021].

[26] A. Subramanian et al., "Effect of airfoil and solidity on performance of small scale vertical axis wind turbine using three dimensional CFD model", *Energy*, vol. 133, pp. 179-190, 2017. Available: 10.1016/j.energy.2017.05.118 [Accessed 15 August 2021].

[27] V. Anil Hemanth and U. Jyothi, "CFD Analysis of a Solid Propellant Retro Rocket Motor using Ansys Fluent", *E3S Web of Conferences*, vol. 184, p. 01054, 2020. Available: 10.1051/e3sconf/202018401054 [Accessed 8 August 2021].

[28] P. Badelwa and V. Kesharwani, "Thermal Simulation and an Analysis on an Exhaust Gas of a Teg Model using Fluent", *International Journal of I.C. Engines and Gas Turbines*, vol. 6, no. 2, pp. 1-19, 2020. [Accessed 14 August 2021].

[29] D. Sofialidis, "HPC with ANSYS Fluent", *PRACE Autumn School 2013 – Industry Oriented HPC Simulations*, 2013. [Online]. Available: https://materials.prace-ri.eu/350/1/hpcAnsys.pdf. [Accessed: 18- May- 2021].

[30] A. Serageldin, A. Abdelrahman and S. Ookawara, "Earth-Air Heat Exchanger thermal performance in Egyptian conditions: Experimental results, mathematical model, and Computational Fluid Dynamics simulation", *Energy Conversion and Management*, vol. 122, pp. 25-38, 2016. Available: 10.1016/j.enconman.2016.05.053 [Accessed 15 August 2021].

[31] P. Kumar and S. Singh, "Flow past a bluff body subjected to lower subcritical Reynolds number", *Journal of Ocean Engineering and Science*, vol. 5, no. 2, pp. 173-179, 2020. Available: 10.1016/j.joes.2019.10.002 [Accessed 11 August 2021].

[32] P. Mondal, M. Rahman and A. Hasan, "Numerical analysis of bio-inspired corrugated airfoil at low Reynolds number", 2016. Available: 10.1063/1.4958388 [Accessed 11 August 2021].

[33] L. Kharulaman, A. Aabid, F. Mehaboobali and S. Khan, "Research onFlows for NACA 2412 Airfoil using Computational Fluid Dynamics Method", *International Journal of Engineering and Advanced Technology (IJEAT)*, vol. 9, no. 1, 2021. [Accessed 6 August 2021].

[34] Ansys, "Choosing the Pressure-Velocity Coupling Method", *National Agency for New Technologies, Energy and Sustainable Economic Development*, 2009. [Online]. Available: https://www.afs.enea.it/project/neptunius/docs/fluent/html/ug/node785.htm. [Accessed: 17- Aug- 2021].

[35] M. Mohamed, G. Janiga, E. Pap and D. Thévenin, "Multi-objective optimization of the airfoil shape of Wells turbine used for wave energy conversion", *Energy*, vol. 36, no. 1, pp. 438-446, 2011. Available: 10.1016/j.energy.2010.10.021 [Accessed 25 June 2021].

[36] T. Fondelli, A. Andreini and B. Facchini, "Numerical Simulation of Dam-Break Problem Using an Adaptive Meshing Approach", *Energy Procedia*, vol. 82, pp. 309-315, 2015. Available: 10.1016/j.egypro.2015.12.038 [Accessed 4 June 2021].

[37] T. Michal et al., "Comparing Unstructured Adaptive Mesh Solutions for the High Lift Common Research Airfoil", *AIAA Journal*, vol. 59, no. 9, pp. 3566-3584, 2021. Available: 10.2514/1.j060088 [Accessed 25 July 2021].

[38] J. Coder and D. Somers, "Design of a slotted, natural-laminar-flow airfoil for commercial transport applications", *Aerospace Science and Technology*, vol. 106, p. 106217, 2020. Available: 10.1016/j.ast.2020.106217 [Accessed 6 May 2021].

[39] V. D'Alessandro, S. Montelpare, R. Ricci and A. Zoppi, "Numerical modeling of the flow over wind turbine airfoils by means of Spalart–Allmaras local correlation based transition model", *Energy*, vol. 130, pp. 402-419, 2017. Available: 10.1016/j.energy.2017.04.134 [Accessed 12 July 2021].

[40] S. Benjanirat, L. Sankar and G. Xu, "Evaluation of Turbulence Models for the Prediction of Wind Turbine Aerodynamics", *ASME 2003 Wind Energy Symposium*, 2003. Available: 10.1115/wind2003-517 [Accessed 18 July 2021].

[41] F. Rizzo, V. D'Alessandro, S. Montelpare and L. Giammichele, "Computational study of a bluff body aerodynamics: Impact of the laminar-to-turbulent transition modelling", *International Journal of Mechanical Sciences*, vol. 178, p. 105620, 2020. Available: 10.1016/j.ijmecsci.2020.105620 [Accessed 6 August 2021].

[42] M. Costes and F. Moens, "Advanced numerical prediction of iced airfoil aerodynamics", *Aerospace Science and Technology*, vol. 91, pp. 186-207, 2019. Available: 10.1016/j.ast.2019.05.010 [Accessed 25 July 2021].

[43] S. Mittal and T. Tezduyar, "A finite element study of incompressible flows past oscillating cylinders and aerofoils", *International Journal for Numerical Methods in Fluids*, vol. 15, no. 9, pp. 1073-1118, 1992. Available: 10.1002/fld.1650150911 [Accessed 3 August 2021].

[44] Airfoiltools, "NLF(1)-0115 (nlf0115-il) Xfoil prediction polar at RE=1,000,000 Ncrit=9", Airfoiltools.com, 2021. [Online]. Available: http://airfoiltools.com/polar/details?polar=xf-nlf0115-il-1000000. [Accessed: 17- Nov- 2021].

An Overview of Passive Flow Control Techniques in Supersonic Flows

1st Zukhruf Liaqat
Department of Aeronautical Engineering
National University of Sciences and Technology
Risalpur, Pakistan
zliaquat.ms13ae@student.nust.edu.pk

2nd Aamer Shahzad
Department of Aeronautical Engineering
National University of Sciences and Technology
Risalpur, Pakistan
a.shahzad@cae.nust.edu.pk

***Abstract*—Fluid flow is characterized by active and passive controls. Active flow control exploits external energy to control flow externally and internally. However, passive flow control used physical devices to regulate the flow of the fluid without incorporating any auxiliary power. Passive control is inherent to air vehicles to achieve desired characteristics smoothly. Most of the times, passive flow control devices are installed from the time of the manufacturing. These devices also come as external kits. The shape and size of the device being installed determines the pressure regulation, here the boundary layer effects are prominent. Several techniques are discussed in this paper with a focus on how they achieve desired flow characteristics by pressure regulation and ultimately contribute positively towards required flight characteristics. Some common passive flow devices include vortex generators, tabs, leading edge slats, cavities, and flow vanes. These physical devices do not need an external energy and change pressure distribution to a desirable form through geometric changes of the surfaces. The phenomena of flow separation and stall are of particular significance when passive flow techniques are under consideration. The weight and drag may experience slight increase but a cost-efficiency trade-off is made to achieve optimum results. The aim behind flow control is to regulate pressure recovery and remove unsteady pressure changes. The techniques of passive flow control are widely used because of their simplicity, affordability, and accessibility.**

Keywords—Auxiliary energy, boundary layer, control devices, flow characteristics, flow separation, passive flow, pressure fluctuations, supersonic regime, vortex generation

I. INTRODUCTION

In fluid dynamics, flow control is a necessary tool to regulate pressure fluctuations in order to control the total drag of the body [1]. The flow controls techniques are primarily used to achieve improved flow characteristics and reduce the unwanted disturbances such as unsteady pressure changes. The flow control techniques are divided into two types: active and passive. Passive control techniques do not require any auxiliary energy and are achieved by the geometric changes most of the time. These flow control techniques are used to improve the flight conditions of air vehicles [2]. The passive flow control manipulates the characteristics of the flow in the boundary layer and eventually affects and controls the mixing of the flow. The passive flow control is achieved by installing several devices which will be briefly discussed in subsequent sections. These devices are the mechanical options aerodynamicists use to achieve flow characteristics. In contrast, an active flow control technique makes use of external energy and is a paid choice usually. Passive flow control techniques have been extensively used due to their simplicity, affordability, and accessibility. The paper presents a review of several passive flow control techniques in the supersonic regime.

II. DISCUSSION

TABLE I: Passive Flow Control Devices with Their Advantages and Disadvantages

CONTROL DEVICE	ADVANTAGES	DISADVANTAGES
Vortex generators	Reduction of stall High controllability at low speeds	Inconvenience in washing and/or painting the wing or surfaces where VG is installed
Leading edge slats	Additional lift creation at different flight sequences such as takeoff, climb, approach and landing at low speeds	Additional weight and structural complexity Creation of high stall angle
Cavities	Drag reduction Noise reduction	Not preferred for high speed flows
Flow vanes	Efficient control device in turbines	High maintenance
Tabs	High aerodynamic performance	Added weight leads to drag production
Corrugations	Enhancement of aerodynamic performance at gliding flight Low membrane stress	Increased surface drag leads to increased fuel consumption

A. Vortex generators

TABLE II: Specifications of a Vortex Generator

SPECIFICATION	DESCRIPTION
Used for	Flow separation Drag generation
Installation	Mostly close to leading edge Various lifting surfaces
Shapes	Triangular (delta, cropped delta) Rectangular (stretched square, trapezium)
Height	Comparable to boundary layer thickness (for MVGs, << BL thickness)

Vortex generator is one of the devices used in techniques employed for passive flow control. In simple terms, it delays the flow separation thus reducing the formation of trailing edge vortices that ultimately lead to the generation of drag on the body. It is an aerodynamic device with varying sizes according to the requirement of the application that is attached to delay the flow separation. In aerodynamics applications, the shape is usually of an airfoil attached to a vane that is placed on the aircraft's wing [3]. The vortex generators are usually triangular or rectangular in shape with a height of approximately equal to boundary layer thickness

and placed on the thickest part of the surface over which they are employed [4].

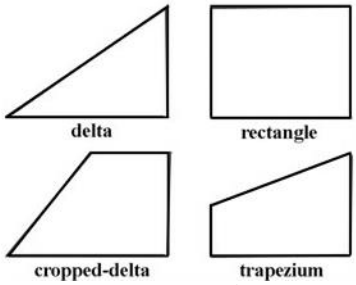


Figure 1: Various shapes of vortex generators

They are attached to the wings and vertical tail of most airliners.

Vortex generators are also used on other aerodynamic control surfaces such as elevators, ailerons and rudders and flaps. The application of vortex generators is used in turbine blades as well [5].

In most of the applications, the vortex generators are placed very close to leading-edge to ensure a smooth fluid flow over the surface all the way to the trailing edge [6]. The vortex generators are given an angle of attack with respect to the local flow to produce an energetic tip vortex that captures the surrounding fluid flow towards itself thus removing the local eddies and directing the flow into slow-moving boundary layer that sweeps across the surface. The vortex generators encourage the creation of the turbulent flow that is less prone to flow separation than the laminar flow [7].

Passive flow control is inherent to most of the aircraft and these vortex generators are present on aircraft from the time of manufacturing. In addition to that, vortex generators are also available in VG kits [8, 9]. One problem that may arise with vortex generators installed on the external surfaces is of icing due to local flow. However, since the vortex generator is placed within the boundary layer, the icing due to local cold flow does not usually arise and hence extra measures to de-ice the surface are not usually needed. The application of vortex generators is subjected to weight and lift considerations [3]. The one added advantage with the employment of such devices with the addition of low weight considerations is that they do increase the maximum takeoff weight but it can be overcome with a tradeoff with enhanced delay in flow separation and hence drag reduction.

In supersonic flow, shock wave and boundary layer interactions are common and not only can change the shock wave structure but also induce accelerated boundary layer development [10]. This can affect the total pressure recovery of the system and hence the need for a technique to control the flow arises. The concept of micro vortex generators (MVGs), although is novel but it has gained much appreciation in the recent past. They have shown better results than conventional suction systems. Usually vortex generators have comparable height with boundary layer thickness. However, VGs smaller in height than BL thickness have also shown effective results with enhanced flow control ability with minimum resistance and such VGs are conveniently named as micro vortex generators. MVGs do not decrease the mass flow rate and have greater potential than suction systems since no power penalties are observed in the former. The vortices generated by the MVGs were experimentally validated where the main purpose of such vortices was to enhance the mixing effect of higher momentum external flow and the lower momentum flow around the wall [2].

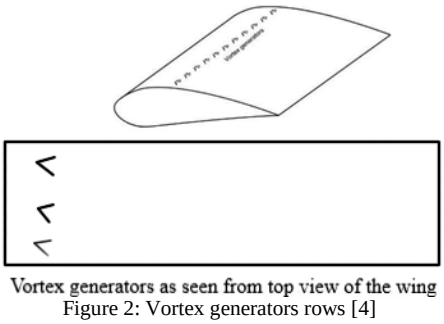


Figure 2: Vortex generators rows [4]

This figure represents the installation of triangular vortex generators throughout the wing structure.

B. Leading Edge Slats

Leading-edge slats are one of the earliest passive flow control techniques employed on aircraft to delay the flow separation and check pressure fluctuations in high-speed flows. These are attached to the leading edge of the airfoils and manipulate the flow in the space between the main body and slat to delay the flow separation. The vortices are generated due to the presence of these slots and vary in size while accelerating the flow. The larger vortices correspond to the presence of a lower Reynolds number while smaller vortices indicate the presence of high Re flow [11]. Due to the installment of slats, the flow gains momentum and transports it to the boundary layer thus energizing it enough to delay the flow separation. The concept of slats in high speed flows is effective since the pressure recovery becomes a significant consideration in supersonic regimes. The increase in drag can be traded off to the advantages provided by the installment of leading-edge slats [12]. Leading-edge slats are effective passive flow control techniques with no requirement of external energy and best suited to delay the stall of the aircraft. They are typically used in fixed as well as retractable slats in high-speed flows [13].

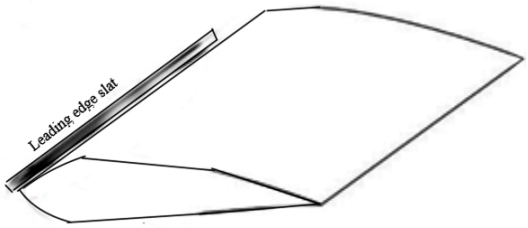


Figure 3: Leading-edge slat [7]

C. Cavities

TABLE III: Features of Cavities Over Airfoil Surfaces

SPECIFICATION	DESCRIPTION
Preferred flight regime	Subsonic
Used for	Generation of pressure gradient due to counter rotating vortices
Installation	Over airfoil's suction surface, mostly at leading edge
Added benefit	Noise reduction

Although more preferred for the subsonic regime, cavities are used for passive flow control in low supersonic flows as well. The basic principle behind mounting a cavity on an airfoil surface is to generate a pressure gradient [6]. The pressure gradient is generated due to the presence of counter-rotating vortices trapped inside the cavity. The presence of these trapped vortices ensures the generation of a low-pressure region and eventually contributes to reducing the total drag. The cavity created in the airfoil's suction surface hosts counter-rotating flows which delay the stall phenomenon thus contributing positively to the lift production [14]. Cavitied airfoils do not work efficiently since the high speed will induce higher pressure fluctuations and geometric changes will be sensitive to such fluctuations. Near transonic and low supersonic flows, they prove to be effective devices for passive flow. The cavity can be introduced at leading or trailing edge, however, leading-edge modifications have been more successful for the transonic regime than their trailing edge counterparts.[15] Not only the cavitied airfoils improve flight characteristics through passive flow control, but these are also an effective way to reduce noise disturbances in the flow. Since open cavities in supersonic flows can create further problems of unsteady pressure tones, spoilers are used to reduce the amplitudes of such disturbances. [16]



Figure 4: Generation of vortices in an airfoil [16]

D. Flow vanes

TABLE IV: Specification of a Flow Vane

SPECIFICATION	DESCRIPTION
Commonly used in	Turbines
Commonly used for	Delaying stall and pressure regulation
Size	Chord length comparable to attached surface
Installation	Above suction surface of airfoil

A typical passive flow control device for turbines, flow vanes benefit the flow by delaying the stall and improving pressure regulation by catering for excessive and unsteady fluctuations in pressure. [15, 17]. The flow vanes have small yet comparable chord length with the main body on which these are installed [18]. They are placed above the suction surface of the airfoil and delay the flow separation thus improving the characteristics of the flow.

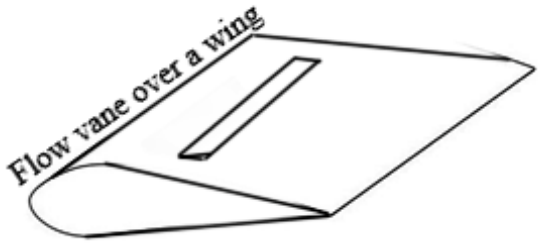


Figure 5: Flow vane over a simplified wing showing the vane and wing surface are attached at root of the flow vane [18]

E. Tabs

TABLE V: Salient Features of a Typical Tab

SPECIFICATION	DESCRIPTION
Installment	Trailing edge of lifting surface
Vortex generation	Counterclockwise
Size and position	Determine flow mixing in high and low momentum regions
Height	Comparable to boundary layer thickness

Tabs or lift-producing tabs are installed on the trailing surfaces of the lifting devices in the form of small plates to provide effective results for flow control. Again, these tabs do not need an external power and control flow through the geometric changes of the body they are attached with [1]. The flap size, height and position relative to the flow determine the mixing of the flow in high and low momentum regions. The height of the tab is measured relative to the boundary layer to have a perspective about the impact on the boundary layer and eventually on flow separation. A typical example of tabs providing passive flow control is Gurney flap [19]. After installation, counter-rotating vortices are produced behind the flap. These flaps encourage flow to stay attached with the surface thus delaying the flow separation [20].

The tabs are installed mainly on the wing airfoils but are also used on the tail surface and have shown commendable results for the increase in the lift at an angle of attack with little increase in lift coefficient with respect to baseline position [1]. These tabs are known as lift-enhancing tabs for the same reason since they favor drag reduction due to their performance on the main airfoil as well as on the tail flaps.

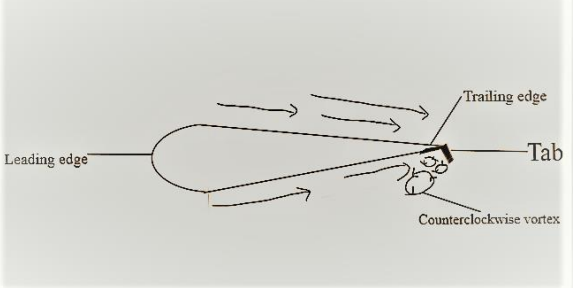


Figure 6: Lift enhancing tab on an airfoil along with counterclockwise vortices [10]

The passive flow control techniques makes use of a variety of different devices such as grooves and ribs, also of high significance in supersonic regime [21]. The principle behind using these devices is to achieve maximum pressure recovery

using least external energy. In many cases, this means a trade-off between cost and efficiency.

F. Corrugations

TABLE VI: Features of Corrugation

SPECIFICATION	DESCRIPTION
Used for	Passive flow control through effective jet mixing in supersonic regime
Shape	Triangular or semi triangular
Installation	Airfoil Nozzle exit

The flow control at supersonic regime often uses the mechanism of corrugation to enhance the effectiveness of the flow jet mixing. At high speeds semi corrugated triangular tabs are employed for flow control processes. The effectiveness of corrugation is measured through pitot pressure determination where the tabs are fixed at nozzle exit at the inclination of 180 degrees from each other. The static pressure is measured at different values of back pressure and the vortices generated due to the presence of the tabs enhances flow mixing as high as Mach 2. Corrugation is used practically to reduce thrust loss and enhance aerodynamic performance. The effect of corrugation will deteriorate propulsive efficiency in low Re flows, yet the advantages of high thrust and lift outweigh the disadvantages.

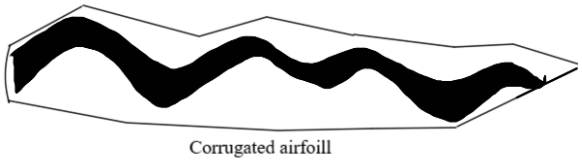


Figure 7: A corrugated airfoil outlining exaggerated pattern inside [22]

III. LIMITATIONS

While passive flow control techniques enable improved flight characteristics without using auxiliary power, instantaneous increases in drag may be observed in some cases such as cavity flows [20]. Moreover, some devices above mentioned work best in low supersonic flow, and assumptions have to be made for high supersonic flow analysis if the same devices are used for passive flow control at higher Mach.

IV. CONCLUSION

Flow control is a necessary requirement for any fluid flow. Two basic control techniques are active and passive flow controls. Passive flow control is achieved by physical devices without an external source of energy while active flow requires a continuous supply of energy. Passive flow manipulates the flow characteristics and is involved in mixing of flow to achieve desirable characteristics. Vortex generator is one of the widely used device to control flow through passive means. It creates vortices and delays production of trailing edge vortices eventually reducing the drag being produced. VGs are installed on lifting as well as control surfaces [23]. Leading edge slats are passive flow control device in high speed and transonic flows that delays the flow separation and reduces pressure fluctuations. They are applicable for both high and low Re flows. Cavities are another passive flow control device that use trapped counter-rotating vortices to achieve required flow characteristics. Among other devices, flow vanes are another common name typically used for turbine flows hence remain in near transonic regions [24]. The main aim of flow vanes is to delay the stall. Many of leading and suction surface devices have been discussed but trailing surfaces also experience passive flow control techniques. The tabs attached to trailing edges of lifting surfaces provide remarkable results in the lift generation and consequent drag reduction due to geometric changes. The constraints of passive flow include weight and drag increases at certain instances; however, a trade-off is made between cost and efficiency to achieve desirable flow characteristics by using only physical devices and without employing external energy.

REFERENCES

[1] M. Asadullah, S. A. Khan, W. Asrar, and E. Sulaeman, "Passive control of base pressure with static cylinder at supersonic flow," *IOP Conf. Ser. Mater. Sci. Eng.*, vol. 370, no. 1, 2018, doi: 10.1088/1757-899X/370/1/012050.

[2] B. Zhang, Q. Zhao, X. Xiang, and J. Xu, "An improved micro-vortex generator in supersonic flows," *Aerosp. Sci. Technol.*, vol. 47, pp. 210–215, 2015, doi: 10.1016/j.ast.2015.09.029.

[3] A. R. Paul, S. Joshi, A. Jindal, S. P. Maurya, and A. Jain, "Experimental studies of active and passive flow control techniques applied in a twin air-intake," *Sci. World J.*, vol. 2013, 2013, doi: 10.1155/2013/523759.

[4] T. M. Reedy, G. S. Elliott, J. C. Dutton, and Y. Lee, "Passive control of high-speed separated flows using splitter plates," *AIAA J.*, vol. 50, no. 7, pp. 1586–1595, 2012, doi: 10.2514/1.J051566.

[5] I. Kim and N. Chokani, "Navier-Stokes study of supersonic cavity flowfield with passive control," *J. Aircr.*, vol. 29, no. 2, pp. 217–223, 1992, doi: 10.2514/3.46147.

[6] J. G. Dudley and L. Ukeiley, "Detached eddy simulation of a supersonic cavity flow with and without passive flow control," *20th AIAA Comput. Fluid Dyn. Conf. 2011*, no. June, pp. 27–30, 2011, doi: 10.2514/6.2011-3844.

[7] Y. V. Pehlivanoglu and B. Yagiz, "Optimization of active/passive flow control parameters on airfoils at transonic speeds," *J. Aircr.*, vol. 48, no. 1, pp. 212–219, 2011, doi: 10.2514/1.C031066.

[8] M. Gad-el-Hak, "Introduction to Flow Control," *Flow Control*, no. 1904, pp. 1–107, 2007, doi: 10.1007/3-540-69672-5_1.

[9] *Applications of Circulation Control Technology*. 2006.

[10] N. Chokani and I. Kim, "Suppression of pressure oscillations in an open cavity by passive pneumatic control," *AIAA 22nd Fluid Dyn. Plasma Dyn. Lasers Conf. 1991*, 1991, doi: 10.2514/6.1991-1729.

[11] K. C. Schadow and E. Gutmark, "Research For Improved Subsonic And Supersonic Combustion AI AA / ASM E / SAE / ASEE 25th Joint Propulsion Conference," 1989.

[12] S. J. Lawson and G. N. Barakos, "Assessment of passive flow control for transonic cavity flow using detached-eddy simulation," *J. Aircr.*, vol. 46, no. 3, pp. 1009–1029, 2009, doi: 10.2514/1.39894.

[13] H. K. and T. S. Youngki Lee, Minsung Kang, "Passive Control Techniques to Alleviate Supersonic Cavity Flow Oscillation," *J. Propuls. power*, vol. 24.

[14] S. B. Verma and A. Hadjadj, "Supersonic flow control," *Shock Waves*, vol. 25, no. 5, pp. 443–449, 2015, doi: 10.1007/s00193-015-0587-y.

[15] J. Sivasubramanian and H. F. Fasel, "Numerical investigation of supersonic axisymmetric wakes with active and passive flow control," *4th AIAA Flow Control Conf.*, no. June, pp. 1–18, 2008, doi: 10.2514/6.2008-3999.

[16] A. J. Saddington, V. Thangamani, and K. Knowles, "Comparison of passive flow control methods for a cavity in transonic flow," *J. Aircr.*, vol. 53, no. 5, pp. 1439–1447, 2016, doi: 10.2514/1.C033365.

[17] A. P. Heffron, "Rotating Stall and Passive Flow Control on Blade Profiles and in Centrifugal Compressors," 2017.

[18] J. S. X. S. B. Richard M. Wood Floyd J. Wilcox and J. M. Allen, "Vortex Flows at Supersonic Speeds," no. TP-211950, p. 94, 2003.

[19] S. A. Khan, A. A. Al Robaian, M. Asadullah, and A. M. Khan, "Grooved cavity as a passive controller behind backward facing step," *J. Adv. Res. Fluid Mech. Therm. Sci.*, vol. 53, no. 2, pp. 185–193, 2019.

[20] B. Yagiz, O. Kandil, and Y. V. Pehlivanoglu, "Drag minimization using active and passive flow control techniques," *Aerosp. Sci. Technol.*, vol. 17, no. 1, pp. 21–31, 2012, doi: 10.1016/j.ast.2011.03.003.

[21] H. Choi, H. Park, W. Sagong, and S. im Lee, "Biomimetic flow control based on morphological features of living creatures," *Phys. Fluids*, vol. 24, no. 12, 2012, doi: 10.1063/1.4772063.

[22] M. E. Abd El-Latief, K. Elsayed, and M. Madbouli Abdelrahman, "Aerodynamic study of the corrugated airfoil at ultra-low Reynolds number," *Adv. Mech. Eng.*, vol. 11, no. 10, pp. 1–18, 2019, doi: 10.1177/1687814019884164.

[23] J. Sivasubramanian and H. F. Fasel, "LES and DES of high Reynolds number, supersonic base flows with control of the near wake," *Proc. - HPCMP Users Gr. Conf. UGC 2006*, pp. 80–88, 2006, doi: 10.1109/HPCMP-UGC.2006.42.

[24] S. Aradag, K. A. Gelisli, and E. C. Yaldir, "Effects of active and passive control techniques on Mach 1.5 cavity flow dynamics," *Int. J. Aerosp. Eng.*, vol. 2017.

Possible Seismo-Ionospheric Anomalies Associated With the Earthquakes Occurred in 2018 Using GNSS TEC: A Statistical Analysis

Muhammad Arqim Adil
Institute of Space Technology
Islamabad, Pakistan
arqamadil3@gmail.com

Munawar Shah
Institute of Space Technology
Islamabad, Pakistan
shahmunawar1@gmail.com

Asim Khan
Institute of Space Technology
Islamabad, Pakistan
khanlaroosh@gmail.com

Ejaz Nazir
University of Agriculture
Faisalabad, Pakistan
ejaznazir428@gmail.com

Mohamed Freeshah
Wuhan University
Wuhan, China
engmfreeshah@yahoo.com

Hamza Bin Babar
University of Agriculture
Faisalabad, Pakistan
cleverhamza143@gmail.com

***Abstract*—The ambient detection of ionosphere momentary changes preceding earthquakes (EQs) is becoming an ever-growing debate with the excel in the satellite technology. In this paper, we study ionospheric irregularities before 11 significant EQs that occurred in 2018 by analyzing Global Navigation Satellite System (GNSS) derived Total Electron Content (TEC) in pursuit of possible detection of the seismic precursors. We carefully choose these EQs so that there should be at least three International GNSS Service (IGS) permanent stations operating around the epicenter and the geomagnetic activity should quiet ($Kp \leq 3$, $Dst \geq -20$). We perform a statistical analysis based on sliding interquartile (IQR) method over TEC for 15 days before and 5 days after each EQ that shows abnormal variations within 10 days before all these EQs. Our analysis shows that the possible EQ induced TEC anomalies have deviated averagely ~4 TECU, with a percentage deviation of about 44%, from the corresponding upper bound (UB) during quiet geomagnetic activities ($Kp \leq 3$). Whereas the other TEC anomalies induced by moderate geomagnetic activities of ~4 Kp show relatively fewer deviations of about 3 TECU (~37%) from the corresponding UB. Moreover, we did not find any proportionality between TEC anomalies and the magnitude of the EQ. However, the sequential EQs, including fore and aftershocks, exhibit a strong proportionality between TEC anomalies and days before EQ. Conversely, our results also explicate the complexness of finding an ionospheric EQ precursor even in such quiet geomagnetic activities.**

Keywords—GNSS-TEC, Ionosphere, Seismic Precursors, 2018 Earthquakes.

I. INTRODUCTION

Natural hazards are the most devastating geological, hydrological, or meteorological events that severely affect human life in terms of fatalities, infrastructure loss, and the environment across the globe. In recent times, scientists have become able to monitor and forecast some meteorological hazards (hurricanes, tornadoes, and floods) in near real-time. But the most destructive geological hazards remain extremely difficult or impossible to predict that includes tsunamis, earthquakes (EQs), volcanoes, and typhoons. Therefore, the timely detection of these natural hazards is a prerequisite to avoid further human loss. Studies have suggested that the geological natural hazards (especially EQs) induce acoustic and gravity waves into the atmosphere that propagates vertically upwards and causes variations in the electron densities of the ionosphere [1]. Besides, some have reported the involvement of whistler waves during a seismic preparation activity [2]. The whistler waves are usually produced through lightning strokes during a thunderstorm activity, where they propagate in the Earth's ionosphere and further in the magnetosphere along the magnetic lines. These studies provide some insights towards the exploration of the physical processes in the atmosphere and the possible EQ forecasting.

The ionosphere is a dispersive layer of the upper atmosphere comprising large free electrons of different gas molecules, mainly oxygen and nitrogen, that spreads between an altitude between ~80 km to 1000 km above the mean sea level [3]. The sun is the primary source responsible for the changes of electron concentrations in this layer, however, some local hazardous events (volcano, typhoons, EQs) are also observed to be transient influencers in this part of the atmosphere [4][5][6]. Furthermore, Freeshah et al. [7] have reported the involvement of some anthropogenic processes as an unexpected outlier that may bring changes in the ionosphere by studying a recent Beirut explosion that killed more than 218 people and leaving more than 7000 to be injured. However, EQs are known to release several trace gases which react with the atmosphere and the reaction consequences bring changes in the atmosphere that could help in the future EQ forecasting through monitoring the electron density variations in the ionosphere through various in-situ and satellite measurements [8][9][10][11]. These findings urged us to conduct a statistical analysis to detect seismic related ionospheric anomalies that may contribute to the possible EQ prediction.

In this paper, $11 > 5.0$ M_w EQs are studied in pursuit of possible detection of the ionospheric anomalies as potential seismic precursors. The purpose in not limited to the inspection of the seismo-ionospheric anomalies but also to closely monitor the space weather conditions. In Section 2, the criteria of EQ selection and data analysis are briefly discussed. Section 3 comprises results and limitations about the detection of the ionospheric anomalies as precursors. Finally, Section 4 and 5 consist of a brief discussion and conclusion of all the results, respectively.

II. CASE STUDIES AND DATA

We have studied the ionospheric effects potentially affected by the EQ phenomenon around the local areas of the corresponding EQs. Generally, the ionosphere is a pleasant residence for a number of other phenomena other like, space weather, magnetic storms, travelling ionosphere disturbances, thunderstorms, and extreme weather events etc. we have

exampled a very few of them here. The induced electron variations from these phenomena are widely reported previously which depicts the vulnerability of the ionosphere to these extreme events [1][5]. However, some strong evidences have been provided about the seismic influences in the ionosphere. Scientists have been continuously warning about the limitation if the using ionosphere as a reference field for EQ forecasting, as the ultimate ionospheric dynamics are constructed space weather events [6]. Considering this, we plan to study EQ from different regions under the solar minimum year of 2018 (to avoid space weather) and the thought is: the ionospheric variations should be local. We formulate criteria such that there should be three IGS stations and geomagnetic conditions should be quiet. Therefore, after applying this filter we can only manage to find 11 such EQs (https://earthquake.usgs.gov/earthquakes/search/). It should be noted that there are thousands and thousands of EQs occur each year but the space weather phenomena don't allow to monitor every single one, the geomagnetic conditions are retrieved from http://isgi.unistra.fr/data_download.php to check any disturbance during the events. The selection of the IGS station to monitor ionosphere is subjected to its location in EQ preparation zone which is calculated by Dobrovolsky et al. [12] formula:

$$R = 10^{0.34M} \quad (1)$$

where M is the magnitude of the EQ and R denotes the radius of the critical region. The detailed information about these selected EQs and their corresponding IGS stations is provided in Fig. 1.

III. Methodology

A. GNSS TEC Estimation

To monitor the ionosphere variations above the epicenter we need the electron concentrations vertically along the line of sight from the epicenter to ionosphere, while the IGS stations returns slant TEC (STEC) values, where STEC is estimated by the total number of electrons in $1m^2$ tube along the signal ray path. Its unit is TEC, where 1 TECU=10^{16} electrons/m^2 [13][14]. Now this STEC is reformulated to estimate the Vertical TEC (VTEC) as:

$$STEC = \frac{f_1^2 f_2^2}{40.28(f_1^2 - f_2^2)}(L_1 - L_2 + \lambda_1(N_1 - N_2) - \lambda_2(N_1 - N_2) + \varepsilon) \quad (2)$$

$$STEC = \frac{f_1^2 f_2^2}{40.28(f_1^2 - f_2^2)}(P_1 - P_2 - (d_1 - d_2) + \varepsilon) \quad (3)$$

$$VTEC = STEC.\left(cos\left(sin^{-1}\left(\frac{R.sin\,Z}{R+H}\right)\right)\right) \quad (4)$$

Where λ, N, P, L, d, ε, f_1, f_2, R, H, and Z are wavelength, ambiguity, pseudo-range, random residual carrier phase frequencies, radii of the Earth, height of the top ionospheric and elevation angle of the satellite [15], respectively.

B. Statistical Analysis

The identification of VTEC ionospheric electron density anomalies endangered by the studied EQs is carried out by using a total of 18 dual-frequency GNSS receiver stations, where the VTEC values are calculated through a temporal resolution of 1-second. We constructed the confidence bounds through calculating the median ($\tilde{X}$) and Inter Quartile Range (IQR) for an interval of 10 days before each value over a period of 15 days before and 5 days after each observational day.

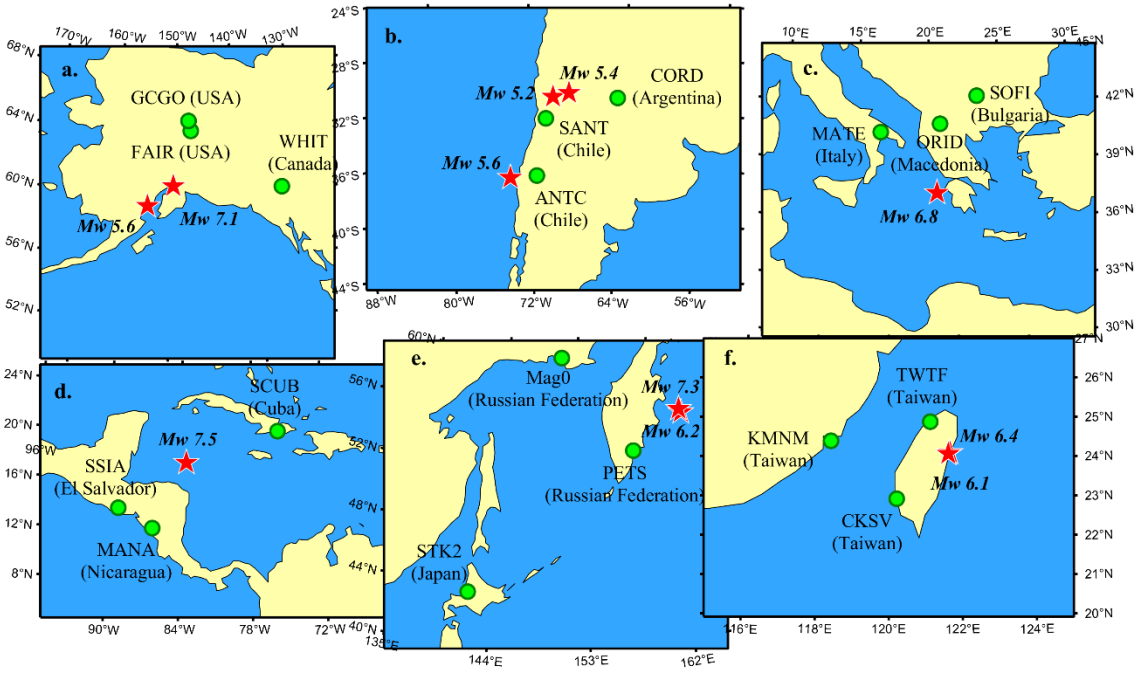


Fig. 1: The geographical locations of 11 EQs (red stars) and IGS stations (green dots) along with their respective country names in which they are operating.

The upper/lower bounds (UB/LB) can be extracted as:

$$UB = \tilde{X} + 1.5IQR \quad (5)$$

$$LB = \tilde{X} - 1.5IQR \quad (6)$$

Eqs. (5-6) demonstrate the formation of the UB and LB, and the TEC values exceeding from either of the limit bounds

will be declared as anomalies with a confidence level of 99.99% [11]. Such a precision in the confidence level makes this method significant one.

On the other hand, through subtraction method, where the actual VTEC values are subtracted from the UB values, differential TEC (ΔTEC) is utilized to quantify potential seismic induced anomalies. The observed TEC (TEC_{obs}) is subtracted from UB to get the deviation in TEC from the normal distribution as:

$$\Delta TEC = \begin{cases} TEC_{obs} - TEC_{UB} \\ 0 \quad if \quad \Delta TEC < 0 \end{cases} \tag{7}$$

The purpose of using this methodology is separately present the geomagnetic and seismic anomalies because the majority of the trend been dismissed.

IV. Results

We present the ionospheric states in terms of GNSS-TEC before M_w > 5.0 EQs occurred during 2018. The EQs, belonging to different regions like Alaska, Argentina, Chile, Greece, Honduras, Russia, and Taiwan are explored. Additionally, the diurnal TEC variations along with differential TEC values are analyzed. The differential TEC values helped a lot to distinguish whether these anomalies are due to seismic interventions or due to geomagnetic disturbances. The ionospheric states before these 11 EQ events that occurred in 6 different regions are discussed below.

The word count limitations of the conference don't allow us to give a comprehensive view of the each event, however, we present the full analysis of a significant M*w* 7.1 Alaska EQ that occurred at 17:29:29 UT on November 30, 2018, while the other EQs will be briefed through statistical results. The geographical coordinates of Alaska EQ are 61.346°N, 149.955°W in latitude and longitude, respectively, while according to the USGS the depth of this EQ was recorded as 47 km (Fig. 1a). For monitoring the ionospheric VTEC variations before this event, we selected 3 IGS stations operating closest and falling under the umbra of the EQ preparation area whose geographical locations are depicted in (Fig. 1a), under observably quiet geomagnetic and solar conditions. One can see in Fig. 2c-e and Table 1 a deviation in maximum ΔTEC values is of about 1.6 TECU at FAIR, 1.2 TECU at WHIT, and 1.3 TECU at GCGO stations, 3 days before the EQ, respectively. Furthermore, the percentage deviations are also recorded as pretty significant where the values exceeded about 56.71% at FAIR, 26.7% at WHIT, and 73.2% GCGO from the corresponding UB. It should be noted that these variations are under silent geomagnetic conditions. The geomagnetic indices timeseries during the observational period is shown in Fig. 2a-b, where a threshold for geomagnetic Kp is represented by a red dashed over the value 3. In any case a value touching or exceeding the threshold line will declare an active geomagnetic activity. Such a scenario can be observed in about 3 days after the M*w* 7.1 Alaskan EQ in Fig. 2b on December 03, 2018, where the geomagnetic Kp values overlaps the declared threshold triggering a geomagnetic activity. Some positive deviations can also be observed on 19th and 20th of November which are pretty consistent with the M*w* 7.1 EQ variations. Interestingly, these variations are the result of an EQ as well, but with a relatively smaller magnitude of M*w* 5.6, which was a foreshock to the gigantic Mw 7.1 EQ, its anomaly details are given in Table 1.

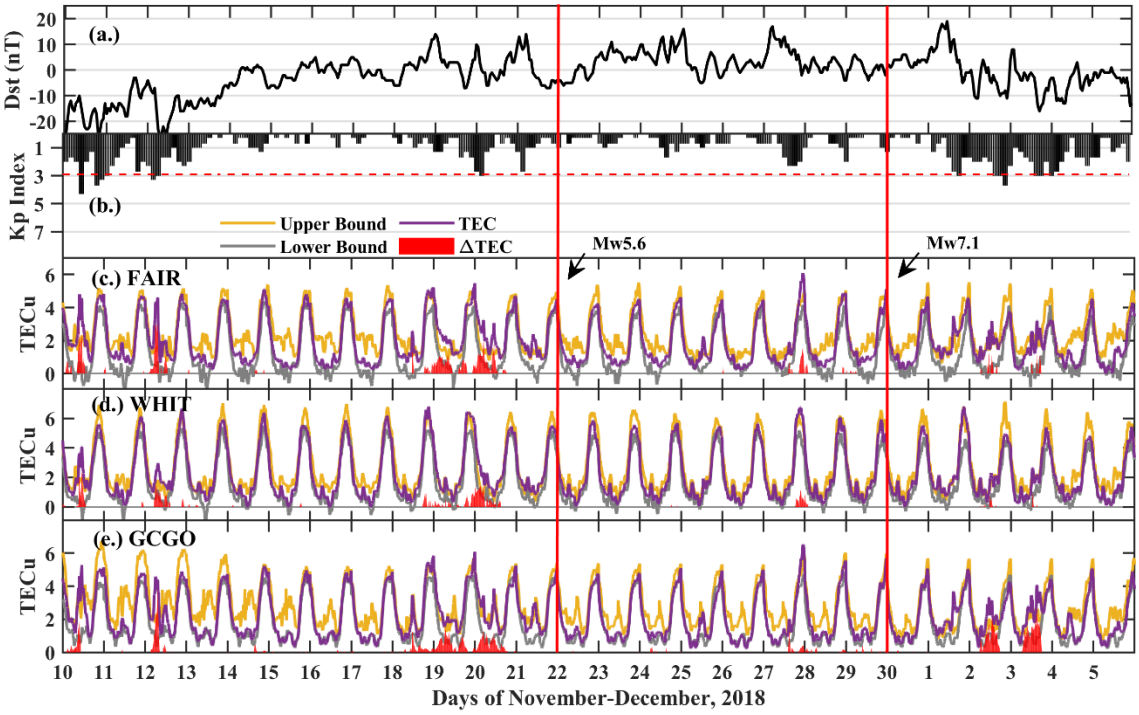


Fig. 2: For Alaska EQ (a.) Geomagnetic Dst (b.) Geomagnetic Kp Index, while GNSS-TEC from (c) FAIR, (d) WHIT, and (e) GCGO.

Table 1: Statistical results of the ΔTEC deviations for SIAs and GIAs

Sr. No	Event	Date	Ave. Max. ΔTEC of SIA	Ave. Max. %TEC for SIA	Geomagnetically Disturbed Day	Ave. Max. ΔTEC for GIA*	Max. Ave. %TEC for GIA	Value of Kp Index
1	5.6	2018-11-21	1.7193	59.62 %	2018-11-12	2.7431	88.35 %	4-
2	7.1	2018-11-30	1.3756	52.20 %	2018-12-03	2.0459	69.35 %	4-
3	5.4	2018-01-28	6.5606	33.54 %	2018-01-24	5.6546	26.68 %	4o
4	5.2	2018 -02-01	5.4180	36.41 %	2018-01-24	5.6546	26.68 %	4o
5	5.6	2018-02-08	6.1690	33.13 %	2018-01-24	5.6546	26.68 %	4o
6	6.8	2018-10-25	3.3180	26.58 %	2018-10-13	N/A	N/A	4+
7	7.5	2018-01-10	7.5472	54.41 %	2018-01-08	4.3924	38.96 %	4-
8	7.3	2018-12-20	1.9925	39.05 %	2018-12-09	1.1133	29.18 %	4-
9	6.2	2018-12-25	1.7730	41.45 %	2018-12-09	1.1133	29.18 %	4-
10	6.1	2018-02-04	6.0543	42.75 %	2018-01-24	2.7532	19.82 %	4o
11	6.4	2018-02-06	9.0018	45.69 %	2018-01-24	2.7532	19.82 %	4o

*Geomagnetically Induced Anomalies

According to Pulinets et al. [17], the possible cause of production of these SIAs is the air ionization process that takes place around the vicinity of a seismic epicenter some days to few months before the seismic jolt. The emission of radon gas due to the stress effect of rocks along the active faults is largely responsible for this air ionization process. This air ionization further causes decrease in the relative humidity and increases the thermal budget of the atmosphere in the form of OLR. Therefore, the anomaly maps of the relative humidity and OLR from NOAA are investigated to confirm the air ionization production that caused the seismo-ionosphere variations on November 19,20, and 28, 2018. Fig. 3 depicts the relative humidity and OLR variations where the humidity decreased to 20% and consequent OLR anomalies increased up to 30 W/m^2 around the epicenters of corresponding EQs that fairly demonstrates the production of air ionization over the epicenters. The Fig. 2 demonstrates an extremely interesting fact about one after another synchronous anomalous pattern where both back to back EQs show a strong proportion in anomalies exhibition and number of days before their corresponding shocks as depicted by Fig. 2c-e.

We adopted the same methodology for other selected EQs (Fig. 1) and the final results are summarized in Table 1. These findings suggested that the SIAs can be useful in the future EQ prediction, but it will be difficult to find a precursor in high geomagnetic conditions.

V. Discussion

The purpose of this paper was not limited to describe the seismic effect on the ionosphere but it was equally devoted to discuss the geomagnetic effects, and how we can distinguish both effects. A brief overview of this discrimination is presented in Table 1 and Fig. 4. This comparison shows that the TEC deviations may deviate averagely about 4.63 TECU from UB for possible seismic anomalies as compared to the geomagnetic anomalies (Kp = 3) whose values are averagely recorded up to 3.39. The production of the air ionization around the corresponding epicenters is main cause behind the generation of these ionospheric anomalies [17]. In a similar analysis, Adil et al. [3] find decreasing humidity with increasing OLR and TEC anomalies before three New Zealand EQs. Whereas the geomagnetically induced anomalies have shown a percentage deviation of 37.47% averagely, which is remarkably less than the percentage deviation of SIA anomalies as shown in Fig. 4. Besides, one should keep in mind that in this analysis the geomagnetic conditions are not that much active and only moderate to low (Kp 3 – 4), so the SIA anomalies are only superior to the moderate geomagnetic conditions. However, severe geomagnetic storms (Kp > 5) will ultimately have higher influences in to the ionosphere where they can even mask the seismic anomalies. Furthermore, some reports favors the SIA up to only 20% [18]. In contrast, our results show deviations of more than 20 % (Fig. 4). Furthermore, the sequential EQs, including fore and aftershocks, exhibit ionospheric anomalies at the almost same number of days as its predecessor (Fig. 5).

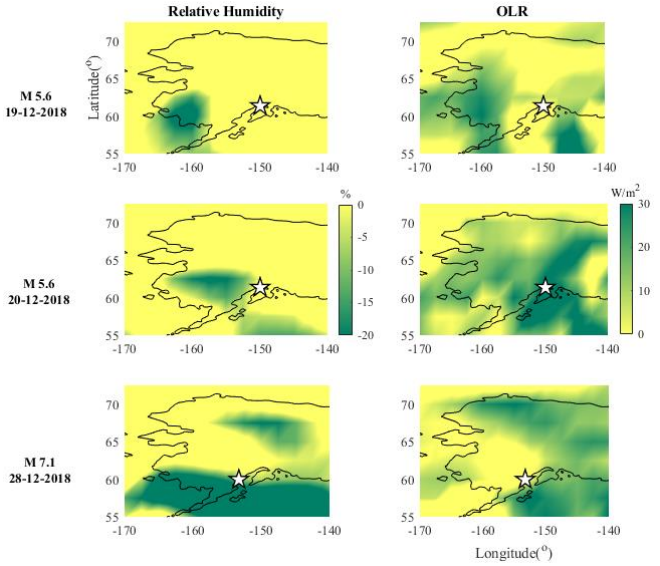


Fig. 3: The anomaly maps of the relative humidity and OLR depicting air ionization over and around the epicenters of both sequential Alaskan EQs on December 19, 20, and 28, 2018. Top two rows describe the variations for M 5.6 while the third row represents the anomalous variations on December 28, 2018. The white stars depict the location of the corresponding epicenters.

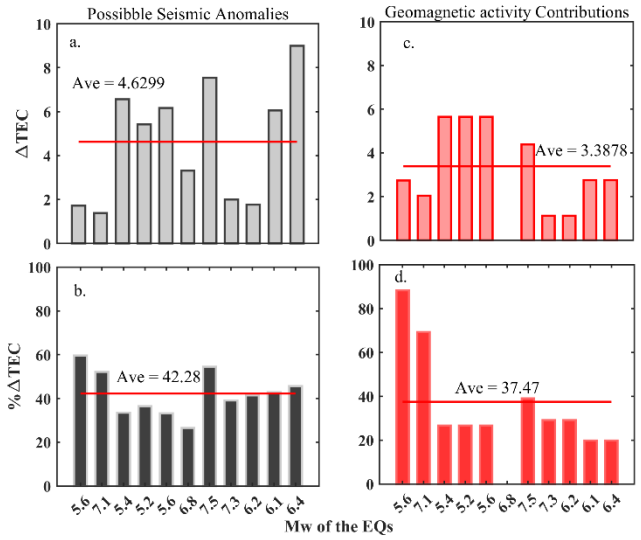


Fig. 4: Max. ΔTEC (upper panel) and % deviations (lower panel) for all EQs.

VI. Conclusion.

We presented EQ related ionospheric anomalies from GNSS TEC of 11 global EQs in 2018 during quiet geomagnetic conditions. Results suggested the TEC anomalies during Kp ≤ 3 geomagnetic activities are the possible seismic anomalies appeared because of the air ionization produced from the increased radon emanations around the epicenters of the 11 corresponding EQ prone regions that induced ionospheric changes through decreasing humidity and increasing the thermal budget of the atmosphere. For seismo ionospheric anomalies, 4 TECU deviation of daily TEC beyond UB is recorded, while moderate geomagnetic activities (Kp=4) recorded about 3.7878. The percentage corresponds to 37.47% for the GIAs, while 42.28% for SIAs. Furthermore, during the observed periods before and after the respective shocks, the EQ induced ionosphere anomalies have shown a better tendency than moderate geomagnetic variations. These results indicate the existence of seismo ionosphere anomalies, however, to further clarify this marvelous phenomenon more dedicated ground and space observations are needed.

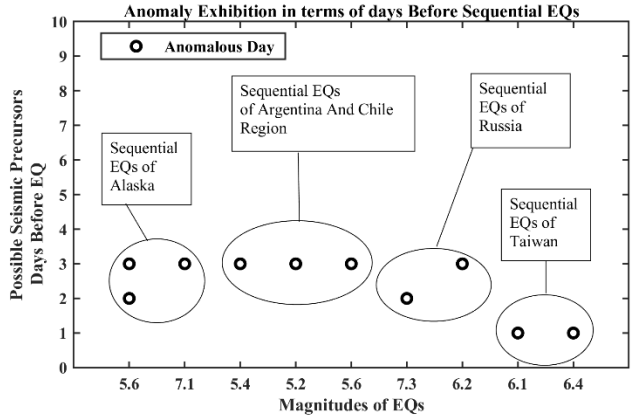


Fig. 5: The anomaly pattern followed by sequential EQs sharing same regions.

Acknowledgment

The authors are thankful to the IGS, USGS, OMNIWEB NASA and NOAA for GNSS-TEC, EQs, geomagnetic and atmosphere data.

References

[1] E. Astafyeva, "Ionospheric Detection of Natural Hazards," *Reviews of Geophysics*, vol. 57, no. 4, pp. 1265–1288, 2019.

[2] M. Parrot and J.-L. Pinçon, "Is There an Earthquake Weather?," *Open Journal of Earthquake Research*, vol. 09, no. 02, pp. 69–82, 2020.

[3] M. A. Adil, A. Abbas, M. Ehsan, M. Shah, N. A. Naqvi, A. Alie," Investigation of ionospheric and atmospheric anomalies associated with three Mw >6.5 EQs in New Zealand," *Journal of Geodynamics*, vol. 145, pp. 101841, 2021.

[4] W. Li, J. Guo, J. Yue, Y. Shen, and Y. Yang, "Total electron content anomalies associated with global VEI4 + volcanic eruptions during 2002–2015," *Journal of Volcanology and Geothermal Research*, vol. 325, pp. 98–109, 2016.

[5] M. Freeshah *et al.*, "Analysis of Atmospheric and Ionospheric Variations Due to Impacts of Super Typhoon Mangkhut (1822) in the Northwest Pacific Ocean," *Remote Sensing*, vol. 13, no. 4, p. 661, 2021.

[6] M. A. Adil, E. Şentürk, S. A. Pulinets, and C. Amory-Mazaudier, "A Lithosphere–Atmosphere–Ionosphere Coupling Phenomenon Observed Before M 7.7 Jamaica Earthquake," Pure and Applied Geophysics, vol. 178, p. 3869–3886 2021.

[7] Freeshah, M., Zhang, X., Şentürk, E., Ren, X., Arqim Adil, M., and Xu, G., "Could the Beirut Explosion perturb the Ionosphere? Pre-results Using TEC-GNSS observations." *EGU General Assembly Conference Abstracts*, pp. EGU21-8990, 2021.

[8] M. A. Adil, E. Şentürk, M. Shah, N. A. Naqvi, M. Saqib, and A. R. Abbasi, "Atmospheric and ionospheric disturbances associated with the M > 6 earthquakes in the East Asian sector: A case study of two consecutive earthquakes in Taiwan," *Journal of Asian Earth Sciences*, vol. 220, p. 104918, 2021.

[9] A. Kiyani *et al.*, "Seismo ionospheric anomalies possibly associated with the 2018 M 8.2 Fiji earthquake detected with GNSS TEC," *Journal of Geodynamics*, vol. 140, p. 101782, 2020.

[10] M. Saqib, E. Şentürk, S. A. Sahu, and M. A. Adil, "Ionospheric anomalies detection using autoregressive integrated moving average (ARIMA) model as an earthquake precursor," *Acta Geophysica*, vol. 69, no. 4, pp. 1493–1507, 2021.

[11] M. Shah *et al.*, "Possible seismo-ionospheric anomalies associated with M > 5.0 earthquakes during 2000-2020 from GNSS TEC," *Advances in Space Research*, Apr. 2022.

[12] I. P. Dobrovolsky, S. I. Zubkov, and V. I. Miachkin, "Estimation of the size of earthquake preparation zones," *Pure and Applied Geophysics PAGEOPH*, vol. 117, no. 5, pp. 1025–1044, 1979.

[13] H. Li, Y. Yuan, Z. Li, X. Huo, and W. Yan, "Ionospheric Electron Concentration Imaging Using Combination of LEO Satellite Data With Ground-Based GPS Observations Over China," *IEEE Transactions on Geoscience and Remote Sensing*, vol. 50, no. 5, pp. 1728–1735, 2012.

[14] D. Roma-Dollase *et al.*, "Consistency of seven different GNSS global ionospheric mapping techniques during one solar cycle," *Journal of Geodesy*, vol. 92, no. 6, pp. 691–706, 2017.

[15] J. Klobuchar, "Ionospheric Time-Delay Algorithm for Single-Frequency GPS Users," *IEEE Transactions on Aerospace and Electronic Systems*, vol. AES-23, no. 3, pp. 325–331, 1987.

[16] M. Saqib, E. Şentürk, S. A. Sahu, and M. A. Adil, "Comparisons of autoregressive integrated moving average (ARIMA) and long short term memory (LSTM) network models for ionospheric anomalies detection: a study on Haiti (Mw = 7.0) earthquake," *Acta Geodaetica et Geophysica*, vol. 57, no. 1, pp. 195–213, 2022.

[17] S. A. Pulinets, D. P. Ouzounov, A. V. Karelin, and D. V. Davidenko, "Physical bases of the generation of short-term earthquake precursors: A complex model of ionization-induced geophysical processes in the lithosphere-atmosphere-ionosphere-magnetosphere system," *Geomagnetism and Aeronomy*, vol. 55, no. 4, pp. 521–538, 2015.

[18] J. M. Forbes, S. E. Palo, and X. Zhang, "Variability of the ionosphere," *Journal of Atmospheric and Solar-Terrestrial Physics*, vol. 62, no. 8, pp. 685–693, 2000.

Analysis of The Atmospheric Anomalies Associated with M_w>6.0 Continental Earthquake in The Afghanistan and Tajikistan

Daboor Sultana
Department of Space Science
Institute of Space Technology
Islamabad, Pakistan
daboorsultana@live.com

Dr. Munawar Shah
Department of Space Science
Institute of Space Technology
Islamabad, Pakistan
shahmunawar1@gmail.com

***Abstract*— The recent advances in space-based atmospheric precursors of earthquakes (EQ) aid in the development of the lithospheric atmospheric coupling system. In this paper, anomalies associated with the atmosphere are investigated in the Central Asian region of M_w>6.0 EQs (Afghanistan and Tajikistan) are examined. The atmospheric precursors are searched in humidity, Aerosol Optical Depth (AOD), and soil moisture from Giovanni (A Web interface to analyze NASA's gridded data). Pre atmospheric anomalies are observed before all three EQs during a 5- 50-day window beyond the upper bounds. On the other hand, post atmospheric anomalies are only observed after the M_w 7.0 Afghanistan EQ within 5 days. The overall analysis shows that pre atmospheric anomalies can be monitored more frequently than post atmospheric anomalies; however, more analyses need to clear the lithosphere atmosphere coupling. There is a lack of possible precursors of the EQs, but the need for more analysis can certainly validate the phenomenon.**

Keywords*— Earthquake; Atmospheric anomalies; Mw> 6.0; Lithospheric-Atmospheric Coupling; AOD; Humidity; Soil Moisture

I. INTRODUCTION

Satellite remote sensing procedures detected the EQ-induced atmospheric precursors at different altitudes before the megathrust over the seismogenic zone. These precursors can be of three types depending on the altitude: (1) Lithospheric precursors occurred around the epicenter on the ground, such as land surface temperature and soil moisture [1], [2] air ionization and humidity variations in the atmosphere near the Earth surface [2], and [3] the ionospheric variations over the seismic prone region. [3-4] According to previous reports, the atmospheric anomalies from different sources over the epicenter of the mainshock event occurred within one to five months before the mainshock [5]. Nevertheless, it depends on the magnitude and local terrain of the event. They further explained that different atmospheric parameters behaved abnormally over the seismic zone within several days to several months before the impending mainshock. On the other hand, the lack of detection of the right anomaly is the selection of appropriate statistical parameters [6]. Therefore, the existence time of the EQ-induced atmospheric anomalies became very essential for the prediction of the megathrust. The multi-parameter-based study of the atmosphere is important for the reliability of the EQ precursor detection and understanding of the complex mechanism of seismic related anomalies. According to previous reports, the enhancement in humidity, AOD, and soil moisture exists before the coastal EQs [7-10]. Nevertheless, the high elevation and heterogeneous geomorphology of the epicentral region could not influence the abnormality in these parameters.

There are different hypotheses about the evaluation mechanism of pre-seismic atmosphere anomalies from remote sensing procedures. Among them, the most compromised theory is the activation of positive holes (p holes) in the stressed rocks in the seismic preparation zone [11]. According to the p-hole hypothesis [11], the positive charge carriers triggered by tectonic forces in the crustal rocks propagate out of the compressed rocks to the nearby atmosphere. Furthermore, it causes the air ionization at the Earth-atmosphere interface in a thin layer and induced significant atmospheric anomalies due to the recombination of p holes. Adil et al. [12] showed from a ray-trace model that a millimeter disturbance at the Earth's surface can be amplified to wave amplitude of 100 m at 100 km altitude up in the atmosphere.

II. DATA AND METHOD

The temporal and spatial atmospheric anomalies before the large magnitude continental EQs are reported based on remote sensing procedures. United States Geological Survey (USGS) provides the EQs information via link (https://earthquake.usgs.gov/earthquakes/) [13-14]. The different parameters of the EQs are listed in Table. 1. We studied three different hypocentral depth EQs (e.g. shallow, intermediate, and deep) on the continental part of the lithosphere in Afghanistan and Tajikistan (Fig. 1). The terrestrial DEM (Digital Elevation Model) data is used for determining the crustal thickness in the study area. The temporal data for DEM is retrieved from NASA via earth explorer (https://earthexplorer.usgs.gov/). Similarly, the Geoid height and Gravity anomaly are obtained from the ICE (https://www.aviso.altimetry.fr/es/applications/geodesy-and-geophysics/geodesy.html). [15-18] these datasets confirm the existence of high topography of the studied EQs epicenters. In this study, we aim to show the consistency in atmospheric anomalies before the continental EQs, which occurred on high terrain in Afghanistan and Tajikistan.

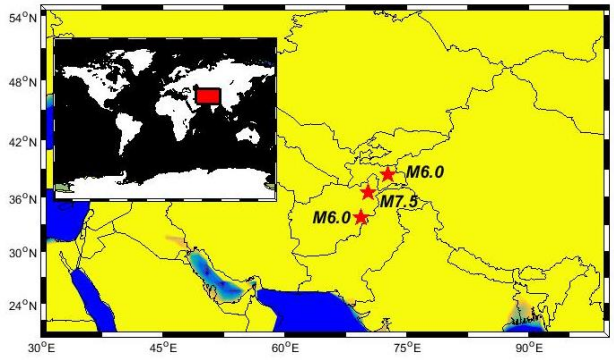


Fig. 1. Epicenter of the three EQs in Asian regions. The red-filled star is for the EQs epicenter.

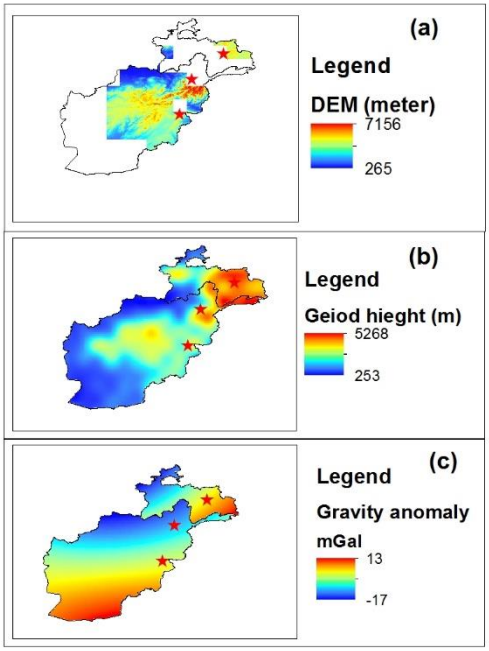


Fig. 2. (a) DEM, (b) Geoid, and (c) Gravity anomaly of the study area.

The atmospheric data (e.g. humidity, AOD, and soil moisture) were retrieved from NASA through GIOVANNI via (http://www.giovanni.sci.gsfc.nasa.gov/giovanni). GIOVANNI is an online data source of remote sensing to assist in atmospheric and meteorology research and maintained by the National Aeronautics and Space Administration (NASA).

Table 1. Information for the three EQs of M_w> 6.0

Earthquake	Occurrence Date	Pre-atmospheric anomalies days	Post-atmospheric anomalies days
M6.0 Afghanistan	**2008-10-05**	**-35 days before**	**Nil**
M6.0 Tajikistan	**2011-01-24**	**-50 days before**	**Nil**
M7.0 Afghanistan	**2005-10-25**	**-5 days before**	**5 days after**

To identify any significant deviation triggered by the EQ, all the variables were studied for 3-4 months before and one month after the mainshock. Furthermore, the anomalies were detected using μ±σ (median ± sigma), which is obtained from the data of (2002-2015). We declared the anomaly as the deviation from normal distribution to a significant level beyond the confidence levels, as the method implemented in [9,10].

III. RESULTS AND DISCUSSIONS

In this study, atmospheric anomalies associated with EQs before three large magnitudes EQs from remote sensing data in the continental portion in Afghanistan and Tajikistan are analyzed. The occurrence anomaly over the epicenter during the EQ preparation period in humidity, AOD, and Soil moisture before the main shock confirmed the synoptic blocking of huge energy appeared in remote sensing procedures. There exist different conclusions in past about the formation of such anomalies at the lithospheric-atmospheric interface over the EQ preparation zone (EPA).

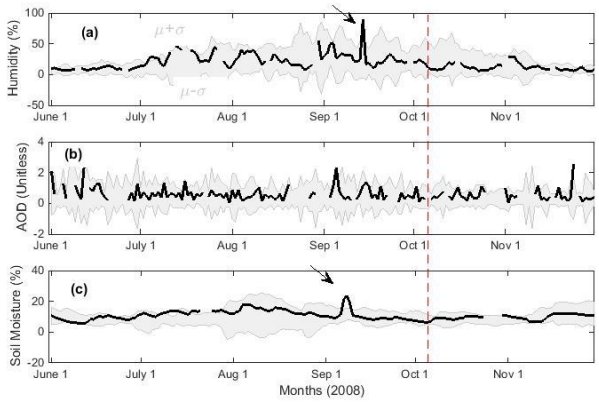


Fig. 2. The analysis of different atmospheric indices with their confidence bounds before and after the 5th October 2008 Afghanistan EQ.

The atmospheric anomalies are clear on the day (-35) before the 2008 Afghanistan EQ (Fig. 2). On the other hand, there are no post-seismic atmospheric anomalies after the mainshock day within the seismogenic zone.

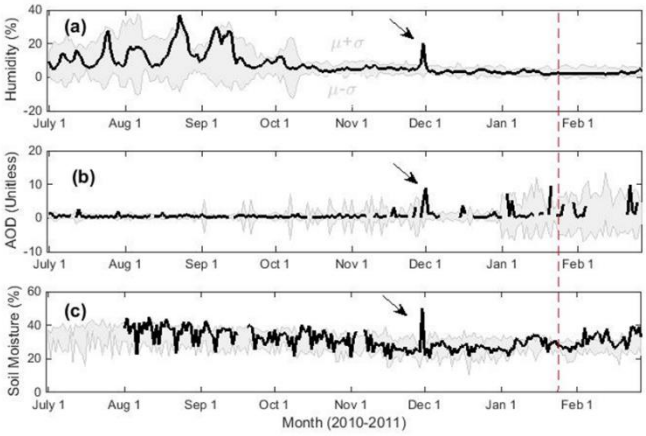


Fig. 3. (a) Humidity, (b) AOD, and (c) Soil Moisture analyses with confidence bounds associated with the 24th January 2011 Tajikistan EQ.

The 2011 Tajikistan EQ shows clear anomalies in AOD on -50 days as a pre-seismic atmospheric perturbation (Fig. 3).

Which is duly verified by the analyses of humidity and soil moisture from different remote sensing satellites data (Fig. 3). As in Figure 4, the -5 day anomalies in the atmosphere are clear within 5 days before the 2005 M7.0 EQ in Afghanistan (Fig. 4). The AOD shows more than 10% variation as an anomaly from the normal distribution of the data (Fig. 4). Similar variations are recorded in humidity and soil moisture in Figures 4a and 4c, respectively.

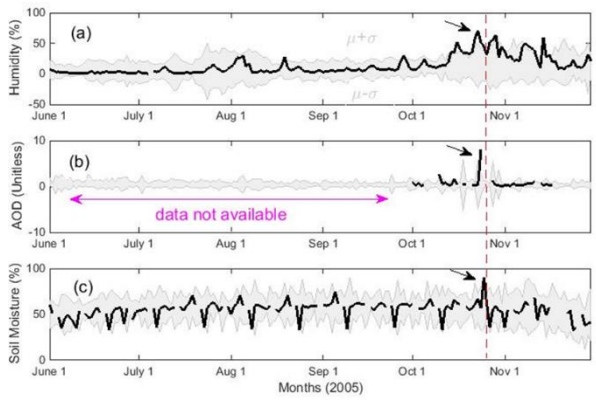


Fig. 4. The analysis of different atmospheric indices with its confidence bounds before and after the 25th October 2005 Afghanistan EQ.

IV. CONCLUSION

In this paper, atmospheric anomalies associated with 3 large magnitude EQs in the continental part of Asia; i.e., Afghanistan and Tajikistan are examined. All parameters were investigated for 3-4 months before and one month after the main EQ event. Furthermore, the anomalies were detected using μ±σ (median ± sigma), which is obtained from the data of (2002-2015). We found different atmospheric parameters behaved abnormally over the seismic zone within several days to several months before the impending EQ. Results show the occurrence of atmospheric anomalies within the EPA in humidity, AOD, and Soil moisture before the main shock confirmed the synoptic blocking of huge energy appeared in remote sensing procedures. We declared the anomaly as the deviation from normal distribution to a significant level beyond the confidence levels of high terrain at the lithosphere-atmosphere interface over the EPA.

ACKNOWLEDGEMENT

The authors are grateful to the Earth Explorer community for the availability of atmospheric indices data. We are obliged by the United States Geological Survey (USGS), ICE for providing information about the EQs, Geoid height, and atmospheric parameters, respectively.

REFERENCES

[1] K. Davies and G. Hartmann, “Studying the ionosphere with the global positioning system,” Radio Science, vol. 32, no. 4, pp. 1695–1703, 1997.

[2] J. Shuang-gen, J. Wang, Z. Hong-ping, and Z. Wen-yao, “Real-time monitoring and prediction of ionospheric electron content by means of GPS,” Chinese Astronomy and Astrophysics, vol. 28, no. 3, pp. 331–337, 2004.

[3] M. Shah, A. Ahmed, M. Ehsan, M. Khan, M. A. Tariq, A. Calabia, and Z. ur Rahman, “Total electron content anomalies associated with EQs occurred during 1998–2019,” Acta Astronautica, vol. 175, pp. 268–276, 2020.

[4] M. Ulukavak, “Deep learning for ionospheric tec forecasting at mid-latitude stations in turkey,” Acta Geophysica, vol. 69, no. 2, pp. 589–606, 2021.

[5] E. Astafyeva, “Ionospheric detection of natural hazards,” Reviews of Geophysics, vol. 57, no. 4, pp. 1265–1288, 2019.

[6] A. Kiyani, M. Shah, A. Ahmed, H. H. Shah, S. Hameed, M. A. Adil, and N. A. Naqvi, “Seismo ionospheric anomalies possibly associated with the 2018 MW 8.2 Fiji EQ detected with GNSS TEC,” Journal of Geodynamics, vol. 140, p. 101782, 2020.

[7] K. Davies and D. M. Baker, “Ionospheric effects observed around the time of the Alaskan EQ of march 28, 1964,” Journal of Geophysical Research, vol. 70, no. 9, pp. 2251–2253, 1965.

[8] S. Pulinets, “Ionospheric precursors of EQs; recent advances in theory and practical applications,” Terrestrial Atmospheric and Oceanic Sciences, vol. 15, no. 3, pp. 413–436, 2004.

[9] S. Jin, G. Occhipinti, and R. Jin, “GNSS ionospheric seismology: Recent observation evidence and characteristics,” Earth-Science Reviews, vol. 147, pp. 54–64, 2015.

[10] M. Free shah, X. Zhang, E. S¸ entu¨rk, M. A. Adil, B. Mousa, A. Tariq, X. Ren, and M. Refaat, “Analysis of atmospheric and ionospheric variations due to impacts of super typhoon mangkhut (1822) in the northwest Pacific Ocean,” Remote Sensing, vol. 13, no. 4, p. 661, 2021.

[11] J. Ahmed, M. Shah, M. Awais, S. Jin, W. A. Zafar, N. Ahmad, A. Amin,M. A. Shah, and I. Ali, “Seismo-ionospheric anomalies before the 2019 Mirpur EQ from ionosonde measurements,” Advances in Space Research, 2021.

[12] M. A. Adil, A. Abbas, M. Ehsan, M. Shah, N. A. Naqvi, and A. Alie, “Investigation of ionospheric and atmospheric anomalies associated with three mw¿ 6.5 Eqs in New Zealand,” Journal of Geodynamics, vol. 145, p. 101841, 2021.

[13] I. Dobrovolsky, S. Zubkov, and V. Miachkin, “Estimation of the size of EQ preparation zones,” Pure and applied geophysics, vol. 117, no. 5, pp. 1025–1044, 1979.

[14] M. Shah and S. Jin, “Pre-seismic ionospheric anomalies of the 2013 mw= 7.7 Pakistan EQ from GPS and cosmic observations,” Geodesy and Geodynamics, vol. 9, no. 5, pp. 378–387, 2018.

[15] A. R. Abbass, M. Shah, A. Ahmed, and N. A. Naqvi, “Possible ionospheric anomalies associated with the 2009 m w 6.4 Taiwan EQ from Demeter and GNSS tec,” Acta Geodaetica et Geophysica, vol. 56, no. 1, pp. 77–91, 2021.

[16] L. He, L. Wu, A. De Santis, S. Liu, and Y. Yang, “Is there a one-to-one correspondence between ionospheric anomalies and large EQs along longmenshan faults?” in Annales Geophysical, vol. 32, no. 2. Copernicus GmbH, 2014, pp. 187–196.

[17] A. Ali, C. Sheng-Chang, and M. Shah, “Continuous wavelet transformation of seismic data for feature extraction,” SN Applied Sciences, vol. 2, no. 11, pp. 1–12, 2020.

[18] H. Li, Y. Yuan, Z. Li, X. Huo, and W. Yan, “Ionospheric electron concentration imaging using a combination of LEO satellite data with ground-based GPS observations over China,” IEEE Trans. Geosci. Remote Sens vol. 50, no. 5 PART 2, pp. 1728–1735, 2012, doi: 10.1109/TGRS.2011.21 964.

Analysis and Comparison of Maximum Power Point Tracking Algorithms for Electrical Power System of the CubeSats

Usman Azeem
Small Satellite Technology and Research Lab, NCGSA
Institute of Space Technology
Islamabad, Pakistan
usmanazeem074@gmail.com

Dr.Rehan Mahmood
Small Satellite Technology and Research Lab, NCGSA
Institute of Space Technology
Islamabad, Pakistan
Rehan.mahmood@ist.edu.pk

***Abstract*— The photovoltaic (PV) system has been used for years as one of the leading renewable energy sources. We are concerned with reducing cost and improving efficiencies today so these natural resources can be tapped and utilized effectively. Using a maximum point tracker (MPT), it is possible to extract maximum power from a PV panel. PV systems have varying output powers based on changes in temperature and irradiance. Charger efficiency must be enhanced. Several maximum power point tracking (MPPT) methods are available to achieve the maximum point, for example, Incremental Conductance algorithm (INC), Perturbation and Observation algorithm (P&O), and a Constant Voltage technique. To measure and evaluate the performance parameters and to test the efficiency and validity of the proposed controller, an entire PV system will be modeled and simulated with Simulink. On the design level, we used Incremental Conductance Method (INC) and Perturb and Observe (P&O) MPPT algorithm. For comparison purposes, the output data of the MPPT is compared to find a significantly better MPPT system.**

Keywords*— *MPPT (Maximum Power Point Tracking), Photovoltic Panel (PV), INC (Incremental Conductance), P&O (Perturb and Observation), Boost converter, Buck Converter, Buck-Boost Converter.

I. INTRODUCTION

EPS electronics, or Electrical Power System (EPS), provide considerable power to nanosats and cubesats.As a long-term cubesat bus, the EPS needs to be flexible as well as efficient. As a result, EPS should be designed to meet specific power requirements, and capable of supporting multiple missions without having to be completely redesigned [1]. In a photovoltaic (PV) a system, solar cells are employed. Various cells are linked in the series to create specific voltage (V) and are linked in parallel to produce specific current (A). Modules are also connected parallelly and in the series to create an array of modules [2].

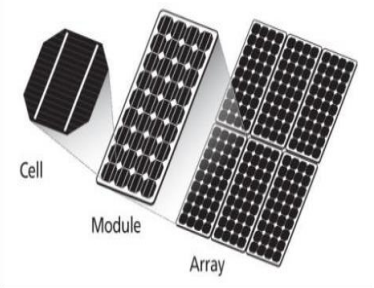


Figure. 1. PV Cell, Module, Array

The optimal PV output current to voltage (I-V) characteristic depends nonlinearly on temperature and irradiance. Photovoltaic arrays are typically designed so that their output power rests at a single point on the graphs of its I-V and P-V. If arrays are continually operated at their maximum power point (MPP), they can generate maximum power. To make cubesats as efficient as possible, it is critical to select a proper MPPT when designing EPS [3]. In this study, two MPPT techniques are compared: perturbation and observation technique and incremental conductance technique.

II. How a Solar cell works

Light energy is converted into electrical energy by solar cells or photovoltaic cells through the photovoltaic effect. PN junctions are the basic building blocks of solar cells. The photovoltaic effect is responsible for the operation of solar cells. Through semi conductive silicon materials, light causes, electrons to move from one layer to another. Electrons are ultimately responsible for producing an electric current. Cells that convert solar radiation directly into electric current are called photovoltaic, which are made from semiconductor materials.

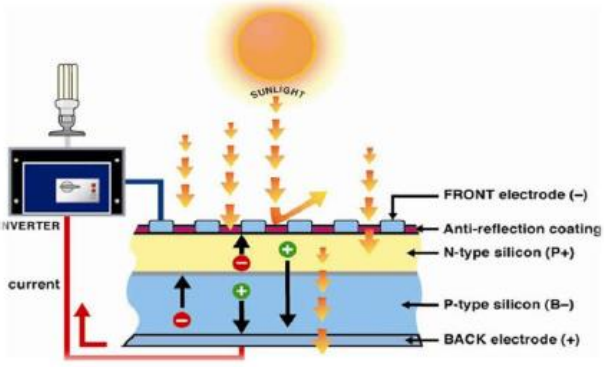


Figure. 2. Photovoltaic cell structure

PN junctions produce electric current in their zones of depletion. A p-n junction has depletion zones caused by electrons diffusing from the n-type to holes of the p-type [3]. By absorption of light by one of these silicon atoms, light will displace electrons, creating a hole and a free electron. The result is the formation of free electrons and holes with sufficient energy to leave the depletion zone. The current will flow (electrons) through the wire when connected between the cathode (n-type silicon) and the anode (p-type silicon). An

electric current is created when the electron attracts the positive charge of the "p-type" material and travels through the load. If an electron is freed from its charge, the negative charge of "n-type" material will attract the electron and cause it to fall towards the back electrical contact. As a result of the electrons entering p-type silicon from the back electrical contact, the electrical neutrality is restored.

We can further describe the PV cell characteristics by using an equivalent circuit as shown in the fig 3. PV models consist of three components: current sources, diodes, and series resistances. The parallel resistance results in a very small leakage resistance in a single module. Under constant temperatures and a constant incidence of light, the current source's output is constant.

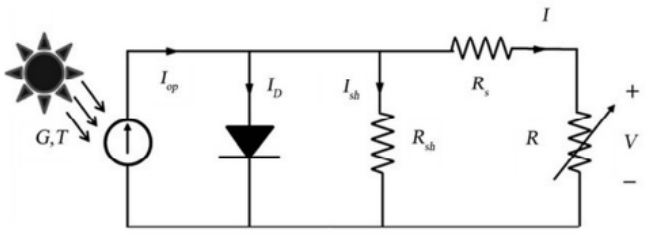


Figure. 3. Equivalent circuit of an ideal PV cell

According to the PV cell model, the equations are as follows: [1]

$$I = Ipv - Id - Irp \quad (1)$$

$$I = Ipv - Io\left(\exp\left(V + \frac{I * Rs}{a * Vt}\right) - 1\right) - V + I * \frac{Rs}{Rp} \quad (2)$$

$$Vt = Ns * K * \frac{T}{q} \quad (3)$$

$$Iph = \frac{G}{Gn}(Ipvn + ki(T - Tn) \quad (4)$$

$$Io = Irs\left(\frac{T}{Tn}\right)^3 * \exp(q * \frac{Eg}{a * k}\left(\frac{1}{Tn} - \frac{1}{T}\right) \quad (5)$$

$$Irs = \frac{Iscn}{\exp\left(\frac{Vocn}{a * Vtn}\right) - 1} \quad (6)$$

Where:

I = solar cell current (A)
V= solar cell voltage (V)
Ipv = photo current (A)
Id=diode current (A)
Io=reverse saturation current (A)
K= boltzman constant
T=solar cell temperature
q= charge of electron
G= irradiance intensity

A solar panel's maximum power can be determined using the IV curve in an ideal position. A graph showing how current varies with voltage is shown below. The peak will provide the best power output for the panel.

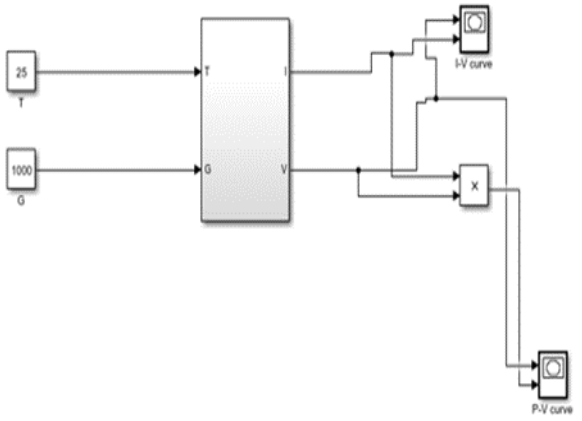


Figure. 4. Schematic of a solar array

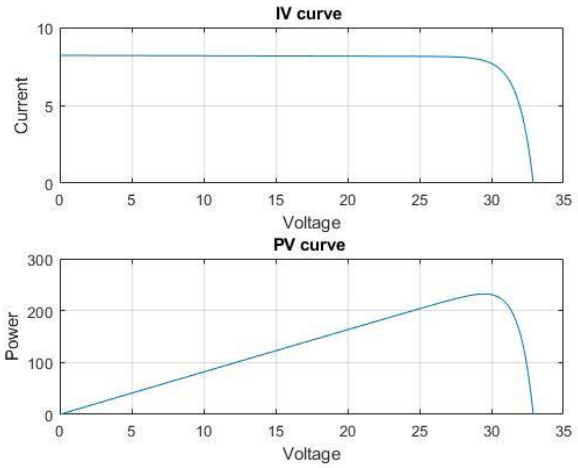


Figure. 5. V-I and P-V curve

Utilizing the IV curve, we can determine the maximum power for a solar panel in an ideal situation. Below is a graph of current versus voltage. The peak represents the maximum power available [7].

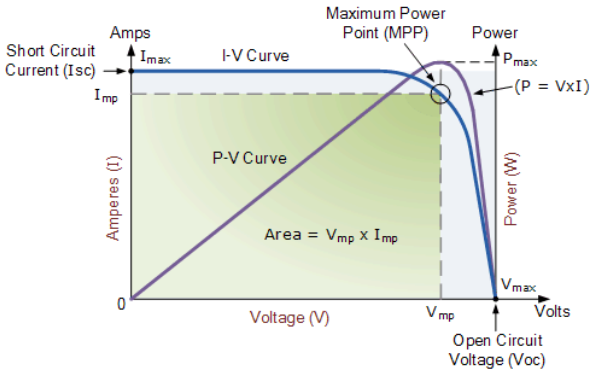


Figure. 6. Basic V-I curve

Solar cells typically produce the following outputs for a given irradiance and operating temperature. According to figure 6. 1. Short circuit current (Isc) is equal to maximum current at zero potential. In an ideal world, if V = 0, Isc = IL [4]. There is a direct relationship between Isc and the amount of sunlight available

2. Voltage of an open circuit (VOC) at zero current is defined as the maximum voltage. An increase in sunlight exponentially increase Voc. In this way, solar cells are excellent for charging batteries.

III. MPPT ALGORITHMS

As the name implies, MPPT is intended to find the maximum voltage and current when using a PV module, which is referred to as the maximum power point. The main MPPT algorithms are.

A. Perturb and Observe technique

The MPP is commonly determined with the help of this method. As a result of this method, the controller adjusts voltage slightly from the array, measures power, and makes adjustments until there is no longer increase in power. We call this method "Perturb and Observe". An important feature of P&O methods is the comparison of (Pn) recent PV power with (Pn-1) previous PV power. Voltage and current are measured to determine a photovoltaic power. This algorithm tries to determine the optimal point in the left or right side of recent position when the difference between previous power and recent power is not equal to zero. When P (n)-P (n-1) is equal to 0, a maximum power is achieved. A voltage will be increased or decreased until the MPP is found [3].

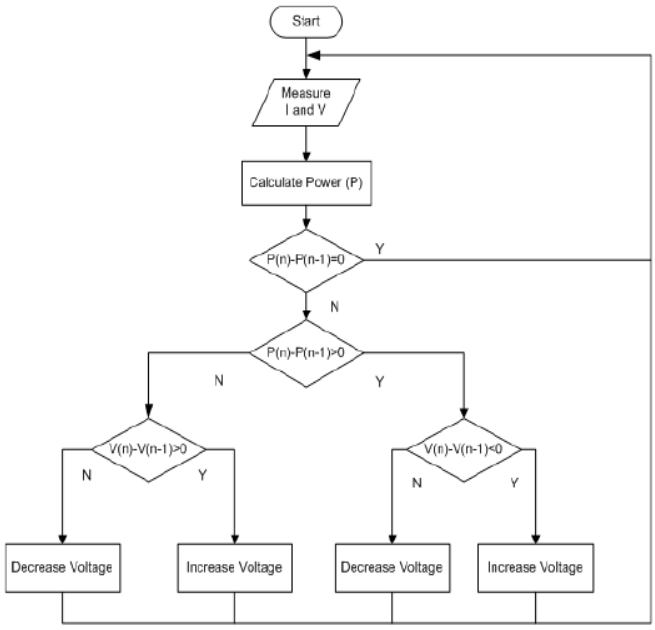


Figure. 7. Perturb and Observe Algorithm

B. Incremental Conductance technique

The incremental conductance method was used to observe a P-V characteristic curve. Power loss is reduced, PV efficiency is improved, and system costs are reduced using this method. The PV module's voltage and current are measured first. Next, it calculates incremental changes, dI (change in current) and dV (change in voltage), by using the current value and previous voltage value. Based on the assumption that the operating point lies on the MPP's left when the inequality equation below is satisfied, so the module voltage must be increased to move it to the right. In the same manner, whenever the condition is satisfied by the inequality equation, we assume that the operating point lies on the right of the MPP, therefore the module voltage must be lowered to put the operating point on the left [6]. According to figure8 INC method, at the MPP, the PV array slope is zero, it slopes positively to the left of the MPP, and it slopes negatively to the right.

MPP is reached when $\frac{dP}{dV}=0$

IF

$$\frac{dP}{dV} > 0 \; then \; Vp < Vmpp \qquad (1)$$

$$\frac{dP}{dV} = 0 \; then \; Vp = Vmpp \qquad (2)$$

$$\frac{dP}{dV} < 0 \; then \; Vp > Vmpp \qquad (3)$$

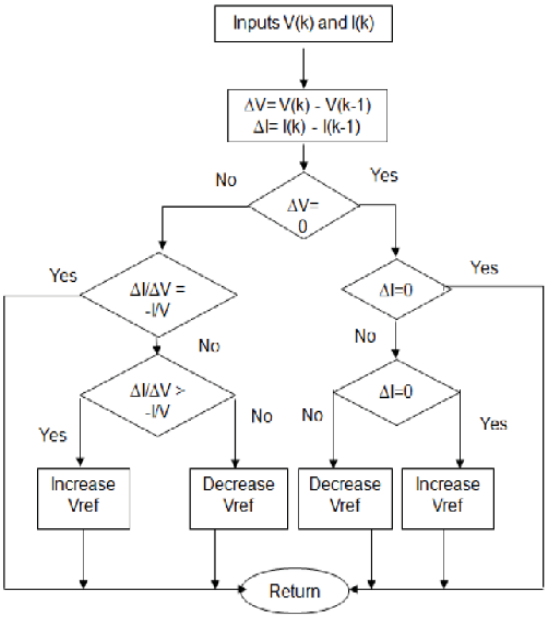


Figure. 8. Incremental Conductance Algorithm

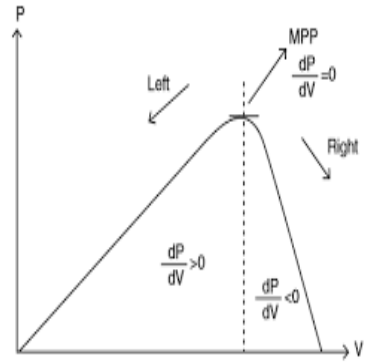


Figure. 9. Incremental Conductance Graph

IV. POWER CONVERTERS

In electronics, DC-DC converters are circuits that change direct current (DC) from one level to another. Typical applications for these DC-DC converters include dc motor drives and switch-mode power supplies [2]. Their input voltage is often unregulated. Due to the magnitude changes in the line voltage, this is obtained by rectifying the line voltage. A switch mode DC-DC converter is employed in

MPPT to regulate the input voltage at the PV MPP and match the load to ensure maximum energy transfer. The basic DC to DC converters considered for analysis are

A. BUCK Converter

Step-down converters, or buck converters reduce voltage while maintaining a constant level of power. Buck converters were designed to improve efficiency and extend battery life, reduce heat, and reduce the size of the device [6]. As DC-DC converters, Buck converters are much more energy efficient than linear regulators because they act as switching converters. The diode is in an open circuit condition when the switch is on, because it is reverse-biased. As a result, an initial current will pass through the load, but the inductor will restrict the current, so it will start charging as well. In other words, there is constant charge build-up in the capacitor that reflects across the load during on time of the circuit.
Energy stored in the inductor L1 decreases when the switch is in an off state and passes through the diode D1. Due to this reverse polarity in the inductor, the diode is in forward-biased condition [6]. In this case the inductor's magnetic field decreases, the current will flow through the load until it runs out of the charge. Generally, Buck converters have a 90% efficiency rate.

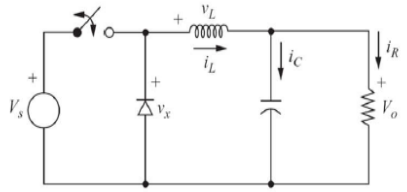


Figure. 10. Buck Converter

B. BOOST Converter

There are many types of switch mode converters, one of which is a boost converter. In other words, it boosts or increases an input voltage [7]. This circuit includes an inductor (L), a MOSFET switch, a diode (D), and a capacitor (C). A switch represents a short circuit when it is turned ON, therefore, there is no resistance in its path, so the DC input source will receive the full amount of current. During the off state, the inductor has reverse polarity. The load resistance eliminates the inductor energy, thereby ensuring a current flow in the same direction through the load. Inductor energy act as an additional source in the combination with the input source, so that the output voltage can also be increased.

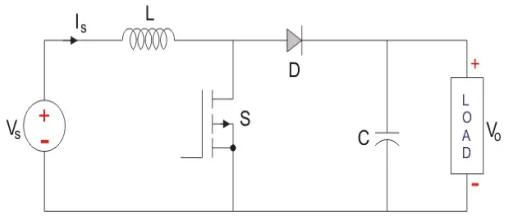


Figure. 11. Boost Converter

C. BUCK BOOST Converter

In order to generate stable current (PV cells) from a high or low input supply, a DC-DC converter with a low ripple output is needed. An effective Buck-Boost converter transforms DC voltage into a higher or a lower voltage [7]. The Buck boost converter is especially useful for tracking PV optimum power. When the switch is on, it creates no resistance to current flow, so all the current flows through it and back to the source. An inductor stores energy while the switch is on. During the off-state, by reversing the inductor's polarity, it releases its stored energy through the load resistance, maintaining the same direction of current, and boosting the output voltage because it serves as both an inductor and a source.

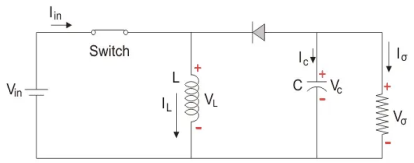


Figure. 12. Buck Boost Converter

V. RESULTS

The INC and P&O methods track maximum power points steadily and determine the operating point at which maximum power is achieved using the proposed method. As described within the method, the controller gives the PWM signal to regulate the voltage, the controller adjusts the voltage by Buck converters, and when the voltage increases, further modifications are attempted until the voltage remains stable.
For the calculations of system performance and to determine how well it performs, this model is needed. The PV voltage is stepped down in the DC/DC buck converter model. To drive the converter switch, the pulse width modulation (PWM) a model is applied. It depends on the duty cycle.

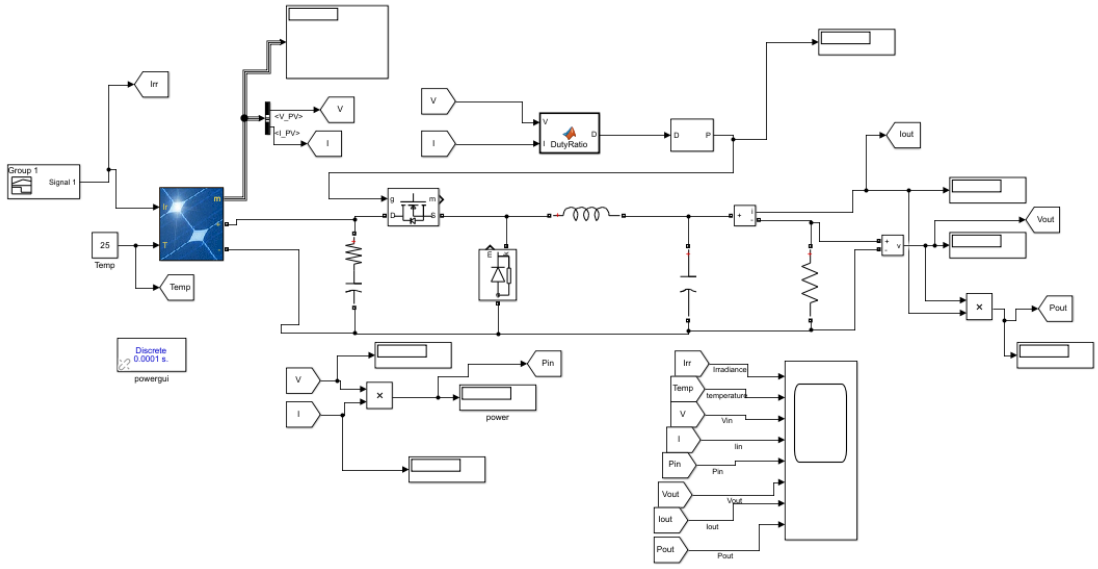


Figure. 13. Mppt Simulation

A. *Perturb and observation method*

Figure shows the Irradiance, Temperature, Solar array Vin, Solar array Iin, Solar array Pin, Iout, Vout, and Pout.

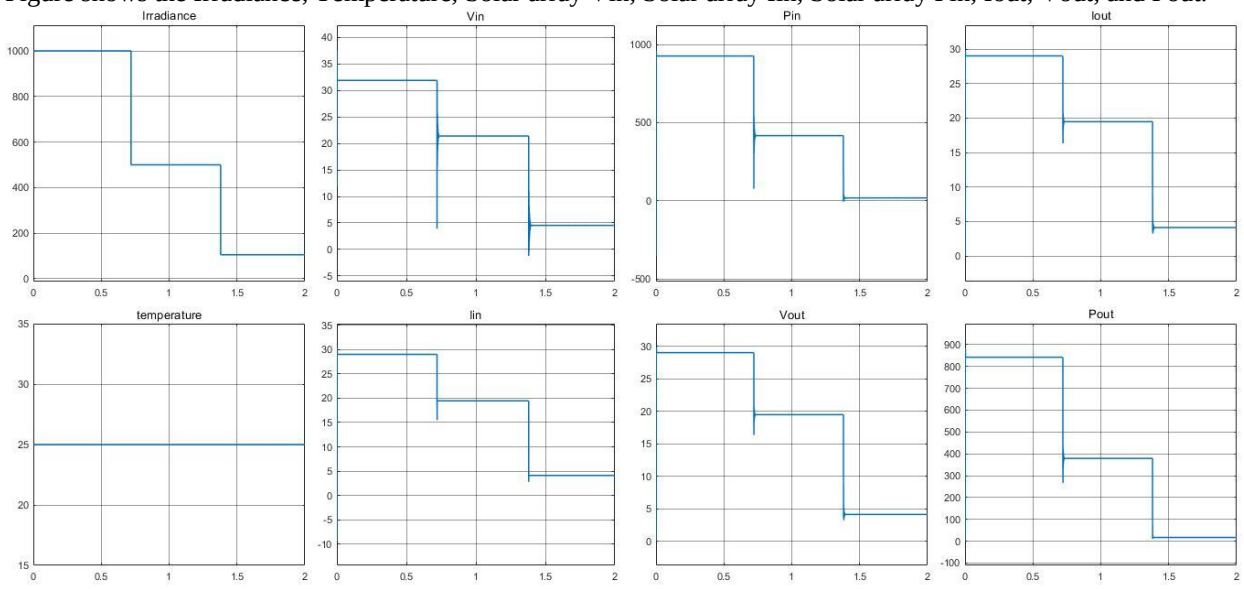


Figure. 14. Irradiance, Temperature, solar array Vin, Solar array Iin, Solar array Pin, Vout, Iout, Pout

B. *Incremental conductance method*

Figure shows the Irradiance, Temperature, Solar array Vin, Solar array Iin, Solar array Pin, Load, Iout, Vout, Pout.

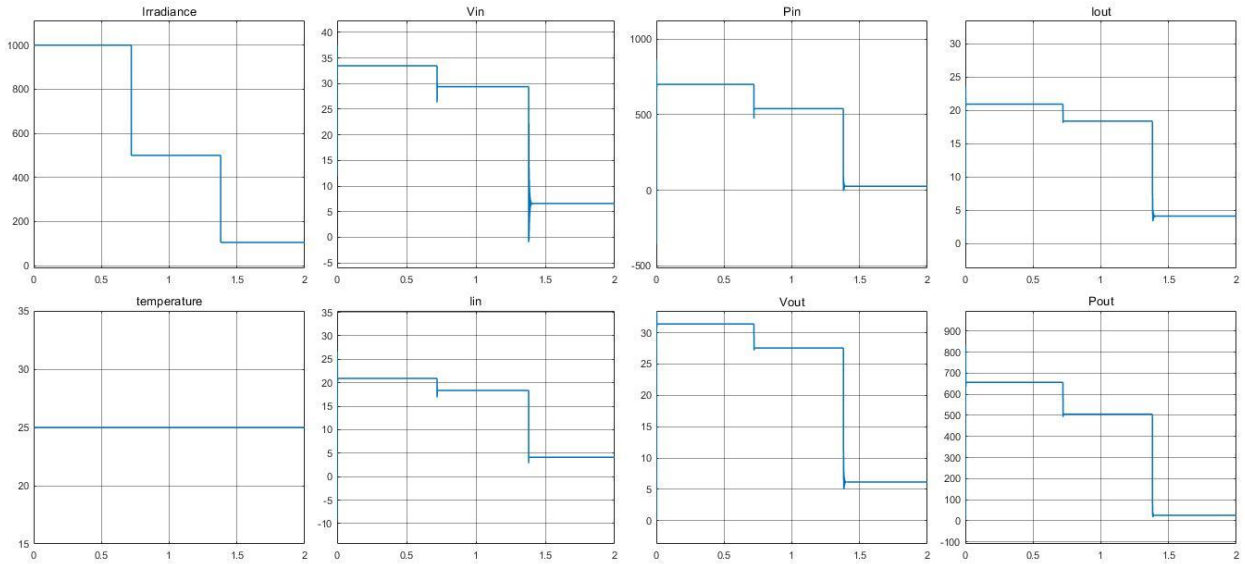


Figure. 15. Irradiance, Temperature, Solar array Vin, Solar array Iin, Solar array Pin, Vout, Iout, Pout

VI. Comparison between Perturbation and Observation Technique and Incremental Conductance Technique

For comparison purposes, the output data of the MPPT is compared to achieve a significantly better MPPT system.

Table I. Comparison between P&O and INC algorithm at Irradiance 1000W/m2

	Perturb and observation	Incremental conductance
Irradiance	1000W/m2	1000W/m2
Temperature	25°C	25°C
Vin	31.93V	33.48V
Iin	29.02A	20.92A
Pin	926.6W	700.5W
Vout	29.02V	31.39V
Iout	29A	20.92A
Pout	842.4W	656.7W
Efficiency	90%	93%

Table II. Comparison between P&O and INC algorithm at Irradiance 500W/m2

	Perturb and observation	Incremental conductance
Irradiance	500W/m2	500W/m2
Temperature	25°C	25°C
Vin	21.42V	29.39V
Iin	19.47A	18.37A
Pin	417.1W	539.9W
Vout	19.1V	27.55V
Iout	19A	18.37A
Pout	379.2W	508.1W
Efficiency	90%	93%

VII. CONCLUSIONS

Based on features such as control variables involved and type of control strategies, circuitry, manufacturing cost, the algorithm technique is considered one of the best mathematical models in use. A comparison is made between the incremental conductance technique and Perturbation and observation technique in this paper, and we find incremental conductance to have a 93% efficiency rate and perturb and observe a 90% efficiency rate. Compared to perturb and observe, incremental conductance is cost-effective and more efficient. Therefore, it is demonstrated that incremental conductance provides a better performance. By using these algorithms, we improve the efficiency of DC-DC converters and improve the dynamics of photovoltaic systems.

ACKNOWLEDGEMENTS

Throughout the thesis, the faculty of Small Satellite Technology and Research Lab (SSTRL) / NCGSA, Institute of Space Technology (IST) guided and supported me in choosing a topic of interest and monitoring my work. I have been enlightened about solar cells and power electronics by them, who has provided various ideas. Throughout this thesis, they helped and guided me in a way which was invaluable.

REFERENCES

[1]. Ananya Dutta, Niloy Barua, Aninda Saha. (2016). Design of an arduino based Maximum Power Point Tracking (MPPT) solar charge controller.

[2]. B Abdelilah1, A Mouna1,2, N KouiderM'Sirdi2 and A El Hossain. (2018). Implementation of Maximum Power Point Tracking (MPPT) Solar Charge Controller using Arduino.

[3]. Hamidullah Kandahari,Rakesh Kumar. (2019). Maximum Power Point Tracking (MPPT) Solar Charge Controller. International Journal for Scientific Research and Development , 7, 6.

[4]. Jesus Gonzalez-Llorente,Eduardo I.Ortiz-Rivera . (2013). Comparison of Maximum Power Point Tracking Techniques in Electrical Power Systems of Cubesats . 27th Annual AIAA/USU Conference on Small Satellites , (p. 6).

[5]. Md. Rokonuzzaman,Md Hossam-E-Haide. (2016). Design and Implementation of Maximum PowerPoint Tracking Solar Charge Controller.

2016 3rd International Conference on Electrical Engineering and Information Communication Technology (ICEEICT), (p. 5).

[6]. Ponugoti, R. S. (2016). Comparative Study of P&O and Incremental Conductance MPPT Algorithms for Photovoltic Systems . International Journal of Innovations in Engineering and Technology(IJIET) , 7.

[7]. Yejee Choi,Monineath Khun,Giselle Verbera. (2017). Maximum Power Point Tracking.

Formation Flying Strategy for Attitude Determination and Control of CubeSat

Muhammad Abubakar Arshad
Small Satellite Technology and Research lab
Institute of Space Technology
Islamabad, Pakistan
aaf7121@ymail.com

Dr.Rehan Mahmood
Small Satellite Technology and Research lab
Head of Department
Institute of Space Technology
Islamabad, Pakistan
rehan_59@hotmail.com

Dr.Mohammad Tahir
Department of Electrical Engineering
International Islamic University
Islamabad, Pakistan
drmtahirmalik2018@gmail.com

***Abstract*— This paper explains the comparison between different types of sensors and actuators used to measure and control the orientation of the spacecraft to determine spacecraft position in space and direction in which it is pointing its target. Typically, sensors used for this purpose are Magnetic, Star, Sun, Earth and Gyro sensors. While, actuator on the other hand is the reaction of the sensor which cause motion or action to keep satellite in the right orientation. For possible two types of controls, active and passive controls [1], we will discuss actuators like reaction wheel, magnetic torque bars and thrusters. The major constraints that take place for small satellite configuration are mainly, size, cost and power specification. Considering all of these, appropriate sensors (magnetometer, sun sensor and earth sensor) are used for low earth orbit (LEO). Presently, use of conical scan earth sensors are being genuinely studied and found to be effective for the use of attitude determination (AD) in small satellite. While, controlling the satellite, it shall concentrate both; an effective instantaneous communication and attitude controls method e.g., magnetic actuation (magnetorquer, permanent magnet and reaction wheels). All in all, the paper holds discussion of different types of sensors and actuators that can be used for small satellite missions, following; strategies of implementing a sensor less Formation Flying method for satellites in (LEO) with minimum budged and improved reliability in the field of small satellite (CubeSat) communication.**

Keywords— *Attitude determination, Attitude controls, CubeSat, Conical Scan Earth sensors, CubeSat Formation Flying, Gyro sensors, Magnetorquer, Magnetic sensors, Magnetic Actuation, Reaction wheels, Sun sensors, Star trackers, Thrusters*

I. INTRODUCTION

The aim of introducing Nano-satellites has evolved over the years. One of the examples of Nano-satellites is CubeSat. The idea of CubeSat processing and developing was proposed by i.e., California polytechnic state university and Stanford University in 1999. They planned to test small satellite flights for low earth orbit communication. CubeSat are typically used by mass research stations for their research and students for their training missions. They are generally of mass ranging to a kilogram and dimensions of 10 x 10 x 10 cm^3 [2]. Such a CubeSat with reaction wheels installed is shown in Fig. 1.

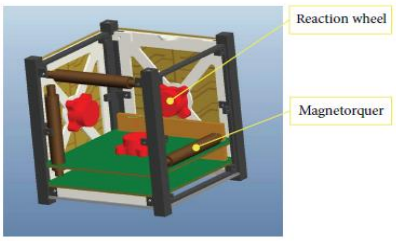


Fig. 1. CubeSat with reaction wheel installed [2]

A satellite mission requires a complete satellite orientation control system. The specific sensors and actuators altogether make up this whole system. CubeSat, a small satellite used for mission, requires not too large and expensive controls systems. Commercial off the shelf and low-cost designs are installed in this small satellite. The sensors (sun, star, earth, gyro, magnetic) and actuators (torque rods, thrusters, reaction wheels) with a detailed study have been implemented to design a more credible attitude control system.

An Attitude Determination and Control Systems, is divided into two parts as stated by [3], the ADCS1 and ADCS2. The ADCS1 performs the simple task of Detumbling of the satellite. The second part, ADCS2, performs the simple task of pointing control. The purpose of introducing these two systems is for reliability and accuracy. It also helps to support in case, if one system fails, the other is present as a backup. The main idea of this paper is to determine the most suitable sensors and actuators that could be used for reliability and accuracy.

The paper discusses the comparison of different types of sensing (determination) and reaction (control) methods, their differences and drawbacks for the satellite mission. First, in section 1, we briefly describe the specification and model of the CubeSat for the mission. Section 2, describes the sensor specification following the section 3 which shows the suitability and credibility. Section 4 explains the list of actuators leading to section 5 detailing the pros and cons of different types of actuators used for spacecraft mission. Section 6 includes the future proposed plan and theory of new ideas. Section 7 concludes the paper.

II. SENSOR AND ACTUATORS SPECIFICATION

The feedback in the control system has no purpose if no suitable sensors are employed. The attitude of the satellite is necessary to be estimated before the deployment and after it is released in space. For this purpose, single or number of sensors are placed to attain the accurate estimation of satellite.

The sensors have two classes in which they are categorized; the reference one and the other are inertial [5]. These both are sensors but the difference is between the frames of references in which they are operated. Sun, star, and earth sensors incorporate the field of reference for their output estimation whereas the inertial sensor includes gyros which work because of the inertial frame. As for the point of convenience of mission, both frames are important for the attitude estimation process.

A. Sun Sensor

Sun sensor or a reference sensor, often a measurement is estimated from a particular reference for the given instant of time. The basic work of a sun sensor is simple, to determine the angle between the base and the incident light falling upon a small opening (slit). They are typically used nowadays in spacecraft missions, however, needs an un-obstructed (clear view of visible light) field of view. As LEO has to face eclipse periods, then somehow AD shall counter that problem and provide a clear reading on the loss of reference (sun). Typically, sun sensors have an accuracy ranging between 0.05-4 degrees [11].

B. Star Sensor

The best and the far more accurate method are using the star sensors for the attitude estimation of the space satellite. The sensor works in a coordinate system, the position of star present at a distance is measured with respect to object (satellite) and then this estimation is fed into system to locate the observed star position from its (star) history of behaviour (movement). This method is accurate (arc second to arc minutes) [11], while its costly, for such small satellite space missions.

C. Magnetic Sensor

The principal object used for the measurement of earth's magnetic field is magnetometer. The use of magnetometer in the space satellite defines the measurement of earth's magnetic field and comparing it with the observed value for the attitude estimation of the satellite. The method is quite convenient to use but some internal and external disturbances during mission makes it inaccurate and falls below from other methods (star and earth references model) used for this particular attitude estimation technique [5].

D. Gyroscope (Gyro Sensor)

The word gyro involves the inertial measurement of the satellite; it is basically a mass spinning around which determines the speed and angle of the spacecraft orientation. The process is entirely blank regarding external references involved around the spacecraft environment. The mechanism is durable with a good accuracy rate if this mechanism coexists with external reference or point.

E. Earth Sensor (Horizon Sensor)

Earth sensors like sun are also known as reference sensors, as they use the reference object to determine the attitude of the space satellite. They are usually an infrared sensor, study the difference of temperatures between earth and space environment. Many spacecraft pointing nadir directions have a wide FOV (field of view) which enables them to view entire earth and stabilize the spacecraft according to it [4]. Earth sensor e.g., Conical Scan earth sensor (CES) used in small satellite uses earth as a reference to point roll and pitch angles for the process of attitude estimation. The compact design of this sensor makes it convenient use for small satellite missions. A CES sensor had been considered a great source of satellite attitude determination application with cost saving and its wide field of view (FOV) [13].

TABLE I. ADVANTAGES AND DISADVANTAGES OF SENSOR TYPES USED IN NANO SATELLITE [[5] [6] [7]]

Sensors	Advantages	Disadvantages
Star sensor	High accuracy	High power consumption Large in size Cost expensive Spinning may cause the sensor to not work properly
Sun sensor	Simple Low power consumption Cheap	During eclipse it does not work Disturbed by earth albedo Some two axis sensors are expensive
Magnetic sensor	Simple sensor Smaller in size Cheaper Available in huge amount	Not much accurate Magnetic field not fully known Only useful for low earth orbits (LEO)
Gyro sensor	Helps in during the eclipse	Large size High power consumption Some of them are expensive
Earth sensor	Simple Earth, the reference is always present	Accuracy affected by sun and moon

F. Credibility of combined Sensor Techique

According to the availability, a reference sensor makes it a lot easier for the estimation procedure, however during eclipse time the reference sensor may fail to achieve the goal, in that case inertial frame of sensor can be used; in conclusive, to perform the Attitude Estimation process of the satellite. Reference and inertial frame of sensors are used altogether [12] e.g., a sun sensor (reference sensor), because of its low cost and less space occupancy, they are highly used sensor for the Attitude Determination process and along using a gyro sensor (inertial sensor) can help the estimation process during eclipse. Similarly, using magnetic actuation with momentum wheels benefits the system controls in providing high pointing accuracies [14].

G. List of Actuators

After studying and intelligent formation from a suitable sensor application the use of actuators comes in hand to control the satellite's attitude. As actuator is nothing but an assembly of mechanical hardware to produce suitable torque in response to the attitude control of the satellite.

H. Reaction Wheels

Reaction wheels mainly involve the moving mechanical parts, which rotate at higher speed [8], they work on the principle of Newton's third law. The mechanical part moves with a great speed and produces torque in the opposite direction of the rotation. However, increasing momentum and small satellite specification this cannot be used extendedly.

I. Control Moment Gyro

Control moment gyros (CMGs) basically provide the active control mechanism for the process of AC of the spacecraft. CMG, composed of a spinning wheel in the center (reaction wheel) attached to one or more gimbals which tilt the angular momentum of the rotor in reaction to certain error in the control systems (Fig. 2). They are considered very quickly, with high response time, however some limitation to their weight and higher cost they are disregarded [8].



Fig. 2. Control Moment Gyros (CMG)

J. Parmanent Magnet

Permanent magnet stabilization is similar to the magnetorquer but the difference which accounts, is about power consumption. The permanent magnet needs no power from the satellite's ADCS (attitude determination and control system), this benefits the two-axis stabilization of the satellite for its entire life. Whereas during flight time, oscillation accomplished, cannot be removed easily by this permanent magnet control which makes it unsuitable for the satellite mission requirement [3].

K. Magnetorquer

The method uses the comparison of produced magnetic field with the earth's magnetic field and finally works on rotating the satellite in particular position until the two get aligned. This is useful and much reliable method to control the satellite in regions with a strong field like, LEO (low earth orbit) because the mechanism involves no mechanical rotation or momentum, where it only compares the measured magnetic field with the reference field (one present in the reference model) [5], however it should be perpendicular to the geomagnetic field of the earth.

L. Thrusters

Thrusters are the key approach in basic satellite attitude control; the method uses Newton's third law in such a way that, expulsion of propellant at high velocity gives a momentum (push) in the opposite direction. In past 2010, reaction control thrusters were used to control the satellite; the mechanism used, was the switching one of those thrusters which were needed to control the stability [9]. Thrusters on one side are found to be effective, by reverting satellite back on track (original in which it was moving) however it occupies mass in satellite which reduces the mission life. Thrusters were officially made an unreliable approach by NASA as the uses of magnetorquer were compared to be effective in orbits closed to earth e.g., LEO [10].

M. Spin Stabilization

The method proposes the rotation of the satellite on its axis; it's particularly a movement which causes a gyroscopic effect to take place by such movement in order to control the attitude of the satellite. Usually spinning satellites are divided into three categories; passive spin, spin with precession control and dual spin [11]. Satellite which are independent of control authority are known as passive spin, contrast to those having spin authority, spins with precession control, however the most effective of them is the dual spin, which is a spinning central mass and a platform of de-spun tracking the target [11]. Although, spin stabilization techniques are found in great number but this kind of method is generally unreliable, as such movement and satellite itself revolving around LEO with great speed would cause disturbance in communication.

TABLE II. DIFFERENT METHODS FOR SATELLITE CONTROL [12]

Method	Degrees of Accuracy	Performance
Reaction Wheels	0.01	Response time is quick High precision
Thrusters	0.1	Quick response time High authority
Magnetorquer	1-2	Are light in weight Low cost Used near Earth
Spin Stabilization	0.1	Simple in use Cheaper Inertially oriented
Control Moment gyro	0.1	Very fast response time High authority

N. Assets and Liabilities

According to the flight configuration and CubeSat compatibility every control has its pros as well as cons; however, for a smooth mission more than one control altogether is required. Like magnetorquers used with permanent magnet make it sufficient for the attitude control of a small satellite.

Based on structure and the type of flight, some controls are left behind; as because of the structure of reaction wheels, that are totally incompatible with CubeSat ADCS, similarly on the other hand considering spin stabilization as the source for control actuator makes it difficult for the satellite to complete its mission (communication) because of such high-speed rotation along its axis. Thruster is considered to be the typical control actuator for satellite, but as their propellant needed

some space to be stored, so, later it could be expelled when needed during attitude control; which deliberately occupies space of ADCS which significantly shortens the life of small satellite.

III. Discussion and analysis

For a particular instant, key is to choose the right sensors and actuators which can be effectively used in the limited and constraints of a small satellite, which involves; power consumption, size and cost of the sensor and actuator used to construct a reliable source of system for attitude determination and its control.

As discussed earlier, main sensors which are used for determination process are Star, Sun, Earth, however, cost of choosing the right sensors for this process depends upon structure, power consumption, size of the sensor, cost and how much efficient it is during communication e.g., the use of gyroscope is not a good choice for the system as its weight and large power consumption makes it inappropriate for the flight. Where using a star tracker or horizon sensor (scan wheel) occupies space and is cost effective, which makes it inconvenient for the process of attitude determination (AD). With limited budget and size (space), leaving choice for only magnetometer, sun sensor and currently most used application of conical scan earth sensor. Sun sensor; cheap and smaller in size makes them suitable for attitude determination. Magnetometer, surpassing every sensor, e.g., during eclipse, sun sensor fails to deliver the information for attitude where magnetometer copes with this abnormality effectively [3]. There is advancement in earth sensors; where conical scan earth sensor has found to be effective in the field of attitude determination of small satellites. With a wide conical field of view (FOV) and a tilt angle of 40 degrees, use of such two sensors in small satellite covers almost all the surface to which it's pointed. Another important aspect, where many satellites use different sensors for three axis spacecraft and transfer orbit operation; conical scan earth sensors can perform these two-operation making it very cost effective for a budgeted satellite system [13].

To control the satellite, actuators system is installed and for firm communication, combination of actuators is used altogether. Using technique, in which magnetorquer and permanent magnet; with low power consumption and a lifespan of lifetime for the permanent magnet make them ideal for the mission. Where, accuracy and light structure for magnetorquer (does not involve any mechanical movement) makes them a wide source of application, collectively, these both make a reliable actuator system for the control of small satellites [3]. In another approach of controls deals in magnetic actuation, use of magnetorquer with momentum wheels (a hybrid system) make a better system for controls of satellite; helping both, damping of mechanical torque and providing better pointing accuracy for satellite [14].

IV. Future Proposal

The paper states the types of sensors used for the attitude estimation and control actuators for the possible control system for small satellite. As with successive research and study in the field of astronomy; students and scientists are working on the new details to make satellite communication easier with limited constraints.

A. Formation Flying of CubeSat

GNSS (Global Navigation Satellite System) is the kind of navigation system which provides autonomous Geo position with global coverage. A good precision and accuracy for position and satellite orientation could be obtained from this GNSS. This area of research is evolving and could later be used for many future experiments by many research students and scientists. Similarly, an approach being studied is use of GNSS in Formation Flying of small satellites and who's computational efficiency is still part of active research i.e., use of interferometric principle for the attitude determination using GNSS phase measurements [15]. This method uses a pair of GPSs (global positioning system) antenna, user can determine the attitude of the satellite using the phase difference between like signals of that antenna pair, which makes this technique more accurate and precise. A similar approach to Satellite Formation Flying (SFF) was the use of line of sight (LOS) and Ranges between the satellites (Deputy and Chief). The method uses a relative state estimation between deputy and chief satellite vehicle using the data acquired from, LOS and ranges between them [16].

For active research, students and many researchers are attracted towards the Formation Flying Strategies of CubeSat, which enables users to build low-cost and higher success rate design for determination process of satellite's orientation like i.e., Relative Attitude and position determination of satellite in Formation Flying of CubeSat, however, this was for the time being only helped for one Satellite (Deputy Vehicle) [17]. Later, in the same research field, successive results lead in determining relative state of multiple small satellites using array signal detection; the method was quite adoptive in sense of Formation Flying, it explains how one satellite (deputy satellite) follows and estimates its attitude with respect to another satellite (chief satellite). The procedure follows, antenna arrays present on both satellite, deputy as well as chief. Furthermore, using angle of arrival and angle of departure attitude knowledge is calculated by deputy satellite relative to chief satellite [18]. This use of Formation Flying in multi-CubeSat enables a sensor free design (free from large volume, size and power consuming sensors) and an approach which is also more extensive in providing better accuracy than GPS based navigation system.

V. Conclusion

This paper contributes in overviewing the basic idea of the sensors and actuators that could be use in the process of attitude determination and control system (ADCS). The different types of sensors, actuators are outlined extensively with their use and drawbacks for AD and CS respectively. This paper can be helpful in the field of designs and implementation of ADCS for Formation Flying Concept for small satellite. The purpose for building this approach is to counter the use of conventional sensors reducing the size, weight and cost. With this report, researchers could use this approach in implementing various designs, flights, and novel approach to determine the orientation of a small satellite using this advance study of GNSS for the Formation Flying of CubeSat [17].

Acknowledgment

The contribution of this paper shows the unique idea of formation flying strategy and it's use in Nano satellite technology, CubeSat in IV. Furthermore, this paper also

shows and explain this different method which briefs how they are different from random conventional sensors technique which wholly makes system crowded and unreliable for specification like, CubeSat.

REFERENCES

[1] P. Hendrik, "Development of attitude controllers and actuatores for solar sail cubesat," March 2011.

[2] M. P. T. W. R. L. Junquan Li, "Design of Atitude control systems for CubeSat-Class nano satellite," *Journal of control science and engineering*, 2013.

[3] Jensen, K. F., & Vinther, K. (2010). Attitude determination and control system for AAUSAT3. *Master's Thesis, Aalborg University*.

[4] Reigber, C., (Ed.) (1996). *Champ, Phase B*. Scientific technical report STR96/13. champ project office.

[5] T. Bak, "Spacecraft attitude determination- a magnetometer approach," *Aalborg University, 1999.*

[6] J. R. Wertz, "Spacecraft aatitude determination and control," *Kluwer academic publishers, 1994.*

[7] Arbinger, C., & Enderle, W. (2000, September). Spacecraft attitude determination using a combination of GPS attitude sensor and star sensor measurements. In *Proceedings of the 13th International Technical Meeting of the Satellite Division of The Institute of Navigation (ION GPS 2000)* (pp. 2634-2642).

[8] Paula Sorolla Bayod " Study and Design of the Attitude control of a CubeSat 1U based on reaction wheels", *Bachelor's Degree Thesis, September 30, 2019*

[9] Curti, F., Romano, M., & Bevilacqua, R. (2010). Lyapunov-based thrusters' selection for spacecraft control: analysis and experimentation. *Journal of guidance, control, and dynamics*, *33*(4), 1143-1160.

[10] Agasid, E., Burton, R., Carlino, R., Defouw, G., Perez, A. D., Karacahoglu, A., ... & Shimmin, R. (2015). *Small spacecraft technology state of the art, NASA, Ames Research Center, Mission Design Division Rept. NASA/TP-2015-216648/REV1, Moffett Field, CA.*

[11] Larson, W. J., & Wertz, J. R. (1992). *Space mission analysis and design* (No. DOE/NE/32145-T1). Torrance, CA (United States); Microcosm, Inc.

[12] CubeSat *Design Specification*. Tech. rep. *California Polytechnic State University, 2009.* url:http://www.cubesat.org/images/{\%}0Ddevelopers/cds {_} rev12.pdf

[13] Fowler, R. Z. (1981). THE USE OF THE CONICAL SCAN EARTH SENSOR IN COMMUNICATION SATELLITE APPLICATIONS. International Foundation for Telemetering.

[14] Tebbani, S., Makarov, M., Maniu, C. S., & Hinostroza, I. (2016, May). Nanosatellite attitude control using electromagnetic actuation. In *4th SONDRA Workshop*.

[15] Garrick, J. 1996. Investigation of Models and Estimation Techniques for GPS Attitude Determination. *In Flight Mechanics/Estimation Theory Symposium 1996 (p. 89).*

[16] Wang, X., Qin, W., Bai, Y., & Cui, N. (2016). A novel decentralized relative navigation algorithm for spacecraft formation flying. *Aerospace Science and Technology, 48, 28-36.*

[17] J. Wang, J. Yuan, R. Zhang, and H. Zhang Relative position and attitude determination for CubeSats and drones using signal direction based on antenna arrays. In *Proc. Int. Astronaut. Congr., Guadalajara, Mexico, Sep. 2016, pp. 1–7.*

[18] Wang, J., Zhang, R., Yuan, J., & Luo, J. (2019). Multi-CubeSat relative position and attitude determination based on array signal detection in formation flying. *IEEE transactions on aerospace and electronic systems, 55(6), 3378-3393.*

[19] Naqvi Najam Abbas and Dr. Li Yan Jun, "The Quest for Optimal Spacecraft Attitude Determination Filtering Algorithm Using GNSS Phase Measurement: An Overview", *2nd International Conference on Signal Processing Systems (ICSPS), 2010.*

Overview of ICUBE-N: National CubeSat of Pakistan

Usman Imran
National Centre of GIS and Space Applications
Institute of Space Technology
Islamabad, Pakistan
usman.imran@mail.ist.edu.pk

Muhammad Asfandyaar Arshad
National Centre of GIS and Space Applications
Institute of Space Technology
Islamabad, Pakistan
asfandyaar @mail.ist.edu.pk

Arooj Shafique
National Centre of GIS and Space Applications
Institute of Space Technology
Islamabad, Pakistan
arooj.shafique @mail.ist.edu.pk

Rehan Mahmood
Department of Electrical Engineering
Institute of Space Technology
Islamabad, Pakistan
rehan.mahmood@mail.ist.edu.pk

Rizwan Mughal
Department of Electrical Engineering
Institute of Space Technology
Islamabad, Pakistan
rehan.mahmood@mail.ist.edu.pk

Hayat Muhammad Khan
Department of Aerospace Engineering
Institute of Space Technology
Islamabad, Pakistan
rehan.mahmood@mail.ist.edu.pk

***Abstract*—** The miniaturized version of satellites encouraged cheap access to space at the university level for research purposes. The miniaturization of electronic components and advancements in engineering technologies have paved the way for developing and launching small, low-cost spacecraft**.** IST initiated the satellite program back in 2010, ICUBE-1 a 1U CubeSat, and was launched in 2013. The second satellite of this program is ICUBE-N, a 3U CubeSat and is in development. The mission's primary goal is to launch ICUBE-N and establish communication with the ground station successfully. The secondary goal is the technology demonstration and data acquisition from different payloads, including a camera. In this work, preliminary design and analysis of different subsystems of ICUBE-N are discussed in detail, along with its required testing and technical support facilities. The presented agile systems engineering approach and components selection will help develop a small budget and educational CubeSats missions.

Keywords— CubeSat, Space Technology, Global Positioning System (GPS), Onboard Computer, Payload, Tracking, tele-command, telemetry (TTC), ADCS

I. INTRODUCTION

Launching satellites for research and space exploration had always been carried out by national space organizations due to huge funding requirements which constrained initiating such projects at the university level. The standardized specifications of CubeSat were defined for educational and research institutes for easy access to space. CubeSat concept containing certain specifications was first proposed by professors at California Polytechnic State University [1] in 1999 which later became a standard for the development of education satellite. Until now, around 1600 CubeSats have been launched since its inception. CubeSat is a small satellite consisting of one or more units where one unit (1U) is of size 10 cm × 10 cm × 10 cm and mass 1.33 kg. CubeSat can be arranged in 2U, 3U, 6U, or multiple unit configuration by following the specifications [2]. CubeSat missions can range from educational projects to technology demonstration [3], science missions like measuring electron precipitation [4] and providing commercial services. The Poly Picosatellite Orbital Deployer (P-POD) [5] built by California Polytechnic University ensures the safety, proper deployment of CubeSats and reduces the concerns of the launch providers. P-POD has gone through various improvements and modifications since its inception.

Institute of Space Technology (IST) started the development of ICUBE-1 [6], a low-cost small spacecraft back in 2009 that was successfully launched in 2013. ICUBE-1 carried an imaging payload that had a low-resolution CMOS camera responsible for taking images of earth. The ground station facility exists already at IST along with a clean box and vibration testing facility.

IST with the support of the Higher Education Commission, Pakistan initiated the project of an experimental nanosatellite named ICUBE-N which is a 3U CubeSat. The different universities in Pakistan will collaborate in the design and development of the payload. ICUBE-N will carry a high-resolution camera as a payload along with other payloads which are yet to be finalized. The development of a clean room is underway and other facilities like thermal vacuum chamber, vibration testing facility and the ground station would be upgraded too.

ICUBE-N project aims to facilitate the students in gaining experience and skills which are essential for the development of nanosatellites. The main objective of ICUBE-N is to design and develop indigenous modules instead of Commercial off-the Shelf (COTS) systems which could help later in capacity building. The secondary mission objective is to successfully collect payload data and communicate with the ground station. The knowledge and experience gained during the operation and development of ICUBE-1 would be utilized in the development of complex subsystems for ICUBE-N. ICUBE-N will enable the involvement of IST students and graduates in all stages of CubeSat development, operation, and launch.

Section II provides the mission overview consisting of ground track and operational modes for ICUBE-N. The detailed system design for the structure, power, communication, onboard computer, attitude determination, and control system and payload are provided in Section III. Section IV explains the engineering facilities consisting of a ground station, clean room, thermal vacuum chamber, Helmholtz coil, and vibration testing facilities. Section V summarizes and concludes the paper followed by acknowledgment and references.

II. MISSION OVERVIEW

The objective of ICUBE-N is to design and develop the subsystem modules indigenously instead of using commercial

off-the-shelf components. In addition to that, ICUBE-N aims to indulge the other universities of Pakistan in the development of payload subsystems as it is the national CubeSat of Pakistan. Apart from this, the aim is to demonstrate the capability of low-cost nanosatellites to observe the properties of the earth's atmosphere and space using scientific payload subsystems. The other objective of ICUBE-N is to bring the onboard components, subsystems, and instruments to the technology readiness level so that they can be implemented in future scientific missions with more reliability.

ICUBE-N is anticipated to be propelled in a low earth orbit (LEO). The altitude of orbit will range from 550-650 km but for investigation, an altitude of 600km is chosen. The LEO is selected so that ICUBE-N is accessible from everywhere on earth. The slant of ICUBE-N is around 97° concurring with the selected parameters. The orbital period of ICUBE-N is 96.62 minutes with a maximum obscure time of 34.27 minutes. The thermal and power generation for ICUBE-N are analyzed considering the worst-case scenario of dawn and midnight. The STK simulation is used for obtaining the ground track of ICUBE-N as shown in Figure 1. ICUBE-N can communicate with the IST ground facility 4-5 times a day with a communication period of 53 minutes per day approximately.

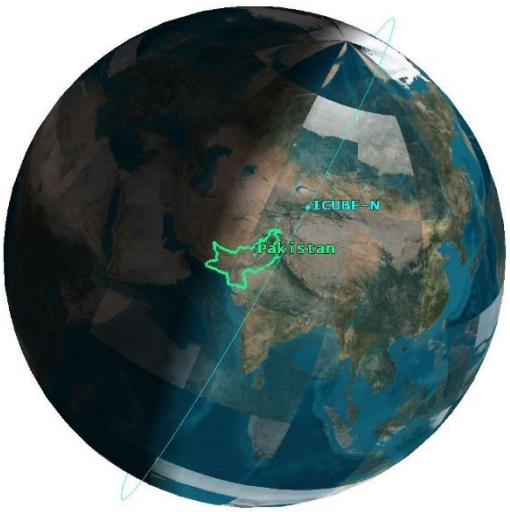


Figure 1 – 3D view of ICUBE-N ground track

There are five operating modes of ICUBE-N which are Normal, Transmit, Payload, Emergency, and Power saving mode. The modes can be changed manually and automatically. It can be shifted manually by sending the telecommand from the ground station. The onboard computer is responsible for automatic switching of the modes depending upon the situation and requirements.

The deployment cycle is initialized instantly after deployment by following the guidelines [2] given in the CubeSat specifications. When the CubeSat is deployed from P-POD, the system bus is connected to the batteries after the release of the deployment switch. A delay of 10-25 minutes is essential before deploying any structure, such as boom or antenna, so that the CubeSats in the same P-POD have enough separation. After deploying successfully, ICUBE-N will be in the power saving mode in which only the onboard computer will be in a power-on state. ICUBE-N will shift to normal mode when the power of batteries reaches the required threshold and performs the check on housekeeping tasks and communication of the beacon signal. The block diagram of operational modes is shown in Figure 2.

ICUBE-N will execute the payload tasks like image capturing, transferring to memory storage, etc. The payload and onboard data are saved on the memory storage device which is later transferred to the ground station. While contacting the ground station, ICUBE-N shifts to transmitting mode to send the data to the ground. It can also receive commands and instructions from the ground station to perform accordingly. In case of any anomaly or undesirable situation, ICUBE-N will switch to emergency mode. ICUBE-N will restart onboard devices in emergency mode and try to bring the system in the power-saving mode.

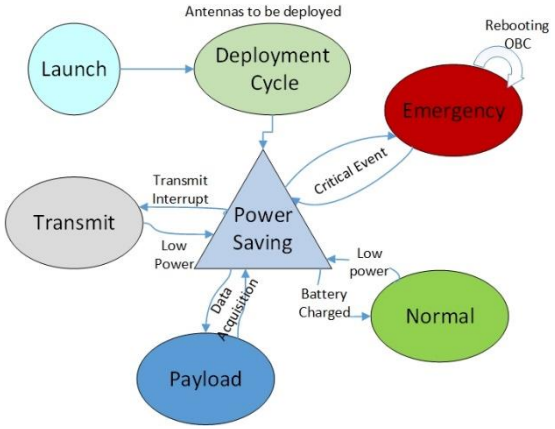


Figure 2 – Operating Modes of ICUBE-N

III. SYSTEM DESIGN

The draconian space environment and payload onboard ICUBE-N demands highly efficient system design considering power, attitude, and control. ICUBE-N consists of various subsystems just like its predecessor [7] ICUBE-1. Each subsystem is developed in-house instead of using COTS modules. The subsystems are described in detail in the following sections and shown in Figure 3.

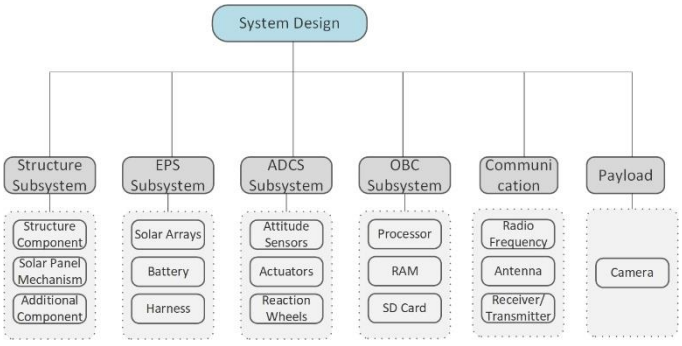


Figure 3 - Subsystems of ICUBE-N

Structure: The structure for ICUBE-N is designed by considering the space material [8] and structural dimensions for the standard CubeSats [2]. After reviewing the available structures, it is determined to develop an in-house structure that would help later in the capacity building. The structure for ICUBE-N is a 3U structure of dimensions 340mm X 100mm X 100mm and mass less than 0.3kg which is very lightweight.

The structure is portable, and all the faces of structures can be removed easily. The structure consists of rails, ribs, standoffs, and L-pieces as shown in Figure 4. The PC104 stacks [9] can be easily placed anywhere within the structure using internal ribs. The choice of materials is critical in any discussion of tiny spacecraft construction. Mechanical qualities like modulus, stress, and toughness, as well as physical features like thermal properties, and radiation resistance, must all be satisfied. These are focused on payload designs, as well as mission readiness and deployment procedures, with knowledge of rideshare safety issues. Protection switches which include the remove before flight pins, footswitch, and the need for spacecraft to be shut off when placed in the deployer, are all considered. The structure is made up of Aluminum 6061-T6 and the surfaces are anodized to prevent the ICUBE-N from external electrical field and radiations.



Figure 4 - Structure of 3U ICUBE-N

Power: The power generating capabilities of CubeSat is always restricted due to its compact physical size. With advancements in solar cell fabrication techniques, it is now feasible to produce Ultra Triple Junction Cells that are more than 30% efficient, nearly twice the efficiency of ordinary Silicon solar cells. Advanced Triple Junction cells will be used in ICUBE-N. ICUBE-N has solar panels on its faces. Each cell has an efficacy of more than 28 percent at room temperature.

The in-house power module has been designed and can offer both regulated and unregulated power at +3.6V and +5.5V. The power supply can also be used with the OBC and other ICUBE-N subsystems. Battery charge regulators are also included. The voltages and currents of the battery and buses, as well as the temperature of the different EPS components, make up the health data of the electrical power system. The data is sent to the OBC through the I2C protocol.

To keep all the systems active during eclipses, rechargeable Li-ion batteries are linked in series with the EPS. Each battery has a voltage of 3.7 volts. Lithium polymer batteries are popular because they have a high storage density and a low rate of deterioration over time. Moreover, each battery has a thermostat device that can be operated via I^2C bus, ensuring that the temperature remains within the working range for optimal efficiency.

Communication: One of the most important subsystems of ICUBE-N is the communication subsystem. A satellite is useless without dependable communication. For uplink and downlink communication in ICUBE-N, amateur radio bands would be employed. Amateurs and hobbyists are welcome to utilize the amateur frequency band, which has few coordination requirements. In addition, several ground stations currently use this frequency range, allowing ICUBE-N to interact with other ground stations. After consulting with the International Amateur Radio Union, the downlink and uplink frequencies would be determined. The uplink for ICUBE-N will be in the VHF band, while the downlink will be in the UHF band. Commands would be sent to the satellite via uplink rate of 1200bps using Audio Frequency Shift Keying. The downlink would employ Binary Phase-shift keying with a transmission rate of 1200 bits per second to collect telemetry data from the satellite. The system of communication can send out a CW beacon in Morse code at regular intervals. It is used to determine the CubeSat and to send data on the spacecraft's fundamental health.

The output power of the transceiver utilized will be around 350mW. For packet communication, the AX25 connection protocol would be utilized. Uplink and downlink will be served by monopole and dipole antenna. The antennas would be positioned at the launch sequence.

On-Board Computer (OBC): The primary goal of an onboard computer is to process and control all the data and connect with other satellite subsystems. ICUBE-N is developing in-house OBC instead of using a commercial off-the-shelf module. The onboard computer (OBC) will consist of EFM 32 microcontroller with external RAMs and ROMs. The block diagram of OBC for ICUBE-N is shown in Figure 5.

The EFM 32 microcontroller is a 32-bit ARM Cortex M4 controller operating at 72MHz. This controller has the

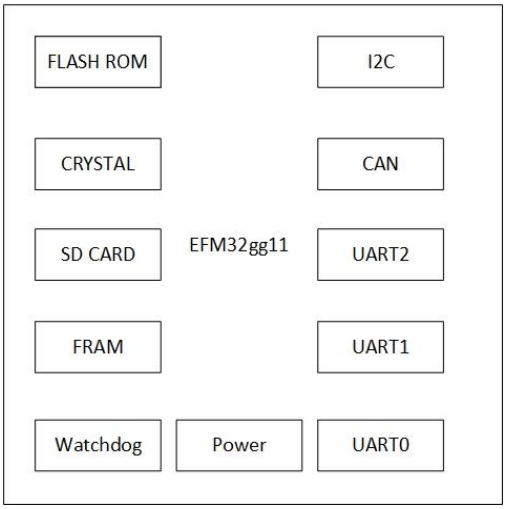


Figure 5 – Block diagram of OBC

capability of SPI interface, SD card, and CAN bus. Its

features include 144 GPIO pins, 2 MB of flash program memory, and 512KB of data RAM. It also hosts an integrated DC buck converter. The serial interfaces consist of UART, Ethernet, I^2C, and CAN controllers. The survey of different electrical bus interfaces is provided in [10]. The microcontroller also hosts two Analog to Digital converters and two Digital to Analog converters. It supports a 16-bit timer and there is a total of 7 timers available. It has a low power consumption of around 80µA in energy mode.

The connections between OBC and other subsystems of ICUBE-N are made through the PC-104 stack. The PC-104 stack consists of 104 pins which are assigned different functions based on the standard so that pins are compatible with other commercially available subsystems. The Micrium operating system which is a real-time operating system (RTOS) is used for programming the EFM32 controller using Simplicity studio.

Some of the libraries from FreeRTOS would also be used in software development. The tests will be performed to validate the working of OBC in the extremely harsh environment of space bearing all the radiations, temperature changes, and vibrations.

Attitude Control: Attitude Determination and Control System (ADCS) is designed and developed instead of purchasing a commercial module as ICUBE-N is following the in-house development strategy. Active control is based on the feedback principle, in which the spacecraft's attitude is sensed and torque is supplied to adjust it. The reaction wheel is used as a common actuator for active attitude control (AAC). The reaction wheel has high power and weight but results in fast and continuous feedback resulting in more efficient control. The control block diagram for AAC is shown in Figure 6.

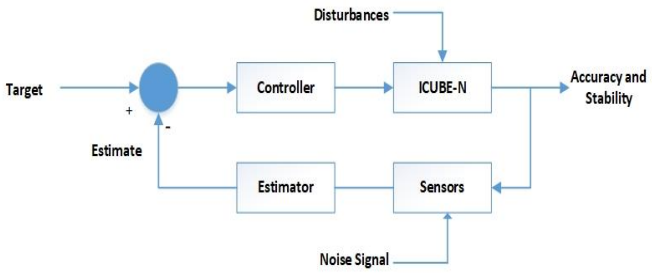


Figure 6 - Control block diagram for active attitude control

The number of reaction wheels equals the number of axes of torque. Usually, three wheels are required for three axes. The vibrations which are induced by imbalances of the reaction wheel are also considered while designing ADCS. Several sensors are also installed on the ADCS module which includes Global Positioning System (GPS), magnetometers, and inertial measurement unit (IMU). The GPS receives data from a number of satellites revolving around the earth and gives an accurate position for our system. The magnetometers get attitude by measuring the magnetic field and comparing it to the modeled magnetic field.

The IMU is an integrated unit that consists of hardware sensors and software. IMU measures rotation with the help of gyroscope by measuring angular rate, translation with help of accelerometers by measuring specific acceleration

Payload: The ICUBE-N is going to have several payloads. One of which is a high-resolution camera. The other payloads are yet to be finalized. The camera with long-range and high-resolution would result in taking better images of the earth for later observation. The images would be saved on the SD card memory and would be later sent to the Ground Centre. The special lens would be considered for the draconian space environment. The image will initially be compressed using the image compression technique because of the lower downlink data rate. The picture compression is carried out by a dedicated microcontroller According to the requirements, the information will be transferred to the Ground Centre.

IV. ENGINEERING FACILITIES

Sophisticated engineering labs are required to effectively design, build, and incorporate the ICUBE-N. To increase the reliability of the spaceship and its components, appropriate test processes are specified [11]. A satellite's certification test verifies that each of the satellite parts and systems is operational and sustainable at launch in the environment of space during its lifespan. Vibration, electromagnetic and thermal tests are among the checks that may be necessary. Moreover, the construction of a base station capable of communicating with the satellite is critical. IST is working to build and enhance the engineering and maintenance infrastructure needed for the ICUBE-N project. Most of the laboratory equipment will be provided by IST. However, other universities and organizations' assistance and testing resources would be used as well.

Ground Station: As part of its space development effort, IST constructed a spacecraft ground station during the development of ICUBE-1. The same ground station would be upgraded to match the needs of ICUBE-N. The ground station is capable of independently getting remote sensing data. With independent Yagi-Uda cross antennas for both lateral and vertical orientation, the base station can send and accept data in the VHF and UHF frequencies. The image of the ground station is shown in Figure 7.



Figure 7 – Ground Station at IST

For receiving S-Band transmissions, a tiny dish is also installed. The alignment of antennas is controlled through computerized software by rotor assembly. A coaxial cable producing 100W of electricity connects the satellite ground

station transceiver to the antennas. It was created specifically for satellite communications. To encode, decode, and packetize digital data, many TNCs are linked to the transceiver. The ground station can follow spacecraft autonomously.

Clean Room: Satellites are built in a clean room to minimize dirt and surface dust, particularly on parts like solar panels. The spacecraft's endurance is improved because of this advancement procedure. IST already has a clean box that was used at the time of ICUBE-1 and is now working on constructing a class 10,000 cleanroom for ICUBE-N.

Thermal Vacuum: The configuration of a CubeSat's thermal subsystems and the trajectory in which it operates influence its thermal requirements. To guarantee the spacecraft's correct operation, all parts and subsystems must withstand high temperatures. The modules and the entire CubeSat will be placed in a TVC to assess and qualify them according to the specified thermal environment. The CubeSat is subjected to a thermal cycle and evaluated in accordance with the requirements [12].

Vibration Testing: ICUBE-N subsystems and elements must all endure the shipping and launch procedure. During its flight, the launch vehicle creates severe vibrations and accelerates by many g's. ICUBE-N structure must be able to withstand these severe vibrations and remain unaltered not just for the mission's success, but also for the health of the other cargo and the launch vehicle. Depending on the launch vehicle, vibrations might vary from 20Hz to 2000Hz.

Helmholtz Coil: ICUBE-N has an active attitude control system that comprises a reaction wheel and a number of sensors like IMU, GPS. The control of ADCS must be tested in a homogeneous magnetic field. Helmholtz coils can be used to create a homogeneous magnetic field. The Helmholtz coil facility is located at IST, and it will be used to evaluate the attitude control system.

Air Bearing: A spherical air bearing for testing the attitude control of ICUBE-N is in the development phase. The air bearing can test the three axes control, pitch, roll, and yaw, for attitude determination and control system module. The whole CubeSat is placed in the air bearing system and the ADCS is tested along all three axes. The spherical air bearing is frictionless, so it can mimic the control of roll, pitch, and yaw in the space environment.

Launch: Small satellites are usually launched alongside the major payload as a piggyback. Furthermore, the primary payload sets the orbital parameters, and the secondary payloads must adapt their missions to fit inside these limits. Due to increased involvement in the CubeSat program from international institutions, the CubeSat association has begun to coordinate CubeSat launches. The launch of CubeSats is also being coordinated by other parties. This lowers total launch and procedural costs, letting mission planners to focus only on satellite construction.

V. CONCLUSION

The initial design and subsystem analysis of ICUBE-N is presented in this paper. ICUBE-N is a 3U CubeSat and will carry scientific payloads. The scientific value intended to be gained from this research will serve as a foundation for the institute's subsequent space missions.

ICUBE-N design emphasizes the development of in-house modules for capacity building instead of the utilization of space-proven components and extensive COTS components. The in-house development includes the design and development of ICUBE-N structure, OBC, ADCS with active attitude control system and electrical power system module. The predicted environmental assessments, as well as the orbital attitude, have been accomplished. Using these simulation settings and analysis findings, an initial engineering model of ICUBE-N is being developed and will be integrated later in the flying model. Subsequent space missions will benefit from the in-house development of ICUBE-N.

ACKNOWLEDGMENT

The authors would like to thank the IST administration for all their support and the Higher Education Commission of Pakistan, and the National Centre for GIS and Space Applications for initiating and funding this project for the development of ICUBE-N, the national CubeSat of Pakistan.

REFERENCES

[1] J. Puig-Suari, C. Turner, and W. Ahlgren, "Development of the standard CubeSat deployer and a CubeSat class picosatellite," in *IEEE Aerospace Conference Proceedings*, 2001, vol. 1, pp. 1347–1353. doi: 10.1109/aero.2001.931726.

[2] CalPoly, "Cubesat design specification," *The CubeSat Program, California Polytechnic State …*, vol. 8651, no. June 2004, p. 22, 2009.

[3] M. R. Mughal *et al.*, "Aalto-1, multi-payload CubeSat: In-orbit results and lessons learned," *Acta Astronautica*, vol. 187, pp. 557–568, Oct. 2021, doi: 10.1016/j.actaastro.2020.11.044.

[4] FORESAIL collaboration *et al.*, "FORESAIL-1 cubesat mission to measure radiation belt losses and demonstrate de-orbiting," *Journal of Geophysical Research: Space Physics*, vol. 124, no. 7, pp. 5783–5799, May 2019, doi: 10.1029/2018JA026354.

[5] W. Lan, R. Munakata, R. Nugent, and D. Pignatelli, "Poly Picosatellite Orbital Deployer Mk III Rev. E User Guide," *California Polytechnic State University T*, vol. The CubeSa, pp. 1–21, 2014.

[6] R. Mahmood, K. Khurshid, A. Zafar, and Q. ul Islam, "ICUBE-1: First Step towards Developing an Experimental Pico-satellite at Institute of Space Technology," *Journal of Space Technology*, vol. 1, no. 1, pp. 5–10, 2011.

[7] R. Mahmood, K. Khurshid, and Q. Ul Islam, "Institute of Space Technology CubeSat: ICUBE-1 subsystem analysis and design," *IEEE Aerospace Conference Proceedings*, 2011, doi: 10.1109/AERO.2011.5747229.

[8] "ECSS-E-ST-32-08C – Materials | European Cooperation for Space Standardization." https://ecss.nl/standard/ecss-e-st-32-08c-materials/ (accessed Sep. 10, 2021).

[9] PC/104 Embedded Consortium, "PC/104 Specification Version 2.6," 2008. Accessed: Sep. 10, 2021. [Online]. Available: www.pc104.org

[10] J. Bouwmeester, M. Langer, and E. Gill, "Survey on the implementation and reliability of CubeSat electrical bus interfaces," *CEAS Space Journal*, vol. 9, no. 2, pp. 163–173, 2017, doi: 10.1007/s12567-016-0138-0.

[11] J. Richard. Wertz and W. J. Larson, "The Space Mission Analysis and Design Process," in *Space Mission Analysis and Design*, Microcosm, 1991, pp. 1–18. doi: 10.1007/978-94-011-3794-2_1.

[12] DNEPR, "Safety Compliance Requirements," no. August 2004, pp. 2–4, 2004.

Design and Development of a Portable Dish Antenna for SATCOM Man-Pack Terminal

Shujaat Hussain
College of Aeronautical Engineering, NUST
Risalpur, Pakistan
shujaatkhan784@gmail.com

Awais Munawar Qureshi
College of Aeronautical Engineering, NUST
Risalpur, Pakistan
awaisqureshi80@cae.nust.edu.pk

Rizwana Kausar
College of Aeronautical Engineering, NUST
Risalpur, Pakistan
rkausar@cae.nust.edu.pk

Mohsin Javaid
Air University
Islamabad, Pakistan
mohsinjavaid87@gmail.com

***Abstract*— In this paper, design analysis of a portable dish antenna for Satellite Communication (SATCOM) application has been presented. SATCOM is of great significance as it can provide coverage over entire globe. RF signals in Ku-band are transmitted over longer ranges after reflection by a parabolic dish antenna. These signals are utilized to send and receive information from remote areas where other communication technologies may fail. The high-gain and high-efficiency offered by a parabolic dish antenna make it suitable for SATCOM, Telecommunication, broadcast and reception applications. However, the procurement of a customized parabolic dish antenna is expensive for developing countries. This paper focuses on the development of a low-cost parabolic dish antenna for SATCOM Man-Pack terminal. The design and construction of a parabolic dish antenna used to intercept RF signals from satellite have been discussed in detail. The proposed design approach offers a number of advantages such as low complexity, high gain and cost-effectiveness. Based on our proposed approach, parabolic dish antenna can be fabricated in a time efficient manner using easily available materials and local resources. The simulation results validate the high-efficiency and high-gain characteristics of our proposed parabolic dish antenna design. A link budget analysis (uplink and downlink) has also been conducted to investigate the atmosphere effects on RF signals propagation in the air. The attenuation factors include atmosphere clouds, gases, rain, noise temperature and beam spreading.**

***Keywords*— Block Up Converter, Intermediate Frequency, Local Oscillator, Low Noise Block, Portable Dish Antenna, Radio Frequency, SATCOM**

I. INTRODUCTION

Portable dish antenna plays a major role in telecommunication, television, military command and control, radio, computer communication and maritime navigation applications. This research is based on design and construction of a parabolic dish antenna for RF signals transmission and reception in Ku-band (12 to 18 GHz) with high gain. Portable dish antenna can provide a high gain in Ku-band and operate in exactly similar fashion as of optical telescope. The parabolic dish antenna can transmit and receive the RF signals to or from any desired location in a satellite orbit. This type of antenna comes in different sizes and shapes, and most commonly use to transmit and receive the satellite guided television signal. Its working principle is similar to that of a television antenna with the exception that it is intended to pick up the weak ultra-high frequency satellite signals. Thereafter, it transforms the signals frequency and passes them through the coaxial cable to the television. One of its main roles is to provide wide range of television signals to the consumers. [1].

II. LITERATURE REVIEW

Parabolic antenna consists of a parabolic reflector which is of curved shape design utilized to direct the radio signals. The most popular of parabolic reflector is the dish antenna or parabolic dish. Reflector antenna can provide extremely high gain at microwave frequencies (300 MHz to 300 GHz). In Ku-band (12 - 18 GHz), it can provide more than 30 dB gain. This high gain is only achievable if the antenna is properly designed and installed at proper angle towards the satellite. The other radiation characteristics (polarization, directivity, efficiency) of a reflector can be improved by properly designing the structural configuration The reflector of the parabolic dish antenna collects the radio waves from satellite and converges the beams of parallel waves at a spot called the focal point (foci). The Low Noise Block (LNB) placed at the focal point transforms the concentrated radio waves into required signal level and shape. After conversion, the signals are forwarded to the receiver circuitry of SATCOM for postprocessing [2]. The diagram of a portable dish antenna is shown in Fig. 1

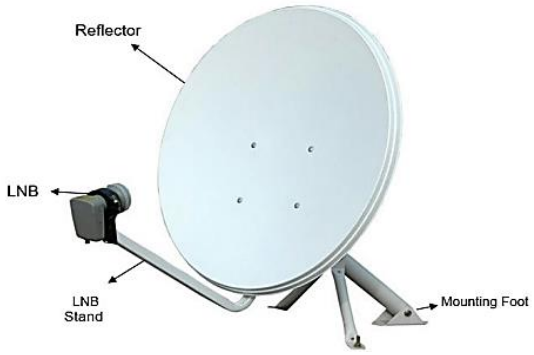


Fig. 1. Portable dish antenna

A. Portable Antenna

Parabolic dish antenna has a transducer that is capable of transmitting and receiving the electromagnetic (EM) waves. The transmitter side transforms the electric current into EM waves while the receiver side converts the EM waves into electrical current. Dish antenna is a type of unidirectional antennas as it can efficiently radiate or receive radio waves in a particular direction. The designing of parabolic dish antenna is a function of its need to the society as compared to other types of antennas and it is the best selection when it comes to the reception of satellite signals. Moreover, parabolic dish antenna is known for its high gain and fast data communication as it can reflect the radio and communication signals very efficiently. EM waves due to their shorter

wavelength require a reasonable small size reflector that is more effective at both the transmitter and receiver end.

Usually, a parabolic dish antenna comprises of a parabolic reflector along with a small antenna. The reflector is made up of metallic material curved into a parabolic shape and then rotated into circular shape with proper diameter. The curving is in such a way that the light source produces a light beam parallel and aligned with the curving axis. The small antenna is placed at the foci of parabolic reflector in order to have better transmission and reception of radio waves through coaxial cable or wave guide. The gain of a portable dish antenna can be improved to a greater extent with proper designing and precise fabrication [3].

B. Materials for Dish Refelector

The most prominent aspect in achieving the stable gain of parabolic dish antenna is the selection of proper material. As the demand for better performance increases for radio waves, the selection of appropriate materials becomes more vital. A suitable material gives higher structure stability to the antenna and provides a better support. In Table I, Aluminium, Steel and Carbon Fibre have been compared based on the price, density, Young's modulus, specific modulus, thermal expansion and heat conduction properties of each material. Based on the availability and cost effectiveness, the Aluminium material has been selected for reflector design.

TABLE I. MATERIAL SELECTION

Properties	Aluminium	Steel	Carbon Fibre
Price per kg in USD	1.79	1.59 - 1.79	27 - 51
Density	2,710	8,050	1,800
Young's Modulus	69	200	90.5 - 190
Specific Modulus (Mm^2/s^2)	26	25	56 - 120
Thermal Expansion (in/F)	13	07	02
Heat Conduction (W/mK)	210	50	5 - 7

C. Dish Antenna Design

The portable dish antenna works in the same way as a reflecting optical telescope. The microwave (MW) signals arriving on parallel paths from distant source, like satellite in our case, are reflected by the reflector to the focal point. As the curve is parabolic, all rays are meet at one focal point. Some difficulties are faced in real-life dish antennas design such as the placement of LNB for receiving MW beams and BUC for transmitting radio signals. The main difficulty is to find the focus point position such that maximum energy may be collected from the receiving signals, transmitted by the satellite, as shown in the Fig. 2 [4].

D. Antenna Feed

Dish antenna reflector consists of a radiating element, BUC or LNB, which acts as a feed system for the antenna. It is placed at the focal point of the parabolic reflecting surface. The energy from the BUC or LNB is focused in such a way that dish antenna transmits or receives electromagnetic signals with minimum attenuation.

E. Low Noise Block

Low Noise Block (LNB) is utilized for the reception of satellite signals (downlink). It consists of a low noise amplifier, a frequency mixer, a local oscillator, band pass filters and an intermediate frequency amplifier. LNB collects the signals in form of microwaves from the satellite as received by the dish. Thereafter, it amplifies the received signals and converts into intermediate frequency signals and forwards to indoor receiver through transmission cable after amplification. The block diagram of LNB is shown in Fig. 3. It comprises an input waveguide, followed by the receiver circuitry. There is a vertical pin at the input waveguide that extracts the electrical current with vertical polarization. The bandpass filter allows only the required MW frequency range and attenuates all other unnecessary frequencies. The low noise amplifier amplifies the signal and feeds to the mixer where it is combined with the local oscillator. Finally, the intermediate signal in Ku-band is filtered and amplified before transmission through cable [5].

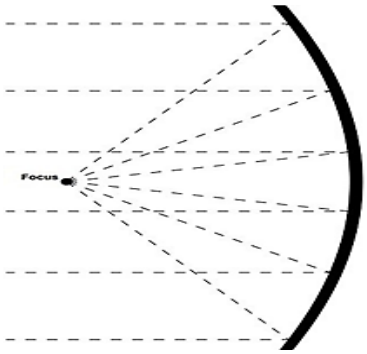


Fig. 2. Operating principle of portable dish antenna

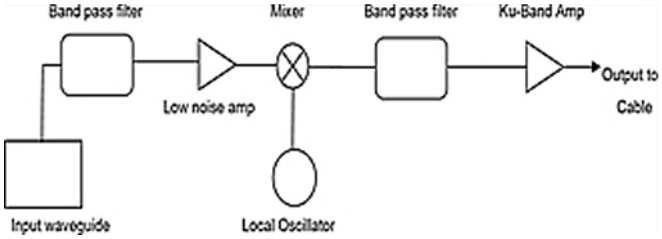


Fig. 3. LNB block diagram

F. Block Up-converter

Block Up-converter (BUC) is utilized for the transmission of satellite signals (uplink). The main function of BUC is to convert a band of lower frequencies into higher frequencies. It is used in combination with LNB. Since the BUC steps up the lower frequencies to higher, it is installed at the transmission side. Whereas LNB steps down the higher frequencies to lower, is mounted at the receiver side.

G. Aperture Gain and Efficiency

The aperture gain of dish antenna is calculated using (1). The efficiency for well-designed dish antenna is often of the order 0.6 – 0.7 [4].

$$G = \varepsilon \frac{4\pi}{\lambda^2} A = \varepsilon \frac{(\pi \mathrm{D})^2}{\lambda^2} \tag{1}$$

H. Satellite Segments

In a satellite communication framework, different tasks are performed. Among these, the principle tasks are circle controlling, elevation of satellite, and checking and controlling of different subsystems. It comprises of two main portions, namely; the Space Segment Subsystem and the Ground Segment Subsystem.

1) *Space Segment Subsystem:* It comprises of following:-
   a) Satellite
   b) Transponder
   c) Tracking, Telemetry and Control System (TT&C)

The satellite is a body that rotates in a specific orbit around the other body. The communication satellite system acts a receiver for receiving the radio waves in the space. The criteria selected for satellite signals transmission and reception is that the frequency range is kept different for both uplink and the downlink so as to avoid interference between the transmitted and received signals. The transponder has two functionalities, the frequency up-conversion of signals at the receiver side and translation of received signals.

2) Ground Segment Subsystem: The ground station provides a communication link to the satellite. The ground segment comprises two subsystems; the receiving earth station and the transmitting earth station.

III. Methodology

In case of satellite communication system, the most important factor to be taken into consideration is the satellite antenna. The better choice of the satellite antenna leads towards an interference free communication between the satellite space stations and the earth units, with high efficiency and the least possible interference of the noise. Therefore, for a feasible communication, there must be a well-defined set of parameters for antenna design. For efficient antenna design, various techniques are adopted such as frequency reuse configuration, multiple beams amount and the circular polarization. The dish antenna model that has been proposed here is efficient enough that fulfills all necessary requirements for a better, noise-free and effective communication between the space stations and the ground units.

A. Design of Offset Reflector Antenna

The designed antenna operates in Ku-band of microwave region. In this band, the frequency range is 10.9 – 12.75 GHz for downlink and 13.75 – 14.5 GHz for the uplink. The commercial offset dishes used for satellite reception at homes generally have major axis dimension of 90 cm. It is designed with an offset parabolic reflector antenna of dimensions 90 cm x 82 cm. This particular design enables to track a number of satellites with low Equivalent Isotropic Radiated Power (EIRP) values or footprints. The our design of a reflector dish antenna with horn antenna at offset point is shown in Fig. 4.

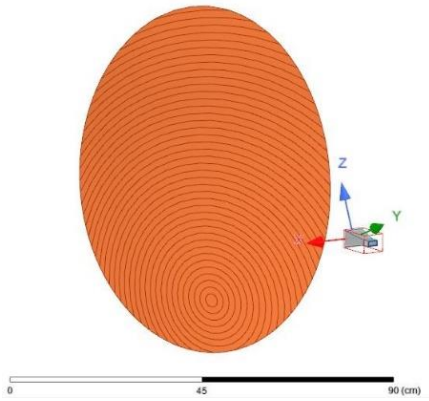


Fig. 4. Reflector design with horn antenna

B. Calculation for Offset Dish Antenna Design

Based on the theoretical and practical studies, following calculations have been made. The tilt Angle is defined as the arcsine of the ratio of short axis to the long axis (2).

$$\theta = arccosine\frac{shortaxis}{longaxis} \tag{2}$$

$$\theta = arccosine\frac{82}{90}$$

$$\theta = 24.34^{\circ}$$

For effective reception of signals in Ku-band, the focal length (f) and diameter (D) ratio must lie between 0.65 – 0.75. The '*f*' value has been taken as 0.70 times the optimum value of '*D*'. Since the value of *D* = 90 cm, the '*f*' value comes out to be 63 cm. This is the focal point where all incoming satellite signals are focused to LNB. The depth of antenna is the deepest point of the dish and has been calculated using (3).

$$depth(d) = \frac{D^2}{16f} \tag{3}$$

$$depth(d) = \frac{90^2}{16(63)}$$

$$depth(d) = 8.03cm$$

IV. Antenna Characterisation Parameters

Following are the simulation results of important antenna characterization parameters that have been considered while designing and developing a parabolic dish antenna.

A. Radiation Pattern

This is the best quantitative description of an antenna that defines how much energy it can concentrate in one direction with reference to other directions. The radiation pattern also informs about the bore-sight maximum gain in a particular direction which in our design is equal to 38.8 dB. The 3D radiation pattern of designed dish antenna is shown in Fig. 5

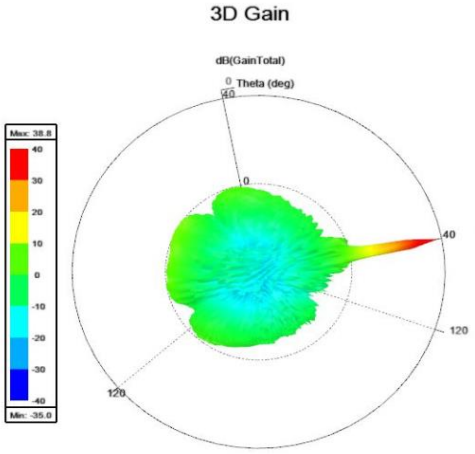


Fig. 5. 3D radiation pattern of designed dish antenna

B. Polar Plot

This plot displays the magnitude and specific response in a particular direction. In this plot, the radiation pattern is taken in a particular plane. For dish antenna, it is on 90-degree angle as shown in Fig. 6. Polar plots provide us the information about Sidelobe Level (SLL) which indicates how large or small are side lobes with reference to main lobe in the radiation pattern of portable dish antenna. Usually, it is the difference between the maximum level at a bore sight of dish antenna and the maximum value of side lobe, expressed in dB.

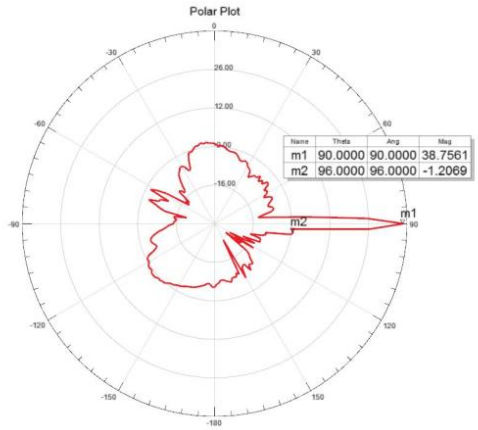


Fig. 6. Side lobe level of designed dish antenna

$$SidelobeLevel\ (SLL) = Max\ Side\ lobe\ Value - Max\ Gain$$
$$SidelobeLevel\ (SLL) = -1{:}2069 - 38{:}7561 = -39{:}963dB$$

C. Half Power Beamwidth (HPBW)

The polar plot can be represented as a 2D plot. The radiation pattern along vertical and horizontal axis are shown in Fig. 7 and 8, respectively. The elevation HPBW (-3 dB) along elevation angle is given in Fig. 7. The azimuth (-3 dB) HPBW along azimuth angle is given in Fig. 8. According to the required specification, the -3 dB HPBW is expected to be equal or less than 1.58 degree. In our design, its value is 0.93 degree along elevation and 1.1 degree along azimuth.

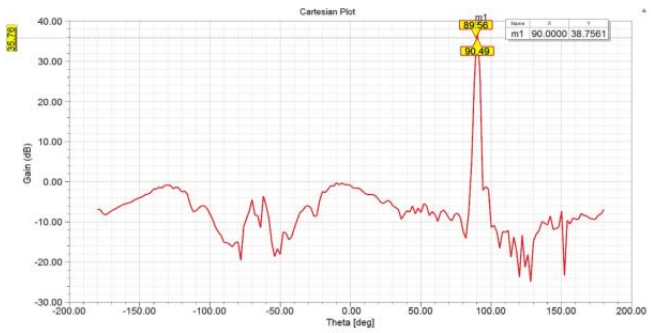


Fig. 7. Elevation (-3 dB) beamwidth of designed dish antenna

$$HPBW = 90.49 - 89.56 = 0.93 \text{ degree}$$

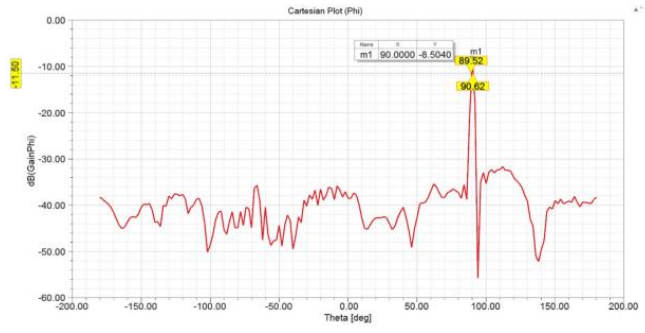


Fig. 8. Azimuth (-3 dB) beamwidth of designed dish antenna

$$HPBW = 90.62 - 89.52 = 1.1 \text{ degree}$$

D. Reflection Coefficient

Reflection Coefficient (S_{11}) is the ratio of reflected to incident wave signal. This parameter explains the reflection of waves due to mediums impedance mismatch. According to given requirements, the S_{11} value should be less than -19 dB for both uplink and downlink link frequency range. The reflection co-efficient of our designed dish antenna is plotted in Fig. 9. It is highlighted that S_{11} value of our antenna is less than -19 dB for both uplink and downlink frequency range.

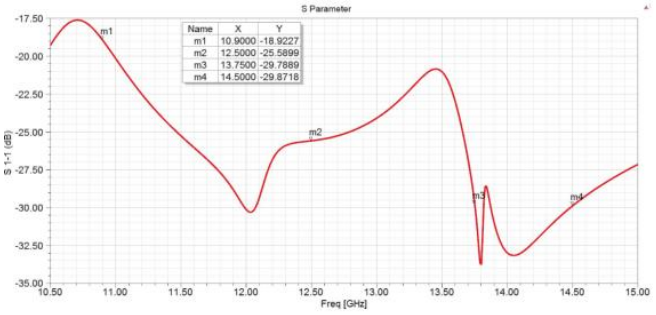


Fig. 9. Reflection coefficient (S_{11}) of designed dish antenna

E. Voltage Standing Wave Ratio (VSWR)

VSWR is the ratio of maximum to the minimum voltage value in a standing wave pattern along the transmission line. According to the given requirements, VSWR parameter value should be less than 1.25 for both uplink and downlink link frequency range. The VSWR of our designed dish antenna is plotted in Fig. 10. It is highlighted that VSWR value of our antenna is less than 1.25 for both uplink and downlink frequency range.

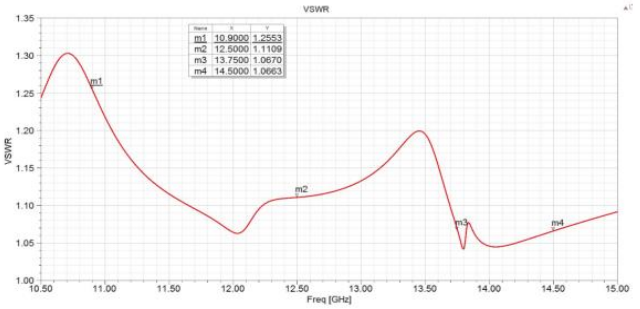


Fig. 10. VSWR of designed dish antenna

V. Link Budget Analysis

A. Link Budget

The link budget is the summation of all gains and losses from the ground segment to the satellite segment. There are two types of link budget.

1) Uplink

In uplink of a satellite circuit, the earth station is transmitting the signal and the satellite is receiving it.

2) Downlink

In downlink of a satellite circuit, the satellite transmits the signals and the earth station receives it.

B. Equivalent Isotropic Radiated Power

The important factor in the link budget analysis is the concept of Equivalent Isotropic Radiated Power (EIRP). It is the sum of transmitted power and the gain of antenna (4), where P_t is the transmitted power in dBW and G_t is the transmitted antenna gain in dB.

$$EIRP = P_t + G_t \quad (4)$$

C. Transmission Losses

Basically, EIRP is the concept of power input to a system at one end and calculating the power at other end while taking into consideration the transmission lines losses as the signal proceeds. Fig. 11 shows the PAKSAT-1R satellite EIRP level.



Fig. 11. PAKSAT-1R satellite EIRP

1) Free-space transmission: The first thing in calculating the losses is the estimation of losses due to the spreading of signals in free-space. The power delivered to a receiver is given as (5), where P_R is the received power in dBW and G_R is the receiver antenna gain in dB.

$$P_R = \frac{EIRP G_R \lambda^2}{4\pi r^2}$$

$$P_R = [EIRP] + [G_R] - 10log\,(4\pi r/\lambda)^2 \quad (5)$$

The signal received at the receiver side can be expressed as the sum of EIRP, the receiver antenna gain and the Free-Space Loss (FSL) as (6), where FSL component is defined as (7) in dB.

$$P_R = [EIRP] + [G_R] - 10log\,(4\pi r/\lambda)^2$$

$$P_R = [EIRP] + [G_R] - [FSL] \quad (6)$$

$$FSL = 10log\,(4\pi r/\lambda)^2 \quad (7)$$

Generally, the wavelength is known instead of frequency and the frequency can be determined using equation (8), where 'c' represents the speed of light and is constant, frequency (*f*) is in GHz and the distance is in Km.

$$\lambda = \frac{c}{f} \quad (8)$$

2) Feeder losses: The losses which are suffered between the antenna and receiver path are known as the feeder losses. Such losses arise from the filters, couplers and the waveguides that connect the receiver antenna to high power amplifier.

3) Antenna misalignment losses: For an ideal case, once the link has been established, the earth and the space station are aligned in such a way that the gain is maximum. In reality, there arise off-axis losses due to misalignment between the satellite and earth. The off-axis losses at the space station are considerable and are taken into account while designing the antennas and the link operations. However, the earth off-axis losses are minimum and are usually of the order of tens of dB.

D. System Noise

The noise power can be determined from the thermal noise sources and is presented as (9), where P_N is the noise power in dBW, T_N is the noise temperature, B_N is the noise bandwidth and *k* is the Boltzmann constant. The noise increases with the increase in temperature of physical surrounding but not always equal to one.

$$P_N = kT_NB_N \quad (9)$$

E. Carrier-To-Noise Ratio

In order to evaluate the performance and efficiency of a communication link, Carrier to Noise Ratio (CNR) is utilized. It is defined as the ratio of carrier power to the noise power at the receiver side (10) and (11). It is the most important parameter in determining the receiving system performance.

$$\frac{C}{N} = P_R - P_N \quad (10)$$

$$\frac{C}{N} = [EIRP] + [G_R/T_S] - [LOSSES] - [B_N] - [k] \quad (11)$$

F. Satellite and Ground Segment Specification

The satellite and ground segment parameters are presented in Table II.

TABLE II. SATELLITE AND GROUND SEGMENT SPECIFICATIONS

Parameters	Specifications
Satellite	PAKSAT-1R
Reflector Diameter	0.6-0.9 m
Transmitter/Receiver Frequency	10.9-14.5 GHz
Data Bit Rate	10 Mbps
Symbol Rate (QPSK)	5 MPs
Bandwidth	6.25 MHz
Transponder Bandwidth	72 MHz
EIRP of Satellite	53 dB
G/T	5 dB

G. Data Bit Rate and Symbol Rate

It measures the rate at which number of bits are transmitted per second. It is also specified by the term baud rate which is the transmission of the number of the symbols per unit time.

1) Quadrature Phase-Shift Keying: This model converts the binary data into two-bit symbol which is further utilized to modulate the carrier signal (12). Against the binary states of zeros and ones, there are four possible states for a symbol. QPSK and 8PSK are used for high speed communications. QPSK modulation is selected to compare the required CNR value with the actual CNR.

$$Symbol\ Rate\ (Rs) = (Data\ bitrate)/2 \quad (12)$$

$$= (10)/2 = 5\ Msps$$

The operating bandwidth can be determined from the symbol rate as (13), where alpha is the roll-off factor which is often around the 0.25 value and *Rs* is 5 Msps. Under these assumptions, it comes out to be 6.25 MHz. According to Table III, the minimum value of CNR for QPSK is 6.42 dB, if 9 bits out of 10 are used. The CNR value must exceed from 6.42 dB for availability.

$$Bandwidth = Rs\,(1 + \alpha) \quad (13)$$

TABLE III. DVB-RCS-S2 ADAPTIVE MODEM CHARACTERISTICS

ETSI EN 302307 DVB S2 Theoretical Performance for Target ModCOD

MODulation	CODing Rate	Es/No	Sym rate	BW (nyq)	C/No	C/N	Spectral Efficiency	Bits/ symbol	Data Rate	Ebi/No	Eb/No	Gross Bit Rate	Info bits	code bits	"overhead"
		dB	Msym/sec	MHz	dBHz	dB	info bit/symbol		Mbps	dB	dB	Mbit/sec	Mbit/sec	Mbit/Sec	
QPSK	1/4	-2.35	41.67	50.00	73.85	-3.14	0.490243	2	20.4268	0.746	-5.360	83.33	20.83	62.50	1.951%
QPSK	1/3	-1.24	41.67	50.00	74.96	-2.03	0.656448	2	27.3520	0.588	-4.250	83.33	27.78	55.56	1.533%
QPSK	2/5	-0.3	41.67	50.00	75.90	-1.09	0.789412	2	32.8922	0.727	-3.310	83.33	33.33	50.00	1.324%
QPSK	1/2	1.00	41.67	50.00	77.20	0.21	0.988858	2	41.2024	1.049	-2.010	83.33	41.67	41.67	1.114%
QPSK	3/5	2.23	41.67	50.00	78.43	1.44	1.188304	2	49.5127	1.481	-0.780	83.33	50.00	33.33	0.979%
QPSK	2/3	3.10	41.67	50.00	79.30	2.31	1.322253	2	55.0939	1.887	0.090	83.33	55.56	27.78	0.831%
QPSK	3/4	4.03	41.67	50.00	80.23	3.24	1.487473	2	61.9780	2.306	1.020	83.33	62.50	20.83	0.836%
QPSK	4/5	4.68	41.67	50.00	80.88	3.89	1.587196	2	66.1332	2.674	1.670	83.33	66.67	16.67	0.800%
QPSK	5/6	5.18	41.67	50.00	81.38	4.39	1.654663	2	68.9443	2.993	2.170	83.33	69.44	13.89	0.720%
8PSK	3/5	5.50	41.67	50.00	81.70	4.71	1.779910	3	74.1629	2.996	0.729	125.00	75.00	50.00	1.116%
QPSK	8/9	6.20	41.67	50.00	82.40	5.41	1.766451	2	73.6021	3.729	3.190	83.33	74.07	9.26	0.637%
QPSK	9/10	6.42	41.67	50.00	82.62	5.63	1.788612	2	74.5255	3.895	3.410	83.33	75.00	8.33	0.633%
8PSK	2/3	6.62	41.67	50.00	82.82	5.83	1.980636	3	82.5265	3.652	1.849	125.00	83.33	41.67	0.968%
8PSK	3/4	7.91	41.67	50.00	84.11	7.12	2.228124	3	92.8385	4.431	3.139	125.00	93.75	31.25	0.972%
16APSK	2/3	8.97	41.67	50.00	85.17	8.18	2.637201	4	109.8834	4.759	2.949	166.67	111.11	55.56	1.10%
8PSK	5/6	9.35	41.67	50.00	85.55	8.56	2.478562	3	103.2734	5.408	4.579	125.00	104.17	20.83	0.858%
16APSK	3/4	10.21	41.67	50.00	86.41	9.42	2.966728	4	123.6137	5.487	4.189	166.67	125.00	41.67	1.11%
8PSK	8/9	10.69	41.67	50.00	86.89	9.90	2.646012	3	110.2505	6.464	5.919	125.00	111.11	13.89	0.77%
8PSK	9/10	10.98	41.67	50.00	87.18	10.19	2.679207	3	111.6336	6.700	6.209	125.00	112.50	12.50	0.77%
16APSK	4/5	11.03	41.67	50.00	87.23	10.24	3.165623	4	131.9010	6.025	5.009	166.67	133.33	33.33	1.07%
16APSK	5/6	11.61	41.67	50.00	87.81	10.82	3.300184	4	137.5077	6.425	5.589	166.67	138.89	27.78	0.99%
32APSK	3/4	12.73	41.67	50.00	88.93	11.94	3.703295	5	154.3040	7.044	5.740	208.33	156.25	52.08	1.25%
16APSK	8/9	12.89	41.67	50.00	89.09	12.10	3.523143	4	146.7976	7.421	6.869	166.67	148.15	18.52	0.91%
16APSK	9/10	13.13	41.67	50.00	89.33	12.34	3.567342	4	148.6393	7.607	7.109	166.67	150.00	16.67	0.91%
32APSK	4/5	13.64	41.67	50.00	89.84	12.85	3.951571	5	164.6488	7.672	6.650	208.33	166.67	41.67	1.21%
32APSK	5/6	14.28	41.67	50.00	90.48	13.49	4.119540	5	171.6475	8.132	7.290	208.33	173.61	34.72	1.13%
32APSK	8/9	15.69	41.67	50.00	91.89	14.90	4.397854	5	183.2439	9.258	8.700	208.33	185.19	23.15	1.05%
32APSK	9/10	16.05	41.67	50.00	92.25	15.26	4.453027	5	185.5428	9.563	9.060	208.33	187.50	20.83	1.04%

VI. Rain Attenuation

In ITU Radiocommunication (ITU-R) model, the rain is related to the input as rain intensity with 0.01% probability level [6-8]. The link budget analysis for PAKSAT-1R in Ku band has been presented in this paper. Rain attenuation for Ku-bands has been calculated. Here, the location of earth station for Islamabad, Pakistan is (33.7167° N, 73.0667° E).

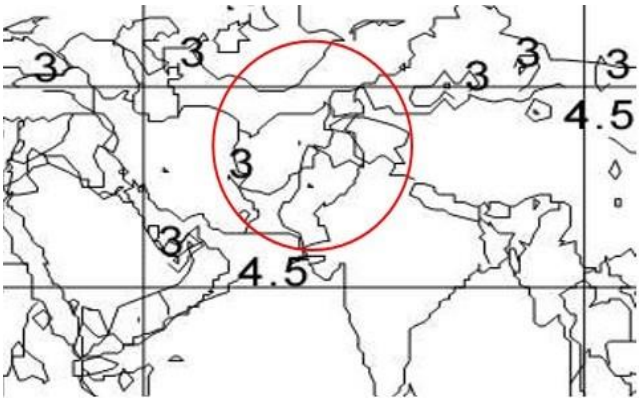


Fig. 12. Pakistan map from the satellite

The elevation angle for the dish antenna is 35.9°, latitude is 33.68° and the Rain Rate for 0.01% of average year, is taken from the Table IV. As per the "ITU" the whole Pakistan is classified into a K-rain region, with having almost 148 mm/hr intensity of the rain. The rain is varied from one city to another city in Pakistan due to which the different cities is classified into different zones. Islamabad is labelled as L-zone with rain amount of 60mm per hour, whereas the cities like Peshawar and Islamabad is identified as K-region with rain intensity of about 42mm per hour.

In order to have a complete availability that is about 99.99 percent for the required length, there is only one requirement of the microwave hop. But if the link is designed with wrong assumptions of the rain, then in such conditions there is need of more than one hop to achieve the objectives.

TABLE IV. ITU Climatic Zones

S. no	percent age of time ⟶ rain regions	1	0.3	0.1	0.03	0.01	0.003	0.001
1	*A*	0.12	0.8	2	5	8	14	22
2	*B*	0.5	2	3	6	12	21	32
3	*C*	0.7	2.8	5	9	15	26	42
4	*D*	2.1	4.5	8	13	19	29	42
5	*E*	0.6	2.4	6	12	22	41	70
6	*F*	1.7	4.5	8	15	28	54	78
7	*G*	3	7	12	20	30	45	65
8	*H*	2	4	10	18	32	55	83
9	*J*	8	13	20	28	35	45	55
10	**K**	**1.5**	**4.2**	**12**	**23**	**42**	**70**	**100**
11	*L*	2	7	15	33	60	105	150
12	*M*	4	11	22	40	63	95	120
13	*N*	5	15	35	65	95	140	180
14	*P*	12	34	65	105	145	200	250
15	*Q*	24	49	72	96	115	142	170

A. Impact of Rain on Wireless Communication

Precipitation causes serious distortion to amplitude level of received signals above 10 GHz frequency. This debasement causes the recurrence of radio waves. Therefore, rainfall is one of the main causes of degradations in received signals. The degradation increases with the increase in radio frequency. As the rain increases the attenuations of desired signal increases. The main factors that contribute to the attenuation are the size of rain drop and the signal frequency. The larger rain sizes increase the scattering and absorption of radio signals. In any kind of communication, either the satellite or terrestrial, the main component is prediction of rain. The mathematical approximation of attenuation due to rain is given as (14), where '*k*' is the constant (k_H or k_V) known as the rain coefficient and α is the rain drop size / shape, and is frequency dependent. Their values can be calculated using (15) and (16).

$$a_r = k\,(R0.01)\,\alpha \tag{14}$$

$$\log_{10} k = \sum_{j=1}^{4}\left(a_j \exp\left[-\left(\frac{\log_{10} f - b_j}{c_j}\right)^2\right]\right) + m_k \log_{10} f + c_k \tag{15}$$

$$\alpha = \sum_{j=1}^{5}\left(a_j \exp\left[-\left(\frac{\log_{10} f - b_j}{c_j}\right)^2\right]\right) + m_\alpha \log_{10} f + c_\alpha \tag{16}$$

The suggested values for all the constants are mentioned in Table V to VIII. Values for coefficient k_H for horizontal polarization are given in Table V and values for coefficient k_V for vertical polarization are given in Table VI. Table VII provides the values for coefficient α_H for horizontal polarization and Table VIII gives the values for coefficient α_V for vertical polarization [9-11].

TABLE V. Coefficient for K_H

j	a_j	b_j	c_j	m_k	c_k
1	–5.33980	–0.10008	1.13098	–0.18961	0.71147
2	–0.35351	1.26970	0.45400		
3	–0.23789	0.86036	0.15354		
4	–0.94158	0.64552	0.16817		

TABLE VI. Coefficient for K_V

j	a_j	b_j	c_j	m_k	c_k
1	–3.80595	0.56934	0.81061	–0.16398	0.63297
2	–3.44965	–0.22911	0.51059		
3	–0.39902	0.73042	0.11899		
4	0.50167	1.07319	0.27195		

TABLE VII. COEFFICIENT FOR α_H

j	a_j	b_j	c_j	m_α	c_α
1	–0.14318	1.82442	–0.55187	0.67849	–1.95537
2	0.29591	0.77564	0.19822		
3	0.32177	0.63773	0.13164		
4	–5.37610	–0.96230	1.47828		
5	16.1721	–3.29980	3.43990		

TABLE VIII. COEFFICIENT FOR α_V

j	a_j	b_j	c_j	m_α	c_α
1	–0.07771	2.33840	–0.76284	–0.053739	0.83433
2	0.56727	0.95545	0.54039		
3	–0.20238	1.14520	0.26809		
4	–48.2991	0.791669	0.116226		
5	48.5833	0.791459	0.116479		

Using coefficient values provided in Table V to VIII, Eq (15) and (16) gives the value of k =0.622 and α =0.2937. After putting these values in (14), the value of specific attenuation is calculated as 0.014391*dB/km*. Thereafter, rain attenuation using Slant Range = 40.15 km and Elevation Angle = 35.9° has been calculated as 0.9855*dB* (18).

$$A_t = a_r\,(L_S); \quad L_s = Slant\ Range/(sin(\theta))$$

$$A_t = 0.014391(40.15/sin\ (35.9))$$

$$A_t = 0.9855dB \tag{18}$$

VII. KU-BAND LINK BUDGET ANALYSIS FOR SATCOM

A. Uplink Budget Analysis

The uplink budget analyses have been presented in Table IX. It provides different parameters values for both the clear sky and rain conditions.

TABLE IX. UPLINK BUDGET ANALYSIS FOR SATCOM IN KU-BAND

Parameters	Clear Sky	Rain	Units
Earth Station EIRP	74.8	74.8	dB
Satellite G/T	05	05	dB/K
Path Loss	205.51	205.51	dB
Rain Attenuation	00	0.9855	dB
Cloud Attenuation	00	01	dB
Gaseous Attenuation	01	01	dB
Transmitter Waveguide Loss	0.4	0.4	dB
Atmospheric Loss	02	02	dB
Polarization Loss	0.1	0.1	dB
Additional Losses	0.6	0.6	dB
Ionospheric losses	0.7	0.7	dB
Pointing loss	0.5	0.5	dB
Feed Loss	0.5	0.5	dB
Total Losses (Lt)	211.81	213.795	dB
Boltzmann Constant	-228.6	-228.6	dB
Noise Bandwidth	67.95	67.95	dB
CNR	28.64	26.6515	dB

B. Downlink Budget Analysis

The downlink budget analysis is directly dependent upon the (G/T) value of receiver. The total temperature of ground segment can be calculated from (19), where T_a is the antenna noise temperature and T_c is the composite noise temperature of the receiver equal to 10 K. T_a is calculated using (20), where T_m is the medium temperature and according to ITU its value ranges from 270 K to 290 K. By putting the values of T_m, T_c and attenuation, we found the value of T_a equal to 66.844 K.

$$T_S = T_a + T_c \tag{19}$$

$$T_a = T_m\,(1 - 10)^{-A/10} + T_c^{-A/10} \tag{20}$$

We have performed the calculations for series NJR2835U/36U/37U/39U of LNB. The Noise Factor (NF) value of this series ranges from 0.8 to 1 dB. For our convenience, we have taken the mean value of NF = 0.9 dB. Using Table X, we have found the corresponding temperature value of LNB at NF = 0.9 dB as 66.78 K [11]. According to ITU-R, the temperature of clear sky is 30 K and total losses temperature is 35.39 K. Therefore, the antenna clear sky temperature is the sum of clear sky temperature and the LNB temperature (21).

$$T = T_{CS} + T_{LNB} \tag{21}$$

$$T = (30 + 35.39) + 66.78 = 132.17\ K$$

$$T_{dB} = 21.211dB$$

TABLE X. NOISE FACTOR AND TEMPERATURE

NF	F	Te
dB		Deg K
0.1	1.02	6.75
0.2	1.05	13.67
0.3	1.07	20.74
0.4	1.10	27.98
0.5	1.12	35.39
0.6	1.15	42.96
0.7	1.17	50.72
0.8	1.20	58.66
0.9	1.23	66.78
1	1.26	75.09
1.1	1.29	83.59
1.2	1.32	92.29

During rain, the value of temperature increases and we have to add the clear sky antenna temperature to the rain temperature (22).

$$T_S = T_{CS} + T_{Rain} \tag{22}$$

$$T_S = 132.17 + 66.844 = 199.014K$$

$$T_{SdB} = 22.986\ dB$$

Since, the temperature of antenna for clear sky and during rain is different, it will affect the value of G/T as following.

$$(G/T)_{clear\ sky} = 38.8 - 21.211$$

$$(G/T)_{clear\ sky} = 17.588\ dB$$

Moreover, the attenuation of radio signals also increases with rain. This results in temperature increase for scattering of communication signals. Subsequently, this affects the G/T factor too.

$$(G/T)_{Rain} = 38.8 - 22.988$$

$$(G/T)_{Rain} = 15.812dB$$

The downlink budget analyses have been presented in Table XI. It provides different parameters values for both the clear sky and rain conditions.

TABLE XI. DOWNLINK BUDGET ANALYSIS FOR SATCOM IN KU-BAND

Parameters	Clear Sky	Rain	Units
Satellite EIRP	53	53	dBw
Ground G/T	17.588	15.812	dB/K
Path Loss	204.87	204.87	dB
Rain Attenuation	00	0.9855	dB
Cloud Attenuation	00	01	dB
Gaseous Attenuation	01	01	dB
Transmitter Waveguide Loss	0.4	0.4	dB
“Atmospheric Loss”	02	02	dB
Polarization Loss	0.1	0.1	dB
Additional Losses	0.6	0.6	dB
Ionospheric losses	0.7	0.7	dB
Pointing loss	0.5	0.5	dB
“Feed Loss”	0.5	0.5	dB
Total Losses (Lt)	210.67	212.655	dB
Boltzmann Constant	-228.6	-228.6	dB
Noise Bandwidth	67.95	67.95	dB
Ground Stn. C/No(10Mbps)	20.568	16.8065	dB
Required C/No (QPSK)	6.42	6.42	dB
Link Margin	14.048	10.3865	dB

VIII. CONCLUSION

In this paper, we have presented the design analysis of a portable dish antenna for SATCOM man-pack terminal application. The designed parabolic dish antenna is composed of aluminum material with 90 x 82 cm size. It can be efficiently utilized for satellite signals transmission / reception in Ku-band. To achieve high gain, offset dish reflector type has been selected that offered more aperture efficiency than other types of portable dish reflector. A horn antenna for feed system of portable dish reflector has also been designed. A maximum gain of 38.8 dB in a particular direction towards the satellite has been successfully achieved. Space and ground segments of SATCOM have also been studied in-depth that helped in performing an accurate link budget analysis. The effect of various atmosphere conditions on RF signals propagation in the air has also been explained. For this purpose, ITU-R models have been efficiently utilized. The attenuation factor due to rain during uplink and downlink communication has been calculated to design an all-weather dish antenna. The CNR value validates that proposed design of portable dish antenna is feasible for SATCOM applications. It can be easily and time-efficiently constructed using available materials and local resources.

REFERENCES

[1] C. Onah, K. Arinzechukwu, and F. Elekwachi, “Designing, constructing and testing a 90 cm parabolic satellite dish using fiberglass material,” *Research & Reviews: Journal of Space Science & Technology*, vol. 2, no. 2, pp. 12–26, 2019.

[2] G. R. Adewale, “Design and construction of a cost-effective parabolic satellite dish using available local materials,” *International Journal of Advanced Materials Research*, 2019.

[3] B. J. Feder, “” taylor howard, 70, pioneer in satellite tv for the home”. new york time. retrieved 19 july 2014,” 15 November 2002.

[4] H. A. Syed Muhammad J. S Ammar N., “A survey paper on security issues in satellite communication network infrastructure,” October-November 2014.

[5] Mahmudul, HM and Sirajum, M. and Syed, N.S. and A.K.M.F.H., and Haque, Shahina and Tasnim, I.R., “Design and development of an lnb based dvb-s receiver,” *International Journal of Engineering and Technology (UAE)*, 2018.

[6] I. Abubakar, J. Din, and H. Y. Lam, “Disparities in the induced rain attenuation between beacon (narrowband) and broadband satellite links in tropical zones,” *Indonesian Journal of Electrical Engineering and Computer Science*, vol. 10, no. 2, pp. 687–695, 2018.

[7] X. Yang and Z. Lidong, “Research on rain attenuation for ka-band satellite communication system,” in *2008 ISECS International Colloquium on Computing, Communication, Control, and Management*, vol. 2. IEEE, 2008, pp. 412–415.

[8] J. S. Ojo, M. O. Ajewole, and S. K. Sarkar, “Rain rate and rain attenuation prediction for satellite communication in ku and ka bands over nigeria.” *Progress in Electromagnetics Research*, vol. 5, pp. 207–223, 2008.

[9] P. Series, “Propagation data and prediction methods required for the design of earth-space telecommunication systems,” *Recommendation ITU-R*, pp. 618–12, 2015.

[10] Z.-w. Zhao, M.-g. Zhang, and Z.-s. Wu, “Analytic specific attenuation model for rain for use in prediction methods,” *International Journal of Infrared and millimeter waves*, vol. 22, no. 1, pp. 113–120, 2001.

[11] M. Zubair, Z. Haider, S. A. Khan, and J. Nasir, “Atmospheric influences on satellite communications,” *Przeglad Electrotechnics*, vol. 87, no. 5, pp. 261–264, 2011.

Design and Simulation of Cost-efficient Reaction Wheel for 1U CubeSat

Pawan Kumar
Department of Space Science
Institute of Space Technology
Islamabad, Pakistan
pawan04@ist.edu.pk

Oscar Lionel
GNSS & Space Education Research Lab
National Center of GIS & Space Applications
Islamabad, Pakistan
lionel_astro@hotmail.com

***Abstract*— Rapid progress in CubeSat technology has made them feasible to be used for different scientific research purposes but the cost associated with different subsystem used in the CubeSat are relatively high which limits student researcher to limit their scope. The attitude control mechanism is an important aspect of a satellite, and for this purpose, this research presents the cost-effective development of a reaction wheel alongside with three-reaction wheels actuation model for 1U CubeSat. In the presented setup, the reaction wheel is developed using a commercial-off-the-shelf (CoTS) component, based upon hard drive disk (HDD). HDD based brushless DC motor and flywheel are utilized for this research. The simulation of the developed reaction wheel for 1U CubeSat is carried out in the Simulink environment using a three-wheel setup and PID based controller with space environment disturbance torques values as initial parameters. The output of the simulation presented the working and response of the purposed reaction wheel against the disturbance torques. The HDD based reaction wheel with one flywheel has potential to produce maximum torque of 37.6 $mN.m$.s at the angular momentum of 6200 rpm and has power consumption ratings from 0.4 watts to 0.7 watts and an operating temperature of -40o C to 75o C. The final design output confirms the use of HDD based components for reaction wheel development. Moreover, the overall cost associated with hardware is comparatively less than the commercially available systems.**

Keywords— Reaction wheel; Attitude Control; Disturbance Torques; Brushless DC Motor; 1U CubeSat, Simulink Model

I. INTRODUCTION

1U CubeSat comes in the category of miniaturized satellite with dimensions of 10 cm × 10 cm × 10 cm and with mass of 1.33 kg and are often developed for research purposes using COTS components[1]. Attitude system of satellite refers to the satellite orientation and position with respect to an object, mostly Earth and the control of this attitude has fundamental importance for payloads, which require orientation in correct direction[2]. Rotation of satellite around Earth subjects it to various kind of disturbance torques, which results in disorientation of satellite, and to counter the disturbances torques, active attitude control systems are employed[3] Advancement in CubeSat technology and its low cost has extended the extent of purposes for which it is being used where many of the missions require high pinpoint accuracy. To provide attitude control of satellite, different mechanisms are utilized which are divided into active and passive attitude control mechanisms.

Reaction wheels are used in active attitude control system of a satellite to provide pinpointing accuracy of orientation the satellite. For two decades, this method of ACS is employed in different CubeSat's design specifically where the pinpoint accuracy is mission requirement[4]. To achieve 3-axis stabilization for a satellite (pitch, roll and yaw), reactions wheels are used in configuration of three to provide stabilization in three directions whilst 4-wheels configuration are also used for redundancy and more torque generation in each axis. In this research, 3-wheel orthogonal configuration is employed for attitude control. The cost-feasibility of the reaction wheel is done by comparing totals cost incurred with the commercially available reaction wheels and also by performance analysis of the developed hardware.

The primarily objective of this research is to introduce a COTS component for the development of reaction wheel and study its feasibility to be used as an actuator in CubeSat missions. For this, a simulation modelled is developed with the parameters of the used COTS component and this model is subjected to various space-environment disturbances to analyze the reaction wheel response. The mathematical model of reaction wheel and attitude control system are defined in MATLAB.

II. SATELLITE ATTITUDE DYNAMICS AND ACTUATION MODELLING

A. Satellite Attitude Dynamics

In space environment, satellite is subjected to different torques, which can be divided into two groups of internal and external torques. Internal torques are produced due to different payload and system inside a satellite whereas external disturbances and the control torque provided by actuators produce external torques. In this research, internal torques are out of scope and will be assumed zero and equations governing the attitude dynamics will only include external torques.

Let M_T be the total external torques affecting the satellite and it comprises of sum of disturbance torques M_D and sum of command torques M_C. Thus, total torque on satellite body can be given as:

$$M_T = M_D + M_C \tag{1}$$

This research focuses on the satellite at the altitude of 600 km, which subjects satellite to disturbance torques due to gravity gradient, aerodynamic torque, Earth's magnetic field and Solar pressure. The dynamic modeling is based upon Newton-Euler formulation where angular momentum deviates relating to the applied torque and is given as:

$$M_T = \frac{d\vec{H}_I}{dt} \tag{2}$$

In this research, reaction wheels are the only source for commanded torque, thus angular momentum H_B of satellite will become:

$$H_B = I_s w_b + h_w \tag{3}$$

Here h_w denotes the angular momentum produced by reaction wheels which is defined by:

$$h_w = C_{rw} I_w w_w \tag{4}$$

Here I_w denotes reaction wheel diagonal inertia matrix where w_w represents reaction wheel angular velocity and C represents the distribution matrix associated with the reaction wheel distribution in satellite body.

By using Newton's Euler method, and taking equation of moment H_b, we will get:

$$\frac{dH_B}{dt} = -w_b(t) \times H_B(t) + M_T \tag{5}$$

By using equation of H_B and h_w from (3) and (4):

$$\frac{dH_B}{dt} = \left[I \frac{dw_b}{dt} \right]_b + \dot{h_w} \tag{6}$$

By comparing (5) and (6), we will get:

$$\left[I \frac{dw_b}{dt} \right]_b = -w_b(t) \times H_B(t) + M_T - \dot{h_w} \tag{7}$$

Now, as reaction wheel are functioned to provide opposite torque to oppose disturbing torque and by using principle of exchange of momentum then commanded torque will became:

$$\dot{h}_w = -M_c \tag{8}$$

$$\frac{dw_b}{dt} = I^{-1}(-w_b(t) \times H_B(t) + M_T + T_c) \tag{9}$$

Equation (9) gives time derivate of angular velocity in body frame whereas commanded torque T_c is also in body frame.

B. Attitude Control Model

In this research, three reaction wheels control each axis of satellite. Whenever satellite is subjected to disturbance torque in any axis, the aligned reaction wheel of that axis provides opposition to overcome that disturbance torque and continues to do so until it reaches saturation[6].

In the case of satellites, four-wheel configuration is used for redundancy but due to mass and size constraint of CubeSat, this model will only employ 3-wheel reaction model. The idea behind choosing the 3-wheel system is due to constraint of CubeSat and relative size and mass of used reaction wheel. In orthogonal formation of reaction wheels, required distribution matrix is given as[7];

$$C_B^{Rw} = [C^1 C^2 C^3]^T = \begin{bmatrix} r_x^1 & r_x^2 & r_x^3 \\ r_y^1 & r_y^2 & r_y^3 \\ r_x^1 & r_z^2 & r_z^3 \end{bmatrix} \tag{10}$$

Above matrix gives matrix for three-reaction wheel in three axis. Number of columns represent the total number of reaction wheel and number of rows represent the axis. In the case of orthogonal configuration, C_B^{Rw} becomes[8],

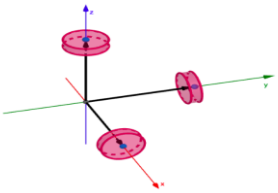


Figure 1 Orthogonal arrangement of reaction wheels

$$C_B^{Rw} = [C^1 C^2 C^3]^T = \begin{bmatrix} 1 & 0 & 0 \\ 0 & 1 & 0 \\ 0 & 0 & 1 \end{bmatrix} \tag{11}$$

The use of distribution matrix provides solution to the problem associated with control allocation between reaction wheel and Euler angles. When satellite is affected by external torque, then this torque command is distributed to all reaction wheels respective to their axis. This is done by using inverse of distribution matrix as shown by below equation[3].

$$H_{rw} = \left[C_{rw}^{body} \right]^{-1} H_{rw}^B \tag{12}$$

The overall angular momentum (H_{rw}) produced by actuation system equals to the sum of individual angular momentum provided by each reaction wheel and can be written as,

$$w_{rw} = [w_{rw1} \; w_{rw2} \; w_{rw3}]^T \tag{13}$$

Thus, by using principle of momentum exchange and by use of (1) to (13), total M_c in each axis comes out to be:

$$M_c^{rw} = \dot{H}_{RW}^B + (w_{IB}^B + H_{RW}^B) = \begin{bmatrix} \dot{H}_{RWx}^B + \vec{H}_{RWz}^B w_{IBy}^B - \vec{H}_{RWy}^B w_{IBz}^B \\ \dot{H}_{RWy}^B + \vec{H}_{RWx}^B w_{IBz}^B - \vec{H}_{RWz}^B w_{IBx}^B \\ \dot{H}_{RWz}^B + \vec{H}_{RWy}^B w_{IBx}^B - \vec{H}_{RWx}^B w_{IBy}^B \end{bmatrix} \tag{14}$$

C. Reaction Wheel Electrical and Mechanical Model

In this research, the reaction wheel hardware and software implementation utilize BLDC motor which speed is controlled electronically by commutation. This commutation becomes source of ripple in torque command, which creates instability, thus use of speed and torque controller are implemented in the model.

To control reaction wheel and to deal with instability, speed and torque control are implemented in the model. The

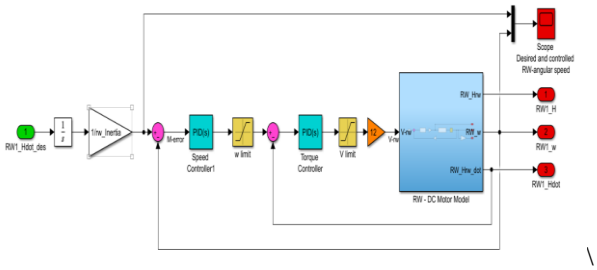


Figure 2 Speed and Torque PID control model

commanded torque is achieved by providing current to the motor hence, torque can be controlled by controlling current supplied to electronic which is done through torque control. In contrast to torque control, speed control is in cascade loop which controls the voltage supplied to the inner loop. This is necessary, because without cascade control more ripple torque is generated which makes system unstable[9].

A simplified model for PID controller is implemented in above model. It can be seen that speed control is in cascade loop whereas toque controller is inside the loop. The above model is based upon model described by Andresen in[7]. This model is linearized and commutation effect is not represented. The bldc motor of reaction wheel has been modelled in under given equation in which armature voltage v is related to armature current I and BLDC motor's angular velocity w.

$$v = R.i + L\frac{di}{dt} + K_s.w \tag{15}$$

In above equation, R represents the stator's resistance, L represents stator's inductance, and $K_s w$ represents electromotive force when conductor is motioned in magnetic field. The torque M_{rw} is represented by following equation[6], which is directly proportional to the torque produced, by motor $Kt.i$ and friction $b.w$.

$$M_{rw} = j_{rw}\frac{dw}{dt} = kt.i + b.w \tag{16}$$

This equation is used to model reaction wheel in Simulink.

III. Disturbance Torques.

Satellites orbiting and revolving around the earth become subjected to different torques, which alter the attitude along the course of satellite time in orbit. These disturbance torques are excellent for modeling attitude control system as it is foremost functionality of reaction wheels to overcome these disturbances[3].

In this research, the selected alattitude lies in LEO orbit and in this orbit, satellite is generally affected by four kind of torques, this torques are[2], [10];

1. Gravity gradient (M_g)
2. Aerodynamic torque (M_a)
3. Solar radiation (M_s)
4. Earth's magnetic field (M_e)

For modeling the system, worst-case scenario will be assumed which will be maximum disturbance torque in all axis, by summing up all the torques and applying them to each axis.

$$M_d = M_g + M_a + M_s + M_e \tag{17}$$

A. Gravity Gradient Torque

Gravitational force is a long-distance force and satellites in Earth's orbit are susceptible to planetary gravitational force, which decreases by $1/r^2$ factor as we move away from center of planet. The attraction due to this force will be more on satellite's lower side as compared with its upper side thus it will produce disturbance torque affecting satellite's attitude. The mathematical expression of gravity gradient for maximum torque can be stated as[6]:

$$M_g = \frac{3_{\mu\oplus}}{2R^3}\left|I_z - I_y\right|\sin(2\theta) \tag{18}$$

In this equation, $\mu_{\oplus}$ is the gravitational parameter of Earth and is multiple of Earth's mass and gravitational constant ($3.986*10^{14}$ m^3/s^2), R denotes orbit radius which in our case is R_e + 600 km, θ denotes maximum deviation of satellite's from Earth's z-axis, and I_x and I_y are satellite's moment of inertia along x and y axis respectively.

In this research, maximum torque is required which will be in the case when sin(2θ) = 1. Hence, torque is calculated by putting the parameters in the equation (18)[1].

B. Magnetic Torque

Earth's magnetic field produce the torque on the outer space bodies, which also includes the different satellites orbiting around Earth. This field give rise to the disturbance torque acting on body. It decreases as we move farther from the Earth nonetheless, it produce noticeable torque in LEO satellites, which can be stated as[4]:

$$M_m = \vec{m} \times \vec{B} \tag{19}$$

Where m is satellite residual dipole that in our case can be estimated from reference case and which comes out to be *~0.01 A.m²* [1], [12] and B is the Earth's magnetic field, which can be stated as[13]:

$$\vec{B} = \frac{2M}{R^2} = 4.7016 \times 10^{-5}\, Tesla \tag{20}$$

Whereas M is magnetic moment of Earth ($M = 7.96\ 10^{15}$ *Tesla.m³)* and R is orbit radius.

C. Aerodynamic Torque

Satellites in LEO orbit is subjected to aerodynamic drag due to their low altitude. This drag results in producing disturbance torque on satellite body. The aerodynamic torque depends upon the difference of satellite's center of pressure and center of mass. The formulation of aerodynamic drag force on satellite is given as[1], [2]:

$$F_{aero} = \frac{1}{2}\rho V^2 C_d A_{ince} \tag{21}$$

Whereas ρ represents atmospheric density at altitude, V is orbital velocity of the satellite, C_d is co-efficient of drag and for CubeSat it values lies between 2 and 2.5 and A_{ince} is satellite surface area subjected to drag.

Putting $\rho = 3.725\ 10^{-12}$ *kg/m³*[12], $V = 7558.5$ *m/s* for altitude of 600 km and $A_{ince} = 0.1\ m^2$ in (21), the F_g comes out to be:

$$F_{aero} = 2.660 \times 10^{-6}\ N \tag{22}$$

For aerodynamic torque,

$$M_a = R_{cp} \times F_{aero} \tag{23}$$

Where R_{cp} is the difference of satellite's center of pressure (c_p) from center of mass (c_p) and this comes to *0.05 m* for maximum torque[12].

D. Solar Radiation Torque

In outer space, due to continuous activity in solar region high energetic particles strike with outer space bodies, which in result give rise to disturbance torque alongside with multiple other factors. In contrast to gravity gradient, solar radiation affect maximizes as we move away from center of Earth. The amount of power per meter^2 emitted by Sun is known as solar flux density and is taken as constant. Solar radiation force is given as:

$$F_{sr} = -p_{sr} c_r A_s \cos(i) \tag{24}$$

Where p_{sr} is sun pressure force applied per unit area which can be calculated by dividing solar flux with speed of light (c) which is given as[14]:

$$p_{sr} = \frac{SF}{c} \quad (25)$$

The torque due to this force can be calculated by[15]:

$$M_s = F_{sr} \times (c_{pSR} - c_g) \quad (26)$$

c_{pSR} in above equation is the point of where solar pressure acts and for maximum torque it should be located at farthest point from the satellite. Its value for CubeSat comes out to be 0.05[14].

The total disturbance torque for each axis is calculated is shown in table 1.

TABLE 1 DISTURBANCE TORQUES

Symbol	Disturbances Torque	Magnitude in Nm
Mg	Gravity gradient	$7.8171 \times 10^{-8} Nm$
Mm	Magnetic torque	$4.706 \times 10^{-7} Nm$
Ma	Aerodynamic torque	$1.3301 \times 10^{-7} Nm$
Ms	Solar radiation torque	$3.645 \times 10^{-9} Nm$
Mmax	Total Torque	$6.850 \times 10^{-7} Nm$

IV. SELECTION AND COMPUTATION OF HARDWARE

A. Electric Motor Selection

The ideal motor for designing reaction wheel should meet satellite's power and size requirement while also generating enough torque to provide command over attitude. Given the requirements, the BLDC motor is selected over simple DC motor. The selection of bldc motor can be justified as due to no brushes, they provide more efficiency and generate more torque on the consumption of small power[16]. Even though the complexity increases while controlling bldc motor as it does not follow the same commutation principle as DC motors but BLDC motor enable to precisely control the torque generated and are more durable than DC motor. Therefore, our primarily consideration for hardware is BLDC motor.

Taking into consideration the research scope of this paper, reaction wheel is developed using hard disk drive (hdd) motor of personal computer. HDD spindle motor and its disks will be utilized for purpose of developing reaction wheel. In HDD, the BLDC motor is used for spindle motor and uses ball bearings. Due to special characteristics of hard disk drives, the motors are built in such a way that they have very low leakage of magnetic field to have no impact on data reading/writing process. Furthermore, they are built to run for a long time and provide high rotations rate on the consumption of less power. Additionally, from literature review it was noted that working temperature of hard drive spindle motor lies between -40° C to 75° C. This makes them perfect to be used in reaction wheel assembly, as they will be subjected to harsh space conditions. The moment of inertia corresponding to hdd spindle motor is [17], [18].

B. Flywheel Selection and Theoertical Calculation

Flywheel are important part of reaction wheel assembly. They are selected to meet the torque generation requirement of a satellite and in our case, for CubeSat. size and material for flywheel is selected by considering constraints, which are size, mass and required storage of angular momentum. In this research[19], the needed moment of inertia has been derived by using needed angular momentum change, this can be expressed as:

$$H_{store} = w_{max} \times \frac{\pi}{30} x I_{motor} \quad (27)$$

In addition, total needed moment of inertia is given as,

$$I_{required} = \frac{H_{min}}{w_{max} \times \frac{\pi}{30} x I_{motor}} \quad (28)$$

This equation implies that total moment of inertia of disk should be,

$$I_{disk} = I_{required} - I_{motor} > 0 \quad (29)$$

Considering the requirements, in this research flywheel selected are the aluminum disks of HDD mounted on spindle motor. The disks are made up of aluminum or ceramics, and comes up with the coating of magnetic material and are perfectly balanced thus, negating the horizontal and vertical motion of disk. The flywheel used in this research has inner radius of 25 mm with the outer radius of 95 mm and has thickness of 1 mm. The mass of one disk is 22.9 g. Thus, the disk moment of inertia is given by (30) and dimensions can be visualized in fig 3[20];

$$I_{zz} = \frac{N_d m_d}{2} (r_2^2 + r_1^2) \quad (30)$$

In (30), N_d is number of disks, m_d is mass of disk, and r_1 and r_2 are disk I inner and outer radius respectively. Putting up the parameters, where $N_d = 2$, $m_d = 22.9$ g, $r_1 = 12.5$ mm and $r_2 = 47.5$ mm. the moment of inertia comes out to be:

$$I_{zz} = 5.5 \times 10^{-5} kg.m^2 \quad (31)$$

The inertia of motor is approximated through literature review[17] and is given as:

$$I_m = 3 \times 10^{-6} kg.m^2 \quad (32)$$

In addition, total moment of inertia is:

$$I_T = I_{zz} + I_m = 5.8 \times 10^{-5} kg.m^2 \quad (33)$$

The nominal angular momentum of hdd reaction wheel at nominal rpm of 3100 is given by:

$$H_{rw} = I_T . \frac{2\pi . rpm}{60} = 18.8\, mN.m.s \quad (34)$$

In addition, the maximum angular momentum at 6200 rpm is given by using (34) is:

$$H_{max\, rw} = 37.6\, mN.m.s \quad (35)$$

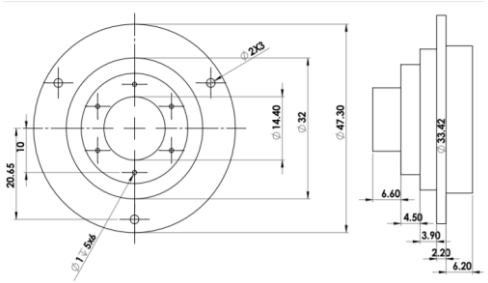


Figure 3 HDD Dimensions

Furthermore, the total torque that can be generated from reaction wheel depends upon rate of change of angular momentum, and depends upon the time taken for reaction wheel to reach nominal angular momentum from rest position. Figure 4 and 5 shows the selected motor with flywheel respectively.

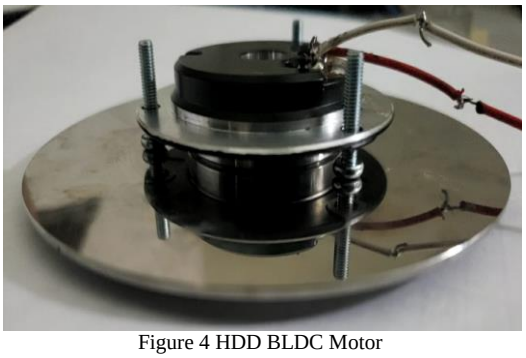


Figure 4 HDD BLDC Motor

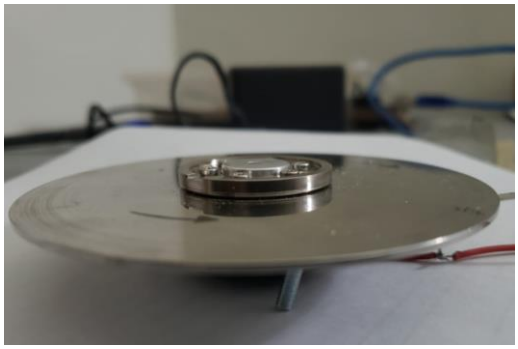


Figure 5 HDD Flywheel

The calculated and approximated[17], [20] parameters for hard drive spindle motors alongside with its electrical parameter are summarized in following table 2.

TABLE-2 HDD CALCULATED PARAMETERS

Parameter	Symbol	Value	Unit
Inductance	Lo	0.48	H
Resistance	R	7	Ω
Voltage	V	3.3 - 5	volts
Motor Field constant	Ke	0.922*10-3((60)/2π))	V/(rad/s)
Motor Torque constant	Kt	$8.8*10^{-3}((60)/2\pi))$	N.m/amp
Damping Coefficient	b	8.85 * 10-3	Nm/(rad/s)
mass	m	0.12	Kg
RW Radius	r	0.047	m
RW height	h	0.012	m
Moment of inertia	IT	5.8 * 10-5	kg m2
Nominal momentum	Hrw	18.8 * 10-3	Nm.s
Max. momentum	Hmaxrw	37.6 * 10-3	Nm.s
Power consumption	P	0.4 – 0.7	W

C. Control Method for Reaction Wheel

The most common method of controlling BLDC motor is Pulse Width Modulation (PWM) signal. In PWM, current signals are provided to the stator to generate commanded torque. The electronic circuit consists of electronic speed controller; Arduino Uno based micro controller and power source. The required angular momentum signal is given through laptop using Arduino language. The schematics of circuit are given in figure 6 and the hardware implementation of circuit is shown by figure 7.

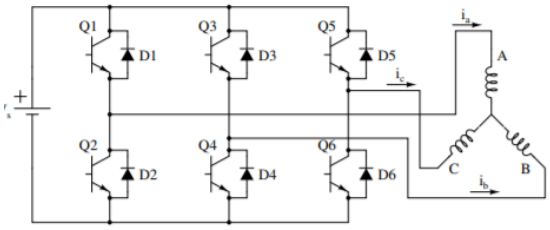


Figure 6 ESC speed control circuit for BLDC motor

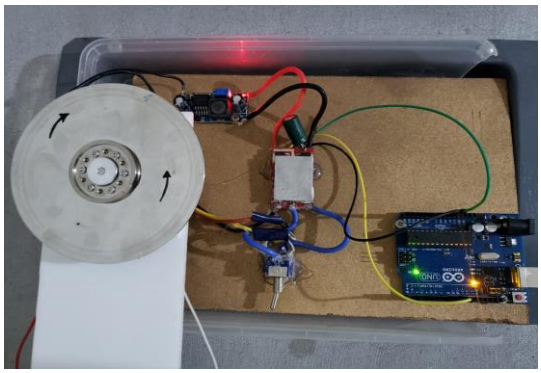


Figure 7 RW Testing System

V. RESULTS AND DISCUSSIONS

This simulation modelling is done for 3-axis stabilization using three reaction wheels aligning with the CubeSat's principle axis. In figure 8, a complete model of actuation model is presented. In this model, input command is 1 X 3

matrix of the maximum disturbance torque in all axis, due to space environment and the output of the model is the response angular momentum and change in angular momentum produced by reaction wheels in their aligned axis. Moreover, figure 9 shows the algorithm used in the modelling of the system.

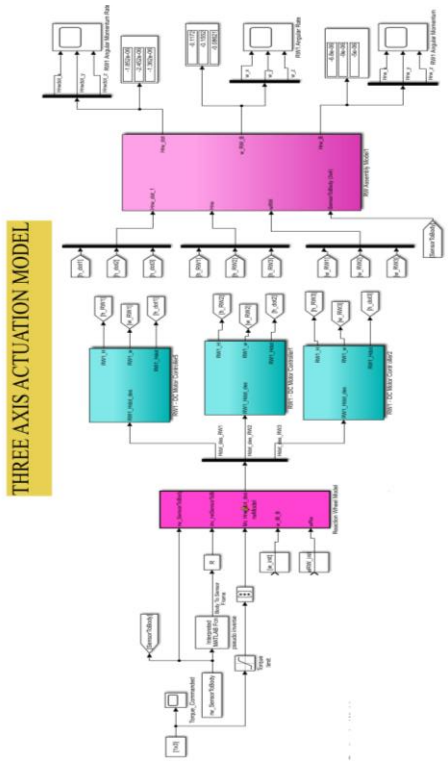


Figure 8 Actuation Control Model - 3-axis Stabilization

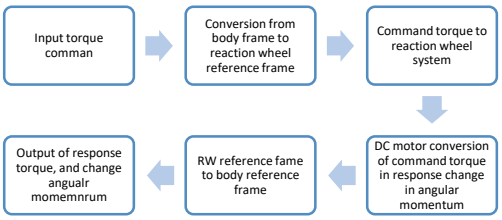


Figure 9 Block diagram of Simulink model implementation

The initial parameters for the simulation model are calculated from the HDD based reaction wheel alongside the conditions used for model are defined by the conditions faced by 1U CubeSat satellite at LEO orbit. The tables for both HDD reaction wheel and 1U CubeSat satellite are shown in the table 3 and 4 respectively, whereas the initial torque offset is the disturbances torques that are summarized in table 1.

TABLE 3 HDD HARDWARE PARAMETERS

HDD Reaction wheel Parameters			
Parameter	***Symbol***	***Value***	***Unit***
Inductance	Lo	0.48	H
Resistance	R	7	Ω
Motor Field constant	Ke	0.922 * 10-3((60)/2π))	V/(rad/s)
Motor Torque constant	Kt	8.8 * 10-3((60)/2π))	N.m/amp
Damping Coefficient	b	8.85 * 10-3	Nm/(rad/s)
mass	m	0.12	Kg
RW Radius	r	0.047	m
RW height	h	0.012	m
Moment of inertia	IT	5.8 * 10-5	kg m2
Nominal momentum	Hrw	18.8 * 10-3	Nm.s
Max. momentum	Hmaxrw	37.6 * 10-3	Nm.s
Power consumption	P	0.4 – 0.7	W
Sampling time	S(t)	0.1	second

TABLE 4 CUBESAT ENVIRONMENT PARAMETERS

Parameter	Value
CubeSat Type	1U
CubeSat Mass	1.33 kg
Surface Area	0.01 m2
C.G. Offset	<0.02, 0.02, 0.02> m
Inertia (Ixx,Iyy,Izz)	<0.01, 0.01, 0.01> A.m2
Dimensions	2.22 10-3 kg
Orbit Altitude	600 km
Earth Angular velocity	7.291 10-5 rad/sec
Drag coefficient	2.2

In figure 10, it is visible that reaction wheel has generated the same torque as commanded torque in all three axes but in opposite direction. This evidently proves that this model of reaction wheel is successfully negating the disturbance torques. Furthermore, total response time taken to negate disturbances is 10 seconds. The values are steeper during startup of reaction wheel which shows that maximum change in torque occurred during initial time and this change become gradual with passage of time.

Evidently, the response torque provided by reaction wheel will be continuous and last until the reaction wheel reach the saturation. For three reaction wheels placed in orthogonal structure, the problem of saturation is met by using magneto torquers rod which reset the reaction wheels when they reach saturation.

In figure 11, angular momentum response of reaction wheel is represented for 3-axis stabilization and response time of angular momentum is shown to the command torque. It is evident from the figure that the total angular momentum of system is in reverse direction of command torque. The linearity of time with angular momentum shows that the controller used for these simulations are working efficiently with minimum settling time.

Figure 12 shows the angular velocity change. In figure, the linearity of time with angular velocity can be seen. This linearity is due to less settling time of PID cascade speed controller. Angular velocity also obeys the same change principle as angular momentum and torque as it also showed response in negative direction to the commanded torque. The reaction wheel response to disturbance torque is linear for the most part of simulation.

The response of model is susceptible to the input provided and model of DC model implemented. The smooth curve of graph represents that the plant function used in the model are well tuned according to the parameters of HDD based RW motor model.

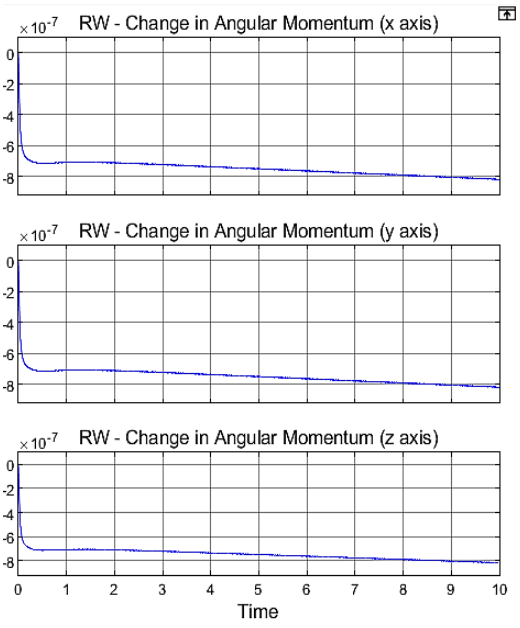


Figure 10 RW response change in angular momentum to torque

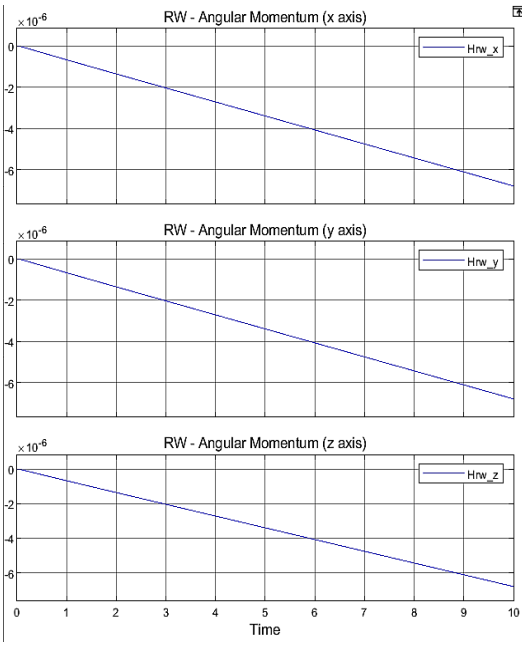


Figure 11 Angular momentum response to command torque

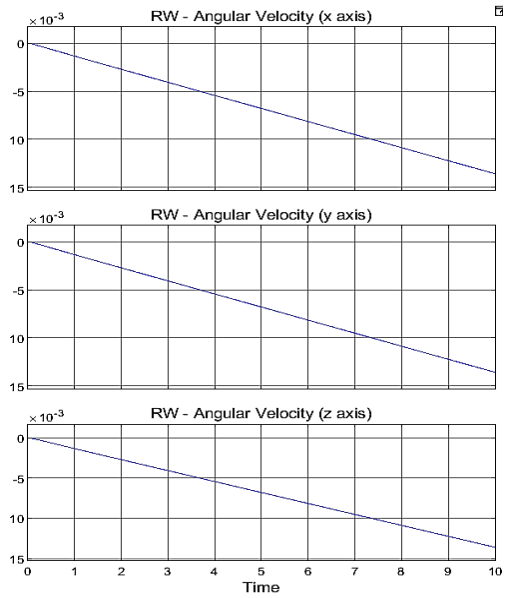


Figure 12 Angular velocity response to command torque

A. *Total Budget*

The cost effectiveness study involves comparing the developed product with the commercially available set of reaction wheels. The major cost cutting is due to the reduce benchmarking tests as the current setup involves already-tested component that has working parameters This research work focused on in-house development of low-cost reaction wheel using hard drive-based BLDC motor and flywheel. Different kind of hard drive are available commercially with different sizes and parameters and most common ones are 2.5" inches and 3.2" inches. For our research, 3.2" inch variant was used for one-dimensional control. Furthermore, for controlling the reaction wheel the drive circuitry is based upon Arduino Uno controller with electronic speed controller/ the total cost incurred in given in table. The cost break down of reaction wheel is for one dimensional. For three dimensional, total cost comes to be $330 which is economical as compared to the commercially available reaction wheels.

TABLE 5 REACTION WHEEL BUDGET DISTRIBUTION

S. No	Component	Cost
1.	3.2" inch Hard drive	$50
2.	Arduino Controller	$10
3.	Drive Circuitry	$40
4.	Miscellaneous	$10
Total Cost		$110

VI. . CONCLUSION

Since the inception of CubeSat technology, many space-based applications shifted to this relatively new technology. Due to cost effectiveness and easy to develop nature, many students led projects are based on CubeSat. Many COTS components are employed for developing subsystem of CubeSat, which includes development of satellite attitude control systems. Moreover, different mechanisms are used for ACS.

The ACS model of satellite was developed using orthogonal formation of three-reaction wheel system. Model design used three reaction wheel model which. Each reaction wheel has a defined motor, which is parametrized in accordance with HDD BLDC motor. The speed and torque are controlled with PID. Furthermore, the model was simulated on the disturbance torque values which were calculated through

the relevant equations. Maximum value of disturbance torque was selected as initial parameters, which was given manually to model. In response, opposing torque was generated by reaction wheel, which suggests that hdd motor-based reaction wheels store enough torque to oppose the maximum torque and can be used to maneuver satellite to required attitude. Saturation problem associated with reaction wheel is not dealt in this research work.

Secondly, prototype of reaction wheel is also developed in accordance with the constraints of 1U CubeSat. The COTS components are hdd based BLDC motor and flywheel. The torque and angular momentum storage of components were calculated using the motor formulas and the calculated values were found out to be accurate enough to control the attitude of satellite precisely.

Conclusively, this research work provides cost efficient method to develop reaction wheel system for 1U CubeSat alongside with actuation model that simulates the working of developed reaction wheel. From the simulations, it can be assessed that reaction wheel system are providing suitable torque to control the attitude of 1U CubeSat.

REFERENCES

[1] J. Li, M. Post, T. Wright, and R. Lee, "Design of Attitude Control Systems for CubeSat-Class Nanosatellite," Journal of Control Science and Engineering, vol. 2013, p. e657182, May 2013, doi: 10.1155/2013/657182.

[2] J. R. Wertz and W. Larson, Eds., Space Mission Analysis and Design. Springer Netherlands, 1991.

[3] H. Polat, "PROTOTYPE DESIGN AND MISSION ANALYSIS FOR A SMALL SATELLITE EXPLOITING ENVIRONMENTAL DISTURBANCES FOR ATTITUDE STABILIZATION," Naval Postgraduate School, Monterey, California, 2016.

[4] J. R. Wertz, D. F. Everett, and J. J. Puschell, Space mission engineering: the new SMAD. Hawthorne, CA: Microcosm Press : Sold and distributed worldwide by Microcosm Astronautics Books, 2011.

[5] "small_spacecraft_technology_state_of_the_art_2014.pdf." Accessed: Sep. 10, 2020. [Online].

[6] S. S. Nudehi, U. Farooq, A. Alasty, and J. Issa, "Satellite attitude control using three reaction wheels," in 2008 American Control Conference, Seattle, WA, Jun. 2008, pp. 4850–4855. doi: 10.1109/ACC.2008.4587262.

[7] Z. Ismail and R. Varatharajoo, "A study of reaction wheel configurations for a 3-axis satellite attitude control," Advances in Space Research, vol. 45, pp. 750–759, Mar. 2010, doi: 10.1016/j.asr.2009.11.004.

[8] D. G. Diez, "Study and Design of the attitude control of a cubesat 1U based on reaction wheels," Politician de Catalunya University, BArcelona, Spain, 2019.

[9] B. Wie and C. M. Raithmayr, "Integrated Orbit, Attitude, and Structural Control Systems Design for Space Solar Power Satellites," Langley Research Center, Hamptom, Virginia, Technical Memorandum NASA/TM-2001-2108554, 2001.

[10] W. F. Hilton, "Spacecraft Attitude Dynamics. P. C. Hughes. John Wiley & Sons, Incorporated, New York. 1986. 564 pp. Illustrated. £48.95.," The Aeronautical Journal, vol. 90, no. 894, pp. 152–152, Apr. 1986, doi: 10.1017/S0001924000015578.

[11] M. D. Griffin and J. R. French, Space vehicle design, 2nd ed. Reston, VA: American Institute of Aeronautics and Astronautics, Inc, 2004.

[12] juan molina, victor ayerdi, and L. Zea, "Attitude Control Model forCubeSats," in Techn Session VII: Attitude Determination and Control Systems, Florianopolis, Brazil, Jan. 2016, vol. 2nd, p. 22.

[13] J. Gießelmann, "Development of an Active Magnetic Attitude Determination and Control System for Picosatellites on highly inclined circular Low Earth Orbits," School of Aerospace, Mechanical and Manufacturing Engineering Science, Engineering and Technology Portfolio RMIT University, Melbourne City, 2006.

[14] D. A. Vallado and W. D. McClain, Fundamentals of astrodynamics and applications, 2nd ed. Dordrecht; Boston: Kluwer Academic Publishers, 2001.

[15] J. Zorita, "Dynamics of small satellites with gravity gradient attitude control," KTH, School of Electrical Engineering (EES), Zurich, 2011.

[16] N. Murugananthan, "STATE SPACE MODELING AND SIMULATION OF SENSORLESS PERMANENT MAGNET BLDC MOTOR," International Journal of Engineering Science and Technology, vol. 2, no. 10, p. 8, 2010.

[17] H. RUOYU, "Moment of inertia and torque performance sensorless measurement for HDD used spindle motors," Thesis, Natioanl University of Singapore, Singapore, 2004.

[18] M. Feng and L. Qu, "Torque Performance Analysis of HDD Spindle Motors Based on Geometrical Interpretation," IEEE Transactions on Magnetics - IEEE TRANS MAGN, vol. 47, pp. 1906–1910, Jul. 2011, doi: 10.1109/TMAG.2011.2131122.

[19] T. Vergoossen, "Design, Integration and Testing of the Delfi-PQ Satellite Reaction Wheel," Delft University of Technology, Delft, 2017.

[20] L. Sahar, E. Edlerman, H. Agalarian, V. Balabanov, and P. Gurfil, "Hard Disk Drive Based Reaction Wheels for CubeSat Attitude Control," Journal of Spacecraft and Rockets, vol. 55, no. 1, pp. 236–241, 2018, doi: 10.2514/1.A33866.

Comparative Study of Image to Image Translation Models for Abnormal Weather Effects Removal

Maria Siddiqua
Department of Computer and Information Sciences
Pakistan Institute of Engineering and Applied Sciences
Islamabad, Pakistan
maria_21@pieas.edu.pk

Naeem Akhter
Department of Computer and Information Sciences
Pakistan Institute of Engineering and Applied Sciences
Islamabad, Pakistan
naeemakhter@pieas.edu.pk

Javaid Khurshid
Department of Computer and Information Sciences
Pakistan Institute of Engineering and Applied Sciences
Islamabad, Pakistan
javaidk@pieas.edu.pk

***Abstract*—Contamination of images by abnormal weather environments such as haze, rain, fog, snow is inevitable as they are naturally occurring weather effects. These weather effects degrade the effectiveness of various computer vision applications like traffic sign detection, audiovisual surveillance, aerial and ground navigation. Therefore, a unified image-to-image transformation model is proposed that is Multi-Modal Contextual Conditional Generative Adversarial Network (MC^{2}GAN) which is capable of eliminating several weather effects that are snowflakes, haze, rain streaks, and fog. The addition of multiple bottleneck layers amid the encoder and decoder of the generator makes the construction of contextually alike output images to the ground truth image given together with the input image as a constraint. The usefulness of MC^{2}GAN is compared with the existing image-to-image transformation networks specifically, pix2pix, cycleGAN, unsupervised image translation (UNIT), contrastive unpaired translation (CUT), and fastCUT visually and numerically. After a thorough examination of supervised and unsupervised networks, it is concluded that our proposed model MC^{2}GAN outpaces other models.**

Keywords—*Street views, image restoration weather effects, image-to-image transformation, conditional adversarial network, context encoders.*

I. INTRODUCTION

In recent times, research in the image restoration domain has gained a lot of consideration due to its immense requirement in various machine vision applications. With the increased commercialization of autonomous vehicles, the need to have clear images for accurate navigation is essential but the weather effects like fog, haze, rain, and snow invade the performance by corrupting its visual quality which results in poor scene visibility. Similarly, images with improved visibility are a requisite for many tasks such as criminal detection and recognition from CCTV footages, computational photography, traffic sign, and lane detection.

In this paper, a comparative study of our proposed network named MC^{2}GAN with different image-to-image translation networks is presented for weather effects removal. The subsequent section of this paper provides a brief outline of previously proposed techniques for the restoration of weather degraded images. Section 3 explains the proposed work. Experimental analysis of the proposed work is specified in section 4. At last, concluding statements are specified in section 5.

II. RELATED WORK

Restoration and enhancement procedures for weather-affected images are classified into two main groupings namely prior-based and deep data-driven methods.

In prior-based methods, assumptions or additional information is provided such as layer, channel, shape, natural, or color prior to our model to generate meaningful outputs. Anparasy Sivaanpu and Kokul Thanikasalam [1] proposed a defogging model which computes the depth map, dark channel, and transmission for the dense fog presence in local scene-specific regions of an image. Yuanyang Zou et al. [2] used logarithmic guide filtering to estimate the general lighting and proposed a self-adaptive method to overcome the defects of dark and bright channel prior. Qiaosi Yi et al. [3] used a method with residual channel prior to preserve the structure in rainy images. Similarly, semantic and geometric priors are exploited for snow removal by Kaihao Zhang et al. [4]. Although prior-based methods have produced remarkable results, in some cases, where the images are heavily degraded by weather effects, the prior-based methods do not guarantee to perform well, the assumptions might disrupt the restoration process.

Owing to the promising results of deep neural networks, the recent focus from prior-based methods is shifted towards deep learning models. For specifically working on images, deep convolutional neural networks (CNN) and generative adversarial networks (GAN) are commonly applied. As compared to the former, the latter approach learns the representation from input to the target distribution, thereby, making it an image-to-image translation problem.

Various algorithms are presently based on CNN for the restoration of weather-affected images. R. Suganya and R. Kanagavalli [5] proposed a hybrid gated recurrent unit and CNN-based scheme for defogging. Mayuri Dongare and Jyoti Kendule [6], introduced a CNN-based dense haze removal network. Similarly, P. Musafira and K. S. Shanthini [7] used the CNN model for removing rain within a single image. Minghan Li et al. [8] introduced an online multi-scaled convolutional light coding model to remove real-time snow.

Recently, many remarkable results are achieved by GAN-based methods for improving visibility. Dong Li et al. [9] performed image defogging using conditional GAN. Amrita Sanjay et al. [10] worked on haze removal using GAN. Yanyan Wei et al. [11] used cycleGAN an unsupervised model with rain attentive detecting for deraining images. Similarly, Aiwen Jia et al. [12] used an attention-based GAN

model for single image snow removal.

An enormous amount of work is accomplished in the field of image enhancement and restoration, but most of the methods are confined to single weather effect removal whereas, our proposed model MC^{2}GAN is capable of handling four weather effects: fog, haze, rain streaks, and snowflakes. A solo model is proposed which is compared to five image-to-image translation models. The comparative analysis shows the reliability of our proposed model.

III. PROPOSED WORK

The goal in this paper is to have weather affected image with either fog, haze, rain, or snowflakes effect and clean it by removing the weather effect. This is considered as an image-to-image translation problem and such a model which does competent image-to-image translations are generative adversarial networks (GANs) which consist of generator and discriminator models. Generator and discriminator work in adversary, each one tries to outperform the other. The generator generates an image as close to the ground truth image as possible to fool the discriminator, whose task is to identify the generated image as real or fake. The output image is generated via GAN in two ways either unsupervised or supervised. In supervised GAN models, paired images are provided to the network for generating output images, while, the unsupervised model takes unpaired images lacking details of the ground truth image corresponding to the input.

Pix2pix [13] is a supervised GAN-based model which takes the ground truth image together with the input image as a condition. Many alternatives of GAN exist from which cycleGAN [14], UNIT [15], CUT [16], and fastCUT [16] are a few of the prominent unsupervised GAN-based models. CycleGAN model works cyclically by generating the output image from an input image and vice versa. UNIT is a coupled version of GAN where the hidden space is shared for learning the target domain. The CUT model tries to compare the small input image areas to its ground truth image areas precisely to achieve maximally similar output images, whereas, fastCUT is a modified version of the CUT model analogous to the cycleGAN model but simpler and has fewer computations as identity loss is not used in it, unlike the CUT model. In this paper, a comparative study of MC^{2}GAN with five image-to-image transforming models: pix2pix, cycleGAN, UNIT, CUT, and fastCUT is reported.

The proposed model MC^{2}GAN is a supervised variant of the GAN model with a generator and discriminator. The generator is made up of eight encoding and decoding blocks with skip connections. Each encoder block has convolutional, batch normalization, and leaky ReLU activation layers, while the decoder block involves leaky ReLU, batch normalization, and deconvolution layers together with two bottleneck layers amidst as shown in Fig. 1, for better encoding the image background. The discriminator network has five encoding blocks alike generator, as shown in Fig. 2, which takes the affected and ground truth images as input, and outputs a guess, 1 if the degraded image is restored and 0 if it is degraded. The condition to produce an output image is alike a ground truth image, and for contextual similarity, bottleneck layers are applied to make the proposed model effective.

The loss function of MC^{2}GAN is stated as

$$L_{GAN}(G, D) = {}_{(m,n)}[\log D(m, n)] + \mathbb{E}_{(m)}[\log[1-D(m, G(n))]] \quad (1)$$

Here m represents input image, n output image, and generator G put efforts in dropping this loss for an adversarial discriminator D that tries to surge it, $G^* = \min_G \max_D L_{GAN}(G, D)$. G* together with L1 distance prevent images to get blurry in the restored images. The discriminator work remains the same, while the generator is held responsible to deceive the discriminator by producing an output image analogous to the ground truth image.

$$L_{L1}(G) = \mathbb{E}_{(m, n)}[||J-G(m)||_1] \quad (2)$$

Therefore, the final loss function is

$$G^* = \min_G \max_D L_{GAN}(G, D) + \lambda L_{L1}(G) \quad (3)$$

Here G* signifies lowest with respect to G of the highest with respect to D. This loss function is improved by training the model with a batch size of 1, learning rate 0.0002, and decay rate 0.99.

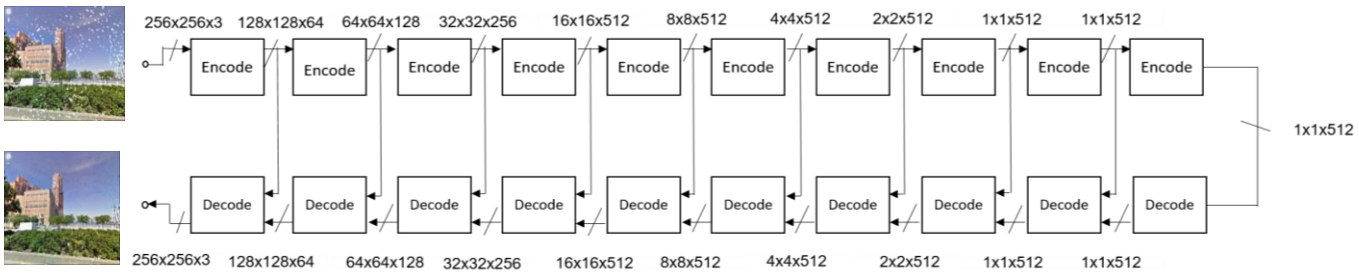


Fig. 1. Block diagram of MC^{2}GAN generator.

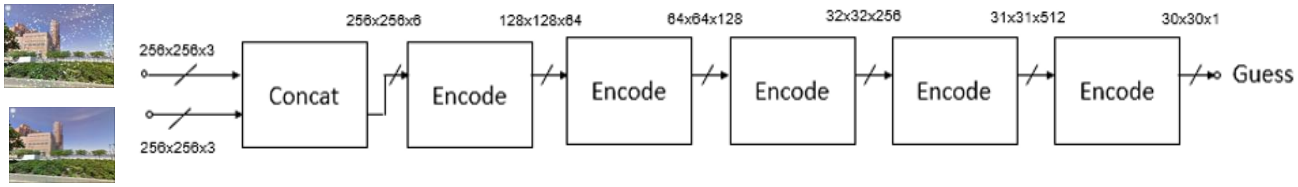


Fig. 2. Block diagram of MC^{2}GAN discriminator.

IV. Results and Evaluations

The proposed model MC^{2}GAN is evaluated and compared both qualitatively and quantitatively with other models. The outcomes are examined and reported in the next sections.

A. Dataset

The emphasis of this work is to enhance the visibility of images with street views. Google street view dataset [17] is used to accomplish this goal. Moreover, a self-made image dataset is created by embedding snow, fog, and rain effects within it using an image augmentation library [18]. A synthetic dataset OTS RESIDE [19] is utilized for haze removal. A paired dataset for training MC^{2}GAN and pix2pix is used, while, cycleGAN, UNIT, CUT, and fastCUT models are trained by an unpaired dataset.

B. Training

All the architectures in this work are trained on an NVIDIA GeForce GTX 1070 GPU system.

C. Qualitative results

The Qualitative comparison of MC^{2}GAN with pix2pix, cycleGAN, UNIT CUT, fastCUT is shown in Fig. 3.

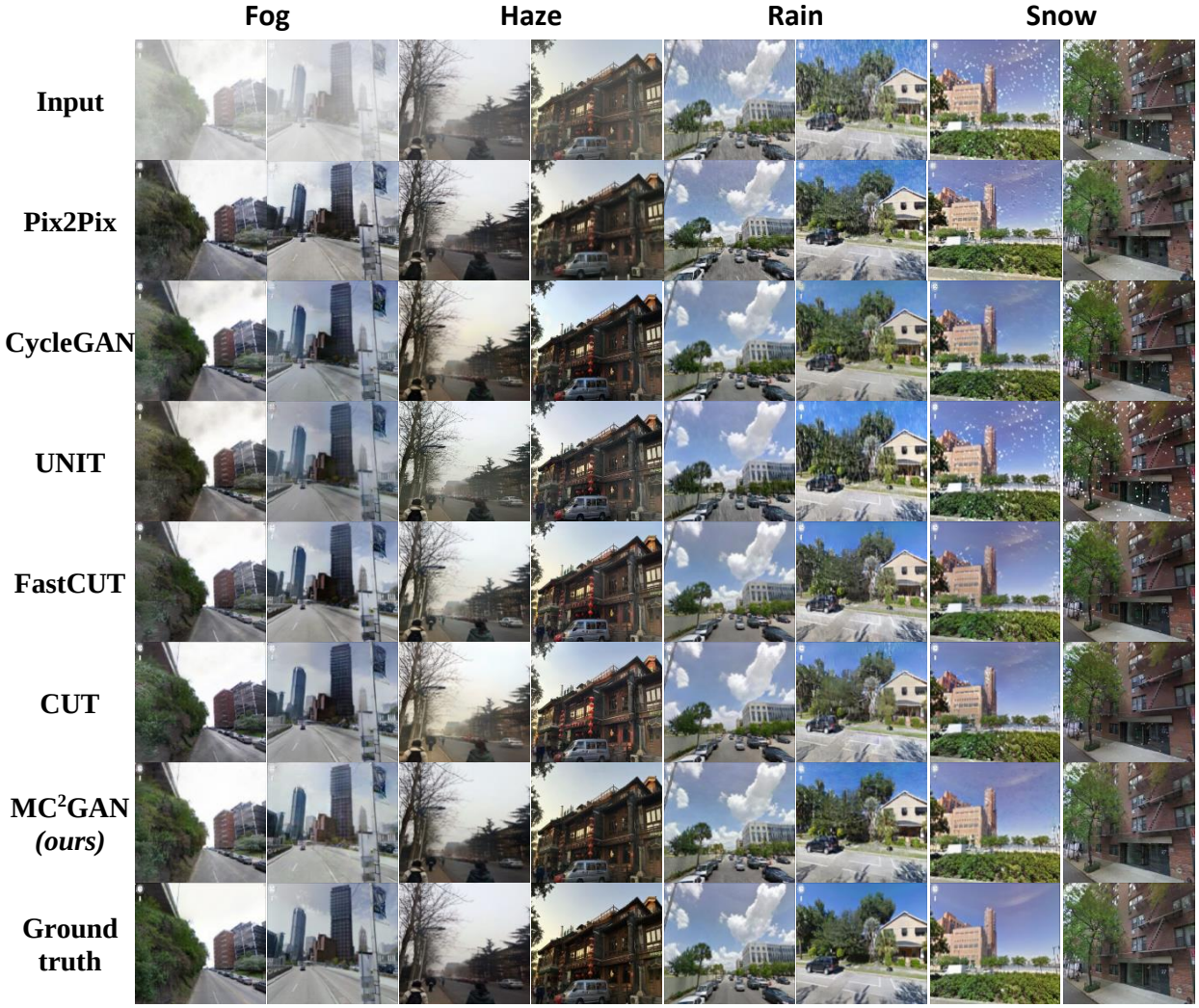


Fig.3. Visual evaluation of MC^{2}GAN results with pix2pix, cycleGAN, UNIT, CUT, and fastCUT model results.

The first row shown in Fig. 3 contains input images provided to our generator model and the latter row shows the ground truth target images. The first column of fog results shows how inefficient pix2pix, cycleGAN, and UNIT are in removing fog from the sky and street, moreover, as compared to the target image, pix2pix, cycleGAN, UNIT, CUT and fastCUT are unable to color the leaves properly on the left side of the image. From column three and four, it can be seen that the haze is still present in all model's results except MC^{2}GAN, which have restored the hazy image properly and also enhanced the image contrast. In case of rain, UNIT has underperformed the most by not removing the rain streaks properly. The results of snowflakes removal are better with MC^{2}GAN, in the rest of the results some of the snowflakes are still present in the output. Though, from the visual comparison, it can be concluded that the output of MC^{2}GAN is maximally analogous to the ground truth image as the effects are removed completely and have improved visual quality than the results of other models. The output of other models is incapable to eliminate the weather effects properly, specifically in the case of snowflakes. Therefore, our model performs well for all input modalities.

The proposed model is also tested on a few dust and lightning images, though the model is not trained on these

images but is still able to improve its visibility as shown in Fig. 4, this shows the generalization power of the proposed model. From Fig. 4, it can be determined that the overall image contrast and scene visibility is boosted. In the case of dust, the brownish shade is removed thereby increasing the clarity of the scene, and the lightning streak in the sky part is also taken out successfully.

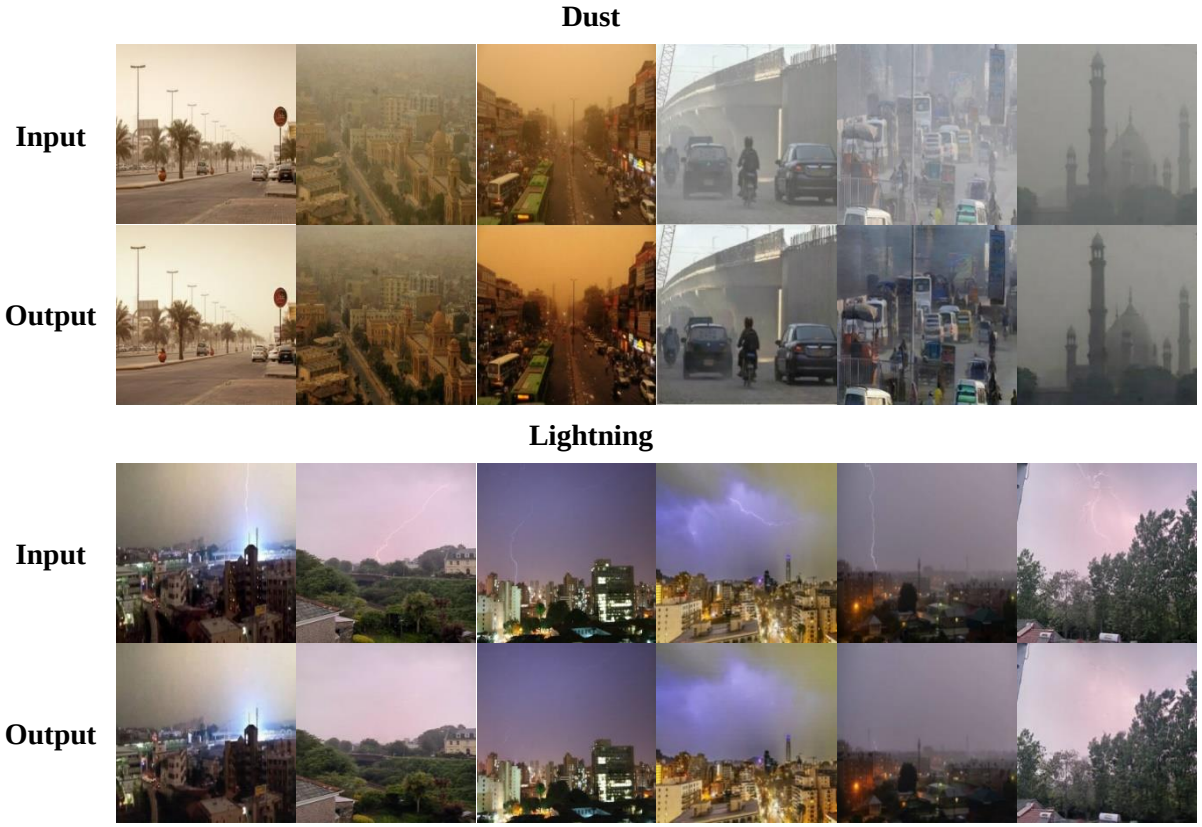


Fig.4. Qualitative results of dust and lightning effect removal.

D. Quantitative results

Two performance measures: Peak Signal to Noise Ratio (PSNR) and Structural Similarity Index Measure (SSIM) are used for quantitative comparison of MC^{2}GAN with other models. PSNR tells the ratio of an image to get corrupted by noise to its maximum power. SSIM is a measure that tells the extent to which the two images are structurally similar. A higher value of PSNR and SSIM is desired. The numerical values of PSNR and SSIM for all models are mentioned in Table I.

TABLE I. PSNR AND SSIM VALUES COMPARISON

Models	***PSNR***	***SSIM***
MC^{2}GAN	**26.2924**	**84.2333**
Pix2Pix	24.3770	80.0911
CycleGAN	23.6015	81.3006
UNIT	22.3177	79.8123
FastCUT	21.0206	72.1580
CUT	20.6191	70.4681

Table I. specifies that MC^{2}GAN has outpaced the other models numerically likewise in PSNR and SSIM values.

V. CONCLUSION

To assess the usefulness of our proposed model in restoring the weather degradations, its comparison with various image-to-image transforming models is presented. Our proposed model MC^{2}GAN is proved to be optimal in improving the weather degraded images both visually and numerically. In the future, more weather effects can be added to the unified proposed model. Training and testing can be done on more images. For comparing the performance of the proposed model, more models can be used.

ACKNOWLEDGMENT

I would like to thank the Data Science Lab of Pakistan Institute of Engineering and Applied Sciences (PIEAS) for giving an outstanding informative atmosphere and up-to-date lab services. This research work was backed by PIEAS Information Technology and Telecom Endowment Fund.

REFERENCES

[1] He, K., Sun, J., Tang, X., "Single Image Haze Removal Using Dark Channel Prior. IEEE Transactions on Pattern Analysis and Machine Intelligence," Vol. 33 No. 12, 2341-2353, 2011.

[2] Tan, Z., Bai, X., Wang, B., Higashi, A., "Fast Single-image Defogging," FUJITSU Sci. Tech. J., Vol. 50 No. 1, 60-65, 2014.

[3] Li, Y., Tan, R.T., Guo, X., Lu, J., Brown, M.S., "Rain Streak Removal Using Layer Priors," In: Proceedings of the IEEE Conference on Computer Vision and Pattern Recognition (CVPR), 2736-2744, 2016.

[4] Lu, Y., Xu, M., Jia, S., Huang, W., "Fast snow removal algorithm based on the maximum value of the degree of polarization and angle of polarization," Physica Scripta, Vol. 94 No. 4, 2019.

[5] Qingjiang, C., Xue, Z., "Image defogging algorithm combined with full convolution neural network," Journal of Applied Optics, Vol. 40 No. 4, 596-602, 2019.

[6] Li, B., Peng, X., Wang, Z., Xu, J., Feng, D., "AOD-Net: All-in-One Dehazing Network," In: Proceedings of the IEEE International Conference on Computer Vision (ICCV), 4780-4788, 2017.

[7] Fu, X., Huang, J., Ding, X., Liao, Y., Paisley, J., "Clearing the Skies: A deep network architecture for single-image rain removal," In: Proceedings of the IEEE Transactions on Image Processing, Vol. 26, 2944-2956, 2017.

[8] Liu, Y., Jaw, D., Huang, S., Hwang, J., "DesnowNet: Context-Aware Deep Network for Snow Removal," In: Proceedings of the IEEE Transactions on Image Processing, Vol. 27, 3064-3073, 2018.

[9] Liu, W., Yao, R., Qiu, G., "A physics based generative adversarial network for single image defogging," Image and Vision Computing, Vol. 92, 2019.

[10] Anvari, Z., Athitsos, V., "Dehaze-GLCGAN: Unpaired single image dehazing via adversarial training," ArXiv, abs/2008.06632, 2020.

[11] Matsui, T., Ikehara, M., "GAN-Based Rain Noise Removal from Single-Image Considering Rain Composite models," IEEE Access, Vol. 8, 40892-40900, 2020.

[12] Jaw, D., Huang, S., Kuo, S., "DesnowGAN: An Efficient Single Image Snow Removal Framework using Cross-resolution Lateral Connection and GANs," IEEE Transactions on Circuits and Systems for Video Technology, 2020.

[13] Isola, P., Zhu, J., Zhou, T., & Efros, A.A., "Image-to-Image Translation with Conditional Adversarial Networks," IEEE Conference on Computer Vision and Pattern Recognition (CVPR), pp. 5967-5976, DOI: 10.1109/CVPR.2017.632, 2017.

[14] Liu, M., Breuel, T., & Kautz, J., "Unsupervised Image-to-Image Translation Networks," *ArXiv, abs/1703.00848*, 2018.

[15] Zhu, J., Park, T., Isola, P., & Efros, A.A., "Unpaired Image-to-Image Translation Using Cycle-Consistent Adversarial Networks," *IEEE International Conference on Computer Vision (ICCV)*, 2242-2251, 2020.

[16] Park, T., Efros, A.A., Zhang, R., & Zhu, J., "Contrastive Learning for Unpaired Image-to-Image Translation," *ArXiv, abs/2007.15651*, 2020.

[17] Zamir, A., Shah, M., "Image Geo-Localization Based on Multiple Nearest Neighbor Feature Matching Using Generalized Graphs," IEEE Transactions on Pattern Analysis and Machine Intelligence, Vol. 36, 1546-1558, 2014.

[18] Image Augmentation Library. [online] https://github.com/aleju/imgaug Last Accessed 6th July 2021.

[19] Li, B., Ren, W., Fu, D., Tao, D., Feng, D., Zeng, W., Wang, Z., "Benchmarking Single-Image Dehazing and Beyond," IEEE Transactions on Image Processing, Vol. 28, 492-505, 2019.

PICK AND PLACE HAND-GESTURED-ROBOT FOR PHYSICALLY CHALLENGED PEOPLE

Muhammad Ihtisham Babar
Department of Aerospace Engineering
CAE,National University of Sciences and Technology, NUST
Islamabad, Pakistan
ihtisham.babar23@gmail.com

Muhammad Ibtisam Babar
Department of Mechatronics Engieering
Air University, AU
Islamabad, Pakistan
ibtisambabar786@gmail.com

Azeema Azhar
Department of Mechatronics Engieering
Air University, AU
Islamabad, Pakistan
azeemaazhar786@gmail.com

***Abstract*— Robots, which are used to pick up an object and transfer it to the desired place, are known as pick and place robots. It can be of any shape and design e.g., a cylindrical robot, spherical, articulate or scara robots providing movement in horizontal, vertical and rotational axes. In this article, development of pick and place robot is discussed. The robot is controlled via NRF communication. The robot comprises of two main parts, robotic vehicle and arm. The robotic vehicle is capable to move in all possible four directions. The movement of the robotic vehicle is controlled by gesture human hand wrest using accelerometer. The movement of the arm is controlled by the gesture of human hand fingers using optical sensors. The controlled movement of robotic arm is such that it can pick and place objects up to weight of 1 kg from any source place to desired destination. The prime aim of the designed robot is to make it feasible for physically challenged people to transfer and get things using hand motion.**

Keywords*— *NRF communication, pick and place robot, accelerometer, optical sensor, hand motion.

I. INTRODUCTION

Robots are one kind of electromechanical device which is operated by its internal circuitry. Robotics is one of the new emerging field of engineering in the upcoming years. The demand of the robot's is increasing significantly from education sector to transportation, restaurant and many other sectors. The traditional robot controlled via wire are very common now a days. But lot of wires make it very difficult to handle and limits the distance covered by the robot. The wireless robot can solve these problems. The wireless robot will be controlled by human hand gestures. The movement of robot is controlled by the hand and finger gestures using microcontroller and optical sensors, which makes it a beneficial robot system for user friendly support, bomb disposal, material handling and to enhance the independence of physically impaired persons [1]. It is a kind of efficient alternative for wired control robot that aids the impaired people which often suffers from physical problems. By making the wireless interface using transmitter and receiver of specific frequency, makes the robot to be controlled very easily. Gesture control is so far a better alternative to voice-controlled devices for controlling the robots as voice controls mostly suffers from interruption of unwanted noise and interface.

The main aim of this paper is to design and fabricate a hand gesture-based pick and place robot controlled by NRF communication for physically challenged people. The robot should be capable to move in all possible four directions (forward, backward, right and left). The robot comprises of robotic vehicle and arm. The movement of the vehicle will be controlled via hand gesture wrest. The movement of the arm will be controlled the motion of fingers. The successful transmission is desired between the transmitter and receiver. Gesture recognition is the main task in the design. The movement will act as an input for the motion of robot. Robot will identify the movement of human hand to complete the certain tasks assigned to it. The sensors on the glove will record and convert the raw mechanical data into electrical signals. This data will be further utilized to make it in understandable format by the system.

II. LITERATURE REVIEW

B. A. Malar [2], designed a basic robot which will be controlled by accelerometer rather than button control. The robot moves according to the motion of the hand. Arduino Uno is used in the design of the system.

Wu. [3], implemented hand-gesture control on a smart robot to take data of hand path with the help of three-axis accelerometer. The hand data is sent to computer wirelessly with the help of an RF module. The received paths are then sorted to one of six control commands for navigating a robot. The dynamic time warping (DTW) algorithm is assumed by the classifier to classify hand path. With the help of hand paths, robot can be controlled by the user.

Thivagar [4], developed a voice-based information controlled robot with the help of Arduino. With the help of "hand gesture", feature user can move robot wirelessly depending on the Radio Frequency, placed on the hand.

Kumar [5], designed a system to record wireless movement and controlled the movement of robot using respirators. Robotics and part of body are connected by a wireless connection. Mainly the robot is controlled by Arduino Uno. The aim was to improve the components and programming for a smart arm controlled by an accelerometer, have been achieved. From the idea that has been made, it obviously shows that development and production of this smart robot is easy, friendly and easy to control.

Herkariawan [6], developed hand gestured controlled Arduino based warfare robot. MPU6050 gyroscope was used to determine the orientation of the robot. Nathan [7], concluded that robots are viable options to replace manual operations and integrations of vision and touch sensors in robots can change the work efficiency significantly.

Ifeoma [8], designed a robot which is able to handle real time instructions using gesture control using Arduino mega and Baron [9], designed single application-controlled NXT robot by tracking calibration using gesture and voice command.

Bodiroza [10], discussed the generalized design method of the gesture vocabulary (GV) for intuitive and natural two-way robot-human dialog. The designed is based on motion gestures using robot waiter (RW) dialog. Zhao [11], discussed about the gesture control technology and its impact on the education sector.

III. System Architecture

The complete system comprises of transmitter and receiver end. The gesture sensing glove is the transmitter end while the robot is the receiving end.

1. The Gesture Sensing Glove (Transmitter End)

The block diagram of the transmission end is shown in Figure 1. The main components of the gloves are the accelerometer, optical sensor, Arduino nano microcontroller and NRF with 2.4GHz transmission module. A separate power bank is used to excited all the components of the gesture sensing glove.

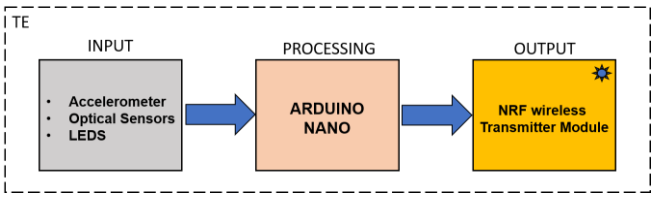


Figure 1 Block diagram of the transmission end

Following are the details of the each component in the transmission end (gesture sensing glove) of the system:-

a. GY-61 Accelerometer

Gy-61 accelerometer is used to detect the exact orientation of glove. It detects the orientation both axes and gives its equivalent analog values to the microcontroller. Gy-61 is a low power, thin, small three axis accelerometer gives easy way to the X, Y and Z axis analog outputs. It is capable of detecting 3g forces in all three axes. It is used commonly in the tilt detecting applications for the shock or vibration evaluation due to dynamic acceleration and static acceleration of gravity [12]. The bandwidth of the accelerometer is selected by the user pin capacitance X out, Y out and Z out. The elective suitable bandwidth depends on the application, X-axis and Y-axis bandwidth is between 0.5 Hz and 1600 Hz, while Z-axis of the bandwidth is between 0.5 Hz and 550 Hz. Accelerometer takes 5V supply for its operation. However, 3.3V on-board regulator is also available letting it to be powered from a 3.3 to 5V power supply source. Its sensitivity is about 300mV/g and is dimension is 20.3mm x 15.7mm. Figure 2 shows the pin configuration of the Gy-61 accelerometer.

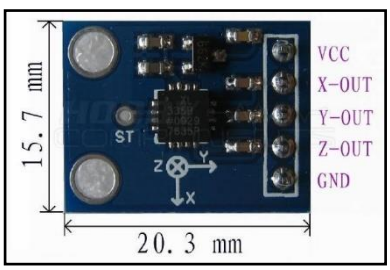


Figure 2 Pin configuration of G-61 accelerometer

b. Optical Sensor

Optical sensor is used here instead of flex sensors, normally used in gesture control systems. Usually Flex sensors are mounted on finger to detect the amount of bend. The change in the internal resistance of flex sensor gives appropriate output to microcontroller. But these flex sensors are very costly. The similar work out can be achieved from a low-cost optical sensor as shown in Figure 3.



Figure 3 Optical Sensor

The optical sensor includes bright LED and LDR (Light Dependent Resistor). The LED and LDR are fixed in at each end of a fixable rubber pipe [13]. When a user bends his finger, the intensity of the light from LED on the LDR changes, the output of the LDR changes accordingly. This change in the output of LDR can be processed by the microcontroller.

c. Arduino NANO

Arduino Nano is used on the glove while Arduino UNO is used on the robotic vehicle. Arduino Nano can be considered as a self-sufficient system with a processor, storage and programmable input/output device and can be used as an implanted system. The Arduino Nano is a small full package circuit based on the ATmega328P; that gives the same specifications of the Arduino UNO but little less.

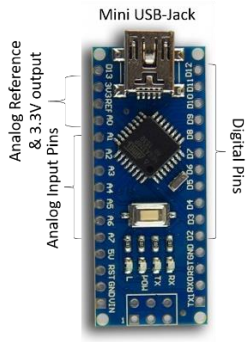


Figure 4 Detail diagram of Arduino NANO

Arduino Nano is another member of the facilely with similar, lesser or more features than Arduino UNO. Arduino Nano Pinout contains 14 digital pins, out of 14; five can be used for built in PWM feature, 8 Pins are for anlog input, 2 Pins are for reset purpose as shown in Figure 4.

d. Wireless Transmission

In the design of our glove system, NRF24L01 wireless transmitter module is used. It runs on frequency band of 2.4 GHz. Its optimal range is 100m which can be increased if the antenna is active. It can work within baud rates of

250 kbps to 2 Mbps. In open area, its range can rise up-to 100 meters, with lower baud rate. The module uses variety of channels which gives a opportunity to have an independently working network modems at the same time. Only 12mA power is consumed by this module during this transmission. The operational voltage of the module is from 1.9 to 3.6V, but the main advantage is that the other pins can endure 5V logic, so it can be easily attached with an Arduino without using any logic level converters. Other characteristics of the NRF radio frequency module is that it is of low cost, easily available and able to make communication possible even through lot of obstacles.

2. Robot (Receiver End)

The receiver end consists of following components:-

a. L298N motor driver and DC motors

The speed of the DC geared motor used here is 125 RPM. Its operating voltage ranges from 5 V to 15 V and draw current of 80 mA to 100 mA. Motors and wheels are shown in Figure 5.



Figure 5 DC Motor mounted on the wheels

b. Servo motors

The servomotor used in the robot is known as Tower Pro MG 945. It has an operating voltage range of 4.8 V to 7.2 V and is capable to provide 10 Kg/cm. The robotic arm will be controlled via Arduino UNO microcontroller and it will be able to grasp, lift and translate objects.

c. Arduino UNO

Arduino UNO boards consists of USB interface, 14 digital I/O pins, out of 14 ports, 6 pins can be used for PWM output and 6 for analog signals [14]. Arduino UNO comes with integral LED, which is attached through pin_{13} as shown in Figure 6.

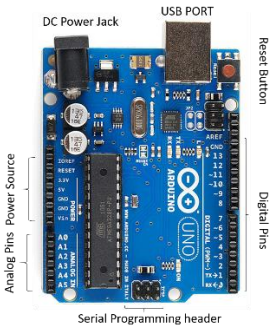


Figure 6 Detail diagram of Arduino UNO

d. Rechargeable battery

The receiver circuit (robotic vehicle) is operated by a 9.4 V rechargable battery.

e. DC Buck Regulator

The servo can operate only on 5V while the receiver cricuit require 9.4V, for this purpose a LM2596 DC-DC buck convertor is used.

f. NRF24L01 with 2.4GHz Receiver Module

Two NRF transceiver are used one as a transmitter in the glove and another as a receiver in the robot. NRF24L01 is an 8-pin board. The pin configuration of NRF24L01 pin 1 and pin 2 will be connected to GND and VCC respectively. Pin 3 is the chip enable used to enable the SPI communication. Pin_4 CSN must be high fir SPI communication. Pin_5 is serial clock used to provides the clock pulse using which the SPI communication. Pin_6 and pin_7 are MOSI (Master Out Save In) MISO (Master in Slave Out) respectively. MOSI and MISO are used to transmit or receive data in SPI communication. The pin configuration of NRF24L01 is shown in Figure 7.

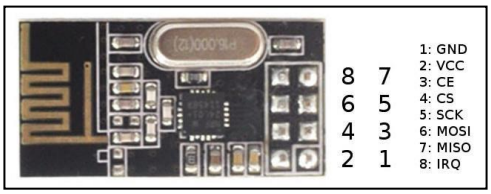


Figure 7 Pin configuration of NRF24L01

The block diagram of the receiver end is depicted in the Figure 8.

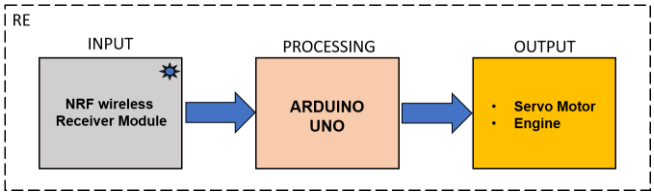


Figure 8 Block diagram of receiver end

IV. ELECTRICAL WIRING

Electrical and electronics components handling is very tedious job in the project. Any miss handling of wires polarity can leads to serious damages. The electrical part of the project is consisting of two circuits i.e., the transmitter circuit and the receiver circuit.

1. The Transmitter Circuit

The movement of the robotic vehicle is controlled by the accelerometer mounted on the glove. The movement of hand that comes from accelerometer is feed into Arduino nano microcontroller board for further processing. The outputs of the accelerometer X-out, Y-out and Z-out are connected to the analog pin A_0, A_1 and A_2 of the microcontroller respectively. The gripper of the robotic arm is controlled by the optical sensor mounted on the two fingers of the glove. The two sensors are connected to the analog pin A_3 and A_4 of the microcontroller. The analog outputs of the accelerometer and

optical sensors are processed by the microcontroller and the output of the microcontroller are transmitted by the NRF module to receiver circuit. The MOSI pin and MISO pin of the NRF module is connect to SPI pins; pin D11 and D12 respectively. The chip enable CE pin of the NRF is connected to pin D_7, CSN pin is connected to pin D_8 and the serial clock SCK is connected to pin D_{13} of the microcontroller. The transmitter circuit is operated by 5V power bank provided for the glove. Figure 9 gives the wiring and circuit diagram of the transmitter.

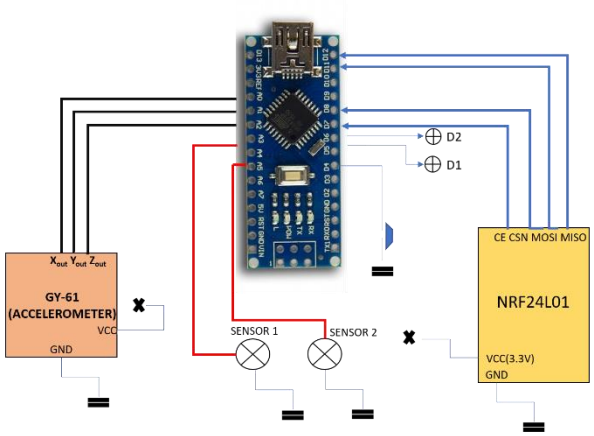


Figure 9 Circuit diagram of transmitter end

2. The Reciever Circuit

The signal transmitted by the NRF of the transmitter is received at the NRF of the receiver on the robotic vehicle. The MOSI pin and MISO pin of the NRF module is connect to SPI pins; pin D_{11} and D_{12} respectively. The chip enable CE pin of the NRF is connected to pin D_7, CSN pin is connected to pin D8 and the serial clock SCK is connected to pin D_{13} of the microcontroller. The code received is processed by the microcontroller and the outputs are generated to operate the motors and servos.

The logical outputs for the motor on the right side of the vehicle are generated from pin_9 and pin_{10} while the left side motor of the vehicle is connected to pin_2 and pin_3 of the microcontroller. The logical inputs of the two servo motors are connected to the pin_5 and pin_6 of the microcontroller. Figure 10 shows the circuit diagram of the receiver.

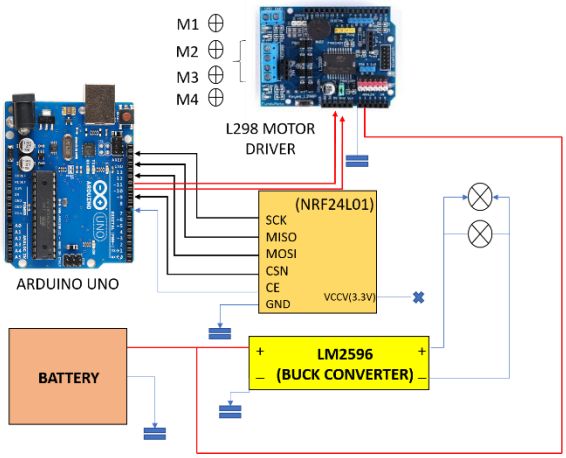


Figure 10 Circuit diagram of receiver end

3. Methodology of Control Motion

Serial Peripheral Interface (SPI) is an interface bus is used to send data between two microcontrollers. The two NRF modules communicates to each other by the SPI protocol. The direction of hand movement is given by the accelerometer. As hand moves, the accelerometer reading varies. This varying signal is sent to Arduino analog input. Arduino board has an integrated 8 bit analog to digital converter. Signal is conveyed to the receiver by the NRF module of the transmitter. The signal is trabsfered to the NRF module of the receiver and is sent to the Arduino digital input for further process. This signal is then transferred to the driver of the motor to rotate the motor such that the robot moves in the desired direction as of hand movement.

The optical sensors also send determinant values to the microcontroller. As the user moves his fingers, the LDR reading varies accordingly. These values are sent to microcontroller analog inputs and a code is generated based on the value of the LDR by the microcontroller which is transmitted to the receiver in order to control the two-servo motor.

V. HARDWARE IMPLEMENTATION

1. Robotic Vehicle

The robotic vehicle comprises of 4 wheels which are attached to the DC geared motors and is controlled by the accelerometer. The vehicle movement have the four motions (Forward, Backward, Left and Right) respectively. The vehicle is controlled by the Arduino UNO on the receiver end through the signal received from the accelerometer on the glove. Four wheels coupled with DC geared motors can be mounted on a wooden base. The forward and backward movement can be achieved by rotating all the four wheels in same direction. For the right turn the RPM of the right-side wheels should be reduced by PWM and for the left turn the RPM of the left side wheels must be lower than RPM of the right-side wheels.

The first part to implement is to design a strong mechanical base for the gesture control robotic vehicle. Base can be made from low weight acrylic with an appropriate dimension of 30cm x 30 cm. Slots of 7 cm are made in order to make space for all the four tires inside the base. Slots are moved 4 cm inward for safety and stability purposes. Wheels can be directly coupled with the DC geared motor. The finally mount all the four DC geared motor to base. Figure 11 shows the CAD model of four wheels coupled with DC geared motor mounted on the base of the robotic vehicle.

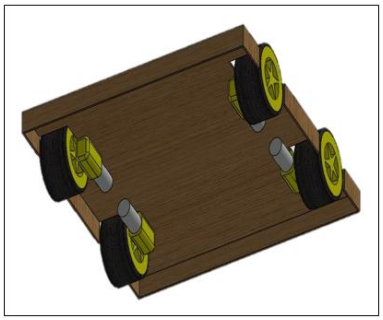


Figure 11 Base of the robotic vehicle

The diameter of the wheel is 6.5 cm while the diameter of the shaft is 0.5 cm.

2. Robotic Arm

Robotic arm is mechanical arm which is statically mounted on the receiver part of the circuit. The gripper on robotic arm can revolve up to 180 degree, which is fixed to the servo motor. Specific load is applied to test the arm for lifting the objects of desired weight (up to 1 kg). The servo motor is used for the purpose of picking and placing the object, because of its the low torque applications. Optical sensor in the transmitter part controls the gripper.

The length of the arm is 12.7 cm. The jaws of the gripper are capable to pick and place an object of width 5cm. Figure 12 shows the CAD model of the robotic arm with opening and closing mechanism. The movement of the arm and micro gripper can be controlled by the servo motor.

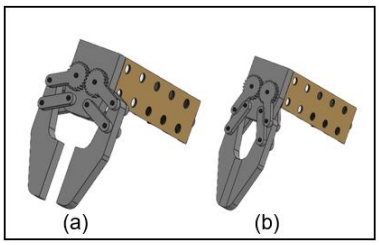


Figure 12 Robotic arm with (a) opened gripper position, (b) closed gripper position

The schematic model of the robotic arm is shown in Figure 13. Several Test is performed to find out the exact limit of the weight that can be easily handled without slipping by the gripping. It is concluded that it can only handle the weight of 1kg, due to the limitation imposed by the gripper and motor.

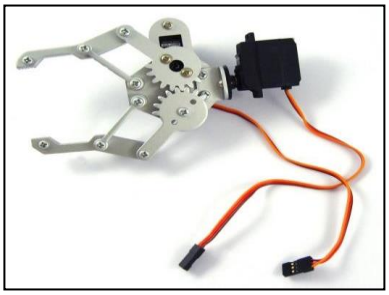


Figure 13 Robotic arm attached with servomotor

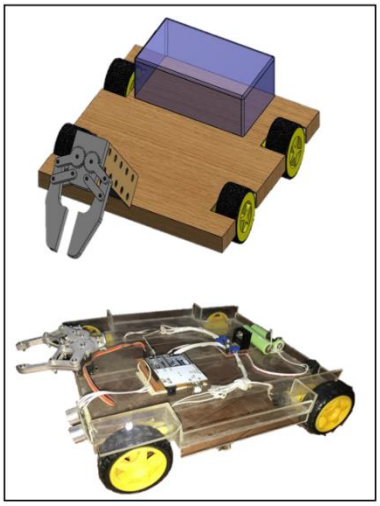


Figure 14 Final model of robot

The complete model of the hand gesture control robot is shown in Figure 14. The base is made in such a way that in future modification, objects can be place on the base with the help of gripper which will make the robot to carry more objects.

VI. TESTING

The accelerometer reading varies between maximum and minimum values, as the user moves his hand. These two values are used to specify the range for each task of robot. If the received value falls between this range, then the equivalent determinant is generated. Then the value of the determinant is received by the microcontroller, which identifies the corresponding movement after processing, and emits signals to move the robot accordingly.

Figure 15 shows the four specific hand gestures that are used to control the robot's motion. When the hand tilts in forward direction, the gesture is identified as the forward motion, and the robot moves forward. The speed of the robot is controlled by the tilt angle. Tilt angle is calculated by the difference between the angle of tilt of hand and the threshold value of forward motion. When the hand tilts in the right direction, the robot identifies the gesture and moves rightward.

Similarly, when hand tilts in the left direction, the robot moves in the left direction. The angle of the tilt of hand defines that whether it is a normal or sharp turn. In a sharp turn a car varies the direction without getting slower. When the user tilts his hand backwards, the robot moves in the reverse direction. To move the robot in the diagonal direction the movement of hand will be in somewhere between two gestures.

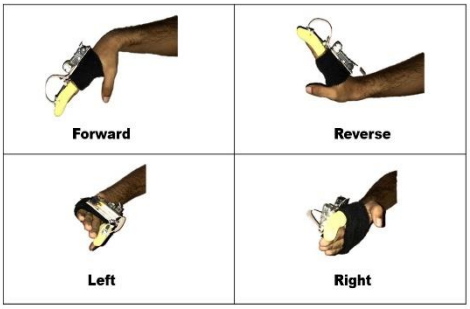


Figure 15 Hand Gestures to control Robot Motion

Two specific gestures to control the movement of the robotic arm and gripper is shown in Figure 16. When the user bends his finger, the gesture is recognized and the arm go in forward direction, when he straightens his finger, the arm goes backward. The gripper is controlled by second finger; the jaws of the gripper closes when the user bends his finger and the jaws of the gripper opens when the finger is straightened.

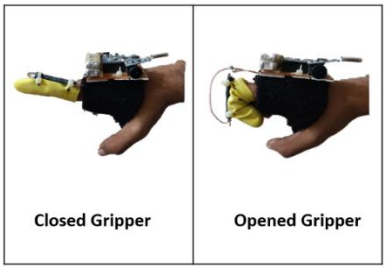


Figure 16 Finger Gestures to control Arm Motion

VII. RESULTS AND DISCUSSION

a. Overall performance analysis

The main purpose of this test is to evaluate the movement response of the pick and place robot. Table 1 shows the movement response of the robot w.r.t different gestures given command. Good means 100 percent accuracy and less depicts accuracy below than 90%.

Table 1 Movement Testing Results

No	Movement	Functions	Responses
1	Hand-Down	Forward	Good
2	Hand-Up	Reverse	Good
3	Tilt Hand Left	Left Direction	Good
4	Tilt Hand Right	Right Direction	Good
5	Close Finger	Close Gripper	Good
6	Open-Finger	Open Gripper	Good

b. Distance testing in open and closed space area

The range testing of the robot is performed to find out actual capability of the robot. Table 2 and 3 shows the behavior of the robot in open and closed space area.

Table 2 Distance Testing in Open space Area

No	Distance (m)	Response	Feedback
1	200	Move	Good
2	400	Move	Good
3	600	Move	Good
4	800	Move	Less
5	1000	No	Less

Table 3 Distance Testing in Closed space Area

No	Distance (m)	Response	Feedback
1	50	Move	Good
2	100	Move	Good
3	200	Move	Good
4	300	Move	Less
5	400	No	Less

The results shows that robot has a range of 800m in open space and 300m in closed space.

c. Weight Testing

The Table 4 shows the tests results of the weight that gripper can carry and hold easily. The results shows that gripper can carry and displace up to 1 kg of weight.

Table 4 Weight Testing results

No	Weight (g)	Pick	Displace
1	200	Yes	Yes
2	400	Yes	Yes
3	600	Yes	Yes
4	800	Yes	Yes
5	1000	Yes	Yes
6	1200	No	No

VIII.COMPARISON WITH PREVIOUS ROBOTS

The designed robot can be controlled within the range of 800m, which is slightly greater than the conventionally designed robots as discussed in literature. Secondly by using the Arduino NANO, and modern receiver, the hand glove system has been made more light weight for the easiness of the user. Thirdly the gripper is controlled only with the movement of finger instead of hand, so that rest of the fingers can be used for multi-tasking in the future version of the robot whereas in previous robots both gripper and robot were controlled by hand. Fourthly, the robot can pick and place the objects up to 1kg easily whereas in previous robots the weight carrying capacity was up to 500g.

IX. CONCLUSION

The purpose of research is to design a pick and place robot using accelerometer sensors attached to a hand glove for the physically challenged people. The designed robot allows the user to control the motion of vehicle and robotic arm by only using the hand and finger. The robot is designed using the accelerometer and optical sensor which is controlled by the Arduino. Finally, a test ready model is developed to implement the idea. The model performed the desired tasks up to the mark. It is concluded that this type of pick and drop robot can help the disable person so that he can use only his hand and finger movement to control the robot for picking the objects.

X. FUTURE WORK

- The robot can only pick the weight up to 1 kg, more powerful motors can be used to pick more weight.
- Camera can be mounted, which could be attached via wireless connection to mobile so that person can pick the things from out of sight places.
- For now, the gripper can only move along single axis, multi axes gripper can be mounted to improve the design.

REFERENCES

[1] S. K. Talakayala, “Design and fabrication of pick and place robotic arm. 2nd National Conference on Recent Trends in Mechanical Engineering, GIST”, Nellore, 2020.

[2] B. A. Malar, "Hand Gesture Control Robot. International Journal of Innovative Technology and Exploring Engineering (IJITEE)", Volume 9, Issue 2,2019.

[3] X. H. Wu, "A Hand-Gesture-Based Control Interface for a Car-Robot. International Conference on Intelligence Robotics and System”, IEEE, Taipei, Japan:2010.

[4] T. Thivagar, "Hand Gesture and Voice Controlled Smart Vehicle. International Journal of Modern Science and Technology", 164-167,2020.

[5] C. P. Kumar, "Gesture Control Robot with Arduino. Material Science and Engineering", IOP Publishing, 2018.

[6] C. Herkariawan “Design control system using gesture control on the Arduino-based warfare”. IOP Conf. Series: Material Science and Engineering,2021.

[7] N. Nathan, “A gesture-controlled system”. International Journal of Science & Engineering Research, 2015.

[8] U. Ifeoma, “Design and Implementation of Arduino-Based Gesture- Controlled System with accelerometer”. International Journal of Recent trends in Engineering and Research,2019.

[9] G. Baron “Gesture and voice driven mobile tribot robot using Kinect sensor”. IEEE International Symposium on Electrodynamic and Mechatronic Systems (SELM), 2013.

[10] S. Bodiroza, “Dynamic gesture vocabulary design for intuitive human-robot dialog”. IEEE 7th ACM/IEEE International Conference on Human-Robot Interaction (HRI), 2012.

[11] L. Zhao “Gesture Control Technology: An investigation on the potential use in Higher Education”. IT Innovation Centre, University of Birmingham, 2016.

[12] R. Grepl, Selection of MEMS Accelerometers for Tilt Measurements. Journal of Sensor,2017.

[13] N. Sabri, "Toward Optical Sensors: Review and Applications. Journal of Physics Conference Series"2013.
[14] L. Louis, Working Principle of Arduino and Using it as a Tool for Study and Research. International Journal of Control, Automation, Communication and Systems (IJCACS),2016.

A Review of Vulnerabilities and Cyber-Security Threats Associated with Overseas Telecom Companies' Operations

M Naveed Tahir
School of Interdiciplinary Enginerring and Sciences (SINES), National University of Sciences and Technology, H-12 Campus
Islamabad, Pakistan
mnaveed.msse20rcms@student.nust.edu.pk

Asim Shahzad
Federal Urdu University of Arts, Sciences and Technology
Lahore, Pakistan
asim.shehzad@fuuastisb.edu.pk

Areeba Azhar
King Edward Medical University
Lahore, Pakistan
areebaazhar383@gmail.com

***Abstract*— Growing technological advancements in Mobile Telecommunication Companies' connectivity services have led them to be a vital component of our daily lives enabling their users to perform routine tasks on the go. On the other hand, this rapid advancement in technology, broadened bandwidth along with tremendous usage have made these companies vulnerable to malware and various security breaching attacks. In addition, vast options of connectivity, device software platforms and telecom services have also made mobile stations critical regarding security and privacy. The current study briefly discussing the telecom infrastructure, reviews vulnerabilities associated with overseas mobile companies, resulting security threats, attacks and their solutions for both mobile stations and switching centres. Vulnerabilities and resulting attacks are classified widely considering various variables. With this categorization, the paper presents an easy and brief view of major vulnerabilities, sources associated with these vulnerabilities, their classification and types which concludes to a critical analysis focusing on why they occur, their effects, possible solutions, contributing internal and external factors and key recommendations for their apprehension and suppression.**

Keywords — cyber-attack, encryption, passive threat, vulnerability, data security and privacy

I. INTRODUCTION

Modern communities have dependent on cyberspace that offers valuable and necessary services for performance of majority of functionality of human life. With the increasing adoption of services based on internet aimed to increase the interactions and connections, the government offices are moving towards transformation of majority of their services online. However, this has led to increasing ratio of cyber-attacks and cyber criminals have been able creating an availability, integrity or confidentiality attack upon networks as well as services. These types of cyber activities may influence or even hinder the essential ICT services. Though research is being done in the field of cyber security, however, it needs to be backed by an authentic assessment of the vulnerabilities which may be associated with various attacks [1]. It is, therefore crucial to analyze these vulnerabilities associated with the operations of Telecom Companies in order to protect our cyber space and further design and implement effective cyber security policies.

Telecom industry in Pakistan is growing at a rapid pace with Pakistan's growing economy being the key factor for its growth. With more than a billion users and four mobile companies, the sector provides employment to a major chunk of population in the country. As this telecom sector is responsible for provisioning of the wide spread services, thus is prone to security and privacy challenges. Majority of the operations being on the Internet necessitates ensuring security and safety of data and information.

This paper contributes a brief yet comprehensive assessment of cyber security threats, security breaches, and vulnerabilities associated with the telecommunication sector in Pakistan linked directly or indirectly to their operations and classified widely based on a number of key variables.

A. Scope and Design of Current Research

The critical data and information gathering required for the study vis-à-vis the access limitation to the telecom companies' infrastructure mainly limited the data acquisition to qualitative research techniques focused on review of pervious researches. As is obvious that no setup or specialized industry would neither share its data highlighting their weak areas and vulnerabilities nor would they allow access into their infrastructure for such sensitive organization level data collection as sharing the knowledge of the vulnerabilities would indirectly mean an in-depth evaluation of their technical infrastructure to an extent so as to identify possible loop holes. Therefore, indirect data collection techniques through literature review remains the method of choice to access the vulnerabilities in form of various cyber security attacks associated with telecom companies. Survey and comparison of telecom security services vis-à-vis the telecom service providers was carried out. The main aim remains assessing the vulnerabilities, attacks which can occur as a result of vulnerabilities, classification of these attacks and any possible solutions already worked upon.

Researchers considered following few questions during the course of research: (a) What is the infrastructure of Telecom sector in Pakistan? (b) What are the security policies and regulatory authorities governing the telecom industry in Pakistan? (c) What is meant by the risks, threats and vulnerabilities associated with telecom sector? (d) What is the basic security architecture? (e) What previous researchers have studied about the vulnerabilities? (f) What are the main sources of vulnerabilities? (g) What are the key vulnerabilities associated with the telecom companies' operations? (h) What kind of attacks are associated with these vulnerabilities? (i) How can these attacks be categorized and classified? (j) What are the implications and possible solutions of the attacks? (k) What could be the way forward to minimize these attacks?

B. Organization of the Paper

The paper is divided into five sections. Section II highlights earlier studies related to the infrastructure of telecom sector, Pakistan's current telecom industry's setup, cyber security issues and vulnerabilities, mobile telecommunications security and vulnerabilities, the authentication issues, data security and privacy. Section III presents an analysis of the related works studied in Section II and summarizes the sources and major vulnerabilities. Section IV documents discussion; we consider some findings and propose some recommendations to minimize the vulnerabilities and associated cyber-attacks. Section V concludes the paper.

II. VULNERABILITIES RELATED TO TELECOM INDUSTRY

A. Threat

A *security threat* may be called as "a potential violation of security" [2]. For instance: (a) unlawful leakage of data (b) unauthorized obliteration or alteration of information or related resources (c) deletion or damage of data (d) disruption or rejection of services (e) impersonation, or masked as a legal entity.

A security threat may be classified as *accidental* or *intentional* and further can be *active* or *passive*.

- An *accidental threat* is one with no premeditated intent such as a system or software malfunction or a physical failure.
- An *intentional threat* is one that is realized by someone committing a deliberate act. Intentional threats may range from casual examination, using easily-available monitoring tools, to sophisticated attacks using special system knowledge.
- An *active threat* is one that results in some change to the state or operation of a system, such as alteration of data or destruction of physical equipment.
- A *passive threat* involves no change of state. Eavesdropping and wiretapping are examples of passive threats.

B. Vulnerability

Vulnerability is "a flaw or weakness that could be exploited to violate a system or the information it contains. If a vulnerability exists, then it is possible for a threat to be realized successfully unless effective countermeasures are in place" [2].

The vulnerabilities associated with the telecom sector may be classified into undermentioned four types :

(a) *Threat model vulnerabilities* resulting from failure to foresee possible future threats.

(b) *Design and specification vulnerabilities* resulting from errors or oversights in the design of a system or protocol and make it inherently vulnerable.

(c) *Implementation vulnerabilities* Introduced by errors or oversights during system or protocol implementation.

(d) *Operation and configuration vulnerabilities* originating from improper usage of options in implementations or weak deployment policies and practices.

C. Pakistan's Telecom Sector Overview

Telecom industry in Pakistan is growing at a rapid pace with Pakistan's growing economy being the key factor for its growth. With more than a billion users and four mobile companies, the sector provides employment to a major chunk of population in the country. The Pakistan Telecommunication Act, 1996 is the key legislation governing the telecom industry [3][4].

The Act proposed the creation of:

- Pakistan Telecommunication Authority (PTA) for purpose of regulating telecom segment.
- Frequency Allocation Board (FAB) to sort out the allocation and further, the assignment of frequency operation band to various telecom operators, broadcasters and private wireless users in Pakistan.
- National Telecommunication Corporation for provision of telecommunication services to government organizations such as defense services, provincial governments and other institutions.
- Pakistan telecommunication Company Limited to provide basic telecom facilities to users.

PTA being the regulatory authority is accountable for formation, operation, maintenance and provisions of telecommunication services in country. In addition, provisioning and reinforcement of licenses to telecom industry's operators is also responsibility of PTA. It provides guidelines, regulates tariffs, investigates complaints and authorizes the approvals for use of various equipment to the telecom companies and service providers [4][5][6].

1) Policies and Deregulation: Mobile cellular policy was launched by Government of Pakistan in 2004 with an objective to promote competition among the cellular companies in Pakistan.it further focused on fair use of frequency bands, encouraging private investments and lay down the rights and obligations of the companies along with customer's facilitations [7].

Broadband Policy was also formulated in the same year to encourage growth of the private sector and appreciate civil service providers to initiate their services. The policy also aimed the provision and development of a high-speed broad band network which would be available without interruption [8][9].

2) Foreign Investment and its Impact on Telecom Sector: Above stated policies coupled with deregulation policy not only encouraged the foreign companies to invest in the telecommunication sector but also enhanced these companies' operations manifold. The Pakistan Board of Investment (BoI) is offering due incentives to these foreign operators to establish and flourish. As per the Pakistan Telecommunication Act PTA is required to [10][5];

"Promote the availability of wide range of high quality, efficient, effective and competitive telecommunication services throughout Pakistan"

As a result, in current situation of security and instability in the country, the massive involvement, operation and data handling being carried out by the foreign telecom companies has led to a number of vulnerabilities and cyber security concerns for their users. Large amount of confidential data is

being transferred or stored via various wireless services, internet connections and direct dialling calls provided by these companies [11][12].

D. Telecom Infrastructure, Cyber Security Issues and Vulnerabilities

Cyberspace offers many services for functioning of modern industrial world and the environment, thereby making the modern communities dependent on it. On the other hand, it has posed a number of challenges. Cyber security is concerned on protecting networks and databases from any cyber security breach, destruction or mutation [13][14][4]. It aims at proposing and providing the capability of influencing the actions of cyberspace thus requiring in-depth knowledge of limitations and vulnerabilities associated with ICT. In today's world, there arises a requirement of thorough and in-depth involvement at various levels of development and operations of the cyber world, including the telecom sector as a major chunk, by the developing countries [9][10].

Although the organization related threats have drawn the attention of researchers and think tanks, however, required attention is not being paid to the vulnerabilities' assessment and cyber security particularly when creating the national security strategies. Cyber security is undoubtedly considered a challenge nowadays for a number of countries including Pakistan [4].

A number of cyber security issues are being faced by Pakistan. Though cyber security issues are threatening the world, security providers in Pakistan have also become alert and concerned due to continuous security breaches and cybercrimes. People and telecom companies' lack of knowledge regarding the importance of digital security is the key reason making them vulnerable to cyber criminals. The two broader aspects of the vulnerabilities associated with the users in telecom sector may be categorized as [5][15];

(a) *External Attacks.* Cyber security attacks on the companies unaware or unable to enforce strict security measures. Ultimately, the company and users, both fall a victim to cyber criminals.

(b) *Internal Attacks.* Risks and vulnerabilities for end users created by the company through various means.

After a number of incidents, the situation has improved and the companies are trying harder to provide digital security to their users. However, the obstacle for a flawless security is the diversity of attacks and old tackling approaches. A rapid advancement is essential because as the technological world is progressing with each passing day, cybercriminals are also getting smarter. Telecommunication companies' major concern is to provide good security setup to be safe from external attacks to allow their end users utilize the services without the concern to digital security [3][4][6][8].

A number of companies are working in Pakistan on threat recognizing systems in order to provide data security. In addition, there are exclusive ways to get better data surveillance technology to prevent mishaps. It appears that digital security companies are currently the only source in Pakistan to hold the vulnerable situation and take the country out of both external and internal threats associated with telecom sector and its operation in the country.

The current cyber security situation can become worsen if the authorities remain unable to get better cyber security through various means as discussed earlier. Acceptance of this vulnerable state by the country / users may make us fall back from our current situation. An excellent collaboration between the technical service providers and security service providers is essentially required to curtail the sensitive situation and the security providers need to be more focused and modified of the security concerns and the possible vulnerabilities to the users and organizations [16][8].

E. Vulnerabilities associated Mobile Telecommunications Security

Mobile telecommunications are developing from agility that is restricted to a particular technological aspect to cross networks flexibility with incorporation of IP. Networks of the future may encompass incorporation of wired as well as wireless networks to provide an extensive new services that is not possible by a sole prevailing network. By utilizing true Fixed Mobile Convergence (FMC), roaming across heterogenous networks is possible. The requirements for the security of each type of access are to be met in various ways, however, all these requirements are be fulfilled for protecting users, assessable networks and applications[4].

Security problems can generally be classified as : -

(a) those arising because of the usage of IP in mobile wireless;

(b) because of usage of various multi-technology networking.

Cyber-attacks put a hazard to wireless networks which utilize IP for the transport protocol. Further, vulnerabilities are prone to appear as a result of the nature of wireless network itself i.e., its mobility. The two most important factors while considering the smartphone based threats and vulnerabilities are [29]: -

(a) Authentication Issues.

(b) Data Protection / Privacy.

1) Authentication Issues: Refrence [17] suggests a mutti-sensors-based protocol for mobile stations for achieving inherent authentication. This system persistently understands patterns of human behaviour as well as the setting by permitting users to utilize smartphone without unsettling user actions. The method can also continuously update and improve the user model. Experiments conducted prove that effectiveness of the model only needs only 10 seconds to execute the it and 20 seconds to sense irregular and bogus requests. Thus, level of accuracy attained by utilizing this model can be up to 90-95% .

Zahid *et al.* [18], suggested an identification system to observe the key users of smartphone in order to distinguish authentic users and quacks. They utilized the data set acquired from twenty-five users for establishing the recommended system. The proposed system has a lesser than 2% fault rate which was observed to be nearly zero once PIN authentication has been done. The authors also coupled their technique with state-of-the-art existing detection methods of the users' keystrokes.

Ref [19] proposed "*Typing authentication and protection" (TAP),* which is basically a virtual key grounded in the typo system of smart phones / devices. The security of smartphone using TAP can be improved with a twostep process i.e. in the login phase and secondly in the post login phase. During first stage, TAP works by controlling the biometric information and morphology of users' hand for protecting the identity

while in the second stage, it controls the TAP virtual key. The conducted experimental trials established the utilization of TAP to conserve security as well as usability of the smart phones.

Reference [20] suggests a non-intrusive validation process using the data collection through orientation sensors in smart phones. Being a new approach, it is functioned by smart devices in a distinctive way whereby orientation sensor is used to store these behavioral biometrics. The authors have concluded that this non-intrusive mechanism may be employed with some intrusive instrument. For instance, using Password or PIN alongside the biometric may enhance the security of the device.

Morris studied on merging qualities of the three different approaches including, hand-written signature, biometrics , face recognition, and voice based systems. Consequently, the author reports authentication accuracy of smartphones which is acceptable for a large variety of applications [21].

Reference [22] state that accessing the network, making user registration is allowed by SIM. As without a SIM and successful verification, mobile phones have no access, so the traffic on the infrastructure of these mobile phones cannot inject. Thus, the enabling SIM is first utilized to conduct an attack and afterwards the usage of such a device by a naïve user makes them involved in the attacks being botnet nodes of the network.

2) Data Protection and Privacy: Authors in Ref [23], studied data protection issue from the perspective of users and investigated need for data security systems for smart devices. Types of the data that are aought to be protected by the users are delineated. Also, the current users practices for data protection are also examined. On the basis of this thorough analysis they showed how different types of data require different security arrangements. The authors have reported the results of an interview based study conducted on a 22 individuals which concludes that although all of the users wish to protect their data, however, the availbe solutions were not found convienient by the users, thus highlighting the need for adaptive and efficient solution.

In his research, Muslokhlove highlights data protection issues against physical threats. The study summarizes the user's requirements for data protection based on surveys and interviews. Requirements for data protection are highlighted after interviews and surveys. It concludes that recognizing the malicious approaches for data access do not cover the requirements of data security and thus remains a number of vulnerabilities [24]. However, authors in Reference [25] believe that privacy of smart devices and the users under their designed framework is protected through semantic policies dependent on settings and privacy of users.

Kodeswaran *et al.* [26] present a framework for implementation of privacy policies in smart phones as well as for data protection. The authors show their framework designed for Android based devices and the results accomplished through that framework.

III. ANALYSIS : ASSESSMENT OF VULNERABILITIES AND RESULTING ATTACKS

In this section, we first identify the main sources of vulnerabilities associated with the telecom sector, then discuss the major vulnerabilities extracted out of the literature and understanding of telecom industry and finally summarize the major attacks on a client's smartphone resulting due to the vulnerabilities associated with telecom companies operation.

A. Sources Associated With Vulnerabilities In The Telecom Sector

Deployment of internet and telecom-based services in various telecom companies operating in Pakistan has increased the incidents of systems' digital security sabotage both from external and internal sources. Though these attacks and incidents are not device or network-specific but commonly used devices and networks are: -

1) Mobile Phones: In the current decade, the smart phone usage has increased significantly as these have become a cheap and convenient source of various services such as sharing and storage of data, online / offline entertainment and games, internet services, phone calls and numerous other applications. Though smartphones provide diverse services, they are burdened with challenges; security and privacy being most important. Most of the smart phones' operations are associated with internet, so security and safety of data is always on the risk. Passwords, PIN and biometric recognition systems are being employed for smart phone authentication, however these measures do not remain reliable with a higher ratio because of guessing and brute forcing can easily counter these measures[28].

Considering the vulnerabilities and cyber security threats associated with the use of smart phones, there are a number of ways of cyber-attacks; a lot of viruses, Trojans and various malware based on smart phone APIs' operations are continuously being developed and mostly they appear as if the user is using a safe software and hence go undetected. Some of these application based tools gather sensitive information of the users for example geo-location without knowledge of the users through GPS based services in smart phone[29][30].

Many smart phones operating systems have been developed such as Microsoft Windows, IOS, Android, Symbian and blackberry. Amongst these Android is the most common due to improved performance. It is based on Linus system architect. It's important to understand that there is a difference between the Desktop OS and the versions created for smart phones. Smart phones enable instant internet connection and communication with friends or gather data and information. As the powerful hardware coupled with advanced operating systems and smart applications increase the capabilities and functionalities of the smart phones, the users become more vulnerable to data security threats since the weaknesses of these systems are continuously being identified and exploited by cyber criminals. These attacks include both; the ones generated by software developer itself and the ones most commonly launched by external agencies in the form of external attacks[31].

Similarly, features including broad band width, multiple interfaces and internet accelerators etc., become a source of viruses spread on the network. Multiple connectivity is associated with high risks and makes the transmission of viruses easier which may further aggravate the threats. Thus, security challenges for smart phone environment may be considered similar to those observed in personal computer environment. "*Threat means possible breach of smart phone's security"* [32][33]. In view of above discussion, smart phone security issues may be summed up into undermentioned categories;

- Authentication problems
- Data protection and privacy
- Vulnerabilities
- Cyber Attacks

2) Internet Services: As a result of rapid adoption and application of internet-based services in pursuit of increased interactions / connectivity, mobile companies are continuously transforming their majority of the services to online. Implementation of internet-based services to such an extent has resulted in an increase in the possibility of security breaches and data thefts despite of the fact that a high-end security measures are also being employed by these mobile operators. Again, the systems are vulnerable to attacks from internal as well as external sources [34][13].

3) Digital Applications: In a developing country like Pakistan where majority of telecom industry are employing the modern IT services extended by telecommunication companies into their infrastructure and the higher authorities are also taking keen interest to use these technologies. These digital applications lead to severe security breach of customers and mobile operators making these companies not secure for their customers.

B. Major Vulnerabilities Associated with Telecom Companies

There are several cyber security attacks and vulnerabilities associated with mobile phone companies operating in Pakistan. The vulnerability can cause insecurity or make the companies a victim to malicious attackers for creating the attacks. These vulnerabilities include the following: -

1) System fault/ defects: This is implausible for any telecommunication company to circumvent defects related to software and hardware. Some companies have faults in their mobile phones. Most of these defects only reveal once the device is put in use with some of these observed earlier and some identified later. Though software related defects can be rectified easily however hardware defects can cause irregularities and rectification is possible through change of hardware or the device architechture. Exploitation of these defects by attackers thus remains inevitable to initiate the attacks on smart phones as well as central data bases[35][15].

2) Insufficient management of applications: Smart devices utilizing the services extended by the telecommunication companies employ a distinctive feature of utilizing flexible APIs in order to develop a number of applications. Nevertheless, if these APIs are not managed properly, it can become a main reason for a variety of cyber crimes. Therefore, mismangement of API appears to be a common reason for code based malicious infections.

APIs can be categorized as Third-Party App Development Open APIs, and Control APIs. Amongst the listed classification of APIs, controlled APIs generally have higher privileges in terms of updating the system, creating files and destroying and fetching data. If somehow, the attackers are able to gain control of these APIs of the companies, attacks can easily be initiated and cyber criminals can exploit the privileges that these APIs can extend to them [36][5][11].

3) Unsecure networks: WIFI technology is being used most commonly by a large number of users. Similarly, other services such as GPS, Cellular Network and Bluetooth are also being used to connecting to internet or any network. There can be two possibilities; either some network device hacker can steal network data packets or the telecom company itself can 'sniff' into the sensitive information. So it is a vulnerability which the end user can overcome by using encryption and related tools in their communication and data / information transfer [37][9].

4) Lack of user's awareness: A potential vulnerability associated with the telecom companies' operations is the lack of awareness of the user to security which must be of prime importance. When the user gets connected to network services provided by the company for downloading data or installing any unknown application, the save button may be linked to some malicious codes thereby being a cause of external security breach or otherwise, the sensitive information passed on to the network for this purpose may be hacked by the service provider [38][15].

Various triggers are set which automatically detect if the required data is being transmitted to steal it for the application developer or the telecom service provider. Activating wireless or Bluetooth can be executed secretly without an indication to the user. So, this is a critical vulnerability associated with telecom sector which can only be overcome with the users' awareness and employing strict security measures [39][6].

C. Vulnerabilities And Attacks On Smartphones Associated With Telecom Service Providers' Operations

In previous sections we have discussed the sources of attacks on users' data and information and the vulnerabilities associated with the telecom companies' operations which when coupled with the identified sources become a cause of security breach by cyber criminals. All computing devices and smart devices are prone to these attacks. These attacks can be broadly grouped into; old attacks and new attacks.

1) OLD ATTACKS

a) Malware: Companies and cyber criminals may launch malwares which attack the users' device by creating an application and providing it for download. Malware is a critical security threat which is slowing the development of wireless applications. It may result into crashing of the data once it is accepted or installed by the user.

b) Radio and Wireless Network Attacks: Services provided by the telecom sector can become prone to the wireless communication intruders who, then, can simulate and launch wireless network based attacks which can be classified as:

- *Active attacks.* These include corruption, spoofing, blockage and modification techniques for data theft.
- *Passive Attacks.* Passive attacks include eavesdropping and sniffing.

The most common technique employed by the intruders or the telecom company onto the vulnerable user in this category of attacks is detecting the information by listening to the communication and data transfer while being broadcasted wireless through the use of malicious nodes. Sometimes a fake Wi-Fi network is created by the intruders to which other users connect and fall a victim of data theft [40][13].

So, it is vulnerability associated with services provided by the Telecom Company which can be dealt by generating encrypted communication and beware of what networks our devices are connected to.

c) Virus: Viruses are software generated by the attackers that infect boot sectors, executable files and even the common files for instance word documents and PDFs etc. Virus actually makes duplication of files which consume system's capacity and capability. They also link the device to unknown source like installation software.

Users remain vulnerable to viruses. A system that can detect and alert smart phones user regarding this vulnerability has been introduced. Using such systems which can study unusual behaviors of the device as well as communication actions taking place within the device to create an alert for the users can help the users to save them from falling a prey to this vulnerability.

d) Worms: These are the programs created by the attacker that replicate the copies from one device to others by employing various transport mechanisms throughout network requiring no interference of the user[7][37].

e) Trojan: Trojan is mostly some useful program that has hidden malicious functions. Intention is to sneak in system by breachng authentication requirements of the administrators. Concerns regarding the security threats pertaining to smart phones users' security are growing as the mobile companies are becoming more complex and dominant for provision of a variety of functions. They are becoming susceptible to the Trojans and viruses of the same class as of personal computers[5][13].

f) Spam: Spam is a malware attachment that can be appended to the digital messages conveyed to the smart phones via electronic mail etc. The attachments appear normal but when a user opens such an attachment, his device gets infected by malicious software such a Trojan or worm. Smartphone zombies are manipulated by the cyber criminals who send junk messages which are used a porthole by the attackers for security breach of smart phones.

2) NEW ATTACKS

a) SMS Based Attack: Another vulnerability associated with services provided by the telecom companies is that a cyber criminal advertises and distributes phishing linkages through SMS. They may also use text messages to feat vulnerabilities. However, applications can be designed to detect this malware and avoid abuse by this vulnerability.

Telecom operators provide a service to their clients to transfer credit / unit through SMS. Subsystem "permission" and ordering mechanism helps establishing haven for SMS based malware and gives them a complete authority over receipt, transmission and hiding of SMS messages. Therefore, malicious confirmations may be kept hidden from telecom operators by the application and have the potential to affect a large set of users and telecom operators.

b) Escalation Attack: These attacks aim to acquire complete access to all the information in a particular device. They may be avoided by employing soft wares that have a scheme to detect and prevent these attacks. If the system or data is called by special components of Andriod based systems, these programs prevent it from happening and thus detection and blockage of the malware is possible.

c) USSD Attacks: USSD stands for Unstructured Supplementary Service Data and serves as a protocol utilized by the operators to run specific functions between user and the operator which include functions such as credit inquiry, sending a prepaid call back etc. USSD mainly consists of these components: interceptor service, permission testing, main activity and boot service.

Smart phones are vulnerable to mainly two types of USSD based attacks by telecommunication operators. The first one is sending an SMS and push notifications network to snip credit. The second one uses the mobile dialer application utilizing USSD protocol being in the background [41][5].

d) USB Connection Attacks: Weaknesses can be exposed in the service provider's system that may be used to pose the vulnerability. Advanced features may be intended to configure and control device.

e) Denial of Service Attack: This category of attacks is usually called DoS attack as it prevents the use of service by operation of data management protocol connection in order to locate the smart phone having Wi-Fi antenna. The attacker creates a false eye Wi-Fi internet access with the help of a device such as laptop, then asks for a Wi-Fi smart phone to terminate the existing mobile broad band connection and link to the created bogus Wi-Fi connection. Once connected, it refrains the targets to connect to other internet links till target user identifies the malicious activity and disables the Wi-Fi. Even the most popular smart phones with IOS and Android are also susceptible to denial of service [42][6]

f) Camera based Vulnerabilities and Attacks: Most of the smart phones have camera and touch screen as essential features. Attacker and service providers can use these features as a tool to attack on the smart phone. Installation of third-party applications from Application stores makes the users vulnerable to attackers. Users fall a victim to the attacks which intend to steal personal information, data and even establish root access to the smartphone or device.

g) Control Flow Attacks: Control flow and runtime attacks include injection of milacious codes or return oriented programming and are one of the most severe threats and critical vulnerability coupled with the services provided by telecom companies. Being common attacks, they have been applied to smart phone applications downloaded by many users [43][5][31].

IV. CRITICAL ANALYSIS AND RECOMMENDATIONS

In today's world of Information Technology, data privacy, vulnerabilities and attacks caused by these vulnerabilities are the key issues related to digital security both for the service providers, mobile stations and the end users. A good and feasible solution to the burning issue of authentication problems can save the users from security attacks. As every user wishes for data protection, therefore data privacy is another key apprehension of clients. Though a considerable breakthrough into the data privacy issue can chiefly be achieved by employing trusted sources and applications, the root cause of most of the attacks is associated vulnerabilities. If these vulnerabilities are addressed, most of the attacks on smartphones and digital data can be saved. In rapidly advancing Information Technology world, achieving 100 % security is difficult, however, continual design and development of the digital security systems keeping in view the associated vulnerabilities can lead to secure mobile stations and networks.

The root cause of most of the attacks is vulnerabilities associated with telecom companies' operations. Based on the study following recommendations are made : -

(a) Mobile companies must introduce active firewalls.

(b) Encryption and authentication algorithm for communication to be improved.

(c) Techniques to avoid denial of service attacks to be introduced.

(d) Proper authentication mechanism to be adopted at mobile switching centers

In view of above stated recommendations, the general cyber-security objectives for ICT networks may be : -

(a) Access to, and use of networks and services to be restricted to only authorized users.

(b) Only authorized users to access and operate on assets they are authorized to access.

(c) Networks to support confidentiality to the prescribed level in the security policies.

(d) All network entities to be held accountable for their own actions.

(e) Networks to be protected against unsolicited access.

(f) Plans to be set in place to address how security breaches are to be handled.

(g) Procedures should be there for restoration of normal operation once a security breach is detected.

(h) The network architecture is to be designed in such a way so that it may support different security policies and various up gradations of different strengths in security mechanisms.

A. Research Limitations

Though extensive efforts have been made to conduct the study and to explore the existing literature as well as telecom infrastructure, however, the study posed a few limitations such as (a) Limited literature particular to Pakistan's telecom industry. (b) Lack of access as well as information sharing by telecom companies due to sensitive and confidential nature of the data. (c) Vulnerabilities present the weakness of service providers and security providers. Moreover, they give a thorough insight into the technical infrastructure of these companies which made the research dominantly qualitative literature review.

B. Ethical Considerations

This research is primarily of qualitative nature and primary as well as secondary sources of information have been used with a main chunk of information gathering from primary sources; wherein the primary sources being the existing literature and conducted surveys and studies. These have been properly cited wherever used throughout the research. Similarly, the secondary sources remained the professionals and experts of the telecom industry who were ensured that their identity would not be shared with anybody and any type of information related to their maintenance setups would be kept confidential.

V. CONCLUSION

In this paper, we first highlight the recent authentication issues, data protection and the evolving privacy problems vis-à-vis presenting the telecom infrastructure. The study investigates vulnerabilities associated with telecom industry operating in Pakistan and attacks that can occur in client's smart phones as a result of these vulnerabilities. Further, sources associated with these vulnerabilities, their broad classification and smartphone vulnerabilities associated with telecom service providers' operations have been discussed. Vulnerability can cause insecurity or make the companies a victim to malicious attacks. We have also identified and categorized these attacks focusing on why they occur, their effects, possible solutions and the contributing internal and external factors. Consistent design and development of the digital security systems keeping in view the associated vulnerabilities, however, can lead to secure mobile stations and networks.

REFERENCES

[1] Hamid, Bushra, N. Z. Jhanjhi, Mamoona Humayun, Azeem Khan, and Ahmed Alsayat. "Cyber Security Issues and Challenges for Smart Cities: A survey." In *2019 13th International Conference on Mathematics, Actuarial Science, Computer Science and Statistics (MACS)*, pp. 1-7. IEEE, 2019.

[2] Telecommunication Standardization Bureau, ITU, "Security in Telecommunications and Information Technology", September 2015.

[3] N. Yildirim, R. Das, and A. Varol, "A Research on Software Security Vulnerabilities of New Generation Smart Mobile Phones," in 2nd International Symposium on Digital Forensics and Security (ISDFS'14), 2014, pp. 6–16.

[4] A. Jawad and M. Shahzad, "Threats of Cyber Security and Challenges for Pakistan", Institute of Information and Communication Technology, University of Sindh, Jamshoro, 76200, Pakistan, Conference Paper · March 2016

[5] A. Awais, H. shabbier, "Pakistan Telecom Sector Overview" Haidermota BNR, Insight, February, 2017.

[6] "Telecom Indicators| PTA" (http://www.pta.gov.pk/index.php/en/telecom-indicators/1). *www.pta.gov.pk*. Retrieved 2018-11-15.

[7] R. van der Meulen, "Gartner says 821 million smart devices will be purchased worldwide in 2012; sales to rise to 1.2 billion in 2013," 2012.

[8] R. van der Meulen and J. Rivera, "Gartner Says Smartphone Sales Grew 46.5 Per Cent in Second Quarter of 2013 and Exceeded Feature Phone Sales for First Time," 2013.

[9] "Global Smartphone Use Continues to Climb, Studies Show." [Online]. Available: http://www.eweek.com/mobile/global-smartphone-use-continues-to-climb-studies-show.html. [Accessed: 30-Oct-2015].

[10] H. Luo, G. He, X. Lin, and X. Shen, "Towards hierarchical security framework for smartphones," in Communications in China (ICCC), 2012 1st IEEE International Conference on. IEEE, 2012, pp. 69–72.

[11] M. Ahmad and N. Musa, "Comparison between android and iOS Operating System in terms of security," in Information Technology in Asia (CITA), 2013 8th International Conference on. IEEE, 2013, pp. 1–4.

[12] M. Goadrich and M. Rogers, "Smart smartphone development: iOS versus Android," in Proceedings of the 42nd ACM technical symposium on Computer science education. ACM, 2011, pp. 607–612.

[13] L. Ma, L. Gu, and J. Wang, "Research and Development of Mobile Application for Android Platform," Int. J. Multimed. Ubiquitous Eng., vol. 9, no. 4, pp. 187–198, 2014.

[14] J. Liu and J. Yu, "Research on Development of Android Applications," in Fourth International Conference on Intelligent Networks and Intelligent Systems. IEEE, 2011, pp. 69–72.

[15] T. Grønli and J. Hansen, "Mobile application platform heterogeneity: Android vs Windows Phone vsiOSvs Firefox OS," in Advanced Information Networking and Applications (AINA), 2014 IEEE 28th International Conference on. IEEE, 2014, pp. 635–641.

[16] 14. D. Tilson, C. Sørensen, and K. Lyytinen, "Change and control paradoxes in mobile infrastructure innovation: the Android and iOS mobile operating systems cases," in System Science (HICSS), 2012 45th Hawaii International Conference on. IEEE, 2012, pp. 1324–1333.

[17] W. Lee and R. Lee, "Multi-sensor authentication to improve smartphone security," in Conference on Information Systems Security and Privacy., 2015, pp. 1–11.

[18] S. Zahid, M. Shahzad, S. Khayam, and M. Farooq, "Keystroke-based user identification on smart phones," in Recent Advances in Intrusion Detection. Springer Berlin Heidelberg, 2009, pp. 224–243.

[19] T. Feng, X. Zhao, B. Carbunar, and W. Shi, "Continuous Mobile Authentication Using Virtual Key Typing Biometrics," in 2013 12th IEEE International Conference on Trust, Security and Privacy in Computing and Communications, 2013, pp. 1547–1552.

[20] C.-C. Lin, C.-C. Chang, D. Liang, and C.-H. Yang, "A New Non-Intrusive Authentication Method Based on the Orientation Sensor for Smartphone Users," in 2012 IEEE Sixth International Conference on Software Security and Reliability, 2012, pp. 245–252.

[21] A. Morris, "Multimodal person authentication on a smartphone under realistic conditions," in Defense and Security Symposium. International Society for Optics and Photonics, 2006, p. 62500D–62500D.

[22] N. Gobbo, A. Merlo, and M. Migliardi, "A denial of service attack to GSM networks via attach procedure," Secur. Eng. Intell. Informatics. Springer Berlin Heidelb., vol. 8128, pp. 361–376, 2013.

[23] I. Muslukhov, Y. Boshmaf, C. Kuo, J. Lester, and K. Beznosov, "Understanding Users' Requirements for Data Protection in Smartphones," in 2012 IEEE 28th International Conference on Data Engineering Workshops, 2012, pp. 228–235.

[24] I. Muslukhov, "Survey: Data Protection in Smartphones Against Physical Threats," in Term Project Papers on Mobile Security. University of British Columbia., 2012.

[25] D. Ghosh, A. Joshi, T. Finin, and P. Jagtap, "Privacy Control in Smart Phones Using Semantically Rich Reasoning and Context Modeling," in 2012 IEEE Symposium on Security and Privacy Workshops, 2012, pp. 82–85.

[26] P. Kodeswaran, V. Nandakumar, S. Kapoor, P. Kamaraju, A. Joshi, and S. Mukherjea, "Securing Enterprise Data on Smartphones Using Run Time Information Flow Control," in 2012 IEEE 13th International Conference on Mobile Data Management, 2012, pp. 300–305.

[27] V. Remenar, S. Husnjak, and D. Peraković, "Research of Security Threats in the Use of Modern Terminal Devices," in 23rd International DAAAM Symposium Intelligent Manufacturing & Automation: Focus on Sustainability, 2012.

[28] Maji and K. Hao, "Characterizing failures in mobile oses: A case study with android and symbian," in Software Reliability Engineering (ISSRE), 2010 IEEE 21st International Symposium on. IEEE, 2010, pp. 249–258.

[29] O. Riva and C. Qin, "Progressive Authentication: Deciding When to Authenticate on Mobile Phones.," in Presented as part of the 21st USENIX Security Symposium (USENIX Security 12)., 2012, pp. 301–316.

[30] F. Al-Qershi, "Android vs. iOS: The security battle," in Computer Applications and Information Systems (WCCAIS), 2014 World Congress on. IEEE, 2013, pp. 1–8.

[31] D. Padmavathi and M. Shanmugapriya, "A survey of attacks, security mechanisms and challenges in wireless sensor networks," arXivPrepr. arXiv0909.0576, vol. 4, pp. 1–9, 2009.

[32] M. A. Dar and J. Parvez, "Smartphone operating systems: Evaluation & enhancements," in 2014 International Conference on Control, Instrumentation, Communication and Computational Technologies (ICCICCT), 2014, pp. 734–738.

[33] J. H. Choi and H.-J. Lee, "Facets of simplicity for the smartphone interface: A structural model," Int. J. Hum. Comput. Stud., vol. 70, no. 2, pp. 129–142, Feb. 2012.

[34] W. Lee and R. Lee, "Multi-sensor authentication to improve smartphone security," in Conference on Information Systems Security and Privacy, 2015, pp. 1–11.

[35] Reddy, G.N. & Reddy, G. 2014, "A Study of Cyber Security Challenges and Its Emerging Trends on Latest Technologies", arXiv preprint arXiv:1402.1842, .

[36] Sebastian Bortnik 2012, Trends for 2013: astounding growth of mobile malware, WeliveSecurity:Security news, views and insight from the ESET experts, ESET Latin America.

[37] Ten, C., Manimaran, G. & Liu, C. 2010, "Cybersecurity for critical infrastructures: attack and defense modeling", Systems, Man and Cybernetics, Part A: Systems and Humans, IEEE Transactions on, vol. 40, no. 4, pp. 853-865.

[38] Threat Track Security 2014, December 12, 2014-last update, Spammers Accelerate Dyre Distribution [Homepage of Threat Track Security],[Online]. Available: http://www.threattracksecurity.com/it-blog/ [2015, January12, 2015].

[39] Z. Farhan, M. Shah, K. Muhammad, J. Qiaser and Z. Sejing, "A Survey on Security for Smartphone Device", *International Journal of Advanced Computer Science and Applications, Vol. 7, No. 4, 2016.*

[40] Telecommunication Standardization Bureau, ITU, "Security in Telecommunications and Information Technology", September 2015.

[41] A. Agrawal and A. Patidar, "Smart Authentication for Smart Phones," Citeseer, vol. 5 (4), pp. 4839–4843, 2014.

[42] P. Schulz and D. Plohmann, "Android security-common attack vectors," in Rheinische Friedrich-Wilhelms-UniversitatBönn, Germany, Tech. Rep, 2012.

[43] C. Pettey and R. van der Meulen, "Gartner says worldwide sales of mobile phones declined 3 percent in third quarter of 2012; smartphone sales increased 47 percent," Gartner),[Online], 2012.

Sentiment Analysis of Social Media Text for Selective World Events and Geographical Segregation

Muhammad Ahsan khan
Institute of Space Technology
Islamabad, Pakistan
71ahsan@gmail.com

***Abstract*— This document covers the domain of natural language processing and the use of natural language processing (NLP) to make a filter on social media (in our case Twitter) text which in return will give us feedback about how a specific topic, entity or scenario is seen or felt by different and huge population. In this paper we are trying to apply sentiment analysis on Twitter. Our final model is going to give us amount of positive and negative tweets about a given input word that we are interested in, such as, event, entity etc. This paper will go briefly through popular neural networks that have been used till 2018 for sentence classification. This paper is not explanation of all the neural network architectures such as those found in surveys rather it will share the author's thoughts regarding implementation of Sentiment Analysis based on practical constraints.**

Keywords— ***NLP, Artificial Intelligence, Text Classification***

I. INTRODUCTION

Sentiment analysis (SA) is a technique in which the aim (obvious by its name as well) is to detect/know sentiments of individual(s) regarding anything that may be a person, place, scenario etc. [2]. In this study we will divide individual's emotions in two categories, that are positive and negative.

SA helps us to have insights on large amount of audience, say for example Apple users all from around the world, which were 1.4 billion in 2020[11]. And hearing views from all of 1.4 billion people is impossible for a human or organization. So, we train our system to diagnose the audience and in return hope that it gives us the crux of what are the demands/wants/sentiments of individuals.

The concept of our study lies in the fact that if those users are kept under consideration and a mechanism is engineered which filters this enormous useless data (comments) into useful data (which our machine can understand), then a machine can quickly analyze the data and can give us how the audience are seeing a particular thing/character/scenario etc. By this, we can save an enormous amount of time and can quickly have our analysis which can prove very beneficial for an organization/company/institution/person.

This paper aims to analyze Twitter data. For this analysis, users from United States of America (USA) are kept under consideration. The final shape of analysis will be to have a GUI (map) that will show the amount of percentage of tweets that are positive and negative about any given input entity/scenario etc. with respect to the States. Since our work's genre is purely based upon research of past popular practices in machine learning/deep learning in text classification, so we will put forward the popular neural architectures we came across in our literature review and describe them briefly theoretically and practically.

II. WORD RERESENTATIONS

A. Word Vectors

Since words are unstructured data, before 2013, generally words were represented as one-hot encodings and that was a massive flaw in the development of neural architecture, as our input vector of words would not have semantics' information in its vectors. The problem was two folds. First was that one-hot encodings (each word's vector length equaled to the number of words in the vocabulary) had a sparse vector of zeros which carried no meaning in the first place. Other problem was the complex computations done in neural network which did not favored/allowed computation due to constraint of computation power by high-end systems back in the days.

In 2013, Google research team made a 'bottle neck' solution for obtaining a lower-dense vector representation of every word in the vocabulary [1]. The concept is equivalent to 'Auto-encoders' neural architectures in which the whole aim is to find a small dimensional vector representation of a given input.

Google team published two papers in the year 2013, both finding lower dimensional vectors which are dense representations.

The whole intuition behind these architectures is to develop a way in which a word can be expressed in regards to its surrounding/context words. If the word gets expressed in this manner, then it is likely that the word's vector is enriched with its semantic nature. This idea also suffices the idea of how we (humans) interpret language/words because according to a famous American linguist, John Firth, whom says, "You shall know a word by the company it keeps."

These architectures have been implemented on very large corpus which has 100 billion of words [3]. This huge amount of data has given us an opportunity to gather the 'connections between the words' or semantics of all words via just few equations.

1: Continous Bag Of Words (CBOW)

In this a context is given as an input and a two-layer neural architecture tries to predict the specific word from whose surroundings the context was taken. In Figure 1, left side, shows a representation of this architecture taken from their

paper [1]. In the input, one-hot encoded words are added and linearly transformed in the first hidden layer and then the hidden layer is linearly transformed again to an output layer which is followed by a hierarchical soft-max (nonlinear function). In the soft-max layer, theoretically, we are intending to maximize the probability of the required word (in one-hot encoding) among all words in the vocabulary. After training/back-propagation, the weights between hidden/projection layer and input layer, and projection layer and output layer are added or concatenated. And these are the new representation of the output word. If the same word comes again as an output (in future iterations) then the resultant matrices are added to its previous dense vector.

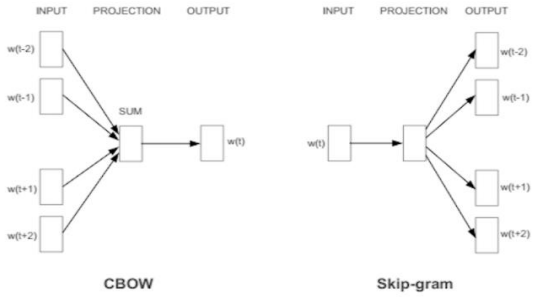


Fig. 1. CBOW (left side) and Skip-gram (right side)

2: Skip-gram

This model is the opposite of CBOW. Here we give an input word and the neural network tries to predict the surrounding words, it is shown in Fig. 1, right sided. In this research paper [2] they have implemented everything similar to CBOW except that the inputs and outputs are now completely opposite in number of words, and a new concept called 'Negative sampling' is also introduced. Previously [1], in the computation of soft-max, the algorithm would take out soft-max of all vocabulary which was very computationally intensive as vocabulary would reach in millions [1]. In Negative-sampling (NS) [2], the algorithm deals this task as supervised classification task rather than unsupervised approach in [1].

For NS, 2 sets are generated. One has proper context and word pairs. The other set has context and word pairs that do not occur in the corpus (they are random pairs). Once context and word are considered from the corpus, the algorithm randomly selects other words that are not pairs. The randomly selected words range from 2 to 5 for large corpus and 5-20 for small corpus [2], these numbers have no proper mathematics behind them as they are taken out by hit and trial method.

So, what it means is that now the neural network has to just change and update weights for the word(s) that are actually the answer(s) and for the random samples. Through this approach, computation power is saved hugely at every iteration because before NS, all of the probability of words were computed (using soft-max function), and now through NS, only word(s) plus 'k' number of bad/incorrect pairs are computed. The formulae which the paper gives for log-likelihood is given in Fig. 2.

$$\log \sigma({v'_{w_O}}^{\top} v_{w_I}) + \sum_{i=1}^{k} \mathbb{E}_{w_i \sim P_n(w)} \left[\log \sigma(-{v'_{w_i}}^{\top} v_{w_I}) \right]$$

Fig. 2. Formula for negative-sampling (from the paper [2])

III. Neural Architectures

A. Convolutional Neural Architecture

In 2014 a one-layer architecture of CNN was proposed by Yoon Kim [3]. The simplicity of the architecture with promising results is the main hype of this paper. It was one of the first paper that used semantic representation of words. Fig. 3 shows its accuracy on different datasets.

In this input word vectors of each sentence were given and 100 filters each of size 2,3 and 4 were applied. It is then passed through a Max-pooling layer which takes out the most significant value out of the vector/matrix. After that they are passed through a fully connected and sigmoid layer. The diagram is shown in Fig. 4.

Though, its results are promising in regards to its simplicity but this architecture is not fit to be used in NLP because this architecture do not full fill the intrinsic property of how a sentence must be read as we humans do. Generally, this architecture is finding a sequence of words in our training data that generally corresponds to our binary classification. It is analogous to how CNN first detect edges in a picture in its early layers and then start to detect minute details such as eyes etc., as the picture go deeper in the network. We can generally say that though the architecture has learned general combination of words but this does not mean that its 'general word's combination' will work on Test data because the amount of vocabulary and the style of interpretation is quite vast in human beings.

Model	MR	SST-1	SST-2	Subj	TREC	CR	MPQA
CNN-static	81.0	45.5	86.8	93.0	92.8	84.7	**89.6**

Fig. 3. Datasets accuracy from the paper

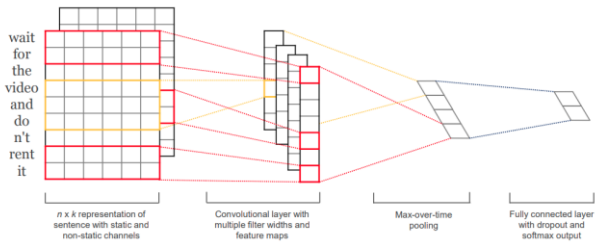


Fig. 4. Architecure of Yoon-Kim's CNN model(taken from its paper [3])

B. Recurrent Neural Network Architectures (RNN)

We humans absorb a text document or a sentence in a sequential manner because we generally go from the first word to the last word of the sentence and try to find out the meaning of the sentence. The meaning of the sentence in our brain evolves from time to time (from start to finish) while we are reading the text. This sequential manner is sort of mimicked in RNNs, as inputs are computed in a sequential manner.

RNN is a dynamic neural network which means that it changes its hidden state with respect to input. Theoretically, it is used in places where a memory or sequential/temporal information is required. Every time step learns an input given at that instant in regards to the previous given inputs/temporals. It is shown in equation 1 and diagram is

shown in Fig. 5. Equation 1 gives the mathematical interpretation of maximum likelihood. In this 'x' terms are the inputs words. Equation 2 represents a generic computation done at each temporal step in which 'g' represents a nonlinear function, x(t) represents input word, a(t-1) represents information from the past temporals, rest of terms are the learning weights. The other most popular architectures used in NLP in sequence modelling (other than RNN) are Long Short-Term Memory (LSTM) [6]and Gated Recurrent Unit [4] which will be discussed later.

The drawback of this (RNN) architecture is the inability to capture long-term-dependencies due to vanishing gradients and exploding gradients [5] as either the architecture does not learn or resist to learn data respectively. During back propagation, the inputs/weights of inputs that are far away from required loss functional node tend to produce either no effect or extreme high effect thus making our learning extremely slow or impossible to learn respectively. This is due to the derivative's contribution at each time step, because when moving from right to left (in back propagation) each temporal step requires its derivative to get multiplied on its temporal step before going further to the left (chain rule in derivative).

Equation 3 shows one derivative effect of the previous temporal towards the present temporal. One can see that how weight is multiplied at the very end. The same multiplication process is done for other previous temporals which means that same weight will be multiplied, but now, with the power of the number of previous temporals from which we are calculating their effect on the required temporal (which is the last layer in our case).

The weights of all temporal steps are the same (RNN has this property because we are trying to capture general representation of data from first temporal to the very end temporal), so if the matrix has the values less than 1 then its multiplication will make the derivative value close to zero which will make the gradient vanish, On the other hand, we will get a very large value if values of the matrix are greater than 1.

RNNs gets addition in layers as input (word) is incremented. This drawback in RNN architecture does not appreciate us to opt it as the 'gradient problem' can be encountered more because the more the temporal steps i.e., input words in a sentence are, the greater is the chance of vanishing or exploding gradients.

To our knowledge there is no research paper which has given analysis about the number of words that would work efficiently on RNNs. On the other hand, we are hoping to have long sequenced texts and if those long sequences are effectively quantified/analyzed then our system would cater all and different kind of Tweets effectively in a practical environment.

$$p(x1,\ldots,xT)=p(x1)p(x2|x1)p(x3|x1,x2)p(xT|x1\ldots xT\text{-}1) \quad (1)$$

$$a^{(t)} = g(W_{aa}a^{(t-1)} + W_{ax}x^{(t)}+b_a) \quad (2)$$

$$d(a^{(t)})/d(a^{(t-1)}) = (\text{inner function derivative}) * W_{aa} \quad (3)$$

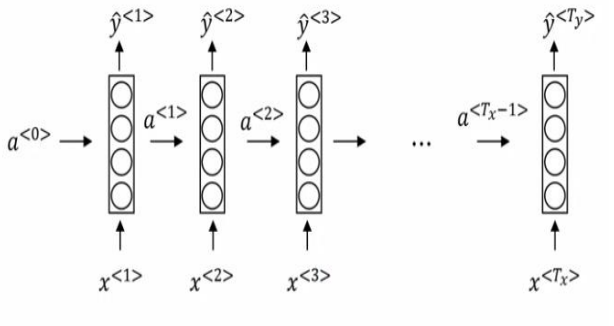


Fig. 5. Basic RNN architecture. Our analysis result will be only on the last output. The other outputs are shown for the reader's understanding to let them know that we can take output at each temporal (if we want to).

C. Long Short Term Memory(LSTM)

There are other solutions to the vanishing and exploding gradient problem rather than introducing new architectures such as gradient clipping and using skip connections in scenario of gradient exploding and vanishing respectively. In gradient clipping we just deduct a user defined value from the slope (gradient) if our gradient gets larger from a specified value in order to retain our learning rate rhythm with respect to our loss curve [4] [5], while in skip connection we add a direct input from past layers which makes the past layer(s)'s information directly accessed by the future time steps [12]. The other approach to overcome the gradient problem is to devise a new neural architecture.

LSTM [6] uses gates to control and propagate the flow of information. It has Input gate, Forget gate, Output gate. Equations 4,5,6,7,8 and 9 are showing the processes done at every temporal. LSTM has the advantage to store information in each time step and carry it forward in time steps (if it realizes that the information is necessary for upcoming temporals).

Theoretically, they are designed in such a way that if an information is seen important at any time step by our machine, then the Forget gate will remember it and carry it for a longer number of time steps thus ensuring long-term-dependency capture (which was the main flaw in RNN), or vice versa.

In the equations the memory is called a Cell. Forget gate (F) decides what shall be kept from previous cell state or changed i.e., updated with new variation. Input gate (I) decides what to write from current time step into the Cell/memory. Output gate (O) decides what part of the overall memory (after addition of the information from the present temporal to the cell state) must be written to the output or hidden state. 'c`' is the new information computed from the current temporal's information for memory. On this intermediate cell state i.e., 'c`', we apply Input gate which takes the necessary information from 'c`' vector, which then gets added to the memory/Cell. 'C' is the overall combination of previous cell state and current cell state, after the application of gates. 'H' is the output given to the next time step which is taken from 'C' or cell state which it thinks is necessary for the next temporal's computation. 'g' corresponds to sigmoid function and the rest of the variables are learning weights.

One can think of it as equivalent to conversating with a person. In which one does not tell everything (what the individual has stored in his mind while hearing the other

person) every time whenever they speak to the other person, rather, the individual just decides what information is necessary to tell from all of the information which the individual has stored in mind.

Here contrary to RNN, we will not have the problem of vanishing or exploding gradient because none of the weights will be repeated with the same value. Another advantage is that there are more weights, so this gives the architecture more expressivity or gives more opportunity to learn the data at each temporal.

$$F^{(t)}= g(W_f\, h^{(t-1)} + U_f\, x^{(t)} + b_f) \quad (4)$$

$$I^{(t)}= g(W_i\, h^{(t-1)} + U_i\, x^{(t)} + b_i) \quad (5)$$

$$O^{(t)}= g(W_o\, h^{(t-1)} + U_o\, x^{(t)} + b_o) \quad (6)$$

$$c`^{(t)}= \tanh (W_{c`}\, h^{(t-1)} + U_{c`}\, x^{(t)} + b_{c`}) \quad (7)$$

$$C^{(t)}= F^{(t)} . C^{(t-1)} + I(t) . c`^{(t)} \quad (8)$$

$$H^{(t)}= O^{(t)} . \tanh (C^{(t)}) \quad (9)$$

D. Gated Recurrent Unit (GRU)

GRUs [9] are equivalent to LSTM but has a smaller number of computations [5]. Here in the explanation, contrary to Cell state/memory (in explanation of LSTM) we will use the term 'hidden state'.

It has an Update gate (U) which decides what part(s) of current and previous temporal's hidden states are to be retained or deleted or changed. It has a Reset gate (R) which decides which information of previous hidden state is necessary to compute the current temporal data. 'h`' is new hidden state of current time/temporal step and 'H' is the combined combination of previous and current hidden states. The general computation for one temporal is shown in Equations 10,11,12 and 13.

Our analysis on temporal based networks found two flaws. According to the paper [5] and to our research there is no concrete evidence (theoretically) in the literature that LSTM or GRU would suffice the problem of long-term-dependency if our input sentence is very long. By 'very long' we mean more than 100 words because we are assuming that our comments of Twitter are not always supposed to be small in length. The other reason is the 'sequential process' of all temporal architectures. This means that second input will start its computation once first input computation is done and so on.

The main reason we see for this is that at the time of RNN and LSTM, the world was not familiar with the concept of parallel processing done with GPUs and researchers did not keep this constraint in the design of their architectures. We in our research are aiming to take maximum advantage of GPU and also find an architecture that ensures a better memory based processing of information of a sentence.

One theoretical intuition we found was that though GRU tries to mimic the same process of LSTM with less computation, it will have a less accuracy on dataset due to less weight matrices learning at each time step as we generally know that the more weight matrices are, the greater would be the learning of the neural network.

One thing we concluded from our study is that due to the vast expressivity of our language, the dense information with respect to temporal (sequence) and the vast vocabulary of semantic nature really makes it hard on sequence models to make them understand on a test set. As one sentence can be written in multiple ways reflecting the same meaning, so intuitively, it seems to us that there is less chance of making our machine understand well as compared to pictures or videos where clues like edges and borders tend to be same regardless of where an object is in the picture (in the case of CNN) [13].

$$U^{(t)}=g(W_u h^{(t-1)}+U_u\, x^{(t)} + b_u) \quad (10)$$

$$R^{(t)}=g(W_r\, h^{(t-1)} + U_r\, x^{(t)} + b_r) \quad (11)$$

$$h`^{(t)}=\tanh(W_h(r^{(t)}.h^{(t-1)})+U_h x^{(t)}+b_h) \quad (12)$$

$$H^{(t)}= (1-u^{(t)}).\, h`^{(t-1)} + u^{(t)}.\, h`^{(t)} \quad (13)$$

E. Transformers/Bi-directional Encoded Representations from Transformers (BERT)

Till now our study summed up to three important constraints. CNN has the ability to capture the sequence for both positive and negative polarities but it is limited to the vocabulary and sequence of vocabulary used in the training data. Sequential architectures have the problem of vanishing gradient even in LSTM [16] as well if input length gets larger. On the other hand in sequential architectures, there is also a lack of parallel computation i.e., ensuring the maximum use of GPU for efficient computation.

These above important constraints were all catered in Transformers architecture back in 2017.

The Transformers architecture [7], Fig. 13 came in 2017 and BERT [8] architecture came in 2018. The Transformers architecture is composed of Encoder and Decoder block. Our study's interest is in their Encoder block as BERT model is established only on Encoders.

Encoder block is based on parallel mechanism (which the sequential neural architectures lacked) that takes in an input of a sentence and tries to induce information of all the words in every word with respect to semantic nature and their respective position in the sentence.

Difference between Transformers and BERT is generally in two ways. BERT has an array of Encoder blocks whereas Transformers architecture has arrays of both Encoder and Decoder. BERT takes in information in a sentence in both direction whereas Transformers architecture computes information from left side only (in translation such as from French to English).

In the architecture, first comes the Positional Encoding (PE) block which is required to give a 'signature' of position to each word because all of the words are processed parallelly. The formulas are shown in Equations 14 and 15. Equation 14 and Equation 15 corresponds to words' dimensions that are at even number and odd numbers respectively. Here 'i' represents the sequence number of the dimension of the word's vector and 'd' corresponds to output's total dimension that the architecture produces after performing computation. In Transformer architecture [7] they use 'd' as 512.

Once the PE is calculated it is then added to the original word's vector respectively. Through this we infuse the position information of every word. Figures from Fig. 6 to Fig. 9 show the effect of how sequence of positional encoding changes as position of the word gets further from the start of the sentence. We can see more '1's' addition to

the dimension of the word's vector as the word gets further from the starting word.

$$PE(pos,2i) = \sin(pos /10000^{2i/d}) \quad (14)$$
$$PE(pos,2i+1) = \cos(pos /10000^{2i/d}) \quad (15)$$

After addition of the sequence information, the next step is to multiply each word with a weighted matrix of Query, Key and Value. These matrices are responsible to convert each word (which we gave in the input) to three new and different representations. The intuition behind Query, Key and Value is the format of a database structure. Key might be a person's name and value will be the person's phone-number. Query on the other hand can be information asked regarding Key and Value such as whether a specific person name with golden phone-number is present or not.

Once the multiplication (linear transformation) is done by the weighted matrices, we will have 3 different representations of one word. For instance, let us assume we have 4 words (of input dimensions of 3) in a sentence shown in Fig. 10. As an example, we are considering the first word. What we do is that we take the first word's Query vector and have dot product multiplication with all the words' Key vector in the sentence (including itself). Which means that first word's Query vector gets multiplied (dot product) with all of the keys' vector separately. Now, after that when all of the dot product multiplications are computed parallelly then we make them normalize and apply SoftMax function so that our dot products answers are brought in range from 0 to 1. Normalization is done by dividing it by the dimension of the vector of key in order to avoid operating very large numbers because there is a possibility that our dot product might result into a very large number [7].

Then we multiply each answer with its own word's Value vector. From this we see that how much each word was contributing individually in regards to the Query vector. Then after that we add all the vectors of all the words. And this is now the final/new representation of the first word (Query word) with respect to all 4 words.

From the above process the first word (Query word) now has all the contextual/surrounding information, achieved parallelly. The diagrams of all processes are shown in Fig. 10, Fig. 11 and Fig. 12. Here we considered 'I' word from the sentence 'I study at school'. The last column in Figure 12 will be summed up to have a contextual representation of word 'I'. This above process will be repeated to all the words and they all will get the same dimensional representation.

The above given process is known as a single 'Head' in the BERT paper. There are a total of 12 heads which means that there are 12 different Queries, Values and Keys for each word. It is referred to as 'Multi-Head' attention, Fig.14.

The intuition behind it is that since the machine can not properly concentrate (or figure out similarity of all words with one another) on each word and find the context which is necessary or important with in a sentence in one go. So, it is wise practice to give our machine room to concentrate on different combination of words in different attention heads. The reason for doing is to enable our model to detect different attentions on different things such as nouns with verbs, nouns with preposition etc.

When all of the attention heads perform their computation parallelly, because none of the processes (heads) are dependent on one another, then we concatenate their results and multiply it by a matrix W^o to bring it down to the dimension of the words that were given at the input.

After that our resultant matrix goes through position wise fully connected layer which means each word is linearly transformed separately in the layer and none of the words are sharing their information with each other.

The above-described whole process is replicated 11 times more in BERT. For our classification purpose we then added a classification layer (that is sigmoid layer) which gets us our final output of whether an input sentence is positive or negative.

The model we use is $BERT_{BASE}$ model which has 12 Encoder layers, with 768 hidden size and 12 Attention heads. Its total parameters are 110Million.

We used a pretrained model of $BERT_{BASE}$ and fine-tuned it. Its training is done on two tasks. Firstly, it is trained on Masked language modelling which means that a big corpus/document is given to BERT and 15% of the words are made hidden/masked from BERT. In training, BERT job is to predict the word that is hidden/masked by looking at the words that are present at either side of the hidden word in the sentence.

The other training approach done on this model is to give 2 sentences from a big corpus. The model is then required to predict whether the second sentence is likely to follow after the first sentence.

The miracle of this model is that this paper is the proof that if a big/huge model is trained well enough then it can work on small problems in that relevant field with just a little fine-tunning [8]. A table from BERT paper is given in Fig.15 which shows its performance compared to other neural architectures.

The reason to pick BERT is not only for best-accuracy-chase rather this algorithm gives us State of the art (SOTA) results on other 11 NLP tasks [8] as well.

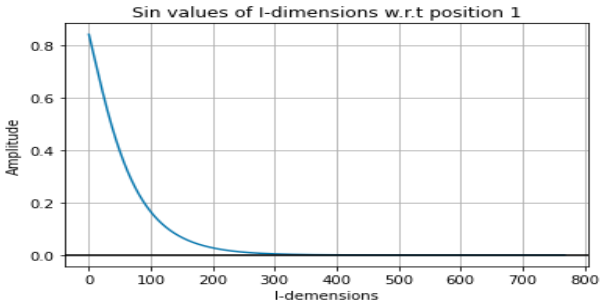


Fig. 6. Sine wave for position 1

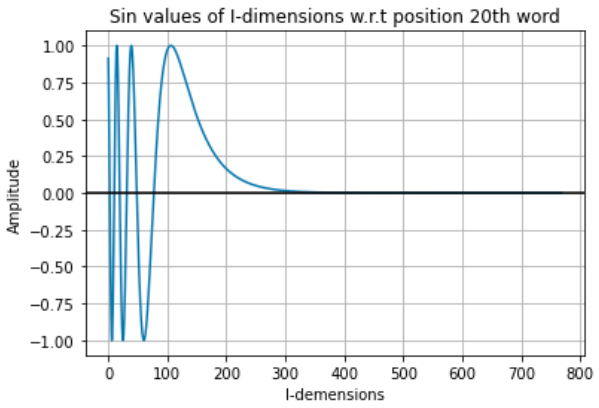


Fig. 7. Sine wave for position 20

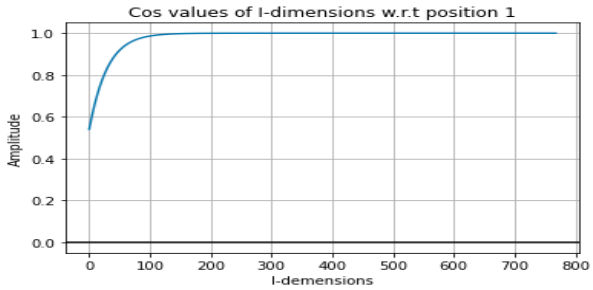


Fig. 8. Cosine wave at position 1

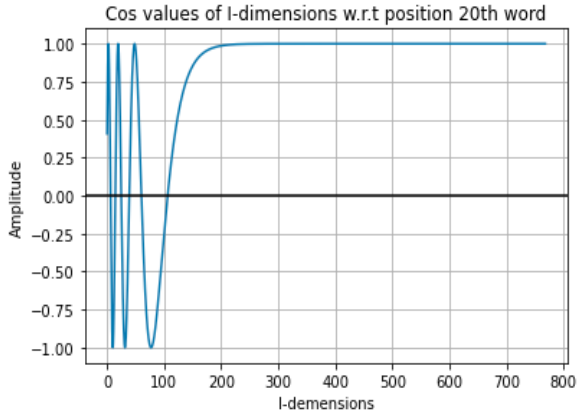


Fig. 9. Cosine wave at position 20

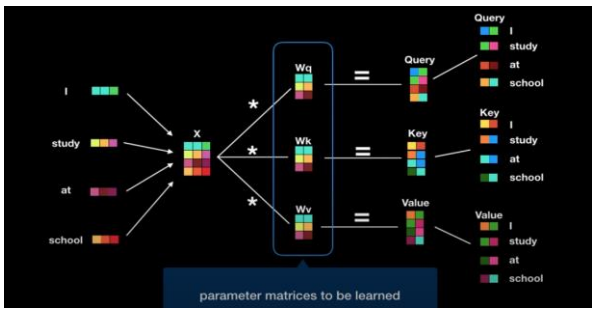


Fig. 10. Linear Transformation of each word into Query, Key and Value[14]



Fig. 11. 'I' computation with repsect to all words[14]

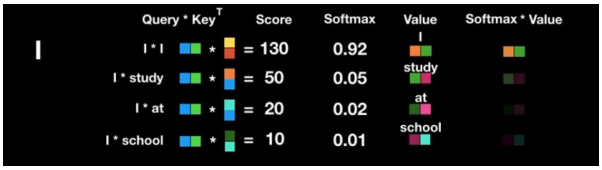


Fig. 12. Soft-max coloumn will now get multiplied with the 'Value' vector of each word. And then all vectors will be added together which will result in vector representation of the word 'I' in that specific sentence[14]

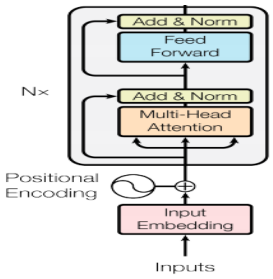


Fig. 13. A Transformer's Encoder block (taken from original Transformers paper)

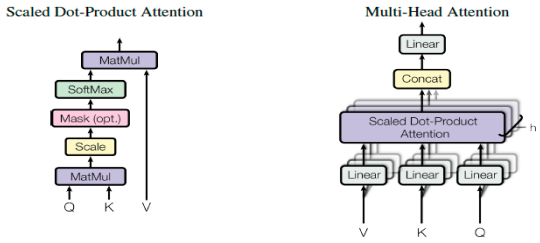


Fig. 14. Left side shows attention mechanism and Right side shows the how Multi-Head phenomena takes place (taken from original Transformers paper)

System	MNLI-(m/mm) 392k	QQP 363k	QNLI 108k	SST-2 67k	CoLA 8.5k	STS-B 5.7k	MRPC 3.5k	RTE 2.5k	Average -
Pre-OpenAI SOTA	80.6/80.1	66.1	82.3	93.2	35.0	81.0	86.0	61.7	74.0
BiLSTM+ELMo+Attn	76.4/76.1	64.8	79.8	90.4	36.0	73.3	84.9	56.8	71.0
OpenAI GPT	82.1/81.4	70.3	87.4	91.3	45.4	80.0	82.3	56.0	75.1
$BERT_{BASE}$	84.6/83.4	71.2	90.5	93.5	52.1	85.8	88.9	66.4	79.6
$BERT_{LARGE}$	**86.7/85.9**	**72.1**	**92.7**	**94.9**	**60.5**	**86.5**	**89.3**	**70.1**	**82.1**

Fig. 15. Accuracy score of BERT on different datasets(taken from original BERT paper)

IV. Training Strategy

As a social media test experiment, it was hard to choose the dataset to train/fine-tune our model on. First problem was the approximate 110 million parameters learning time because we are training all the weights (due to TensorFlow documentation), as our one epoch of 200000 sentences took

around 2 hours on Google Colab. The other problem was how to effectively tackle every kind of Tweet as some Tweets would use standard english, some would use slang language etc.

We decided to use SENT140 dataset that contain 1.6 million tweets of binary classification, Movie reviews and SST-2 data set that contains 10662 and 50000 binary classified sentences respectively.

We took 100000 sentences each from both of the classes of SENT 140 dataset. We took all of the sentences from SST2 dataset for the training. We took 4000 sentences from Movie Review dataset only (that had equal number of sentences with respect to polarity). We merged them and shuffled them. We also made the combined dataset lower case. For testing, we used the remaining sentences in Movie Review dataset.

This strategy was induced to see how robust our proposed neural model is in practical terms after Fine-tuning. First reason is that these differnet datasets were taken in order to train our model on different genre of sentences such as personal opinions, accusations, general comments, informal language etc, because this combined dataset will have data that will be similar to real-time Tweets on which we are going to build our application. Second reason is that we are testing on that dataset whose training data is in a low proportion in training phase. The test results will depict our neural model authenticity of understanding binary classified sentiment analysis. Though all three datasets correspond to the same classification but we are taking account the different platforms (twitter and movie reviews) and their data-collection's time as well, because there is a chance that at different platforms the ways/style of writing can be different, and even the time can also play its part as fashion of writing changes [15].

Thus we belief that our analysis has important meaning in analyzing how effective the understanding of our model is in regards to the nature of a sentence because in standard practice of machine learning, we gather a dataset from a certain controlled environment, may that be a specific topic, platform, group of selected indivduals, or even the person(s) whom is/are collecting the raw dataset(s). What we are trying to point out is that there is a chance that there could be a certain 'biasness' of some sort of nature in the datasets. If these constraints are kept under consideration then it must help our model correctly analyze a sentence in a practical environment.

The test results on this dataset gave us a 84.6 percent of accuracy. From this we can interpret that how robust our new model is.

We think that this is a novel idea that we have established in our strategy. We, to our best knowledge do not think that this strategy is used in any of the literature before in the field of sentiment analysis.

V. Geogrpahical Output

We used TWINT library in Python to filter out Tweets with respect to a keyword, from co-ordinates of States of America. We then used Folium library to create GUI map of America. After testing the tweets on our model we then counted how much percent were tweets postive and negative and then we represented them on our map. The picture of a GUI is given in Fig. 16.

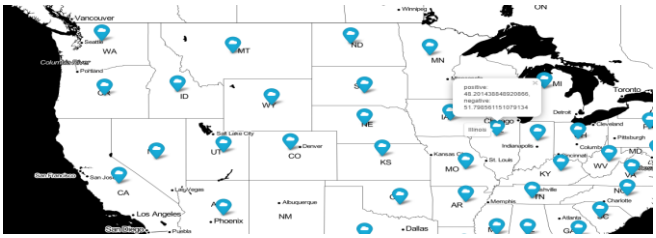


Fig. 16. A 'part' of our full map of United states. One can see the percent of tweets regarding an event from the state of Illinois

VI. Conclusion

We hope that our paper will ensure to save a lot of time of the young researchers by giving a bird's-eye view of popular neural architecutures' theoretical framework with respect to practical constraints. We also showed how a practical application can be made through sentiment analysis i.e. working on real time Tweets. By our findings we conclude that why it is necessary to study BERT model, additionaly it will also help young researchers to not only have promising results on sentiment analysis rather on other 11 NLP tasks as well [8]. On the other hand, BERT model will also help young researchers grasp the concepts of other architectures 'a bit more easily' that came after BERT such as Transformer-XL, GPT-2 and GPT-3 etc because they all use Transformers architecuture's concept in some sort of way.

References

[1] K. C. G. C. J. D. Tomas Mikolov, "Efficient Estimation of Word Representations in Vector Space," *arXiv preprint arXiv:1301.3781*, 2013.

[2] Mikolov, T., Sutskever, I. and Chen, K., 2013. *Distributed Representations of Words and Phrases and their Compositionality*. Cornell University.

[3] Y. Kim, "Convolutional Neural Networks for Sentence Classification," *Association for Computational Linguistics*, vol. Proceedings of the 2014 Conference on Empirical Methods in Natural Language Processing (EMNLP), p. 1746–1751, 2014.

[4] Chung, J., Gulcehre, C., Cho, K. and Bengio, Y., 2014. *Empirical Evaluation of Gated Recurrent Neural Networks on Sequence Modeling*. Cornell University.

[5] Y. Bengio, P. Simard and P. Frasconi, "Learning long-term dependencies with gradient descent is difficult," in IEEE Transactions on Neural Networks, vol. 5, no. 2, pp. 157-166, March 1994, doi: 10.1109/72.279181.

[6] S. Hochreiter and J. Schmidhuber, "Long Short-Term Memory," in Neural Computation, vol. 9, no. 8, pp. 1735-1780, 15 Nov. 1997, doi: 10.1162/neco.1997.9.8.1735.

[7] vaswani, A., Shazeer, N., Parmer, N., Uszkoreit, J., Jones, L., N. Gomez, A., Kaiser, Ł. and Polosukhin, I., 2017. *Attention is all you need*. nips.cc.

[8] Devlin, J., Chang, M., Lee, K. and Toutanova, K., 2018. *BERT: Pre-training of Deep Bidirectional Transformers for Language Understanding*. arXiv.org > cs > arXiv:1810.04805.

[9] K. C. B. van Merrienboer Caglar Gulcehre and D. Bahdanau, "Learning phrase representations using RNN encoder–decoder for statistical machine translation," *Arxiv.org*. [Online]. Available: http://arxiv.org/abs/1406.1078v3. [Accessed: 31-Aug-2021].

[10] S. Albawi, T. A. Mohammed, and S. Al-Zawi, "Understanding of a convolutional neural network," in *2017 International Conference on Engineering and Technology (ICET)*, 2017.

[11] M. Potuck, "Apple hits 1.5 billion active devices with ~80% of recent iPhones and iPads running IOS 13," *9to5Mac*, 28-Jan-2020. [Online]. Available: https://9to5mac.com/2020/01/28/apple-hits-1-5-billion-active-devices-with-80-of-recent-iphones-and-ipads-running-ios-13/. [Accessed: 18-Nov-2021].

[12] *Arxiv.org*. [Online]. Available: http://arxiv.org/abs/1512.03385v1. [Accessed: 21-Nov-2021].

[13] L. Zhang, S. Wang, and B. Liu, "Deep learning for sentiment analysis: A survey," *Wiley Interdiscip. Rev. Data Min. Knowl. Discov.*, vol. 8, no. 4, p. e1253, 2018.

[14] "Transformer (Attention is all you need)," 28-Apr-2019. [Online]. Available: https://www.youtube.com/watch?v=z1xs9jdZnuY&list=RDCMUCxP77kNgVfiiG6CXZ5WMuAQ&index=26. [Accessed: 21-Nov-2021].

[15] F. Can and J. M. Patton, "Change of writing style with time," *Comput. Hum.*, vol. 38, no. 1, pp. 61–82, 2004.

[16] M. O. Topal, A. Bas, and I. van Heerden, "Exploring Transformers in Natural Language Generation: GPT, BERT, and XLNet," *arXiv [cs.CL]*, 2021.

Autonomous Drone Navigation using Deep Convolutional Neural Network

Muhammad Arif Arshad
Pakistan Institute of Engineering and Applied Sciences
Pattern Recognition Lab, DCIS
Islamabad, Pakistan
engrarifarshad@gmail.com

Saddam Hussain Khan
Pakistan Institute of Engineering and Applied Sciences
Pattern Recognition Lab, DCIS
Islamabad, Pakistan
hengrshkhan822@gmail.com

Muhammad Waleed Khan
Pakistan Institute of Engineering and Applied Sciences
Pattern Recognition Lab, DCIS
Islamabad, Pakistan
Waleed@pieas.edu.pk

Suleman Qamar
Pakistan Institute of Engineering and Applied Sciences
Pattern Recognition Lab, DCIS
Islamabad, Pakistan
m.sulemanqamar@gmail.com

Asifullah Khan*
Pakistan Institute of Engineering and Applied Sciences
Pattern Recognition Lab, DCIS
Islamabad, Pakistan
asif@pieas.edu.pk*

***Abstract*— Drones are unmanned aerial vehicles utilized for a broad range of functions, including delivery, aerial surveillance, traffic monitoring, architecture monitoring and even in War field. Indeed, drones confront significant obstacles while navigating independently in unstable and highly dynamic environments. In comparison with the standard "map-localize-plan" approaches, this research paper investigates an information-driven strategy to address the issues mentioned above. For this purpose, a convolutional neural network (CNN) is proposed to pilot a drone across city streets safely. Every input image generates two outputs: a steering angle for the drone's movement whilst dodging the hindrances and the possibility of a collision for alerting the Unmanned Aerial Vehicle (UAV) far away from spotting risky situations and responding quickly. However, gathering enough data in an unorganized outside area such as a metropolis is a challenge. It is not easy to collect data for the sake of the pilots, so data is used, which is collected by mounting a camera on the cars and bikes. This paper suggests that data collected by automobiles and bicycles can be used to train a UAV that would not threaten other vehicles or pedestrians. Dataset is divided using the train-test split method. Despite being trained on urban roads from the perspective of urban cars, the navigation strategy of the proposed architecture is very generalized. The high recall (99.38%), great accuracy (97.78%) and good f-score (94.81%) of the proposed technique suggest that it can be used for autonomous driving of drones. The proposed technique masters a navigation strategy that accomplishes a relatively higher level of accuracy, recall, f-score and precision, which shows that it outperforms previous approaches in the literature.**

Keywords*— *Residual Network, Drone, Convolutional Neural Network, Perception and Autonomy

I. INTRODUCTION

Unmanned Aerial Vehicles (UAVs) are one of the most significant disciplines in recent technology, with autonomous drones being a key study focus. Self-flying, also called self-piloting, refers to a drone's capacity to conduct aerial movements without the assistance of a person. In this case, autonomy is defined as the drone's decision to run the aforementioned self-flying activities without the need for human intervention. Manually operating UAVs is challenging, as is deploying many sensors on a drone. As a result, it is planned to build drones that will be controlled by a single front and rear camera, from which the drone would get real-time visual information and act independently.

CNNs have emerged as one of the most potentially fruitful avenues in the computer vision field in recent years, delivering outstanding results in a variety of vision recognition tasks, including pose estimation [1], face recognition [2], digit recognition [3][4], image classification [5][6] medical analysis[7], content-based image retrieval [8][9] and object and pedestrian detection [10][11].

Due to its usage and suitability on commercially feasible drones that are often implemented with a fourth-looking camera and lack additional power-hungry or heavyweight sensors, vision-based navigation has recently received great attention. Simultaneously, advances in machine learning have improved visual navigation capabilities, like Deep Neural Networks (DNNs) have enabled the creation of tail-to-tail learning methods [12], learn-able parameters are used for feature extraction in it. While the previous method has limited generalization capabilities, DNNs offer visual navigation in real-world contexts where visual appearances are inevitably diverse.

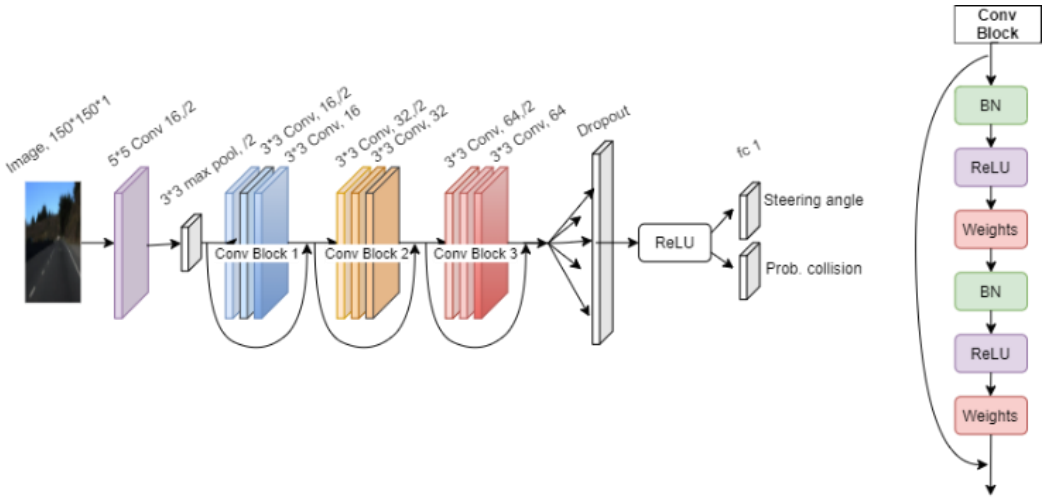
Recently, new deep learning techniques have been producing excellent results in a variety of domains [13][14][15]. Reinforcement learning (RL)-based techniques, in particular, suffer from a significant rise in sample complexity, making them unsuitable for usage by UAVs in safety-critical settings. Successful flying policies, on the other hand, maybe learned using supervised-learning approaches. [13][15][16] however, it hasn't worked out how to collect enough expert trajectories from replicating yet. In addition, as mentioned by [16] drones must learn how to react in risky circumstances just like human pilots.

Clearly, a UAV effectively flying in the streets must follow the road and react to risky circumstances in the same manner that any other manned ground vehicle would. As a result, we introduce employing the information acquired from ground automobiles incorporated in the above-mentioned settings already. The dronet architecture is customized by modifying the initial and final layers to be compatible with the input feature map dimensions and output multi-class challenge (2 classes). Comprehensively, contributions made by this work are as followed:

- We proposed a model named as customized modified residual-Dronet architecture that can predict the steering angle and collision probability

Table 1: Quantitative findings on regression and classification tasks: For the steering regression task, EVA and RMSE are calculated, while for the collision prediction job, Average accuracy and F1-score are assessed. In comparison to the considered baselines, our model performs admirably. Despite having a small number of parameters, Modified Residual-Dronet performs admirably on both tasks.

Model	EVA	RMSE	Avg. Accuracy	F-Score	Recall	Num. Parameters	Num. Layers
Random Baseline	-1 ± 0.022	-0.3 ± 0.001	$50 \pm 1\%$	0.3 ± 0.001	-	-	-
Constant Baseline	0	0.34	75.6%	0.00	-	-	-
VGG-16 [17]	0.712	0.097	96.6%	0.921	-	$2.6 * 10^7$	50
Resnet 50 [18]	0.795	0.119	92.7%	0.847	-	$7.5 * 10^6$	16
Dronet [12]	0.737	0.109	95.4%	0.901	-	$3.2 * 10^5$	8
Modified Residual-Dronet	0.99	0.48	97.78%	0.9481	0.9938	$8.2 * 10^4$	8



(a) (b)

Figure 1: (a) Modified Residual-DroNet is a branched CNN which anticipates the steering angle and collision probability from a single 150 x 150 grey-scale frame. A ResNet-8 consists of three residual blocks (b) forms the common component of the architecture, which is accompanied by dropout and non-linearity ReLU. Following that, the architecture is divided in two fully connected layers and out of those two, one for prediction of steering angle and other for inferring a probability of collision

which helps in safely navigation of a drone in urban situations.

- The proposed model has been employed on "Udacity" and "Collision" datasets, collected from automobiles and bicycles. The "Udacity" dataset is basically used to calculate the steering angle, and the "Collision" dataset is used to predict the probability of collision.
- The proposed model outperforms the existing state of the art CNN models.

Despite our system's impressive outcomes, we don't want to change the standard "map-localize-plan" drone navigation approaches; instead, we want to explore if a likewise task can be performed with a single shallow neural network. Traditional and learning-based techniques, we believe, will eventually complement one another.

II. Related Work

Obstacle detection and avoidance challenges are comparable to autonomous navigation. Obstacle detection systems are centered on either machine learning algorithms or machine vision methods. There are numerous techniques for drone navigation and obstacle avoidance in the existing literature. The sensory input and processing required for the controlling of flying platforms vary greatly across these methods.

The challenges of obstacle detection and avoidance are inextricably intertwined with those of autonomous navigation in terms of their complexity. Object detection approaches for identifying barriers are based on either machine learning algorithms or computer vision techniques.

To assess the device form, figure out the existence of hindrances, after that execute course devising, a UAV flying outside is generally equipped with GPS field, and optical sensing devices [19]. However, due to construction, massive rushes, and dynamic states in metropolitan regions, these types of activities are still likely to suffer, resulting in significant unobserved inaccuracy in the assessment of system state.

DNN has recently attracted a lot of attention for their ability to teach control rules directly from raw sensory input. There



Figure 2: (a) Images from Udacity were utilized for learning the steering angles. (b) Images were collected in order to determine the likelihood of a collision. No-collision frames are in the green box, whereas collision frames are in the red box.

are two types of approaches: reinforcement learning (RL) methods [15][20] and supervised learning methods [14], [16][17][21][22].

Antonio Loquercio developed a Deep Convolutional Neural Network model named Dronet in his paper [12] which can safely fly a drone across a city's streets. For every input image, Dronet produces two outputs a steering angle which controls the directions of the UAV and encounter possibility that allows the UAV to identify risky conditions and respond quickly. For training a deep CNN, the proposed technique leverages footage captured by a drone-mounted camera during real or simulated flights that approximately follow the intended path.

Maria Tzelepi proposed a human crowd detection technique [24] which uses deep Convolutional Neural Networks (CNN) for driving the autonomous UAV. The goal of the research is to develop light architectures that can successfully discriminate between swarmed and non-swarmed images taken by drones, as well as crowd heat maps which could be useful for semantically improved flight blueprints by designating no-fly zones.

III. Methodology

Our learning approach seeks to anticipate the probability of collision and predicting a steering angle using the drone's forward-looking camera in real-time. These may be translated into control flying instructions, allowing a UAV to fly safely around objects while avoiding collisions. The resulting Architecture is shown in Figure 1.

For the reduction of complexity of the architecture, the proposed methodology is mutually used by two jobs to some extent, but it is then split into two branches at the end. One of the two jobs is steering angle which is a regression problem, while the other one is collision probability prediction which is a classification problem. Because the two objectives are so dissimilar, we recommend separating the last fully connected layer of the network. We exclusively use images acquired by manned vehicles throughout the training. Images collected from bicycles are used to understand the likelihood of a collision, while images captured from cars are used to learn steering angles.

A. Learning Methodology

The ResNet-8 design is followed by a 0.5 dropout and a ReLU non-linearity in our network that the two jobs share. Figure 1 shows the blocks of the residual network.

The success of Resnet can be attributed to its learning idea, which enables it to handle vanishing/exploding gradient problems in extremely deep networks. To improve model performance, we tweaked this design choice. Tasks stop sharing parameters at the last ReLU layer, and then the path is separated for both steering angle and probability of collision using two separate, fully connected layers. The steering angle is output by the first, while the collision probability is output by the second. The latter, strictly speaking, is an index that quantifies the network uncertainty in prediction rather than a Bayesian probability. We still refer to it as a probability.

To train the collision and steering predictions, we use binary cross-entropy (BCE) and mean square error (MSE), respectively. Despite the fact that the network design is suitable for reducing perplexity and time taken to process, a naive joint optimization faces severe convergence issues due to the extremely varied gradient magnitudes produced by each loss. Using no weighting among the two losses during the learning phase, in particular, leads towards convergence to unsatisfactory and weak results. That can perhaps be described due to the magnitude differences in gradients between classification and regression tasks towards the beginning of training, which could make optimization challenging [25]. Because the MSE gradients' standards are relative to the absolute steering error, the regression job's gradients are initially much higher. As a result, as we progress through the training process, we place more emphasis on classification loss. Applying a constant loss weight between the two losses or not will almost need considerably prolonged optimization duration and possibly leads to sub-optimal efficiency for the reasons described above. This is a form of curricular learning [25]. This may be regarded as a sort of curricular learning. More specifically, the BCE weight coefficient is (1), but the MSE weight coefficient is always 1. We used decay = 1/10 and epoch_0 = 10 for our trials.

$$\boldsymbol{L_{tot} = L_{MSE} + \max\left(0, 1 - e^{-decay(epoch_0 - epoch)}\right) * L_{BCE}} \quad (1)$$

The Adam optimizer[26] is employed with 0.001 learning rate and decay rate of 10^{-5}. For optimization, hard mining is used for learning the most difficult samples. In particular, for each epoch, we choose the k samples with the greatest loss and calculate the overall loss using Equation 1. We set the value of k to decrease with time.

B. Dataset

We utilize one of the freely accessible datasets from Udacity's project [27] to learn steering angles. Nearly 60,000 images of car driving are split across five experiments, 1 for testing and 4 for training. Every experiment saves images from three cameras (left, centre, and right) and data from the GPS, IMU, brake, steering angles, throttle, gear, and speed. To learn the probability of collision from images, We utilize a dataset that is freely available online from Dronet's project [12]. They collected the dataset by mounted the GoPro camera on the bicycle's handlebar. And drive the bicycle in multiple city areas, attempting to mix up the sorts of barriers (vehicles, people, plants, construction sites) and appearance of surroundings. As a result, the drone can generalize in a variety of settings. This dataset has 32000 images spread across 137 sequences. In these sequences, frames are labelled as 0 (no collision) if the distance from the obstacle is enough, which means there is less chance of collision, and those frames in which there are some obstacles are labelled as 1 (collision). Frames labelled as 1 (i.e. collision frames) are that kind of data that is very difficult for a drone to gather yet required for the development of a reliable as well as safe technique.

C. Drone Control

The UAV is instructed to fly with a forward velocity of V_k and a steering angle of θ_k using the outputs. The network uses the probability of collision to regulate the forward velocity: when the collision probability is zero, vehicles are commanded to move with the maximum velocity i.e. V_{max}, and it stops when the probability of collision is close to 1. The forward velocity is filtered using a low pass filter $0 < \alpha < 1$ as shown in Equation 2.

$$\boldsymbol{V_k = (1-\alpha)V_{k-1} + \alpha(1-P_t)V_{max}} \quad (2)$$

Similarly, the predicted steering angle is also converted into a yaw angle (rotation around the z-axis). We transform s_k from the [-1, 1] range to the required yaw angle θ_k in the $[\frac{-\pi}{2}, \frac{\pi}{2}]$ range and low pass filter it as shown in Equation 3.

$$\boldsymbol{\theta_k = (1-\beta)\theta_{k-1} + \beta\left(\frac{\pi}{2}\right)S_k} \quad (3)$$

Lastly, in conclusion, a novice dynamic navigation strategy that will operate a drone accurately with just only a single forward-looking camera is developed. Our method has the advantage of being able to calculate a collision probability using one image, excluding any prior knowing the platform's velocity. Our belief is that the proposed architecture will be making decisions based on the range between noticed items in the sphere of vision [18].

IV. Experimental Setup

The experimentation conducted to evaluate our suggested technique is presented in this portion, along with the set of performance measures to assess the correctness of the model.

A. Regression and Classification Results

We initially analyze our model's regression performance using the Udacity dataset's testing sequence [28]. We utilize two measures to measure steering prediction performance: Root Mean Square Error (RSME) and Explained Variance Ratio (EVA). We utilize F-score and average classification accuracy to evaluate collision prediction performance. Table 1 compares Modified Residual-Dronet architecture with several known architecture from the literature [16][27][29]. Weak baselines include a constant estimator that anticipates 0 for steering angle always and "no collision," as well as a random estimator. The above-mentioned findings imply this while being 317 times smaller than the previous best design. Our method outperforms it in terms of prediction accuracy. Additionally, a favorable contrast to the VGG-16 network [17] demonstrates a utilization for the residual learning scheme in terms of generalization, as described in Section III-A. As demonstrated in Table 1, Figure 4, Figure 5 and Figure 6. Our design achieves a great performance as compared to other models in the literature.

B. Performance Metrics

Various common performance indicators are used to assess the performance of the implemented models. Accuracy, recall, and F-score are examples of these measures. Equation 4 measures the total number of accurate assignments and is used to determine accuracy. The proportion of actual collision

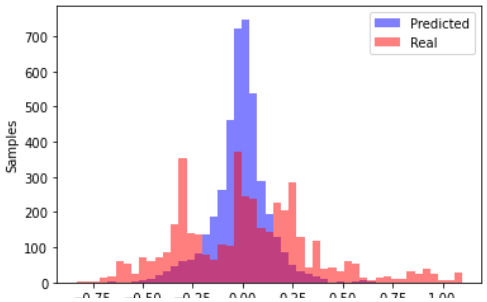


Figure 3: Model performance: Anticipated vs Actual steering of Udacity testing sequence dataset using the Probability Density Function (PDF).

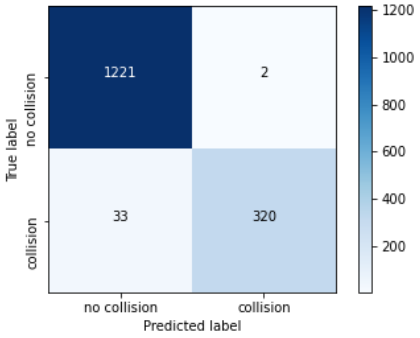


Figure 4: Confusion matrix for collision categorization based on the obtained dataset's testing images. The percentage of samples in each group is shown by the numbers in this matrix.

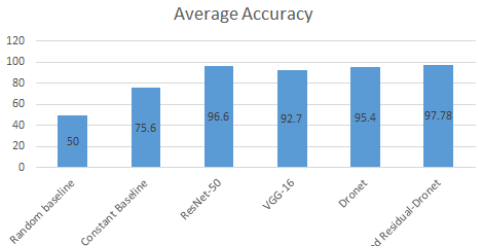


Figure 5

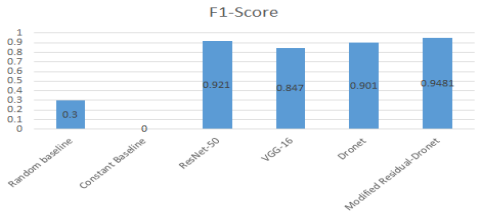


Figure 6

probability predictions is measured by recall Equation 5. Equation 6 specifies the F-score.

$$\boldsymbol{Accuracy} = \frac{\boldsymbol{True\ Positive + True\ Negative}}{\boldsymbol{Total\ number\ of\ samples}} \quad (4)$$

$$\boldsymbol{Recall} = \frac{\boldsymbol{True\ Positive}}{\boldsymbol{True\ Positive + False\ Negative}} \quad (5)$$

$$\boldsymbol{F - Score} = \boldsymbol{2} * \frac{\boldsymbol{Precision} * \boldsymbol{Recall}}{\boldsymbol{Precision + Recall}} \quad (6)$$

V. Discussion

Both conventional and learning-based techniques have advantages and limits, and our methodology is no exception. The benefits include allowing a drone to securely explore previously unexplored areas utilizing our easy learning and control approach. Unlike prior techniques, there is no need to be given or construct an online map of the environment, pre-define collision-free destinations, or find inside it. Furthermore, we exhibited intriguing generalization skills across a wide range of circumstances. It might be a useful supplement to standard "map-localize-plan" techniques in navigation related activities such as airborne delivery. Indeed, unlike CNN-based methods [21], the flying strategy that we offer may successfully fly in significant unknown circumstances, excluding the need for any re-training or fine-tuning. Furthermore, our technique may be suitable for platforms with limited resources because of the relatively basic and efficient network design. The drawbacks include the nimble dynamics of drones that aren't completely utilized. So this is not feasible to unambiguously assign the robot an objective for achievement, such as in previous CNN-based controllers [16][22][30]. There are various options for dealing with the restrictions described above. When a high chance of collision is expected, one may construct 3D collision-free paths to make use of the drone agility, as shown in [29].

It is not difficult to estimate the distance to the target [30] if the 2D map is known. one may give the distance to the target or use the new learning approaches developed for ground vehicles [31] for the generalization of the goal-driven problems. Furthermore, as shown in [32], a measure of uncertainty might be added to our system to make it more resilient.

VI. Conclusion

In this paper, we introduced a CNN model capable of safely piloting a drone across city streets. Because gathering data in such an unregulated environment using UAV is both risky and time-consuming, our model learns to fly by emulating automobiles and cyclists, which already obey the laws of the road. This model forecasts the collision probability and required steering angle simultaneously with the high accuracy (97.78%), precision (99.38%), and f1-score (94.81%) compared to other architectures in the literature, allowing a UAV to react quickly to unexpected occurrences and hurdles. Through extensive testing, it is proved that a drone can be trained for navigation in urban areas by simulating manned automobiles. Furthermore, intriguing abstraction skills across a broad range of circumstances is exhibited. It might be a useful supplement to standard "map-localize-plan" techniques in navigation related activities such as airborne delivery.

References

[1] A. Toshev and C. Szegedy, "Deeppose: Human pose estimation via deep neural networks," in *Proceedings of the IEEE conference on computer vision and pattern recognition*, 2014, pp. 1653–1660.

[2] Y. Taigman, M. Yang, M. Ranzato, and L. Wolf, "Deepface: Closing the gap to human-level performance in face verification," in *Proceedings of the IEEE conference on computer vision and pattern recognition*, 2014, pp. 1701–1708.

[3] D. Ciregan, U. Meier, and J. Schmidhuber, "Multi-column deep neural networks for image classification," in *2012 IEEE conference on computer vision and pattern recognition*, 2012, pp. 3642–3649.

[4] Y. LeCun *et al.*, "Learning algorithms for classification: A comparison on handwritten digit recognition," *Neural networks Stat. Mech. Perspect.*, vol. 261, no. 276, p. 2, 1995.

[5] C. Szegedy *et al.*, "Going deeper with convolutions," in *Proceedings of the IEEE conference on computer vision and pattern recognition*, 2015, pp. 1–9.

[6] S. H. Khan, A. Sohail, and A. Khan, "COVID-19 detection in chest X-ray images using a new channel boosted CNN," *arXiv Prepr. arXiv2012.05073*, 2020.

[7] S. H. Khan, A. Sohail, M. M. Zafar, and A. Khan, "Coronavirus disease analysis using chest X-ray images and a novel deep convolutional neural network," *Photodiagnosis Photodyn. Ther.*, p. 102473, 2021.

[8] A. Babenko, A. Slesarev, A. Chigorin, and V. Lempitsky, "Neural codes for image retrieval," in *European conference on computer vision*, 2014, pp. 584–599.

[9] J. Wan *et al.*, "Deep learning for content-based image retrieval: A comprehensive study," in *Proceedings of the 22nd ACM international conference on Multimedia*, 2014, pp. 157–166.

[10] R. Girshick, J. Donahue, T. Darrell, and J. Malik, "Rich feature hierarchies for accurate object detection and semantic segmentation," in *Proceedings of the IEEE conference on computer vision and pattern recognition*, 2014, pp. 580–587.

[11] P. Sermanet, K. Kavukcuoglu, S. Chintala, and Y. LeCun, "Pedestrian detection with unsupervised multi-stage feature learning," in *Proceedings of the IEEE conference on computer vision and pattern recognition*, 2013, pp. 3626–3633.

[12] A. Loquercio, A. I. Maqueda, C. R. Del-Blanco, and D. Scaramuzza, "Dronet: Learning to fly by driving," *IEEE Robot. Autom. Lett.*, vol. 3, no. 2, pp. 1088–1095, 2018.

[13] S. Ross *et al.*, "Learning monocular reactive uav control in cluttered natural environments," in *2013 IEEE international conference on robotics and automation*, 2013, pp. 1765–1772.

[14] T. P. Lillicrap *et al.*, "Continuous control with deep reinforcement learning," *arXiv Prepr. arXiv1509.02971*, 2015.

[15] A. Giusti *et al.*, "A machine learning approach to visual perception of forest trails for mobile robots," *IEEE Robot. Autom. Lett.*, vol. 1, no. 2, pp. 661–667, 2015.

[16] D. Gandhi, L. Pinto, and A. Gupta, "Learning to fly by crashing," in *2017 IEEE/RSJ International Conference on Intelligent Robots and Systems (IROS)*, 2017, pp. 3948–3955.

[17] K. Simonyan and A. Zisserman, "Very deep convolutional networks for large-scale image recognition," *arXiv Prepr. arXiv1409.1556*, 2014.

[18] K. He, X. Zhang, S. Ren, and J. Sun, "Deep residual learning for image recognition," in *Proceedings of the IEEE conference on computer vision and pattern recognition*, 2016, pp. 770–778.

[19] S. Scherer *et al.*, "River mapping from a flying robot: state estimation, river detection, and obstacle mapping," *Auton. Robots*, vol. 33, no. 1, pp. 189–214, 2012.

[20] S. Shen, Y. Mulgaonkar, N. Michael, and V. Kumar, "Multi-sensor fusion for robust autonomous flight in indoor and outdoor

environments with a rotorcraft MAV," in *2014 IEEE International Conference on Robotics and Automation (ICRA)*, 2014, pp. 4974–4981.

[21] Y. Zhu *et al.*, "Target-driven visual navigation in indoor scenes using deep reinforcement learning," in *2017 IEEE international conference on robotics and automation (ICRA)*, 2017, pp. 3357–3364.

[22] G. Kahn, T. Zhang, S. Levine, and P. Abbeel, "Plato: Policy learning using adaptive trajectory optimization," in *2017 IEEE International Conference on Robotics and Automation (ICRA)*, 2017, pp. 3342–3349.

[23] N. Smolyanskiy, A. Kamenev, J. Smith, and S. Birchfield, "Toward low-flying autonomous MAV trail navigation using deep neural networks for environmental awareness," in *2017 IEEE/RSJ International Conference on Intelligent Robots and Systems (IROS)*, 2017, pp. 4241–4247.

[24] M. Tzelepi and A. Tefas, "Human crowd detection for drone flight safety using convolutional neural networks," in *2017 25th European Signal Processing Conference (EUSIPCO)*, 2017, pp. 743–747.

[25] Y. Bengio, J. Louradour, R. Collobert, and J. Weston, "Curriculum learning," in *Proceedings of the 26th annual international conference on machine learning*, 2009, pp. 41–48.

[26] A. KingaD, "A methodforstochasticoptimization," *Anon. Int. Learn. Represent. SanDego ICLR*, 2015.

[27] M. Mancini, G. Costante, P. Valigi, T. A. Ciarfuglia, J. Delmerico, and D. Scaramuzza, "Toward domain independence for learning-based monocular depth estimation," *IEEE Robot. Autom. Lett.*, vol. 2, no. 3, pp. 1778–1785, 2017.

[28] A. Kazakova, Y. Cho, and C.-G. Lee, "OSCAR: An Open-Source, Self-Driving CAR Testbed," 한국정보과학회 학술발표논문집, pp. 720–722, 2018.

[29] S. Yang, S. Konam, C. Ma, S. Rosenthal, M. Veloso, and S. Scherer, "Obstacle avoidance through deep networks based intermediate perception," *arXiv Prepr. arXiv1704.08759*, 2017.

[30] M. Pfeiffer, M. Schaeuble, J. Nieto, R. Siegwart, and C. Cadena, "From perception to decision: A data-driven approach to end-to-end motion planning for autonomous ground robots," in *2017 ieee international conference on robotics and automation (icra)*, 2017, pp. 1527–1533.

[31] W. Gao, D. Hsu, W. S. Lee, S. Shen, and K. Subramanian, "Intention-net: Integrating planning and deep learning for goal-directed autonomous navigation," in *Conference on Robot Learning*, 2017, pp. 185–194.

[32] C. Richter and N. Roy, "Safe visual navigation via deep learning and novelty detection," 2017.

Parameter Identification and Optimization of Permanent Magnet DC Motor using Nonlinear Least Square Error Method

1st Raja Muhammad Sohail Khan
College of Aeronautical Engineering
National University of Sciences and Technology,
Risalpur, Pakistan
msohail@cae.nust.edu.pk

2nd Hamza Malik
College of Aeronautical Engineering
National University of Sciences and Technology,
Risalpur, Pakistan
hmalik@cae.nust.edu.pk

3rd Hammad Munawar
College of Aeronautical Engineering
Nautional University of Sciences and Technology,
Risalpur, Pakistan
h.munawar@cae.nust.edu.pk

***Abstract*— Parameter identification and optimization of any system play an important role in system modeling and subsequent control system design. DC motors are frequently employed in industry for their ease of use and control. Dynamic models of motors based on motor parameters are used to design the control systems. However, for designing sophisticated control systems accurate motor parameter values are required. This paper presents a technique for the identification and optimization of these parameters for any permanent magnet DC motor using the non-linear least square method. Parameters and speed response are measured using experimental readings from data acquisition equipment and exploiting analytical relationships of PMDC motor dynamics. These experimental values are used to optimize nominal motor parameters using the non-linear least square error method. A computer-based algorithm is employed to minimize the error in several iterations based on the non-linear least square error function. The results show that the non-linear least square error method was able to minimize the relative error below the set tolerance which resulted in the close matching of simulated and measured responses of the motor. These optimized motor parameters can be utilized to design a sophisticated control system for various applications.**

Keywords— estimation, nonlinear least square error method, parameter optimization, PMDC motor

I. INTRODUCTION

In industrial control systems, DC motors have various applications as they can be easily modeled and controlled. However, in certain scenarios, a precise and accurate model of the DC motors is required to achieve optimum control system design. In such a case, the nominal values for motor specifications provided by the manufacturer in its data-sheet are not sufficient to achieve the desired optimum performance of the required control system design. This is especially the case when cheaper DC motors are used where values provided in the manufacturer's data-sheet have considerably large tolerances making it difficult to achieve the desired goal. In addition to this, another downside of selecting cheap motors is that no specifications with respect to electrical and mechanical parameters is provided especially if selected DC motor is part of some other product as a whole e.g. a linear actuator. Various techniques have been identified and implemented to model the accurate DC motor model. System identification methods [1]–[4] usually employing MATLAB System Identification toolbox can be utilized for determining motor's parameters. Other than System Identification, [5], [6] utilized the algebraic identification method while, [7] implemented the inverse theory technique and [8] applied the moments method. Least Square Error (LSE) is the most common technique for parameter estimation as it involves the minimization of squared error between the simulated and measured (experimental) responses of DC motor. The same technique is employed by [9] whereas, a recursive approach to LSE is employed by [10]. DC motor parameters can also be estimated using Artificial Neutral Network [11], where an added advantage is that parameter estimation could be achieved by utilizing adaptive learning method in an online scenario. The accurate DC motor parameters identified using the mentioned approaches are used to model the DC motor which is then subsequently utilized for accurate controller design as implemented in [6], [11] and [7]. An approach like this paper is implemented in [9] utilizing the MATLAB constraint optimization technique which also involves the curve fitting method based on LSE technique. Another very important aspect to look for, before selection of parameter estimation techniques, is the identification through inexpensive and readily available basic testing apparatus. In addition to this, the employed technique should consist of a short testing cycle. This is especially useful when quick prototyping of controller-based systems is performed. In this paper, a DC motor parameter identification approach based on Simulink Design Optimization technique is presented. The motor used was a part of actuator (shown in "Fig. 1") required for linear actuation in Stewart Platform. The measured parameters and speed response of DC motor are used to estimate and find the optimum parameter values based on nonlinear LSE technique in parameter estimation tool of Simulink.

A. DC Motor Background Theory

The schematic diagram for a permanent magnet (PM) DC motor is shown in "Fig. 2". The electro-mechanical schematic for a DC motor system can be used to develop DC motor's transfer function after applying the basic circuit analysis techniques. The key DC machine relationships used to obtain the required transfer function are shown as (1). The transfer function equates input voltage (V) to the output motor speed (ω) as shown in (2). The nomenclature of all variables and constants is shown in "TABLE I".

$$T = kI, \quad V_c = K_b\omega, \quad V = E + IR \tag{1}$$

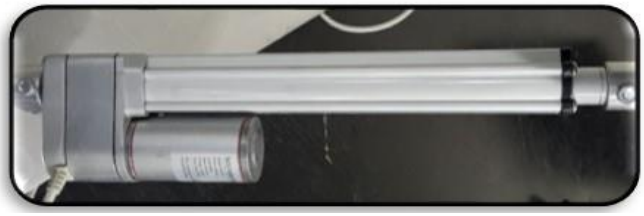


Fig. 1. Linear actuator used as legs of Stewart platform

$$\frac{\omega_m(s)}{V(s)} = \frac{K_m}{J_m R s + R B_m + K_b K_m} \quad (2)$$

B. Methodology

The overall methodology for implementing an optimum control design of linear actuator of Stewart platform is divided into four sections i.e. experimental measurement of motor parameters, parameter estimation (optimization) using Simulink MATLAB, controller design using optimized parameter values, and finally implementation and verification of results by implementation on actual system. Initially, the electrical and mechanical parameters (Jm; Bm; R; L; Km; Kb) of DC motor of the linear actuator were determined from DC motor model and experimental measurements on DC motor. In addition to this, Motor speed response was also measured at its rated voltage using required experimental setup. This was followed by estimation and optimization of measured parameters using MATLAB Simulink constrained optimization technique. The constraint optimization technique compared the measured speed response with the simulated speed response obtained using nominal values of DC motor parameters. The optimum parameters achieved using this technique can be used to design an accurate controller for the actuators for further integration on a Stewart platform.

II. EXPERIMENTAL MEASUREMENT OF DC MOTOR PARAMETERS

A. Experimental Setup

The acquisition hardware to carry out parameter measurements and finding the speed step response consisted of DC motor (disassembled from linear actuator), quadrature encoder, DC power supply, Digital Oscilloscope, Digital Multi-meter, National Instruments Data Acquisition Device (NI-DAQ), HBridge motor driver (L298) and LABVIEW / MATLAB installed CPU.

TABLE I. NOMENCLATURE

State Variable (unit)	Description
V_α (V)	Supply voltage
R (Ω)	Armature resistance
L (H)	Armature inductance
I_α (A)	Armature current
ω (rad/s)	Back EMF of the motor
J_m (kg/m^2)	Inertia of the motor
B_m (Nms/rad)	Damping coefficient
K_m (Nm/A)	Torque constant of the motor
K_b $(V/rad/s)$	Back EMF constant
τ_{mech} (s)	Mechanical time constant
τ_{elec} (s)	Electrical time constant

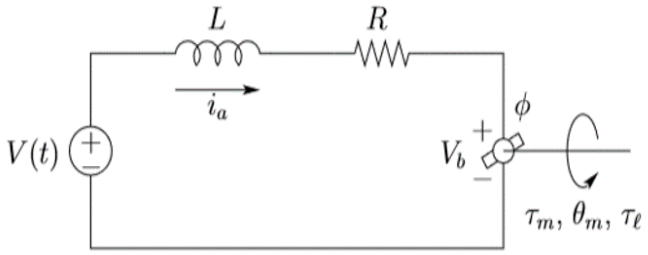


Fig. 2. Schematic diagram for permanent magnet DC motor (adapted from [12])

B. Armature Resitance (R)

Motor stall test is usually employed to determine the DC Motor's armature resistance. The two common methods used for measuring the armature resistance are as follows:

1) Multimeter: After noting any zero offset in the ohmmeter, measure the resistance across DC motor positive and negative terminals. Removing the zero offset will give the correct measurement reading. Due to the chance of DC motor brush to be in-contact with commutator, the measured resistance may vary at different rotor positions. To cater for this, repeated measurements were taken at different rotor positions and averaged out to get the final armature resistance.

2) Voltage and Current Measurement: The measured values obtained using multi-meter will tend to be slightly inaccurate due to capacitive and inductive losses of the sensors inside multi-meter. To avoid this, another method can be used to determine near-accurate resistance. In this method, a DC voltage supply is used to excite the motor at its rated voltage while clamping the motor's rotor in a fixed position. The current flowing through the motor's terminals is measured to find the armature resistance. As specified previously, repeated measurements are taken at different rotor positions and averaged out. As the resistance is sensitive to rotor position, a number of rotor positions should be tested and the average taken.

C. Armature Inductance (L)

DC motor's armature inductance can be measured by exciting the end terminals of the motor with a low voltage AC supply while measuring the voltage drop across the series resistance such as 1K Ohm added to motor's path [13]. The circuit diagram showing the given configuration is shown in "Fig. 3". The impedance (Z) can then be calculated using the equation shown in (3) while equivalent series resistance (RESR) and total phase (α) can be calculated using (4) and (5), respectively. The voltages V_A, V_B and phase difference θ between the two voltages can be measured using a digital oscilloscope. The armature inductance can then be found using (6) where f denotes the frequency of the AC supply voltage.

$$Z = \frac{V_B}{\sqrt{V_A^2 - 2V_A V_B \cos(\theta) + V_B^2}} \quad (3)$$

$$R_{ESR} = Z\cos(\alpha) \quad (4)$$

$$\alpha = \theta - \tan^{-1}\frac{-V_B \sin(\theta)}{V_B - V_A \cos(\theta)} \quad (5)$$

$$L = \frac{Z sin(\alpha)}{2\pi f} \quad (6)$$

D. Motor Torque Constant (K_m) / Back EMF Constant (K_b)

Both these motor constants are based on physical and geometrical properties of the DC motor. Factors such as number of turns and magnetic flux density are the main contributors. By neglecting any non-ideal electrical and mechanical losses, we can assume that the motor torque constant and back EMF constant are equal. Based on this, only back EMF constant will be measured. Under steady state conditions, the voltage to current relationship is reduced to the (7). Using this relationship under no-load, DC motor is excited

Fig. 3. Circuit diagram for measuring inductance

using a DC power supply while incrementing the voltage from zero to its rated voltage in small steps. The current and speed of the motor are measured during each iteration. The speed of the motor was measured using a quadrature encoder via National Instruments Data Acquisition Device (NI-DAQ) while current readings were recorded from DC power supply. The back EMF voltage (V_c) was calculated using (2) at each iteration and was plotted to get a trend line with speed (rad/s) on x-axis and voltage (volts) on y-axis. The back EMF constant can be calculated using (7).

$$V = IR + K_b\omega \tag{7}$$

E. Damping Coefficeint (B_m)

Based on the electrical and mechanical relationships of motor torque shown in (8) and (9), the damping coefficient (B_m) can be simplified under steady state conditions after canceling the derivative term as shown in (10). When excited under its rated voltage, the measured current, speed and torque constants can be used to calculate the damping coefficient.

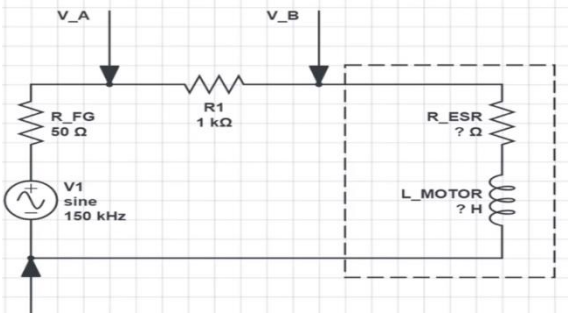
$$\tau_m = K_m I \tag{8}$$

$$\tau_m = J_m\, I\, \frac{d\omega}{d_t} + B_m\omega \tag{9}$$

$$B_m = \frac{K_m I}{\omega} \tag{10}$$

F. Motor Inertia (J_m)

The motor inertia (J_m) can be measured by simply measuring the mechanical time constant (τ_{mech}) and using the relationship given by (11). The mechanical time constant can be measured by switching off the running motor by opening the electrical circuit while recording the time series data of speed of motor using quadrature encoder data acquired using NI-DAQ (LabView software).



$$\tau_{mech} = \frac{J_m}{B_m} \tag{11}$$

G. Speed Step Response

The speed response measured using experimental procedure acts as the reference (final) response to be achieved in parameter estimation and optimization algorithm implemented using Simulink Design Optimization technique in MATLAB. “Fig. 4” shows the equipment setup for speed measurement. In order to obtain the speed step response, 12 VDC was given manually as step input repeatedly till 10 seconds and the resultant speed response of DC motor was acquired using NI-DAQ (LABVIEW) attached through quadrature encoder with DC motor. The obtained response is shown in “Fig. 5”.

III. Parameter Estimation and Optimization

In order to optimize the DC motor model parameters based on the measured speed response, a toolbox of MATLAB Simulink known as Design Optimization is utilized. It is a numerical optimization technique that estimates and tunes the Simulink model parameters and performs two specific tasks, which are:

1) Calibration of DC motor model parameters with experimentally measured data to enhance the accuracy of the model.
2) Find the model parameter values that fulfill the design requirements. This is achieved using a user interface called parameter estimation tool, which is used to estimate and optimize the parameters of the model.

The significance of this method is that, it can even find the unknown parameters based on the physically measured speed data. The simulated response must match the measured response to find the optimum estimates of the model parameters. The overall process after collection of

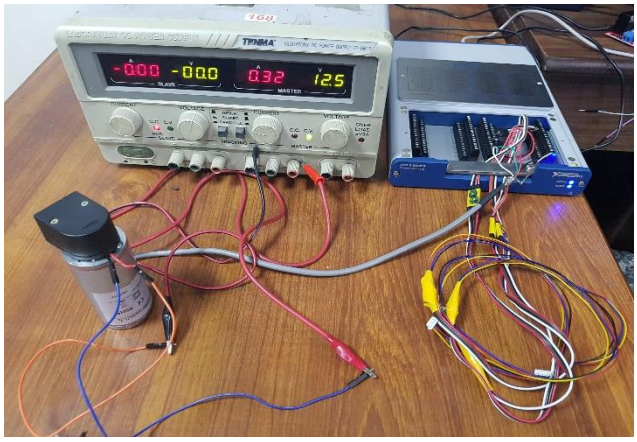


Fig. 4. Motor speed measurement experimental setup

experimental data is as follows:-

a) Specification of parameters to be estimated in the user interface (inital and final ranges, initial guesses (if known))
b) Build the simulink model of DC motor based on nominal values
c) Find optimum estimates based on suitable algorithm (non-linear least square)
d) Repeat with other experimental data-sets for verification

A. *Parameter Estimation Tool in Simulink*

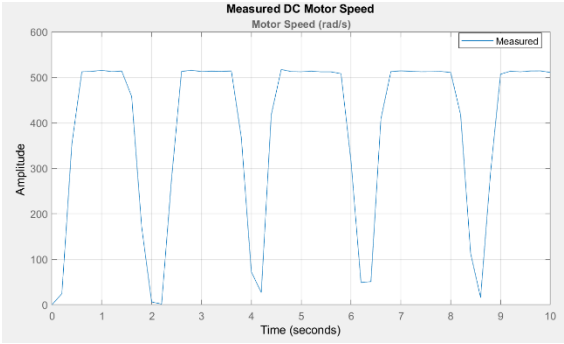


Fig. 5. Measured speed response of DC motor

Based on the optimization problem, parameter estimation tool in Simulink MATLAB is used to find the optimum parameters for DC motor. The parameter estimation tool requires specifying certain variables and options which are as follows:-

a) Design parameter variables (x: R, L, B_m, J_m, K) of DC motor to be estimated

b) Defining variables bounds ($x_{min} \leq x \leq x_{max}$) - limits of design parameters to be estimated, as parameter values cannot be negative, so lower limits were set to zero.

c) Selection of suitable objective function: calculates difference between measured and simulated response of DC motor model. It iteratively tunes the parameter variable values to obtain the simulated speed response (y_{sim}) that tracks the reference signal (y_{ref}) which in this case is measured speed step response. It minimizes the estimation error ($e(t)$) defined as,

$$e(t) = y_{ref}(t) - y_{sim}(t) \qquad (12)$$

Simulink design optimization tool consists of various algorithms such as nonlinear least square (NLS), Gradient Descent (GD), simplex search (SS) etc. The algorithm implemented in this paper is NLS as it is considered to be most suitable algorithms for parameter estimation of DC motor model. [14]

B. *Estimation Procedure*

The Simulink model for DC motor with nominal / measured parameter values was developed to get the simulated response. The Simulink model with input set as voltage and output set as speed is shown in "Fig. 6". Afterwards, following procedure is adopted to carry out the estimation: -

a) In DC motor Simulink model, Parameter Estimation from Analysis tab was selected to open a new session of parameter estimation tool for DC motor.

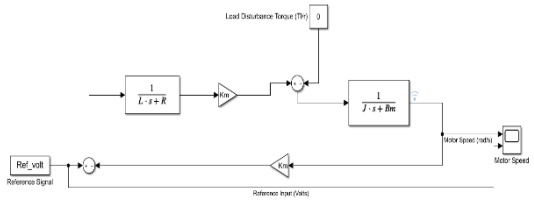


Fig. 6. Simulink model

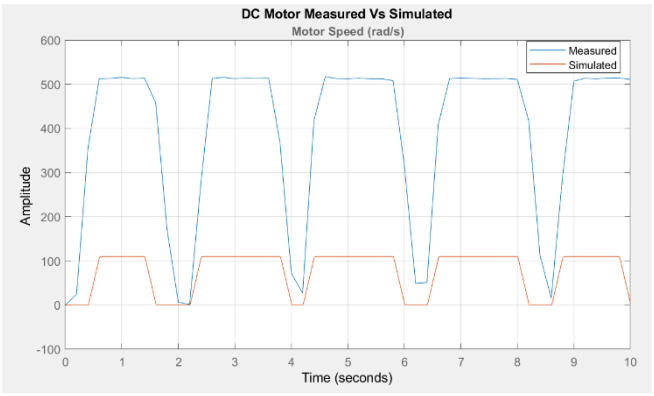


Fig. 7. Initial Measured and simulated responses

b) DC motor parameters used for simulation were selected in Select Parameters option. Meanwhile, the lower bounds were also set to zero.

c) A New Experiment was created and the measured speed data was imported. The Plot and Simulate option was selected to plot the measured and simulated response on the same window as shown in "Fig. 7".

d) After specifying the objective function SSE, stimation was run using Estimate option.

After several iterations, the estimation stops after the selected objective function has converged and the simulated response closely matched the measured response giving the final estimated parameter values.

IV. RESULTS AND DISCUSSIONS

After 28 iterations, the optimization stopped because the relative sum of square of errors (SSE) (5.76e-4) minimization function came below its defined tolerance of 1e-3. Moreover, the simulated response came very close to the measured plot as shown in "Fig. 8". The changing parameter values as estimation algorithm was iteratively executing to reach the optimum point are shown in "Fig. 9". Whereas, the initial and tuned parameters are shown in "TABLE II". It can be seen in "Fig. 8" that the simulated response is closely following the measured response other than a few milliseconds delay in some points. The parameter values achieved using this optimization technique can be used in accurate controller design for DC motor. The same optimized model along with its controller design can then be used in actual controller implementation of the linear actuator and verified. The achieved controller gains and overall system response can then be compared with the previously implemented model for further analysis.

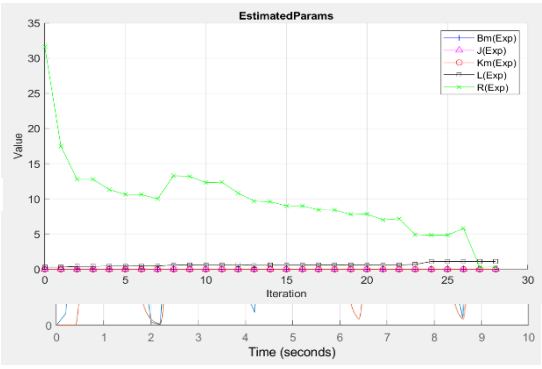


TABLE II. MEASURED / NOMINAL AND TUNNED PARAMTERS OF DC MOTOR

Parameter (unit)	Measured / Nominal	Tunned
$R\ (\Omega)$	31.64	0.3342
$L(H$		
$J_m(kg/m^2)$	1.66e-14	3.289e-11
$B_m(Nmsrad)$	2.54e-7	3.9675e-7
$K_m\ (Nm/A)$	9.916e-4	0.0018

Fig. 9. Iterative plot of parameter values

V. Conclusion

The main parameters governing the dynamic equations of the PMDC motor were measured and subsequently used to generate a Simulink model of DC motor. These values also act as the initial estimates in Simulink Design Optimization algorithm. In addition to this, the actual speed response of PMDC motor was measured experimentally which also act as the final reference response to be achieved in the optimization algorithm. After executing the parameter estimation tool in Simulink, it was observed that the resultant simulated response was very closely following the measured response. The tuned parameters achieved during this optimization are the accurate values based on which accurate and precise control of DC motor can be achieved.

VI. Future Work

Coupled model of DC motor and linear actuator can be obtained by augmenting rotary to linear dynamics in DC motor transfer function. This complete model can be simulated in MATLAB using optimized DC motor parameter values obtained in this paper. This can lead to accurate controller design, which can finally be implemented in actual Stewart platform equipment.

Acknowledgment

The authors would like to thank the anonymous reviewers and the editors for their time and efforts in reviewing the paper and giving valuable suggestions which greatly improved this paper.

References

[1] A. Simpkins, “System identification: Theory for the user, (ljung, l.; 1999)[on the shelf],” IEEE Robotics & Automation Magazine, vol. 19, no. 2, pp. 95–96, 2012.

[2] H. Unbehauen and G. Rao, “A review of identification in continuoustime systems,” Annual reviews in Control, vol. 22, pp. 145 171, 1998.

[3] J. C. Basilio and M. V. Moreira, “State-space parameter identification in a second control laboratory,” IEEE Transactions on Education, vol. 47, no. 2, pp. 204–210, 2004.

[4] G. F. Franklin, J. D. Powell, M. L. Workman et al., Digital control of dynamic systems. Addison-wesley Menlo Park, CA, 1998, vol. 3.

[5] G. Mamani, J. Becedas, V. Feliu-Batlle, and H. Sira-Ramirez, “Openloop algebraic identification method for a dc motor,” in 2007 European Control Conference (ECC). IEEE, 2007, pp. 3430–3436.

[6] G. Mamani, J. Becedas, and V. Feliu-Batlle, “On-line fast algebraic parameter and state estimation for a dc motor applied to adaptive control,” in Proceedings of the World Congress on Engineering, vol. 2, 2008.

[7] M. Ruderman, J. Krettek, F. Hoffmann, and T. Bertram, “Optimal state space control of dc motor,” IFAC Proceedings Volumes, vol. 41, no. 2, pp. 5796–5801, 2008.

[8] M. Hadef, A. Bourouina, and M. Mekideche, “Parameter identification of a dc motor via moments method,” 2008.

[9] S. Adewusi, “Modeling and parameter identification of a dc motor using constraint optimization technique,” International Journal of Mechanical and Civil Engineering, ISSN, pp-46-56, vol. 13, 2016.

[10] R. Krneta, S. Antic, and D. Stojanovi ´ c, “Recursive least squares method ´ in parameters identification of dc motors models,” Facta universitatisseries: Electronics and Energetics, vol. 18, no. 3, pp. 467 478, 2005.

[11] A. Rubaai and R. Kotaru, “Online identification and control of a dc motor using learning adaptation of neural networks,” IEEE Transactions on industry applications, vol. 36, no. 3, pp. 935–942, 2000.

[12] M. W. Spong and M. Vidyasagar, Robot dynamics and control. John Wiley & Sons, 2008.

[13] “Kde-dms kde direct device manager software for uas electronic speed controller (esc) series.” [On line]. Available: https://www. kdedirect.com/collections/uas-multirotorelectronics/products/kde-dms?page=specs

[14] W. Koech, S. Rotich, T. Rotich, and F. Nyamwala, “Dynamic model of a dc motor-gear-alternator (mga) system,” Asian Research Journal of Mathematics, vol. 1, pp. 1–16, 2016.

Threats to the Navigation of Drone Based Delivery Services

Imtiaz Nabi,
National Center of GIS and Space Applications,
Institute of Space Technology,
Islamabad, Pakistan
Imtiaznabi8@gmail.com

Salma Zainab Farooq
Institute of Space Technology
Islamabad, Pakistan
zaineb.farooq@ist.edu.pk

Sunnyaha Saeed
National Center of GIS and Space Applications,
Institute of Space Technology,
Islamabad, Pakistan
Sunnyahasaeed3@gmail.com

***Abstract*—Drone-based delivery services are expected to have massive commercial deployment in the upcoming years. The potential for drones to deliver goods across different terrains, at an unprecedented speed, has been attracting both investors and customers alike. Medical supplies, pesticides, ammunition, and other variety of goods can be transported more quickly and efficiently by using fixed-wing and rotary-wing unmanned aerial vehicles (UAVs). These delivery drones, however, require a sound navigation system that can guide and navigate them properly from one place to another. Global navigation satellite systems (GNSS) have been playing a vital role in drone-based delivery services as they provide navigation services by employing size, weight, power, and cost efficient hardware. However, satellite-based navigation systems are vulnerable to several threats, which turn drone-based delivery into a complete disaster causing collateral damage to goods and human infrastructure. This paper highlights some of the main threats to the GNSS-based navigation with regards to drone delivery services.**

Keywords—Global Navigation Satellite Systems (GNSS), Global Positioning System (GPS), Zipline, Amazon Prime Air, Drone Based Delivery Services, GNSS Jamming, GNSS Spoofing

I. Introduction and Background

Unmanned Aerial vehicles (UAVs) or drones are known for their military applications. They have proven themselves as solemn force multipliers by showing effectiveness in reconnaissance, surveillance, and armed combat e.g., "MQ 8b Fire Scout" currently used by the United States of America [1]. In recent years, with the emergence of the Internet of Things (IoT), the capabilities of UAVs have extended to numerous civilian sectors. One major application is agriculture, where drones are used to spray pesticides in the fields [2] as well as monitoring the crops [3]. Other applications include, forest fire monitoring [4], emergency and health management services [5], traffic monitoring [6], search and rescue (SAR) operations [7] and even fast food industry [8]. The company "Zipline" operating in Rwanda, East Africa, helps to provide blood and other emergency medical supplies to distant hospitals using UAVs [9]. Zipline has proven itself quite helpful by timely supplying blood and medicines to patients in need, and thus saving thousands of lives.

The concept of drone-based delivery service has attracted different companies, such as Amazon (Prime Air drone), Google (Project Wing drone), and German logistic company Deutsche Post DHL (Parcelcopte drone) to adopt it to improve their quality of service and customer satisfaction [8]. According to [10], the net shipping cost of Amazon Prime Air, employing drone based service model, would reduce to 8.6% of the cost of conventional delivery services. Drone-based delivery services are expected to reduce time and cost of delivery and assist in environmental protection as they use eco-friendly Lithium batteries as power source [10]. However, there are some challenges in the way of UAV based delivery system. In literature, different issues have been discussed regarding, the battery life, design of the vehicle [11]– [13] and path planning of delivery drones [14]. However, these aren't the only problems in the way of UAV based delivery network. One of the most important issues is the navigational threats. These threats include GPS/GNSS jamming and spoofing. These navigational threats, if not catered for, pose physical, loss and financial risks [8].

Commercial UAVs depend on GNSS/GPS for their guidance and navigation [2]. Nonetheless, GNSS is vulnerable to interference from different sources, posing threats to drone-based delivery services, endangering goods and human infrastructure. This paper highlights the main threats to GNSS-based navigation of delivery drones, namely jamming and spoofing, and their impact on the service. The flow of the paper is as follows; Section II of the paper introduces jamming and a brief description of the countermeasures that can be adapted to counteract these effects. Section III of the paper details spoofing, its threats to GNSS based navigation of delivery drone and finally the countermeasures. Finally, conclusion is drawn in section IV after reviewing all the threats.

II. GNSS Jamming

One of the challenges towards the navigation of autonomous drone-based delivery services is GNSS signal jamming. Jamming is the generation and transmission of signals, with enough power, towards the victim receiver that leave it unable to track GNSS signals [11] (Figure 1). There are multiple jamming incidents reported by literature that confirm the effect of intentional and unintentional RF interference on GNSS navigation based devices. One of the most well-known jamming incidents in the GNSS community is in January, 2007 in San Diego, California during a naval exercise. The technicians jammed radio signals and unknowingly also jammed GNSS signals, resulting in disruption of GNSS service As a result, Naval Medical Center emergency pager stopped working. Besides that, the harbor traffic management system also failed and the Air Traffic Control (ATC) had to use a backup to maintain the flow of air traffic. The problem of GNSS disruption was unknown for three days [11]. Moreover, several other reports confirm that GNSS signals are prone to

signal jamming leading to unwanted situations during signal outage [12].

Authors of [2] concluded that jamming signals depend upon two main parameters; the power of signals and distance of the jamming source from the victim receiver. In addition to this, jamming signals have two main characteristics; jamming to signal ratio (J/S) and central frequency. The nearer the GNSS signal jammer to the victim receiver, the greater will be power of the jamming signal [13]. Thus, it can overpower the carrier to noise ratio (C/N_0) of GPS/GNSS receivers which is the basic acquisition parameter of these receivers [14].

Delivery drones that have safety-coded firmware can easily be landed when exposed to GNSS/GPS jamming signals. It is because jamming of both GNSS signals and command and control link (C2 link) triggers their built-in safety feature [15]. This increases the risk of stolen goods that the delivery drone was carrying to its destination. Besides that, jamming signals can also cause these unmanned aerial vehicles (UAVs) to crash, thus endangering humans and animal lives and such an incident has been reported by [16].

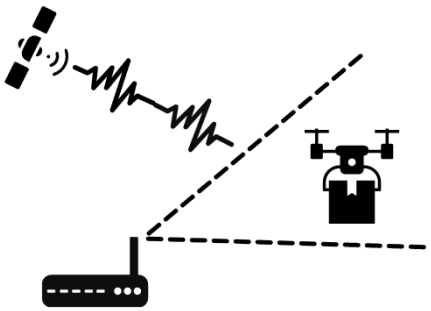


Fig. 1. GPS Jamming

With regards to jamming, figure 2 illustrates some of the countermeasures that can be adapted [11].

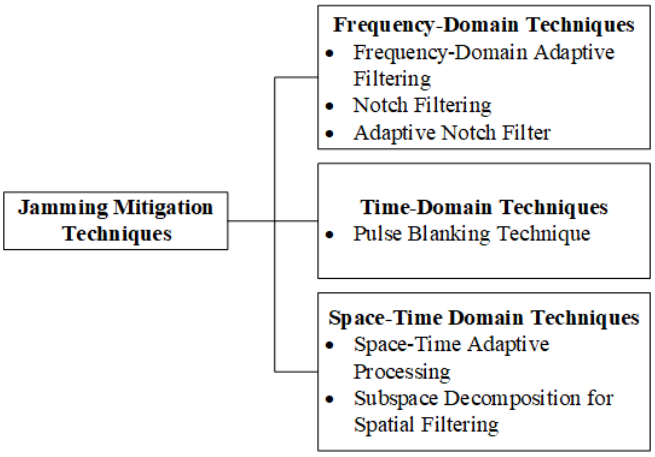


Fig. 2. Classification of GNSS Jamming mitigation techniques

III. GNSS SPOOFING

GNSS spoofing or structured interference can be defined as the act of transmission of falsified signals towards the victim receiver to achieve one of the four main objectives; distraction, destruction, hijacking, or apprehension [2]. Due to the transmission of counterfeit signal, GNSS spoofing proves to be a lot more dangerous than GNSS signal jamming. It is because in case of spoofing the attacker can transmit signals with false information that can even allow the attacker to gain full control off the target. In the case of delivery drones, they can easily be landed and captured by the attacker without risk of damaging the package that the UAV was carrying. A GNSS spoofing attack can be of two main types; "meaconing" or "fabrication" [2]. Both meaconing and fabrication are discussed in detail in the following sections after the mathematical description of spoofing attacks. During GNSS Spoofing attacks the victim receiver receives both authentic and fake signals simultaneously. The combined signals can be modeled at the input of the victim receiver as follow:

$$y^{a}_{RF,l}(t) = \sum_{l=0}^{N_s-1} s_{RF,l}(t) + n_l(t) + a(t) \quad (1)$$

Here a in superscript indicates that the receiver is under attack while $s_{RF,l}$ is the authentic signal. The term $n_l(t)$ is noise component of the signal and $a(t)$ is the component from the attacker. The attacker's component can be modeled as:

$$a(t) = \sum_{l=0}^{N_a-1} s'_{RF,l} + n_a(t) \quad (2)$$

In equation (1.2) $n_a(t)$ is the number of counterfeit replicas $s'_{RF,l}$ is the signal generated by the spoofer and $n_a(t)$ represents additional noise contribution. Signal generated by spoofer can be affected by demodulation or estimation errors and during imperfect synchronization, the counterfeit signal includes a residual modulation term due to difference in frequency Δf_l and phase φ_l between both the real and counterfeit signal. Due to this reason, the signal can be modeled as.

$$s'_{RF,L}(t) = A_l(t)\hat{s}_{RF,l}(t-\tau_l(t))\cos(2\pi\Delta f_l(t) + \Delta\varphi_l) \quad (3)$$

In the above equation $A_l(t)$ represents the ratio between amplitude of fake replica signals and authentic signals, $\hat{s}_{RF,l}$ is the estimated signal, and $\tau_l(t)$ is the relative delay between them. The values of both $A_l(t)$ and $\tau_l(t)$ can be either constant or vary with time depending upon the type of attack.

Spoofing attacks can be of different types and levels depending upon the objectives of the attacker [1]. Several types of spoofing attacks are discussed in the following section. Although different review papers can be found on spoofing attacks, however, in this paper we have summarized all the attacks to provide an understanding and show spoofing as a potential threat to drone-based delivery networks

A. Meaconing

Meaconing can be defined as the recording, delaying, and rebroadcasting of the GNSS signals [2]. It is the most basic type of spoofing attacks, however, it still can be dangerous in some situations. It requires a signal repeater or hardware that can record and replay signals. In the case of meaconing, the signal received from visible satellites is not separated from the reception phase [3]. In addition, a relative delay is added to the signal due to which the

meaconing signal arrives at the target or victim receiver with a positive delay.

During a successful meaconing attack, the number of fake signals matches the number of available satellites in view. The main feature of meaconing attacks is that the attacker generates an exact replica of the signals with a constant amplification factor and delay. In addition, a noise figure is introduced into the signal due to the meaconer hardware component. The noise figure from the meaconer hardware components is not negligible and it increases the noise power. However, no residual modulation is introduced in case of spoofing attacks [3] i.e. $\Delta f_l(t) = 0$ and $\Delta \varphi_l = 0$

B. Simplistic Spoofing Attack

A simplistic GNSS spoofing attack is considered fabrication of GNSS signals, using commercial GNSS signal simulators, to broadcast signals towards target receiver to distract it from its true path (Figure 2). Signal simulators are easily available on GitHub or can be created using Matlab/Simulink environment. Simplistic attacks may be easier to implement, however, they are not consistent and time-synchronized with the real signals. Signals generated by the GNSS simulators usually have higher power as compared to real signals. In addition, slight discrepancy in the navigation message such as old ephemeris data, etc. can affect the counterfeit signal. Also, the attack generated by simplistic spoofer may represent satellites that are not visible on the scene.

Due to these shortcomings, such types of attacks can easily be countered with basic anti-spoofing algorithms. Apart from that, in most cases, the attacker has to jam the signal first to lose lock on the real signal and then inject the stronger signal which is then locked by the receiver [3]–[5]. Though it can lead to disastrous situations once successfully carried out but this technique is still a naive approach to GNSS spoofing and can easily raise an alarm about signal spoofing due to jamming of the signals first.

C. Intermediate Spoofing Attack

In contrast to the simplistic attack, the intermediate attacks are far more advanced in nature. In these types of attacks, the attacker is able to determine the time, location, and satellite information from the received signals, and then makes believable counterfeit signals by synchronizing the local codes and carriers (Figure 3). For carrying out a successful attack, the counterfeit signals must be synchronized with the authentic ones by code-phase within at least half a chip. In addition to this, the knowledge about the relative positions of the spoofer antenna and target antenna and the receiver dynamics must also be known for successful attacks. In case of intermediate spoofing, each tracking channel is attacked by first code-phase alignment, and then signal power is increased gradually. It must be kept in mind that the signals are synchronized due to which the Δf_l parameter is negligible.

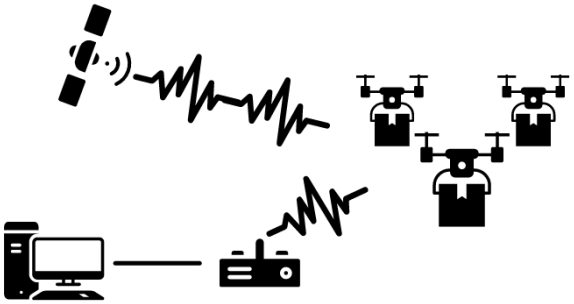


Fig. 3. Simplistic Spoofing Attack: A signal simulator based spoofing attack

Intermediate spoofing attacks are harder to detect using basic anti-spoofing algorithms due to the synchronization of the code phase. However, they can be detected using complex measures such as angle of arrival defense. A possible implementation of a portable civilian GPS spoofer is described in [6] which can be implemented for the development of a sound counter spoofing algorithm.

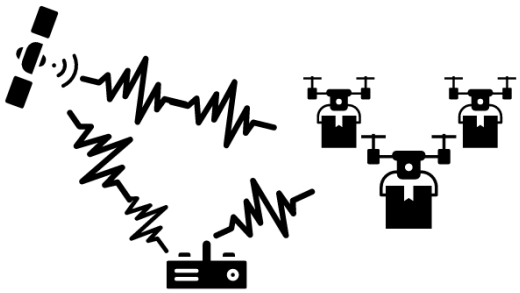


Fig. 4. Intermediate Spoofing Attack: A receiver spoofer architecture

D. Sophisticated Spoofing Attack

The sophisticated spoofing attack is the most advanced technique of spoofing attack. It requires sub-centimeter-level knowledge about the attacker's antenna phase center and the target antenna phase center. In addition to this, the fake signals are accurately synchronized with the real ones due to which the phase and frequency differences becomes negligible. Such types of attacks can easily distract a receiver with advanced anti-spoofing algorithms due to the nature of the attack as they can easily suppress the authentic signals as well.

Sophisticated spoofing attacks can be extremely hard to detect even using advanced countermeasures such as angle of arrival defense. However, they can be countered through cryptographic techniques such as signals authentication [3].

The spoofing attacks and their countermeasures are listed in Table I and II respectively

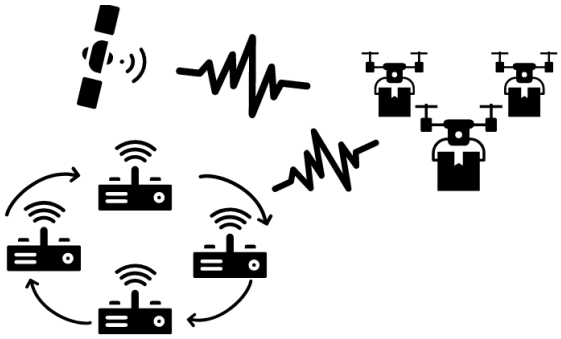


Fig. 5. Sophisticated Spoofing Attack: A chain of spoofers synchronized together and has information about the victim's antenna phase center

IV. CONCLUSION

Drone-based delivery networks can be a major productive innovation as they can easily reduce the cost and time of delivery to various locations. Due to which many marketing giants are in a race to adopt this system. Amazon, Google, DHL have already conducted tests and are highly interested in such a system. However, there are many challenges that drone-based delivery services have to face and overcome. Apart from the weight of the payload & package, battery life, structure of drones, and weather condition, navigation is the most important aspect of such services which must be reliable and fool-proof. Since drones rely on GNSS for their guidance and navigation and GNSS can easily be compromised with signals jamming and spoofing which can result in unwanted situations. Therefore, they must be equipped with solid anti-jamming and anti-spoofing algorithms to fight against several GNSS threats and make drone-based delivery more reliable and easy.

TABLE I –SPOOFING ATTACKS AND THEIR SPECIFICATIONS

Type Of Attack	Hardware Requirement	Context Requirement	Difficulty of Detection
Meaconing	GNSS antenna, Low noise amplifier (LNA), RF Transmitter	Must be located in proximity to target receiver, LNA gain, and power level must be adapted according to the distance from the target.	Easy [11]
Simplistic Spoofing Attack	Signal simulator, power amplifier, RF transmitter	The transmitting antenna must be close to the target	Very Easy [11]
Intermediate Spoofing Attack	Modified receiver with transmitting front end	Target receiver antenna position and velocity must be accurately known	Hard [11]
Sophisticated Spoofing Attack	Multiple phase-locked receivers-spoofers	Sub-centimeter level knowledge about target antenna phase center position and velocity	Extremely Hard [11]

TABLE II – SPOOFING MITIGATION TECHNIQUES

Countermeasure Type	Complexity	Robustness	Limitation
Navigation Message Authentication	System: Low Receiver: Low	Robust against simplistic attacks	Fails against meaconing and intermediate spoofing
Spreading Code Authentication	System: Medium Receiver: Medium	Robust against simplistic and intermediate	Fails against meaconing
Navigation Message Encryption	System: Medium Receiver: Medium	Robust against simplistic attacks	Fails against intermediate, sophisticated, and meaconing attacks
Spreading Code Encryption	System: high Receiver: High	Robust against simplistic, intermediate, and sophisticated	Fails against meaconing

REFERENCES

[1] K. Wesson and T. Humphreys, "Hacking Drones," *Sci. Am.*, vol. 309, no. 5, pp. 54–59, Oct. 2013, doi: 10.1038/scientificamerican1113-54.

[2] S. Z. Khan, M. Mohsin, and W. Iqbal, "On GPS spoofing of aerial platforms: a review of threats, challenges, methodologies, and future research directions," *PeerJ Comput. Sci.*, vol. 7, p. e507, 2021, doi: 10.7717/peerj-cs.507.

[3] F. Veroustraete, "The Rise of the Drones in Agriculture," *EC Agric.*, vol. 2, no. 2, pp. 325–327, 2015.

[4] C. Yuan, Y. Zhang, and Z. Liu, "A survey on technologies for automatic forest fire monitoring, detection, and fighting using unmanned aerial vehicles and remote sensing techniques," *Can. J. For. Res.*, vol. 45, no. 7, pp. 783–792, Apr. 2015, doi: 10.1139/cjfr-2014-0347.

[5] J. C. Rosser, V. Vignesh, B. A. Terwilliger, and B. C. Parker, "Surgical and Medical Applications of Drones: A Comprehensive Review," *JSLS : Journal of the Society of Laparoendoscopic Surgeons*, vol. 22, no. 3. NLM (Medline), Jul. 01, 2018. doi: 10.4293/JSLS.2018.00018.

[6] F. Outay, H. A. Mengash, and M. Adnan, "Applications of unmanned aerial vehicle (UAV) in road safety, traffic and highway infrastructure management: Recent advances and challenges," *Transp. Res. Part Policy Pract.*, vol. 141, pp. 116–129, Nov. 2020, doi: 10.1016/j.tra.2020.09.018.

[7] S. Mayer, L. Lischke, and P. W. Woźniak, "Drones for Search and Rescue," p. 7.

[8] M. Knobloch, "What impedes Consumers' Delivery Drone Service Adoption ? A Risk Perspective Arbeitsberichte aus dem Fachbereich Informatik," no. 1, 2020.

[9] E. Ackerman and E. Strickland, "Medical delivery drones take flight in east Africa," *IEEE Spectr.*, vol. 55, no. 1, pp. 34–35, 2018, doi: 10.1109/MSPEC.2018.8241731.

[10] Jung, Sunghun and kim hyunsu, "Analysis of Amazon Prime Air UAV Delivery Service," *J. Knowl. Inf. Technol. Syst.*, vol. 12, no. 2, pp. 253–266, 2017, doi: 10.34163/jkits.2017.12.2.005.

[11] T. Cokyasar, W. Dong, M. Jin, and İ. Ö. Verbas, "Designing a drone delivery network with automated battery swapping machines," Comput. Oper. Res., vol. 129, p. 105177, May 2021, doi: 10.1016/j.cor.2020.105177.

[12] T. Cokyasar, "Optimization of battery swapping infrastructure for e-commerce drone delivery," Comput. Commun., vol. 168, pp. 146–154, Feb. 2021.

[13] T. Cokyasar, "Delivery drone route planning over a battery swapping network," in Procedia Computer Science, 2021, vol. 184, pp. 10–16, doi: 10.1016/j.procs.2021.03.013.

[14] H. Huang, A. V. Savkin, and C. Huang, "Reliable Path Planning for Drone Delivery Using a Stochastic Time-Dependent Public Transportation Network," IEEE Trans. Intell. Transp. Syst., pp. 1–10, 2020, doi: 10.1109/TITS.2020.2983491.

[12] F. Dovis, *GNSS Interference Threats and Countermeasures*. Artech House, 2015.

[13] T. Westbrook, "The Global Positioning System and military jamming: The geographies of electronic warfare," *J. Strateg. Secur.*, vol. 12, no. 2, pp. 1–16, 2019, doi: 10.5038/1944-0472.12.2.1720.

[14] D. Silva, "GPS Jamming and Spoofing Using Software Defined Radio," 2017.

[15] *GNSS — Global Navigation Satellite Systems*. Springer Vienna, 2008. doi: 10.1007/978-3-211-73017-1.

[16] P. Tedeschi, G. Oligeri, and R. Di Pietro, "Leveraging Jamming to Help Drones Complete Their Mission," *IEEE Access*, vol. 8, pp. 5049–5064, 2020, doi: 10.1109/ACCESS.2019.2963105.

[17] C. G. L. Krishna and R. R. Murphy, "A review on cybersecurity vulnerabilities for unmanned aerial vehicles," in *SSRR 2017 - 15th IEEE International Symposium on Safety, Security and Rescue Robotics, Conference*, Oct. 2017, pp. 194–199. doi: 10.1109/SSRR.2017.8088163.

[18] J. Bhatti and T. E. Humphreys, "Hostile Control of Ships via False GPS Signals: Demonstration and Detection," *Navig J Inst Navig*, vol. 64, no. 1, pp. 51–66, 2017, doi: 10.1002/navi.183.

[19] L. Dobryakova and E. Ochin, "On the application of GNSS signal repeater as a spoofer," *Zesz Nauk Akad Morska W Szczecinie*, vol. nr 40 (112, no. 112, pp. 53–57, 2014.

[20] T. E. Humphreys, B. M. Ledvina, M. L. Psiaki, B. W. O'Hanlon, and P. M. Kintner, "Assessing the spoofing threat: Development of a portable gps civilian spoofer," *21st Int Tech Meet Satell Div Inst Navig ION GNSS 2008*, vol. 2, pp. 1198–1209, 2008.

Investigation of Pre-Seismic Ionospheric and Atmospheric Anomalies before Mw 6.1 El Salvador Earthquake on October 28, 2018

Abdur Rafeh Abbasi
Institute of Space Technology
Islamabad, Pakistan
abdurrafehabbasi@hotmail.com

Abdul Hanan Hamid
Institute of Space Technology
Islamabad, Pakistan
abdulhanan.geo@gmail.com

Muhammad Arqim Adil
Institute of Space Technology
Islamabad, Pakistan
arqamadil3@gmail.com

Daboor Sultana
Institute of Space Technology
Islamabad, Pakistan
daboorsultana@live.com

Saqib Mehdi
Institute of Space Technology
Islamabad, Pakistan
sqbmehdi@gmail.com

Erman Senturk
Kocaeli University
Kocaeli, Turkey
erman.senturk@kocaeli.edu.tr

***Abstract*— Seismo-ionospheric anomalies (SIA) from space and ground instruments can provide deep insights over the epicenter of future earthquakes (EQ). An earthquake may disrupt the lower as well as upper ionosphere through several coupling mechanisms during the EQ preparation periods. This paper analyzes the temporal variations in Total Electron Content (TEC) from Global Positioning System (GPS), Outgoing Longwave Radiation (OLR), and Air Temperature (AT) from GIOVANNI-AIRS and MODIS, respectively, before El Salvador EQ that occurred on October 28, 2018. The temporal TEC observations retrieved from the International GNSS Service (IGS) stations of Managua and Guatemala cities, laying within the earthquake preparation area (EPA), showed a positive ionospheric response from 2 to 3 TECu from the corresponding upper bound about 2-6 days before the EQ. The variations are found based on the confidence interval of median and associated interquartile range for 10 days before and 5 days after the main shock. The bounds are calculated from continuous analysis of 10 days before and after the observed day. Additionally, sudden increments in atmospheric AT and OLR were also found consistent with ionospheric TEC variations that indicate an EQ-induced atmospheric environment. Furthermore, to monitor the space weather conditions during the observation period for the EQ, we examined the solar wind speed (V_{SW}), solar radio flux (F10.7) solar activity, disturbance storm-time (Dst), Kp geomagnetic activity indices to distinguish SIA. The mutual enhancements in atmospheric and ionospheric parameters might be due to the abrupt energy released by this EQ that exhibits a lithosphere-atmosphere-ionosphere coupling (LAIC).**

Keywords—Earthquake, GPS-TEC, Ionosphere, OLR, Space Weather

I. INTRODUCTION

Advancement in space science and research intrigues many modern-day researchers to study the space atmosphere and its impact on human life and planet Earth. Scientists analyze space-based ionospheric observations to study the earth's atmosphere and their impact on lithosphere-atmosphere-ionosphere coupling (LAIC) related to seismic activity [1][2][3][4]. Particularly forecasting of EQs via seismo-ionospheric anomalies is now getting debate among researchers. This paper analyzes ionospheric and atmospheric anomalies that occur during the EQ period. The analysis shown in this research is one of the EQ events that occurred in the El Salvador region of Mw 6.1 in the southwest of the Acajutla region in El Salvador on 28 October 2018.

Researchers introduced many theories and hypotheses that indicated ionospheric anomalies before EQs [5][6][7][8]. However, it is not yet confirmed, and no one culminates this topic with an explicit definition. As far as the researchers are concerned, many theories have been introduced like comparing local TEC with global TEC; solar activity, and analyzing with variations of f0F2 and NmF2 [9] [10]. Recent studies also observed numerous pre-seismic ionospheric abnormalities in TEC, Nmf2 (F2 peak electron density), and hmF2 (F2 peak height) [11][12][13], yet, the underlying mechanism is unclear and more research is still required in this field. The relationship between lithosphere-ionosphere coupling is not pursued entirely and is largely open for research [14]. Outgoing Longwave Radiation (OLR) is also very important when observing the anomalous behavior of LAIC, as it measures the amount of energy released from the ground to outer space and atmosphere which is considered another important source of finding seismic related anomalies in the ionosphere [15]. Ouzounov et al., [16] use multi-sensors and thermal infrared radiations (TIR) i.e., OLR to investigate atmospheric response and process before impending EQ in China from 2008 to 2014. A study indicated ionospheric perturbations developed within the few days before the happening of the seismic activity that was monitored by DEMETER and GNSS-TEC [17]. Many researchers work in the LAIC mechanism to investigate a chain mechanism during the EQ phenomena. A researcher examined the seismic precursors by analyzing the LAIC phenomena using the positive holes or p holes [2]. According to Kuo et al., [2] stress in the lithosphere emanates the positive charge carriers that result in a disturbance in the ionospheric and atmospheric parameters.

Seismo-ionospheric irregularities over the EQ preparation zone can be conferred by two different techniques; positive holes (p hole) emission [18] [19] and Radon emanation from EQ-prone regions [20] [21]. Radon emanation is argued by Freund et al., [18]. According to a study [18], stress caused in the rocks in the epicenter of EQ releases the radon that emanates the Earth's surface, that result tends to vary the air ionization near the lithosphere. Consequently, these phenomena are responsible to cause abnormalities in the atmospheric and ionospheric behavior over the EQ breeding zone. Radon discharge from the EQ

breeding zone due to future seismic preparation period, initiates processes like air ionization and ion recombination subsequently propagating to the ionosphere by variating air temperature (AT) and relative humidity [18] [19].

Solar radiation and geomagnetic activity are also driving forces that cause trouble in the ionosphere. Therefore, it is mandatory to exclude the factor of storms before examining SIA. Therefore, researchers are quite reluctant to examine SIA under storms. Gonzalez et al., [22] characterized that if the value of Dst is between -50nT to -30nT, it is considered a weak storm. While from -100nT to -50nT, a moderate storm is considered, and below -100nT storm is considered as a strong geomagnetic storm. Furthermore, positive Dst is considered by the consequence of solar wind pressure.

This paper analyzes pre-seismic and post-seismic GNSS-TEC data that occurred on 28 October 2018 at 22:23 UTC in the Southwest region of Acajutla, El Salvador. The magnitude of the EQ was 6.1 (Mw) and the depth of the EQ was 22km from the surface of the earth. Furthermore, this research also investigates geomagnetic indices i.e., Dst, Kp, and solar index V_{SW}, f10.7 to discriminate seismo-ionospheric anomalies with solar or geomagnetic activities. Additionally, AT and OLR are also examined to analyze the atmospheric abnormalities and justify GNSS-TEC.

II.DATA AND METHOD

In this paper, TEC is being analyzed and anomalies were observed concerning EQ. The epicenter of the EQ was 13.035^0 N and 90.369^0 W, 85 km from the southwest region of Acajutla, El Salvador (Table 1). TEC is a very important constituent in EQ forecasting studies, but earlier researchers were found to be very selective as they always associated the TEC anomalies with EQ without checking the nature of geomagnetic storms during that EQ happening [23]. Therefore, before observing TEC, solar and geomagnetic indices are analyzed in this study. Space weather data are retrieved from the OMNI website (https://omniweb.gsfc.nasa.gov/).

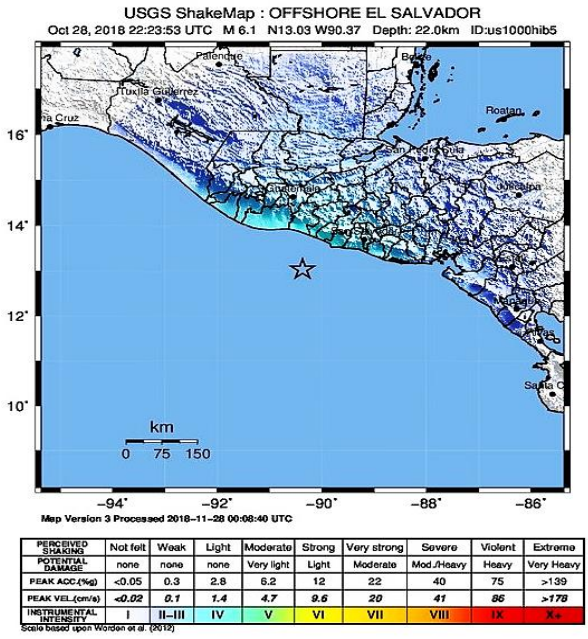


Fig. 1. Shake Map of Mw 6.1 El Salvador EQ (https://earthquake.usgs.gov/earthquakes/eventpage/us1000hib5/shakemap/intensity).

OLR is an important constituent in the prediction of EQ that depends on AT. As OLR is taken from the top of the atmosphere, it is considered an important source of predicting lithosphere-ionosphere anomalies as energy radon raises from ground to atmosphere and will provide a better justification for the observed anomalies. The change in OLR data is dependable with changes in other atmospheric parameters [24]. Therefore, we analyze the OLR as well as AT by collecting the data for 16 days from October 18, 2018, to November 02, 2018. The anomaly can be detected in OLR by applying the limit bounds on OLR data. OLR data is freely available in (https://giovanni.gsfc.nasa.gov/giovanni/).

The ionosphere primarily consists of Total Electron Content (TEC), which plays a very vital role in the ionosphere. Most researchers use TEC to analyze and observe anomalies in the ionosphere before the EQ [25][26][6]. Therefore, this research also uses TEC data to analyze the behavior in the ionosphere for 10 days before and 5 days after the impending EQ. To examine TEC variations, TEC data is utilized from two different International GNSS Service (IGS) stations located in Managua and Guatemala cities. These stations are available near the epicenter and within the earthquake preparation area (EPA). We used the Dobrovolsky formula to calculate the EPA [27].

$$\rho = 10^{0.43M} \quad (1)$$

In (1), M indicates the scale of an EQ where ρ is considered as the area of the affected region, which is in km unit.

Slant TEC (STEC) from the GNSS ground-based stations is acquired alongside the ray-path from the satellite to the GNSS receiver [28][29]. To examine vertical TEC (VTEC), STEC has been derived from the IGS ground-based stations using the equation.

$$STEC_a^h = -\frac{f_2^2 f_1^2}{(f_1^2 - f_2^2)40.3}\left[P_{4,a}^h - c\ (DCB_a + DCB^h)\right] \quad (2)$$

From the above (2), f_1 and f_2 are the GPS dual frequencies, c is the speed of light, $P_{4,a}^h$ is the differences between smoothed code measurements while DCB_a and DCB^h are differential code biases for the satellite and receiver [30]. Furthermore, to convert STEC into VTEC following equation has been applied to STEC:

$$VTEC = STEC\ x\ cos\left[arcsin\left(\frac{Rsinz}{R+H}\right)\right] \quad (3)$$

From the eq. (3), H is defined as the altitude of the ionospheric layer from the surface of the Earth, R is considered as the radius of Earth while "z" concerning the Earth is considered as the zenith angle of the satellite [31]. The station-based TECs are calculated by weighting or surface interpolation of vTECs [32].

$$TEC = \sum w(\varepsilon)VTEC \Big/ \sum w(\varepsilon) \quad (4)$$

TEC is denoted as TECu, where is denoted as a unit (therefore, 1 TECu is equal to 10^{16}el/m^2). Ciraolo et al., [29] use TEC data extracted from the TEC stations that lie within EPA.

To find the TEC variations, a running median upon the basis of quartile is performed. Inter-quartile range (IQR) uses the information of pre ten days of the seismic activity and five days after the seismic activity. Discrepancies were found based on the confidence interval of median ($\widetilde{X}$). Now for the limit bounds, we use the following equations to define the Upper Bound (UB) and Lower Bound (LB):

$$UB = \tilde{X} + IQR \quad (5)$$

$$LB = \tilde{X} - IQR \quad (6)$$

For the detection of abnormalities in the time series, a confidence interval of about 95% is declared, it is suggested that if the observed TEC gets a higher peak than normal distribution is anomalous. Hence, we can visualize the abnormality in the time series by plotting (5-6). A similar median-quartile methodology was used to examine the changes in the OLR and AT. In addition, we used (5-6) for OLR data to generate UB and LB as well.

Detrended TEC (dTEC) is applied on vTEC to further scale the GPS-TEC anomalies [33]. dTEC extracted from vTEC using the following equation:

$$dTEC = \begin{cases} TEC - LB; & while\ TEC < LB \\ 0; & while\ LB \le TEC \le UB \\ TEC - UB; & while\ TEC > UB \end{cases} \quad (7)$$

Table 1. Information about the EQ

Information about the EQ

Magnitude	Country	Location	Date and Time	Preparation Zone [km]
6.1 Mw	El Salvador	13.035^{0}N 90.369^{0}W	2018-10-28 22:23:53 (UTC)	564.94

Information about the IGS stations

Station Name	Location	Distance from Epicenter [km]	Max. dTEC [TECU]	Max. OLR [W/m^2]	Max. AT [^{o}K]
GUAT	14.590^{o}N 90.520^{o}W	136.73	3.886	299	279
MANA	12.149^{o}N 86.249^{o}W	417.47	3.597		

III. RESULTS AND DISCUSSION

This study examines morphological features associated with the El Salvador EQ that occurred on 28 October 2018 by utilizing GPS-TEC, OLR, and AT datasets. Space weather phenomena play a decisive role in ionospheric dynamics [25]. Therefore, before the investigation of the ionospheric seismic interventions, the space weather conditions should be monitored carefully. Fig. 2a and 2c show the time series of Dst and Kp magnetic activity indices. These indices suggest the weak magnetic activity before the main seismic shock, where the Dst index ranges within ±20 nT and Kp (Planetary K-index) range is below than 3 [34]. Fig. 2b and 2d show the time series of V_{SW} and f10.7 solar activity indices. The Solar wind speed ranges show a low-speed V_{sw} (i.e., 300-500 km/s) [35][36][37]; 1-2 days before the EQ, the index values reached 421 km/s. f10.7 values vary between 66-71 sfu before the seismic activity, which indicates quiet or low-solar activity. The low ranges of the space weather indices supported the indication that the abnormalities noticed before the El Salvador EQ may be associated with the impending seismic activities.

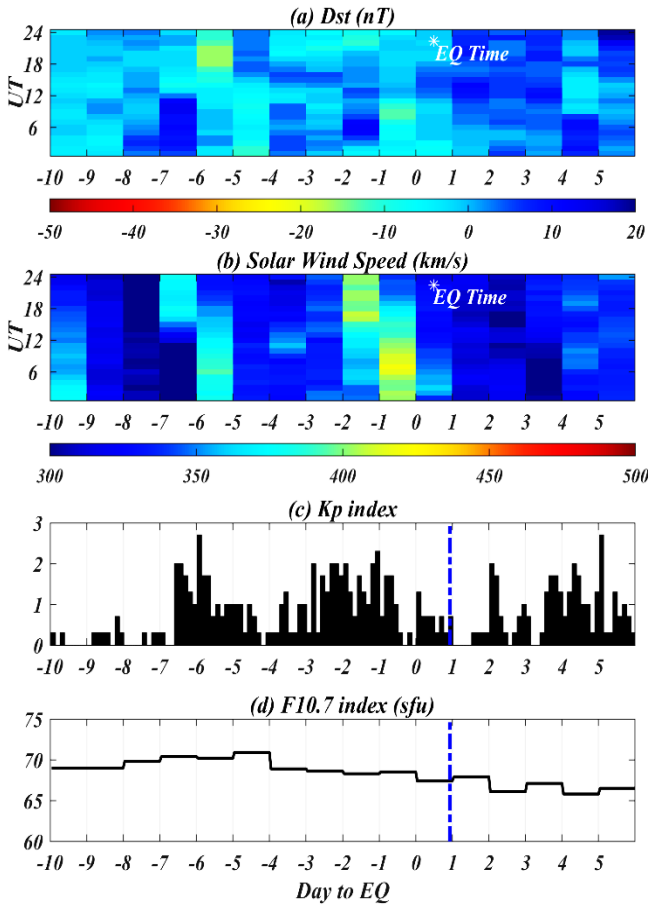


Fig. 2. Depicts the space weather indices 10 days before and 5 days after the El Salvador EQ.

The quiet geomagnetic and solar indices provide a great opportunity to monitor the ionosphere conditions that might experience seismic interferences. Before analyzing the ionosphere directly, we prefer to start analyzing the lower atmospheric conditions by considering the OLR and AT variations. Fig. 3 provides the temporal variations observed during the observed period. It can be seen that the positive variations in the AT started on 22 October 2018 (6 days before the EQ) that lasted for three continuous days till 24 October 2018 and went back to normal afterward. Then a severe change in AT was observed on 26 October 2018 (2 days before the EQ) where the temperature raised to 279^0K (maximum during the observation period). [21] explained that radon released by a tectonic movement initiates several processes in the atmosphere such as air ionization due to the dropped relative humidity. These ionizations lead to changes in the air temperature (depending on the region) which further variates the OLR. From Fig. 3, one can observe that OLR measurements have undergone sudden increments between 22-26 October 2018 (2-6 days before the EQ) that may be induced by increased AT due to increased radon around the EQ preparation zone. Similar findings were reported by [24], where they find mutual anomalies in the OLR and AT within 5 days before M 7.8 Nepal EQ. These mutual enhancements indicate an increased radon activity around the EQ periphery that might lead to ionosphere disturbances.

the ionospheric variations were monitored by two IGS stations falling within the EPA named GUAT and MANA. The details about the locations of these stations and the recorded measurements are depicted in Table 1. The temporal TEC time series for 15 days within the seismic period, along with the dTEC values, are represented in Fig. 4. Significant anomalies in the terms of dTEC can be observed between 22-26 October 2018 (2-6 days before the EQ), where a deviation of about 3 TECU can be observed at both stations, simultaneously. It can be observed that anomalies exhibited by OLR, AT (Fig. 3), and ionospheric TEC (Fig. 4) correlate perfectly with each other which indicates a LAIC coupling phenomenon. In another study, Ouzounov et al., [3] observed different aspects of synchronized TEC and OLR abnormalities inside 5 days period while examining the Tohoku EQ of M_w 9.0. Jianyong et al., [38] also analyzed similar abnormalities in ionospheric GPS-TEC as impending seismic forerunners using a compact system of GPS receivers around the region of the Wenchuan seismic zone. Hence, we suggest that mutual ionospheric-atmospheric analysis may provide significant contributions to future EQ forecasting.

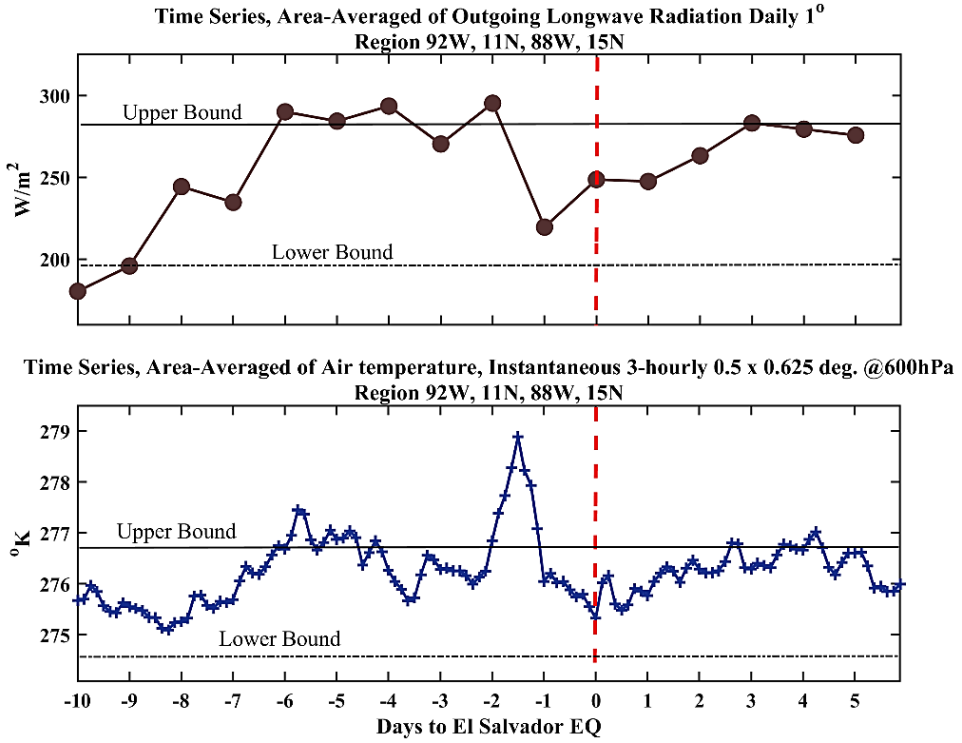


Fig. 3. Time series datasets for AT and OLR over the EQ's region. The red dotted line represents EQ day.

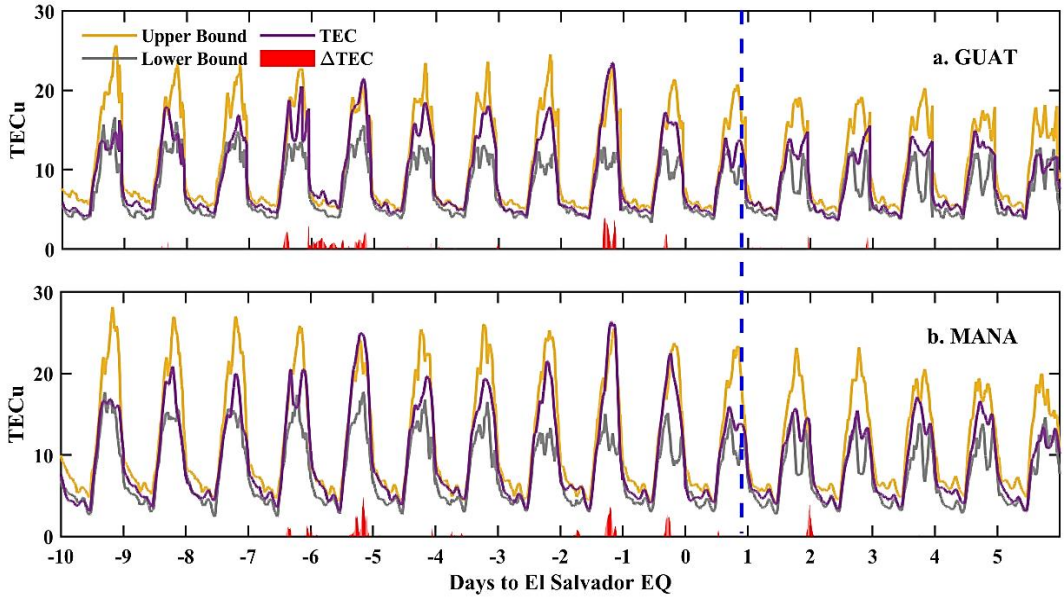


Fig. 4. Analysis of TEC and dTEC values recorded at (a) GUAT and (b) MANA stations, respectively, during 15 days

IV. CONCLUSION

The motivation of this research is to investigate the seismic-induced ionospheric-associated abnormalities that occurred before the El Salvador EQ. LAIC is the focus of the analysis throughout this study. Before processing the data, solar and geomagnetic indices are being analyzed. To analyze the data, we opted for two different GNSS stations, named GUAT and MANA, within the EPA. The ionospheric TEC observations were treated under a statistical analysis based on confidence bounds where considerable deviations of 2 to 3 TECu were observed on October 23-26, 2018. The anomalous AT and OLR observed on October 23-26, 2018, that showed consistency with the TEC anomalies, may be attributed to the increased radon emanations around the El Salvador EQ preparation zone that consequently disturbed the ionosphere. Interestingly, the anomalous response in the atmospheric-ionospheric parameters was enhancing concerning days to the EQ. As the maximum response was observed just 2 days before the EQ which was initiated 6 days ago. Henceforth, we can say from the derived results that observed anomalies can be a possible precursor to the impending EQ. Even though, these results propose the relation between EQ and SIA yet more analysis require to indicate a persuasive part in calculating EQ.

ACKNOWLEDGMENT

The authors are very thankful to NASA, GIOVANNI, and IGS for sharing the GPS-TEC, OLR, and Space weather indices data. We also pay our gratitude to the USGS for providing the seismic catalog and regional EQ information.

REFERENCES

[1] M. Hayakawa, Y. Hobara, "Current status of seismo-electromagnetics for short-term earthquake prediction. Geomatics," Natural Hazards and Risk, 1(2): 115-155, 2010.

[2] C. L. Kuo, L. C. Lee, and J. D. Huba, "An improved coupling model for the lithosphere-atmosphere-ionosphere system," Journal of Geophysical Research: Space Physics, 119(4), 3189-3205, 2014.

[3] D. Ouzounov, S. A. Pulinets, A. Romanov, K. Tsybulya, D. Davidenko, et al., "Atmosphere-ionosphere response to the M9 Tohoku earthquake revealed by multi-instrument space-borne and ground observations: Preliminary results," Earthquake Science, 24(6), 557-564, 2011.

[4] X. Zhang, K. Hattori, T. Tramutoli, "Preface to the special issue on electromagnetic phenomena related to seismic and volcanic activities from EMSEV in 2016," Earthquake Science 30(4): 165-166, 2017.

[5] D. Ouzounov, M. Kafatos, G. Guiliani, S. A. Pulinets, J. Y. Liu, et al., "Observing of pre-earthquake transients features in the Earth atmosphere-ionosphere environment associated with M6.4 and M7.1 Ridgecrest, California, Earthquakes of July 2019," American Geophysical Union, 2019.

[6] A. R. Abbasi, M. Shah, A. Ahmed, N. A. Naqvi, "Possible ionospheric anomalies associated with the 2009 M w 6.4 Taiwan earthquake from DEMETER and GNSS TEC," Acta Geodaetica et Geophysica, 1-15, https://doi.org/10.1007/s40328-020-00325-1, 2020.

[7] A. Kiyani, M. Shah, A. Ahmed, H. H. Shah, S. Hameed, M. A. Adil, N. A. Naqvi, "Seismo ionospheric anomalies possibly associated with the 2018 Mw 8.2 Fiji earthquake detected with GNSS TEC," Journal of Geodynamics, 140, 101782, 2020.

[8] M. Parrot, V. Tramutoli, J. Y. Liu, S. A. Pulinets, et al., "Atmospheric and ionospheric coupling phenomena related to large Earthquakes," Natural Hazards and Earth System Sciences Discussions, 2016.

[9] E. M. Ovalle, M. A. Bravo, C. U. Villalobos, A. J. Foppiano, "Maximum electron concentration and total electron content of the ionosphere over Concepción, Chile, prior to the 27 February 2010 earthquake," Advances in Space Research, 52(7), 1274-1288, 2013.

[10] F. Basciftci, C. Inal, O. Yildirim, S. Bulbul, "Comparison of regional and global TEC values: Turkey Model," International Journal of Engineering and Geosciences, 3(2), 61-72, 2018.

[11] J. Y. Liu, Y. I. Chen, Y. J. Chuo, C. S. Chen, "A statistical investigation of pre earthquake ionospheric anomaly," Journal of Geophysical Research, 111, A05304, 2006.

[12] K. Heki, "Ionospheric electron enhancement preceeding the 2011 Tohoku-Oki Earthquake," Geophysical Research Letters, 38, L17312, 2011.

[13] S. Kalita, B. Chetia, "A novel approach for ionospheric total electron content earthquake precursor and epicenter detection for low-latitude," International Journal of Engineering and Geosciences, 5(2), 94-99, 2020.

[14] E. Senturk, M. S. Cepni, "A statistical analysis of seismo-ionospheric TEC anomalies before 63 M w≥ 5.0 earthquakes in Turkey during 2003–2016," Acta Geophysica, 66(6), 1495-1507, 2018.

[15] N. Venkatanathan, B. Kaarthick, C. Priyadharshini, "OLR anomalies prior to big earthquakes (Mw> 6.0)–A case study on earthquakes of India's neighboring region occurred during the year 2012," New Concepts Global Tecton, 1(3), 34-44, 2013.

[16] D. Ouzounov, S. A. Pulinets, et al., "Atmosphere response to pre-earthquake processes revealed by satellite and ground observations. Case study for few strong earthquakes in Xinjiang, China (2008-2014)," Annals of Geophysics, 63(5), 2020.

[17] K. Ryu, M. Parrot, S. G. Kim, K. S. Jeong, J. Chae, S. A. Pulinets, K. I. Oyama, "Suspected seismo-ionospheric coupling observed by satellite measurements and GPS TEC related to the M7.9 Wenchuan earthquake of 12 May 2008," Journal of Geophysical Research: Space Physics, 119(12), 10,305–10,323, 2014.

[18] F. T. Freund, A. Takeuchi, B. Lau, A. Al-Manaseer, C. Fu, N. Bryant, et al., "Stimulated infrared emission from rocks: assessing a stress indicator," eEarth, 2, 1–10, 2007.

[19] F. T. Freund, I. G. Kulahci, G. Cyr, J. Ling, M. Winnick, J. Tregloan-Reed, M. M. Freund, "Air ionization at rock surfaces and pre-earthquake signals," Journal of atmospheric and solar-terrestrial physics, 71, 1824–1834, 2009.

[20] S. A. Pulinets, D. Ouzounov, L. Ciraolo, R. Singh, G. Cervone, A. Leyva, M. Dunajecka, A. V. Karelin, K. A. Boyarchuk, A. Kotsarenko, "Thermal, atmospheric and ionospheric anomalies around the time of the Colima M 7.8 earthquake of 21 January 2003," Annales Geophysicae 24(3), 835–849, 2006.

[21] S. A. Pulinets, and D. Ouzounov, "Lithosphere – Atmosphere – Ionosphere Coupling (LAIC) model – An unified concept for earthquake precursors validation," Journal of Asian Earth Sciences 41 (4–5), 371–382, 2011.

[22] W. D. Gonzalez, L. A. Joselyn, Y. Kamide, et al., "What is a geomagnetic storm?" Journal of Geophysical Research Space Physics. 99 (A4), 5771-5792, 1994.

[23] J. Ahmed, M. Shah, W. A. Zafar, M. A., Amin, T. Iqbal, "Seismoionospheric anomalies associated with earthquakes from the analysis of the ionosonde data," Journal of Atmospheric and Solar-Terrestrial Physics, 179, 450-458, 2018.

[24] M. Shah, M. Khan, H. Ullah, S. Ali, "Thermal Anomalies Prior to the 2015 Gorkha (Nepal) Earthquake from Modis Land Surface Temperature and Outgoing Longwave Radiations," Geodynamics and Tectonophysics, 9, 123-138, 2018.

[25] E. L. Afraimovich, E. I. Astafieva, M. B. Gokhberg, V. M. Lapshin, V. E. Permyakova, G. M. Steblov, S. L. Shalimov, "Variations of the total electron content in the ionosphere from GPS data recorded during the Hector Mine earthquake of October 16, 1999, California," Russian Journal of Earth Sciences, 6(5), 339-354, 2004.

[26] E. Senturk, M. S. Cepni, "Performance of different weighting and surface fitting techniques on station-wise TEC calculation and modified sine weighting supported by the sun effect," Journal of Spatial Science, 64(2), 209-220, 2019.

[27] I. P. Dobrovolsky, S. I. Zubkov, V. I. Miachkin, "Estimation of the size of earthquake preparation zones," Pure and applied geophysics, 117(5), 1025-1044, 1979.

[28] J. Y. Liu, Y. J. Chuo, S. J. Shan, Y. B. Tsai, Y. I. Chen, S. A. Pulinets, S. B. Yu, "Pre-earthquake ionospheric anomalies registered by continuous GPS TEC measurements," In Annales Geophysicae, 22(5), 1585-1593, 2004.

[29] L, Ciraolo, F. Azpilicueta, C. Brunini, A. Meza, S. M. Radicella, "Calibration errors on experimental slant total electron content (TEC) determined with GPS," Journal of Geodesy, 81(2), 111-120, 2007.

[30] A. Sekertekin, S. Inyurt, S. Yaprak, "Pre-seismic ionospheric anomalies and spatio-temporal analyses of MODIS Land surface temperature and aerosols associated with Sep, 24 2013 Pakistan Earth-TEC findingsquake," Journal of Atmospheric and Solar-Terrestrial Physics, 200, 105218, 2020.

[31] J. A. Klobuchar, "Ionospheric time-delay algorithm for single-frequency GPS users," IEEE Transactions on aerospace and electronic systems, (3), 325-331, 1987.

[32] E. Senturk, H. Livaoglu, M. S. Cepni, "A Comprehensive Analysis of Ionospheric Anomalies before the Mw 7·1 Van Earthquake on 23 October 2011," The Journal of Navigation, 72(3), 702-720, 2019.

[33] M. A. Tariq, M. Shah, M. Hernández-Pajares, T. Iqbal, "Pre-earthquake ionospheric anomalies before three major earthquakes by GPS-TEC and GIM-TEC data during 2015–2017," Advances in Space Research, 63(7), 2088-2099, 2019.

[34] S. Mehdi, M. Shah, N. A. Naqvi," Lithosphere atmosphere ionosphere coupling associated with the 2019 M_w 7.1 California earthquake using GNSS and multiple satellites," Environmental Monitoring and Assessment 193**(**501), 2021.

[35] S. R. Cranmer, "Coronal holes and the high-speed solar wind," Space Science Reviews, 101(3-4), 229-294, 2002.

[36] J. Zhang, M. W. Liemohn, J. U. Kozyra, M. F. Thomsen, H. A. Elliott, J. M. Weygand, "A statistical comparison of solar wind sources of moderate and intense geomagnetic storms at solar minimum and maximum," Journal of Geophysical Research, 111(A01104), 2006.

[37] D. H. Brautigam, M. S. Gussenhoven, D. A. Hardy, "A Statistical Study on the Effects of IMF B_z and Solar Wind Speed on Auroral Ion and Electron Precipitation," Journal of Geophysical Research, 96 (A4), 5525-5538, 1991.

[38] L. Jianyong, M. Jianyong, Y. Xinzhao, Z. Rui, S. Hongbo, H. Yufei, "Ionospheric total electron content disturbance associated with May 12, 2008, Wenchuan Earthquake," Geodesy and Geodynamics, 6 (2), 126–134, 2015.

Uplifting Agriculture through Information and Communication Technology and Geospatial Applications: A Review of Potential Tools and Techniques

Muhammad Adnan Shahid
Department of Irrigation and Drainage,
University of Agriculture, Faisalabad
Faisalabad, Pakistan
muhammad.shahid@uaf.edu.pk

Saif Ullah Khan
Agricultural Remote Sensing Lab
University of Agriculture, Faisalabad
Faisalabad, Pakistan
saifullahsaifi29@gmail.com
(Correspondent Author)

Subhe Seeme
Agricultural Remote Sensing Lab
University of Agriculture, Faisalabad
Faisalabad, Pakistan
subhe.seeme@uaf.edu.pk

Muhammad Danish Majeed
Agricultural Remote Sensing Lab
University of Agriculture, Faisalabad
Faisalabad, Pakistan
kambohdanish@gmail.com

Muhammad Saqlain
Agricultural Remote Sensing Lab
University of Agriculture, Faisalabad
Faisalabad, Pakistan
msaqlain5432@gmail.com

***Abstract* - In Pakistan, agriculture is the back bone of country's economy and largest contributor in the GDP, i.e. 19.2%, providing employment to a large chunk of labor force, as around 70% of population depends on agriculture for its livelihood. Therefore, the role of the agriculture is indispensable to the wellbeing of the nation, poverty alleviation, employment generation, and food security. Large-scale population and labor shift from rural to urban areas along-with other constraints including shrinking of arable land due to horizontal urban advancement, water shortage and climate change have resulted in shrinking agricultural growth. Innovations and involvement of latest technologies in agriculture is the need of hour to increase the agricultural productivity. Agricultural data collection by using Remote Sensing (RS) techniques is an efficient method. Radar imagery and satellite based optical technology can be used for data acquisition, analysis, monitoring, and mapping. Various factors can be studied with greater accuracy through digital image processing (supervised or un-supervised classification, image enhancement, and spectral slicing). Similarly, in-situ observations can be integrated using ICT based tools to different geospatial and crop models for flood monitoring, drought assessment, crop production forecast, and estimation of crop water requirement and acreage under different crops. These advances may prove to be the foundations for the future research**

Keywords:- GIS and RS, ICT, digital agriculture, hazards mitigation.

I. INTRODUCTION

Agriculture is one of the major pillars in the economy of Pakistan contributing 19.2% in the GDP and providing employment to 38.5% of the labor force. More than 65-70% of the population depends upon agriculture for its livelihood (PES 2021). Application of Remote Sensing (RS) and Geographic Information System (GIS) techniques in the field of agriculture can be utilized beneficially for the good will of the farming community, as it can be helpful for natural resource management (Kumar et al., 2015). Every farmer aims at producing the food in a cost-effective manner. The usage of GIS and remote sensing in agriculture is helping the farmers to increase their production, reducing input costs, and achieving more efficient utilization of their land. In the country like Pakistan, where agriculture is major source of country's economy, government can use these applications in order to get information about types of the crops grown, area under cultivation, and expected yield, as well as monitoring and mitigating natural hazards including floods and droughts.

The major aspect of remote sensing is the spectral information, which can be employed to estimate the canopy parameter in crop modeling that ultimately determines the crop growth stages and crop health. Moreover, GIS and Remote Sensing can be used to analyze land use/ land cover and assess any significant changes in it due to drought, floods and other extreme weather events (Bill, 2018). Similarly, remote sensing can be used for identification of pest infestation and diseases. Water resources can also be monitored by the use of geospatial techniques, as well as using ICT based tools. Thus, the major uses of GIS and remote sensing in the agriculture may be summarized as identification of crops, area estimation under a certain crop and assessment of its condition, biomass and yield estimation, water resources management, soil moisture monitoring and management, agro meteorology, and irrigation management by scheduling irrigations precisely (Nain, 2017).

Areas of food insecurity can also be identified by using various tools in GIS. This may help ending the global

hunger by eliminating its root causes. Data collection through remote sensing either directly or by installation on the farm implements allows the farmers to perform different farm operations precisely. For example, if combine harvesters are equipped with GPS tracking units, it could help measuring crop yield and moisture content at the exact locations in the field at the time of harvesting. Similarly, crop growth monitoring along-with different kinds of stress identification and their management may help enhancing agricultural productivity and natural resources sustainability.

II. PRECISION AGRICULTURE

With the introduction of precision agriculture, focus has been made to develop a system in which the management practices are selected according to the site condition. All this has become easy with the introduction of satellite based image analysis. Similarly, for the assessment of real-time agricultural land-scape, the usage remote sensing has been increased. The basis of the system is data acquisition using modern technologies. With the integrated use of technologies including Global Positioning System (GPS), GIS and RS, yield monitoring, assessment of soil related problems, plant health, pest population, and incorporation of different inputs can be done as per requirement (Seelan et al., 2003, (Gassner et al., 2012, Fountas and Gemtos, 2016, Davis et al., Shafi et al., 2019)

III. LAND USE LAND COVER CLASSIFICATION

Existing natural surface features (forests, hills, rivers etc.) are termed as land cover, whereas, the land use features are those modified by human beings (urban, rural settlements, canal, orchards, etc.) For identification of different surface features, their hierarchical classification, and its role in the study of global change is known as land use/ land cover mapping. It is largely affected by human activities such as environmental problems that lead to deforestation and biodiversity loss. Therefore, management and future planning for critical decision making can be provided by available data on land use and land cover. Unplanned and uncontrolled changes in land use and land cover are due to growing population and increasing socio-economic problems (Kaul and Sopan, 2014).

Mismanagement of agricultural, range and forest lands leads to severe environmental problems such as floods, landslides that alter the land use and land cover. Satellite imagery can be used to detect pixel by pixel change for determination of land use/ land cover maps. In different geographical studies, land use and land cover mapping has always remained very important. It is composed of basic information of features and their locations such as area, location, shape, and pattern. For identification of land use and land cover properties throughout the year, geo-registered multi temporal remote sensing data is very beneficial, and in extensive regions in terms of cost, accuracy, and manual errors, it is far better than manual surveys.

In comparison to the manual surveys, where there is a great chance of negligence of different features, synoptic view of the area can be captured through imagery or aerial photography, and nothing can be remained unobserved in this case. Figure 1 shows the LULC map developed for a canal command area.

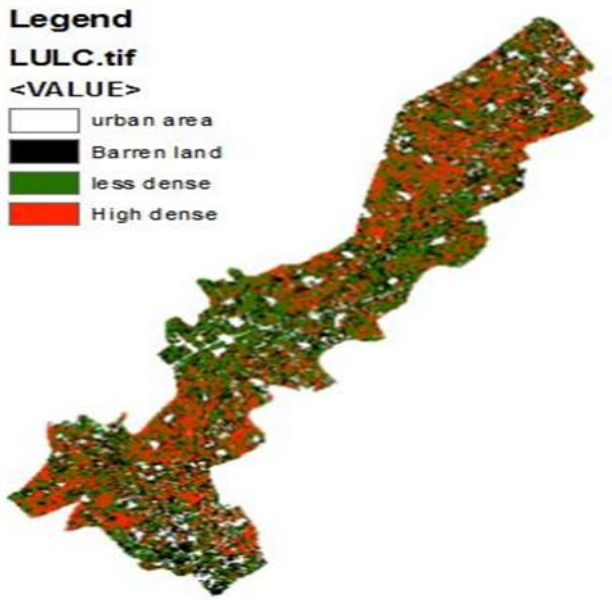


Figure 1. LULC Classification for a Canal Command (Work conducted under Ignite funded project of the authors).

IV. RAINFALL ESTIMATION AND ANALYSIS

Rainfall measurement is necessary in order to determine water requirements of the crops. Moreover, rainfall is one of the major input parameters of hydrological models. Climate and meteorology highly influence the agriculture. Several agro-meteorological parameters e.g. surface albedo, surface temperature, solar radiation, and evapo-transpiration can be accurately and frequently estimated through satellite metrology. To develop correlation and weighted regression model, minimum and maximum temperature and rainfall data are the prime agro meteorology inputs, as crop water demand assessment can be done by subtracting the amount of useful rainfall from ET (Kumar et al., 2015). Satellite-based rainfall estimations have been made possible through different missions including Tropical Rainfall Measuring Mission (TRMM) and Global Precipitation Measurement (GPM). In addition, GIS can be successfully used to develop rainfall raster datasets based on point rainfall data, as well as for rainfall data management by developing interpolated rainfall maps. Such rainfall datasets and graphs can be developed on daily as well as monthly basis to perform different kind of analysis. Figure 2 presents an interpolated rainfall map for Faisalabad for the month of July, 2018.

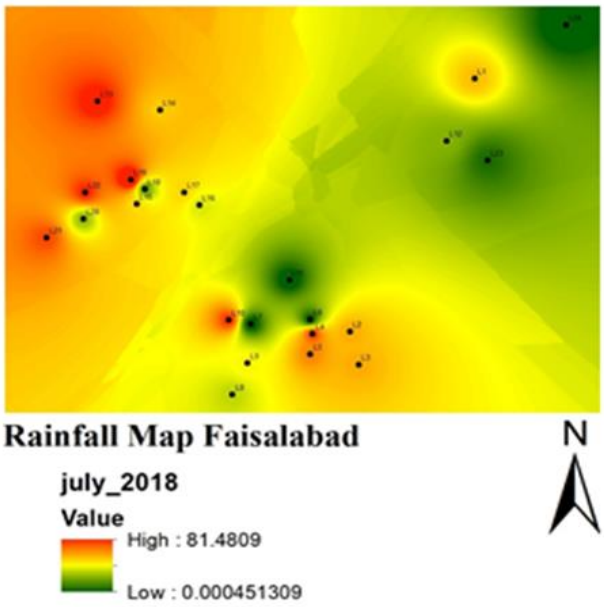


Figure 2. Monthly rainfall interpolation map of Faisalabad for July, 2018 (Work conducted under PARB funded project No.947 of the authors).

V. FLOOD MONITORING

World population is facing great threats from the hydro-meteorological natural hazards like floods. These threats and their impacts on human beings must be assessed in order to combat these issues timely. From agriculture point of view flood, the monitoring is necessary in order to avoid the huge damages to crops and livestock especially during monsoon rainfall spell. Moreover, flood water harvesting can be beneficially used for different applications either agriculture or domestic, but in order to do that flood monitoring and forecasting is essential. The flood monitoring has become necessary due to increased frequency and intensity of such events under changing climate. Remote sensing technology has made it easier to obtain data at much larger scales than the area which could be covered through field-based instruments and methods. Information about flooded areas at different temporal and spatial scales can be gathered through satellite imagery. For management of natural disaster extensive multi-temporal spatial data is needed. In this regard, usage of GIS can be helpful for early warning, monitoring and disaster management (Bannert, 2000). In order to understand the effects of flooding in a particular area such as roads, airport, buildings, streets, and railways, flood inundation mapping is done. Flood inundation or vulnerability mapping can be performed by geo-statistical analysis of a historic archive of satellite imageries. Figure 3 presents such flood inundation/ vulnerability map for District Jhang.

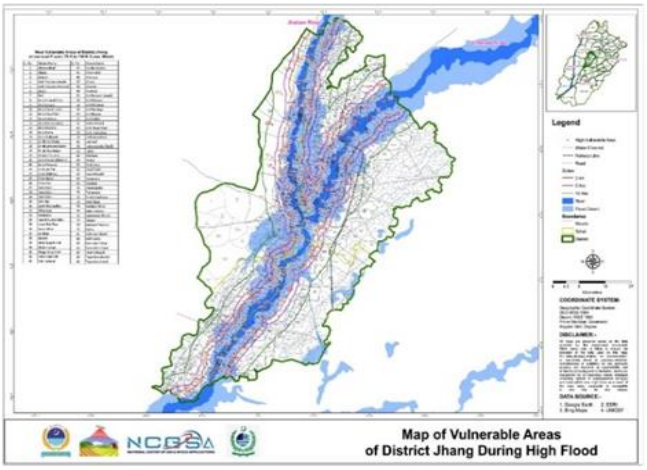


Figure 3. Flood Vulnerability Map for District Jhang; activity performed in Agricultural Remote Sensing Lab.

In addition to direct assessment of flood affected areas from imagery, different RS data like Digital Elevation Models integrated with flow data and other parameters in hydraulic models like HEC-RAS may also be used to develop flood inundation and velocity maps for a river floodplain. Figure 4 presents such flood inundation map for Kalabagh to Chashma reach of Indus river developed using HEC-RAS model.

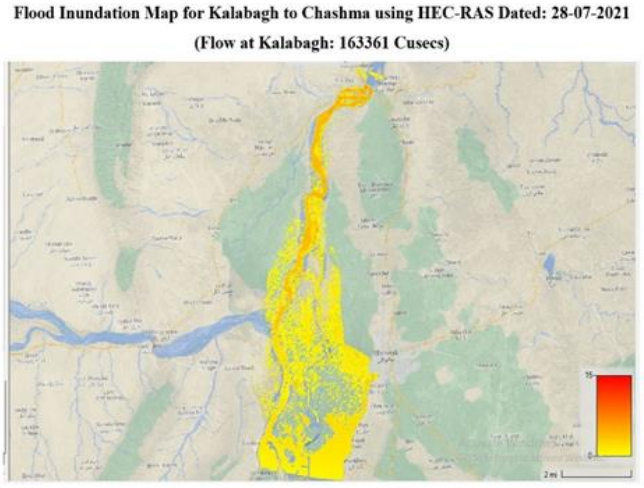


Figure 4. Flood inundation map for Kalabagh to Chashma Reach (Work conducted under the NRPU project No.7431 of the authors).

Geospatial techniques integrated with hydrologic models may also be used for real time monitoring or prediction of any possible flood event and providing flood warnings. For this purpose, the geospatial data in the form DEM, real time rainfall and other parameters including soil and land cover characteristics have integrated to develop hydrologic models for specific river catchments to predict downstream flows and any possible flood situations. Figure 5 presents the hydrographs developed for Poonch and Chenab rivers using such approach in HEC-HMS.

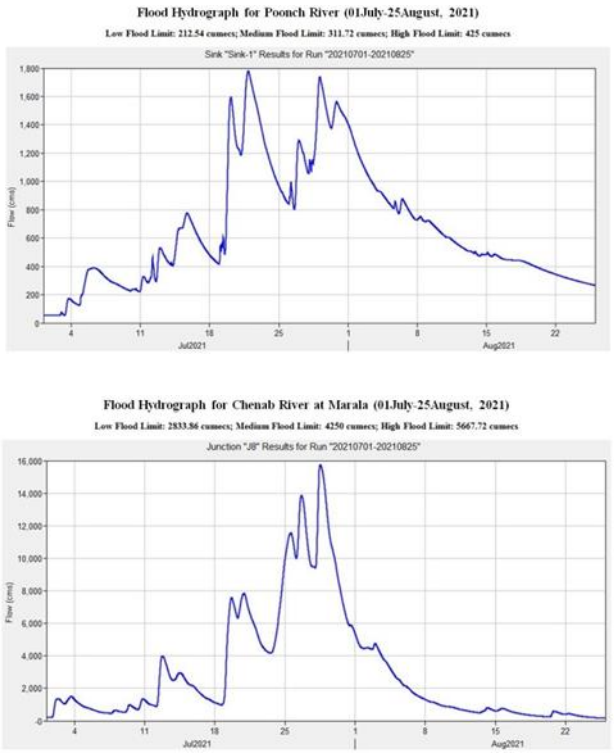


Figure 5. Flood hydrographs for Poonch and Chenab rivers developed using HEC-HMS (Work done under TDF02-117 project of the authors).

VI. CROP INVENTORY

Remote sensing and GIS can be effectively used for identification of crops to determine cropping patterns and perform crop mapping. For a country having agriculture based economy, it is important to have knowledge of the various kinds of crops grown, expected yield, and area under the certain crops. Crop modeling is done by using the spectral information, and strongly related to the canopy parameter on the basis of which crop growth stages and crop health is determined and yield can be estimated (Singh et al., 2002; Ferencz et al., 2004; Zhang et al., 2004; Prasad et al., 2006; Ahmad et al., 2018; Ahmad et al., 2020). Various maps can be created by a combination of satellite images and survey data, which would ultimately give the evidence to the agribusinesses such as seed and fertilizer companies, about the land owners and area under cultivation. Thus, in inventorying data base on different crops, remote sensing can play a significant role. It aids in higher precision of data estimation by reducing the amount of field data to be collected (Kingra et al., 2016).

6 IRRIGATION MANAGEMENT

Agriculture is one of the major water consuming fields and more than 90% water is used in agriculture sector for irrigating the crops. Therefore, irrigation management by proper scheduling and precise application is necessary. Remote sensing data integrated with ICT tools may play a key role in the former part, i.e. determining exact water demands and scheduling irrigations as per needs (Hunsaker et al., 2005; Sultan et al., 2008; Singh et al., 2009; Glenn et al., 2011; Kamble et al., 2013; Yameen et al., 2019) Based on the concept of ET and crop coefficients and water requirements estimation using remote sensing, an irrigation advisory has already been developed (www.uafimis.com) and being employed to provide ET-based irrigation scheduling guidelines to the farmers, which is helpful in reducing water losses by shifting towards precision irrigation to increase per acre yield and water productivity.

In addition to precise scheduling, use of High Efficiency Irrigation System (HEIS) such as drip and sprinkler techniques may help reducing major portion of water application losses. Drip irrigation is more efficient than traditional methods of irrigation including flood, basin and furrow irrigation systems. However, real benefits of these HEIS may be achieved by automation, which is possible by integrating ICT-based tools to perform irrigation need assessment, as well as automatically apply the required amount.

VII. CONCLUSION

With increase in population, the pressure on the natural resources is increasing globally. Sustainable agriculture is necessary to meet the challenges of food security and geospatial data can be successfully used for this purpose, as it is necessary in the current scenario as well as for future generations (Joshi et al., 2002). In the developing countries, where resources are limited, remotely sensed data is a cheap source for their management. Tremendous opportunities are available for the scientists and data analysts in the form of application of RS and GIS in modelling and mapping and employing ICT based tools. A brief review of potential opportunities and options has been presented in this paper, which are already being employed or may be a great breakthrough in future. Integrated use of these geospatial techniques and ICT based tools may be greatly helpful to utilize the resources in efficient manner and uplift the agriculture sector in Pakistan.

REFERENCES

[1] Ahmad, I., Saeed, U., Fahad, M., Ullah, A., ur Rahman, M. H., Ahmad, A., & Judge, J. (2018). Yield forecasting of spring maize using remote sensing and crop modeling in Faisalabad-Punjab Pakistan. Journal of the Indian society of remote sensing, 46(10), 1701-1711.

[2] Ahmad, I., Singh, A., Fahad, M., & Waqas, M. M. (2020). Remote sensing-based framework to predict and assess the interannual variability of maize yields in Pakistan using Landsat imagery. Computers and Electronics in Agriculture, 178, 105732

[3] Ara, M.J., and S.A. Chief. 2019. EFFECT OF FLOODS ON FARMER ' S LIVELIHOOD : A CASE STUDY FOR BUILDING AGRICULTURE RESILIENT TO FLOODS IN. 8(2): 334–344.

[4] Bannert, D. 2000. XXXIII: 113–117.

[5] Bill, R. 2018. Remote sensing and GIS. gis.Science - Die Zeitschrift fur Geoinformatik (2): I. doi: 10.1201/9780429326349-15.

[6] Ferencz, C., Bognar, P., Lichtenberger, J., Hamar, D., Tarcsai, G., Timár, G., ... & Ferencz- Árkos, I. (2004). Crop yield estimation by satellite remote sensing. International Journal of Remote Sensing, 25(20), 4113-4149.

[7] Glenn, E. P., Neale, C. M., Hunsaker, D. J., & Nagler, P. L. (2011). Vegetation index-based crop coefficients to estimate evapotranspiration by remote sensing in agricultural and natural ecosystems. Hydrological Processes, 25(26), 4050-4062.

[8] Hunsaker, D. J., Pinter, P. J., & Kimball, B. A. (2005). Wheat basal crop coefficients determined by normalized difference vegetation index. Irrigation Science, 24(1), 1-14.

[9] Joshi, C., J. De Leeuw, and I.C. Van Duren. 2002. REMOTE SENSING AND GIS APPLICATIONS. (Graph 1).

[10] Israel, D.C. 2012. Economic and Welfare Impacts of Disasters in East Asia and Policy Responses. (December): 553–599.

[11] Hunsaker, D. J., Pinter, P. J., & Kimball, B. A. (2005). Wheat basal crop coefficients determined by normalized difference vegetation index. Irrigation Science, 24(1), 1-14.

[12] Kamble, B., Kilic, A., & Hubbard, K. (2013). Estimating crop coefficients using remote sensing-based vegetation index. Remote sensing, 5(4), 1588-1602.

[13] Kaul, H.A., and I. Sopan. 2014. Land Use Land Cover Classification and Change Detection Using High Land Use Land Cover Classification and Change Detection Using High Resolution Temporal Satellite Data.

[14] Kingra, P.K., D. Majumder, U. Banga, K. Vishwavidyalaya, and S.P. Singh. 2016. Application of Remote Sensing and Gis in Agriculture and Natural Resource Management Under Changing Climatic Conditions. (October). doi: 10.5958/2395-146X.2016.00058.2.

[15] Kumar, N., S.. Yamaç, and A. Velmurugan. 2015. Applications of Remote Sensing and GIS in Natural Resource Management. J. Andaman Sci. Assoc. 20(1): 1–6.

[16] Nain, A.S. 2017. Application of remote sensing and GIS in agrometeorology. J. Agrometeorol. 19(Special Issue): 21–25.

[17] Prasad, A. K., Chai, L., Singh, R. P., & Kafatos, M. (2006). Crop yield estimation model for Iowa using remote sensing and surface parameters. International Journal of Applied Earth Observation and Geoinformation, 8(1), 26-33.

[18] Seelan, S.K., S. Laguette, G.M. Casady, and G.A. Seielstad. 2003. Remote sensing applications for precision agriculture : A learning community approach. 88: 157–169. doi: 10.1016/j.rse.2003.04.007.

[19] Singh, R. A. N. D. H. I. R., Semwal, D. P., Rai, A., & Chhikara, R. S. (2002). Small area estimation of crop yield using remote sensing satellite data. International Journal of Remote Sensing, 23(1), 49-56.

[20] Singh, R. K., & Irmak, A. (2009). Estimation of crop coefficients using satellite remote sensing. Journal of irrigation and drainage engineering, 135(5), 597-608.

[21] Sultan, S., & Ahmad, I. (2008). Determination of daily regional scale actual evapotranspiration for Indus sub-basin using Landsat ETM+. Pakistan Journal of Meteorology (Pakistan).

[22] Yameen, Q. (2019). Normalized Difference Vegetation Index as a Tool for Wheat Crop Coefficient and Evapotranspiration Estimation: A case study of Nankana Sahib District Pakistan. Acta Scientific Agriculture, 3, 32-39.

[23] Zhang, F., Wu, B. F., & Luo, Z. M. (2004). Winter wheat yield predicting for America using remote sensing data. Journal of remote sensing, 8, 611-617.

Atmospheric Monitoring Using Artificial Intelligence Models & Applications

Muhammad Mubeen
PMAS AAUR, Rawalpindi
Islamabad, Pakistan
mubeenkhalid656@gmail.com

Dr. Shahid Mahmood
PMAS AAUR, Rawalpindi
Rawalpindi, Pakistan
shmahmood@uaar.edu.pk

Moosa Bin Saif
PMAS AAUR, Rawalpindi
Islamabad, Pakistan
moosabinsaif157@gmail.com

***Abstract*—**in this paper we discuss Artificial intelligence and the role it plays in atmospheric monitoring through the use of different models and sensors. With the discovery of greenhouse gases and global warming atmospheric monitoring has become an essential requirement. With the help of Artificial intelligence we can fulfill that requirement. AI tools revolutionize the monitoring process through accurate data gathering and forecast information. In the use of AI there are risks and negative effects but its applications are vast. AI can help in Atmospheric monitoring through its integration in machine and sensors. PSO-SVM model (The Support Vector Machine (SVM) would be a methodology for categorizing data that could be split linearly that uses fundamental classification concepts) and MODIS model (This Moderate Resolution Image Spectroradiometer (MODIS) is indeed a payloads imaging sensor. The movement of aerosol-borne contaminants could now be tracked overland, Atmosphere and ocean surfaces thanks to NASA's Moderate-resolution Imaging Spectroradiometer) were discussed in this project.

Keywords*—*Atmospheric Monitoring, AI Models, Air Quality, Artificial Intelligence

I. INTRODUCTION

Exposure to dirty and polluted air quality for a long duration of time has long term health consequences, including the capacity of Lungs will be lost, and the function of the lungs will be affected and decreased—development of some diseases including such, emphysema, asthma, possibly cancer and bronchitis. Poor governance, a lack of research competence, ignorance, incompetence, national/international wars, and political turmoil have all contributed to inattention to air pollution, despite millions of people dying as a result of it across the world. [1]

Air pollution has a range of effects on agriculture. Ground-level ozone could lower agricultural crop and commercial forest production, stunt tree seedling development and survival, and make plants more vulnerable to disease, insects, and some other environmental stresses like harsh weather.[2]

Annually, an average of seven million people is going to die of air pollution throughout the world. According to WHO statistics, nine out of ten persons breathe air exceeding WHO recommended limits and contains high concentrations of pollutants, particularly low- especially middle-income nations bearing the brunt of the burden. The World Health Organization (WHO) is assisting countries in combating air pollution. Air pollution is a severe danger to society and the environment, from haze hanging overhead cities to smoking within the house. Dementia, cardiovascular disease, lung disease, and acute and chronic pulmonary illnesses are among the approximately 4.2 million fatalities caused by exposure to air pollution each year.[3]

II. LITERATURE REVIEW

In the US, the EPA separates the most often employed models under three categories: dispersal models, photo catalytic models, and receptor models. Air pollution models are a crucial technological tool for determining temporal and spatial development, internal mechanisms, and root causes. Simultaneously, it aids in the establishment of a quantitative relationship among "pollution reduction" as well as "quality improvement," and even the transfer between environmental management and planning toward a more quantitative, more refined approach. [4]

Ambient air models are an essential tool for analyzing and resolving environmental issues. Air quality modelling technology has advanced rapidly in recent years, as well as a variety of ambient air models have already been widely used in the research of environmental air pollution. [5]

Various air quality systems have also subsequently become widely utilized in various fields, including necessary scientific research, environmental management, especially environmental impact assessment and decision-making. [6]

III. ATMOSPHERIC MONITORING AND AI

- Monitoring is done to maintain record the air quality throughout order to collect data and improve it.
- SO2, smoke, and suspended particles seem to be the most refined indications.
- The findings are gathered by either a central organization and monitored on some kind of daily basis.
- Spectrometry, conductance, impact and effect, and aerometry are used to assess SO2, the primary pollutant in urban and industrial environments.

Artificial Intelligence

The replication of human intelligence by machines, particularly computer systems, is generally known as artificial intelligence (AI). Computer algorithms, natural language processing (NLP), voice recognition, and machine vision are examples of major AI applications. Computer software programs that analyze the audio and pictures

through surveillance inability to track persons, cars, objects, and situations would be used in artificial intelligence-based sensor networks.

Atmospheric Monitoring

Everywhere else on the planet, this same Copernicus Atmosphere Monitoring Service (CAMS) offers uniform as well as quality-controlled data concerning air pollution levels and health, solar power, greenhouse gas emissions, and climate change. You must monitor environmental air whether you're to know precisely what would be in the atmosphere you are inhaling. Scientists studying air pollution, including transportation, will benefit from a system comprising scientists and researchers monitoring pollution levels. [7]

- NASA monitors air pollution using satellites circling the Earth. Aerosol data by NASA's Terra, Aqua, as well as Suomi-NPP satellites are used by air quality forecasts.
- A new sensor dubbed known as Multi-Angle Imaging system for Aerosols, called MAIA, has been being developed by NASA for use on a prospective spacecraft expedition. MAIA will aid scientists in determining the size, composition, and amount of aerosols throughout our atmosphere.

AI to Measure Air Pollution

We can measure air pollution through different machines and sensors through AI.

Machine:

- We can use machines to measure air pollution in different ways. We can teach machines by machine learning how to measure air pollution, and AI does the process of machine learning.
- Researchers can utilize support vector regression (SVR), a common machine learning approach to anticipate pollutant and particle levels and estimate the overall air quality index.

Sensors:

- We can use different sensors to detect air pollution through AI algorithms.

IV. AI APPLICATIONS USED FOR ATMOSPHERIC MONITORING

This Air Quality Monitoring challenge necessitates thorough, specific instance knowledge and perhaps even the creation of practical, environmental format string event forecasting, as mandated by law. Artificial Intelligence (AI) methodologies and related computer algorithms to supply reliable results could be used to achieve both goals.

Air pollution could then be managed more successfully attributable to Artificial Intelligence (AI). Artificial intelligence (AI) can help cities monitor, communicate, persuade, measure, identify, forecast, advise, decrease, and control air pollution.

Air Pollution Sensors

An air quality sensor is an electronic device that measures the amount of polluted air around them. They are suitable for both indoor as well as outdoor use. Through all the Air Quality System, the EPA keeps track of air quality data.

An air quality sensor is an electronic device that measures the amount of polluted air around them. They are appropriate for intended as well as environmental use. Through Air Quality System, the EPA keeps track of air quality data.

Purple Air employs laser particle detectors PMS5003 as well as PMS1003. 0.3, 0.5, 1.0, 2.5, 5.0, and 10um small particles are counted using all these sensors. This sensor uses a sophisticated algorithm to determine the PM1 from these particulate counts. [8]

Electrochemical Sensors

The electric current passes through conductive material when a magnetic field moves. This generated electrical current may be measured with an electromagnetic sensor.

Electromagnetic (EM) (possibly magneto elastic) stressed sensor technology with steel cable stress monitoring. Microstructure, as well as temperature, have essential roles for magnetization but also magneto elasticity. The EM sensor's construction and setup are depicted.

Optical particle sensors measure the scattered light by particles to measure particulate pollution. Electromagnetic sensors measure the absorbance from infrared light to detect chemicals, including carbon monoxide and Carbon dioxide. [9]

NDIR Sensor

When infrared radiation reacts with gas particles, infrared light at specific wavelengths is captured mainly through gas molecules, producing these gas molecules to vibrate. Gas sensors that use NDIR (Non-Dispersive Infrared) identify a reduction in infrared transmission light that is proportional by gas concentration.

The infrared source, sensor, optic filter, gaseous cell, and machine learning circuits make up an NDIR sensor module. Two detectors and two optical filters having varying frequencies are positioned in the front of the detector in some kind of a single measurement, multiple wavelengths gas sensor monitor. For detecting even a target gas, infrared light captured mostly by target gas travels through with an active filter with such a specific bandwidth. [10]

Operating Principle

Mid-infrared radiation passing through with a sample gas causes gas molecules to resonate with infrared light at their natural frequency inside this spectrum region in which the intensity level of infrared seems to be equal to the natural intensity with gas molecules, actually results throughout infrared absorption besides gas molecules inside the form with molecular vibration.

This Lambert-Beer law describes the relationship between infrared transmittance with gas concentration:

$$T = I / I0 \; e - ecd$$

VOC Sensor

These are the sensors that measure the VOC present in the atmosphere. VOCs are a broad category of carbon-based (organic) compounds (chemicals) present in various man-made & naturally present solids and liquids. Compounds are called volatile because they evaporate quickly at ambient temperature.

- Benzene/BTEX Monitor
- Series-900 VOC Fixed Monitor

Aeroqual VOC Sensors

Photoionization Detector (PID) and Gas Sensitive Semiconductor (GSS) are two main types of VOC measuring sensors offered by Aeroqual. Both sensors

generally non-selective, which means sensors can measure a wide range of VOCs.
They were calibrated against isobutylene to achieve this, recognizing and responding to such a wide variety of VOCs with variable degrees and sensitivity.
Each kind has a measuring range that has been standardized against a subset of VOCs. VOC detectors of the PID type seem to be more durable and can detect a broader range of VOCs. [11]

Measuring Target VOC Sensors

Targeted VOC measures are helpful in regulated contexts (e.g., laboratory, research) when the targeted chemical is employed, but control process and safety and health concerns are present. Any defined correction factor has been hired to assess a specific VOC to find the exact value using isobutylene used during sensor calibration. Furthermore, no additional VOCs should really be introduced in the monitoring area to avoid the border. The sensor may be adjusted towards the targeted VOC and use a calibrated gas of both the target compound for increased accuracy. [12]

Measuring Mixed VOC Sensors

To evaluate air pollution, mixed VOC measurements are widely employed to indicate the existence of VOCs within uncontrolled situations (e.g., workplaces, outdoor). In just this case, the assessment is utilized as a proxy for the presence and concentration of VOCs within the atmosphere. Because some VOCs might impact the readout more often than others, this phenomenon known as cross-interference assessment is just a guide for air quality.

CO_2 Sensor

The carbon dioxide sensor monitors the quantity of infrared (IR) radiation absorbed per carbon dioxide molecule can determine atmospheric carbon dioxide concentrations. Carbon dioxide measurement is essential for monitoring various industrial operations as well as indoor environmental quality.
NDIR sensors seem to be spectroscopic detectors that use carbon dioxide's unique absorption to detect this in a gaseous phase. The infrared detector, the interfered filter, a lighting tube, and an infrared emitter are all part of it. This gas is injected or dispersed into another light pipe, and also the electronics detect the wavelengths and optical emission.
Chemicals carbon dioxide sensor is composed up of polymer and heteropolysiloxane based sensitive sheets. They consume extremely little energy and may be made smaller to fit within microelectronic devices.[13]

Wireless Sensor Network

Current air pollution measuring methods are costly and spatially constrained. Atmospheric monitoring in either a larger area is indeed not possible due to these constraints. However, combining a contemporary low-cost sensor with either a wireless sensor network (WSN) is necessary to receive actual data from multiple sites and generate a comprehensive pollution map.
The primary objectives of this work are to create a low-cost multi-sensor module for measuring air pollution, along with WSN protocols allowing data collecting and data aggregation. Another board like this has been designed and manufactured by us. Standardization from each sensor is performed by comparing data transmission utilizing some of the numerous radio technologies alongside fault-tolerant topology control to preserve data correctness. [14]

MODIS

This Moderate Resolution Image Spectroradiometer (MODIS) is indeed a payloads imaging sensor. The movement of aerosol-borne contaminants could now be tracked overland Atmosphere and ocean surfaces thanks to NASA's Moderate-resolution Imaging Spectroradiometer (MODIS). As little more than a result, CSR and MOD employees successfully adapted MODIS statistics to numerous types of pollutants and have an influence on Texas air quality on even a regular basis. The findings show that MODIS data-related products can identify and monitor pollution movement.
MODIS offers the platform for creating advanced analytical products that might establish a cost-effective yet accurate environmental monitoring system used in concert with ground-based measurements. [15]

V. AI MODELS USED FOR ATMOSPHERIC MONITORING

The goal for the air pollution model is always to estimate environmental air pollutants generated by industrial operations, unintentional releases, or transportation, for example. Air quality modelling has been used to determine the pollutant's higher concentrations and even the source of unusually significant concentrations. The extra contribution toward the current load may be predicted in advance with projects throughout the planning process, and emission circumstances can be optimized.
Mean annual measurements and short-time maximum values have been of interest depending upon these air quality criteria established for both the contaminant in consideration. The proposed methodology can be used to simplify it:

- There is no variation in emission circumstances throughout time.
- During transportation, the weather conditions do not alter.
- Winds speed exceeding one m/s.

Stochastic Model

Stochastic modelling is a type of financial modelling and is used to aid in the decision-making process. Utilizing random variables, this form of modelling estimates the likelihood of possible possibilities under various situations.
Data is presented, and results are predicted using stochastic modelling, accounting for a certain amount of volatility or unpredictability. Companies across a wide range of sectors can use stochastic modelling to enhance their business operations and boost profits. Planners, strategists, and portfolio managers within the financial sector utilize stochastic modelling to control their rights and obligations and optimize their portfolios. [17]

A Case Study in which stochastic model in atmospheric monitoring is described given below:

Applying AI-enabled methodology IOT pollution detectors, the stochastic model from this work was effectively used in environmental dynamics.
The results show that the suggested technique is well adapted to determining air quality in various parts of a city and forecasting PM concentration. Its resulting model employs previous atmospheric data to determine the causal relationship between atmospheric variables and PM concentrations and correctly forecast micro pollutant concentrations.

MACC Model

MACC (Monitoring Atmospheric Composition and Climate) monitors the structure of the Upper atmosphere that predicts air quality using a weather prediction technique based upon modelling and data integration.

It offers data that is critical for understanding environmental issues as well as verifying and refining climate models. There is also knowledge on how to preserve one's health and make the most of solar power generating. MACC is working on creating real atmospheric environmental benefits for operational use. [16]

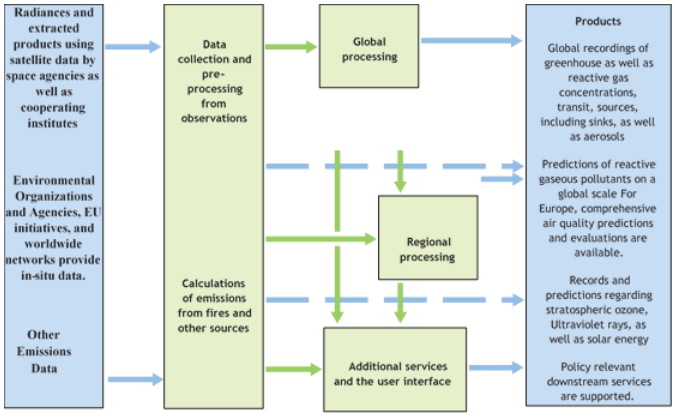


Figure 1

Some Points of MACC Model

- The acquisition and pre-processing collecting observational data and the supply of predictions regarding surface emissions from essential species are the two primary components for MACC.
- Data assimilation and modelling systems that offer fundamental monitoring and warning products and technologies that can provide derived materials are included in regional and global processed chains.
- Providers of downstream services and some other consumers' interfaces.

PSO-SVM Model

The Support Vector Machine (SVM) would be a methodology for categorizing data that could be split linearly that uses fundamental classification concepts. By integrating kernel principles within high dimensional space, SVM was intended to operate with non-linear situations. The researchers employed Particle Swarm Optimization (PSO) and improved SVM performance to overcome their drawbacks. [18]

Case Study

- That is, taking these meteorological factors into account would increase the SAPCF accuracy substantially.
- However, different climatic conditions may have varying impacts on the concentrations of contaminants in the atmosphere. Heavy winds, for example, may transport pollutants across vast areas.
- As a result, wind speed and direction are more essential when compared to many other meteorological parameters. The same climatic element might have distinct impacts in different parts of the world.
- As a result, the influence of climatic factors on pollutant concentrations in the atmosphere must be examined.

To establish a new PSO method for obtaining the best SVM parameters. The automated optimization technique is possible with our suggested PSO–SVM model, which also solves the SVM's precursor concentration problem. [19]

VI. Impact of Artificial Intelligence (AI)

Artificial intelligence has the potential to significantly enhance the efficiency of our workplaces while also augmenting the job that humans can accomplish. Whenever AI takes away mundane or risky activities, it frees understand the more significant labor to focus on tasks that need creativity as well as empathy, amongst many other things.

Environmental Impact of AI

By monitoring fuel reduction emissions, CO2 removal, assisting in the development of greener transportation systems, monitoring deforestation, as well as forecasting extreme weather events, AI can speed global efforts to preserve the environment and save resources. [20]

Increase of CO2

AI would be a huge carbon emitter in and of itself. The scientists calculated that perhaps the carbon footprint from training any single large language model is about 300,000 kilograms of carbon dioxide emissions when they converted this energy usage towards approximate carbon emissions and power expenses.

Not Sustainable Use of Energy

The development in acceptance of machine learning, a field of artificial-intelligence methods that relies on processing massive quantities of data, is primarily to blame for the current increase throughout AI's power usage. "Deep learning models, which are also substantial computational formalism with thousands of millions or billions more features, would be used in modern machine learning techniques.

VII. Conclusion

In this world where technology is evolving at a high rate in order to match the needs and demands of people there is a necessity to keep check and balance of what these demands are costing us. With high demand rate there is high risk involved. This risk could have disastrous effects in the near or upcoming future so we need to monitor this risk with most accurate and efficient technology. Artificial intelligence is that technology. In assessing different models and applications of Artificial Intelligence for atmospheric monitoring it was observed that AI integration in monitoring system can revolutionize the monitoring process. With AI monitoring system we can collect accurate data of atmospheric gases and their concentration with minimum error possibility. We can also predict any changes in the atmospheric composition based in the data collected. AI application in monitoring system can help achieve atmospheric stability.

References

[1] "Spare The Air," 2021. [Online]. Available: http://www.sparetheair.com/health.cfm.

[2] "Frotiers In Public Health," Frotiers In, 2021. [Online]. Available:

https://www.frontiersin.org/articles/10.3389/fpubh.2020.00014/full.

[3] World Health Organization, 2021. [Online]. Available: https://www.who.int/health-topics/air-pollution#tab=tab_1.

[4] W. e. al, "Air pollution terrain nexus: A review considering energy generation and consumption," *Renewable and Sustainable Energy Reviews*, 2019.

[5] A. e. al, "Airborne PM10 and lead concentrations at selected traffic junctions in Khyber Pakhtunkhwa, Pakistan: Implications for human health," *Atmospheric Pollution Research*, pp. 1320-1325, 2019.

[6] Bei et al., "Impacts of local circulations on the wintertime air pollution in the Guanzhong Basin, China," *Science of The Toral Environment*, 2017.

[7] 2. Bei et al., "Impacts of local circulations on the wintertime air pollution in the Guanzhong Basin, China," *Science of The Total Environment*, 2017.

[8] Ilocis, [Online]. Available: http://www.ilocis.org/documents/chpt55e.htm.

[9] Microsoft, 2021. [Online]. Available: https://www.microsoft.com/en-us/education/hackingstem/electromagnets.

[10] "FIGARO," 2018. [Online]. Available: https://www.figaro.co.jp/en/technicalinfo/principle/ndir-type.html.

[11] Aeroqual, 2021. [Online]. Available: https://www.aeroqual.com/voc-sensors-monitors.

[12] "Aeroqual," 2021. [Online]. Available: https://www.aeroqual.com/voc-sensors-monitors.

[13] "AZO Sensors," 2021. [Online]. Available: https://www.azosensors.com/article.aspx?ArticleID=234.

[14] 2. Bathiya et al., "Air pollution monitoring using wireless sensor network," *IEEE*, 2017.

[15] 2. Hutchison et al., "Applications of MODIS satellite data and products for monitoring air quality in the state of Texas," *Atmospheric Environment*, pp. 2403-2412, 2003.

[16] 2. Pour et al., "Spatiotemporal regionalization of atmospheric dust based on multivariate analysis of MACC model over Iran," *Atmospheric Research* , 2021.

[17] 2. Lee et al., "A stochastic model of particulate matters with AI-enabled," *Microelectronic Engineering*, 2020.

[18] 2. Chen et al., "A hybrid PSO-SVM model based on clustering algorithm for short-term," *Technological Forecasting & Social Change*, 2019.

[19] 2. Chen et al., "A hybrid PSO-SVM model based on clustering algorithm for short-term," *Technological Forecasting & Social Change*, 2019.

[20] "PC," 2020. [Online]. Available: https://www.pcmag.com/news/ai-could-save-the-world-if-it-doesnt-ruin-the-environment-first.

Unsupervised Classification of Hyperspectral Images using PCA and K-Means

Ayesha Malik
Department of Electrical Engineering
Institute of Space Technology
Islamabad, Pakistan
ayesha.malik17@mail.ist.edu.pk

Mamoona Waheed
Department of Electrical Engineering
Institute of Space Technology
Islamabad, Pakistan
mamoona17@mail.ist.edu.pk

***Abstract*—The visualization of hyperspectral images in display devices, having RGB colour composition channels is quite difficult due to the high dimensionality of these images. Thus, principal component analysis has been used as a dimensionality reduction algorithm to reduce information loss, by creating uncorrelated features. To classify regions in the hyperspectral images, K-means clustering has been used to form clusters/regions. These two algorithms have been implemented on the three datasets imaged by AVIRIS and ROSIS sensors.**

Keywords—Hyperspectral image, HSI, PCA, K-means clustering, unsupervised, classification, bands, satellite, ROSIS, AVIRIS

I. INTRODUCTION

Remote Sensing is the data collection of earth's surface, by measuring the reflected signal at various wavelength bands to form a spectral signature from objects at long distances, via either of the two techniques: infrared sensing or optical remote sensing (via satellite's optical sensor) [1]. Based on the number of bands, satellite images are classified into: panchromatic, multispectral and hyperspectral images.

Attaining hyperspectral image datasets depends on imaging spectrometers that image in continuous, narrow regions of electromagnetic waves [2]. Due to which, they have high spectral resolution that describes boundaries and composition of an object and can help in image classification, which is the most active part of research. Classifying hyperspectral images may seem difficult due to their high dimensionality, missing labels, variation in data due to spatial locality and poor image quality due to noise or background interference etc.

Hyperspectral image classification methods are as such [3]: supervised, unsupervised and semi-supervised. Supervised classification makes use of prior data knowledge. An example of this method is the support vector machine (SVM). On the contrary, unsupervised classification is not based on any prior data knowledge. A common method is K-means clustering and its aim is to obtain a meaningful output from the set of unlabelled data via clustering/grouping [4].

Hyperspectral imaging (HSI) is used for [5]: agricultural and water resources control (e.g. identifying crops, lakes etc. [4]), document imaging and mineralogical mapping of earth surface.

The large hyperspectral data, increases processing complexity and time. The solution is to effectively reduce data to apply various processing methods e.g. classification, that will help find the number of regions in hyperspectral image [6].

The remainder of this paper is broken down as follows. Section 2 presents the literature review of work done in the field. Section 3 defines the problem statement. Methodology is explained in Section 4. Dataset used and classification results form Section 5. Finally, concluding remarks alongside future work are given in Section 6.

II. LITERATURE REVIEW

Prior to remote sensing, geological surveys were done manually. Now, technological advancements help capture hyperspectral images via satellites and enable algorithms to help classify the data in a matter of moments [4].

Colour images have intensity values in three bands i.e. RGB, whereas, hyperspectral images contain more than hundred bands in discrete intervals from visible to infrared region [7]. HSI obtains the spectrum for each pixel in the image frame to identify target areas.

Hyperspectral images are characterized by two resolution types, namely [5]: spatial and spectral. Spatial resolution is the relationship among image pixels and is inversely proportional to patch size i.e. smaller the patch, greater the details. Whereas, spectral resolution is measured as the number of bands and range of electromagnetic spectrum, by the sensor.

High dimensional hyperspectral data lacking labelled samples can result in Hughes phenomenon i.e. reduced accuracy in classification. This can be overcome by techniques of dimensionality reduction e.g. Principal component analysis (PCA), Discrete wavelet transform and Independent component analysis (ICA) [1]. The first few principal components of PCA result in 70 percent correct classification rate [6].

Previously, only spectral information was being used to achieve hyperspectral image classification upon high dimensional data via support vector machine (SVM) , neural networks etc. [3]. Whereas, some classification approaches work on reducing high-dimensional data first and then using clustering methods.

Supervised deep classification of hyperspectral images returns almost 100 percent accurate results [8]. Classification methods are based on parametric and non-parametric classifiers or supervised and unsupervised classifiers [9]. Each having its own limitations [10]. Classifying regions help study the geographic location and boundaries of a certain patch that is imaged by the satellite.

Existing work is related to either PCA related schemes or discriminant analysis-based schemes. One of the prominent work done is based on both of these schemes, that is by using PCA for dimensionality reduction and SVM for classification [11].

SVM, a supervised learning method, is effective in high dimensional spaces and is accurate for classification. It requires a smaller number of training samples and labels [1]. However, SVM is computationally expensive. Thus, unsupervised classification methods such as K-means clustering , K- nearest neighbour, Neural networks are a better solution where pixels are to be assigned to clusters without using prior knowledge [12]. K-means accounts for 78.3% accuracy for classification [13].

III. Problem Statement

During hyperspectral data analysis, the following challenges are faced:

- High computational cost
- Storage of a few hundred megabytes required
- Redundancy due to correlation of neighbouring image bands. This high dimensional redundant data needs to be catered for, to efficiently apply processing techniques [14].

The aim of this research paper was to implement dimensionality reduction and K-means classification, in order to find the number of regions present in each hyperspectral image and colour label them to differentiate those classified regions.

IV. Methodology

To achieve the goal of this paper, two-stage process was implemented i.e. first, data dimensionality was reduced, followed by K-means clustering. PCA is a standard dimensionality reduction algorithm for hyperspectral images [12] that aims to remove the correlation among bands [1].

Clustering works by grouping pixels and iteratively updating the centroid of a group. The centroid represents mean spectral signature of all pixels in a cluster [8].

A. Importing libraries in Python to load and process data

- numpy: for multidimensional arrays and matrices
- scipy: to load .mat file (hyperspectral dataset)
- sklearn: to import PCA and K-means
- matplotlib: to create figures and plots
- spectral: to use functions for hyperspectral data processing
- import h5py: to import data of HDF5 binary format

B. Dimensionality Reduction via PCA

PCA is a classical, unsupervised dimensionality reduction method which does not require labels [14] and preserves most of the spectral information in a compact number of principal components [1]. Its governing principal is that the neighbouring bands of hyperspectral images are highly correlated, which would mean that they often convey almost the same information. Most of the information may only be contained in the first few bands [6].

The basic principle used in PCA is the eigenvalue decomposition of the covariance matrix [1]. The eigenvalues represent the variance in the direction of the eigenvector.

It must be remembered that PCA is a dimension reduction tool, not a classifier. Thus, a classifier is fit onto the PCA-transformed data.

To choose the number of principal components required to describe a dataset, explained variance ratio graph was plotted (number of components vs. cumulative explained variance). Components which had greater than 95 percent cumulative explained variance were chosen i.e. 8 principal components in this case for all three hyperspectral datasets, as shown in Fig. 1 for Pavia. The curve depicts how much of the total, 102-dimensional variance is contained within the first N components. The same approach was used to select principal components for Cuprite and Moffett.

C. K-means clustering

K-Means being an unsupervised method, groups data into ‘k’ number of user defined clusters. To help decide the number of clusters, elbow method was used i.e. for each value of k (e.g. in the range 1 to 10) , the sum of squared distances from each data point to its centre(distortion) was calculated.

Elbow is the point of inflection on the curve which is the optimal value of k. According to this method, k=5 for Pavia (as shown in Fig. 1) and Cuprite data sets, k= 6 for Moffett [3].

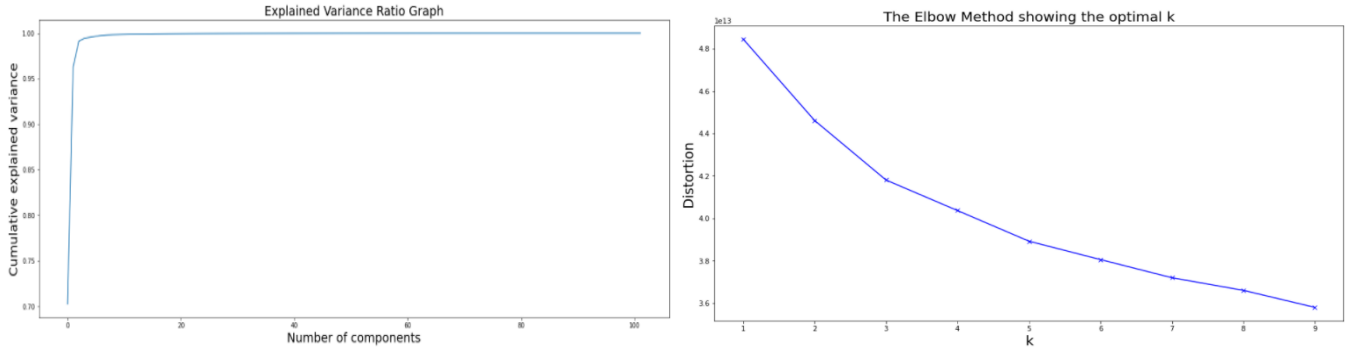


Fig. 1. Explained Variance and Elbow graph for Pavia dataset

V. EXPERIMENTATION AND RESULTS

In accordance with the problem statement, three hyperspectral images were utilized [1]. The classification of different regions was done for the following datasets acquired by their respective sensors:

A. *ROSIS(Reflective Optics System Imaging Spectrometer) Pavia Centre:* covers Pavia, northern Italy having 102 spectral bands.

B. *AVIRIS* (Airborne Visible Infrared Imaging Spectrometer) datasets:
   1) *Cuprite:* covers Cuprite in Las Vegas, U.S having 224 channels.
   2) *Moffett Field:* covers Moffett airfiled, CA, U.S. having 224 channels.

Unsupervised classification was applied on the above stated hyperspectral images using python libraries. The datasets have the following dimensions i.e. rows, columns and bands, respectively:

- Pavia: 1096*715*102
- Cuprite: 512*614*224
- Moffett: 753*1923*224

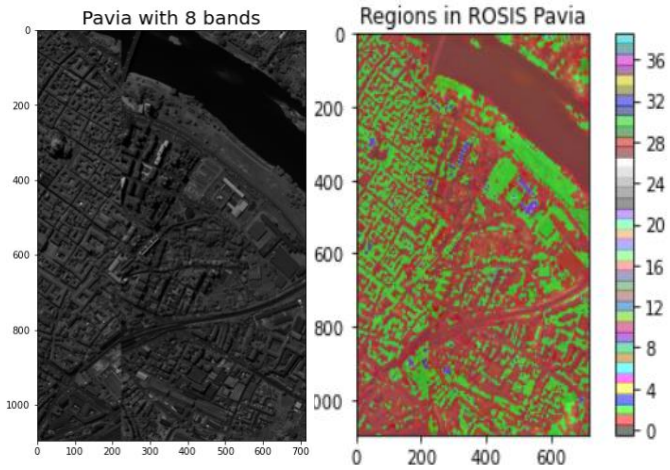
The reshape command was used to reshape the data, by multiplying the actual rows and columns to form the current rows and the original bands were retained as columns e.g. Pavia was reshaped to 783640*102.

To visualize the explained variance ratio, its cumulative sum was plotted which helped select the number of principal components to be retained as shown in Fig. 2 (a), Fig. 3 (a), Fig. 4 (a), that display the images with 8 principal components.

After reducing the dimensions of all three datasets, k-means was applied using the elbow method to assign 'k' optimal clusters. Fig. 2 (b), Fig. 3 (b) and Fig. 4 (b) are the colour-labelled clusters formed for Pavia, Cuprite and Moffett, respectively. The axes of Fig. 2 to Fig. 4 represent the rows and columns of the respective images in 2D.

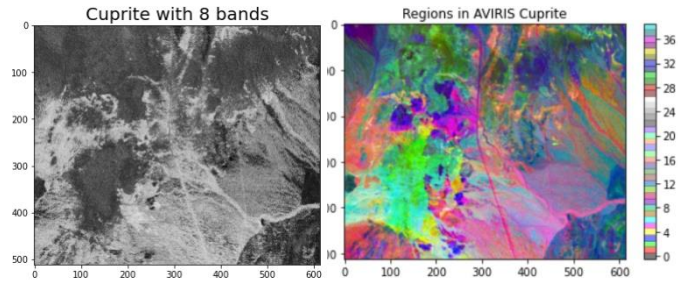
The 'KMeans' command used in python formed clusters with equal variance to minimize 'within cluster sum of squares' (WCSS). For data with high dimensionality, Euclidean distances increase. Thus, implementing a dimensionality reduction algorithm like Principal component analysis (PCA) before K-means clustering can help overcome this problem.

The number of clusters/regions formed for Pavia are 4 after 15 iterations, whereas, for Cuprite and Moffett there are 5 clusters after 15 iterations. In simple words, the algorithm segments the image by clustering pixels into classes which have spectral similarity e.g. roads, trees, water bodies, soil etc.



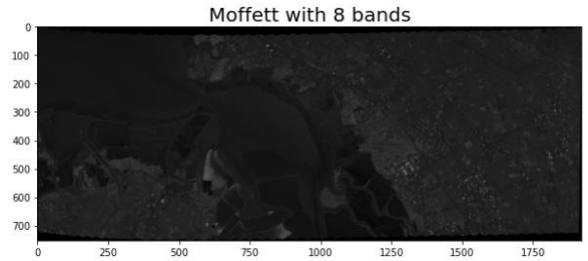
(a) (b)

Fig. 2. Pavia results (a) 8 principal components after PCA. (b) K-means clustering result.

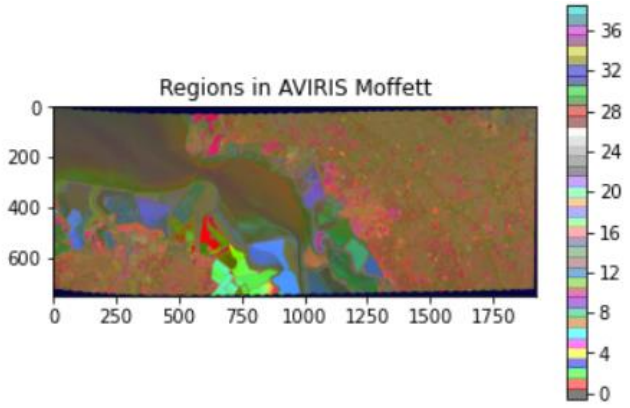


(a) (b)

Fig. 3. Cuprite results (a) 8 principal components after PCA. (b) K-means clustering result.



(a)



(b)

Fig. 4. Moffett results (a) 8 principal components after PCA. (b) K-means clustering result.

VI. Conclusion and Future work

Hyperspectral images contain wide-ranged spectral information that is used to identify and differentiate objects. Classification is the process of assigning objects to classes with homogeneous characteristics. This paper is firsthand examination of: dimensionality reduction via PCA and unsupervised classification via K-means to cluster the three hyperspectral datasets with the goal of finding number of regions based on some similarity in the datasets. Initially, SVM was being used for clustering. However, due to computational expenses, it was dismissed. With K-means, clusters have been formed without any prior knowledge i.e. labels.

One of the limitations of PCA for dimensionality reduction is the loss of spectral information, as a result of selecting principal components by only considering variance and not the spectral position [15]. Another approach of efficiently clustering data and finding number of regions can be: supervised classification, by breaking the dataset into training and test sets.

Data Set

[1] M Graña, MA Veganzons, B Ayerdi, "GRUPO DE INTELIGENCIA COMPUTACIONAL(GIC)," [Online]. Available: http://www.ehu.eus/ccwintco/index.php/Hyperspectral_Remote_Sensing_Scenes. [Accessed 8 May 2021].

References

[1] T. Subba Reddy and J. Harikiran, "Hyperspectral image classification using support vector machines," IAES Int. J. Artif. Intell., vol. 9, no. 4, pp. 684–690, 2020, doi: 10.11591/ijai.v9.i4.pp684-690.

[2] B. Rasti et al., "Feature Extraction for Hyperspectral Imagery: The Evolution from Shallow to Deep: Overview and Toolbox," IEEE Geosci. Remote Sens. Mag., vol. 8, no. 4, pp. 60–88, 2020, doi: 10.1109/MGRS.2020.2979764.

[3] W. Lv and X. Wang, "Overview of Hyperspectral Image Classification," J. Sensors, vol. 2020, 2020, doi: 10.1155/2020/4817234.

[4] C. R. Addanki, S. A, and V. R. A, "Study of the Clustering Algorithms for Hyper Spectral Remote Sensing Images," J. Hyperspectral Remote Sens., vol. 10, no. 2, p. 117, 2020, doi: 10.29150/jhrs.v10.2.p117-121.

[5] M. J. Khan, H. S. Khan, A. Yousaf, K. Khurshid, and A. Abbas, "Modern Trends in Hyperspectral Image Analysis: A Review," IEEE Access, vol. 6, no. June, pp. 14118–14129, 2018, doi: 10.1109/ACCESS.2018.2812999.

[6] C. Rodarmel and J. Shan, "Principal component analysis for hyperspectral image classification," Surv. L. Inf. Sci., vol. 62, no. 2, pp. 115–122, 2002.

[7] S. Ranjan, D. R. Nayak, K. S. Kumar, R. Dash, and B. Majhi, "Hyperspectral image classification: A k-means clustering based approach," 2017 4th Int. Conf. Adv. Comput. Commun. Syst. ICACCS 2017, pp. 0–6, 2017, doi: 10.1109/ICACCS.2017.8014707.

[8] H. Yadav, A. Candela, and D. Wettergreen, "A Study of Unsupervised Classification Techniques for Hyperspectral Datasets," IGARSS 2019 - 2019 IEEE Int. Geosci. Remote Sens. Symp., pp. 2993–2996, 2019, doi: 10.1109/igarss.2019.8900501.

[9] S. Sattar, H. A. Khan, and K. Khurshid, "OPTIMIZED CLASS-SEPARABILITY IN HYPERSPECTRAL IMAGES," in 2016 IEEE International Geoscience and Remote Sensing Symposium (IGARSS), 2016, pp. 2711–2714, doi: 10.1109/IGARSS.2016.7729700.

[10] I. A. Huqqani and K. Khurshid, "Comparative study of supervised classification of urban area hyperspectral satellite imagery," J. Sp. Technol., vol. 4, no. 1, pp. 1–9, 2014.

[11] A. Rehman, "Project Report: Hyperspectral Image Principal Component Analysis and Classification." 2018.

[12] F. Masood, I.-H. Qazi, and K. Khurshid, "Saliency-based visualization of hyperspectral satellite images using hierarchical fusion," J. Appl. Remote Sens., vol. 12, no. 04, p. 1, 2018, doi: 10.1117/1.jrs.12.046011.

[13] S. A., "Hyperspectral Image Classification Using Unsupervised Algorithms," Int. J. Adv. Comput. Sci. Appl., vol. 7, no. 4, pp. 198–205, 2016, doi: 10.14569/ijacsa.2016.070425.

[14] K. Kotwal and S. Chaudhuri, "Visualization of hyperspectral images using bilateral filtering," IEEE Trans. Geosci. Remote Sens., vol. 48, no. 5, pp. 2308–2316, 2010, doi: 10.1109/TGRS.2009.2037950.

[15] H. A. Khan, M. M. Khan, K. Khurshid, and J. Chanussot, "Saliency based visualization of hyper-spectral images," Int. Geosci. Remote Sens. Symp., vol. 2015-Novem, pp. 1096–1099, 2015, doi: 10.1109/IGARSS.2015.7325961.

Implementation of the Maximum Cross Correlation (Mcc) Method In Python for Ocean Current Estimation Over the Arabian Sea

Sheeza Khalid
Geospatial Research and Education Lab
Dept. of Space Science
Institute of Space Technology, (IST)
Islamabad, Pakistan
khalidsheeza@gmail.com

Waqas A. Qazi
Geospatial Research and Education Lab
Dept. of Space Science
Institute of Space Technology, (IST)
Islamabad, Pakistan
waqas.qazi@grel.ist.edu.pk

***Abstract*— Ocean currents are an important parameter in physical oceanography because they act to neutralize the temperature difference between different areas in the oceans. These parameters are important for reduction of shipping cost, and also the dispersal of many life forms also depends on them. The Arabian Sea switches direction annually due to strong monsoon winds and results in changing rainfall patterns seasonally. A few studies have mapped ocean currents in the Arabian Sea using radar altimetry data, however these methods generate only geostrophic currents, have low resolution, and also cannot function well near the coasts. A relatively higher resolution total ocean currents measurement from satellites does not exist for the Arabian Sea over a long time-series. The Maximum Cross-Correlation (MCC) method has been used with Advanced Very High Resolution Radiometer (AVHRR) data in various studies to extract currents in different regions of world. For this study, we have implemented the MCC method in Python with the aim of utilizing AVHRR optical remote sensing image sequential pairs over the Arabian Sea for ocean current generation. The AVHRR level-1B images are first corrected for brightness temperature and then re-projected, to be ready for ingestion in the MCC algorithm, which is implemented in Python as a combination of different functions on pair of images to extract ocean currents. Results represent the velocity vector of ocean currents in the study area. The estimated velocity vectors are then masked with a threshold for the correlation factor and filtered for removal of outliers, for the generation of the final ocean currents map.**

Keywords*— Advanced Very High Resolution Radiometer (AVHRR), Arabian Sea, Brightness Temperature, Maximum Cross Correlation (MCC) Method, Ocean Currents.*

I.INTRODUCTION

Satellite oceanography is the field of remote sensing in which monitoring and study of ocean is focused. Platforms of satellite give advantage to sensors in viewing oceans. These advantages include wide synoptic coverage at higher resolution, and daily sampling, which can produce good time series analysis over a period of many years. These advantage can help in differentiating the remote sensing from all other such techniques. Satellite sensors are used to monitor oceans are of two types active and passive. Visible sensors provide various types of data like suspended particulates, upwelling and chlorophyll. Various parameters like salanity, surface temperature and its roughness are measured by active microwave sensors. Whereas, sea surface temperature is measured more accurately by passive infrared sensors. [1]

In the field of satellite oceanography, the study of ocean currents is an important aspect to deal with oceanic phenomena. The earth's rotation is one of the parameter which influence the sea current. Moreover, salinity, moon's gravitational pull and winds also influence the ocean currents. The Earth's rotation influences currents through the Coriolis Effect acts perpendicular to the direction of motion of the ocean current and to the earth's rotational axis [2].

This study uses Maximum Cross Correlation Method (MCC) to estimate ocean currents over the Arabian Sea. In 1986, Emery et al.[3] developed the technique to compute advective sea surface velocities using cross correlations between sequential infrared satellite images. In 1990, Tokmakian et al. [4] evaluated the method of estimating sea surface velocities from sequences of Advance Very High Resolution Radiometer (AVHRR) and Coastal Zone Color Scanner (CZCS) images using MCC Method. In 1992, Kelly & Strub[5] conducted the research in which two methods of estimating surface velocity vectors from AVHRR data were applied to the same set of images and the results were compared with in situ and altimeter measurements. In 2002, Bowen et al.[6] performed research for ocean surface circulation estimation by automated tracking of thermal infrared features in pairs of sequential satellite imagery. In 2007, Crocker et al. [7] on the basis of many existing studies on MCC analysis developed the comparison analysis for the currents retrieval but the main focus of this study is to evaluate the potential of technique which uses velocities of the current acquired from thermal imagery as compared the technique of MCC. In 2016, Warren et al. [8]attempted to automatically estimate surface current velocities from satellite-derived thermal or visible imagery but faced limitations in the availability of cloud free sequential images. Published in 2017, the work of Heuze et al. [9] analyses the accuracy of such an estimation of surface current fields retrieved with the maximum cross correlation (MCC) method, here used to track patterns of Advanced Very High Resolution Radiometer (AVHRR) brightness temperature between 224 pairs of consecutive images taken between January and December 2015 in the western Mediterranean Sea. Another 2017 study by Heuze et al. [10] focused on using model outputs instead of satellite images, to assess biases induced by this method, for four different seas of Western Europe. In October 2017, Liu et al. [11] studied the computational results of data analysis of two satellites with the help of MCC technique. One of these satellites is known as Visible Infrared Imaging Radiometer Suite (VIIRS), whereas, the other one is known as Moderate Resolution Imaging Spectroradiometer (MODIS).

Rainfall patterns in the Arabian Sea changes annually due to various parameters; and directional change of surface

circulation is the most important of all these. A few studies as Kalyani et al.[12] and Eremeev et al.[13] have mapped ocean currents in the Arabian Sea using radar altimetry data, however these methods generate only geostrophic currents, have low resolution, and also cannot function well near the coasts. A relatively higher resolution total ocean currents measurement from satellites does not exist for the Arabian Sea over a long time-series. Hence for this study, we have implemented the MCC method in Python with the aim of utilizing AVHRR optical sequential pairs images in the region of the Arabian sea for ocean current generation.
The study area map of the Arabian Sea is shown in Fig.1.

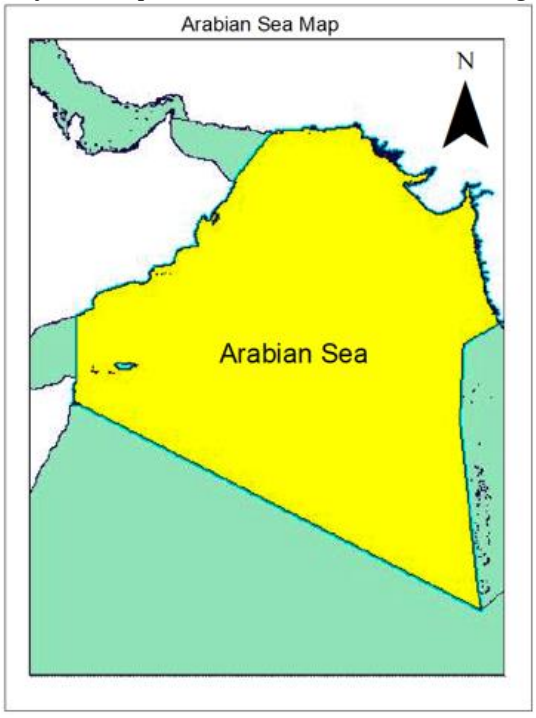


Fig. 1. Study Area Map.

According the change of the season the winds of monsoon change their directions from north-east to south-west. It is noted that the direction of wind in summer season is usually from sea towards land in a clockwise manner, whereas in winter season these winds blow from south-west parts of Asia towards the sea. These winds cause heavy showers in the regions of countries of sub-continent like Pakistan, India and Bangladesh. These are the cyclic effects which not only influence the climate of land but they have impacts on the Arabian Sea as well. Ocean temperatures are also influenced by the local winds due to the landlocked property of the Arabian sea in its north. [14].

II.DATA PRE-PROCESSING METHOD

The Channel 4 data which is related to the temperature of black body is used in this study, which is also known as the brightness temperature with a wavelength of 10.8 µm of Local Area Coverage-1.1km (LAC) format level 1B product of AVHRR data. The sequential pair of 27th May, 2019 with time of capturing of first image is 01:03:56 GMT and that of second image is 03:04:28 GMT are firstly corrected for the brightness temperature using the equation:

$$T = A + B.\mathrm{T}^{*} \quad (1)$$

Where T^{*} is the Brightness temperature band (channel 4) while A and B are correction factors.

This correction is performed using band math of SNAP software. Further we perform the reprojection of the pair images. As shown in Fig.2.

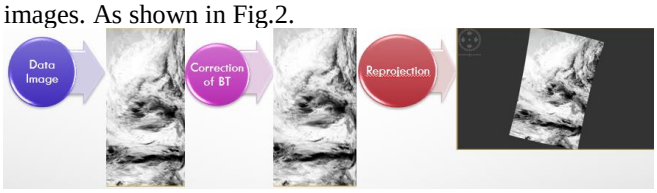


Fig. 2. Data preprocessingn (Non-corrected image, corrected image and the reprojected image (from left to right)).

III.OCEAN CURRENT ESTIMATION FROM MCC METHOD

The pre-processed pair of images are exported in GeoTiff format for the further processing in Python where various steps are performed for the extraction of velocity vectors whose detail sequence is shown in the flow chart in Fig.3..

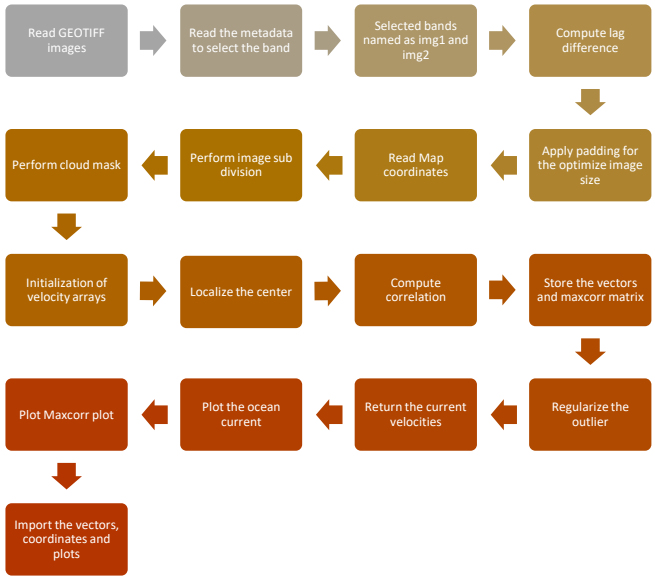


Fig. 3. Sequence of MCC Method in Python.

For the estimation of ocean currents first we select the corrected brightness temperature band. We need to compute the time difference between the pair images, so after computing time lag we apply padding to optimize the image size. Further we extracted the auxiliary data then develop the window filter to divide images in sub section for the ease of processing. After that for cloud masking the cut off threshold of value -1 for normalized brightness temperature is executed with reference to Heuze.et al [9].
After initializing the velocity arrays to store values of vector we performed the normalized cross correlation function to compute the velocity vectors for the plotting of ocean currents.
The MCC method utilizes two images. It cross-correlates one image by the other image through a specified template window and corresponding search window. Displacement vector is calculated in this technique, which is divided by the time lapse of these two images, and hence it yields the velocity of the ocean currents. The computed vectors are finally regularized to remove any outlier in computation and regularized velocity vectors are at last used to plot the estimated ocean currents over the Arabian Sea.

IV.RESULTS AND DISCUSSIONS

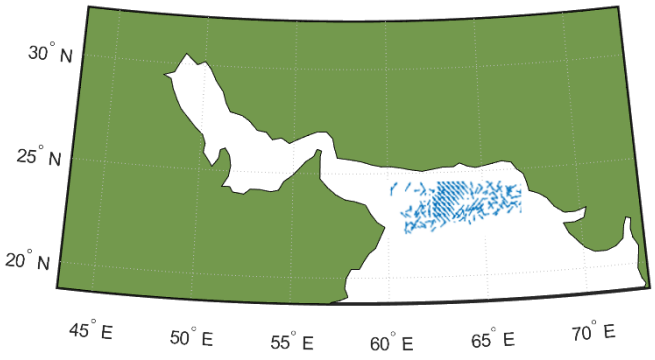
The parameters whose setting effect the accuracy of the MCC method are template window size, search window size and maximum retrieved velocity; in this work we used template window and search window size as 10m while the maximum velocity is set by $1ms^{-1}$. The estimated ocean current map for the sequential pair image of 27th May, 2019 (time of capturing of first image is 01:03:56 GMT and that of second image is 03:04:28 GMT) is shown Fig.4 and the average maximum correlation co-efficient value for the result is 0.33 ms^{-1} whereas the 2D correlation map is also given below depicting the value of maximum correlation co-efficient for each vector. The range of the co-efficient is 0-1 so higher the correlation co-efficient value better the derived current and is more accurately directed.

In this study the major difficulties faced are that first the selection of properly registered images and then to convert the MATLAB code into PYTHON was the challenge because both languages have different syntax and have different kind of function for same task, for example in MATLAB reference matrix is read just through command while in PYTHON it has specific single function to perform all information extraction of image at once.

Also, in this study we observed that for automated code the PYTHON is more efficient and quicker as compared to MATLAB as in MATLAB multiple functions are executed for the image information extraction while in PYTHON single function performed that task. Also once designed the code in PYTHON is completely automated only manual input needed is the pressing of run command.

This algorithm consumed approx. 5 minutes to execute for the one pair image on I3 processor computer so it is understood that more advanced the processor is more efficient and quicker will algorithm will work.

Hence, this study conclude that PYTHON is more efficient for execution of MCC Method as compared to MATLAB.



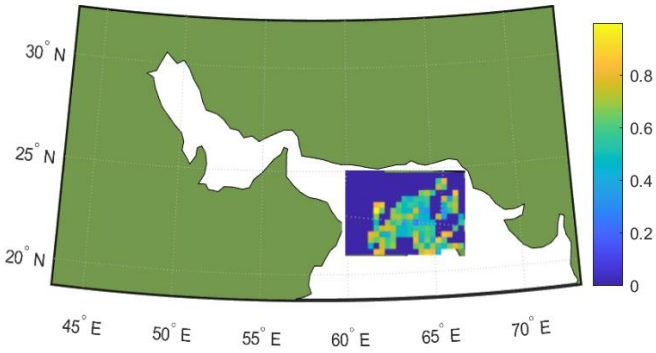


Fig. 4. Derived ocean current over the Arabian Sea and correlation plot of derived ocean currents (from top to bottom).

V.FUTURE RECOMMEDATIONS

Further in future the same algorithm with few loops' execution can be implemented for the large number of sequential images even for the years of data.
Also, the automated application can be designed using this code as the base.

SUMMARY

This study has shown that the correlation between two sequential images can be utilized to yield the ocean currents. Brightness temperature data provided by AVHRR for the Arabian Sea is used in this study. A high level of correlation of sequential images is demonstrated through MCC algorithm as shown in the results. This technique is sensitive to some of the parameters which effect the results of this technique to a large extent. Setting of these parameters is of prime importance. These parameters are:

- Template window size (first image).
- Max. velocity.
- Search window size (second image).
- Correlation cutoff.

Retrieval of surface currents in almost real-time manner is possible by the AVHRR provided data with the help of MCC technique. It is important to mention here that the cloud free nature of the images are very important for highest level of correlation. The average maximum correlation observed for the pair is $0.33ms^{-1}$.

REFERENCES

[3] W. J. Emery, A. C. Thomas, M. J. Collins, W. R. Crawford, and D. L. Mackas, "An objective method for computing advective surface velocities from sequential infrared satellite images," *Journal of Geophysical Research: Oceanography*, vol. 91, no. C11, pp. 12865–12878, Nov. 1986.

[4] Tokmakian, R.T., P.T. Strub, and J. McClean-Padman, Evaluation of the maximum cross-correlation method of estimating sea surface velocities from sequential satellite images, *Journal of Atmospheric Oceanic Technology*, 7, 852-865, 1990.

[5] K. A. Kelly and P. T. Strub, "Comparison of velocity estimates from advanced very high resolution radiometer in the Coastal Transition Zone," *Journal of Geophysical Research: Oceanography*, vol. 97, no. C6, pp. 9653–9668, Jun. 1992.

[6] M. Bowen, W. Emery, J. Wilkin, P. Tildesley, I. Barton, and R. Knewtson, "Extracting Multiyear Surface Currents from Sequential Thermal Imagery Using the Maximum Cross-Correlation Technique," *Journal of Atmospheric Oceanic Technology*, vol. 19, pp. 1665–1676, Oct. 2002.

[7] R. Crocker, D. Matthews, W. Emery, and D. Baldwin, "Computing Coastal Ocean Surface Currents From Infrared and Ocean Color Satellite Imagery," *IEEE Transactions on Geosciences and Remote sensing* vol. 45, pp. 435–447, Mar. 2007.

[8] M. A. Warren, G. D. Quartly, J. D. Shutler, P. I. Miller, and Y. Yoshikawa, "Estimation of ocean surface currents from maximum cross correlation applied to GOCI geostationary satellite remote sensing data over the Tsushima (Korea) Straits," *Journal of Geophysical Research: Oceanography*, vol. 121, no. 9, pp. 6993–7009, Sep. 2016.

[9]C. Heuzé, G. Carvajal, L. Eriksson, and M. Soja-Wozniak, "Sea Surface Currents Estimated from Spaceborne Infrared Images Validated against Reanalysis Data and Drifters in the Mediterranean Sea," *Remote Sensing*, vol. 9, p. 422, May 2017.

[10] C. Heuzé, G. K. Carvajal, and L. E. B. Eriksson, "Optimization of Sea Surface Current Retrieval Using a Maximum Cross-Correlation Technique on Modeled Sea Surface Temperature," *Journal of Atmospheric Oceanic Technology*, vol. 34, no. 10, pp. 2245–2255, Aug. 2017.

[11] J. Liu, W. Emery, X. Wu, M. Li, C. Li, and L. Zhang, "Computing Coastal Ocean Surface Currents from MODIS and VIIRS Satellite Imagery," *Remote Sensing*, vol. 9, p. 1083, Oct. 2017.

[12] C. Kalyani Devasena, S. P. Subramaninan, and M. M. Ali, "Study of seasonal current variability in the Arabian Sea using Geosat altimeter data," *International Journal of Remote Sensing*, vol. 16, no. 14, pp. 2691–2701, Sep. 1995.

[13] V. N. Eremeev, A. N. Zhukov, A. S. Zapevalov, N. E. Lebedev, and A. A. Sizov, "Seasonal Variations of the Arabian Sea Level Anomaly Fields," *Oceanology*, vol. 54, no. 3, pp. 289–297, 2014.

[14] V. F. Banzon, R. E. Evans, H. R. Gordon, and R. M. Chomko, "SeaWiFS observations of the Arabian Sea southwest monsoon bloom for the year 2000," *Deep.-Sea Research Part 2*.

Landslide Hazard Assessment And Monitoring In Azad Kashmir Using Sentinel-1 InSAR Data

Labeeqa Zaheer
Geospatial Research & Education Lab
Institute of Space Technology
Islamabad, Pakistan
labeeqazaheer95@gmail.com

Waqas A.Qazi
Geospatial Research & Education Lab
Institute of Space Technology
Islamabad, Pakistan
waqas.qazi@grel.ist.edu.pk

***Abstract*— Landslides are frequent pervasive geological hazards that pose a serious threat to people, infrastructure, and the natural environment in mountainous regions with steep slopes. Azad Kashmir lies in the Western Himalayan range and is characterized as a subtropical highland climatic zone. Varying mountainous terrain slopes, relief, and heavy rainfall during the monsoon season cause frequent landslides and interrupt human activities, damage roads, and cause displaced buildings, and houses. In such steep topographic areas with vulnerable conditions, information about slope stability is an important task for landslide risk assessment. Differential Synthetic Aperture Radar Interferometry (D-InSAR) is a useful InSAR technique for detection, analysis, and monitoring of slow-moving landslides. Differential InSAR measures line of sight (LOS) displacement by exploiting information relating to phase difference. In this study, single look complex (SLC) SAR imagery from Sentinel-1 C-band sensor product has been used to evaluate landslides over Azad Kashmir region. Both ascending and descending pass image pairs were used to generate interferograms for the period of October 2014 to November 2015. Ascending and descending pairs were processed separately in European Space Agency Sentinel Application Platform (ESA SNAP). Displacement values of highly unstable areas that keep high coherence over a period are calculated. Low-coherence areas and decorrelating land-cover types such as agriculture and dense forest are removed from the analysis. Results are then displayed in the form of displacement maps showing unstable areas that may be at risk for further landslides.**

Keywords— Interferometric Synthetic Aperture Radar (InSAR), Landslide

I. INTRODUCTION

Landslides are amongst the most common natural disasters worldwide, resulting in loss of human life, blockage of roads and rivers, resettlement, and also damage natural resources. They are primarily triggered by earthquakes, intense rainfall, changes in groundwater, a disturbance or change of slope and volcanic activity. Satellite remote sensing techniques offer the capability for mapping and characterization of landslides and assist in the development of guidelines for sustainable land-use planning.

Spaceborne Synthetic Aperture Radar (SAR) remote sensing has advantage over optical remote sensing due to availability of both day and night time images regardless of cloud coverage. Moreover, the coherence of microwave signals helps to detect topographical and deformation changes by processing the phase signals. This forms the basis for the SAR Interferometry (InSAR) and Differential Interferometric Synthetic Aperture Radar (DInSAR) techniques, which have now become been widely used in the field of earth and environmental sciences for detecting and measuring surface displacements, land topography, land changes, land subsidence, ground water levels, soil moisture, snow accumulation, etc. up to millimeter precision. Differential InSAR method measures displacement in the line of sight (LOS) direction by exploiting phase information and compute a phase difference image called interferogram[1]. External DEM is used to remove or minimize phase contribution introduced by surface topography.

Azad Kashmir region is highly susceptible to landslide events due to its complex geological setting combined with active seismicity, easily erodible lithology, coarse terrain, monsoonal climate, deforestation, and accelerated erosion due to construction on steep slopes[2]. The region is deeply dissected by small and large river valleys and people live on the fragile mountain slopes. In such environments, monitoring and analysis of landscape is essential to reduce any preventable loss of life and damage of property. In the past, a number of studies using optical remote sensing data have been carried out to measure land instability in the study area. Optical remote sensing shows greater dependency on atmospheric conditions. Shehzad [3] implemented repeat pass Differential InSAR (DInSAR) in the study area by using Envisat ASAR imagery, and analyzed the long-term impact of the Kashmir 2005 earthquake on major landslide areas by generating displacement maps for the period of 2007-2010. With the launch of Sentinel-1 in 2014, systematic and regular acquisitions of SAR data is made possible. Sentinel-1 has a shorter temporal baseline characterized by high spatial

coverage and a greater ground resolution with respect to Envisat ASAR and other previous C-band radar systems[4].

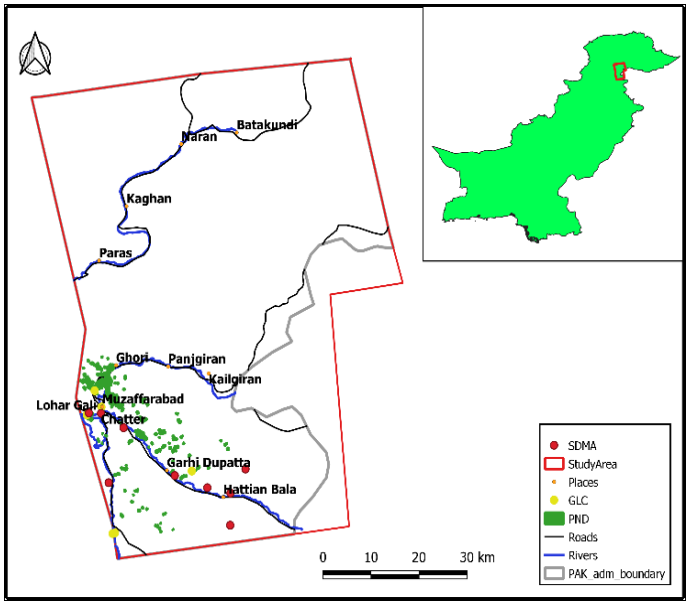
The current study illustrates the potential of Sentinel-1 data, with the aim of detecting regions of relatively high displacement rates in the study area. In future, these unstable areas will be prone to landslides and associated destruction.

A. STUDY AREA

Azad Kashmir is located in northwestern part of the Himalayas range, Pakistan. Geologically, the Himalayan mountain range is the youngest and most dynamic system in the world and is specifically famous for the recurrent seismic activities, varying slopes, land sliding, earthquakes and flash floods[5]. The study area terrain is mountainous and has a subtropical highland climate.

The dominating land cover type is agriculture and dense forest[6]. Muzaffarabad is the capital city of Azad Kashmir and is situated at the confluence of the Neelum and Jhelum rivers. Khagan, Neelum and Jhelum are three principle valleys in study area. In winter season, snowfalls occurs above 1500m elevation. Snow accumulates in steep mountainous slopes and then shed in late spring. High temperature occurs in the summer months. Monsoon season starts in late June and ends in August. Heavy precipitation occurs during monsoon season, results in landslides, and flooding. The study area map with some of the active landslide areas are shown in Fig.1 below

Fig. 1. Study area map of Azad Kashmir



Landslide areas and locations from various sources like State of Disaster Management Authority (SDMA), Planning and Development Department (PND), Global Landslide Catalogue (GLC) by NASA are displayed in the study area map. These datasets were taken from [3].

II. METHODOLOGY

Sentinel-1 operates in C-band (5.405 GHz central frequency f, and 5.547 cm wavelength λ) onboard the two satellites Sentinel-1A and Sentinel-1B. Single look complex (SLC) products in Interferometric Wide (IW) swath mode were downloaded from the European Space Agency (ESA) Copernicus Open Access Hub[7]. IW mode captures three sub-swaths i.e. IW1, IW2, IW3. Each sub-swath contains one image and one polarization channel.
The footprint of both ascending and descending pass SLC images over the study region is shown in Fig.2 below

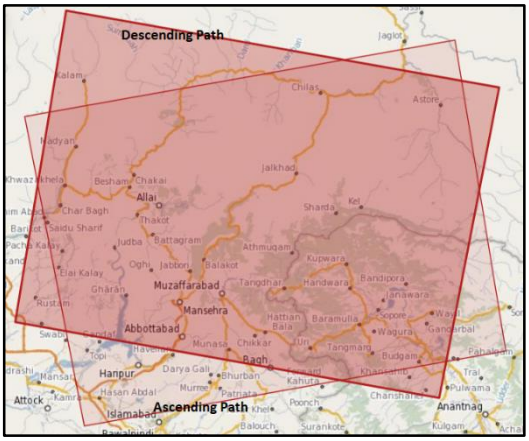


Fig. 2. Spatial foot prints of the ascending and descending passes over the study region

The acquired data is in right-looking direction and has singlePolarization (VV). Relative orbit of ascending pass images is 100 while for descending pass images relative orbit is 107. The data was downloaded for the period of October 2014 to November 2015**.** After data acquisition, InSAR image pair selection has been done. Interferometric pairs must be of the same path number and must cover the same area. Images with different flight directions (ascending vs descending) cannot serve as interferometric pairs. Moreover, image pair selection should consider seasonal variations, atmospheric conditions, and perpendicular and temporal baseline values. It is better to have an image pair of same season, low perpendicular baseline and temporal difference to avoid decorrelation and coherence loss in the area of interest (AOI). Complete list of descending and ascending pairs used in this study is shown in the table I and II below

TABLE I. SENTINEL-1 DESCENDING INTERFEROMETRIC PAIRS USED IN THE STUDY

Sr No	Descending Pairs			
	Reference Image	***Secondary Image***	***Temporal Baseline (Days)***	***Perpendicular Baseline (Meters)***
1	13-Oct-14	06-Nov-14	24	52
2	06-Nov-14	30-Nov-14	24	8
2	30-Nov-14	17-Jan-15	47	-67
4	17-Jan-15	10-Feb-15	23	-59
5	17-Jan-15	30-Mar-15	72	20
6	17-May-15	10-Jun-15	24	-13
7	17-May-15	28-July-15	72	4
8	28-July-15	21-Aug-15	24	-4
9	21- Aug-15	25-Nov-15	96	20

TABLE II. SENTINEL-1 ASCENDING INTERFEROMETRIC PAIRS USED IN THE STUDY

Sr No	Ascending Pairs			
	Reference Image	*Secondary Image*	*Temporal Baseline (Days)*	*Perpendicular Baseline (Meters)*
1	24-Oct-14	17-Nov-14	24	-55
2	24-Oct-14	11-Des-14	47	49
2	11-Des-14	04-Jan-15	24	-82
4	04-Jan-15	28-Jan-15	23	28
5	04-Jan-15	21-Feb-15	47	-1
6	04-Jan-15	17-Mar-15	71	2
7	28-Jan-15	10-Apr-15	72	96
8	04-May -15	21-Jun-15	48	-8
9	21- Jun-15	08-Aug-15	48	-36
10	08-Aug-15	01-Sep-15	24	92

A total of 19 interferometric pairs were formed for the landslide analysis using Alaska satellite facility (ASF) baseline tool[8]. Perpendicular and temporal baseline distribution of all granules within a given InSAR stack is visualized through ASF baseline tool. Multiple reference images were used in order to decrease the chance of coherence loss. InSAR pairs with perpendicular base line less than 100m and temporal baseline less than 100 days were shortlisted for the analysis.

Both ascending and descending interferometric pairs were processed separately in ESA's Sentinel Application Platform (SNAP). The processing steps are shown in the methodology flowchart in Fig.2 below.

Since the study area lies in IW2 sub-swath of SLC image, so processing has been only applied on IW2 sub-swath for analysis.

Phase unwrapping has been done using SNAPHU algorithm. Low coherence areas need more computational time in phase unwrapping and it is quite useless to unwrap them. So, only those areas were unwrapped which have coherence > 0.4. Dense forest and agriculture areas were masked out for final displacement map because dense vegetation leads to coherence loss, and agriculture areas are mostly on plain slopes and soil changes in agriculture areas can also lead to coherence loss.

Absolute phase calibration was performed on the displacement maps. Muzaffarbad city urban areas were considered as stable points for this purpose and used as zero displacement reference point for InSAR displacement measurements. Landslide inventory data taken from[9] and data collected from SDMA, PND and GLC (shown in Fig.1) were overlaid on final displacement maps and further analysis was performed on these selected areas.

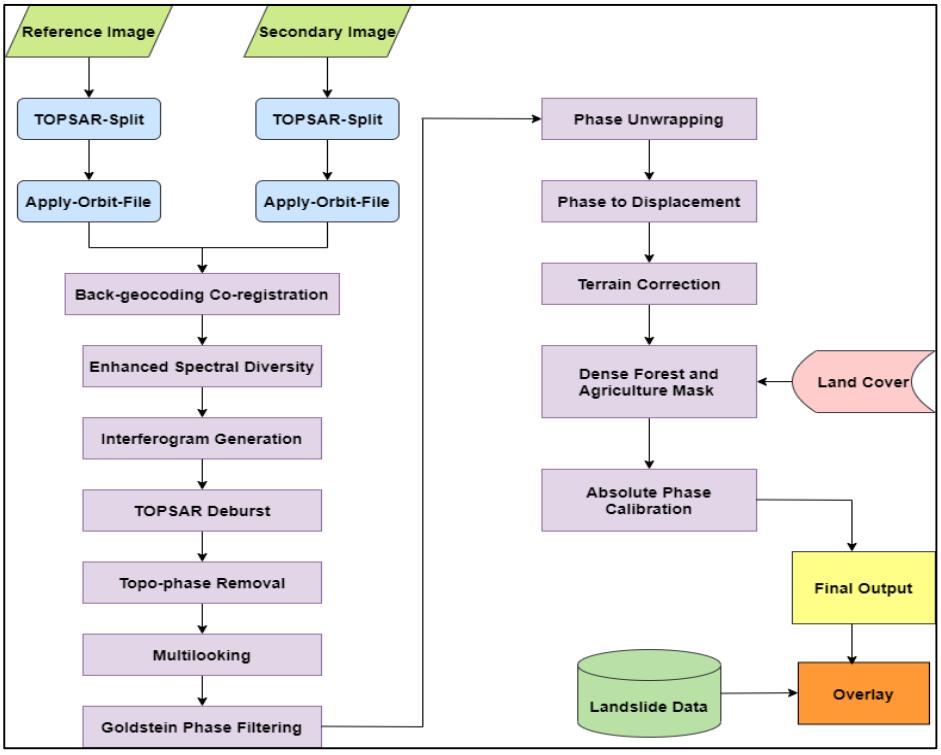


Fig. 3. Methodology flow chart

III. Results And Analysis

Interferograms along with coherence were generated for each interferometric pair for both ascending and descending pairs. Only landslide areas which were highlighted by the sources of SDMA, PND, GLC and landslide inventory data in the study area were considered for analysis.

Also it was very challenging to consider small landslide areas for analysis because of the non-availability of confirmed ground truth data for other landslide areas. The areas with low coherence show noise and one cannot be sure about the displacement values on that areas. Overall, coherence for areas under investigation for landslide analysis did not show very high values especially in ascending pairs.

In ascending pairs, it has been found that the interferogram of pair no 9 (21-Jun-15 - 08-Aug-15) and pair no 10 (08Aug-15 -01-Sep-15) shows highest displacement values as compared to other ascending pairs. Displacement values on the selected landslide areas ranges between -3.0 to 8.0 cm in pair no 9 and ranges between -24.0 to 32.0 cm in pair no 10 and coherence is also relatively high in both the pairs. Pair 9 and pair 10 displacement and coherence are shown in fig.3 and fig.4 below respectively. In both fig. left panel (a) shows displacement while right panel (b) shows coherence.

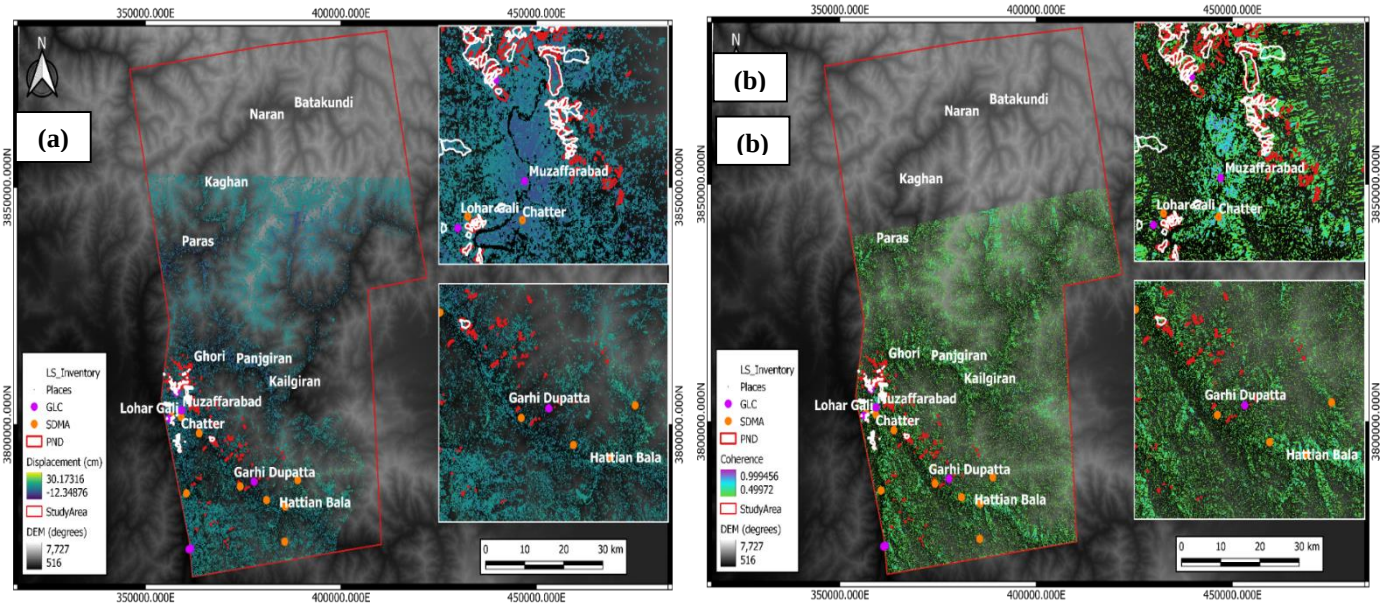


Fig. 4. Ascending pair no 9 (21-Jun-15 - 08-Aug-15)

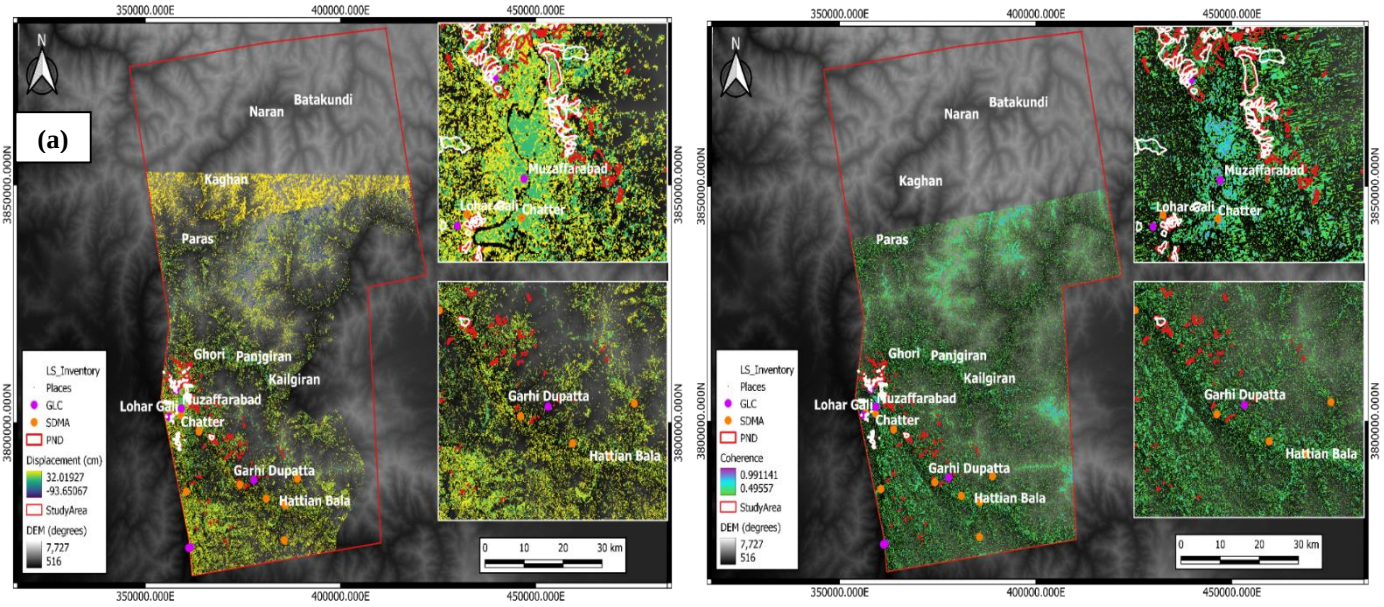


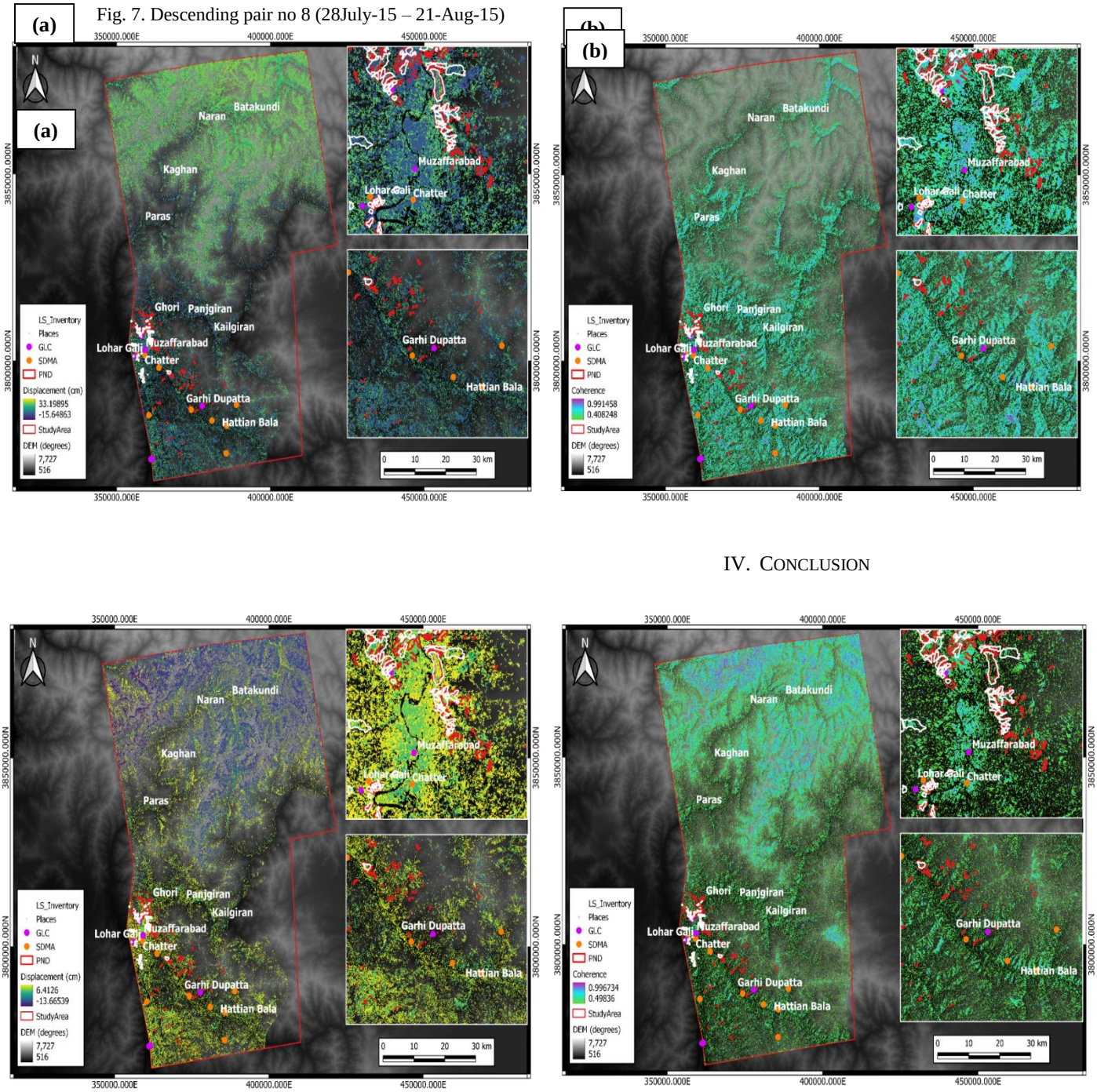
Fig. 5. Ascending pair no 10 (08Aug-15 -01-Sep-15)

In descending pairs, it has been found that the interferogram of pair no 2 (06-Nov-14 - 30-Nov-14) and pair no 8 (28July-15 - 21-Aug-15) shows highest displacement values as compared to other descending pairs. Displacement values on the selected landslide areas ranges between -5.0 to

23.0 cm in pair no 2 and ranges between -2.0 to 6.0 cm in pair no 8 and coherence is also relatively high in both the pairs. Pair 2 and pair 8 displacement and coherence are shown in fig.5 and fig.6 below respectively. In both fig. left panel (a) shows displacement while right panel (b) shows coherence.

Fig. 6. Descending pair no 2 (06-Nov-14 - 30-Nov-14)

Fig. 7. Descending pair no 8 (28July-15 – 21-Aug-15)



IV. Conclusion

Both ascending and descending pairs of Sentinel -1 SLC images were utilized to monitor slope instability in selected areas of Azad Kashmir by applying DInSAR technique. The ascending and descending pairs were treated separately and only those areas for landslides were selected that were highlighted by the SDMA, PND, and GLC landslide inventory data. Displacement maps were generated for the period of October 2014 to November 2015 and areas were

highlighted in displacement maps that showed significant displacement high values (areas of instability).

Areas selected for landslide analysis mainly include Muzaffarabd, Chatter, Lohar Gali, Garhi Dupatta and Hattian Bala. Three landslide locations are found significant in a sense of destabilization with respect to other locations. These locations were selected on the basis of displacement and coherence values in both ascending and descending pairs. The results shows highest destabilization in Hattian Bala and Lohar Gali as compared to any other landslide locations in the study area. Garhi Dhupatta also shows instability in some of the pairs but relatively less in comparison with Hattian Bala and Lohar Gali. June- September period are found to be more favorable for instability. Heavy precipitation and the monsoon period is the main reason for landslide instability in the study area.

V. REFERENCES

[1] X. Zhou, N. Chang, and S. Li, "Applications of SAR Interferometry in Earth and Environmental Science Research," Sensors, vol. 9, pp. 1876–1912, 2009, doi: 10.3390/s90301876.

[2] M. Shafique, M. van der Meijde, and M. A. Khan, "A review of the 2005 Kashmir earthquake-induced landslides; from a remote sensing prospective," *J. Asian Earth Sci.*, vol. 118, pp. 68–80, 2016, doi: 10.1016/j.jseaes.2016.01.002.

[3] K. Shehzad, "Landslide Identification , Assessment and Quantification in Azad Kashmir Using Repeat-Pass Synthetic Aperture Radar (SAR) Interferometry," M.S. Thesis, Institute of Space Technology, 2017.

[4] M. Del Soldato *et al.*, "Monitoring ground instabilities using SAR satellite data: A practical approach," *ISPRS Int. J. Geo-Information*, vol. 8, no. 7, 2019, doi: 10.3390/ijgi8070307.

[5] A. ur Rahman, A. N. Khan, and A. E. Collins, "Analysis of landslide causes and associated damages in the Kashmir Himalayas of Pakistan," *Nat. Hazards*, vol. 71, no. 1, pp. 803–821, 2014, doi: 10.1007/s11069-013-0918-1.

[6] F. M. Qamer *et al.*, "Mapping deforestation and forest degradation patterns in Western Himalaya, Pakistan," *Remote Sens.*, vol. 8, no. 5, pp. 1–17, 2016, doi: 10.3390/rs8050385.

[7] Scihub.copernicus.eu. 2021. [Online] Available at: <https://scihub.copernicus.eu/dhus/#/home>

[8] Search.asf.alaska.edu. 2021. *ASF Data Search*. [Online] Available at: <https://search.a (ASF Data Search, 2021)sf.alaska.edu/#/?searchType=Baseline%20Search>

[9] S.U. Shah, "Spatio-Temporal Change and Hazard Detection of the 2005 Kashmir Earthquake-Induced Landslides," M.S. Thesis, National Centre of Excellence in Geology , University of Peshawar, 2015.

Modeling & Simulation of BSAR (Bi Static Synthetic Aperture Radar) system using Reflected BeiDou B1I Signals

Hassan Sadiq
Department of Space Science, IST
Islamabad, Pakistan
hassanniazi948@gmail.com

Muhammad Shoaib ul Hassan
Department of Space Science, IST,
Islamabad, Pakistan
shoaibulhassan365@gmail.com

Mohammad Usman
ABM SATUMA (PVT) LTD Islamabad
Islamabad, Pakistan
musman751@hotmail.com

***Abstract*—The BeiDou Navigation Satellite System is the recent addition in the GNSS (Global Navigation Satellite Signals) community. Direct BeiDou signals are used for navigation and positioning purposes. This research endeavor intends to utilize the reflected signals as they can provide an opportunity for passive radar applications. A bi-static radar system is formed by the BeiDou satellites, a modified BeiDou receiver, and its signal processing components (antennas). The Bi-static radar (BSAR) can be utilized for passive detection of targets and /or any movement or changes. Firstly, power budget analysis will be calculated for BeiDou B1I signals and compared with GPS L1 signals. Later the whole Bi-static Radar scenario will be simulated as closely and faithfully as possible and a matched filter technique will used to improve the image resolution. The simulation will be carried out under different conditions and in a detailed manner, and efforts will be made to validate that BeiDou signals can be used as an illuminator or "transmitter of opportunity" for passive BSAR applications with acceptable image resolution.**

Keywords— Analysis of Power Budget, BSAR, BeiDou B1I signal,

I. INTRODUCTION

The BeiDou is a Chinese Global navigation satellite system and recently it became fully operational [1]. Primarily, the system provides Global, highly precise, reliable and stable position and velocity information to the user. Secondarily, the system signals after reflection can be an opportunity and utilized for passive remote sensing applications[2]. In numerous application of remote sensing BeiDou reflected signals can be used like measurement of soil moisture content over the land, bio mass, and bi-static imaging [3]–[6]. BEIDOU-3 design comprises of three GEO, three IGSO, and 24 MEO satellites, with backup satellites in orbit. [6], [7].

A BeiDou modified receiver with its components of signal detection(antennas) and BeiDou satellites, formed a BeiDou based bi-static radar system. In applications of remote sensing BSAR (bi-static synthetic aperture radar) systems can be used[8]. In BSAR scenario both receiver and transmitter are separated and the distance between them is called based line and the angle is called bi-static angle. The complete scenario is depicted in Fig. 1.

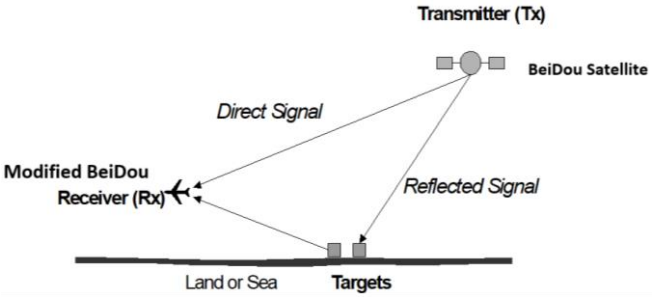


Fig. 1. The BSAR scenarion

As BeiDou has become fully operational and thus the availability of BeiDou signals it is a great opportunity for researchers. BeiDou system is a transmitter of opportunity and can be used in this research to illuminate the target in an area of interest. It eliminates the requirement of dedicated transmitter for this purpose[9]. With compared to hefty specialized transmitters, the power consumption of BeiDou-based bi-static radar is quite low. As the system cross section is differ from the mono static radar for this system too, has the ability of detection of stealthy targets.

However, the power of BeiDou direct signal is low and after the reflection their power is further reduced by the reflecting surface and difficult to detect. These low power signals can be used in many applications of remote sensing after applying some signal processing techniques [10]. During this research endeavor, the image of target will be generated in the area of interest by using reflected signals as the reflected signals has valued information about the reflecting surface. Thus, the BeiDou reflected signals have great potential and can be used in various remote sensing applications like measuring soil moisture content, ice age/thickness, wind speed, passive remote sensing, and ocean remote sensing [3][11][12][8].

The use of BeiDou as an opportunity transmitter eliminates the requirement for a specialized transmitter. Thus, the BeiDou system gives an excellent chance for this type of study; fortunately, such an expensive system has already been constructed and maintained, and it covers a large region and is available 24 hours a day. By selecting appropriate BeiDou satellites and optimizing for geometry in terms of signal power and visibility, direct and reflected signals may be received.

BeiDou radio navigation signals are right-hand circularly polarized (RHCP), and their polarization changes when they

reach the Earth's surface or any other object after reflection. These signals may become circularly polarized on left-hand (LHCP).

Received and locked direct signals from a certain satellite are used to acquire and identify reflected signals. The commercial receivers available in the market have an RHCP antenna that can only receive direct signals and not able to receive reflected signals. The BeiDou signals must be captured and received in digital format, and the signals must be stored in order to do post-remote sensing and imaging of the selected area. To receive the BeiDou signal after reflection, a high gain antenna with circularly polarized on the left hand is used. This information is obtained by the use of a circuit with the proper reference signal and sampling frequency. Receiving a weak signal with a poor SNR at a continuous data rate (minimum of 20 M samples/s) using suitable techniques is a significant problem. This received data is then sent to the processing system.

To create image of a certain selected area BeiDou direct and reflected signals will be manipulated using technique of digital signal processing. The SAR methodology is employed in which it is required to maintain the movement of receiver or Bi-static radar in spatial sphere of influence. As mentioned above, with the use of suitable hardware the BeiDou reflected signal from the object will be acquired, on a mobile object (UAV or aerial platform) the hardware will be arranged for the synthetic aperture effect as demonstrated in Figure 1 to achieve the needed change in geometry. Range Resolution is a very important parameter for the image reconstruction from the reflected BeiDou signals based on bi-static radar architecture. On the same orientation, the Radar system may identify two or more objects at different ranges.

The range resolution is determined as.

$$\delta_r = \frac{C}{2B\cos\left(\frac{\beta}{2}\right)} \qquad (1)$$

Where B denotes the transmitted signal's bandwidth and β is the bistatic angle. As a result, range resolution is affected by signal bandwidth and bi-static angle. For better resolution we improve the bandwidth of the signal. BeiDou signal is transmitted at higher bandwidth, as compared to GPS signals, therefore range resolution is improved**.**

BeiDou B1I signal is transmitted at frequency of 1561.098MHz with a ranging code. The ranging code is unique for each satellite and freely available for all civilian users. When compared to GPS 'L1' signals, these new signals will be more accurate and compatible with remote sensing. This system has become fully operational[1].

For verification of their suitability for remote sensing application, accuracy and compatibility, the power budget analysis is necessary. The analysis for power budget and the influence of clutter on passive target detection and imaging has been interpreted[9] [13]

At 1572.42 MHz, the GPS transmits the L1 civilian signal together with the coarse acquisition (C/A) code. The chip rate of the BPSK modulation of C/A code is 1.023 and the duration is one millisecond. Because of the narrow bandwidth and low L1 signal strength, the GPS L1 signal has a bandwidth of 2.046 MHz, made it difficult to detect the reflected signal using conventional signal acquisition techniques. The Chinese navigation system BeiDou B1I signal is design for civilian purpose and freely available publicly. BeiDou send B1I Signal at frequency of 1561.098MHz, 2.046MHz is the chip-rate of the signal and duration is 1milli second has bandwidth of 4.092MHz. The BeiDou B1I signal Ranging length is 2-times longer than the GPS L1 signal, due to higher bandwidth BeiDou B1I signal has better signal to noise ratio and spatial resolution then GPS L1 frequency signal.

These signals, in practice, travel a greater distance, but have a lower power spectral density than noise. A code sequence generated locally that is longer than conventional receivers and correlated with the received signals from this efficient and better processing gain can be achieved. Correlation may be done in two ways: coherent and incoherent.

The reflected signal is weaker than the direct signal as a result of the scattering process and the extra route travelled. The output may be lower than the noise level even after coherent correlation. A sequence of waveforms can be gathered and non-coherent summation can be performed to speed up the processing even further. However, some doppler or doppler ambiguity removal will be required in this instance, or else the correlation peak would grow and become comparatively flat, most likely due to drift in-phase and doppler related to temporal and spectral variation.

Power budget analysis has been performed in this paper for scenario depicted in Fig. 1. The simulation results for GPS L1 and BDS B1I signals are analyzed.

II. ANALYSIS OF THE GPS L1 SIGNAL POWER BUDGET

The GPS L1 signal is analyzed first for the bi-static radar power budget, followed by the BeiDou B1I signal. The signal transmitted power is represented with P_t and the gain of transmitter is represent with G_t, R_1 represent the range from transmitter to target and it is around 22,000 Km. From receiver to target the range is represented as R_2 and it is the slant range [14] and is given by.

$$R_2 = \sqrt{\frac{Pt\ GtGr\lambda^2\sigma}{(4\pi)^3 R1^2 P_r}}\ km \qquad (2)$$

The power received at the receiver's antenna is represented by

$$P_r = \frac{Pt\ Gt}{4\pi R1^2 4\pi R2^2} * \sigma A_{ef} \qquad (3)$$

Where $A_{e.f}$ is receiver antenna effective area

$$A_{ef} = \frac{\lambda^2 * Gr}{4\pi} \qquad (4)$$

The strength of the reflected signal is determined by the receiver's antenna gain and the radar's cross-section. A target can be easily detected with a greater RCS, and other factors on which detection depends is the size of target, material, and shape.

For the receiver and Bi-static radar the signal to noise ratio is given by [14].

$$SNR = \frac{Pt\ GtGr\lambda^2\sigma}{(4\pi)^3 R1^2 R2^2 KTB_n} \qquad (5)$$

Where receiver antenna gain is G_r, power received at receiver is P_r, the noise of receiver is $N_r = kTB_{n\ and}$ λ is GPS L1 signal wavelength. When $R_1=R_2$ the SNR is maximum however GPS satellite is transmitting signal at height of 22,000 Km. The target to receiver range is limited to 1000 m. The graph in figure (2) shows GPS L1 frequency SNR verses Range plot with 10 m^2 cross-section target. As expected, Radar of passive microwave imaging of this type has the basic limitation, poor

SNR even for short-range. However, the SNR can be increased significantly by correlating the signal for longer period resulting in more processing gain and improvement in the SNR. With the coherent and non-coherent summation, the correlation value can be increased, as noise is uncorrelated therefore SNR will be enhanced.

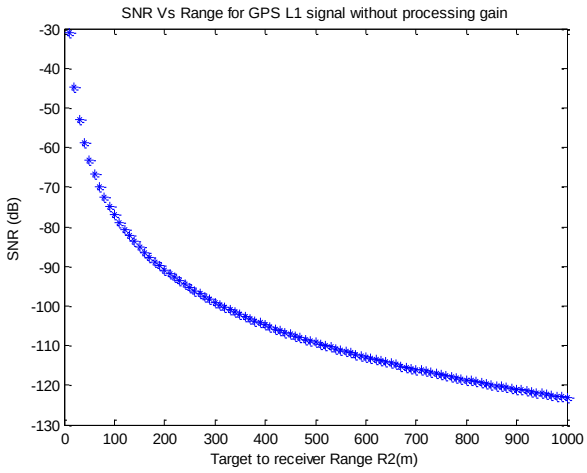


Fig. 2. Without processing gain SNR Vs Range for GPS L1 signal

Fig. 2. shows GPS L1 signal simulation result for SNR verses range. By simulation, the SNR will be calculated at different ranges from 0-1000m. The SNR is -70dB for the range of 100m for GPS signal. With such a low SNR, recovery of signal is extremely difficult. The SNR attained by comparing the signal over a prolonged period is given by [15].

$$SNR = \frac{Pt\ GtGr\lambda^2\sigma}{(4\pi)^3 R1^2 R2^2 KTB_n} G_{sp} N^{0.8} \quad (6)$$

Where N represents the maximum non-coherent number of samples and G_{sp} represents the processing gain. The non-coherent summing is useful for obtaining the desired gain since it requires a larger number of samples (N) than the coherent summation.

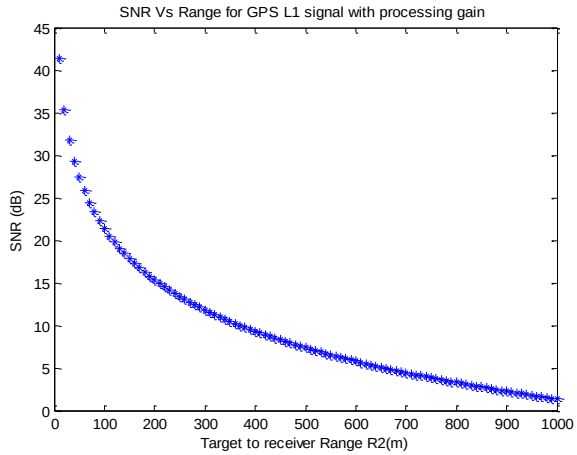


Fig. 3. with processing gain, SNR Vs Range for GPS L1 Signal

The SNR for the GPS L1 signal is 43dB, as shown in Figure 3. SNR will be improved with non-coherent summation while correlating the signal for a longer period, the SNR is 22dB at the range of 100m and therefore detection is possible. Therefore, the reflected signal can be utilized for the application of remote sensing. The parameters and their values are summarized in Table 1 that will be used for "the GPS L1 signal's power budget analysis".

TABLE I GPS L1 Variables values for analysis

No.	Variables	Value	Unit
1	(P_t) is power of transmitted signal	40	Watt
2	(G_t) is antenna gain of transmitter	13	dB
3	(G_r) is antenna gain of receiver	30	dB
4	Bandwidth	2.046	MHz
5	(Nr) is level of noise of receiver	-131	dB
6	(TQ) is interval of processing	0.1	Second

III. BeiDou B1I Signal Power Budget Analysis

The results of using the BeiDou B1I signal for remote sensing have been compared to those of using the GPS L1 signal. BeiDou B1I power budget study revealed signal, in same scenario as shown in section II, the parameters employed for BeiDou B1I signal strength budgeting are listed in Table II.

TABLE II BeiDou B1i Variable values for Analysis

No.	Variable	Value	Unit
1	(P_t) is power of transmitted signal	43	Watt
2	(G_t) is antenna gain of transmitter	15	dB
3	(G_r) is antenna gain of receiver	30	dB
4	Bandwidth	4.092	MHz
5	(Nr) is level of noise of receiver	-131	dB
6	(TQ) is interval of processing	0.1	Second

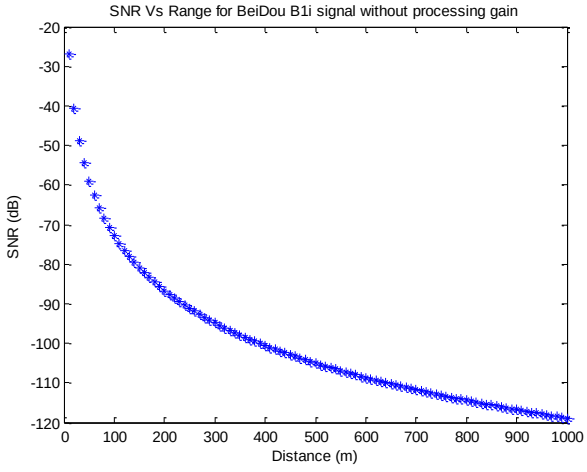


Fig. 4. Without processing gain SNR Vs Range for BeiDou B1I Signal

TABLE III Comparison of Range and SNR

S/N	Target to receiver range R2 (m)	Without processing gain		With processing gain	
		L1 SNR (dB)	B1I SNR (dB)	L1 SNR (dB)	B1I SNR (dB)
1	10	-31	-27	41	45
2	50	-63	-59	27	31
3	100	-77	-73	21	25
4	200	-91	-87	15	15
5	500	-109	-105	7	11
6	800	-118	-114	3	7
7	1000	-123	-119	1	5

Fig. 4. shows BeiDou B1I signal simulation results for SNR vs Range plot. Through simulation, the SNR will be calculated at different ranges from 0-1000m. The SNR is -25dB for the range of 100m for BeiDou B1I signal which is better than the GPS L1 signal.

By comparing the signal over a longer period of time, the SNR can be improved and the results are shown in Fig. 5. As a result, by correlating for a longer time, the SNR may be enhanced with processing gain. As $G_{sp}=BT_Q$, the processing gain is calculated by multiplying B by TQ, where B is the bandwidth and TQ is the processing interval.

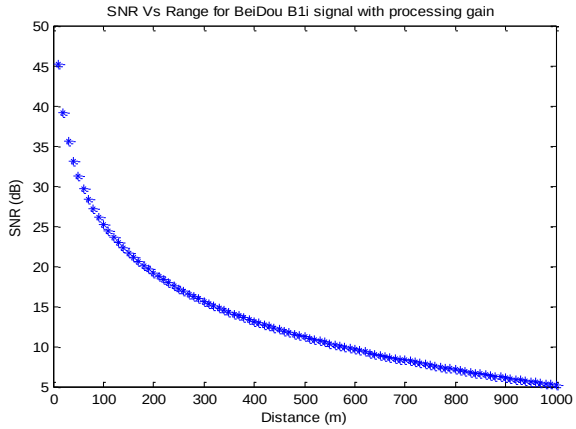


Figure 5 with processing gain SNR Vs Range for BeiDou B1I Signal

The SNR for the BeiDou B1I signal is 25dB with processing gain at a target range of 100 m, which is better than the GPS L1 signal. A comparison of Target to receiver ranges and SNR has been summarized in Table 3 for reflected GPS L1 signal and B1I signal of BeiDou.

REFFERENCE

[1] M. Li and Y. Yuan, "Estimation and Analysis of BDS2 and BDS3 Differential Code Biases and Global Ionospheric Maps Using BDS Observations." *Remote Sensing* 13.3 (2021): 370.

[2] M. Martin-Neira, "A passive reflectometry and interferometry system (PARIS): Application to ocean altimetry." *ESA journal* 17.4 (1993): 331-355.

[3] S. Yan, H. Zhou and J. Gong, "GNSS imaging: A case study of tree detection based on BeiDou GEO satellites." *Progress In Electromagnetics Research C* 84 (2018): 227-240.

[4] T. Zeng, T. Zhang, W. Tian, C. Hu, and X. Yang, "Bistatic SAR Imaging Processing and Experiment results Using BeiDou-2 / Compass-2 as Illuminator of Opportunity and a Fixed Receiver," *2015 IEEE 5th Asia-Pacific Conf. Synth. Aperture Radar(APSAR)*, pp. 302–305, 2015.

[5] S. H. Yan, F. Zhao, N. C. Chen and J. Y. Gong, "Soil moisture estimation based on BeiDou B1 interference signal analysis." *Science China Earth Sciences* 59.12 (2016): 2427-2440.

[6] C. Huang, Z. Li, J. Wu, Y. Huang, H. Yang and J. Yang,"Multistatic Beidou-Based Passive Radar for Maritime Moving Target Detection and Localization." *IGARSS 2019-2019 IEEE International Geoscience and Remote Sensing Symposium*. IEEE, 2019.

[7] "BeiDou Navigation Satellite System Signal In Space Interface Control Document," no. February, 2019.

[8] F. Xuezhen, "Passive SAR with GNSS transmitters: Latest results and research progress." *2017 IEEE International Geoscience and Remote Sensing Symposium (IGARSS)*. IEEE, 2017.

[9] B. Mojarrabi, J. Homer, K. Kubik and I. D. Longstaff, "Power budget study for passive target detection and imaging using secondary applications of GPS signals in bistatic radar systems." *IEEE International Geoscience and Remote Sensing Symposium*. Vol. 1. IEEE, 2002.

[10] M. Usman, and D. W. Armitage. "Acquisition of reflected gps signals for remote sensing applications." *2008 2nd International Conference on Advances in Space Technologies*. IEEE, 2008.

[11] T. Yang, W. Wan, X. Chen, T. Chu, and Y. Hong, "Using BDS SNR observations to measure near-surface soil moisture fluctuations: Results from low vegetated surface," *IEEE Geosci. Remote Sens. Letters 14.8(2017):1308-1312*.

[12] T. Zeng, T. Zhang, W. Tian, C. Hu, and X. Yang, "Bistatic SAR imaging processing and experiment results using BeiDou-2/Compass-2 as illuminator of opportunity and a fixed receiver," *2015 IEEE 5th Asia-Pacific Conf. Synth. Aperture Radar, APSAR 2015*.

[13] V. Behar, H. Kabakchiev and C. Kabakchiev, Detectability of Air Targets using Bistatic Radar Based on GPS L5 signals." *2011 12th International Radar Symposium (IRS)*. IEEE, 2011.

[14] E. P. Glennon, A. G. Dempster, and C. Rizos, "Feasibility of air target detection using GPS as a bistatic radar." *Positioning* 1.10 (2006).

[15] S. Erker, S. Thölert, J. Furthner, and M. Meurer "L5–The New GPS Signal." *Proceedings of IAIN* (2009): 27-30.

Flood Mapping and Crop Damage Assessment using Sentinel-1 SAR GRD and Optical Data through Google Earth Engine

Tariq Abbas
Geospatial Research and Education Lab, Institute of Space Technology, Islamabad, Pakistan.
tariqabbas750@gmail.com

Waqas A. Qazi
Geospatial Research and Education Lab, Institute of Space Technology, Islamabad, Pakistan.
Waqas.qazi@grel.ist.edu.pk

I. ABSTRACT

This study deals with the flood mapping and crop damage assessment for the District of Mirpur Khas, Sindh using microwave Synthetic Aperture Radar (SAR) and optical satellite remote sensing datasets. Floods are one of the most disastrous events across the world and their impact needs to be evaluated and analyzed timely to alleviate and manage the associated damages. The main objective of this study is to delineate the flood extent and assessment of associated damaged crop for the flood that occurred due to monsoon season from August to September 2020 using SAR-based imagery provided by ESA Sentinel-1 satellites and Moderate Resolution Imaging Spectroradiometer (MODIS) global landcover data on a cloud-based Remote Sensing and Digital Image processing platform i.e., Google Earth Engine (GEE). SAR imagery is a more appropriate choice than optical for flood mapping because it has low dependency on weather conditions and can provide day/night images in the situation of emergency because it is independent of solar illumination. MODIS data can be used for crop damage assessment because it gives the global landcover data with a temporal resolution of 1 day. SAR data in VH-polarization and Otsu thresholding provide reliable results for flood mapping.

Keywords— Flood Mapping, Flood Extent, Damage Assessment, SAR, GEE (Google Earth Engine)

II. INTRODUCTION

Floods are one of the heaviest natural disastrous events and bring many casualties with them [1]. Floods are needed to be managed timely by the concerned authorities to mitigate the hazardous impact. But for this purpose, we require early information to estimate the spatial extent of the flood to deal with the emergency response [2]. Since 1928, Pakistan has faced many heavy floods and most of the floods come in the monsoon time-period from July to September. Matee et al. [20] has mentioned some renowned floods of 1928, 1929, 1955, 1973, 1976, 1980, 1988, 1992 and 2010 [18]. Since 1948 to 2008, floods in Pakistan have claimed 7,000 lives and caused many infrastructure and crop losses with 7.7 million acres inundated zones. Spaceborne remote sensing plays a key role in flood mapping [3,4]. Optical remote sensing can be used for flood mapping on basis of high reflectance in RGB (Red, Green, Blue) and low reflectance in Near Infrared (NIR) bands [5,6,7]. Although optical remote sensing can also be used for flood mapping but only in good weather condition. Generally, in-practice, flood occurs in bad weather condition with rainfall and heavy clouds which make deficient the use of optical sensor at such situation when we need cloud-free imagery. In addition, optical sensors are not well-suited for detecting inundated vegetated areas [8].

SAR is widely used in monitoring flood events because SAR transmits microwave signals which remain unchanged by the weather conditions like cloud, fog, smog, etc and can image the area at any time of day. SAR is used for urban flooding because its longer wavelengths have high penetration tendency. In SAR imagery built-up area gives high backscatter and appears brighter due to corner reflection and water appears dark due to its smooth surface backscattering mechanism [9,10]. Therefore, SAR has been used in such situation by many researchers. Although SAR data has great potential for flood mapping but it is challenging to assess the damages with SAR data due to limitation of temporal resolution. In such situation, Moderate Resolution Imaging Spectroradiometer (MODIS) sensors can play a vital role for crop damage assessment due to its temporal resolution of producing imagery twice a day. It gives data two times a day. Though its spatial resolution is coarser as compared to Sentinel-1 SAR data i.e., 250 m to 1000 m. MODIS uses Shortwave Infrared (SWIR) band which is sensitive to soil and vegetation [24].

Generally, there are two types of techniques that can be used for flood mapping. The first technique uses machine learning [11,12], and the second uses a threshold-based mechanism [13,14]. The 1st technique is not used widely for near real time flood mapping because it requires the field survey for training samples which is hard to collect at the time of co-event (flood) [15,16]. The second technique (threshold-based) can be performed manually or automatic and it seems more effective as compared to the prior mentioned technique. The manual threshold approach is a bit difficult because it needs knowledge of some number of training sampling [14,17]. This may also cause inaccurate or less accurate flood mapping due to wrong classification of water pixels and non-water pixels [14]. However, the

automated threshold technique does not use training data and is used for automated separation of water and non-water pixels [18,19].

There are certain automated threshold techniques and the Otsu image threshold is one of them [21,22] and is widely used for flood mapping [19]. Otsu method requires less interaction and is less complex and computes the threshold from a histogram of an image. Otsu method provides a more precise flood map for large areas using Sentinel-1 GRD SAR data [19].

Although, many researchers like [19,22] used Sentinel-1 and manual threshold method and those studies showed appropriate results but those analysis were limited due to time demand, to download and process the datasets and their execution on desktop-based tools. These issues limit the early response for flood mapping to decision makers and other concerned authorities. That is why sometimes these types of tools do not suit for an early and timely response. On the other hand, Google Earth Engine (GEE), a cloud based Remote Sensing and Digital Image processing tool, enables such type of analysis for an early response over large areas. Google Earth Engine has ingested and makes available a large variety of datasets of different satellites for user utilization [23].

The main objective of this study was to demarcate the flooded areas combining the automatic threshold method using Sentinel-1 SAR data and crop damage assessment using MODIS optical data in the GEE cloud-based platform for an early and precise flood mapping for the area of Mirpur Khas, Sindh, Pakistan for the flooding event of August to September, 2020.

III. STUDY AREA

The PMD (Pakistan Meteorological Department) had reported in late August 2020 that monsoon's heavy rains in parts of the Sindh province have affected the districts of Mirpur Khas, Hyderabad, Sukkur, and Larkana. The districts of Karachi, Hyderabad, and Mirpur Khas were declared "calamity-affected areas" [25]. Keeping the above-mentioned scenario in mind it was decided to choose Mirpur Khas, Sindh, Pakistan as study area.

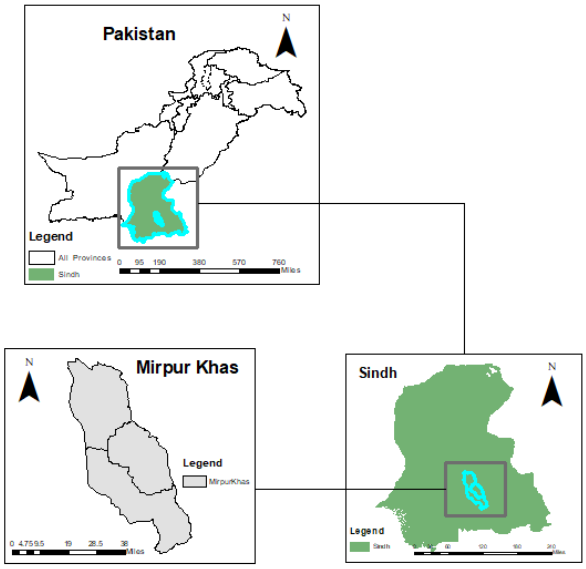


Figure 1: Study Area Map

Mirpur Khas is one of the largest cities of Sindh Province and is located in the south-east of the province Sindh. Mirpur Khas city comes at the 33rd number in the list of largest cities across the country and at 5th number in the list of largest cities of Sindh Province. There are 7 sub-division and 3 tehsils in Mirpur Khas division. It has 233,916 population according to census 2017 [26].

IV. DATASETS

The following datasets were used to execute this research analysis.

A. Sentinel-1

Sentinel-1 is one of 5 missions of Copernicus by the European Space Agency (ESA), operating in all weather, day, and night conditions and produces Synthetic Aperture Radar (SAR) imagery up to 10 m in resolution in the Interferometric Wide Swath (IW) mode, in C band. The Sentinel-1 constellation consists of 2 sensors ("A" & "B") and its revisit period or temporal resolution is 12 days for one satellite and 6 days for both combined. Sentinel-1 data is delivered by ESA in two formats: Single Look Complex (SLC) & Ground Range Detected (GRD). SLC data is used mostly for interferometric SAR applications. Also, to be noted that GEE has ingested only GRD SAR data [27]. Sentinel-1 SAR GRD data was used to highlight change detection and to delineate the flood map.

B. JRC Global Surface Water Mapping Layers

JRC Global Surface Water Mapping Layers is basically a derived product of Landsat datasets. This dataset is generated using Landsat 5, 7, 8's different scenes from 16-03-1984 to 31-12-2020. It classifies each pixel into water or non water area [28]. This dataset was used to classify water and non-water areas on the basis of pixel values.

C. SRTM DEM

The Digital Elevation Model (DEM) which is used in the analysis is Shuttle Radar Topography Mission (SRTM) DEM at 3 arc-second resolution. It was used to remove

signals that were weak backscattered from the topographic area and to extract slope information.

D. MODIS

Moderate Resolution Imaging Spectroradiometer (MODIS) was launched by NASA in 1999 on board Terra Satellite and later in 2002 on Aqua. MODIS gives a moderate spatial resolution from 250 m to 1000 m with a temporal resolution of 1 day [29]. MODIS land cover product is the only dataset that gives global coverage and is available in GEE. MODIS was used to estimate the damaged cropland of the study area.

E. Vector data

The Study area's administrative boundary shapefile was used to extract the exact area of interest.

V. METHODS AND MATERIALS

The following methodology for delineation of flood extent and assessment of damaged crop was performed as shown in Fig.2. 3 criterions (Polarization, Orbit pass, and filter) were defined to analyze that which are suitable for said study. Total 08 images were analyzed. First of all, 8 images of before and after flood were accessed in Google Earth Engine (https://code.earthengine.google.com/) considering the following mentioned parameters.

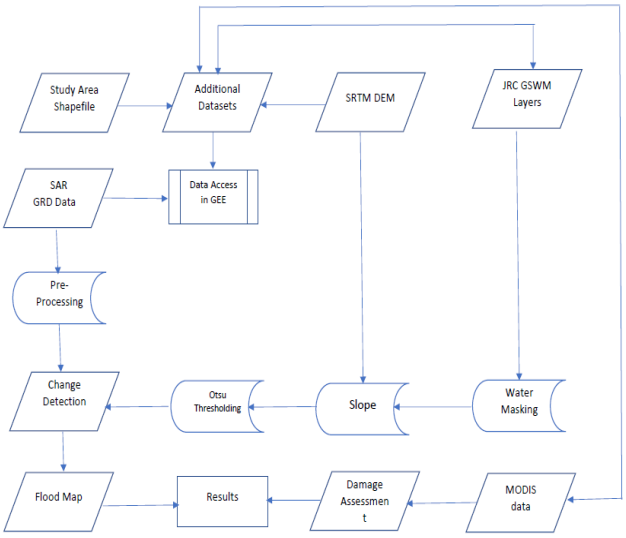


Figure 2: Flowchart

Polarization (VH, VV) & Orbit Pass (Ascending/Descending) as shown in Fig.3. Polarization plays a vital role in backscattering mechanism. Hess et al. analyzed the best results in co-pol channel and suggested its use for flood mapping i.e., HH-pol [30]. However, HH and HV polarizations are available just for some maritime and polar regions and HH-pol data for the said study area was unavailable [26].

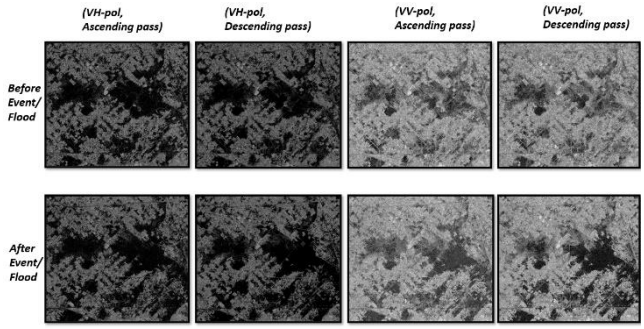


Figure 3: Comparison of VH-pol, VV-pol & Ascending, and Descending orbit pass

The next step was to choose polarization between VV and VH. VV-pol, causes volume scattering in inundated vegetated areas because it is sensitive to rough water, and may provide less information or may cause misclassification [32]. Schumann et al. [31] suggested that in the absence of HH-pol data the other preferable choices are VH and HV polarized data, HV-pol data was unavailable for the study area therefore, VH was chosen.

When Sentinel-1is in ascending pass (Northward) it looks at the area towards west and when it descends (Southward) it is observing towards east [33]. The study area falls in southeast of Province Sindh. Therefore, for this study descending pass was chosen. In Fig.4 flood can be observed more precisely in Descending orbit pass than Ascending orbit pass.

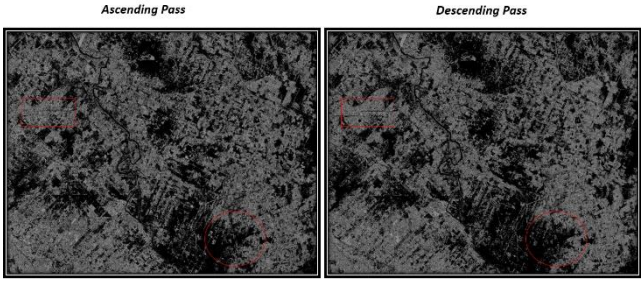


Figure 4: Ascending & Descending Orbit Pass comparison

After selecting VH-pol and descending pass, 2 filters were applied on the images of before and after flood to reduce the speckle-noise. A comparison was also made to highlight the efficiency of which filter can suppress more noise, shown in Fig.5. Observed areas of Deh No. 150 are on the West side, Deh No. 155 are on North side, and Deh No. 160 are on South side. Dark areas are depicting sandy areas due to smooth surface backscattering mechanism. There is also bog area and agriculture land features that exist there and highlighted areas are showing difference between the focal median and focal mean filters results. Focal mean filter can suppress more noise than that of focal median filter.

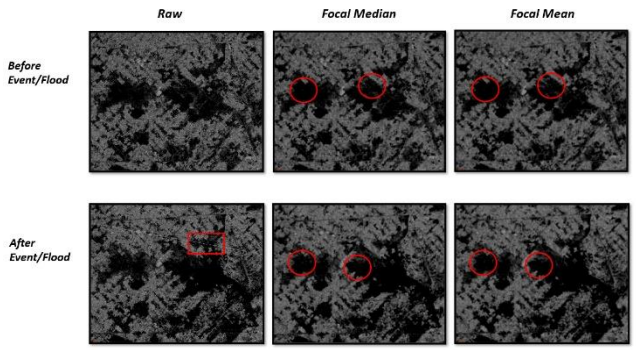


Figure 5: Comparison of Mean & Median Speckle-reducing filters

After selecting VH-pol, descending pass and mean filter slope were calculated using NASA's SRTM DEM 3 arc-second resolution. Then using JRC water layer, a difference layer was created in which the water bodies or water pixels existing for time greater than 10 months were given permanent water label and were masked from flood area. An automated thresholding value of -20.95 dB was generated using Otsu algorithm in GEE and a histogram was generated as shown in Fig.6. Succeeding auto-threshold value, change detection was calculated and flood map was prepared. In the histogram it can be seen maximum value is falling at -20.95 dB. And finally, using MODIS global coverage data crop layer was extracted and was overlayed on SAR after flood image as shown in Fig.7. An assessment of damaged crop due to flood was made which can be seen in Fig.9, highlighted with red circle in green color with flooded area layer on SAR after flood image.

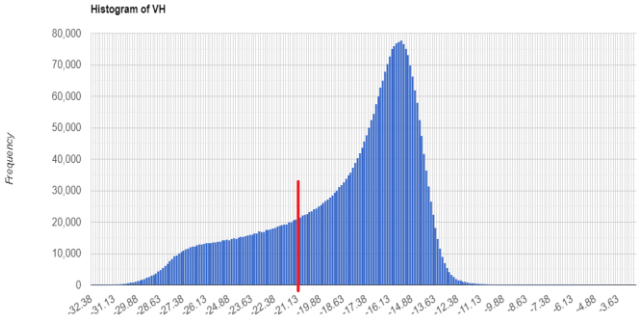


Figure 6: Histogram

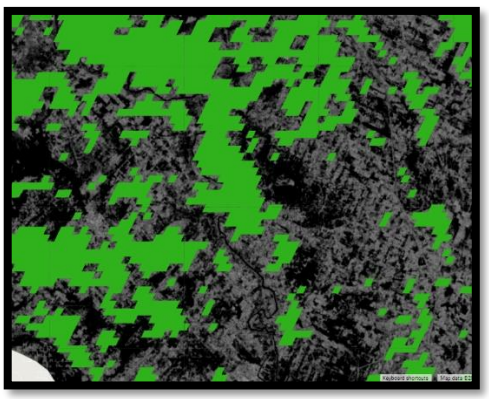


Figure 7: Crop layer overlaying on SAR image after flood

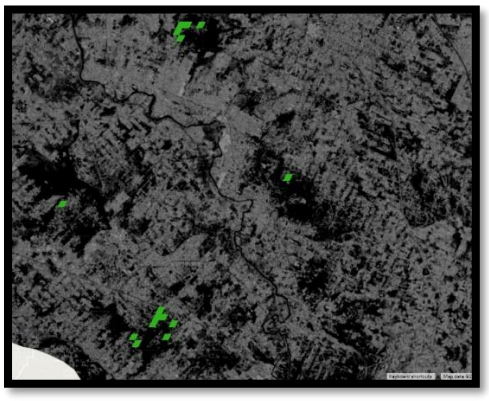


Figure 8: Damaged crop layer overlaying on SAR image after flood

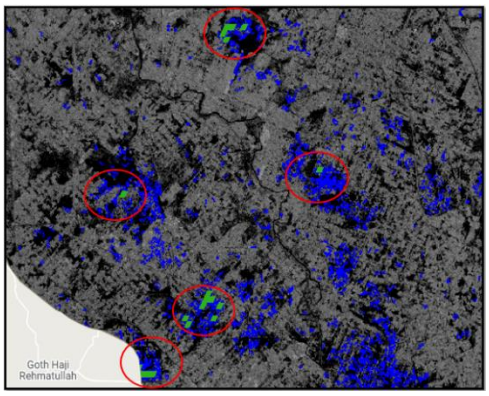


Figure 9: Damaged crop layer overlaying on SAR image after flood with flooded areas layer

VI. RESULTS AND DISCUSSION

Here is the result of the said analysis.



Figure 10: Study Area

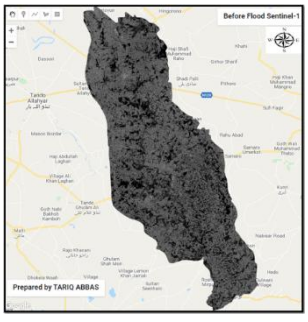


Figure 11: Image before flood

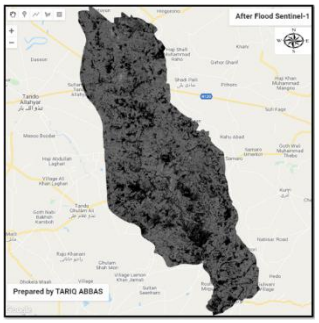


Figure 12: Image after flood

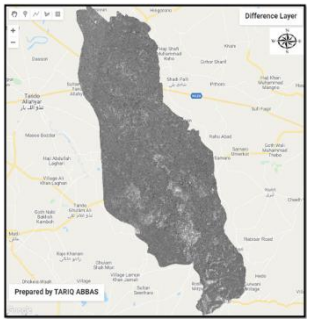


Figure 13: Difference layer

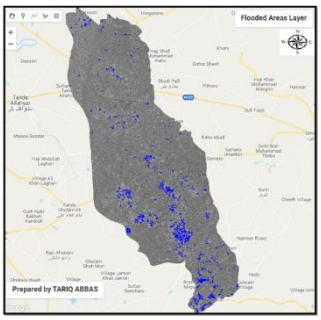


Figure 14: Flood layer overlaying on difference layer

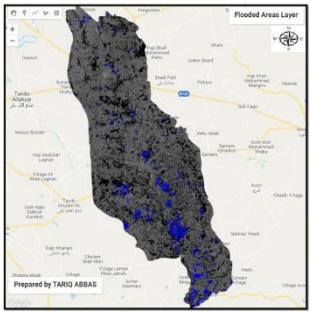


Figure 15: Flood layer overlaying on image before flood

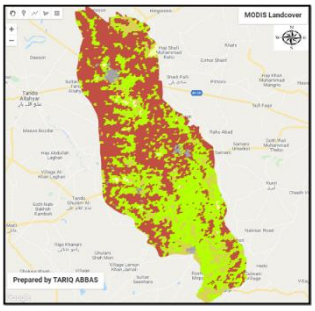


Figure 16: MODIS landcover

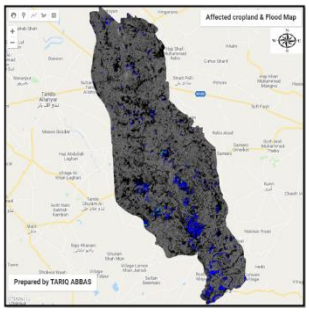


Figure 17: Flood & damage assessment layers overlaying on image before flood

During the flooding season, concerned authorities i.e., NDMA, PMD etc, require updated and timely information to demarcate the affected area, to manage the situation, and mitigate the associated losses. Regarding this situation, a spatio-temporal analysis was made in which Spaceborne SAR GRD data was used to locate the flooded areas and MODIS data was used to assess the associated damages. Fig.10 is showing the study area administrative boundary, Fig.11 is showing the Sentinel-1 SAR GRD image of pre-event taken on 21/09/2019, Fig.12 is showing the Sentinel-1 SAR GRD image of post-event taken on 21/09/2020, Fig.13 is depicting difference layer (DL) that was obtained by "(1)".

$$DL = Image\ after\ event \div Image\ before\ event \quad (1)$$

Then JRC Global Surface Water Mapping layer was accessed and its 'Seasonality' band was chosen to classify the permanent or seasonal water. Values were assigned on the basis of the following "(2)" and "(3)". Permanent water was given a value of '0' and seasonal or flood water was given a value of '1'. After classifying the permanent and flood water slope was calculated using SRTM DEM of 3 arc resolution to further refine the flood results.

$$Water\ existance > 10\ months = Permanent \quad (2)$$

$$Water\ existance < 10\ months = seasonal \quad (3)$$

Fig.14 is showing flood layer in blue overlaying on difference layer, Fig.15 is showing flood layer (in blue) overlaying on the image of pre-event.
MODIS data was used because it gives global land coverage, selected 'LC_Type1' band and cropland was extracted and then overlayed on flood layer. Fig.16 showing is MODIS global landcover coverage, Fig.17 is showing the final result of the analysis in which water in blue and damaged crop detected due to flood in green can be seen.

VII. CONCLUSION

National Disaster Management Authority (NDMA) had reported that disastrous rainfall affected the districts of Mirpur Khas, Karachi, Hyderabad, Badin etc. The flood of September 2020 in Mirpur Khas caused many casualties in the form of lives, infrastructure, and crops. Flood mapping and associated damages should be evaluated quickly to provide near real time flood information to concerned authorities to mitigate the losses. It is somehow challenging to compute flood mapping on a desktop-based system that could not be much helpful for timely response. This study might be helpful for flood mapping using SAR data integrated with automated threshold technique (Otsu) and its associated damages with MODIS data on a cloud-based platform i.e., GEE. While starting an analysis using SAR data one must be aware of basic SAR principles and backscattering parameters i.e., frequency & polarization etc. HH-pol gives the best result of inundated areas but in the absence of HH-pol, the next better option is VH-pol and that can provide reliable results. Otsu algorithm can be used for automated thresholding in GEE. In case of emergency, GEE can be used as key tool to access the spaceborne data. MODIS data has its own benefits, in regard of resolutions although it has coarser spatial resolution with a good temporal resolution and damages can be assess using it.

REFERENCES

[1] J.-M. Martinez and T. Le Toan, "Mapping of flood dynamics and spatial distribution of vegetation in the Amazon floodplain using multitemporal SAR data," *Remote sensing of Environment*, vol. 108, no. 3, pp. 209-223, 2007.

[2] J. García-Pintado, D. C. Mason, S. L. Dance, H. L. Cloke, J. C. Neal, J. Freer and P. D. Bates, "Satellite-supported flood forecasting in river networks: A real case study.," *Journal of Hydrology*, vol. 523, pp. 706-724, 2015.

[3] L. Landuyt, A. V. Wesemael, G. J.-P. Schumann, R. Hostache, N. E. C. Verhoest and F. V. Coillie, "Flood mapping based on synthetic aperture radar: An assessment of established approaches," *IEEE Transactions on Geoscience and Remote Sensing*, vol. 57, no. 2, pp. 722-739, 2018.

[4] Y. Li, S. Martinis, S. Plank and R. Ludwig, "An automatic change detection approach for rapid flood mapping in Sentinel-1 SAR data," *International journal of applied earth observation and geoinformation*, vol. 73, pp. 123-135, 2018.

[5] A. Twele, W. Cao, S. Plank and S. Martinis, "Sentinel-1-based flood mapping: a fully automated processing chain," *International Journal of Remote Sensing*, vol. 37, no. 13, pp. 2990-3004, 2016.

[6] S. Long, T. E. Fatoyinbo and F. Policelli, "Flood extent mapping for Namibia using change detection and thresholding with SAR," *Environmental Research Letters*, vol. 9, no. 3, p. 035002, 2014.

[7] P. A. Townsend and S. J. Walsh, "Modeling floodplain inundation using an integrated GIS with radar and optical remote sensing," *Geomorphology*, Vols. 21 (3-4), pp. 295-312, 1998.

[8] N. G. Pricope, "Variable-source flood pulsing in a semi-arid transboundary watershed: the Chobe River, Botswana and Namibia," *Environmental monitoring and assessment*, vol. 185, no. 2, pp. 1883-1906, 2013.

[9] L. L. HESS, J. M. MELACK and D. S. SIMONETT, "Radar detection of flooding beneath the forest canopy: a review," *International Journal of Remote Sensing*, vol. 11, no. 7, pp. 1313-1325, 1990.

[10] D. C. Mason, I. J. Davenport, J. C. Neal, G. J.-P. Schumann and P. D. Bates, "Near Real-Time Flood Detection in Urban and Rural Areas Using High-Resolution Synthetic Aperture Radar Images," *IEEE transactions on Geoscience and Remote Sensing*, vol. 50, no. 8, pp. 3041-3052, 2012.

[11] H. Shahabi, A. Shirzadi, K. Ghaderi, E. Omidvar, N. Al-Ansari, J. J. Clague, M. Geertsema, K. Khosravi, A. Amini , S. Bahrami , O. Rahmati , K. Habibi , A. Mohammadi, H. Nguyen , A. M. Melesse , B. B. Ahmad and A. Ahmad, "Flood Detection and Susceptibility Mapping Using Sentinel-1 Remote Sensing Data and a Machine Learning Approach: Hybrid Intelligence of Bagging Ensemble Based on K-Nearest Neighbor Classifier," *Remote Sensing*, vol. 12, no. 2, p. 266, 2020.

[12] X. Shen , D. Wang , K. Mao, E. Anagnostou and Y. Hong , "Inundation Extent Mapping by Synthetic Aperture Radar: A Review," *Remote Sensing*, vol. 11, no. 7, p. 879, 2019.

[13] E. Psomiadis, "Flash flood area mapping utilising SENTINEL-1 radar data," in *Earth Resources and Environmental Remote Sensing/GIS Applications VII (Vol. 10005, p. 100051G)*, Eidenburgh, UK, 2016.

[14] P. Manjusree, L. P. Kumar, . C. M. Bhatt, G. S. Rao and V. Bhanumurthy, "Optimization of threshold ranges for rapid flood inundation mapping by evaluating backscatter profiles of high incidence angle SAR images.," *International Journal of Disaster Risk Science*, vol. 3, no. 2, pp. 113-122, 2012.

[15] R. Kumar, "Flood Inundation and Hazard Mapping of 2017 Floods in the Rapti River Basin Using Sentinel-1A Synthetic Aperture Radar Images," *Applications and Challenges of Geospatial Technology. Springer, Cham*, pp. 77-98, 2019.

[16] L. Peter, M. Matjaž and O. Krištof, "Detection of Flooded Areas using Machine Learning Techniques:Case Study of the Ljubljana Moor Floods in 2010," *Disaster Advances*, vol. 6, no. 7, pp. 4-11, 2013.

[17] R. Malinowski, G. Groom, W. Schwanghart and G. Heckrath , "Detection and Delineation of Localized Flooding from WorldView-2 Multispectral Data," *Remote Sensing*, vol. 7, no. 11, pp. 14853-14875, 2015.

[18] M. Ul Haq, M. Akhtar, S. Muhammad, S. Paras and J. Rahmatullah, "Techniques of Remote Sensing and GIS for flood monitoring and damage assessment: A case study of Sindh province, Pakistan," *he Egyptian Journal of Remote Sensing and Space Science*, vol. 15, no. 2, pp. 135-141, 2012.

[19] H. Cao , H. Zhang, C. Wang and B. Zhang, "Operational Flood Detection Using Sentinel-1 SAR Data over Large Areas," *Water*, vol. 11, no. 4, p. 786, 2019.

[20] M. S. Sardar, . M. A. Tahir and M. I. Zafar, "Poverty in Riverine Areas : Vulnerabilities, Social Gaps and Flood Damages," *Pakistan Journal of Life and Social Science*, vol. 6, no. 1, pp. 25-31, 2008.

[21] J.-H. Xue and Y.-J. Zhang, "Ridler and Calvard's, Kittler and Illingworth's and Otsu's methods for image thresholding," *Pattern Recognition Letters*, vol. 33, no. 6, pp. 793-797, 2012.

[22] C. Vishnu, K. Sajinkumar, T. Oommen, R. Coffman, K. Thrivikramji, V. Rani and S. Keerthy, "Satellite-based assessment of the August 2018 flood in parts of Kerala, India," *Geomatics, Natural Hazards and Risk*, vol. 10, no. 1, pp. 758-767, 2019.

[23] N. Gorelick, M. Hancher, M. Dixon, S. lyushchenko, D. Thau and R. Moore, "Google Earth Engine: Planetary-scale geospatial analysis for everyone," *Remote sensing of Environment* , vol. 202, pp. 18-27, 2017.

[24] X. Xiao, S. Boles, J. Liu, D. Zhuang, S. Frolking, C. Li, W. Salas and B. MooreIII, "Mapping paddy rice agriculture in southern China using multi-temporal MODIS images," *Remote sensing of environment* , vol. 95, no. 4, pp. 480-492, 2005.

[25] PMD, "Flood Forecasting Division," Pakistan Meteorological Department, 2021. [Online]. Available: https://ffd.pmd.gov.pk/homepage/.. [Accessed April 2021].

[26] Google Earth Engine, "Synthetic Aperture Radar (SAR) Basics," Google, 2021. [Online]. Available: https://developers.google.com/earth-engine/tutorials/community/sar-basics. [Accessed April 2021].

[27] Google, "Wikipedia," Google, 2021. [Online]. Available: https://en.wikipedia.org/wiki/Mirpur_Khas. [Accessed April 2021].

[28] Google Earth Engine, "Earth Engine Data Catalog," Google, 2021. [Online]. Available: https://developers.google.com/earth-engine/datasets/catalog/JRC_GSW1_3_GlobalSurfaceWater. [Accessed April 2021].

[29] NASA, "MODIS," NASA, 2021. [Online]. Available: https://modis-land.gsfc.nasa.gov/. [Accessed April 2021].

[30] . L. L. Hess and M. J. M. , "Mapping wetland hydrology and vegetation with synthetic aperture radar," *International Journal of Ecology and Environmental Sciences*, vol. 20, no. 1-2, pp. 74-81, 1994.

[31] G. Schumann, R. Hostache, C. Puech, L. Hoffmann, P. Matgen, F. Pappenberger and L. Pfister, "High-Resolution 3-D Flood Information From Radar Imagery for Flood Hazard Management," *IEEE transactions on geoscience and remote sensing*, vol. 45, no. 6, pp. 1715-1725, 2007.

[32] R. Manavalan, "Review of synthetic aperture radar frequency, polarization, and incidence angle data for mapping the inundated regions," *Journal of Applied Remote Sensing*, vol. 12, no. 2, p. 021501, 2018.

[33] P. Tarikhi, "INSAR OF AQUATICBODIES," *ISPRS-International Archives of the Photogrammetry, Remote Sensing and Spatial Information Sciences*, vol. 39, pp. 85-90, 2012.

Prototype of an Autonomous Farming Robot: A Smart Farming System

Moaz Rao
Dept. of Avionics Engineering
The Superior University Lahore
Lahore, Pakistan
rao.moaz1@gmail.com

Muhammad Shaarif Younas
Dept. of Avionics Engineering
The Superior University Lahore
Lahore, Pakistan
shaarif.younas302@gmail.com

Nauman Latif
Dept. of Avionics Engineering
The Superior University Lahore
Lahore, Pakistan
nauman.latif@superior.edu.pk

Ahmad Hammad
Dept. of Avionics Engineering
The Superior University Lahore
Lahore, Pakistan
ahmad.hammad@superior.edu.pk

Sadia
Dept. of Avionics Engineering
The Superior University Lahore
Lahore, Pakistan
sadianamal1998@gmail.com

Ilyas Mahmood Qureshi
Dept. of Avionics Engineering
The Superior University Lahore
Lahore, Pakistan
ilyas.mahmood@superior.edu.pk

***Abstract*— The automated household products in recent technology are adding day by day, we have proposed an autonomous CNC farming project that works on a microcontroller-based Cartesian coordinate system. We present you a Farming Robot that is designed similar to the 3D printer or milling machine in shape and similar precise to perform operation that includes irrigation, seeding, weeding and monitoring soil moisture. This paper briefly describes our project that will assist farmers in monitoring and controlling various activities of farming via Arduino and other components. The status of agricultural parameters is notified to the farmer, allowing him to make appropriate decisions on time. The major benefit of this system is that it is semi-automated, meaning that the farmer makes the choice rather than a completely automated system that results in precision agriculture. It also gets around existing traditional procedures that demand a lot of money, energy, labor, and time. As it's the demand of the environment to have such a product that can grow healthier food in this gradually variant environment and climate change.**

Keywords— computer numerical control (CNC), farming, bot,

I. Introduction

The Agricultural production has kept up with food production due to the industrial and petrochemical revolution, but only at the cost of soil, the environment, and human health. Technological advancements and economies of scale have been driving the increase, but this drive is plateauing and a paradigm shift is needed. Conventional agriculture methods are unsustainable and need to be re-evaluated.

The farming industry has seen a gradual increase in accuracy and precision due to technologies such as GPS and short-range radio. Autopilots, digital mapping, computer vision, and variable rate devices are among the latest innovations. Through the application of these technologies, free-driving tractors are gradually adapted to realize more of the benefits of precision agriculture. By placing the tooling equipment on tracks rather than driving a tractor, Farming robot takes a completely new approach to precision agriculture. A similar method has been used for decades in printers, machine tools, and, more recently, 3D printers, CNC machines, and more. It incorporates Arduino as well as other components.

Farming robot is an autonomous machine designed as a CNC machine. It performs various acts related to farming such as watering, weeding, seeding and it monitors and grows your crops.

II. Literature Review

Crop data can be managed by agricultural management system in such a way that results are orchestrated to address customized solution for each farm by data driven management [1]. Watering system can be managed by automatic plant robot with scheduling system. In which various tests and tools are including like humidity test, soil moisture test and testing of moisture [2]. Smart farming system using sensors such as infrared sensor which is used to regulate the speed of motor. And opto coupler converts electrical signal into light and activates the switches [3]. The farming robot provides information via the internet, as well, which makes the system remotely and flexible. In Pakistan 40% people depend on agriculture for sustainable living [4]. AgroTutor is a mobile application that can take data from framers and give the appropriate advice related to their farming. Also, it provides weather information to farmers. And for business, it also provides the data of historical yield potential and local benchmarking information [5]. Advanced technology, such as the internet of things (IOT), plays an important role in streamlining the process for producers. Harvesters, robotic weeding machines, unmanned aerial vehicles (UAVs), and other automatic machinery are currently helpful to growers in

terms of crop monitoring [6]. Existing research on digitization in agriculture and rural areas does not provide a complete picture of current and future effects. As a result, additional digitized equipment are needed to fill in the gaps in advanced farming techniques' outputs [7]. A method assisted by a mobile object for detecting crop disorder outbreaks and managing them using permitted control strategies. The system ask for the soil and field selection and suggest the ideal condition in which color, shape, distribution pattern etc. are included through which disorder can identify and overcome timely [8]. Capacitive sensors may be used to assess soil moisture efficiently, and a cost drop is possible while maintaining sufficient accuracy. Analog or digital SDI-12 outputs are available for use with the sensor. The sensor's two primary components (oscillator and microcomputer) were chosen because they are general-purpose products with a high temporary availability for manufacturing [9]. Wetting and drying events were detected by the sensors TDR315, CS655, GS1, SM100, and CropX. Based on root mean square error (RMSE), the TDR315, CS655, and GS1 sensors had sufficient accuracy rate for guided watering at the site with low salt concentration and low clay component (LSLC), but not at the site with high salt concentrations and high clay component (HSHC) [10]. Sensor data is needed as input in the automation system application. Sensors in automation systems are used to create a system that works autonomously to regulate performance of the system. Because there are various aspects to consider while constructing an industrial automation system. Water temperature control, irrigation control, fertilization, and oxygen saturation in the water must all be taken into account [11]. There is a screening system in addition to the automation system used in agriculture. This 48-hour screening system makes use of a wireless sensor network (WSN). This screening system monitors conditions in real time [12]. Farmers will benefit from the device since it will provide them with real-time data (temp, humid, soil humidity, Ultraviolet index, and Infrared index) from their farm, allowing them to take the required actions to increase crop production while conserving natural resources (water, fertilizers) [13]. Management of water resources is by far the most sub-vertical (28.08%), followed by agricultural production (14.60%), and finally smart farming (14.60%). (10.11 %). The measuring of surrounding temperature (24.87 %) and ecological moisture (24.87%) yielded the best results in terms of sensor data collecting (19.79%). Other sensor data includes moisture levels (15.73%) and soil pH. (7.61 %). According to statistics, Wi-Fi is the most widely used technology in IOT application development (30.27 %), followed by digital technology (21.10 %) [14]. Smart agricultural designs based on Internet - Of - things technologies may effectively implement the function of real-time data transfer and information processing while also advancing smart agriculture development. Agriculture IOT is an IOT application system that goes through the creation, processing, and distribution of agricultural products. [15].

III. Problem Statement

In this era of automation, there should be such a technology as a smart home device that can automate the farming services on one click for the people who have no farming background so that the agriculture gets promoted as well as healthy food production keeps growing.

IV. Methodoly

Farming robot is an open source robot which works on 3D CNC based operations. We have taken this open concept and try to make it in our own way. In our design circuitry controllers and two stepper motors for x-axis are fixed unlike to the farming robot which is an open source machine. Also, farming robot they are using thread rod for the z-axis movement unlike to this, we have used belt and pulley mechanism to achieve the vertical linear actuation. These are the two major differences in the mechanical structure of our farming robot.

Also, we are designing our own coded firmware which will further implement on cloud computing in future.

A. *Material selection*

As we are designing the machine for both open and closed environment, therefore, we have taken the material selection seriously.

For mechanical structure, we are using anodized aluminum made extrusions as they have high strength against humidity and corrosion. Also, it's not such thermal conductive which makes it almost immune to thermal expansion so that it cannot creates any dimension error in mechanical structure. It's also weather proof and no oxidizing property [16].

For the farming tools and parts, we are using ultraviolet (UV) protected plastics so that it cannot harm or cause any kind of contamination to the food.

B. *Cad model*

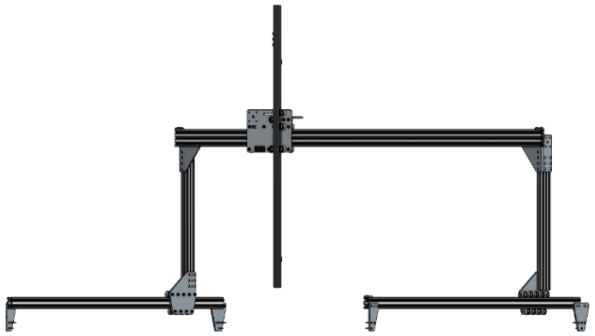


Figure 1: Computer Aided Design CAD model of Farming Robot

C. Hardware selection

For our farming robot, we have selected the material from open builds open source parts for CNC as they are the pioneers of the CNC building.

There is a total of 28 components are used.

- 1.20x40mm V slot aluminum extrusion (17) ft. in total
- 2.20x20mm V slot aluminum extrusion (3 ft.)
- 90-degree L-plates (4 in total)
- The two of these 90-degree L-plates are used to mount the V slots arms of X-axis on the X-axis small carriage plates. And the other two 90-degree L plates are used to mount Y-axis gantry V slot with arms of X-axis.
- V slot Wheels (24 in total)
- These wheels roll over the extrusion to give the smooth movement for actuation. 16 of them are used on 4 carriage plates on two V-slot of X-axis, 4 of them are used on the universal gantry plates on V slot of Y-axis and 4 of them are used another universal gantry plate mounted with main gantry plate to give the vertical actuation to Z-axis V-slot.
- Carriages plates
- These plates are used to carry the whole moveable frame in which arms are directly mounted to these plates with help of L-bar.
- Gantry plates
- 5M bolts
- M3 bolts
- These are used to mount motors with connecting plates over the extrusions and universal gantry plates.
- M5 nuts with washers
- There are used to mount frictionless pulleys, L bars and rollers.
- M5 T nuts
- These are used to mount the extrusions with each other, to mount the connecting plates for stepper motors with V slots, L-plates, belts etc.
- GT 2 belt
- These belts are used to move X, Y, and Z-axis extrusions with the help of stepper motors.
- 20 teeth GT2 pulley
- It mounts on the stepper motor D shaft to push and pull the belt.
- Bearing pulleys
- These are used to roll the belts around the v slots.
- Motor connecting plates
- These are used to mount the motors with a V slot and gantry plates.
- Tool kit
- Drag chain cable carriers

  These are flexible hollow structures used to guide, support, and protect cables, and water lines when in motion
- wires

  4 core and 3 core and single core wire is used to supply power to stepper motors, water pump, limit switches and encoders.

D. General layout & working

After burning the code into Arduino, Arduino will call for the input coordinates from user. After getting the coordinates and computing the required movement, it runs the stepper motors according to the loops as stepper motor achieves one rotation in 200 steps because it covers 1.8 degrees in each step so that the PWM (pulse width modulated) signal should have to be sent in a loop in a condition to achieve the given coordinate using motor drivers accordingly through which the robot will go on to the specified coordinate and perform the farming task assigned to it.

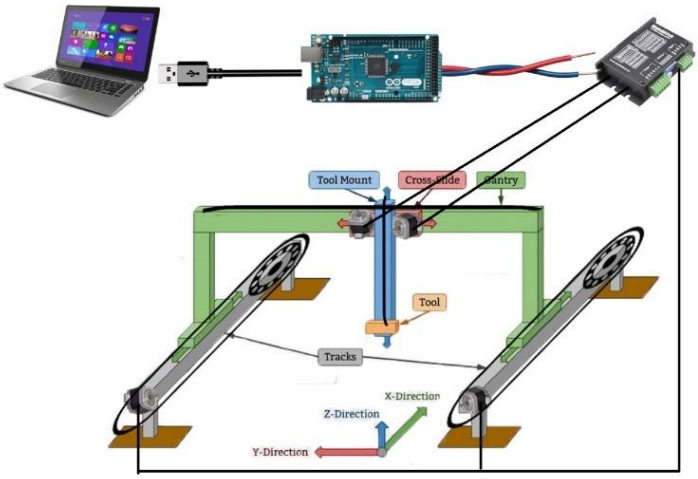


Figure 2: coordinate system and connection layout of Farming Robot

E. Block diagram

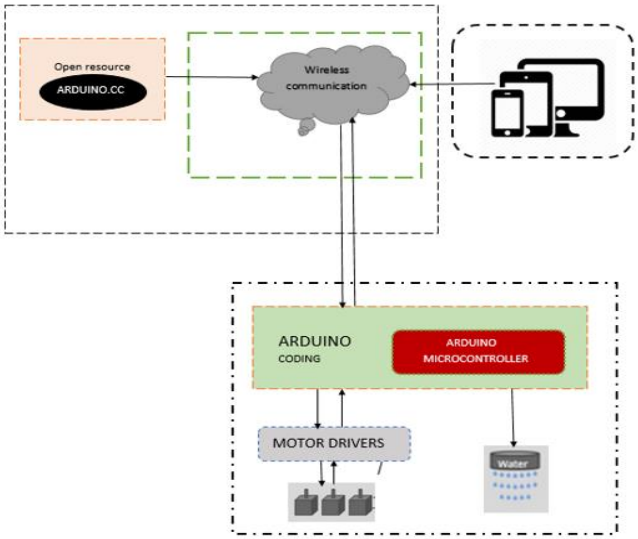


Figure 3: Block Diagram of info flow in Farming Robot

This is the big picture of our project in which our future work is also included. For now we are giving input from PC but in future we can give input from mobile, laptop or wirelessly by making a cloud storage. From cloud storage, input will go to Arduino then it will burn the input. Input will go to motor drivers and drivers will give the input to motors.

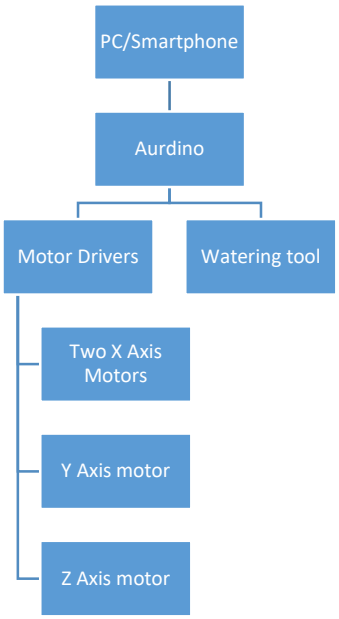


Figure 4: General Flowchart of central idea of Farming Robot

F. Schematic diagram

In block diagram it shows the flow of the input. PC/ smart phone gives the input to the Arduino which goes to motor drivers and watering tool. From motor drivers it goes to all the motors. First it goes to two X Axis motors then to Y and Z axis motors.

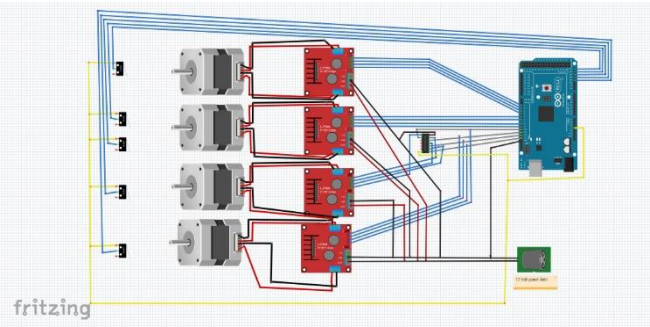


Figure 5: schematic diagram of Farming Robot

G. Electronics

- Arduino Mega
- Motor Drivers L298N
- Stepper motors NEMA 17
- Limit Switches
- HEX Inverting IC
- LED strip light
- Water pump
- Relay switch
- Motor encoders
- Power supplies 12V and 5V

H. Software Selection

ON SHAPE

We have used on shape online software to design the CAD model of Farming Robot.

ARDUINO IDE (integrated development environments)

We have used Arduino IDE software for Programming and motor synchronization.

FRITZING

We have design the schematic diagram on fritzing software.

V. Discussion

Our project is design and development of CNC based farming robot. So, we design and developed the mechanical system of the farming robot. In which we used the aluminum material. Then we develop the coordinate system and control parameters in which x-axis movement via two synchronized stepper motors. Y-axis movement via single stepper motor. And z-axis movement via single stepper motor. We designed and develop the spraying mechanism of our robot which is successfully working. Agriculture sprayers are complete spray systems engineered for generating pressure to drive spray fluid from a tank out to the sprayer's nozzle to crop or soil. Sprayers are most often used for the administration of water, insecticides, pesticides, herbicides, and fertilizer.

VI. Future work/Conclusion

The problem was that there should have to be a product that can automate the farming services as a household machine and our Farming Robot is doing it perfectly but the software framework of the robot is still in progress due to more Future plans but the research work has been done and prototype made and testing is under process. In future, we are designing our own coded firmware which will further implement on cloud computing in future. Also, in open source farming robot, the farming tools are changed by the electromagnetic system which are few of them. Unlike to this, we are working on to design 4 in 1 fixed tool which rotates at 90 degrees to change the tool which is already embedded on it. In this way, our design is more sophisticated, and price controlled than the open source farming robot. Also, farming robot is environment suitable machine as its produce healthier food than the mass production of the locally available food as it monitors your farming 24 hours. It works best even in different climates as well.

VII. References

1. M. Chetan Dwarkani, R. Ganesh Ram, S. Jagannathan, and R. Priyatharshini, "*Smart farming system using sensors for agricultural task automation*," *Proc. - 2015 IEEE Int. Conf. Technol. Innov. ICT Agric. Rural Dev. TIAR 2015*, no. May, pp. 49–53, 2015, doi: 10.1109/TIAR.2015.7358530.

2. S. Suakanto, V. J. L. Engel, M. Hutagalung, and D. Angela, *"Sensor networks data acquisition and task management for decision support of smart farming*," *2016 Int. Conf. Inf. Technol. Syst. Innov. ICITSI 2016 - Proc.*, 2017, doi: 10.1109/ICITSI.2016.7858233.

3. M. Chetan Dwarkani, R. Ganesh Ram, S. Jagannathan, and R. Priyatharshini, "*Smart farming system using sensors for agricultural task automation*," *Proc. - 2015 IEEE Int. Conf. Technol. Innov. ICT Agric. Rural Dev. TIAR 2015*, no. Tiar, pp. 49–53, 2015, doi: 10.1109/TIAR.2015.7358530.

4. M. M. Galgalikar, "*Real-time automization of agricultural*

environment for social modernization of indian agricultural system," *2010 2nd Int. Conf. Comput. Autom. Eng. ICCAE 2010*, vol. 1, no. March, pp. 286–288, 2010, doi: 10.1109/ICCAE.2010.5451949.

5. Bayas, J. C. L., Gardeazabal, A., Karner, M., Folberth, C., Vargas, L., Skalský, R., Balkovič, J., Subash, A., Saad, M., Delerce, S., Cuaresma, J. C., Hlouskova, J., Molina-Maturano, J., See, L., Fritz, S., Obersteiner, M., & Govaerts, B. (2020). "*Agrotutor: A mobile phone application supporting sustainable agricultural intensification". Sustainability (Switzerland)*, *12*(22), 1–10. https://doi.org/10.3390/su12229309

6. Khan, N., Ray, R. L., Sargani, G. R., Ihtisham, M., Khayyam, M., & Ismail, S. (2021). "*Sustainability Current Progress and Future Prospects of Agriculture Technology: Gateway to Sustainable Agriculture"*. https://doi.org/10.3390/su13094883

7. Rolandi, S., Brunori, G., Bacco, M., Scotti, I., & Michailidis, A. (2021). "*The Digitalization of Agriculture and Rural Areas: Towards a Taxonomy of the Impacts"*. https://doi.org/10.3390/su13095172

8. [Sivagnanasundaram, J., Goonetillake, J., Buhary, R., Dharmawardhana, T., Weerakkody, R., Gunapala, R., & Ginige, A. (2021). "*Digitally-Enabled Crop Disorder Management Process Based on Farmer Empowerment for Improved Outcomes: A Case Study from Sri Lanka*." https://doi.org/10.3390/su13147823

9. González-Teruel, J. D., Torres-Sánchez, R., Blaya-Ros, P. J., Toledo-Moreo, A. B., Jiménez-Buendía, M., & Soto-Valles, F. (n.d.). (2021). "*Design and Calibration of a Low-Cost SDI-12 Soil Moisture Sensor"*. https://doi.org/10.3390/s19030491

10. Datta, S., Taghvaeian, S., Ochsner, T. E., Moriasi, D., Gowda, P., & Steiner, J. L. (n.d.). "*Performance Assessment of Five Different Soil Moisture Sensors under Irrigated Field Conditions in Oklahoma*." https://doi.org/10.3390/s18113786

11. Rajaoarisoa, L. H., M'sirdi, N. K., & Balmat, J. F. (2012). *"Micro-climate optimal control for an experimental greenhouse automation". 2nd International Conference on Communications Computing and Control Applications, CCCA 2012*. https://doi.org/10.1109/CCCA.2012.6417903

12. Momirović, N., Vasić, B., Raičević, D. and Oljača M.: *"Technical systems for microclimate control in greenhouses", Agricultural Engineering, Faculty of Agriculture, Universities in Belgrade, Institute of Agricultural Engineering,* No.4, 2007

13. Doshi, J., Patel, T., & Bharti, S. K. (2019)." *Smart Fanning using IOT, a solution for optimally monitoring fanning conditions". Procedia Computer Science*, *160*, 746–751. https://doi.org/10.1016/j.procs.2019.11.016

14. A. A Raneesha Madushanki, Malka N Halgamuge, W. A. H. Surangi Wirasagoda and Ali Syed, "*Adoption of the Internet of Things (IoT) in Agriculture and Smart Farming towards Urban Greening": A Review International Journal of Advanced Computer Science and Applications*(IJACSA), 10(4), 2019. http://dx.doi.org/10.14569/IJACSA.2019.0100402

15. Li, C., & Niu, B. (n.d.). "*Design of smart agriculture based on big data and Internet of things*". *Research Article International Journal of Distributed Sensor Networks*, *2020*(5). https://doi.org/10.1177/1550147720917065

16. Technical datasheet anodized aluminum (n.d.) https://www.trotecmaterials.com/downloads/dl/file/id/555/product/0/technical_datasheet_anodized_aluminium.pdf

17. Aronson, R. landon. (2013)." *Humanity's open-source automated precision farming machine"*. https://farm.bot/blogs/news/the-farmbot-whitepaper?_pos=5&_sid=048d7d7b4&_ss=r

DESIGN AND CFD ANALYSIS OF OUTER AERODYNAMICS OF 10KW HORIZONTAL-AXIS WIND TURBINE

Noman Ahsan
Department of Mechanical Engineering
University of Engineering and Technology Lahore (Narowal Campus), Pakistan
Noman.ahsan.513@gmail.com

Saqlain Abbas*
Department of Mechanical Engineering
University of Engineering and Technology Lahore (Narowal Campus), Pakistan
saqlain.abbas@uet.edu.pk

Muhammad Ahmad
Department of Mechanical Engineering
University of Engineering and Technology Lahore (Narowal Campus), Pakistan
Muhammadahmad.pak17@gmail.com

Ijaz Ali
Department of Mechanical Engineering
University of Engineering and Technology Lahore (Narowal Campus), Pakistan
Mijazali38@gmail.com

Zulkarnain Abbas
Department of Mechanical Engineeering
NFC, Institute of Engineering and Technology Multan, Pakistan
zulkarnain@nfciet.edu.pk

Muhammad Umair Shahid
Department of Electrical Engineering
Khawaja Fareed University of Engineering and Information Technology
Rahim Yar Khan, Pakistan
ushahid@kfueit.edu.pk

***Abstract*— During past years, wind power has been widely recognized and used as a renewable energy resource. However, there exists sufficient difference in the available wind perspective and the overall power production. Pakistan has very good wind potential, especially in the provinces of Sindh and Baluchistan. In the current research study, a 10,000-watt horizontal axis wind turbine (HAWT) is designed for the Taftan, Baluchistan region to meet the energy requirements of Pakistan. For designing the blade profile, the Blade Element Momentum method is used and CFD is utilized for analysis of the designed profile.**

Keywords— ***Aerodynamics, Wind turbine, TSR, Warlock, CFD analysis***

I. INTRODUCTION

It is very difficult for developing countries, including Pakistan, to fulfill the whole population's energy needs. To extract energy from renewable resources has become the need of the hour [1]. Energy consumption, energy conversion, and utilizing energy in a sustainable way have been used and recognized a lot for rotating machinery [2, 3]. There are different renewable resources such as solar, wind, biomass and hydropower potential [4]. The government of Pakistan is struggling hard to overcome the energy crisis by initiating mega power projects to achieve sustainable development goals [5, 6]. The method to extract the energy from wind is getting mature and reliable all over the world [7-12]. Several parameters are required to obtain the optimal design of a wind turbine, including the number of blades, blade material, blade length, rotor diameter, tip speed ratio, the wind cut in and cut out speed, rated power, tower height, etc.

In this research, a computational analysis has been conducted and presented to study the profile of designed 10KW wind turbine for backward areas in Pakistan. The proposed work provides a pollution-free, decentralized, and reliable energy framework.

II. DESIGN PARAMETERS

Analyzing the wind speed in different districts of Pakistan, the Taftan, Baluchistan region is selected in this study for the design of 10KW HAWT. The gearing method is the planetary gearbox.

Table 1. Design parameters

Generator	**Type**	**Permanent magnet 3-phase AC electrical**
	Max Power	14 KW
Rotor	Configuration	Horizontal Axis
	Length of Blade	4.61 m
	Rotor Diameter	3.2 m
	Swept Area	66.76 m^2
	Rotor Speed	126.8 rpm
	Tip Speed Ratio	7.2
Wight	Rotor	1,000 kg
Tower	Hight	50 m
	Material	Stainless steel
	Wind	Upwind

By using Warlock design parameters, the final shape of the wind turbine with tower height is drawn on SOLIDWORKS 2020 by using the loft command.

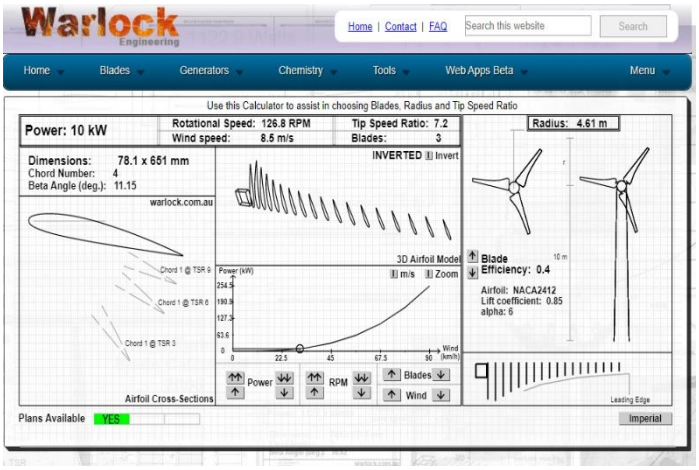


Fig.1 Warlock calculator.

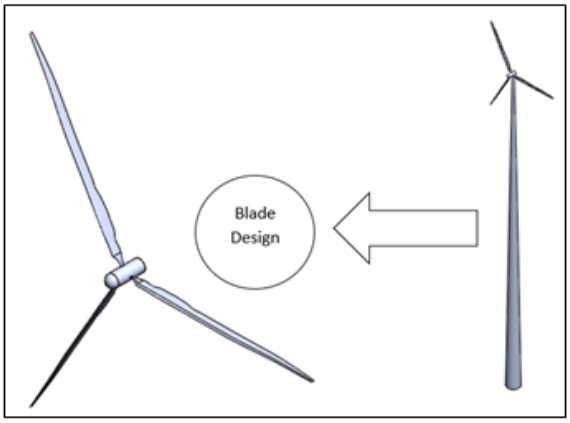


Fig.2 Design with tower height

The power of turbine is calculated by using following formula;

P actual = ½ ρ v3 A * Cp
P actual = 10045.57 W
Density of Air = ρ =1.225 kg/m^3,
wind speed = v = 8.5 m/s
swept area = A = 66.76 m^2
Power coefficient=Cp = 0.398
Rotational speed= w=12.27 rad/s or 126.8rpm

The power coefficient is characterized as the ratio of the examination between genuine power produced by the rotor edge with the power following up on the liquid. The following relation is used to calculate power coefficients at different TSR on the different number of blades using different pitch angles.

$$C_p = \frac{1}{2}(\beta - 0.0220\theta^2 - 5.6)e^{-0.17\beta}$$

Where,

$\beta = TSR\ at\ different\ number\ of\ blades$
$\theta = pitch\ angles$

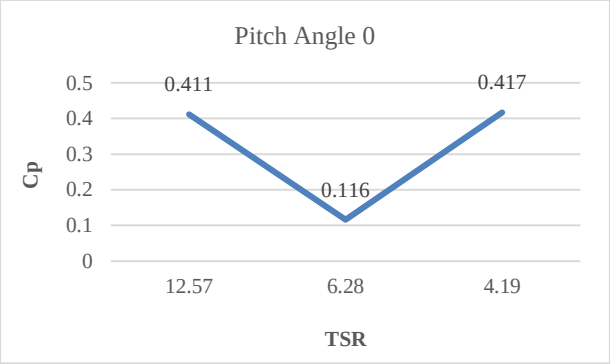


Fig.3 Relation between TSR and C_p for $\theta = 0°$, n= 1,2 & 3

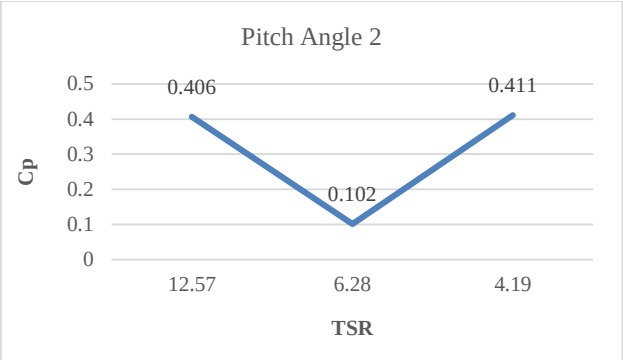


Fig.4 Relation between TSR and C_p for $\theta = 2°$, n= 1,2 & 3

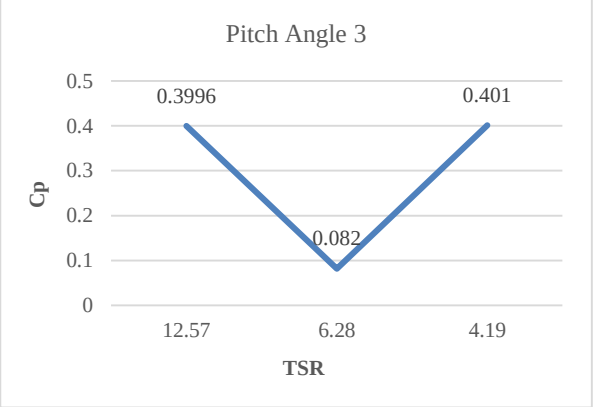


Fig.5 Relation between TSR and C_p for $\theta = 3°$, n= 1,2 & 3

III. SIMULATION ANALYSIS

To justify the proposed design, computational fluid dynamics (CFD) analysis is also conducted in the current study. Meshing is performed on ANSYS 19.2, with element size 845.4mm, while the number of elements and nodes are 1055282 and 185556, respectively. The wind turbine design is accomplished by using given conditions and the K-epsilon turbulence model.

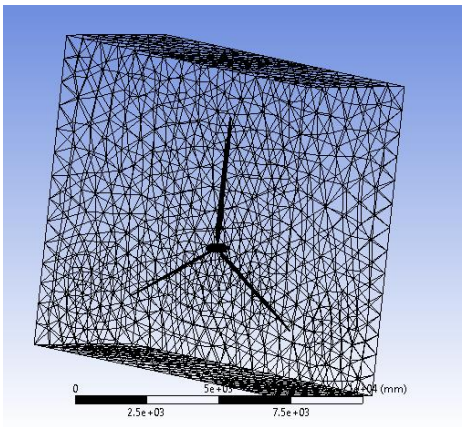


Fig.6 Dissection part of meshing

The lift coefficient (C_l) of the wind blade is calculated 0.26 from Ansys, while the value of drag coefficient (C_d) for airfoil is 0.04.

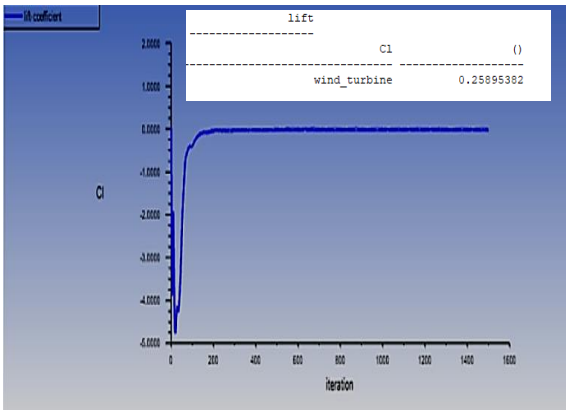


Fig. 7 lift coefficient

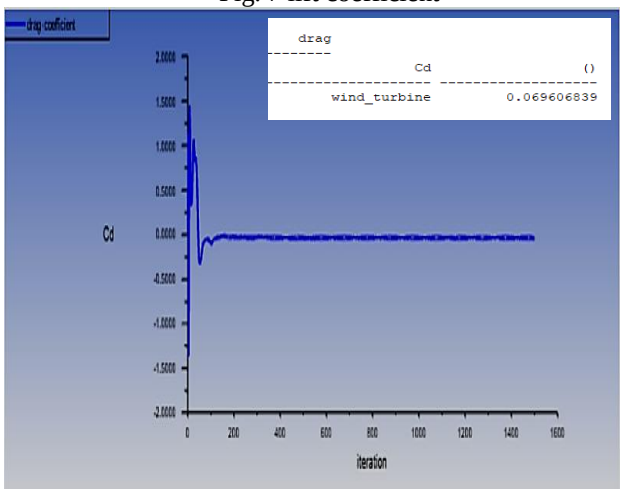


Fig. 8 drag coefficient

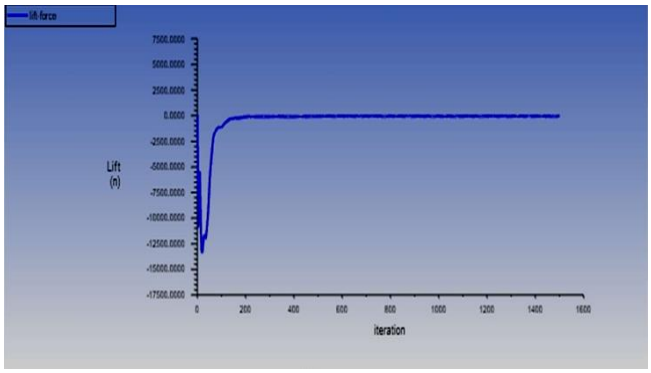


Fig. 9 Lift Force

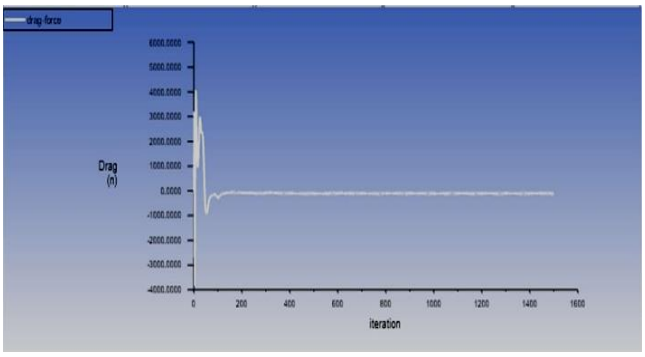


Fig. 10 Drag Force

The power can be calculated as;

P = T*w

As torque on a wind turbine is calculated (774.24 Nm) from Ansys, so power will be

P = 774.24*12.27

P = 9499.92W

Flow distributions are analyzed using the whole model as shown in Fig.11, It can be seen that the blade generate motion due to the high lift coefficient.

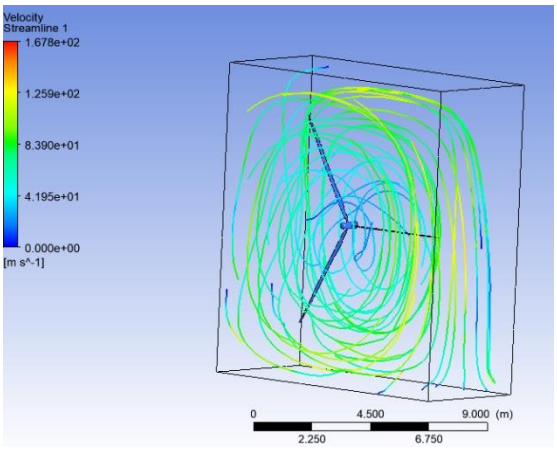


Fig.11 Wind distribution on the whole turbine

The pressure distribution is being taken from the front view and it shows the cut section at the middle of HAWT. It represents that the tip of the wind blade shows a decrease in pressure. An airfoil is a 2-dimensional wing segment that addresses basic wing execution qualities. The pressing factor circulation and lift coefficient are significant boundaries that portray the conduct of airfoils. The pressing factor circulation is straightforwardly identified with the lift created via airfoils.

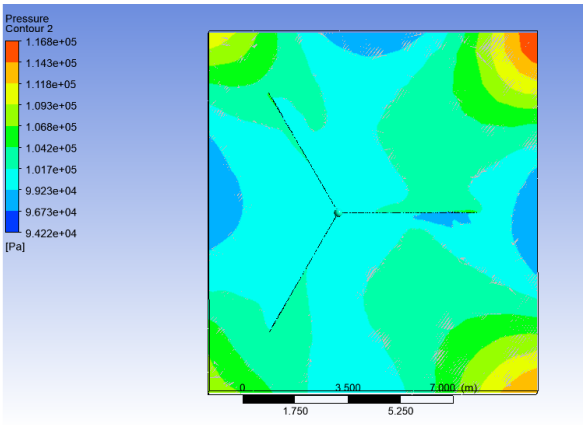


Fig.12 Front view of pressure distribution on the whole turbine

Further, the pressure distribution is also analyzed by using a side view plot distribution to observe the pressure variation on the blade of the designed model.

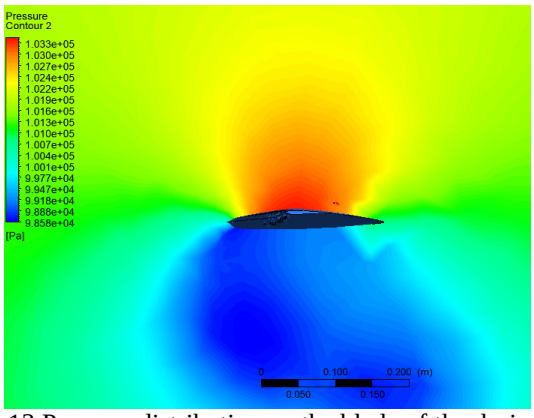


Fig.13 Pressure distribution on the blade of the designed model.

It can be observed from Fig. 13 that in the upper red region of the blade the pressure is high, while the lower side of the blades shows the lower pressure so that it generates motion in the wind blade.

IV. Conclusion

The current research has proposed a design for HAWT to satisfy the energy needs at the microscopic level in Pakistan. All the determined outcomes have been verified utilizing computational analysis. The wind turbine design is accomplished by using the specified conditions and the K-epsilon turbulence model. From simulation results, it is clear that there exists difference in pressure between the lower and upper end of turbine blade. Hence, these computations validate the proposed wind turbine design to provide a decentralized, sustainable and reliable energy framework.

Acknowledgement

The authors of this paper acknowledge the support received from UET Lahore, Pakistan to complete this study.

References

1. Asif M. Sustainable energy options for Pakistan. Renewable and Sustainable Energy Reviews, 2009, 13: 903-909.
2. Xu Q, Lin A, Cai Y, Ahmad N, Duan Y, Liu C. Numerical analysis of aerodynamic characteristics of exhaust passage with consideration of wet steam effect in a supercritical steam turbine. Energies, 2020, 13(7):1560.
3. Fawzy H, Zheng Q, Ahmad N, Jiang Y. Optimization of a Swirl with impingement compound cooling unit for a gas turbine blade leading edge. Energies, 2020, 13(1):210.
4. Abbas T, Bazmi A. A, Bhuttoo A. W, et al. Greener energy: Issues and challenges for Pakistan solar energy prospective. Renewable and Sustainable Energy Reviews, 2014, 31: 258-269.
5. Ghaffar M. A. The energy supply situation in the rural sector of Pakistan and the potential of renewable energy technologies. Renewable Energy, 1995, 6(8): 941-976.
6. Mallawi K.Y, Badr M.A. A practical approach for selecting optimum wind rotors. Renewable Energy, 2003, 28: 803-822.
7. Reiche D, Bechnerger M. Policy differences in the promotion of renewable energies in the EU member states. Energy Policy, 2004, 32: 39-52.
8. Brondstead P, Holmes J .W, Sorensen B. F. Wind rotor blade materials technology. European Sustainable Energy Review, 2008, 2: 36-41.
9. Stol K. A, Zhao W.X, Wright A.D. Individual blade pitch control for the controls advanced research turbine (CART). Journal of Solar Energy Engineering, 2006, 128: 498-505.
10. Reiche D, Bechnerger M. Policy differences in the promotion of renewable energies in the EU member states . Energy Policy, 2004, 32: 39-52.
11. Brondstead P, Holmes J W, Sorensen B F. Wind rotor blade materials technology. European Sustainable Energy Review, 2008, 2: 36-41.
12. Stol K A, Zhao W X, Wright A D. Individual blade pitch control for the controls advanced research turbine . Journal of Solar Energy Engineering, 2006, 128: 498-505.

Autonomous Unmanned Aerial Vehicle for Agricultural, Security, Emergency and Other Uses

Dr. Amir Rashid Chaudhry
COMSATS UNIVERSITY
Islamabad, Pakistan
amir.rashid@comsats.edu.pk

Javid Rashid Ch.
FAMBZZHH
Islamabad, Pakistan
ch.javid@hotmail.com

Dr. Imran Tahir
FAMBZZHH
Islamabad, Pakistan
dr.imran.tahir@gmail.com

Tayyaba Shafaq
COMSATS UNIVERSITY
Islamabad, Pakistan
tayyabashafaq.tts@gmail.com

Imaan Shahid Raja
COMSATS UNIVERSITY
Islamabad, Pakistan
Imaanshahidraja@gmail.com

Salman Amir
COMSATS UNIVERSITY
Islamabad, Pakistan
salman.aamir96@gmail.com

Zohair Anjum
COMSATS UNIVERSITY
Islamabad, Pakistan
zohair381@gmail.com

Nabeel Uddin Sheikh
COMSATS UNIVERSITY
Islamabad, Pakistan
nabeeluddin222@gmail.com

Abstract-- This research is the extension of the work* [1] *revolves around exploration of possibilities of using technology to solve some major problems, with minimum capital and immediate results. These problems include, but are not limited to, Security, Health Emergencies, Agricultural limitations, Cutting down of Trees and Lack of Mobility in hard-access regions. The primary focus was laid on mobility and on an all-in-one solution. In this regard, the use of Unmanned Aerial Vehicles (UAVs), also known as Drones was investigated. It was observed that a Multi-Purpose Drone, designed and built upon a Modular Platform, can prove to be an innovative solution to the problems mentioned above. A drone can access areas which might never be possible to access on foot otherwise, and it can infiltrate hostile regions with no threat of loss of life. Essentially, a drone can be an eye in the sky and prove crucial in many different scenarios. Building upon this idea further, our team explored the possibilities of this. As discussed above, the platform must be modular. That is, the aircraft is to have different swappable modules which can be conveniently swapped-on or swapped-off, depending on the required use on a given instance.

Keywords— UAV, Drone, Autonomous, Aerial, Security, Surveillance, Patrolling, Facial Recognition, Agriculture, Forestry, Tree Plantation, Reforestation, Seed Plantation, Emergency Response, Payload, Remote Controlled

I. INTRODUCTION

Drones as unmanned aerial vehicles which can either operate anonymously once they have been programmed with a certain set of commands, or they can be operated remotely by an operator-also known as a drone pilot. Drones come in different sizes and forms. They can be large enough to carry missiles, or small enough to fit inside the palm of a hand.

The upside of using an aerial drone platform, as opposed to robots or land drones, is the significantly higher level of mobility it comes with. With a drone, the terrain is never a limitation. Drones can reach spots which might otherwise never be accessible on foot or on wheels. This ability can be crucial in a series of possible events, i.e., when a hiker on a hillside needs emergency first-aid or when a high-security sensitive area needs to be patrolled [2]. This technology has been researched upon to offer solutions to multiple problems. To accomplish this, use of existing technology coupled with innovation to create a product with a diverse set of features has been explored. The consideration for the technology was to be modular.

This aspect is primarily what has been missing in the previous work on this technology. A lot of research has been performed to explore different uses of drones, however, minimal thought has been put towards making this technology all-purpose. Many excellent drones have been developed, but all of them are usually only good for one single purpose. Our research explores the use of one single drone for multiple purposes.

It has to have a fixed basic structure with additional swappable modules which can be swapped on or off depending on the nature and intended purpose of the flight. As part of the research, a total of four unique modules were explored: Agricultural Spray module, Seed-firing module, Health and Emergency module and Security and Surveillance module.

The rest of this article is structured as follows: Section 2 offers the literature review of drone technology, its evaluation and architecture. In Section 3, we describe three modules of the technology. The basic assembly and software is discussed in Section 4 and Section 5 respectively . Section 6 contain the working mechanism Section 7 provides the result and some discussions on future research directions. Finally, Section 8 draws the conclusion

II. LITERATURE SURVEY

The world is moving at a fast pace and it keeps changing. With this change, the technology in use also keeps evolving rapidly. Products and services are being vastly improved with time, a process which is as essential as technology itself. The agenda behind this wave of improvement is clear, it is a race towards efficiency, practicality, and sustainability for the greater good of the planet. Old ways are being discarded for

modern, more efficient, and practical solutions to problems surrounding us. Under these circumstances, directing efforts towards innovation to help make the world a better place is a responsibility which befalls every researcher. Our aim, too, is to develop technology which can cater to a wide range of problems with minimum resources required. In this regard, the primary candidate is a UAV (Unmanned Aerial Vehicle), more popularly known as a Drone.

Because of their adaptability and cost adequacy, drones are becoming solid partners in battling against natural issues and contentions, for example, crop assessment [3] and study work for the investigation of flood protections. In light of these realities, organizations, benefit and non-benefit establishments, and solitary substances are attempting to foster ventures that can take on the obligations also, benefits that the UAV bring to the table. Yearningly, this may altogether affect a change on the debates also, confusions on environmental change. In spite of the fact that there is actually just one of numerous most completed chips away at seed-apportioning airplane models, the writing audit on this work will zero in on concentrates on that utilization drones on farming fields[4]. Most different ventures center around making mechanical developments that might conceivably diminish or add to the worldwide soundness of forests and reforestation strategies. AirBoard Agro [5] is an industrial agriculture drone built for precision agriculture and environmentally responsible farming. This drone has a default spray system length of 10 meters.

As mentioned above, a lot of research has been done with regard to drone technology and exploration of different possible uses of drones. However, the main limitation of this previous work done is that all the researches are limited to very few uses of drone technology at a time. The innovative point of our research is to develop a drone technology which is multi-purpose and can serve to multiple uses simultaneously. The upside of using this technology platform, as opposed to robots or land drones, is the significantly higher level of mobility it comes with. With a drone, the terrain is never a limitation. Drones can reach spots which might otherwise never be accessible on foot or on wheels. This ability can be crucial in a series of possible events, i.e., when a hiker on a hillside needs emergency first-aid or when a high-security sensitive area needs to be patrolled. This drone will be designed to offer solutions to multiple problems. To accomplish this, existing technology will be coupled with innovation to create new technology with a diverse set of features. The research is to be modular. It would have a fixed basic structure with additional swappable modules which can be swapped on or off depending on the nature and intended purpose of the flight.

III. METHODOLOGY

Seed Gun:

The Seed-Gun module is one of the two agricultural modules. As the name suggests. This module hosts a purpose-built gun capable of firing seedballs into the soil. In this regard, a mechanism was designed specifically for this purpose. This mechanism consists of a seedball container, an air compressor, a servo motor, air valves, an Arduino, a 3D-printed flap, Motor-driver IC (Integrated Circuit), a loading chamber and a barrel. Seedball container is placed with an opening at the bottom. The gravitational force forces the seed balls out of this opening. The opening has strategically been designed to be barely wider than the seedballs. This allows only one seedball to pop out of the opening at a time. Below the opening is placed a 3D-printed flap, controlled by a servo motor. This servo is connected to an Arduino using a motor-driver IC.

As the servo receives a signal from the Arduino, it rotates its shaft, which then opens the flap. This sequence is timed to only allow one seedball pass into the loading chamber, after which the flap closes again. After passing through the flap, the seedball then passes through an open Arduino-controlled valve. Once the seedball passes, the valve closes. Now, the seedball is in the loading chamber, between two valves. In this loading chamber is another junction which connects the chamber to the compressor.

Both the valves are closed and the compressor builds up pressure inside the loading chamber. When the pressure reaches the required value, the second valve is opened immediately using the Arduino. This pushes the seedball into the barrel at a high speed, essentially firing it straight into the soil below.

Agricultural Spray:

This is the second of the two Agricultural modules, after Seed Gun. This module has been developed keeping in mind the rising demand for food with which the agriculture sector needs to keep up. Methods used in agriculture are often traditional and usually have models which require a large working force. This makes the process, from sowing to harvesting, time-consuming and inefficient. This project aims to solve this problem by minimizing the amount of time and labor force required. Using this drone-mounted spray module, area of one acre would be covered in about 10 minutes. On multiple batteries, one drone alone would cover hundreds of acres in one day. While at it, the drone may also fly autonomously over an area pre-defined on the map using Mission Planner software. This significantly reduces the human input required.

It involves a tank with a 5-liter capacity to hold the spraying liquid. This tank has a plastic build which is preferred due to its lightweight. Moreover, the tank has a compact design which can easily fit between the drone's landing gear. This tank is coupled with a 4-nozzle system which helps efficiently spray the liquid onto the surface/crop below. The nozzles should be as far as possible from each other on the landing gear edges, to ensure maximum spray area with minimum spray overlap regions. The nozzle system is controlled with an Arduino board and both these components are powered by the onboard battery.

Security Module:

The Security module caters to the security aspect. In this, the drone would be equipped with a high-resolution camera coupled with an FPV (First Person View) kit [6]. This equipment gives the capability to run facial-recognition algorithms on to the feed from the camera, in real time. This data can be sent back to an operator who can analyze it.

Emergency/Delivery Module:

This module has been designed with disaster management in consideration. In this module, a carrying mechanism has been designed with an air-drop functionality. That is, the drone would be able to carry a payload to a location and drop it while it is still airborne, without having

to land. This is crucial for first-aid missions when the drone may have to do back-to-back flights without wasting time on landing or take-off repeatedly. The technology has been designed with a payload capacity of 10 kilograms, which is ample for carrying light medical equipment and first-aid kits, or even blood bags. This whole functionality can additionally be also utilized in the logistics sector for a speedy delivery of couriers and mail.

IV. BASE ASSEMBLY

Chassis:

For the chassis, ZD850 frame was explored. This is a hex copter frame [7] which would allow to mount up to twelve motors, two on each arm. This would play a significant part in obtaining a high payload capacity. The frame is made up of carbon fiber which is a strong yet extremely light material. This weight-saving is important for a higher flight time. The frame is foldable, which provides easier mobility when not in flight.

Propellers:

Propellers play a vital role in the flight and thrust of the aircraft. For this purpose, twelve high-strength carbon fiber 2255 propellers can be used. These propellers have a length of 22 inches and pitch of 5.5 inches. These are fully compatible with multi rotor disc brushless motors. The positioning of propellers is crucial. Hex copter has alternate positions of propellers, clockwise and counterclockwise.

Motors:

Each motor has one propeller. 360kv motors would be used which can revolve up to 360 times per minute each. Each motor produces a thrust of 800 to 900 grams.

Electronic Speed Controller (ESC):

ESCs allows the flight controllers to control and adjust the speed of motors, so the aircraft can move in any direction, at variable speeds.

Flight Controller:

Flight Controller receives the signal from the pilot and transmits it to the ESCs to control the drone.

Radio Receiver:

Radio receiver only receives the signals from the pilot.

Battery:

5200mAh Lithium polymer battery was used to ensure ample flight time.



Fig. 1: Drone with arms folded spray tank attached



Fig. 2: Arms open

V. SOFTWARE

Software is a crucial part of this project. It is here where all sorts of calibrations are performed, such as transmitter controls calibration, ESC (Electronic Speed Control) calibration, GPS (Geo-Positioning Satellite) calibration and compass calibration. In addition to this, flight of the drone also has major dependability on the software. Software would be used to determine flight path and to set waypoints along the path. All of these functions to be configured on the Mission Planner software.[8] For surveillance, a continuous path would be defined around a perimeter to patrol it. For the agricultural modules, the aim would be to fly the drone within a defined area, with waypoints scattered all over it so that maximum area can be covered by spray or seed-gun.

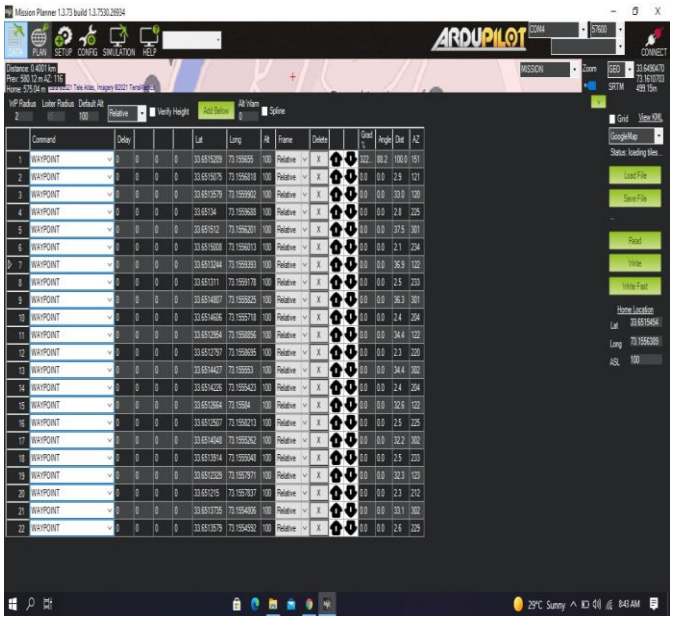


Fig. 3: Waypoint configuration in Mission Planner

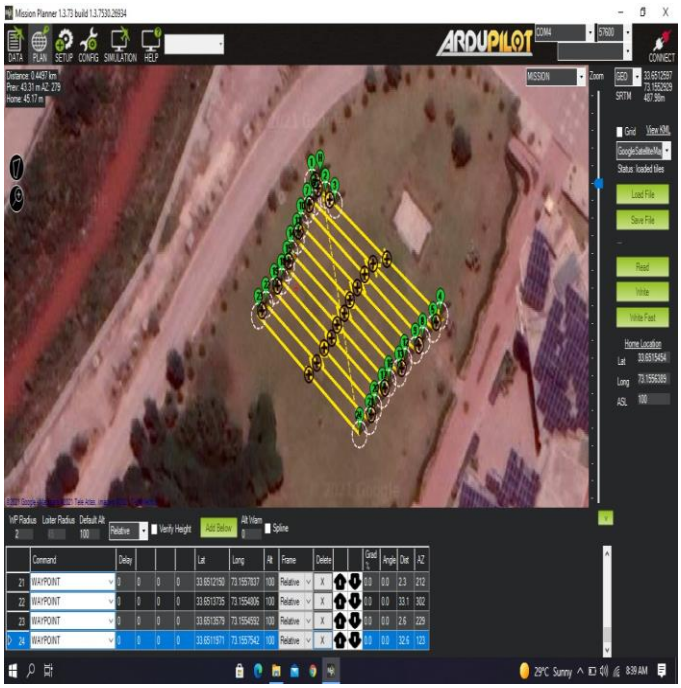


Fig. 4: Path for Agricultural needs

Also, facial recognition is integration is an important part of the software section.

Processing of the image:

Figure 6 shows the processing of an image to improve its quality. Although color images can carry more information about facial expression, 2-D Grey images are more popular in terms of emotion detection. For capturing images, we use a high-definition camera. This stage detects information of interest by smoothing out the image, by removing unwanted noise and enhances the quality of the image captured. It includes normalizing and filtering of the image. It also eliminates the redundancy of the image characteristics. Facial Expression Extraction identifies the information of facial expression like motion, shape of basic facial features. It is considered an interesting part as it extracts useful information from the image. The information extracted is on the premises of facial and appearance features.

Facial expression depends on mood and sentiments. Many facial specifications were extracted from a human face image and used to train specialized neural networks. The best performing specialized convolution neural networks were recruited into decision-making classes which form an integrated Convolution Neural Network (CNN). The integrated CNN is then analyzed using data extracted from the image used during training and testing.

The classification part assembles the information extracted, gathers it together according to certain parameters and helps in their efficient identification. It is a composite procedure as it may be pretentious by many factors. At last, emotions are recognized by looking at the outcome separated by various parameters and estimations.

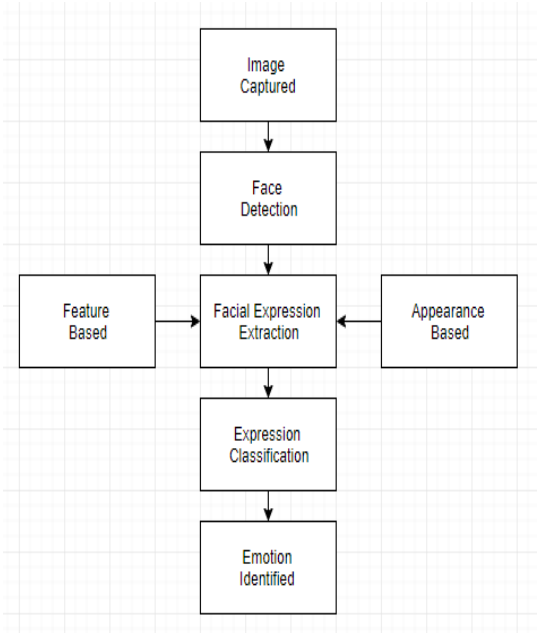


Fig 5: Working of Identification of emotions

While the procedure is to some degree complex, face recognition calculations regularly start by examining human eyes. Eyes comprise of what is known as a valley area which is one of the least demanding highlights to recognize. When eyes are identified, calculations are the initiated to recognize facial locales including eyebrows, lips, nose, nostrils, and the iris. When the calculation construes that it has distinguished a facial area, it then applies extra tests to approve whether it has, truth be told, identified a face.

The main working of facial expression detection [9] will work as follows.

- Detect mouth landmarks
- Collecting the data set
- Feature extracting
- Training the algorithm

- Statistic evaluation of algorithms
- Building program

The part on which we have focused is face-detection. for that, we have used Haar-cascade classifiers [10]which are used for object detection, for which it has been trained. While detecting the face, we obtain facial landmarks detection which will help us to tell the machine about expressions. As seen in fig.6. these numbers are landmarks of facial expressions. Landmarks are the areas of the focus around fiducial facial parts. Facial form captures the inflexible and unbending facial disfigurements because of head developments and outward appearances.

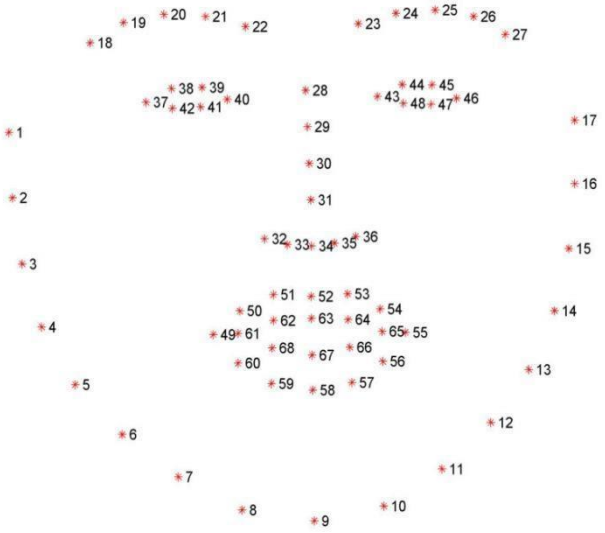


Fig 6: Facial landmarks detection

The next step is to make a dataset of lots of images, we will use a data set of images available on the internet and by using them we'll generate our data set and then it will sort the correct expression from those images in the data set, we'll use some machine learning algorithms to detect facial expression. As shown in the following figure (fig 7) we've approximately more than 40,000 pics for the database and training of the model.

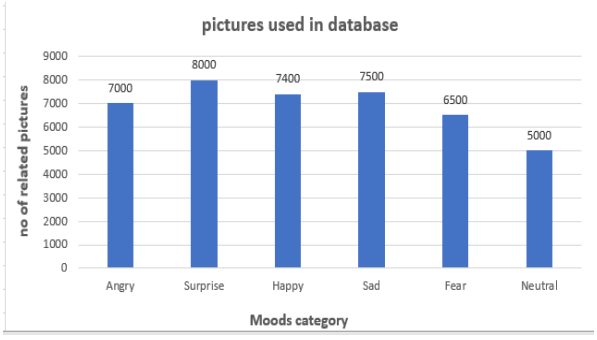


Fig 7: graph of pictures used in the database

Algorithm used:

A Convolutional Neural Network (CNN) is a Deep Learning algorithm that can take in a large amount of data, assign significance (learnable loads and predispositions) to distinct perspectives/questions in the data, and then separate them. When compared to other grouping calculations, the amount of pre-handling necessary in a CNN is significantly less. While channels are hand-designed in primitive approaches, CNNs can achieve expertise with these channels/attributes with enough preparation.

CNN's are frequently utilized in image recognition on databases utilizing CNN and picture classification learning procedure is shockingly quick.

At the point when applied to facial recognition, CNNs accomplished a huge reduction in mistake rate. CNN's were utilized to survey video quality in a target path after manual training of data set.

The Haar Cascade classifier uses the Haar Wavelet approach to examine pixels in a picture and divide them into squares based on their function. The features observed in any image are extracted using integral image concepts. Haar Cascades employs deep learning algorithms that choose several key features from a broad number of parameters to get an efficient outcome. Classifiers then employ cascade methods to recognise faces and expressions in images. Instead of calculating 2,500 highlights for each window, we considered cascading. We analyse 2,500 highlights in x different cascadings. In many cascading directly, we can now tell if there is a face or not. If I find a face in a photograph during the cascade, the photograph is passed on to the next course. In the unlikely event that no face is discovered, we can proceed to the next window. As a result, the time complexity is reduced. [11].



Fig. 8: Path for patrolling

VI. WORKING

The main working mechanism of this drone is the operation of the connected different modules on the drone. All the modules are controlled by a DC servo motor, connected to a

5V power supply. Figure 9 shows the working mechanism of drone and its components.

At first, the operator should know the exact location of the target by relying on pictures, videos, or the satellite-scanned images. After that, the operator defines the area for the main operation based on the collected information.

Secondly, the operator uses the mission planner software to generate the waypoints for the drone and defines the distance between those waypoints as well. The software saves those waypoints and generates the coordinates as a rectangular area to assign the path for the drone, and the mission path is defined as we can see in figure 8.

Lastly, SD card connected to the Arduino stores all the coordinate by using the Mission Planner software. The software sends all the data to the flight controller by using telemetry radios. The Arduino on the ground station is also connected to the Arduinos placed on the drone by using XBee's radios for communicating with each other. DSMX protocol manages all the commands from the ground station. The ground station uses a telemetry radio system over the MAVLink to get the information from the flight controller board. This setup allows a strong connection between the ground station and the drone with all its modules. The ground station can be used to control and track the movement and position of the drone. The connection I seamless with minimum delay, so there is no disruption or risk. The ground controller can control the flight of the drone as well as its connected modules. This includes remote operation of seed dispensing module, agricultural spray module, surveillance module and delivery module. Additionally, the connection between the radio transmitter and the drone is based on the DSMX protocol which is a very reliable connection. This allows the drone to fly upto a 5 kilometer range of the transmitter. This range is crucial for operation in far-off and hard-access areas where the operator is forced to maintain a distance from the drone due to unfavorable conditions of safety or terrain.

The protocol used for the connection between the ground controller and the drone is the MAVLink protocol. It connects a computer with the drone using a telemetry module which is based on two hardware parts. One part is connected to the laptop, while other connected directly to the drone. On the first switch on, both these parts are kept in close proximity. This enables them the kick off an automatic pairing exercise. After a few seconds, both the parts of the telemetry module are paired and start to blink in sync. This telemetry module then provides a stable connection between the computer and the drone and helps transfer location and position data, such as gps and compass co-ordinates to determine the position and altitude of the drone.

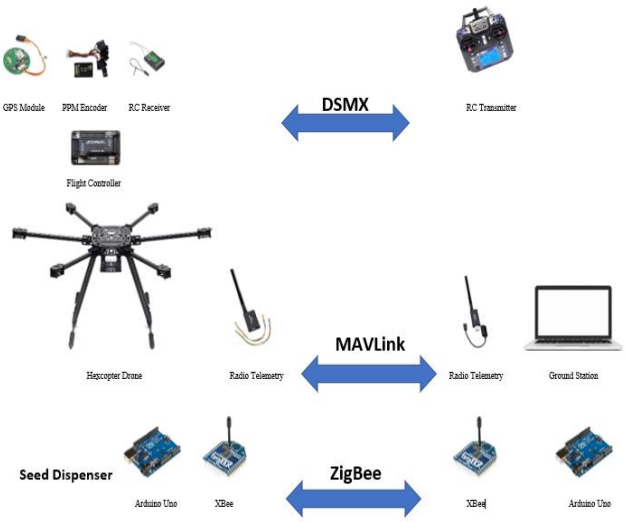


Fig. 9: Working Mechanism

VII. RESULTS

This technology can be deployed for several uses**.**

1-Law Enforcement Agencies:

LEAs can utilize such a drone to perform Surveillance and Patrolling operations with its built-in facial recognition and path-following functionality. Deployment can also be done on the battlefield to assist troops, to watch out for any potential threats. This can significantly lower the risk faced by the personnel on the ground.

2- Agriculture/Reforestation:

Such a drone will also be equipped with a seed-planting module which can effectively shoot seed-balls in the soil to maximize the output of agricultural land and to help in planting trees. Furthermore, a spraying kit can also be added to enable crop-spray.

3-Health Emergency:

The third module is to allow rapid transport of medical aid, such as first-aid kits, medicines and blood bags to areas which otherwise may have a limited access on-foot or on-wheels.

4- Delivery of Goods:

In addition to medical equipment, the drone may also be installed with a heavy payload capacity which will enable it to carry heavy loads over long distances. This can be utilized by courier and food delivery services to significantly speed up their networks.

VIII. CONCLUSION

We strongly believe that this research work will help the humanity in an efficient by using extremely state of the art

technology, moreover, its usability and utility in many different areas can mark the difference by comparing it with old fashioned methods already available. The core emphasis of the research is on surveillance and Patrolling operations with developed facial recognition and path-following functionality along with seed-planting module which can effectively shoot seed-balls in the soil to maximize the output of agricultural land and to help in planting trees and also spraying kit also added to enable crop-spray. The developed drone can do rapid transport of medical aid, such as first-aid kits, medicines and blood bags to areas which otherwise may have a limited access on-foot or on-wheels, furthermore, it's designed in a way that enables to carry heavy payload capacity over long distances. This can be utilized by courier and food delivery services to significantly speed up their networks. This is triumph proof that with the rising global population and the ever-increasing congestion, going airborne is the future and a significant step towards prosperous and peaceful world in future.

REFERENCES

[1] Chaudhary, A. R., Ch, J. R., Tahir, I., Shafaq, T., & Rajja, I. S. (2021, March). UNMANNED AUTONOMOUS ABABEEL SYSTEM FOR SEED PLANTATION UTILIZING SPECTRAL CAMERA ANALYSIS USING DRONE TECHNOLOGY. In BOOK OF ABSTRACTS (p. 319).Erico Pinheiro Fortes (2017). Seed Plant Drone for Reforestation. The Graduate Review Article 7, Volume 2:13-26.

[2] Sanjana, P., & Prathilothamai, M. (2020, March). Drone design for first aid kit delivery in emergency situation. In 2020 6th international conference on advanced computing and communication systems (ICACCS) (pp. 215-220). IEEE.

[3] Na, S. I., Park, C. W., So, K. H., Ahn, H. Y., & Lee, K. D. (2019). Photochemical Reflectance Index (PRI) mapping using drone-based hyperspectral image for evaluation of crop stress and its application to multispectral Imagery. Korean journal of remote sensing, 35(5_1), 637-647.

[4] Hovhannisyan, T., Efendyan, P., & Vardanyan, M. (2018). Creation of a digital model of fields with application of DJI phantom 3 drone and the opportunities of its utilization in agriculture. Annals of agrarian science, 16(2), 177-180.

[5] AirBoard (2019, October 15). Agricultural Drone. https://www.airboard.co/agro/.

[6] Smolyanskiy, N., & Gonzalez-Franco, M. (2017). Stereoscopic first person view system for drone navigation. Frontiers in Robotics and AI, 11.

[7] Arief, U. M., Subiyanto, S., Andrasto, T., Sukamta, S., Sulistyawan, V. N., Sarwono, E., ... & Putra, A. D. H. (2021, March). Design of hexacopter UAV system for disinfectant spraying. In IOP Conference Series: Earth and Environmental Science (Vol. 700, No. 1, p. 012023). IOP Publishing.

[8] https://ardupilot.org/planner/

[9] Zeng, Z., Fu, Y., Roisman, G. I., Wen, Z., Hu, Y., & Huang, T. S. (2006). Spontaneous emotional facial expression detection. *J. Multim.*, *1*(5), 1-8.

[10] Cuimei, L., Zhiliang, Q., Nan, J., & Jianhua, W. (2017, October). Human face detection algorithm via Haar cascade classifier combined with three additional classifiers. In *2017 13th IEEE International Conference on Electronic Measurement & Instruments (ICEMI)* (pp. 483-487). IEEE.

[11] Clarke, Roger. The Regulation of Civilian Drones' Impacts on Behavioural Privacy. 30(3) COMPUTER LAW & SECURITY REVIEW 286–305. June 2014. https://lccn.loc.gov/2009217103

Simulations For Boundary Layer Flows And Heat Transfer Of Cross Fluid Over A Moving Flat Plate

Mazhar Shehzad
Research Centre For Modelling and Simulation
National University of Sciences and Technology
Islamabad, Pakistan
mshehzad.mscse16@rcms.nust.edu.pk

Ammar Mushtaq
Research Centre For Modelling and Simulation
National University of Sciences and Technology
Islamabad, Pakistan
ammar.mushtaq@rcms.nust.edu.pk

***Abstract*—During the past century, rheology has emerged as a new science which deals with the deformation of matter. Metal spinning, wire drawing, polymer extrusion, blood circulation, food industry, and pressure-sensitive adhesion, etc are a few of the potential application areas. Now in most of these applications materials are non-Newtonian and involve rotation, extrusion, and heat exchange. Therefore, understanding the rheology is critically important to improve the quality of product development, methodology, and resource utilization. The goal of this research is to present the boundary layer equations for three dimensional fluid flow and heat transfer of cross fluid over a shretching sheets. Systems of governing partial differential equations are converted into highly non-linear ordinary differential equations by introducing suitable similarity transformations. By using the bvp4c process, the governing ODEs are solved numerically, and the influence of the related parameters of practical importance such as skin friction coefficient and Nusselt number are calculated. The momentum boundary layer demonstrates the elevation impact of the growing local Weissenberg number. The contrary phenomenon for the thermal boundary layer was found. The temperature function has an exceptional S-shaped profile indicating the existence of an adiabatic case for the large enough wall to ambient temperature ratio. Structures of the momentum boundary layer along with Velocity fields demonstrated the identical enhancement tendency for the rising Weissenberg number.**

Keywords—non-Newtonian flows, Cross fluid, Numerical Simulations

I. INTRODUCTION

An American chemistry professor first coined the term "Rheology" which he inspired from the Greek word "πανταρει" meaning "everything flows". During the past century, rheology has emerged as a new science which deals with the deformation of the matter. The rheological studies are focused on dealing with applied stress and strain. As all materials have rheological properties thus rheology is relevant in many fields. Examples include metal spinning, wire drawing, concrete technology, plastic processing, polymer extrusion, paint flows, blood circulation, cosmetics, food industry, and pressure-sensitive adhesion, etc. Now understanding rheology is critically important in order to improve the quality of product development, methodology, and resource utilization. Particularly to the food industry where most materials are Non-Newtonian, Rotating flows in mixtures, extruders, and heat exchangers are widely common [1]. Blasius [2], pioneered in studying the motion of flow on a stationary flat plate. Then later, Leslie Howarth proposed the theory of turbulence in aerodynamics as well as in fluid dynamics [3]. The influence of the boundary layer over a moving plate was then scrutinized by Sakiadis [4-5]. By extending the work of Sakiadis, Crane [6] was able to work for the problem of stretching flat plate and found the exact solution of boundary layer equations. But all these studies were carried out for Newtonian fluids. We need non-Newtonian fluids Because of its broad spectrum of industries applications. Various studies have been carried out on momentum and heat transfer and of non-Newtonian fluids [7-8]. Today many studies are being carried out for many other physical investigations of micropolar fluids, power law, Maxwell fluids, second-grade fluids, etc. So the complex fluids particles like suspensions, turbulent shear flows, can be described using the theory of micropolar fluid flows. [9-14] worked on micropolar and power-law fluids. The power-law model refers to non-Newtonian fluids which are time-independent. Power-law model is sufficient for many non-Newtonian fluids to explore the shear stress and shear rate measurements. In spite, the power-law model has a strong engineering influence, but it cannot explore the normal stress differences. In this regard, we will consider a special type of differential equations of fluids for which the analytical solutions are available. These differential fluids are the class of second-grade fluids [15-17]. This model refers to determining the normal stress results. A significant amount of research on the physical analysis of the laminar boundary layer flows across solid surfaces has been published [18-25]. When a moving surface is subjected to suction or blowing. As polymer is a flexible substance, the geometry of the filament surface may stretch during ejection, causing the surface velocity to disturb from being uniform.. The thermal radiation over a continually stretching surface has taken on excellent significance Due to its use in a wide range of manufacturing and scientific uses, such as the manufacture of plastics, metallurgy, crystal processing, and many others. Plastic sheet drawing. The performance of the final product relies on cooling and stretching rates. The boundary layer flows over a continuously moving surface First mentioned by Sakiadis [4]. Rees and Bassom [26] predicted the flow of a micro-polar fluid flow over a flat surface(Blasius boundary layer) while Soundalgekar and Takhar proposed a similarity evaluation of flow and heat transfer over a continuously flowing semi-infinite plane of micro-polar fluid [27]. The above section shows that although a huge amount of research has been carried out on the boundary layer flows for Newtonian and non-Newtonian fluids. However, to investigate the shear-thinning/thickening region most popular non-Newtonian Model used is the Power Law model. Despite its ability to present a vast class of non-Newtonian fluids, it has its limitations in presenting fluids with severe high and low shear rate. In 1965 Cross [28] introduce a model that caters to a wider sub-section of generalized Newtonian fluids which can detect both the flow rate in the power-law region as well server high and low shear rate range. Now, with the available computing resources and advancement in numerical techniques to tackle highly nonlinear equations such as arising in modelling of Cross fluid, researchers have started working on problems with many folds complexity. Khan et al [29] in 2016 worked on momentum and the heat transfer of the cross

fluid over the stretch surface. In 2017 Khan et al [31] reported on cross-axisymmetric flow and heat transfer across a radially stretched surface. In 2019, Sultan et al [32] explored theoretical elements of thermophoresis and Brownian motion with the activation energy for the 3-D flow of the cross fluid. For the validations purpose the results of the power-law index against temperature profile were compared with Kumari nath[33]. Several researchers have carried out experimental studies on the Cross model over the previous two centuries. Escudier et al. carried out an experimental study and the results on the fluid flow were presented by applying the Cross model to the generalized Newtonian fluid. Xie and Jin studied the Cross Rheology equation to get the free surface flow of non-Newtonian fluids. An experimental method, namely the WC-MPS technique, was used to determine the Cross model's four rheology parameters for the numerical application of the Cross equation Therefore, still, a lot of potential fluid scenarios can be modelled and solved for an in-depth understanding of flow and heat transfer of the Cross fluid model.

II. GOVERNING EQUATIONS

The conservation equations of mass, linear momentum, and energy for the flow of an incompressible fluid

$$\nabla \cdot V = 0 \tag{1}$$

$$\rho \frac{\partial V}{\partial t} = \nabla \tau \tag{2}$$

$$\rho c_p \frac{dT}{dt} = \tau . L - \nabla q \tag{3}$$

Where V is the velocity vector, τ is the Cauchy stress tensor, $c_p$is the specific heat constant, ρ is the density, q is the heat flux, L and $\frac{d}{dt}$ are the material derivatives, T is the fluid temperature. The Cauchy stress tensor for the fluid is defined as,

$$\tau = -PI + \mu^* A_1 \tag{4}$$

Where μ^* is the cross model, P is the pressure, I is the identity tensor, A_1 is the first Rivlin-Ericksen tensor.

$$A_1 = L + L^T, \qquad L = \nabla V \tag{5}$$

$$\dot{\gamma} = \sqrt{\frac{1}{2} tr(A_1)^2} \tag{6}$$

Due to this consideration, (4) will get the following form.

$$\tau = -PI + \mu_0 \left[\frac{1}{1 + (\Gamma\dot{\gamma})^{1-n}}\right] A_1 \tag{7}$$

Through Cartesian coordinates for two-dimensional flow, we consider the velocity field of the form

$$V = [u(x,y), v(x,y)] \tag{8}$$

Keeping in view the shear rate (6) can be written as

$$\dot{\gamma} = \left[4\left(\frac{\partial u}{\partial x}\right)^2 + \left(\frac{\partial u}{\partial y} + \frac{\partial v}{\partial x}\right)^2\right]^{\frac{1}{2}} \tag{9}$$

Putting (8) in (1) and (2) while keeping in mind (7) and Eq (9) a straightforward calculation gets the following form.

$$\frac{\partial u}{\partial x} + \frac{\partial v}{\partial y} = 0 \tag{10}$$

$$u\frac{\partial u}{\partial x} + v\frac{\partial u}{\partial y} = -\frac{1}{\rho}\frac{\partial p}{\partial x} + \nu\frac{\partial}{\partial y}\left[\frac{\frac{\partial u}{\partial y}}{1 + \left\{\Gamma\left(\frac{\partial u}{\partial y}\right)\right\}^{1-n}}\right] \tag{11}$$

III. PROBLEM FORMULATION

Consider a two-dimensional incompressible flow and heat transfer of cross fluid over a moving flat surface. Plate (located at y=0) moving outside the boundary layer with the constant velocity U_w and U_∞ be the fluid velocity. A study on the analysis of heat transfer is carried out due to nonlinear heat flucuations. Also the combined effects of Joule heating and viscous dissipation were considered. The plate is at constant temperature T_w, while T_∞ implicitly denotes the temperature of the ambient liquid.

$$\frac{\partial u}{\partial x} + \frac{\partial v}{\partial y} = 0 \tag{12}$$

$$u\frac{\partial u}{\partial x} + v\frac{\partial u}{\partial y} = \nu\frac{\partial}{\partial y}\left[\frac{\frac{\partial u}{\partial y}}{1 + \left\{\Gamma\left(\frac{\partial \mathrm{u}}{\partial \mathrm{y}}\right)\right\}^{1-n}}\right], Uw < U_\infty \tag{13a}$$

$$u\frac{\partial u}{\partial x} + v\frac{\partial u}{\partial y} = -\nu\frac{\partial}{\partial y}\left[\frac{-\frac{\partial u}{\partial y}}{1 + \left\{\Gamma\left(-\frac{\partial \mathrm{u}}{\partial \mathrm{y}}\right)\right\}^{1-n}}\right], U_w > U_\infty \tag{13b}$$

$$u\frac{\partial T}{\partial x} + v\frac{\partial T}{\partial y} = \alpha\frac{\partial^2 T}{\partial y^2} - \frac{1}{\rho Cp}\left(\frac{\partial q_\gamma}{\partial y}\right) \tag{14}$$

Due to parallel free stream and nonlinear thermal radiation the following boundary conditions are produced.

$$\begin{aligned} u = U_w, v = 0, \;\; T = T_w \text{ at } y = 0 \\ u \to U_\infty, T \to T_\infty \text{as } y \to \infty \end{aligned} \tag{15}$$

where x, y are the coordinates along and normal to the plate. u, v are the velocity components along the x and y directions, ν is the kinematic viscosity, T is the fluid temperature, α is the thermal diffusivity, C_p is the specific heat at constant pressure and q_r is the radiative heat flux.

The radiative heat flux q_r is given by the Rosseland approximation as :

$$q_r = -\frac{4\sigma^*}{3k^*}\frac{\partial T^4}{\partial y} \tag{16}$$

This is further simplified

$$q_r = -\frac{16\sigma^*}{3k^*}T^3\frac{\partial T}{\partial y} \tag{17}$$

So (14) will get the final form

$$u\frac{\partial T}{\partial x} + v\frac{\partial T}{\partial y} = \frac{\partial}{\partial y}\left[\left(\alpha + \frac{16\alpha^* T^3}{3\rho C_p k^*}\right)\frac{\partial T}{\partial y}\right] \tag{18}$$

Where σ* denotes Stefan-Boltzman constant and and k^* denotes the mean absorption coefficient.

Now introduce the corresponding similarity transformation for the Eq (13-15).

$$\eta = y\sqrt{\frac{U}{2\nu x}}, u = Uf'(\eta),$$
$$v = \sqrt{\frac{U\nu}{2x}}(\eta f' - f), \theta(\eta) = \frac{T - T_\infty}{T_w - T_\infty} \tag{19}$$

Where $f(\eta)$ represent the dimensionless stream function and $\theta(\eta)$ represent the non-dimensional temperature. The required continuity (12) is satisfied while (13) and (14) with boundary conditions (15) are transformed into the following form.

$$f'''[1 + sign(\gamma - 0.5)(1-n)(Wef'')^n] + ff''[1 + (Wef'')^n]^2 = 0 \tag{20}$$

$$\theta''[1 + Rd(1 + (\theta w - 1)\theta)^3] + 3Rd\left[(+(\theta w - 1)\theta)^2(\theta w - 1)\theta'^2\right] + Prf\theta' = 0 \tag{21}$$

$$f(0) = 0, f'(0) = 1 - \gamma, \theta(0) = 1, \quad f'(\infty) \to \gamma, \quad \theta(\infty) \to 0 \tag{22}$$

Where $\gamma = \frac{U_\infty}{U}$ is the velocity ratio parameter, $We = \frac{U\Gamma R_e^{\frac{1}{2}}}{x\sqrt{2}}$ is the Weissenberg number, $\theta w = \frac{T_w}{T_\infty}$ is the temperature ratio parameter, $Pr = \frac{\nu}{\alpha}$ is the Prandtl number and $Rd = \frac{16\alpha T_\infty^3}{3KK^*}$ are the radiation parameter. The expression provided for the local skin friction coefficient and the local number Nusselt are:

$$C_f = \frac{\tau_w}{\frac{1}{2}\rho U^2}, \quad N_u = \frac{xq_w}{k(T_w - T_\infty)} \tag{23}$$

Where τ_w is local wall shear stress and q_w is described as surface heat flux.

$$\tau_w = \tau_{xy}|_{y=0} = \left[\eta_0 \frac{\frac{\partial u}{\partial y}}{1 + \left\{\Gamma\left(\frac{\partial u}{\partial y}\right)\right\}^{1-n}}\right]_{y=o}, \tag{24}$$
$$q_w = -k\frac{\partial T}{\partial y}|_{y=0}$$

In the illumination of the Eq. (19) we obtain dimensional forms of the local skin friction coefficient and the local Nusselt number as:

$$\frac{1}{2}Re^{\frac{1}{2}}C_{fx} = \frac{f''(0)}{1 + \left(Wef''(0)\right)^{1-n}}$$
$$-Re^{-\frac{1}{2}}Nu_x = [1 + Rd\{1 + (\theta w - 1)\theta\}^3]\theta'(0) \tag{25}$$

IV. Numerical Solution

In order to solve the higher-order differential problems numerically. They are converted into a system of 1st order equations using new variables. Therefore, let $y_1 = f; y_2 = f'; y_3 = f''; y_4 = \theta$ and $y_5 = \theta'$. The equivalent first-order equations are as follows:

$$y_1' = y_2; y_2' = y_3; \tag{26}$$

$$y_3' = \frac{-y_1 y_3[1 + (Wey_3)^n]^2}{[1 + \text{sign}(\gamma - 0.5)(1-n)(Wey_3)^n]}; \tag{27}$$

$$y_4' = y_5; \tag{28}$$

$$y_5' = \frac{-Pry_1y_5 - 3Rd[(1 + (\theta w - 1)y_4)^2(\theta w - 1)y_5^2]}{[1 + Rd(1 + (\theta w - 1)y_4)^3]} \tag{29}$$

with boundary conditions

$$y_1(0) = 0;\ y_2(0) = 1 - \gamma; y_4(0) = 1;$$
$$y_2(\infty) = \gamma;\ y_4(\infty) = 0 \tag{30}$$

The solution of Eq. (26-30) is obtained using the fifth order Runge-Kutta integration technique with the following initial conditions

$$y_1(0) = 0;\ y_2(0) = 1 - \gamma;\ y_3(0) = u_1$$
$$y_4(0) = 1;\ y_5(0) = u_2 \tag{31}$$

This solution can agree with the original BVP for suitable values of u_1 and u_2.

V. Results and Discussion

Using MATLAB code the boundary value problem is solved. To make sure that the accuracy of obtained computations and validation of the code we have reproduced the results of [18]. After code validation now we will examine the impact of various evolving parameters on the velocity and temperature flow field. The obtained results are tabulated in Tables 1-3. Table 2 is designed to provide a skin friction

coefficient and Table 3 provides heat transfer rate numerical values for various values of relevant parameters.

Fig 3 indicates variation in horizontal velocity with an improvement in the velocity ratio γ. It is observed that the velocity function f' rises and that the thickness of the boundary layer declines when $0 < \gamma < 0.5$ increases. There is no boundary layer formation at γ=0.5. In this region, the free stream velocity is less than the velocity of the plate. The impact of the power-law index 'n' on the velocity profile and fluid temperature profile is shown in Fig.1 and Fig.2 for two different values of γ=0.2 and γ =1. The examination of these graphs demonstrates that the velocity profiles and momentum boundary layer thickness exhibit a progressive trend for both (γ<0.2 and γ>1) with increasing power law of index. The effect of the power-law index 'n' on the temperature profile is observed in Fig 4. In Fig.4 the thermal boundary layer reveals a declining tendency while rising the power law of the index. The physical explanation for this behaviour is that the fluid is facing less resistance because of low viscosity which causes the fluid's velocity to increase and its temperature to fall.

Fig 5 and 6 show the behaviour of the velocity profiles and temperature profile corresponding to a change in Weissenberg's local number. The study of the figures(5-7) reveals that We trigger the velocity of the fluid to increase and decaying in the temperature of the fluid. Physically, an enhancement in the Weissenberg number value We causes the velocity of the fluid to boost and the temperature of the fluid to decrease.

Fig 7 Displays the effect of Prandtl number Pr on the temperature profile for fixed n and We values. Prandtl number is the resultant of viscosity, Specific heat, and thermal conductivity. Furthermore, Pr regulates the relative velocity and thermal boundary layers thickness. Keeping in view all the above aspects that smaller Prandtl liquids lead to speedier heat diffusion in thicker thermal boundaries as compared to higher Prandtl liquids in thinner boundaries. Through the increase of Pr the thermal boundary layer thickness declines and the thermal transfer rate at the plate is increased. Perhaps it can be assured that the Prandtl number can be used to upgrade the cooling rate in the conductive liquid flow. The influence of temperature ratio θw on temperature is shown in Fig.8. The higher temperature ratio parameter θw indicates a higher plate temperature compared to ambient temperature. Due to which the temperature of the fluid rises because of the hotter surface. Fig 9 indicates that, regardless of the range of values chosen for the velocity ratio γ the temperature θ rises with a growing trend in γ.

Table 1:Numerical validation for Newtonian Fluid Case

γ	*Cortell [18]*	*Present*
0	−0.627547	−0.627555
1	0.469602	0.469600

Table 2:Numerical findings Local skin friction for various values of velocity ratio γ, power law index n and Weissenberg number We.

γ	n	We	$f''(0)$
0	0.6	0.8	- 0.443939
0.4			- 0.106581
1			0.625574
0.2	0.1	0.2	- 0.87292
	1.2		- 0.357323
1	0		0.664115
	1		0.496975
0.3	0.8	0.5	- 0.213935
		1.5	- 0.184016
		2	- 0.171461

Table 3:: Numerical findings for Local Nusselt number against different values of power law index n, Weissenberg number We, velocity ratio γ, Temperature ratio θw, Prandtl number Pr, Rd Radiation parameter.

Pr	γ	n	We	θw	Rd	$\theta'(0)$
6.2	0.3	0.2	0.8	1.5	1	- 0.610192
		0.8				- 0.644514
		1.2				- 0.640061
	0	0.8				- 0.738588
	0.7					-0.545214
	1					-0.485732
	0.3		0.5			- 0.641106
			1.5			- 0.647132
			2.5			- 0.651992
0.7	0.6		0.8			- 0.191498
2						- 0.347346
7						- 0.690414
				1		- 1.37613
				1.6		- 0.842045
				2		- 0.603513

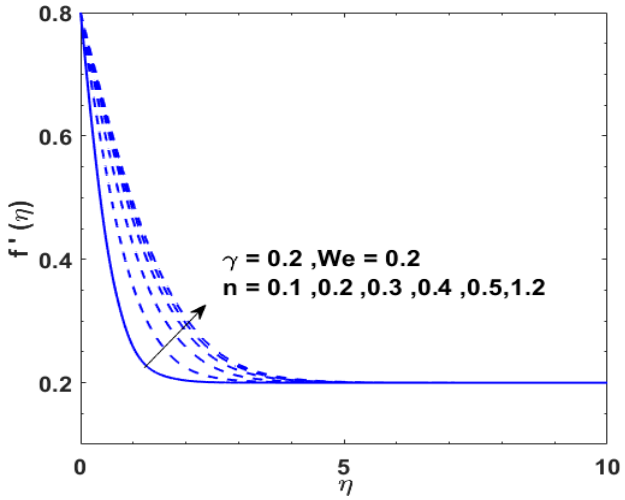


Fig 1: *Velocity curve f' Variation against η for different values of n for Skiadas $\gamma = 0$*

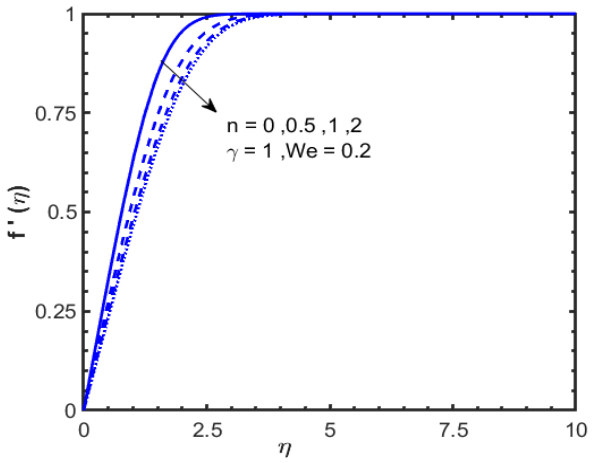


Fig 2: Velocity curve f' Variation against η for different :values of n for Blasius $\gamma = 1$.

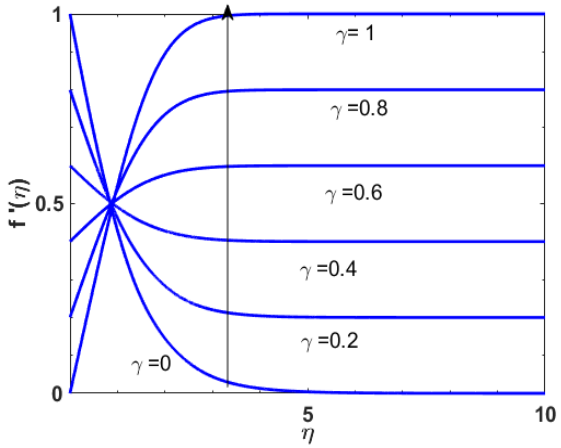


Fig 3: *Velocity curve f' Variation against η for different values of γ*

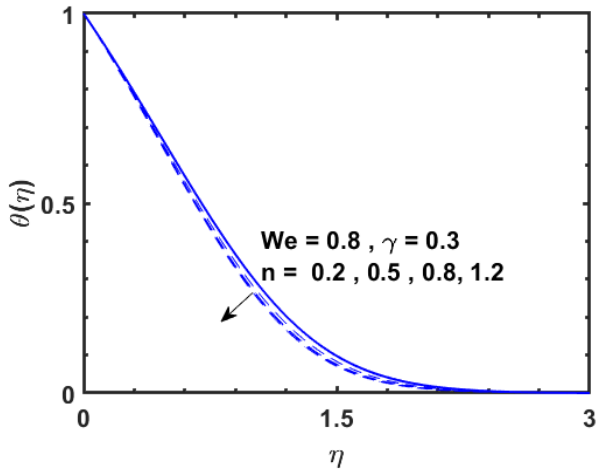


Fig 4: *Temperature curve θ Variation against η for different values of n*

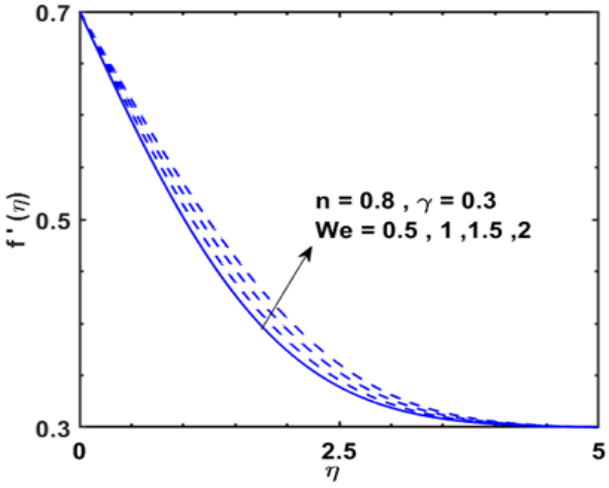


Fig 5: *Velocity curve f' Variation against η for different values of We.*

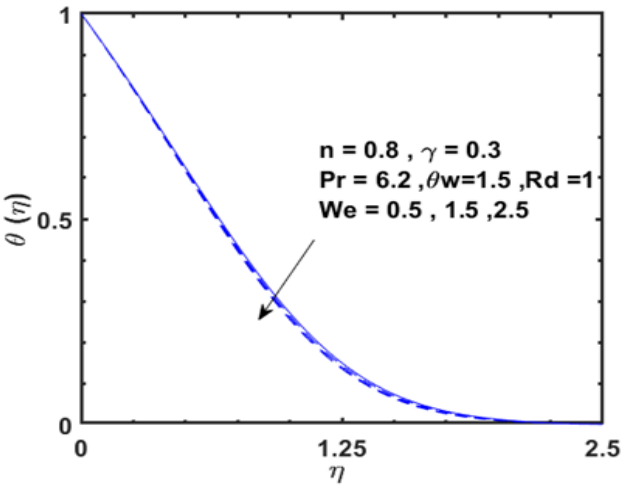


Fig 6: *Temperature curve θ Variation against η for different values of We.*

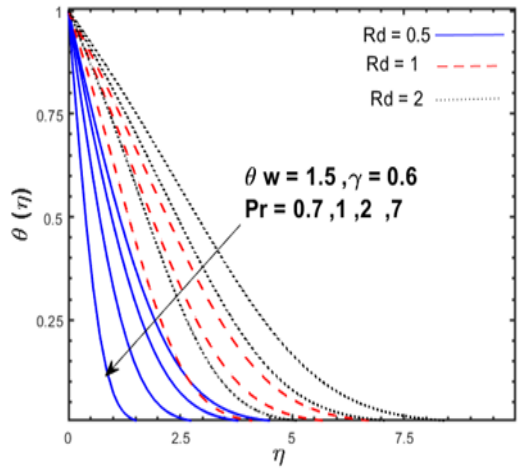


Fig 7: *Temperature curve θ Variation against η for different values of Pr.*

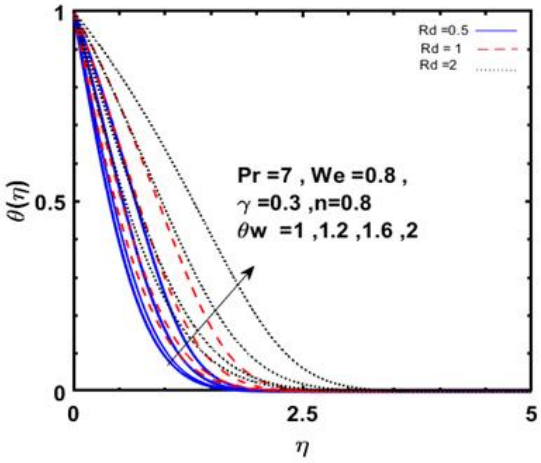


Fig 8: *Temperature curve θ Variation against η for different values of θw.*

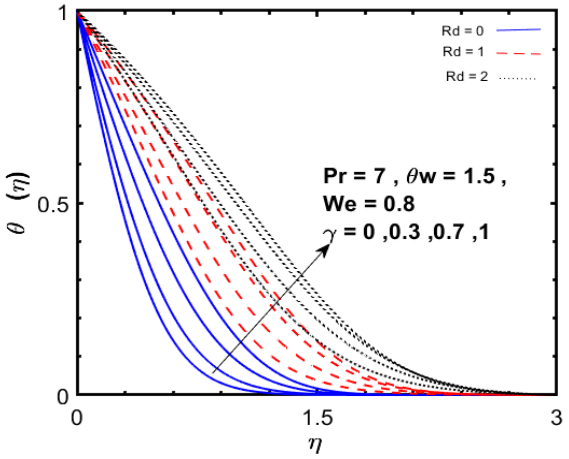


Fig 9*: Temperature curve θ Variation against η for different values of γ*

VI. Concluding Remarks

This study is seminal work in the development of cross fluid flow boundary layer equations. Modeled partial differential equations of cross fluid were Simplified by implementing appropriate similarity transformations and numerical technique using the bvp4c scheme. The key conclusions can be summarized as

- The increasing power-law index values culminated in the velocity of fluid elevation while a decrease in the thermal boundary layer was observed.
- The velocity profiles reach the velocity of the free stream at a great distance from the plate, demonstrating that the momentum boundary layer thickens as the velocity ratio increases.The heat transmission rate and the temperature of the plate increased.
- The momentum boundary layer and Velocity fields are demonstrated the elevation impact of the growing local Weissenberg number. The contrary phenomenon for the thermal boundary layer was found.
- The Prandtl number's elevated values reduced the temperature profile and the thermal boundary layer thickness.
- The temperature rises in the region and from the plate the heat flux reduces as θw is increasing.

Acknowledgment

I would first like to thank my thesis advisor Dr. Ammar Mushtaq (RCMS, NUST). The expertise was invaluable in the formulating of the research topic and methodology.

References

[1] Steffe, Steffe, J.F. Rheological Methods in Food Process Engineering, Freeman Press (1992)

[2] Blasius, H. Grenzschichten in Flüssigkeiten mit kleiner Reibung. Zeits. Math. Phys, 56, 1-37 (1908).

[3] Howarth, L. On the Solution of the Laminar Boundary Layer Equations. Proceedings of the Royal Society of London. Series A, Mathematical and Physical Sciences 164 547–579 (1937).

[4] Sakiadis, B. C. Boundary ‐ layer behavior on continuous solid surfaces: I. Boundary ‐ layer equations for two ‐ dimensional and axisymmetric flow. AIChE J. 7, 26–28 (1961).

[5] Sakiadis, B. C. Boundary ‐ layer behavior on continuous solid surfaces: II. The boundary layer on a continuous flat surface. AIChE J. 7, 221–225 (1961).

[6] Crane, L. J. Flow past a stretching plate. Zeitschrift für Angew. Math. und Phys. ZAMP 21, 645–647 (1970).

[7] Acrivos, A., Shah, M. J. & Petersen, E. E. Momentum and heat transfer in laminar boundary ‐ layer flows of non ‐ Newtonian fluids past external surfaces. AIChE J. 6, 312–317 (1960).

[8] Tashtoush, B., Kodah, Z. & Al-Ghasem, A. Heat transfer analysis of a non-Newtonian fluid on a power-law stretched surface with suction or injection for uniform and cooled surface temperature. Int. J. Numer. Methods Heat Fluid Flow 10, 385–396 (2000).

[9] Schowalter, W. R. The application of boundary ‐ layer theory to power ‐ law pseudoplastic fluids: Similar solutions. AIChE J. 6, 24–28 (1960).

[10] Eringen, A. Theory of Micropolar Fluids. Indiana Univ. Math. J. 16, 1–18 (1966).

[11] Pakdemirli, M. Boundary layer flow of power-law fluids past arbitrary profiles. IMA J. Appl. Math. 50, 133–148 (1993).

[12] Hassanien, I. A., Abdullah, A. A. & Gorla, R. S. R. Flow and heat transfer in a power-law fluid over a nonisothermal stretching sheet. Math. Comput. Model. 28, 105–116 (1998).

[13] Jalil, M., Asghar, S. & Mushtaq, M. Analytical solutions of the boundary layer flow of power-law fluid over a power-law stretching surface. Commun. Nonlinear Sci. Numer. Simul. 18, 1143–1150 (2013).

[14] Andersson, H. I., Bech, K. H. & Dandapat, B. S. Magnetohydrodynamic flow of a power-law fluid over a stretching sheet. Int. J. Non. Linear. Mech. 27, 929–936 (1992).

[15] Dunn, J. E. & Fosdick, R. L. Thermodynamics, stability, and boundedness of fluids of complexity 2 and fluids of second grade. Arch. Ration. Mech. Anal. 56, 191–252 (1974).

[16] Dunn, J. E. & Rajagopal, K. R. Fluids of differential type: Critical review and thermodynamic analysis. Int. J. Eng. Sci. 33, 689–729 (1995).

[17] Hayat, T. & Khan, M. Homotopy Solutions for a Generalized Second-Grade Fluid Past a Porous Plate. Nonlinear Dynamics. 42 (2005).

[18] Cortell, R. Flow and heat transfer in a moving fluid over a moving flat surface. Theor. Comput. Fluid Dyn. 21, 435–446 (2007).

[19] Gupta, P. S. & Gupta, A. S. Heat and mass transfer on a stretching sheet with suction or blowing. The Canadian Journal of Chemical Engineering. 55 744–746 (1977).

[20] Salleh, M. Z., Mohd Rohni, A. & Amin, N. Boundary Layer Flow Due to a Moving Flat Plate in Micropolar Fluid. J. Teknol. 43, (2005).

[21] Siekman, J. The laminar boundary layer along a flat plate. Z. Flugwiss. 10, 278–281 (1962).

[22] Tsou, F. K., Sparrow, E. M. & Goldstein, R. J. Flow and heat transfer in the boundary layer on a continuous moving surface. Int. J. Heat Mass Transf. 10, 219–235 (1967).

[23] Hayat, T., Iqbal, Z., Qasim, M. & Obaidat, S. Steady flow of an Eyring Powell fluid over a moving surface with convective boundary conditions. Int. J. Heat Mass Transf. 55, 1817–1822 (2012).

[24] Mustafa, M., Hayat, T., Pop, I. & Aziz, A. Unsteady boundary layer flow of a Casson fluid due to an impulsively started moving flat plate. Heat Transf. - Asian Res. 40, 563–576 (2011).

[25] Ellahi, R., Alamri, S. Z., Basit, A. & Majeed, A. Effects of MHD and slip on heat transfer boundary layer flow over a moving plate based on specific entropy generation. J. Taibah Univ. Sci. 12, 476–482 (2018).

[26] Rees, D. A. S. & Bassom, A. P. The Blasius boundary layer flow of a micropolar fluid. Int. J. Eng. Sci. 34, 113–124 (1996).

[27] Soundalgekar, V. M. & Takhar, H. S. Flow of micropolar fluid past a continuously moving plate. Int. J. Eng. Sci. 21, 961–965 (1983).

[28] Cross, M. M. Rheology of non-Newtonian fluids: A new flow equation for pseudoplastic systems. J. Colloid Sci. 20, 417–437 (1965). [5

[29] Khan, M., Manzur, M. & Rahman, M. Boundary-layer flow and heat transfer of cross fluid over a stretching sheet. Therm. Sci. 23, 307–318 (2019).

[30] Hayat, T., Khan, M. I., Tamoor, M., Waqas, M. & Alsaedi, A. Numerical simulation of heat transfer in MHD stagnation point flow of Cross fluid model towards a stretched surface. Results Phys. 7, 1824–1827 (2017).

[31] Khan, M., Manzur, M. & ur Rahman, M. On axisymmetric flow and heat transfer of Cross fluid over a radially stretching sheet. Results Phys. 7, 3767–3772 (2017).

[32] Sultan, F., Khan, W. A., Ali, M., Shahzad, M., Irfan, M., & Khan, M. Theoretical aspects of thermophoresis and Brownian motion for three-dimensional flow of the cross fluid with activation energy. Pramana - J. Phys. 92, 1–10 (2019).

[33] M. Kumari and G. Nath, Bangalore, India MHD boundary-layer flow of a non-Newtonian fluid over a continuously moving surface with a parallel free stream. Acta Mechanica 146, 139 150 (2001)

Design, Analysis and Fabrication of Composite Curing Compressive Mold for Aerospace Applications

Muhammad Ayaz Ahmad
Aerospace Engg Dept,
College of Aeronautical Engineering, NUST
Risalpur, Pakistan
mayaz@cae.nust.edu.pk

Sabih Ahmad Khan
Aerospace Engg Dept,
College of Aeronautical Engineering, NUST
Risalpur, Pakistan
skhan.ms01mecae@student.nust.edu.pk

Syed Irtiza Ali Shah
Aerospace Engg Dept,
College of Aeronautical Engineering, NUST
Risalpur, Pakistan
irtiza_shah@gatech.edu

Hamza Akbar Khan
Aerospace Engg Dept,
College of Aeronautical Engineering, NUST
Risalpur, Pakistan
hakbar.88eccae@student.nust.edu.pk

Taimur Ali Shams
Aerospace Engg Dept,
College of Aeronautical Engineering, NUST
Risalpur, Pakistan
taimur.shams@cae.nust.edu.pk

Abstract—An undeniably significant development in the aviation business is the utilization of composite materials, as these empower designers to conquer the boundaries made by utilizing metals. Composite materials have assumed a significant part in weight reduction, and consequently they are utilized for both primary applications and segments of all space apparatus and airplane from UAVs and sight-seeing hot air balloon to military aircraft, space transport and traveler carriers. During this research, an extensive literature review has been performed related to composite curing techniques and processes. As it is known that many of the aircraft components including skin panels, wing-box and even landing gear struts are being made up of composite materials, therefore, specimen manufacturing for testing and qualification of defined curing process and material becomes the paramount. Composite curing using compressive molds is considered to be the most widely used and economical process in this field. In the same context, a compressive mold was designed and developed to study the effect of temperature and pressure for finalization of the curing cycle for various thicknesses of composite specimen. CAD assembly of the designed mold was modeled in SOLIDWORKS®. The design was kept simple for ease of manufacturing and cost effectiveness. Static structural followed by transient thermal analysis for different materials were performed in ANSYS® to validate the structural integrity of manufacturing materials under high temperature and pressure environment required for curing of composite materials. Based on these analysis, final design and material needed for manufacturing of compressive mold were finalized followed by fabrication of mold. Use of this fabricated mold is aimed to define curing cycle for different composite based pre-preg materials of various thicknesses being used in the ongoing and future research projects for aerospace applications.

Keywords— Composite Curing, Compressive mold, Design, ANSYS, Structural Analysis, Transient Thermal Analysis, Structural Integrity.

I. INTRODUCTION

Composite curing is an essential process to enhance the strength of composite products being formed. Over the years, researchers have developed various methods for curing composite materials. Each method has its own benefits and are mainly used to improve the strength of products being manufactured by composite materials. During the curing cycle, single monomers, and oligomers, blended in with or without a curing agent, react to frame a tridimensional polymeric network. In the initial segment of the reaction, branched atoms with different structures are formed, and their sub-atomic weight increments in time with the degree of the response until the organization size is equivalent to the size of the framework [1]. The leftover particles begin to exist together with the plainly visible organization until they respond with the organization making other crosslinks. The crosslink thickness increments until the framework arrives at the finish of the synthetic reaction. Restoring can be started by heat, radiation, electron shafts, or compound added substances. To cite from IUPAC: relieving "may or probably won't need blending in with a substance restoring agent." Thus, two wide classes are a) curing actuated by synthetic added substances (likewise called restoring specialists, hardeners) and (b) curing without added substances. A halfway case includes a combination of resin and added substances that requires outer upgrade (light, heat, radiation) to instigate curing. The relieving technique relies upon the resin and the application. Specific consideration is paid to the shrinkage actuated by the curing [2]. Normally little estimations of shrinkage (2-3%) are desirable. The aim of this research was to design, analyze and fabricate a compressive mold for curing of different composite based pre-preg materials. Specimen needed to validate mechanical properties of cured composite materials as per ASTM standards would be manufactured using the fabricated mold under different temperature and pressure environment. Qualified material and curing cycle would then be recommended for different aerospace applications including landing gear struts.

II. METHODOLOGY

In the first phase of this research, various methods for curing were studied and the pros and cons of each were compared. Curing process involving compressive mold was selected based on cost effectiveness, material availability and availability of fabrication facility. A reference mold used for manufacturing of main landing gear strut of a lightweight aircraft was taken as a base model.

That mold consists of a temperature regulator b3sed on four thermocouples and a pressure mechanism based on five screw jacks pressure mechanism having maximum capacity of 15 tons. Glass fiber prepreg material is used to manufacture main landing gear struts of a lightweight aircraft using reference mold. The process of curing begins by carefully heating and applying pressure simultaneously. The heat is increased gradually and is held for several minutes at several different temperatures for the cross linking to take place. The resin is removed simultaneously as the pressure is applied till the required thickness of the final product is achieved. After the curing process is completed, final product is allowed to cool for 48 hours and is finally removed from the mold. Two test specimens are obtained from the final product and subjected to shear and bending tests as per ASTM standards.

On qualification of these tests, the final product (main landing gear struts) is declared fit for installation on aircraft. Reverse engineering approach was used to develop a small size compressive mold capable of making specimen of composite materials of required length, width, and height for testing as per ASTM standards. Glass fiber-based specimen were required to be manufactured and qualification of small size compressive mold was subjected to clearance of bending and shear strength tests of these specimen [3]. After qualification of these tests, fabricated compressive mold was cleared for future research work related to various thicknesses, materials, and finalization of curing cycles.

This project required the use of SOLIDWORKS® and ANSYS® software. The initial models were developed in SOLIDWORKS® and the analysis were carried out using ANSYS® software. ANSYS® was used for the structural and thermal analysis. Our research methodology involved following steps and is depicted as:

1. The Study of different techniques conventionally used for composite curing.
2. Selection of suitable manufacturing techniques based on various parameters studied earlier.
3. To select base line design for reference and detailed study of the reference mold to understand the governing design principles.
4. Detailed design and assembly of different parts of mold in SOLIDWORKS®.
5. Selection of the most appropriate design with ease of manufacturing and useability.
6. Structural and thermal analysis at different temperature and pressures using higher fidelity tools.
7. Finalization of mold for fabrication.
8. Development of the composite curing mold.

III. Literature Review

A thorough literature review was carried out for better understanding of methods involved in composites curing and controlling physical and chemicals changes occurring during the curing process. Composite curing is a chemical process used in polymer chemistry and process engineering to toughen or harden a polymer material through the cross-linking of polymer chains [4].

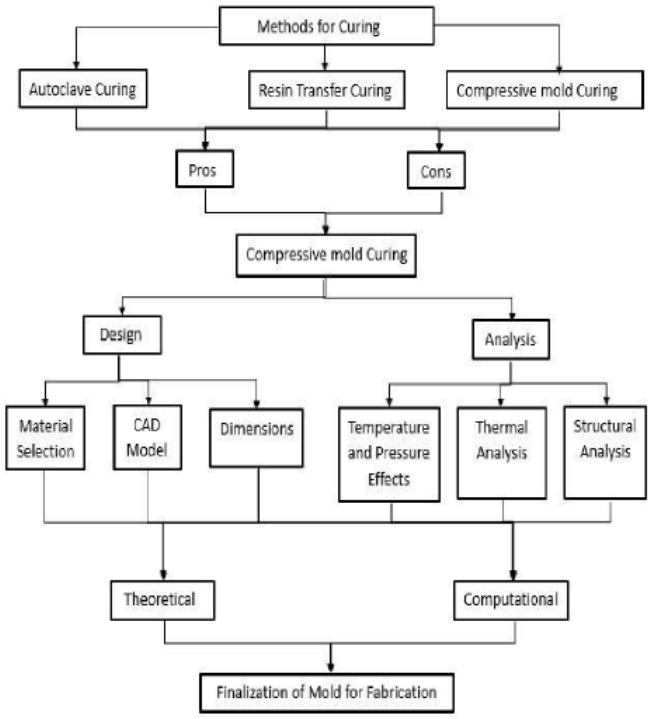


Fig. 1. Research methodology for the design and development of Composite curing mold.

Even though it is most strongly associated with the development of thermosetting polymers, the term curing can be applied to any method that results in a solid product from a liquid solution. The curing of composite resins is divided into three stages: pre-gel, gel point, and post-gel. To compensate for shrinkage forces, the material can flow and undergo molecular rearrangement during the pre-gel process. There is a predominance of linear polymer chains during this phase [5]. The resin then transitions from the flow state (pre-gel) to the viscous state (post gel), establishing its gel stage. During the post gel process, the resin loses its flowing capacity and transmits the stress generated by polymerization shrinkage to the tooth-restoration interface. At this point, cross links predominate in the polymer structure.

The curing process can be carried out by using various techniques. Each of these techniques have their own advantages and disadvantages. The technique used for composite curing depends on the cost and strength requirement of the designer. The various methods for composite curing are as follow:

1. Autoclave Curing
2. Resin Transfer Molding
3. Compressive Molding

A typical curing profile contains two ramps and two isothermal holds. The first ramp and isothermal hold, which are typically in the 240-280°F range, are used to enable the resin to flow (bleed) and volatiles to escape. The viscosity drops dramatically during this process due to the fracturing of cross polymer chains by heating. The polymerization component of the cure cycle is represented by the second ramp and hold. During this point, the resin viscosity drops slightly due to the addition of heat and then rises dramatically as the resin's kinetics initiate the cross-linking process. The resin gels

into a solid, and the cross-linking process continues throughout the second isothermal hold, which is usually between 340-370°F for epoxy resin systems. The resin is usually kept at this cure temperature for 4-6 hours to enable the cross-linking process to complete [6-8].

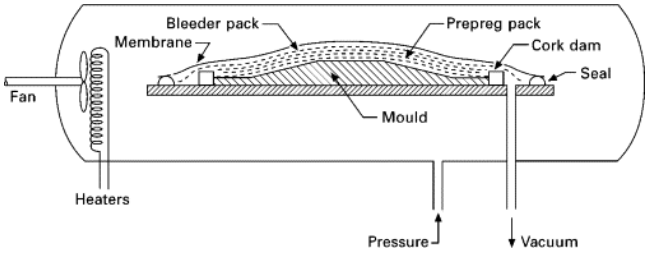


Fig. 2. Schematic diagram of the Autoclave [9].

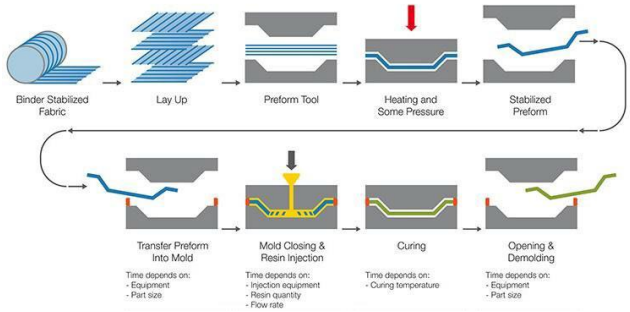


Fig. 3. Working Principle of Resin Transfer Molding (RTM) [10].

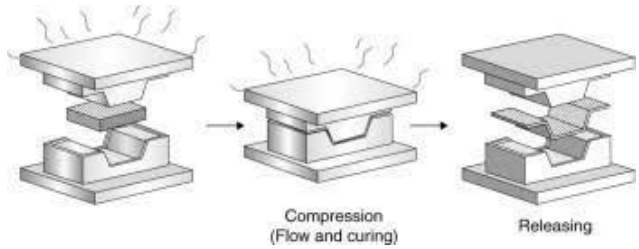


Fig. 4. Working Mechanism of Compression Molding [11].

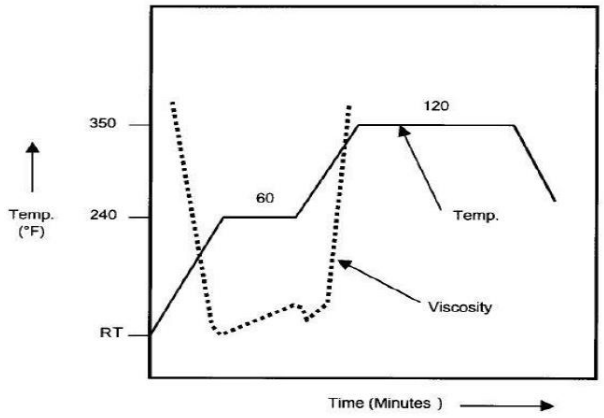


Fig. 5. Composite Curing profile for temperature and pressure during manufacturing [8].

For curing of composite materials, use of compressive mold is considered to be the most economical solution. However, selection of material for manufacturing of compressive mold is very critical as curing cycle involves high temperature and pressure environment. Material Selection is one of the critical issues of any designing project as it affects the weight, performance, and efficiency of the product. Some of the frequently utilized materials are aluminum, mold steel, die steel and stainless steel for making compressive molds. Material properties must be provided for the analysis as it is nearly impossible to simulate or analyze the model without the definition of material properties.

IV. Design of Composite Curing Mold

The design requirements of a compressive mold required for curing of composite materials are as follow:

1. The product should be light weight for ease in transportation.
2. The product should have high strength and thermal conductivity.
3. The product should be able to sustain high pressure and temperature environment.
4. The product should be able to accommodate varying thicknesses of composite specimens.
5. The product should be economical.
6. The product should be easily manufacturable.
7. The design should be compact and easy to use.

A baseline design of compressive mold used to cure thick composite beams (landing gear strut) of fiber glass based composite material was selected to study and understand the complete curing process. This thick composite beam is used as a full-scale main landing gear strut of a lightweight aircraft. However, for research purpose a small-scale compressive mold was aimed to be manufactured to cure test specimens before manufacturing of a full-scale composite product.



Fig. 6. The side walls and heating element of the reference mold in disassembled form.

A. CAD Modelling of Mold

Computer aided model is the prerequisite of any design project. 3D CAD allows engineers to not only design in 3D but also animate aspects to better visualize the working of a concept. It also helps the customers to better understand the features of their required product[[12, 13]. Various models were designed as per the required dimensions of specimens to be cured. All these designs were modeled in SOLIDWORKS® and were then imported to ANSYS® for further computational analysis. The static structural analysis under high temperature was carried out for all these models using different materials. The upper plate of the mold was subject to a pressure of 15 ton using screw jack mechanism. A uniform controlled temperature was provided by heating rods placed in upper and lower plates. The structural analysis was conducted to qualify the mold design and material for given pressure and thermal loads. Final design of the mold is shown in figure 7.

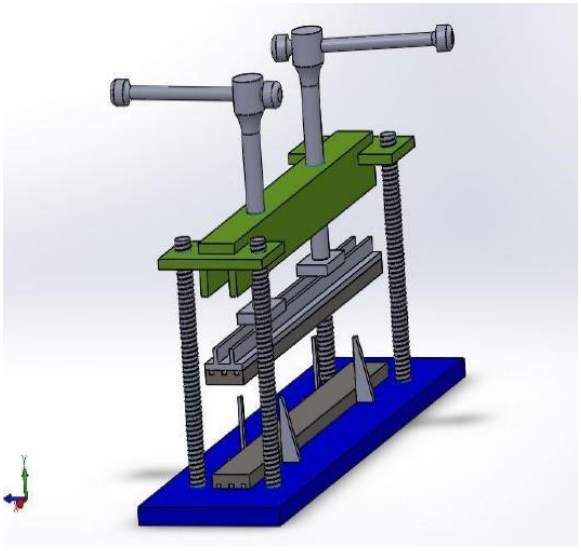


Fig. 7. Completed assembly of the mold to be developed designed in SOLIDWORKS®.

B. Mold Component design

The design is kept remarkably simple for ease of manufacturing. It has the following components:

1) Screw Jacks

The pressure is applied on the mold through a screw jack mechanism for the purpose of compression of the composite pre-pregs sheets and are placed on the top plate. It was estimated that maximum of 17.5 tons force which comes out to be 33.18 ton-force/ ft_2 pressure (32 bar approx.) can be applied on baseline model. However, approximately 40 % of this force is applied. The screw Jack mechanism shown in figure 8.

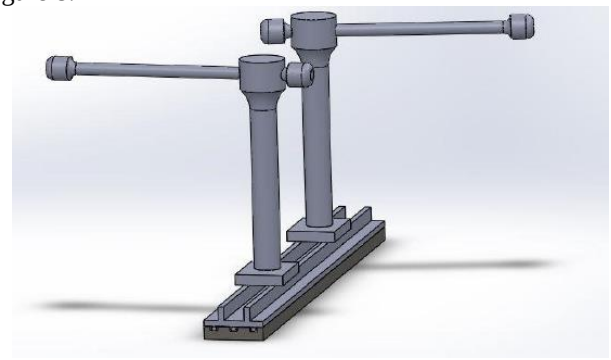


Fig. 8. Manual screw jack mechanism of pressure application.

2) Heated Pressing Plates

A minimum of 6 heating rods were placed at the top and bottom of the mold for uniform heating throughout the mold at temperatures up to 250ºC. Six heating rods were used to cater for the failure of any rod during curing process. These rods are operated through a Control Box having magnetic connectors, breaker, temperature controller, and other items which are required for application of temperature under control environment. The controller measures up to 400ºC. Such a high temperature is kept in case of studying curing methods of other composite materials. At least two thermocouples are placed in each pressing plate at edges and center of the mold to measure and show a uniform temperature in digitally.

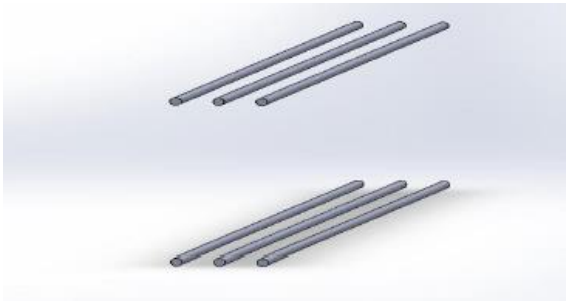


Fig. 9. Heating elements to provide the required heating temperature.

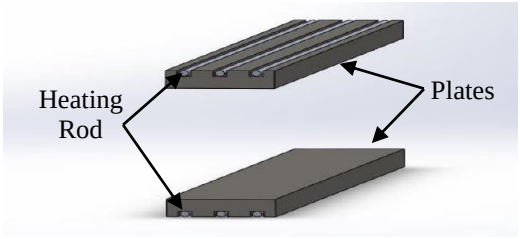


Fig. 10. Heating rods enclosed in plates for curing through both ends.

3) Thickness Measurement Gauge

A manual thickness gauge was set on the sides of the rod which was used to read the thickness of the composite material when pressure is applied to it. The main aim of the pressure jacks is to achieve the required thickness of the composite material being cured. The thickness gauge determines the thickness of the composite material under curing. alongside the thickness gauge are side plates which holds prepreg sheets in place and do not let them slip sideways.

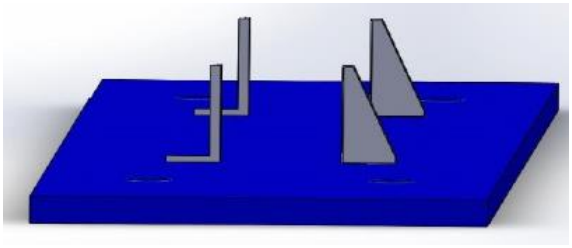


Fig. 11. Thickness plates and side plates.

V. Computational Analysis Of The Compressive Mold

Analysis of the designed molds was carried out in ANSYS®. At first, the mesh was defined followed by boundary conditions. A structural analysis and transient thermal analysis were carried out. The Analysis was carried out using different materials which are used in mold manufacturing and are readily available in the market. Some of these materials are as follows [5]:

1. Aluminum
2. Carbon steel
3. Titanium Alloy
4. P-20 pre-hardened mold steel

A. Mesh Convergence

Mesh convergence was carried out and hence the following parameter has been finalized after the mesh convergence study as depicted in Table :

TABLE I. Meshing parameters of converged solution

Nodes	1292296
Elements	509139
Element type	Tetrahedral
Element size	5 mm

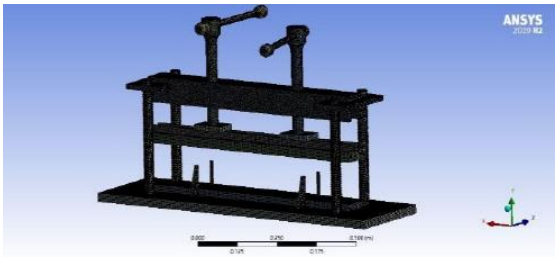


Fig. 12. Meshing of the mold.

B. *Boundary Conditions*

Boundary conditions are defined for the assembly prior to the analysis. For this purpose, mechanism of the mold (the upper tool and the lower plate) were kept fixed to the four rods. The heating rods were placed inside the heated pressing plates. The upper heated pressing plate was attached to the base of the screw jack pressure mechanism while the lower heated pressing plate was fixed to the lower plate. The screw Jack mechanism could apply a pressure of 33.18 ton-force/ ft2 (32 bar approx.). However, approximately 40 % of this force as applied on baseline model was applied. There was no mechanism to calculate the pressure as the use of pressure was only to compress and achieve the desirable thickness of the specimen. The maximum temperature which could be conducted through heating rods was 400ºC but the working temperature for the mold was around 200ºC which is considered sufficient for the most of composite material. The Boundary Condition for Static Structural Analysis and transient thermal are depicted in figure 13 and 14, respectively.

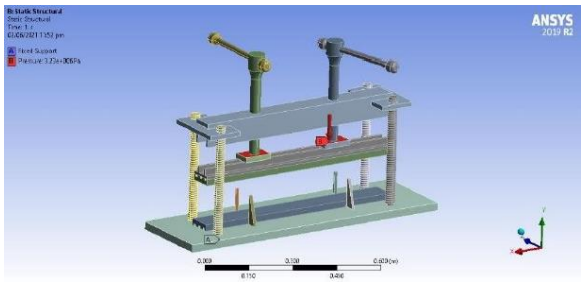


Fig. 13. Boundary conditions for static structural analysis.

C. *Analysis with Aluminum*

Aluminum alloys, with their flexibility, versatility, and minimal effort, offer numerous favorable circumstances over steel and different materials for mold makers. Results of analysis using aluminum material are as follows:

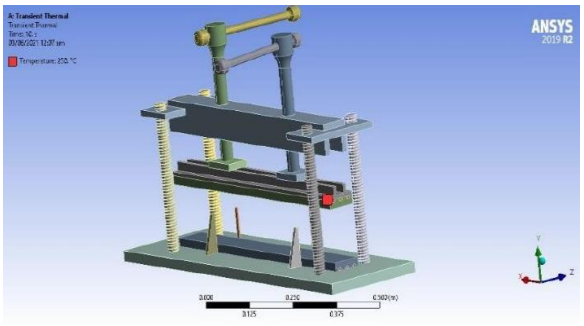


Fig. 14. Boundary conditions for transient thermal analysis.

1) *Transient Thermal Analysis*

The mold underwent a variable change in temperature over time while pressure was applied simultaneously. The maximum temperature which the heating rods could provide was around 400ºC but the working temperature was around 200ºC. The transient thermal analysis was carried out at a temperature of 200ºC. The results are as shown below as figure 15.

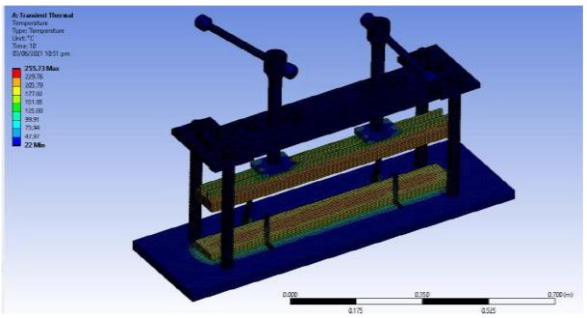


Fig. 15. Aluminum Transient Thermal Analysis.

The results indicated that the Aluminum material is a good conductor of heat and the thermal stresses on it are negligible.

2) *Total Heat Flux*

The heat flux for the mold using aluminum as the material was carried out and results are as shown:

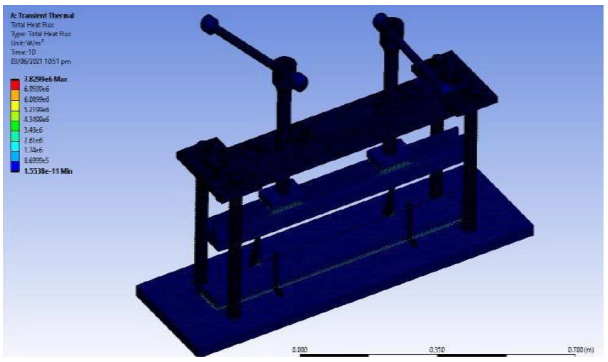


Fig. 16. Aluminum Heat Flux.

3) *Maximum Principal Stress*

The result for maximum principal stresses occurring on the assembly is as follows:

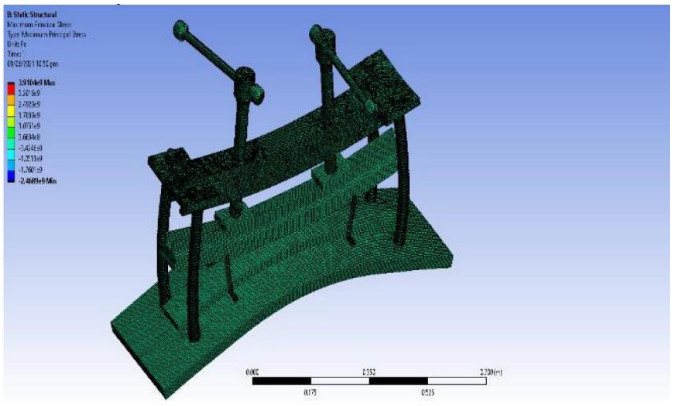


Fig. 17. Maximum Principal Stress of Aluminum.

4) Factor of Safety (FOS)

The results indicated that a max stress of 152.33 MPa occurs on the mold. The Ultimate Tensile Strength of the Aluminum alloy is 310 MPa. Hence the Factor of Safety is calculated as:

$$\boldsymbol{FOS = 2.035}$$

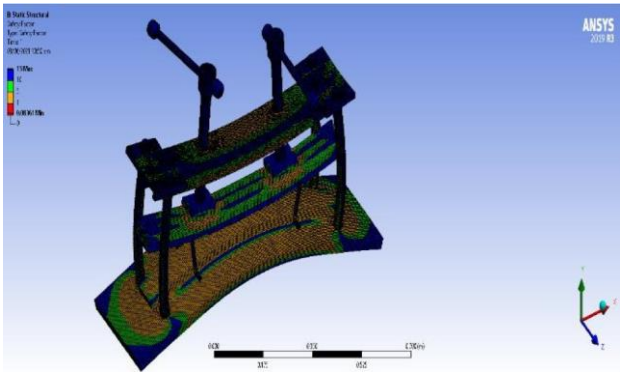


Fig. 18. FOS for Aluminum.

The Aluminum Alloy material qualifies for the compressive mold.

D. Analysis With Carbon Steel

Carbon steel is an exceptional kind of steel that, as the name proposes, has a higher convergence of carbon than different sorts of steel. Other forms of steel have a generally low carbon substance of about 0.05% to 0.3%. In correlation, carbon steel has a carbon substance of up to 2.5%. Over two percent carbon may sound irrelevant, however it presents a few alluring advantages that are not found somewhere else. Results of analysis using carbon steel material are as follow:

1) Transient Thermal Analysis

The mold underwent a variable change in temperature over time while pressure was applied simultaneously. The maximum temperature which the heating rods could provide was around 400ºC but the working temperature was around 200ºC. The transient thermal analysis was carried out at a temperature of 200ºC. The results are as shown.

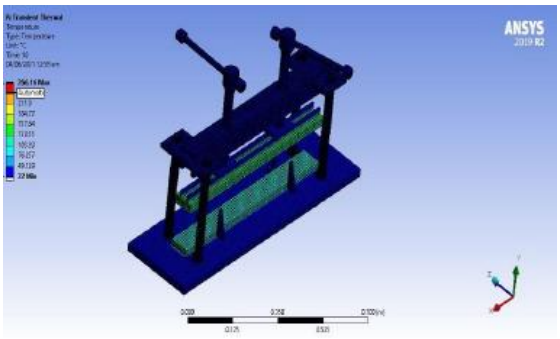


Fig. 19. Transient Thermal Analysis.

The results indicated that the material carbon steel is a good conductor of heat and the thermal stresses on it are negligible.

2) Total Heat Flux

Heat flux for the mold using carbon steel was carried out and results are as shown in figure 20:

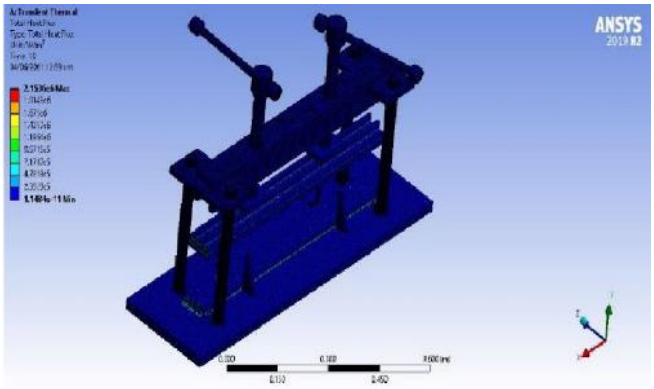


Fig. 20. Carbon Steel Total Heat Flux.

3) Maximum Principal Stress

The result for maximum principal stresses occurring on the assembly is as follows:

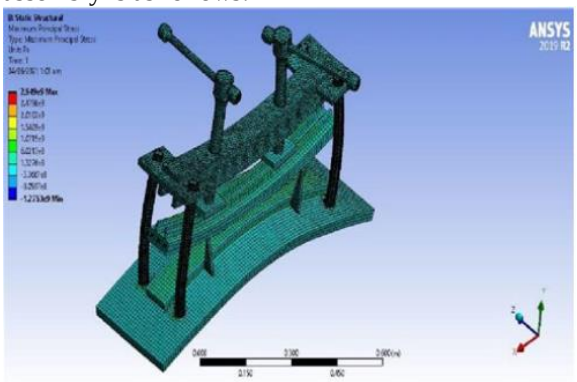


Fig. 21. Maximum Principal Stress.

4) Factor of Safety (FOS)

The results indicated that a max stress of 932.5 MPa occurs and the min stress -416.09 MPa occurs. The negative sign indicates compression. The Ultimate Tensile Strength of the Carbon Steel is 635 MPa. Hence the Factor of Safety is calculated as 4.81 and is also shown in figure.22.

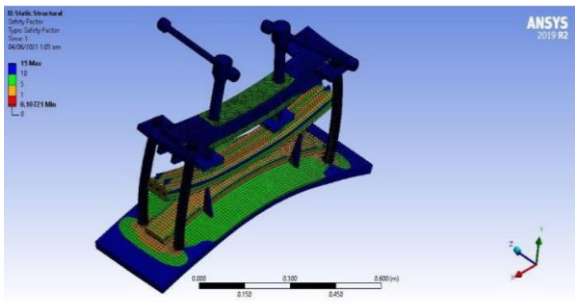


Fig. 22. FOS of Carbon Steel.

5) Principal Elastic Strain

The results for principal elastic strain occurring on the assembly is as follows:

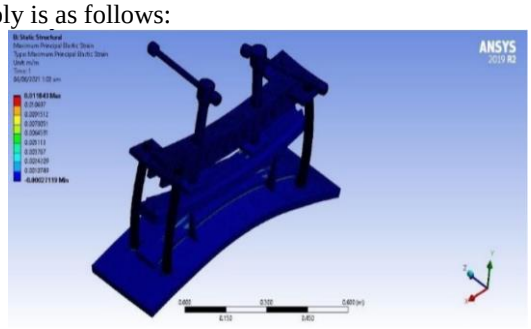


Fig. 23. Carbon Steel Maximum Principal Elastic Strain.

The results show that the maximum strain to be.015007 and the minimum strain to be 0.00165.

6) Total Deformation

The total deformation of the carbon steel assembly while undergoing pressure and temperature is shown as follows:

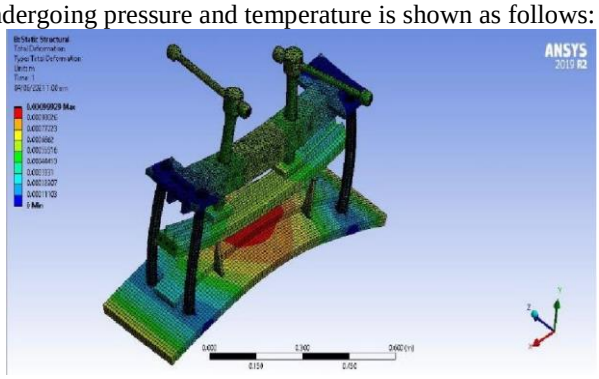


Fig. 24. Carbon Steel Total Deformation.

The results for carbon steel indicate that the assembly will be fully functional without any sort of damage to the assembly during the curing process. All the other materials i.e., Titanium alloy and P-20 pre-hardened mold steel will also qualify but the analysis was not carried out as these materials are very expensive and difficult to machine.

A comparison of the aluminum and carbon steel shows that carbon steel is less costly, and it has particularly good manufacturability. Moreover, it can be heat treated and hardened to get more strength and it has a good durability and finishing ability. Therefore, carbon steel is preferred for this Mold assembly.

VI. Fabrication Of Designed Mold

After the design and analysis phase, fabrication of the mold was undertaken. On the basis of results obtained, carbon steel was finalized as the material was easily accessible and cheaper. Basic design layout, modeling, analysis, and fabrication of the compressive mold was carried out. The fabricated mold was tested by curing a composite specimen to verify the application of its pressure mechanism and conduct of heat through heating rods. These specimens were qualified for bending and shear strength tests as per ASTM standards which ultimately qualified the fabricated mold as well.

The mold was fabricated in a way that it has the following advantages:

1. The height of the mold was kept flexible by changing the vertical rods.
2. The mold was designed to accommodate around 200 pre impregnated sheets, but the fabrication is done such that we can accommodate more than 200 sheets by changing the height as mentioned above.
3. The control box is designed such that it can work on both single phase and 3 phase power sources.

The fabricated mold is as shown:

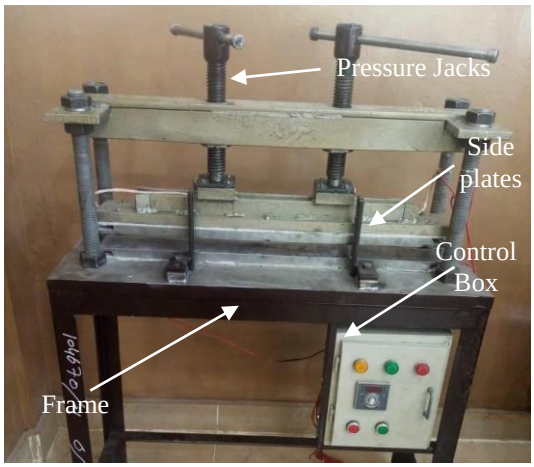


Fig. 25. Fabricated Compressive Mold Front View.

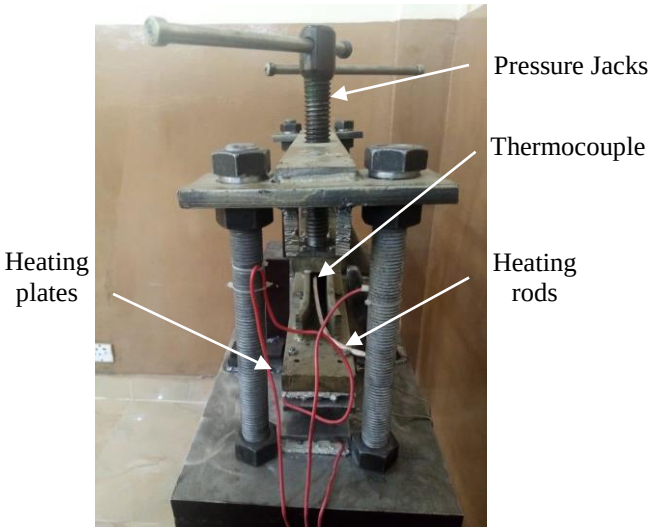


Fig. 26. Fabricated Compressive Mold Side View.

VII. Conclusion

The basic design layout, modeling, analysis, and fabrication of compressive mold for curing of composite materials were carried out. The purpose of this mold is to

conduct experiments and research work related to curing cycle of different composite materials. The compressive mold provides a controlled environment for the curing of composite pre-pregs materials at elevated temperature and pressure. Structural analysis was carried out prior to the fabrication of mold. The material selected for fabrication is based on the availability in market, price, ease in manufacturing and qualification through computational analysis. After the experimental verification of the mold through a series of shear and bending stress tests as per ASTM standards (D790 and D2344), the mold is qualified for further studies involving use of various composite materials and varying thicknesses.

VIII. ACKNOWLEDGEMNT

Authors acknowledge receipt of a grant from Higher Education Commission (HEC) of Pakistan under TDF 03-332 project for completion of this research project.

REFERENCES

[1] N. Ismail, A. Sulong, N. Muhamad, D. Tholibon, M. MdRadzi, and W. Wanlbrahim, "Review of the Compression Moulding of Natural Fiber-Reinforced Thermoset Composites: Material Processing and Characterisations," *Pertanika Journal of Tropical Agricultural Science*, vol. 38, no. 4, 2015.

[2] I. Baran, K. Cinar, N. Ersoy, R. Akkerman, and J. H. Hattel, "A review on the mechanical modeling of composite manufacturing processes," *Archives of computational methods in engineering*, vol. 24, no. 2, pp. 365-395, 2017.

[3] H. Thuis, "The development of composite landing gear components for aerospace applications," 2004.

[4] P. Sormunen and T. Kärki, "Compression molded thermoplastic composites entirely made of recycled materials," *Sustainability*, vol. 11, no. 3, p. 631, 2019.

[5] A. Trende, B. Åström, and G. Nilsson, "Modelling of residual stresses in compression moulded glass-mat reinforced thermoplastics," *Composites Part A: Applied Science and Manufacturing*, vol. 31, no. 11, pp. 1241-1254, 2000.

[6] R. Upadhyay, "Compression molding of composites: Mold heating system design," *Advances in Polymer Technology: Journal of the Polymer Processing Institute*, vol. 8, no. 3, pp. 243-264, 1988.

[7] R. A. Tatara, "Compression molding," in *Applied plastics engineering handbook*: Elsevier, 2017, pp. 291-320.

[8] F. Campbell, "Curing: It'sa Matter of Time (t), Temperature (T) and Pressure (P)," *Manufacturing Processes for Advanced Composites*, pp. 175-221, 2003.

[9] P. J. Halley, "Rheology of thermosets: the use of chemorheology to characterise and model thermoset flow behaviour," in *Thermosets*: Elsevier, 2012, pp. 92-117.

[10] A. Ahmadova, "Numerical modelling of porosity generation, movement, and compaction during the RTM process."

[11] C. Park and W. Lee, "Compression molding in polymer matrix composites," in *Manufacturing techniques for polymer matrix composites (PMCs)*: Elsevier, 2012, pp. 47-94.

[12] M. Barone, D. Caulk, and M. Panter, "Experimental verification of an optimal thermal design in a compression mold," *Polymer composites*, vol. 7, no. 3, pp. 141-151, 1986.

[13] M. A. Kuczmarski and J. C. Johnston, "Improved thermal design of a compression mold," *Advances in Polymer Technology*, vol. 26, no. 2, pp. 86-99, 2007.

Liberation Points of Space

Ms. Hadia Batool
Fazaia Bilquis College of Education, PAF Base Nur Khan
Rawalpindi, Pakistan
guriahadia16@gmail.com

Ms. Sumaira Abbasi
Fazaia Bilquis College of Education, PAF Base Nur Khan
Rawalpindi, Pakistan
sumaira_abbasi09@yahoo.com

***Abstract*— In the world of space, in the region of zero gravity, some places are found to have balanced forces and can be proved as stable areas of space. On the basis of three-body problem, in any system of two celestial massive bodies, these points are present by Nature and act as parking places of space. By years, this phenomena is used by agencies to explore many areas of space. They are total 5 in number and categorized as stable and unstable Libration points. Their stability depends upon how much an object, placed there, can change its initial position after experiencing small perturbation. These points act as point of equilibrium where spacecraft may be parked to make observations.**

***Keywords*—** Balanced Gravity, Gravitational Law, Imaginary and Real Eigen Values, Linear Stability Analysis, Three-body Problem

I. Introduction

Gravity, as an attractive force, is always pulling you down, but there are places in the solar system where gravity balanced out so nicely and agencies use them as *"Parking places" of space* [3]. Nature is on them and has already been using them for billions of years. These are named as "*Libration points*". They are actually stable location in space where the combined effect of force of gravity of two large bodies, equalizes the centrifugal force felt by a much smaller third body. All matches up in a way that causes a smaller object to maintain a stable position relative to larger bodies.

These are points in space where forces of gravity of larger bodies and orbital motion of a smaller body balanced each other and result motion with zero velocity. They are also known as "*Lagrangian points*" or "*L-points*" [2]. If a spacecraft uses a Libration point close to Earth, there are many benefits to the locations with low fuel controls. As *Mainzer* said, "A spacecraft placed at a lagrangian point would be able to do more".

II. Literature Review

In the light of astrophysics theory, many studies have been made about Galaxy's objects. From the special case of n-body problem, we have considering the three-body problem and demonstrating its specific solutions for both collinear and triangular three masses. Some of the contributions are:

Isaac Newton (1643 - 1727), Newton's laws of motion make bases for the three body problem, by taking the initial positions and velocities of three point-masses.

Leonard Euler (1707 - 1783), solved the first three-body problem considering the system of Sun, Earth and moon during collinear eclipse motion.

Joseph-Louis Lagrange (1736 - 1813), contributed for the solution of equilateral triangle in 1772.

Both these concept (collinear and equilateral problems) constitutes the base for the trace of discovery of Libration points.

III. Machanism

The mechanism of Libration points actually works of the pace of space object relative to the pace of Earth. Objects at L-points remain in the same position relative to the Earth. The orbital period of Earth is 365 days per year and so that is for satellites at L-points. [1]

Simply the orbital period of L-points are all same about 365 days but at different places. This is how the benefit of these points is that there is no need for much fuel for continuing the motion of spacecraft or telescope in space and also no much need to have some controlling office on Earth, because naturally the objects place there with move with the relative speed of the Earth.

The proposal of using the system of "Libration points" of the Earth-Sun system is for various purposes, including to design spacecraft orbits which explores a large region of space in the vicinity of Earth, using low-fuel control.

IV. Structure of L-Points

Libration points are total 5 in number which are naturally present in system of any two celestial bodies.

First 3 points are located on the same line with L_1 approximately 1.5 million km from Earth towards the Sun. Also L_2 is approximately 1.5 million km from Earth in the direction opposite the Sun. And L_3 is located on the side of the Sun opposite to the Earth, as being completely hidden by the Sun. L1, L2 and L3 are termed as *"Collinear Libration points"*. While, L_4 is located close to the Earth's orbit at 60° ahead of Earth and L_5 is located close to the Earth's orbit at 60° behind the Earth figured as creating the apex of two triangles. That's why L4 and L5 are termed as *"Triangular Libration points".*

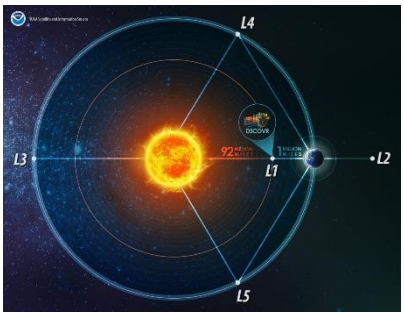


Figure (1): Structure of L-points

V. Stability Analysis

To examine the stability of these points, we will assume some

structural composition of this system. This concept consist of primary mass, secondary mass and an object at some of L-points. Let the mass of primary, Sun, is (1-μ) and secondary mass, Earth, is denoted by μ. The position of the object at L-point is denoted under the circular restricted three body problem, by the reference of center of mass on a line between primary and secondary masses. The distance of primary to the center is μ and the center of mass from secondary is (1-μ). These distances between the masses is sums to unity. The collinear points are lie on a straight line having y-axis points as zero [6]. And the triangular points are based in the form of equilateral triangle, placed at a position of its vertex, with the length equals to unity. The base of these equilibrium point is the `Law of Universal Gravitation'.

Using the Law of Gravitation:

$$F_0 = \frac{-m_0 m_1 r_1}{r_1^3} + \frac{-m_0 m_1 r_2}{r_2^3} \qquad (1)$$

Where; $r_1^2 = (x_1 - x_0)^2 + (y_1 - y_0)^2$,

and $r_2^2 = (x_2 - x_0)^2 + (y_2 - y_0)^2$.

Proceeding (1);

$$\frac{F_0}{m_0} = -\frac{m_1 r_1}{r_1^3} - \frac{m_2 r_2}{r_2^3}. \qquad (2)$$

Also, from 2nd Law of motion F=ma,

Equation (2) become:

$$a_0 = -\frac{m_1 r_1}{r_1^3} - \frac{m_2 r_2}{r_2^3}. \qquad (3)$$

Further we will use inertial frame of reference with ξ, and η.

Equation of motion in inertial frame are:

$$\ddot{\xi} = (1-\mu)\frac{\xi_1 - \xi_0}{r_1^3} + \mu\frac{\xi_2 - \xi_0}{r_2^3}, \qquad (4)$$

and

$$\ddot{\eta} = (1-\mu)\frac{\eta_1 - \eta_0}{r_1^3} + \mu\frac{\eta_2 - \eta_0}{r_2^3}. \qquad (5)$$

Using inertial axis components as:

$$\xi = x\cos t - y\sin t, \quad \text{and} \quad \eta = x\sin t + y\cos t.$$

Now by taking double derivative of both ξ, and η, we get:

$$\ddot{\xi} = (\ddot{x} - x - 2\dot{y})\cos t - (\ddot{y} - y + 2\dot{y})\sin t. \qquad (6)$$

and

$$\ddot{\eta} = (2\dot{x} + \ddot{y} - y)\cos t + (\ddot{x} - x - 2\dot{y})\sin t. \qquad (7)$$

Putting values of ξ, and η in (4) and (5), we are:

$$\ddot{\xi} = [\frac{(1-\mu)(x_1 - x_0)}{r_1^3} + \mu\frac{(x_2 - x_0)}{r_2^3}]\cos t - [\frac{(1-\mu)(y_1 - y_0)}{r_1^3} + \mu\frac{(y_2 - y_0)}{r_2^3}]\sin t. \qquad (8)$$

$$\ddot{\eta} = [\frac{(1-\mu)(x_1 - x_0)}{r_1^3} + \mu\frac{(x_2 - x_0)}{r_2^3}]\sin t + [\frac{(1-\mu)(y_1 - y_0)}{r_1^3} + \mu\frac{(y_2 - y_0)}{r_2^3}]\cos t. \qquad (9)$$

Comparing (6) and (7) with (8) and (9) respectively with similar terms taken as:

$$a = (\ddot{x} - 2\dot{y} - x),$$

$$b = (\ddot{y} + 2\dot{x} - y),$$

$$c = [\frac{(1-\mu)(x_1 - x_0)}{r_1^3} + \mu\frac{(x_2 - x_0)}{r_2^3}],$$

$$d = [\frac{(1-\mu)(y_1 - y_0)}{r_1^3} + \mu\frac{(y_2 - y_0)}{r_2^3}].$$

Now the resulting equations are:

$$a\cos t - b\sin t = c\cos t - d\sin t. \qquad (10)$$

$$b\cos t + a\sin t = c\sin t + d\cos t. \qquad (11)$$

Now, by multiplying (10) by cos (t) and (11) by sin (t);

We get (a=c), as:

$$(\ddot{x} - 2\dot{y} - x) = [\frac{(1-\mu)(x_1 - x_0)}{r_1^3} + \mu\frac{(x_2 - x_0)}{r_2^3}]. \qquad (12)$$

Also, by multiplying (10) by -sin(t) and (11) by cos(t);

We get (b=d), as:

$$(\ddot{y} + 2\dot{x} - y) = [\frac{(1-\mu)(y_1 - y_0)}{r_1^3} + \mu\frac{(y_2 - y_0)}{r_2^3}]. \qquad (13)$$

These are our required two equations of motion for a satellite.

Now for simplifying these equations we will use an effective potential for approximate method, in order to simplify complex systems, called as “Pseudo-Potential”.

And we introduce it by a function U as:

$$U = \frac{1}{2}(x_0^2 + y_0^2) + \frac{(1-\mu)}{r_1} + \frac{\mu}{r_2}.$$

Derivate U with respect to x_0:

$$\frac{\partial U}{\partial x_0} = x_0 + (1-\mu)\frac{(x_1 - x_0)}{r_1^3} + \mu\frac{(x_2 - x_0)}{r_2^3}. \qquad (14)$$

Derivate U with respect to y_0:

$$\frac{\partial U}{\partial y_0} = y_0 + (1-\mu)\frac{(y_1 - y_0)}{r_1^3} + \mu\frac{(y_2 - y_0)}{r_2^3}. \qquad (15)$$

Now equation (12) can be rewrite as:

$$\ddot{x_0} - 2\dot{y_0} = x_0 + (1-\mu)\frac{(x_1 - x_0)}{r_1^3} + \mu\frac{(x_2 - x_0)}{r_2^3} \qquad (16)$$

And also equation (13) can be rewrite as:

$$\ddot{y_0} - 2\dot{x_0} = y_0 + (1-\mu)\frac{(y_1 - y_0)}{r_1^3} + \mu\frac{(y_2 - y_0)}{r_2^3}. \qquad (17)$$

By comparing (14) and (15) with (16) and (17) respectively, we have;

$$\ddot{x_0} - 2\dot{y_0} = \frac{\partial U}{\partial x_0}. \qquad (18)$$

$$\ddot{y_0} - 2\dot{x_0} = \frac{\partial U}{\partial y_0}. \qquad (19)$$

Now, Multiplying (18) and (19) by derivative of x_0 and y_0, then adding both equations we get:

$$\ddot{x_0}\dot{x_0} + \ddot{y_0}\dot{y_0} = \frac{\partial U}{\partial x_0}\frac{dx_0}{dt} + \frac{\partial U}{\partial y_0}\frac{dx_0}{dt} \qquad (20)$$

Since, U is the function of both x_0 and y_0:

So,

$$\frac{\partial U}{\partial x_0}\frac{dx_0}{dt} + \frac{\partial U}{\partial y_0}\frac{dx_0}{dt} = \frac{dU}{dt}.$$

Also,

$$\ddot{x_0}\dot{x_0} = \frac{1}{2}\frac{d}{dt}\dot{x_0^2}, \quad \text{and} \quad \ddot{y_0}\dot{y_0} = \frac{1}{2}\frac{d}{dt}\dot{y_0^2}.$$

Putting these 3 expressions in (20) and multiplying by ‘dt’ we have:

$$\frac{1}{2}d\dot{x_0^2} + \frac{1}{2}d\dot{y_0^2} = dU.$$

On integrating this expression, we get:

$$\dot{x_0^2} + \dot{y_0^2} = 2U - C.$$

It is required equation to represents the region of satellite with zero velocity.

Now,

It is to be determined that all of these Libration points are not fully stable. Some of them are stable while others are unstable points. In order to analyze their stability we will further perform some of the calculations in order to find out the Eigen values for each L-point. For this, we will see the behavior of object at those places by slightly displaced them from their position. If the position of object at any L-

point is displaced by the smaller amount X and Y. In other words, the object's position is perturbed by its initial value (x_L , y_L) into (x_L+X , y_L+Y).

By proceeding (18) and (19) and solving the following determinant:

$$\begin{vmatrix} (\frac{d^2}{dt^2} - \frac{\partial^2 U}{\partial x_0^2})X & (-2\frac{d}{dt} - \frac{\partial^2 U}{\partial x_0 \partial y_0})Y \\ (-2\frac{d}{dt} - \frac{\partial^2 U}{\partial x_0 \partial y_0})X & (\frac{d^2}{dt^2} - \frac{\partial^2 U}{\partial y_0^2})Y \end{vmatrix} = 0.$$

The resulted equation we have is:

$$\lambda^4 + \lambda^2(\frac{\partial^2 U}{\partial y_0^2} - \frac{\partial^2 U}{\partial x_0^2} + 4) + \frac{\partial^2 U}{\partial x_0^2}\frac{\partial^2 U}{\partial y_0^2} - (\frac{\partial^2 U}{\partial x_0 \partial y_0})^2 = 0. \quad (21)$$

Solving terms for (21) using values of U, r_1 and, r_2 we have:

$$\frac{\partial^2 U}{\partial x_0^2} = 1 - \frac{(1-\mu))}{r_1^3} - \frac{\mu}{r_2^3} + \frac{3(1-\mu)(x_1 - x_0)^2}{r_1^5} + \frac{3\mu(x_2 - x_0)^2}{r_2^5}. \quad (22)$$

$$\frac{\partial^2 U}{\partial x_0 \partial y_0} = 3[\frac{(1-\mu)(x_1 - x_0)(y_1 - y_0)}{r_1^5} + \frac{\mu(x_2 - x_0)(y_2 - y_0)}{r_2^5}]. \quad (23)$$

$$\frac{\partial^2 U}{\partial y_0^2} = 1 - \frac{(1-\mu)}{r_1^3} - \frac{\mu}{r_2^3} + \frac{3(1-\mu)(y_1 - y_0)^2}{r_1^5} + \frac{3\mu(y_2 - y_0)^2}{r_2^5}. \quad (24)$$

Now, for "*collinear-points*" (along x-axis at the line joining Sun and Earth), all the y-points are zero: $y_0 = y_1 = y_2 = 0$. This means the terms ($y_1 - y_0$) and ($y_2 - y_0$) are zero in all equations. Further solving (31), (32) and (33) and putting the resulting values in (21), the required equation in terms of **λ** is:

$$\lambda^4 + \lambda^2(2 - A) + (1 + A - 2A^2) = 0 \quad (25)$$

Similarly, for '*triangular-points*' (in the form of equilateral triangle), having all sides of equal length, so; $r_0 = r_1 = r_2 = 0$. Also using $x_1 = -\mu$, $y_1 = 0$, $x_2 = 1-\mu$ and $y_2 = 0$, the resulting equation (21) in terms of **λ** becomes:

$$\lambda^4 + \lambda^2 + \frac{27}{4}\mu(1-\mu) = 0. \quad (26)$$

By using quadratic formula for solving (25) and (26), we get the following expressions for Eigen value **λ**:

$$\lambda^2 = -\frac{2 - A \pm \sqrt{-8A + 9A^2}}{2} \quad \text{For collinear points} \quad (27)$$

$$\lambda^2 = -\frac{1 \pm \sqrt{1 - 27\mu(1-\mu)}}{2}. \quad \text{For triangular points} \quad (28)$$

Where;

$$A = \frac{(1-\mu)}{r_1^3} + \frac{\mu}{r_2^3}.$$

Now, if we specify our results for the system of Sun and Earth.

We can find out exact value of **λ** for all Libration points, with using following values:

Mass of Sun; Primary mass = $1-\mu = 1.989\times10^{30}$

Mass of Earth; Secondary mass = $\mu = 5{,}972\times10^{24}$

Also the values of r_1 and r_2 for all the libration points as been determined by using the restricted three-body problem and gravitational law between Sun and Earth. The resulted values are:

L-Points	r_1 (km)	r_2 (km)	'A'
L_1	1.505×10^8	1.5×10^6	2.35×10^6
L_2	1.535×10^8	1.5×10^6	2.319×10^6
L_3	152.09×10^6	304.18×10^6	5.65×10^5

Table (1): Calculated values of r_1 and r_2

Putting all these values in (27) and (28), to get Eigen values for each L-point. The resulting values for stability analysis are:

L-Points	**λ**^{2}	**λ**
L_1	469500	6.95×10^2
L_2	2.3×10^6	1.516×10^6
L_3	1125000	1.06×10^3
L_4	$8.95\times10^{27}\,i$	$9.46\times10^{13}\,i$
L_5	$8.95\times10^{27}\,i$	$9.46\times10^{13}\,i$

Table (2): Resulting Eigen values

Thus, we get a no. of real and imaginary Eigen values for all L-points.

VI. RESULTS

If all **λ**-values are real, the exponential terms containing **λ** will increase with time and the object will drift away from the equilibrium point toward infinity. Thus real Eigen values represent unstable L-points. The resulted values shows that as being 'unstable' L_1, L_2 and L_3 are placed in saddle nodes and small perturbation would set them 'falling' in either direction and they need station keeping. Thus 'Collinear Libration points' are *"Unstable L-Points"*.

However, if **λ**-values are imaginary, the position of the object will oscillate about the equilibrium points and then become stable. Hence, imaginary Eigen values represent the stable L-points. From the above resulted values L_4 and L_5 being stable, feel attractional forces of gravity from both bodies toward them in the same ratio and the resultant acceleration will not tend them fall out of orbits and it will not drift away and maintain its equilibrium position [4]. Thus, Triangular L-Points are *Stable L-Points.*

VII. CONCLUSION

Being unstable places means under the effect of small perturbation the object doesn't resist its initial position and so there is chances to leave position at L-point and attain another. For this reason, to control objects at *collinear L-points*, there is need of some station on Earth to keep that object in its place.

But being stable, triangular L-points doesn't need any sort of station-keeping. This interesting phenomena is attractive to all space missions with low-fuel contain.

VII. SPACE MISSION

Space missions are formally the sending of manned or unmanned vehicles into space, beyond the Earths gravitational effect, by setting its specific orbital velocity for exploring the facts of Universe, for gathering data about activities in space, for the structural views of other planets, and for many other purposes.

To set a satellite for space missions, some controlling centers have to be created at Earth so that to controls its pace and its orbital location. Along with this controlling system, a huge amount of fuel is needed by satellite or spacecraft to keep itself into a stable orbital position, to prevent any destructions.

The position of Libration point is servable with more benefits because the vehicle at such point doesnt need any controlling station and it can work using low-fuel control. This makes L-points beneficial for this reason and thus there are many space missions working at L-points. As per structural position of Libration Points, the space missions working are as followed:

- **Space mission at L_1**:
  - *Deep Space Climate Observatory* (DSCOVR); Launched in 2015, for the observation of solar wind for affecting many events of space weather like geomagnetic storms, by NASA.
  - *Solar & Heliospheric Observatory* (SOHO); Launched in 1996, to study internal structure

of the Sun, its outer atmosphere and origin of Solar wind. SOHO marks 20 years watching the Sun, by ESA.



Figure (2): SOHO

- **Space mission at L_2:**
  - *Wilkinson Microwave Anisotropy Probe* (WMAP); Operating from 2001 to 2010, to measure temperature differences across sky in the cosmic microwave background, by NASA.
  - *James Webb Space Telescope* (JWST); Started in 2002, and will be launched in 2021. Its function include observing some of the distant events and objects in the Universe and direct imaging of exoplanets, by ESA. It is successor to Hubble Telescope [5].



Figure (3):JWST

- **Space mission at L_3:**

As per structure of L_3, it is always hidden by the Sun. So there is no space mission for the working at L_3 till now because it has no direct approach [8]. It can be supposed that L3 is the living place for aliens hidden by human beings

- **Space mission at L_4 and L_5:**

It is observed that some of the natural objects, such as asteroids and meteoroids, are positioned stably at Triangular L-points.



Figure (4): Asteroids

Some of asteroids found at L_4 and L_5 of Sun-Earth system are:

- *Asteroid 2010 TK7*, is the first discovered "tadpole" orbiting L4, companion to Earth
- *Asteroid 2010 SO16*, is a "horseshoe" companion to Earth, orbiting L5 with high inclination.
- *STEREO A*, in 2009, made its closest pass to L4, slightly faster than Earth.
- *STEREO B*, in 2009, made its closest pass to L5, slightly slower than Earth.

There are also some of the proposed missions toward *L_4 and L_5.*

VIII. Libration Points as Libration Areas

Libration points are indeed points, of infinitesimal in size, they can be named as Libration areas. Surrounding all L-point, is an extended zone where a spacecraft can conveniently put itself in an orbit that require little fuel to maintain



Figure (5)

Each object form halo orbit around the Libration points [7]. Halo orbit is possible due to the gravitational interpolation between two massive bodies, and that creates a small area of stability for the third smaller body.

On the basis of this work, we will extend this concept for Mars-Moon system. As many of the space mission has been starting to reach Mars an exploring life there. So the discovery of **Mars-Moon Libration points** will enhance the possibility of reaching Mars with more ease.

References

[1] Oscar Perdomo, Relativistic Lagrange points, May 15, 2016.
[2] Thomas Greenspan, Stability of Lagrangian points, January 7, 2014.
[3] Elizabeth Howell, Lagrangian points: Parking places in space, August 22, 2017.
[4] Markeev A. P, Libration points in celestial mechanics and space dynamics, 1978.
[5] Cacolici and Kyle Alexander, 'Stability of Lagrange points: James Webb Space Telescope'.
[6] Sean P. Kemp, Stability at Triangular Lagrange point for a Three-Body Problem, May 2015.
[7] Klarreich, Lagrangian points of the Earth-Sun system.
[8] Elena Fantino, Spacecreaft trajectories to L3 point of sun-earth system, November 2010.

Deinococcus Radiodurans As A Chassis For Synthetic Biology Experiments In Space Biology

Muneef U. Rehman
Institute of Integrative Biosciences, CECOS University of IT and Emerging Sciences, Phase 6, Hayatabad, Peshawar, Pakistan
Peshawar, Pakistan
muneef.rehman450@gmail.com

Khudeja Salim
CECOS-RMI Precision Medicine Lab, Rehman Medical Institute, Phase 5, Hayatabad, Peshawar, Pakistan
Peshawar, Pakistan
khudeja@precisionmedicine.pk

Faisal F. Khan
CECOS-RMI Precision Medicine Lab, Rehman Medical Institute, Phase 5, Hayatabad, Peshawar, Peshawar
Institute of Integrative Biosciences, CECOS University of IT and Emerging Sciences, Phase 6, Hayatabad, Peshawar, Pakistan
Department of Bioengineering, University Of Engineering and Applied Sciences, Swat, Pakistan
Peshawar, Pakistan
faisal@cecos.edu.pk

Abstract*—The design and construction of new biological parts, devices, and systems, including the re-design of existing, natural biological systems for beneficial purposes, is referred to as synthetic biology. Engineered systems are then deployed in living host cells referred to as a chassis or cell-free systems. One such promising candidate for a strong chassis is Deinococcus radiodurans owing to its viability in extreme conditions, efficient proteomic shielding, production of novel carotenoids and high transformability. Interplanetary space travel and the colonization of Mars come with several key challenges due to the extreme environment. Various microbes have been reported to have capabilities that can help them survive harsh Martian and space conditions such as Deinococcus geothermalis, Bacillus subtilis, Pseudomonas aeruginosa, Candida albicans, Escherichia coli and Micrococcus luteus. In this study, we explored the natural potential of D. radiodurans by the identification of individual features it possesses as an optimal chassis. An analysis of transcriptomic datasets from the literature, revealed 14 Differentially Expressed Genes (DEGs) that confer survival and ideal chassis features to D. radiodurans. This data can be used to construct a desirable synthetic biology device (chassis) that could be used for experiments in space and on Mars.

Keywords*—Deinococcus radiodurans, synthetic biology, chassis, LEO, Martian and space conditions

I. INTRODUCTION

A. Introduction to Space conditions and Interplanetary travel

Interplanetary space travel and the colonization of Mars encapsulates certain challenges, featuring extreme environments. Primarily, two prominent stressors of concern are the solar radiation and microgravity. Space radiation consists of high-charge particles (HZE's) and Galactic Cosmic Rays (GCR's) having high penetrability, ionization and oxidation strength [1]. Also, Earth's gravity in the Low Earth Orbit is not in the downward direction, like on Mars ($1/3^{rd}$ G) and Earth's moon ($1/6^{th}$ G) which causes physiological changes, that can include less bone and muscle density because of the shifting of the blood to the head region [47].

B. Details of Martian Conditions

Space and Martian conditions including Cosmic Ionizing Radiation (CIR), Ultraviolet Radiation (UV), desiccation, low temperatures, variable pressures and vacuum have an adverse effect on living organisms [2]. Space and Mars environment both have a high flux of cosmic and solar particle events (SPE's) [1], combined solar radiation on Mars varies seasonally, in summer the radiation calculated on the southern hemisphere of Mars has been shown to be roughly 13000 kJ m^{-2} of wavelength > 400nm substantially decreasing in winter [3].

C. Concept Explaining Transfer of Life

Studies have been performed to understand the concept of a rocky transfer of life (microorganisms) now termed as Lithopanspermia [5]. One such study demonstrated the increased survivability of *Deinococcus geothermalis* biofilm cells under UV-radiation, when supplemented with S-MRS (A Martian soil Analog) as compared to the non-supplemented biofilm [2]. In other experiments, spores and cells of *Bacillus subtilis* and *Chroococcidiopsis* genus were used in simulations by encapsulating them inside the meteorites and exposing them to different stress conditions [5].

D. Model Organisms in Space and their Negative Effects

Microbes accompany humans to the space-craft environment, different studies have demonstrated the effect of microbial communities on crew health and craft components [43]. Space shuttle flight STS-95 mission aboard the ISS illustrated *P. aeruginosa*, which formed biofilms when exposed to polycarbonate filters and microgravity [44]. Reference [45] showed that the air and surface contaminants of the LEO stations can affect crew health and equipment integrity. The importance of microbes surviving in a confined environment raises concerns like antimicrobial resistance and increased virulence among pathogens [43]. *Staphylococcus* spp. have been shown to develop increased antibiotic resistance and virulence when infected human subjects were living on the International Space Station (ISS) [46]. These analogs provide

substantial data which can help space missions and more successful.

E. Synthetic Biology and Chassis

Synthetic Biology is a field encapsulating living organisms and how we can engineer them to perform different functions, determine their applications and solve various problems related to a specific industry. Synthetic biologists study, design, re-design whole new organisms and existing genomes.

In Synthetic biology, a term, referred to as a chassis which is a host organism genetically designed to maintain a stable configuration and perform functions specified by genetic constructs. The selection of a suitable chassis usually follows two approaches, the first one is the nearest wild type approach and the second is standard chassis approach. The nearest wild type method involves the selection of a chassis on the basis of specific functions that it performs, these abilities of the host are then honed in the lab to maximize its performance, the standard chassis approach enables the synthetic biologist to choose from the already well-understood and highly alterable chassis. [20].

F. Common prokaryotes and eukaryotes Used as Chassis

Other microbes, like *E. coli* which was engineered as a chassis to express type IV pili system and a synthetic peptide to produce Electrically Conductive Protein Nanowires (e-PNs), ultimately producing electricity using the atmosphere [32]. *S. cerevisiae* was also used as a chassis for the production of a wide array of biochemical and biochemistry products [48].

G. Synthetic Biology and Deinococcus radiodurans

D. radiodurans consists of key features that are necessary for a functioning chassis [21, 22, 23, 7]. Genes associated with these features are also well-known [22, 24, 25, 26]. Considering *D. radiodurans*, an IGEM team from Wuhan, China (XHD-Wuhan-China) synthesized a recombinant *D. radiodurans*, two engineered plasmids (gabY-pRADK and gcd-pRADK) were used to promote the dissolution of phosphates in the Martian soil to enable optimal plant growth. Regarding other projects, Team Botchan.Lab, Tokyo did not use *D. radiodurans* but introduced three of its genes (recA, pprM, pqqE) into *E. coli* to make it more resistant, although, the results of the project are not recorded yet.

H. Introduction to Deinococcus radiodurans

Deinococcus radiodurans was first discovered in irradiated cans of spoiled meat [6]. The Genome size of *D. radiodurans* is 3,284,156 bp present as 2 chromosomes, 1 plasmid, 1 Megaplasmid (223kb) and 3195 genes [7]. *D. radiodurans* cells form non-sporulating colonies and are red in color due to the presence of unique pigment known as deinoxanthin [8]. The Deinococcaceae family consists of more than 60 recorded species [7, 9]. It is a polyextremophile bacterium that is extremely tolerant to desiccation, harsh temperatures, ionizing radiation and variable fluences of UV-radiation, its extreme radio-resistance enables it to survive up to 15000 kGy of radiation during stationary phase with no cell damage or loss of viability [10].

I. Repair Mechanisms of Deinococcus radiodurans and In Space

Reference [11] described the efficient DNA repair in *D. radiodurans* owing to its ability to repair thousands of DSB's [12] and exploiting a mechanism named as the Extended Synthesis-Dependent Strand Annealing (ESDSA). It contains multiple copies of its chromosomes during its exponential phase (log) and stationary phase enabling it to perform the annealing process repeatedly [13]. *D. radiodurans* ultrafiltrate (without proteins) enabled it to prevent protein oxidation and carbonylation, which was also able to protect human Jurkat T-cells with no inflicted viability damage up to 16kGy, which signifies the importance of Mn complexes in the organism [14]. Furthermore, because of this resistance, *D. radiodurans* has been subjected to simulated Low Earth Orbit (LEO) conditions and stress conditions onboard the ISS to assess its survival [17, 18, 19].

J. Aim of the Research

The main aim of this research is to identify the genes that are associated with the different features that can make *D. radiodurans* an ideal chassis which can be used for synthetic biology experiments. Additionally, we want to further our understanding regarding the genes that can be used to build an entirely new genetic circuit (chassis) of *D. radiodurans* capable of performing novel functions and applications.

II. MATERIALS AND METHODS

A. Studying features of an optimal chassis

Literature review was performed to identify the reported features of an optimal chassis. A total of 3 papers were selected which were screened to identify the features fundamental for a chassis. These identified features were then used as reference to identify relevant features in *D. radiodurans* that qualify for a synthetic biology chassis. Reported methods that could be used to incorporate the missing features in the microbes were also identified. [22, 21, 23].

B. Identification of the genes associated with the features

For comparative analysis, gene IDs, protein IDs and gene annotation were added to the list of chassis features. Information regarding the genes was obtained from the literature [7, 22, 27] and protein knowledge databases like Uniprot (release 2021_03), String dB (V.11.5), Kyoto Encyclopedia of Genes and Genomes (KEGG) (release 99.1) and Panther (V.16.0).

C. Comparative and Differential Expression Analysis

The single dataset was filtered on the basis of molecular response of *D. radiodurans* under Low Earth Orbit (LEO) conditions. Gene expression data analysis was performed using Maxquant, Fragments Per Kilobase of transcript per Million mapped reads (FPKM) while comparing LEO and control cells in the transcript dataset, respectively [17]. Comparative analysis of the chassis genes with the chosen dataset (transcripts) was conducted in R (V.4.1.0) using plyr and dplyr packages.

Differential expression of extracted genes corresponding to each chassis feature was analyzed in the transcript dataset. Ground control (ctrl) and LEO FPKM values contained in the dataset were used, these normalized values were divided in the order LEO/Ctrl to obtain $\log_2$ fold change values for each

of the common genes (obtained through comparative analysis). For the visualization of the Differentially Expressed Genes (DEGs), Q-values (from the dataset) and $\log_2$ fold change values calculated were used to construct volcano plots, upregulated and downregulated genes were visualized by $\log_2$FC values (Table. 1) and the corresponding Gene_Locus_IDs. The data was analyzed and was used for construction in R (V.4.1.0) utilizing plyr, dplyr, EnhancedVolcano and ggplot2 packages.

D. Enrichment Analysis for study of the genes

The chassis relevant genes selected from the literature were analyzed and an enrichment analysis was performed using Gene Ontology (GO) (V.2021-08-18) and KEGG (V.99.1) databases. Gene_Locus tags of *D. radiodurans* were uploaded in the database for detailed cellular activities of the genes. Cellular components, biological processes and molecular functions of the differentially expressed genes were extracted and used to construct a combined bar plot signifying the vital functions of the genes (see Figure. 5). The bar plot was constructed by utilizing ggplot2 package of R (V.4.1.0).

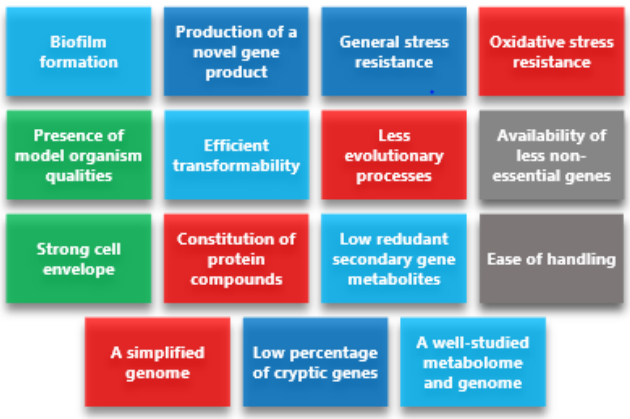
E. Literature Review DEGs

A brief literature search was done, a total of 10 papers were selected from PubMed to learn individual functions of the differentially expressed genes, consequently, these detailed descriptions were analyzed further to create correlations with the chosen chassis features to understand the predicted response of *D. radiodurans* in space.

III. Results

A. Fifteen features were identified for D. radiodurans as a chassis

Eighteen chassis features were identified for *D. radiodurans* as a strong chassis which can be used in Synthetic Biology. These features consisted of properties like biofilm formation, constitution of protein compounds, a simplified genome, a well-studied metabolome and genome, absence or low percentage of cryptic genetic segments, presence of model organism attributes, an ease of handling, availability of less non-essential genes, low redundancy of secondary gene metabolites, efficient transformability, ease of handling, production of a distinct gene product, survival robustness and oxidative stress resistance, strong cell envelope (increased toughness) and low vacancy for evolutionary processes.



characterize an optimal chassis. Features more efficient in *D. radiodurans* (green and light green), features weak in *D. radiodurans* (cyan, blue and light blue)

After screening, the non-molecular aspects of the chassis feature list were removed and ten significant molecular characteristics were selected (Figure. 1). These features were selected on the basis of genes pertaining in *D. radiodurans*. Comprehensive literature review revealed the processes that can be used to incorporate the missing relevant features in *D. radiodurans*, multiple strains of the same microbe can be generated by introducing specified deletions in the genome by a process called λ red type homologous recombination, other methods include comparative analysis of stipulated sequences. Furthermore, techniques like Repeat fusion PCR-based gene disruption and 5-fluoroorotic acid mediated ura4-negative selection were also identified. Bottom-up approaches included sequencing of the whole genome, its subsequent combining through Golden Gate Assembly, Gibson Assembly and Transformation-associated Recombination Cloning (TAR). However, *in silico* tools including Bio Studio revealed the virtual assembly of the desired genome but other than those, less computational methods were mentioned.

B. 134 genes found to be associated with ideal chassis features

A total number of ten final categories were created and a total number of 134 genes were associated (see Figure. 3) (some categories used the same genes). Categories were classified as biofilm formation, constitution of protein compounds, high transformability, production of a novel gene product, survival robustness and oxidative stress resistance, low percentage of cryptic genes, strong cell envelope, general stress resistance genes were annotated.

Out of the 134, 10 genes were involved in biofilm formation in *D. radiodurans*, mostly they consisted of genes encoding membrane autotransporters, quorum sensing, attachment, pathway and interaction proteins. 1 gene was pinpointed that contributes in the production of a cofactor involved in stress circumvention.

Seven genes contributed to the transformability in *D. radiodurans*, these are involved in genetic competence, translocation of DNA, DNA processing and recombination of the environmental DNA. Additionally, 8 genes are involved in the production of a novel carotenoid (deinoxanthin), most of these genes encode monooxygenases, prenyltransferases, oxidoreductases, phytoene synthases and carotenoid desaturases. 41 genes selected regulate and promote oxidative stress resistance in *D. radiodurans* [22] and which abundantly include dismutases, catalases, peroxidases, kinases and thioredoxins. Five genes studied showed some high evolutionary potential and as expected were involved in DNA repair, replication and homologous recombination. Interestingly, 3 genes were cryptic, classified as uncharacterized genes with no annotated functions. Robust cell envelope category encapsulated 7 known and uncharacterized genes encoding proteins which operate membrane maintenance, structure and protein transport. Furthermore, 55 genes were added in the general stress resistance category, DNA replication machinery, UV-resistance, desiccation tolerance, DNA repair machinery and manganese complexes genes are the major runners during the incidence of individual stressors.

C. Differential Expression highlighted genes involved in stress resistance

Comparative analysis between the 134 chassis genes and the 3164 entries in the transcript dataset yielded 134 common entries (see Figure. 4). Out of these 134 genes, 17 were statistically significant (q_value < 0.05) $\log_2$ fold change ($\log_2$FC) values calculated were -2 < x < 1. Most of these genes were involved in DNA repair and recombination, some of them are involved in cellular response to desiccation and radiation. Regarding functions, most of these are associated with DNA binding, ion binding, a minor fraction show peroxidase, helicase and endonuclease activity.

Differential Gene Expression analysis revealed a total of 25 genes, out of the 134, which were all statistically significant i-e. q_value < 0.05. 14 genes were differentially expressed (q_value < 0.05, -0.5 > $\log_2$ FC > 0.5) (see Table. 1). DR_0070, DR_1998 and DR_2263 protect cells by cleaving of peroxides, sequestration of oxidative damage and circumvention of ionizing radiation damage by genome reconstitution. Interestingly, analysis of the data showed the presence of some hypothetical genes with uncharacterized functions. DR_0972 and DR_1021, DR_1916, DR_B0135, DR_1709, DR_1538, DR_1913, DR_0715, DR_A0259, DR_1172 and DR_B0092 were involved in catalyzation of the DNA repair process, unwinding DNA and RNA by nucleic acid binding, stabilization of the protein-RNA complex, membrane-mediated manganese ion transfer, maintain DNA supercoiled structure and glycosylase activity. Although some genes passed the p_value threshold, differential expression was not seen in the plots when $\log_2$ FC cutoff was set to 1 and 2. Hence, the above-mentioned results were obtained when it was set to 0.5 (see Figure. 2). Enrichment analysis revealed the above-mentioned functions for the 14 Differentially Expressed Genes (see Figure. 5), the remaining 11 genes that were only significant in relevance to the $\log_2$ FC values function by binding to heme groups and metal ion groups, others act by binding to sulfur-iron clusters, regulating gene expression by sensing various stimuli in the environment and by predicted synthesis of deoxyribonucleotides due to the breakdown of ribonucleotides (ribonucleotide reductases). KEGG showed results for 4 genes (katA, DR_A0259, recG and G/U mismatch-specific DNA glycosylase) that were involved in different pathways, Gene Ontology showed results for all of the 14 genes with their molecular functions, biological processes and cellular components, however, significant results were not found in GO regarding the cellular component category.

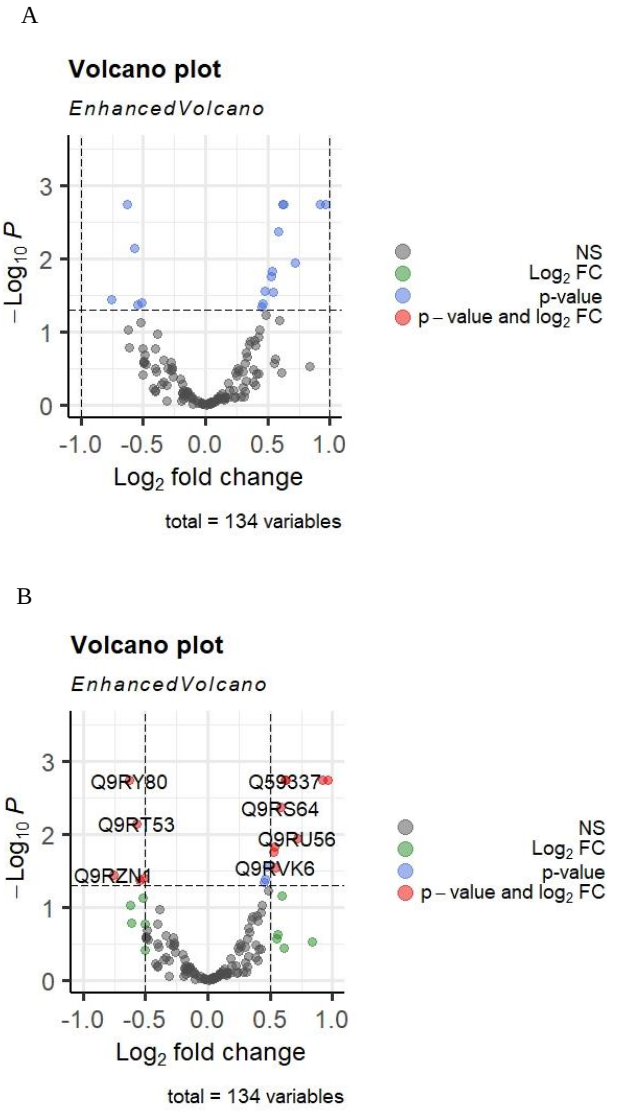


Figure 2. A Log2FC cutoff of 0.5, 1 and p-value cutoff of 0.05 was set to identify differentially expressed genes using a volcano plot. Log2FC when set to (A) 1 did not emanate any significant results, (B) 0.5 value showed differential expression of 14 genes.

Table 1. A table showing the Differentially Expressed Genes (DEGs) with their corresponding q_values and log2FC values.

Protein_ID	Protein_Annotation	q_value	log2FC
Q9RY80	Single-stranded_DNA-binding_protein_DdrB_(DNA_damage_response_protein_B)	0.001832	-0.63028
Q59337	Catalase_(EC_1.11.1.6)	0.001832	0.622565
Q9RYQ0	Catalase_(EC_1.11.1.6)	0.001832	0.627562
Q9RV58	Protein_DR_1172	0.001832	0.918069
Q9RWF4	G/U_mismatch-specific_DNA_glycosylase	0.001832	0.964494
Q9RS64	DNA_protection_during_starvation_protein_1_(EC_1.16.-.-)	0.0042968	0.583822
Q9RT53	DNA_gyrase_subunit_A_(EC_5.99.1.3)	0.007216	-0.56861
Q9RU56	Osmotically_inducible_protein_C	0.0113271	0.719853
Q9RTP8	Divalent_metal_cation_transporter_MntH	0.0147415	0.540193
Q9RVQ0	Uncharacterized_protein	0.0175056	0.528973
Q9RVK6	Uncharacterized_protein	0.028716	0.54165
Q9RZN1	DNA_protection_during_starvation_protein_2_(EC_1.16.-.-)	0.0358975	-0.75703
Q9RZJ2	RNA_helicase,_putative	0.0401479	-0.50988
Q9RT50	ATP-dependent_DNA_helicase_RecG_(EC_3.6.4.12)	0.0429147	-0.54466

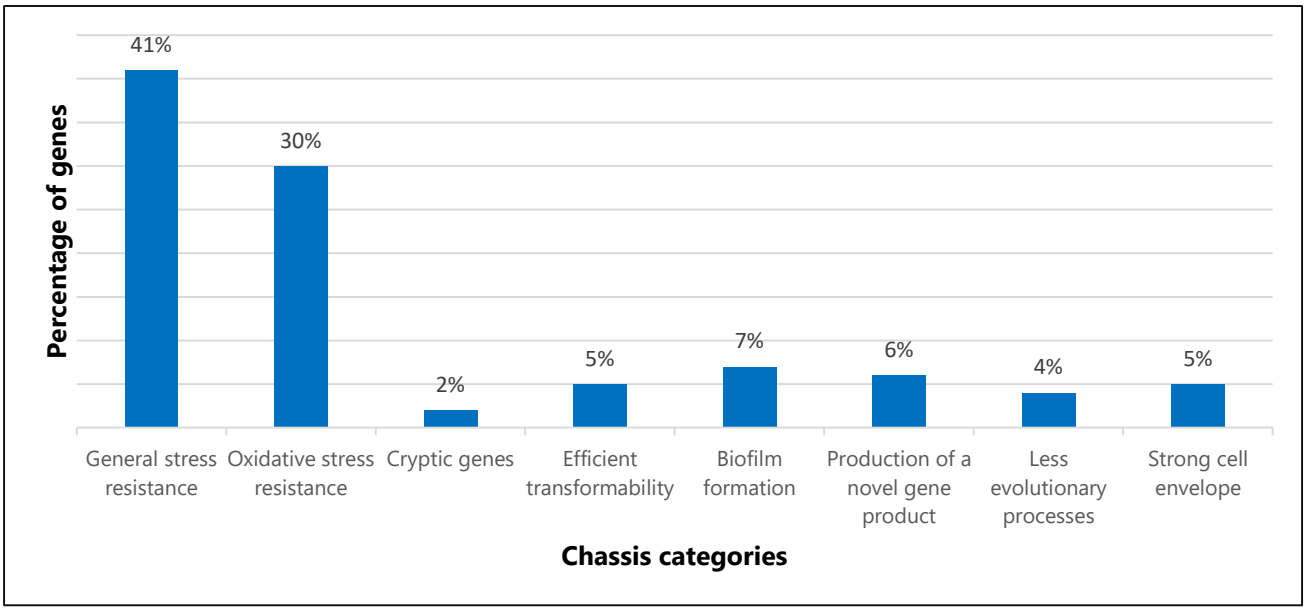


Figure 3. A bar chart showing the percentage of genes associated with each chassis feature category

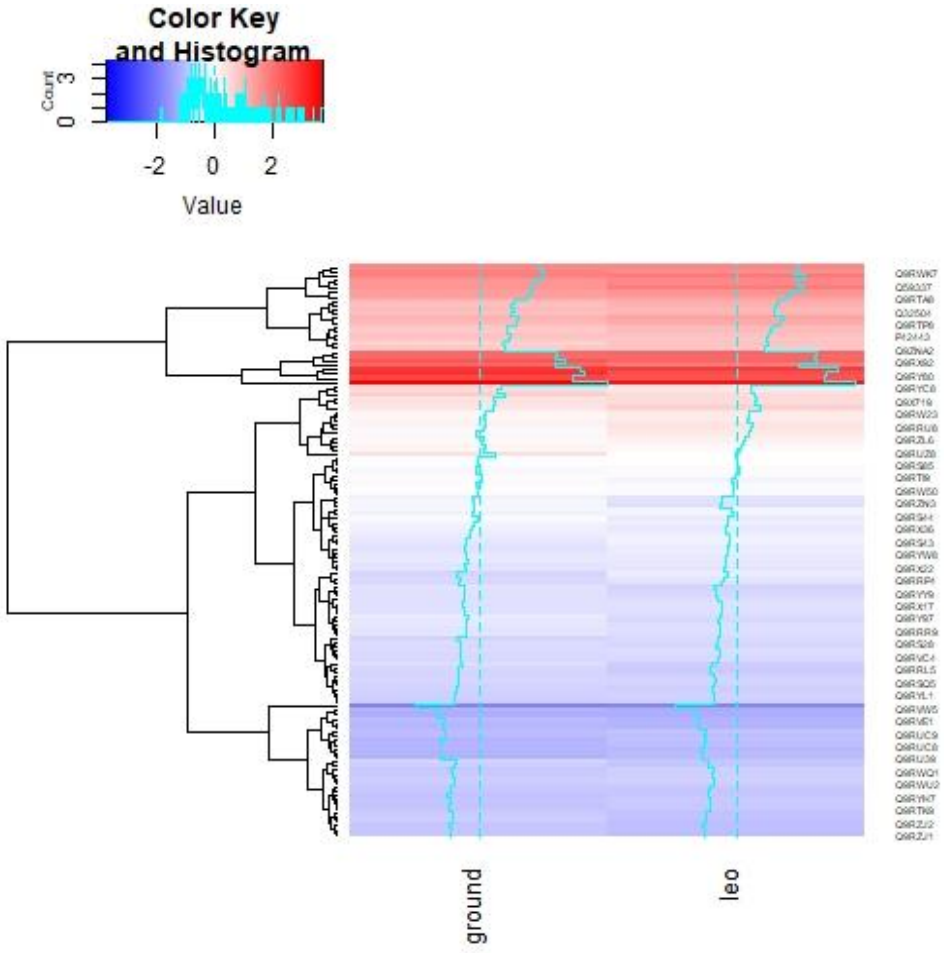


Figure 4. A heatmap showing the comparative expression of the selected 134 genes on the ground (ctrl) and exposed to LEO conditions aboard the ISS (from the dataset)

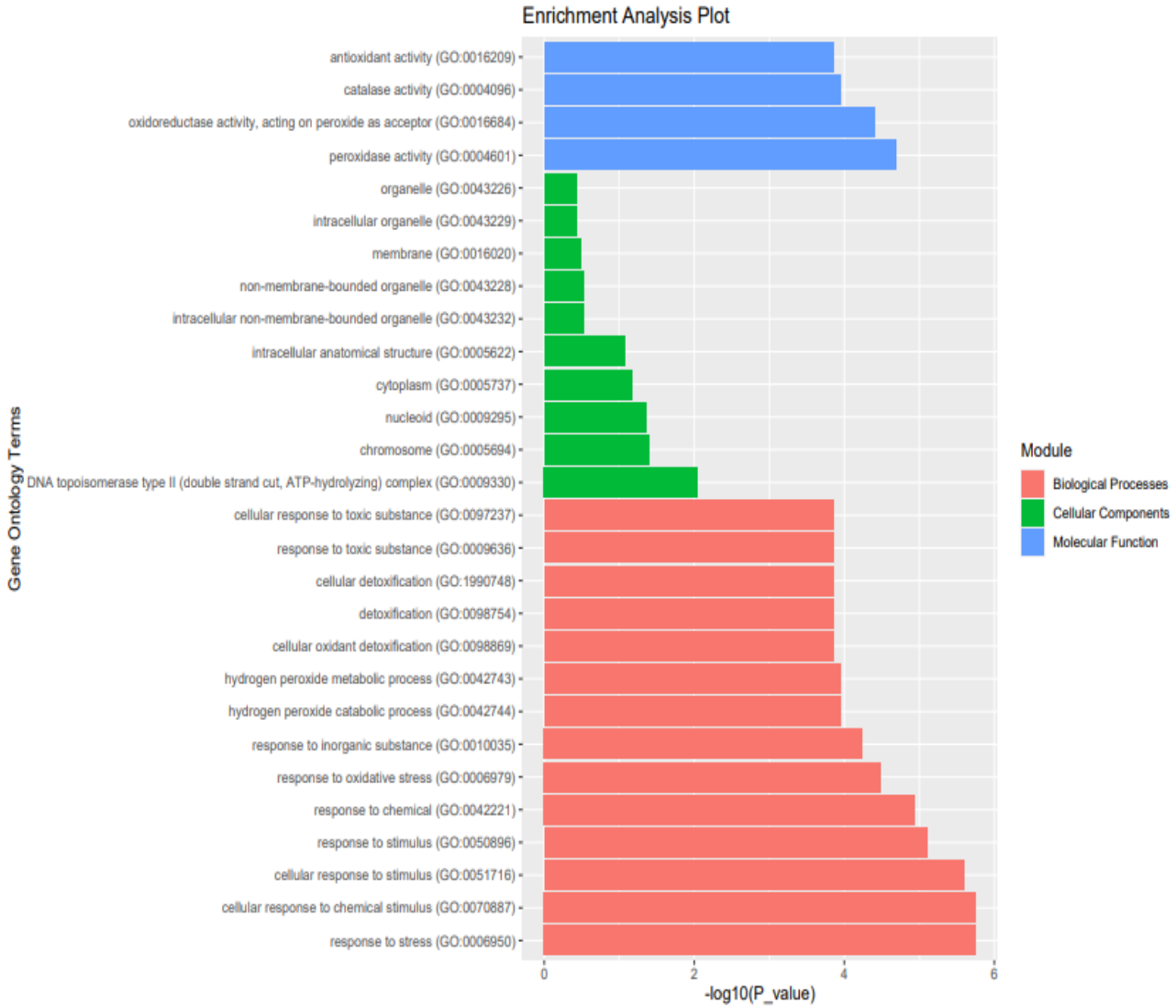


Figure 5. Enrichment analysis bar plot of the 14 Differentially Expressed Genes. X-axis shows the p_value (—log10 to amplify the small value), Y-axis shows the Gene Ontology (GO) Terms and their assigned IDs.

IV. DISCUSSION

The reported findings are reported on the basis of differential gene expression, comparative analysis and literature search that the identified specific genes associated with each chassis feature were differentially expressed in the LEO

environment, which modifies our understanding of the relationship existing between the genes associated with the features of an efficient chassis and the apparent differences induced on their expression under various stress conditions. Genes associated with repair mechanisms and ion transport were upregulated, interestingly, genes with the similar functions were also downregulated. Most of the significant genes belonged to the high transformability, survival robustness and oxidative stress resistance (Figure. 3).

Our findings indicate that there is a cross-talk between individual chassis features of *D. radiodurans* and corresponding genes associated with it, this data can provide a better understanding about the individualized functions of these genes and how they make *D. radiodurans* an optimal chassis for space-related applications. Although most of DEGs were involved in DNA repair, recombination and alleviation of oxidative stress, a gene (DR_1709) related to Mn (II) transport (mntH) was upregulated in the LEO conditions as compared to the ground control (ctrl) which suggests protein protection by circumventing the production of oxidative protein products as demonstrated [14]. The manganese transporter gene alleviates oxidative stress which might give *D. radiodurans* a substantial advantage as a chassis over other less resistant microbes in extreme space environments or future missions to Mars. Moreover, two of the catalases (DR_1998, DR_A0259) that were significantly expressed under LEO conditions, can be the repercussion of the negative effects of ionizing radiation on the water content of *D. radiodurans* causing radiolysis, consequently, aiding the production of ROS (H_2O_2 and O_2^-), which causes these catalases to catalyze the disproportionation of H_2O_2 as peroxidases [33]. Superoxide dismutases (sodA and sodC) genes in *D. radiodurans* are also involved in preventing oxidation [22], however they were absent from the list of DEGs, this might suggest that the LEO conditions were not challenging enough for *D. radiodurans* survival due to which a few of its chassis specific genes were upregulated. Although, many genes in *D. radiodurans* are not well characterized our results identified three of them (DR_0972, DR_1021, DR_1172) that were also upregulated in the LEO environment, which may have various roles in repair mechanisms, cell morphology, biofilm formation and oxidative stress resistance. These cryptic genes might provide some genetic characteristics that could contribute to *D. radiodurans* extended survival; however, the presence of such genes proposes a correlation with the cryptic gene segment feature mentioned above (Figure. 1), to study this relationship requires additional molecular studies to better understand their tasks and how they can enable us to utilize *D. radiodurans* as a synthetic device.

Growth and proliferation of *D. radiodurans* are affected in the LEO and simulated space environment or under prolonged exposures to radiation (Ionizing and UV-radiation) [34], the primary genes/proteins involved in growth during of recovery of *D. radiodurans* from ionizing radiation are also involved in oxidation prevention, Reference [35], described DR_1172 as a desiccation tolerance gene/protein and is shown as uncharacterized gene/protein in our data, is also shown to be contributing to growth after its exposure. DNA gyrase subunit A and ATP Dependent DNA helicase (recG) have a reported role in efficient growth of *D. radiodurans* [36, 37], downregulation of these two in our calculated data indicates (Table. 1) their involvement in repair mechanisms including base-excision repair, recombination and radio-resistance, additionally, this also might portray *D. radiodurans* ability to allocate majority of its genes/proteins in the prevention of stress and oxidation rather than growth during LEO exposure.

In different microbes, reactive oxygen species (ROS) are produced which cause DNA damage, ROS are generated in consequence to desiccation, starvation, radiation etc. These factors, including H_2O_2 can also engage in reduction by Fe^{2+} to form hydroxyl radicals which can cause further damage to the cellular chemistry [38]. Two of the proteins that prevent and combat against the ROS are the gene/proteins known as Dps-1 and Dps-2 (DNA protection during starvation), these act by binding to DNA followed by the stimulation of Fe^{+2} oxidation to Fe^{+3} to make it non-reactive through Fenton reactions [38]. Our data (Table. 1) shows that both of these genes/proteins (dps-1 and dps-2) were differentially expressed, of which dps-1 is upregulated and dps-2 is downregulated, contradictory to the results of [38] which showed the superior ability of dps-2 to combat ROS by low affinity binding to DNA and the inability of dps-1 to protect against ROS damage because of the formation of less stable iron complexes. This upregulation of dps-1 as compared to the ground ctrl may suggest that ROS production in *D. radiodurans* aboard the ISS was mild which caused the effective genes/proteins (dps-2) against oxidative damage to downregulate and instead managed the situation by utilizing a high affinity DNA binding gene/protein (dps-1), because of the cell's low utility. Apart from this, the ground ctrl cells showed increased transcription of replication proteins, transposases and ribosomal proteins (RlmN, RpmC and RtcB) were also common in all the control replicates, this observation was consistent with our data (Table. 1) which showed the downregulation of the RNA helicase gene (DR_B0135) which might be needed to proliferate efficiently under normal conditions. One of the most important methods of DNA repair in *D. radiodurans* is base excision repair, Uracil-DNA glycosylases perform mismatch repair by excising uracil from DNA as part of the pathway, the incorrect addition of uracil to the DNA molecule is the consequence of error during replication or by cytosine deamination, causing G: U and A: U mismatches [39, 40]. Reference (39), described the DNA glycosylase from *D. radiodurans* and how it is specific to G: U and A: U mismatches unlike *E. coli*, in accordance with this study the results show the upregulation of G/U and A/U mismatch DNA glycosylase which suggests the activation of base excision repair in the LEO exposed cells.

Among other antioxidant systems in *D. radiodurans* like thioredoxins, glutaredoxins and peroxiredoxins, there are also a whole family of oxidative stress resistance genes/proteins known as the OsmC which consists of three subtypes: Ohr, OsmC and YhfA [41]. Three proteins: DR_1857, DR_1538 and DR_1177 encoded by *D. radiodurans*, are from the OsmC family, OsmC in *D. radiodurans* is conserved in other *Deinococcus* species, these proteins are peroxidases and catalyze the disproportionation of H_2O_2 into its unreactive form. Moreover, ddrB gene (DR_0070) in *D. radiodurans* is sensitive to IR [42] which is also validated by our results by its significant upregulation, under IR exposure, DR_1538 in our data (Table. 1), shows differential expression and is upregulated under LEO conditions, which demonstrates that

this peroxidase has a direct activity in alleviating *D. radiodurans* oxidant load.

Although, results were statistically significant (when log2FC was set to 0.5), the $\log_2$FC values of all genes were less than 1 which suggests that there was no substantial difference in the expression of the genes when cells were exposed to LEO conditions outside the ISS (see Table. 1) [17], this could have been due to the protective effects of ozone layer that filters out the harmful radiation, regardless this low intensity of radiation combined with other stress factors of space were able to initiate a low yield defensive response in the *D. radiodurans.*

Additionally, the diversity of our results was limited by the smaller number of genes that were associated with their respective chassis features, there may have been other genes that contribute to the properties of *D. radiodurans* as a chassis. Although, computational data shows recognizable results, some of these DEGs have multiple roles which might explain why the magnitude of their differential expression was low, to understand this phenomenon, a study needs to be designed that explores specialized functions of individual genes and how these genes are connected with other elements of the genome. Furthermore, the information gathered in this research can be used to explore *D. radiodurans* in space conditions while considering each of its features as a chassis.

ACKNOWLEDGMENTS

We thank Arsalan Riaz (Precision Medicine Lab) and Abdus Salam (Precision Medicine Lab) for providing their expertise regarding the R program, Laiba Shah (Precision Medicine Lab) for providing helpful insight throughout our research and Hina Zamir (Precision Medicine Lab) for proofreading the manuscript.

REFERENCES

[1] Afshinnekoo et al. 2020. Fundamental Biological Features of Spaceflight: Advancing the Field to Enable Deep-Space Exploration. Cell, 183(5), 1162–1184. https://doi.org/10.1016/j.cell.2020.10.050

[2] Frösler, J., Panitz, C., Wingender, J., Flemming, H. C., & Rettberg, P. (2017). Survival of Deinococcus geothermalis in Biofilms under Desiccation and Simulated Space and Martian Conditions. Astrobiology, 17(5), 431–447. https://doi.org/10.1089/ast.2015.1431

[3] Mancinelli, Rocco & Klovstad, Melisa. (2000). Martian soil and UV radiation: Microbial viability assessment on spacecraft surfaces. Planetary and Space Science. 48. 1093-1097. 10.1016/S0032-0633(00)00083-0.

[4] Horneck et al. 2003. Critical issues in connection with human missions to Mars: protection of and from the Martian environment. Advances in space research : the official journal of the Committee on Space Research (COSPAR), 31(1), 87–95. https://doi.org/10.1016/s0273-1177(02)00662-2

[5] Horneck, G., Klaus, D. M., & Mancinelli, R. L. (2010). Space microbiology. Microbiology and molecular biology reviews : MMBR, 74(1), 121–156. https://doi.org/10.1128/MMBR.00016-09

[6] Anderson et al. (1956). Studies on a radio-resistant micrococcus. I. Isolation, morphology, cultural characteristics, and resistance to gamma radiation. Food Technology, 10, 575-578.

[7] Gerber, E et al. (2015). Deinococcus as new chassis for industrial biotechnology: biology, physiology and tools. Journal of applied microbiology, 119(1), 1–10. https://doi.org/10.1111/jam.12808

[8] Laurent Lemée, Evelyne Peuchant, Michel Clerc, Martin Brunner, Hanspeter Pfander. Deinoxanthin: A New Carotenoid Isolated from Deinococcus radiodurans. Tetrahedron / Tetrahedron [London]; Tetrahedron Suppl; Tetrahedron (London), 1997, 53 (3), pp.919-926. ⟨10.1016/S0040-4020(96)01036-8⟩. ⟨hal-00155200⟩

[9] LaGier M. J. (2017). Predicted Cold Shock Proteins from the Extremophilic Bacterium Deinococcus maricopensis and Related Deinococcus Species. International journal of microbiology, 2017, 5231424. https://doi.org/10.1155/2017/5231424

[10] Minton K. W. (1994). DNA repair in the extremely radioresistant bacterium Deinococcus radiodurans. Molecular microbiology, 13(1), 9–15. https://doi.org/10.1111/j.1365-2958.1994.tb00397.x

[11] Zahradka et al. (2006). Reassembly of shattered chromosomes in Deinococcus radiodurans. Nature, 443(7111), 569–573. https://doi.org/10.1038/nature05160

[12] Krisko, A., & Radman, M. (2013). Biology of extreme radiation resistance: the way of Deinococcus radiodurans. Cold Spring Harbor perspectives in biology, 5(7), a012765. https://doi.org/10.1101/cshperspect.a012765

[13] Battista J. R. (1997). Against all odds: the survival strategies of Deinococcus radiodurans. Annual review of microbiology, 51, 203–224. https://doi.org/10.1146/annurev.micro.51.1.203

[14] Daly, M. J et al. (2010). Small-molecule antioxidant proteome-shields in Deinococcus radiodurans. PloS one, 5(9), e12570. https://doi.org/10.1371/journal.pone.0012570

[15] Lim, S., Jung, J. H., Blanchard, L., & de Groot, A. (2019). Conservation and diversity of radiation and oxidative stress resistance mechanisms in Deinococcus species. FEMS microbiology reviews, 43(1), 19–52. https://doi.org/10.1093/femsre/fuy037

[16] Tian, B., Xu, Z., Sun, Z., Lin, J., & Hua, Y. (2007). Evaluation of the antioxidant effects of carotenoids from Deinococcus radiodurans through targeted mutagenesis, chemiluminescence, and DNA damage analyses. Biochimica et biophysica acta, 1770(6), 902–911. https://doi.org/10.1016/j.bbagen.2007.01.016

[17] Ott, E et al. (2020). Molecular repertoire of Deinococcus radiodurans after 1 year of exposure outside the International Space Station within the Tanpopo mission. Microbiome, 8(1), 150. https://doi.org/10.1186/s40168-020-00927-5

[18] Panitz, C., Frösler, J., Wingender, J., Flemming, H. C., & Rettberg, P. (2019). Tolerances of Deinococcus geothermalis Biofilms and Planktonic Cells Exposed to Space and Simulated Martian Conditions in Low Earth Orbit for Almost Two Years. Astrobiology, 19(8), 979–994. https://doi.org/10.1089/ast.2018.1913

[19] Tsai, C. H., Liao, R., Chou, B., & Contreras, L. M. (2015). Transcriptional analysis of Deinococcus radiodurans reveals novel small RNAs that are differentially expressed under ionizing radiation. Applied and environmental microbiology, 81(5), 1754–1764. https://doi.org/10.1128/AEM.03709-14

[20] Kuldell, N. (2015). Biobuilder. Sebastopol, CA: O'Reilly.

[21] Chi, H et al. (2018). Engineering and modification of microbial chassis for systems and synthetic biology. Synthetic and systems biotechnology, 4(1), 25–33. https://doi.org/10.1016/j.synbio.2018.12.001

[22] Liu, Y., Liu, L., Li, J., Du, G., & Chen, J. (2019). Synthetic Biology Toolbox and Chassis Development in Bacillus subtilis. Trends in biotechnology, 37(5), 548–562. https://doi.org/10.1016/j.tibtech.2018.10.005

[23] Kim, J et al. (2016). Properties of alternative microbial hosts used in synthetic biology: towards the design of a modular chassis. Essays in biochemistry, 60(4), 303–313. https://doi.org/10.1042/EBC20160015

[24] Wang, Y., Xu, G., Wang, L., & Hua, Y. (2019). Distinct roles of Deinococcus radiodurans RecFOR and RecA in DNA transformation. Biochemical and biophysical research communications, 513(3), 740–745. https://doi.org/10.1016/j.bbrc.2019.04.042

[25] Chen, Z., Tang, Y., Hua, Y., & Zhao, Y. (2020). Structural features and functional implications of proteins enabling the robustness of Deinococcus radiodurans. Computational and structural biotechnology journal, 18, 2810–2817. https://doi.org/10.1016/j.csbj.2020.09.036

[26] Ithurbide et al. (2020). Natural Transformation in Deinococcus radiodurans: A Genetic Analysis Reveals the Major Roles of DprA, DdrB, RecA, RecF, and RecO Proteins. Frontiers in microbiology, 11, 1253. https://doi.org/10.3389/fmicb.2020.01253

[27] Ott, E et al. (2017). Proteometabolomic response of Deinococcus radiodurans exposed to UVC and vacuum conditions: Initial studies prior to the Tanpopo space mission. PloS one, 12(12), e0189381. https://doi.org/10.1371/journal.pone.0189381

[28] Rothfuss, H., Lara, J. C., Schmid, A. K., & Lidstrom, M. E. (2006). Involvement of the S-layer proteins Hpi and SlpA in the maintenance of cell envelope integrity in Deinococcus radiodurans R1. Microbiology (Reading, England), 152(Pt 9), 2779–2787. https://doi.org/10.1099/mic.0.28971-0

[29] Jiang, S et al. (2017). DrwH, a novel WHy domain-containing hydrophobic LEA5C protein from Deinococcus radiodurans, protects enzymatic activity under oxidative stress. Scientific reports, 7(1), 9281. https://doi.org/10.1038/s41598-017-09541-2

[30] Farci, D et al. (2014). New features of the cell wall of the radio-resistant bacterium Deinococcus radiodurans. Biochimica et biophysica acta, 1838(7), 1978–1984. https://doi.org/10.1016/j.bbamem.2014.02.014

[31] Zhang, L., Yang, Q., Luo, X., Fang, C., Zhang, Q., & Tang, Y. (2007). Knockout of crtB or crtI gene blocks the carotenoid biosynthetic pathway in Deinococcus radiodurans R1 and influences its resistance to oxidative DNA-damaging agents due to change of free radicals scavenging ability. Archives of microbiology, 188(4), 411–419. https://doi.org/10.1007/s00203-007-0262-5

[32] Ueki, T et al. (2020). An Escherichia coli Chassis for Production of Electrically Conductive Protein Nanowires. ACS synthetic biology, 9(3), 647–654. https://doi.org/10.1021/acssynbio.9b00506

[33] Kobayashi, I et al. (2006). Characterization of monofunctional catalase KatA from radioresistant bacterium Deinococcus radiodurans. Journal of bioscience and bioengineering, 101(4), 315–321. https://doi.org/10.1263/jbb.101.315

[34] Kawaguchi, Y et al. (2020). DNA Damage and Survival Time Course of Deinococcal Cell Pellets During 3 Years of Exposure to Outer Space. Frontiers in microbiology, 11, 2050. https://doi.org/10.3389/fmicb.2020.02050

[35] Liu, Y et al. (2003). Transcriptome dynamics of Deinococcus radiodurans recovering from ionizing radiation. Proceedings of the National Academy of Sciences of the United States of America, 100(7), 4191–4196. https://doi.org/10.1073/pnas.0630387100

[36] Wu, Y., Chen, W., Zhao, Y., Xu, H., & Hua, Y. (2009). Involvement of RecG in H2O2-induced damage repair in Deinococcus radiodurans. Canadian journal of microbiology, 55(7), 841–848. https://doi.org/10.1139/w09-028

[37] Kota, S., Charaka, V. K., & Misra, H. S. (2014). PprA, a pleiotropic protein for radioresistance, works through DNA gyrase and shows cellular dynamics during postirradiation recovery in Deinococcus radiodurans. Journal of genetics, 93(2), 349–354. https://doi.org/10.1007/s12041-014-0382-z

[38] Reon, B. J., Nguyen, K. H., Bhattacharyya, G., & Grove, A. (2012). Functional comparison of Deinococcus radiodurans Dps proteins suggests distinct in vivo roles. The Biochemical journal, 447(3), 381–391. https://doi.org/10.1042/BJ20120902

[39] Moe, E., Leiros, I., Smalås, A. O., & McSweeney, S. (2006). The crystal structure of mismatch-specific uracil-DNA glycosylase (MUG) from Deinococcus radiodurans reveals a novel catalytic residue and broad substrate specificity. The Journal of biological chemistry, 281(1), 569–577. https://doi.org/10.1074/jbc.M508032200

[40] Lindahl T. (1974). An N-glycosidase from Escherichia coli that releases free uracil from DNA containing deaminated cytosine residues. Proceedings of the National Academy of Sciences of the United States of America, 71(9), 3649–3653. https://doi.org/10.1073/pnas.71.9.3649

[41] Shin, D. H et al. (2004). Structure of OsmC from Escherichia coli: a salt-shock-induced protein. Acta crystallographica. Section D, Biological crystallography, 60(Pt 5), 903–911. https://doi.org/10.1107/S0907444904005013

[42] Norais, C. A., Chitteni-Pattu, S., Wood, E. A., Inman, R. B., & Cox, M. M. (2009). DdrB protein, an alternative Deinococcus radiodurans SSB induced by ionizing radiation. The Journal of biological chemistry, 284(32), 21402–21411. https://doi.org/10.1074/jbc.M109.010454

[43] Taylor P. W. (2015). Impact of space flight on bacterial virulence and antibiotic susceptibility. Infection and drug resistance, 8, 249–262. https://doi.org/10.2147/IDR.S67275

[44] McLean, R. J., Cassanto, J. M., Barnes, M. B., & Koo, J. H. (2001). Bacterial biofilm formation under microgravity conditions. FEMS microbiology letters, 195(2), 115–119. https://doi.org/10.1111/j.1574-6968.2001.tb10507.x

[45] Novikova N. D. (2004). Review of the knowledge of microbial contamination of the Russian manned spacecraft. Microbial ecology, 47(2), 127–132. https://doi.org/10.1007/s00248-003-1055-2

[46] Schiwon, K et al. (2013). Comparison of antibiotic resistance, biofilm formation and conjugative transfer of Staphylococcus and Enterococcus isolates from International Space Station and Antarctic Research Station Concordia. Microbial ecology, 65(3), 638–651. https://doi.org/10.1007/s00248-013-0193-4

[47] Demontis, G. C., et al. (2017). Human Pathophysiological Adaptations to the Space Environment. Frontiers in physiology, 8, 547. https://doi.org/10.3389/fphys.2017.00547

[48] Jouhten, P et al. (2016). Yeast metabolic chassis designs for diverse biotechnological products. Scientific reports, 6, 29694. https://doi.org/10.1038/srep29694

Event Rate of Extreme Mass Ratio Inspiral Systems in M32 Galaxy

Muhammad Waqas [1,2]
[1]*Department of Space Science*
[2]*Space and Astrophysics Research Lab (SARL), National Center of GIS and Space Applications (NCGSA), Institute of Space Technology, Islamabad*
waqaspu86@gmail.com

Asad Ali[1,2]
[1]*Department of Applied Mathematics & Statistics*
[2]*Space and Astrophysics Research Lab (SARL), National Center of GIS and Space Applications (NCGSA), Institute of Space Technology, Islamabad*
asad.ali@ist.edu.pk

Rafia Sarwar[1,2]
[1] *Department of Space Science*
[2]*Space and Astrophysics Research Lab (SARL), National Center of GIS and Space Applications (NCGSA), Institute of Space Technology, Islamabad*
rafu2010@gmail.com

***Abstract*—After growing consensus of scientific fraternity that, there exist a black hole (MBH) in the center of every galaxy. The surrounding environment of MBH in the galactic center contains a very dynamic presence of stellar cluster giving rise to systems comprising of a massive black hole (MBH) and a population of stellar-mass compact-object (CO), typically stellar-mass black hole (BH), neutron stars (NS) and white dwarfs(WD). As the COs become gravitationally bound with the central MBH forming extreme mass ratios binary systems, having prolonged 10^4 to 10^5 cycles, which are anticipated candidates for future space-born Laser Interferometer Space Antenna (LISA) to detect gravitational waves from these inspiralling binaries. These CO-MBH systems are producing complex gravitational waves (GW) during their evolution with weak strain amplitudes, leading to the last stable orbit around the MBH. We inspect the relationship between signal–to–noise ratios (SNRs) and informative parameters of these gravitational wave generating binary sources, and developed a generalized linear model inferring their properties. Intrinsic parameters of Analytical Kludge (AK) waveform model were restrained, by employing the well-established understanding of the MBH to extrapolate the scaling relation, which envisages a fiducial fit for back–of–envelop computations of SNRs. We compute the averaged probability of 9.39 EMRI events detectable in LISA mission lifetime, to occur in M32 galaxy, considering the sensitivity of the LISA detector.**

Keywords—Compact Objects (COs), Analytical Kludge Waveform(AKW), Laser Interferometer Space Antenna (LISA), Extreme Mass Ratio Inspirals(EMRIs), Massive Black Hole (MBH)

I. INTRODUCTION

Over the last few decades, astrophysical understanding of galactic centers in galaxies has increased dramatically. Giving consideration to space based telescope like Hubble

Space Telescope (HST) and ground based telescopes which improved their observation results by using adaptive optics, they have studied kinematics of stars or gas in the exotic sub parsec region for distant and milli parsec region of Milky Way galaxy. Remarkable conclusion is drawn from these results that a dark compact object sitting in the center of every galaxy, most probable a MBH of 10^6 to 10^9 $M_\odot$. The nucleus of galaxy contain star cluster, ranging from 10^7 to 10^8 stars with in a few parsec around MBH. In nucleus of galaxy, star densities are around $10^6 pc^{-3}$ and their relative velocities vary from 100 kms^{-1} to 1000 kms^{-1}. These velocities are dependent on mass of central MBH, and their mutual scaling relationship is represented by $M_\bullet - \sigma$ [1].

Interaction between stars & MBH in galactic center occur either by gas produced by stars which then accreted onto the MBH or stars can directly plunge into MBH following radial orbit or inspiral gradually loosing angular momentum in form of GWs & giving rise to EMRI systems. Both interactions contribute to overall mass and spin of MBH. LISA, space-based mission in collaboration with European Space Agency (ESA) will be realized in 2034, which will have a sensitivity range to detect these GWs producing events in milli-Hertz [10^{-4} to 10^{-1} Hz] window [2], produced by MBH of billion solar masses, orbited by few solar mass COs.

On the available observed data, velocity dispersion $M_\bullet - \sigma$ and luminosity relation, 0.01 Mpc^{-3} is the MBH density in the local universe. In Milky Way, M31 and M32 galaxies, observationally it is of scientific knowledge that they possess MBH and a compact stellar nucleus in the galactic center. Since the mass of the COs are 10^0 - 10^2 $M_\odot$, their mass ratio is typically $q = m / M \sim 10^{-4}$ - 10^{-5} . That's why they are termed as extreme-mass-ratio-inspirals (EMRIs), these binary systems are likely to radiate GWs with in most sensitive frequency range of LISA. This places them in a most probable GWs radiating sources detectable by the LISA mission. EMRIs systems evolve right in the heart of galaxy, near to MBH, where sufficient number of COs and stellar remnants are available for capture by the black hole and cusp of stars has been formed around them, even if they have gone through any recent merger. Strain sensitivity of LISA facility lies at 3 mHz, most of the potential sources for this frequency spot should have a MBH of the order of 10^6 $M_\odot$. In EMRI systems, COs mass range is normally 4 orders of magnitude smaller than the mass of the SMBH. This can be considered as the perturbation, to background space-time of the central object. Every black holes is unique, and can be characterized by three parameters mass, spin and charge. Since electromagnetic repulsion is much stronger than gravitational attraction (about 40 orders of magnitude), assuming that astrophysical black holes have negligible net charge, we consider the Kerr metric, where black holes are described only by their mass and spin. Orbital inclination by the spin axis leads to considerable effect as Kerr MBHs involves axisymmetric geometry contrary to symmetric geometry of Schwarzschild MBHs. Stellar dynamics play most important role in EMRI system evolution, as capture of COs principally depends on stellar dynamics in vicinity of MBH whilst orbiting it with high velocities, Strong Mass Segregation (SMS) and scrambled eccentricities become very important too. COs follow eccentric orbits, with relativistic dynamics, till the last stable orbit(LSO), but these parameters depend upon the initial moment of EMRI system when CO is initially captured by MBH. As EMRI evolve and number of orbits go high, strength of GW signal increases and it can be observed effectively till Last Stable

Orbit (LSO). COs orbit mostly in the strong gravitational field before falling into MBH. In this process of orbiting and inspiralling CO dissipates orbital energy and angular momentum, emitting continuous GWs of the order of milli-Hertz, detectable by LISA band.

We will use foundation work of [4] inspiral orbit using waveform simulation by Barack and Cutler, 2004 [5] at the later orbital stages of EMRIs till before CO falls into MBH. EMRIs are formed mostly from, eccentric trajectories emerging from scattering processes and N-body gravitational effect of neighboring stellar species. Yet, few of the COs are ejected to higher orbits by these dynamical processes that may never arrive at the formation stage of an EMRI. The expeditious waveform amplitude of GW of EMRI waveform will be orders of magnitude less than that of detectors noise, nonetheless, detection of few such events the mass and spin parameters of the MBH. It will demystify MBH, and it can be wholly described in terms of no-hair theorem.

Gravitational waveforms from such inspiraling sources have significant prospective for gravitational physics.

Primary goal of this project is to compute event rates of EMRIs in M32 (NGC221) galaxy, anchoring a MBH in its galactic nucleus. In introduction (1) by primitive deliberation of gravitational wave source extreme mass-ratio inspirals (EMRIs) genesis, knowing that such exotic source is the most probable candidate detectable, by space-based laser interferometer space antenna (LISA). LISA mission with the help of European Space Agency (ESA) will be realized in 2034 and it will have detection window of the entire sky probing GWs emitting sources up to the red-shift of the order z = 20. New Gravitational wave Observatory (NGO) will revealing a hidden Universe where electromagnetic spectrum principally cannot probe.We will establish an understanding of the environment around MBH, surrounded by COs of different mass range and the impact of various astrophysical processes on the event rates of EMRIs, and computing formalism for event rate in section (2). Further in (3), we will discuss our approach towards EMRI waveform construction by playing the reduced parameter space for our own good in context with computation ease. Signal processing, Sensitivity of detector and spectral density assessment to obtain Signal to noise ratio will be discussed in (4). Section (5) will include the results and future implications of this work.

II. Event Rate in M32 Galaxy

Observations suggest the presence of $10^7 M_\odot$ of stars in galactic center of M32 galaxy by closely studying its luminous density profile. These stellar density profiles only represent the brighter species present in the galactic center, where as COs like Black Holes (BH) which are heavier of all COs, and orbit very close to MBH are not included because of obvious reasons. But they are potential candidates of EMRI forming systems.

EMRI formation depends upon the astrophysical processes like Strong Mass Segregation, resonant relaxation, tidal disruption, triaxiality and density profiles of galactic centers. Event rates of EMRI counts in any galaxy is very uncertain, as we are studying M32 galaxy exclusively, we will use very optimistic astrophysical presumptions.

A. MBH Population in Universe

MBH masses and spins are crucial to understand in the quest of Event rate estimation. MBH possessing higher spin distributions will produce more EMRIs. In LISA detectable range of MBH. Distribution of these MBH evolve as a function of spin and masses co-moving at particular red-shift z. Estimation of such galaxies in local universe which host MBH in their centers in co-moving volume of local universe is a challenging problem. Formation of EMRIs depend upon cusp-formation around MBH (Babak et al., 2017) in galactic centers, if a galaxy has gone through a recent merger such that the cusp has disrupted around its central MBH, those systems are out as a candidate of EMRI formation. We are studying M32 galaxy, which observably has found to have a cusp formed around its central MBH (Amaro-Seoane et al., 2007; T.L, 1998), and mass of M32 MBH is $2.5 \times 10^6 M_\odot$ (Karachentsev et al., 2004). The z - independent scaling relation of mass function is (Babak et al., 2017).

$$dn/d\,(lnM) = n_o\left(M/3 \times 10^6 M_\odot\right)^B \qquad (1)$$

here M is the mass of MBH, for LISA detectable MBH range n_o is .0002 Mpc^{-3} , and B is 0.3, considering lower limit of EMRI event rate.

B. Intrinsic Rates of Stellar Remnants around MBHs

Stellar remnants (WDs, NSs or stellar mass BHs) orbiting around MBH in GC, their properties contribute to formation of EMRI processes. MS stars nearing SMBH faces tidal disruption and do not resist the tidal forces by SMBH. NSs which have evolved through different evolutionary paths reflect distinctive signatures through dissimilar distribution peak and mass cutoff values. Binary NSs systems and neutron star-white dwarf systems show consistent respective peaks at $1.33_\odot$ accretion of $0.22_\odot$ and $1.55_\odot$ suggesting significant mass which has occurred during the spin-up phase. where as the simulated BH mass range was $[.5-100]M_\odot$ (Abbott et al., 2020). Cusp isformed around dynamically relaxed clusters around MBH, heavier species sink closer to MBH, resulting in SMS (Amaro-Seoane and Preto, 2011) and become the most probablysource of EMRI formation. WDs mass range is fraction of solar mass, thereforewe set the range of COs to be $[.5-100]M_\odot$around MBH to be very wide, to understandtheir effect on resulting GWs sources EMRIs. Intrinsic rate of COs around MBH is given by Power law:

$$R = R_o\left(M/10^6\, M_\odot\right)^a \qquad (2)$$

where a = {−.15, −.25, −.25} with event rates R_o = {400, 7, 20}Gyr^{-1} for BHs, NSs and WDs respectively [9]. Given estimated intrinsic rate R are results of MCMC simulations and does not include the direct plunges. Direct plunges refer to the captures in which CO scatters to the radial orbits and plunges directly without undergoing the inspiral stages.

C. Formalizing Event Rate

To formalize event rate we will be needing number density of comoving MBHs, EMRIs formation intrinsic rate, and mission life time. Whilst running our wave form models we chose mission life time to be 2 years. M32 galaxy exist at .77MPc from Milky way galaxy, having redshift of z = 0.00017 in distance, we ignore this red shifted component of comoving volume for simplicity and negligible effect. Spins of MBH is still highly uncertain, hence, the ∫p(a)da is normalized to 1 which is the probability density function pdf of spin parameter, ranging from 0 to 1. So,

$$N_{EMRI} = t_{life} \times \int_{Mmin}^{Mmax} R \times dn/d\,(lnM)\big(d(lnM)\big) \quad (3)$$

where $M_{min} = 10^4 M_\odot$ and $M_{max} = 10^7 M_\odot$ [10]. Dirac Delta function is applied to the above expression so that limit of

integral converges only when M approaches M. of M32 galaxy and zero elsewhere.

III. EMRIs IN M32 GALAXY

Essential features of General Relativity (GR) has been contemplated by using Analytical Kludge Waveform Model (AK). This waveform model AK, takes in account of lowest order quadrupole moment that retains effect of radiation reaction & effect of orbital precession. AK waveform model improves the rate at which waveform evolves and yet reflecting its all characteristic features. Additionally, the probability of EMRI event happening strongly depends upon capture processes of COs, which can only be determined by dynamical astrophysical stellar processes going on in the closest vicinity of MBH, orbiting around it with high velocities and random eccentricities. As LISA constellation itself will be cart-wheeling and orbiting, it will induce additional Doppler modulations to the receiving signal, that put together reduced mode frequency approximation realized by (Cutler, 1998). We choose this model considering its computational efficiency in comparison to the available range of waveform models.

AK waveform model considers COs instantaneous orbital trajectories as Newtonian in MBH vicinity, assuming background manifold to be flat. In start of EMRI evolution, trajectories of CO orbits are taken to be Keplerian ellipses, and in later stages of EMRIs, relativistic effects are introduced stimulated through PN approximation equations. Appended relativistic effects take account of radiation reaction which is (circularizing and inspiralling) affiliated to CO path in phase–space course and precessions of orbital plane through out formation space.

GWs can be represented completely in three coordinate systems, Barycentric ecliptic coordinate system around solar system, coordinates of MBH at galactic center, and co-rotating coordinates of detector which principally uses low-frequency approximation proposed by (Cutler, 1998) [11] respectively. After choosing source coordinate, Waveform signal is constructed in $h^{+,\times}$ polarizations that is based upon Peters–Mathews work, these effects are then translated into strain amplitude $h_{I,II}$ and with the antenna response functions $F^{+,\times}$, sky location and polarization angle of source is taken in Barycentric coordinate system.

Full representation of EMRI waveform can be done by 17 physical parameters including both intrinsic–extrinsic parameters. If we neglect the spinning effects of CO, 14 parameters are left to consider and are expressed as λ_{AK}= $\{\nu_0, M, \mu, e_0, \gamma_0, \Phi_0, \alpha_0, \theta_S, \varphi_S, i, \tilde{a}, \theta_K, \varphi_K, D_L\}$. They contribute to the evolution of waveform. Parameters are chosen, when capture of CO occur by MBH at t = 0, subscript zero implies that. All of these parameters are chosen to be dimensionless. Extrinsic parameters are dependence on the location of source and orientation of detector. Where Polar angle of MBH spin axis is θ_K and azimuthal angle of MBH spin axis is φ_K. θ_S and φ_S are the source latitude and longitude in ecliptical coordinate system. Distance to the source is D_L which is in Mpc. Intrinsics parameters are ν_0 (Initial orbital frequency), M (Mass of MBH), μ (Mass of CO), e_0 (Initial eccentricity), i (orbital inclination angel) , $\tilde{a}$ (Spin of MBH), γ_0 (initial direction of pericenter), Φ_0 (initial azimuthal orbital phase angle) and α_0 is the initial azimuthal angle of orbital angular momentum [5].

It is still a large Parameter space as far as waveform generation is concerned by grid based or MCMC methods. Global mode of such multi dimension parameter space is computationally very intensive. Our project is specifically for M32 galaxy, so, we have information from observational astronomy, like mass, sky location and distance to MBH, in that way parameter space is left with 10 parameters only.

A. Model Parameters

Our work surrounds Event rate EMRIs of M32 galaxy, where MBH of $M_\bullet = 2.5\times10^6\, M_\odot$ sits in the galactic center [18]. Because we are specific to a single galaxy, we can further reduced our EMRI parameter space, by limiting the parameters of locality, mass of MBH, distance to the source, this reduces the complexity of waveform model. M32 galaxy exists at .77MPc, having redshift of z = .00017 in distance, ignoring z-component for simplicity and its negligible effects in comoving volume. Let the set of parameters be, $\lambda = \{\lambda_0, \lambda_1, \lambda_2, ..., \lambda_z\}$ where superscript "z" is the tell of parameter number. Selection range for parameters is as follows:

- Using stellar kinematics, Hubble Space Telescope (HST) imaging, and Jeans Anisotropic Models mass of MBH is $M_\bullet$ of $2.5 \pm 0.5 \times 10^6\, M_\odot$ and astronomical distance $D_\bullet$ = .77Mpc [18].
- Spin "a" is key intrinsic parameters with the strongest impact on the inner-most stable orbit. hence, to nullify the expected discrepancy in the magnitude of spin angular momentum $\tilde{a} = S/M^2$, we take it to be uniformly distributed U [0, 1].
- We use the J2000.0 coordinates: Ecliptic latitude θ_s and ecliptic longitude φ_s are fixed to be -40.86638889 and 10.67541667 respectively.
- Mass of COs intrinsically defined by its type, e.g BHs, NSs, WDs or low mass Main Sequence (MS) stars. We introduced a randomized uniform distribution of μ within $U[.5, 100]M_\odot$
- Initial eccentricity was taken in uniform distribution between U[0.15, 0.25].
- Initial orbital frequency ν_0 at t = 0 of CO's capture by MBH is taken to be uniform between $\sim 2 - 5$ mHz.
- Spin vectors are taken to be isotropic and symmetrically distributed. Three angles corresponding to the initial phase space trajectory and naively, taken between $U[0, 2\pi]$.

Initial orbital frequency are set in such a way that EMRI system evolve and inspirals up to the Last Stable Orbit (LSO) for a fixed duration of 2 years. Bank of sampling is obtained to have statistically significant results. For each sample, We generated randomized set of parameters as discussed above. We used the noise model of (Barack and Cutler, 2004) and sampled 10^5 mission realizations.

IV. SIGNAL ANALYSIS

If strain amplitude of waveform signal is s(t), and it is the time-dependent linear sum of GW signal denoted by h(t) and noise n(t). We are reviewing the signal analysis in the prospect of classic LISA design model by (Barack and Cutler, 2004) [5], were noise n(t) is taken to be non-correlated and normal (Gaussian), having zero mean. Modifications for LISA will require contributions of updated analytic noise distributions. We are using low frequency approximation in which triangular formation of LISA detector is assumed to be indistinguishable 2-armed detectors, held perpendicular to each other, and will detect strain $h^{+,\times}$ signal. This approximation considers LISA constellation to be statically at equal distance (Cutler,1998) [11]. If strain amplitude is $h_{I,II}$ (t) detected at each detector is I and II, then these signals at each detector $h_{I,II}$ are effectively Michelson interferometers response, and emerge out as linear sum of perturbative polarization amplitude $A^{+,\times}$(t) and geometric antenna response functions $F_{I,II}$ (t) of detector's channels I and II, respectively, and the response functions $F_{I,II}$ (t) depends upon the sky location of the source translated in detector's coordinates.

Waveform model templates are constructed on the basis of chosen astrophysical model and its parameter set. Inner product tells how the signal is variant in comparison to a template and this quantification is called SNR [19]. Inner product function evaluates the amount of weight by which the two time-dependent Fourier transformed signals are different is called optimal filtering, it solely depends upon sensitivity of the detector, which is

$$\rho^2[h] = 4\Re\left(\int_0^\infty h^*(f)h \quad (f)/S_n(f)\, df\right) \qquad (4)$$

where h(f) representing the measure of Fourier Transformed (FT) waveform signal detected, $S_n(f)$ defined one-sided Power Spectral Density (PSD) of the detector's noise and ρ(h) is SNR. If SNR is higher than 20, then we will consider that signal to be detectable.

A. *LISA Sensitivity*

We have used frequency dependent LISA sensitivity curve approximated by Cutler (2004) which is primarily being contributed by single-link optical metrology noise, single test mass acceleration noise and galactic confusion noise.

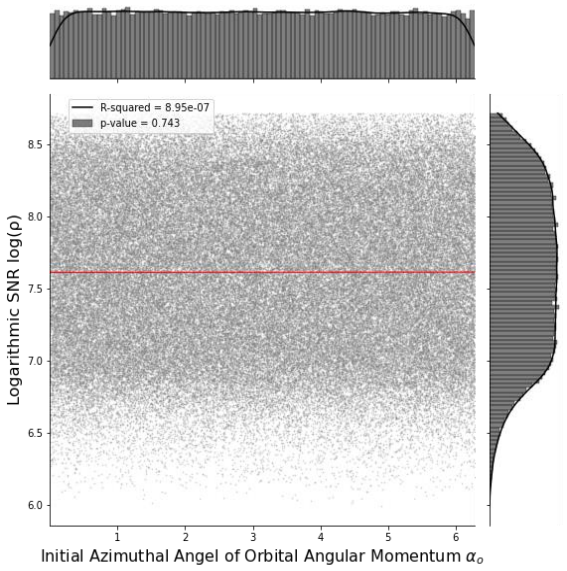
V. RESULTS AND APPLICATIONS

In our research to estimate EMRI event rate, we studied LISA detectors and its techniques for detection of GWs, summarized astrophysics of EMRIs and processes effecting its formation, evolution and event detection formalization. We broaden our signal analysis base and reviewed LISA sensitivity curve and power spectral density analysis to estimate SNRs. Theoretical waveforms model for EMRIs visualizations were performed by Analytical Kludge Waveform model by (Barack and Cutler, 2004). Code we used to generate bank of waveforms were based on previous work of (Ali et al., 2012).

A. Estimates of SNR with EMRI Parameters

Initial orbital frequencies has positive correlation with SNRs. We express SNR in logarithmic scale as it is a positive quantity and by log plots we can better understand the behavior of SNR with sensitive parameters of EMRIs. We will be expressing statistical indicators like R^2 index and $p-$value, which will tell the goodness of regression model. Initial orbital frequency has R^2 index of 0.762 with very significant p-value of $p = 0$. This linear relation of initial orbital frequency and SNR marks out that how orbits of COs around MBH at time of its capture will affect SNRs. This strong inter-dependency can also be observed in scaling relation of SNRs where orbital frequencies are translated into semi-major axis a to compliment the scaling relation of SNRs. Next most sensitive parameter is mass of CO,it has a lower $R^2 = 0.011$ value than initial orbital frequency and has $p-\text{value} < 1.81 \times 10^{-295}$. From rest of the parameters, it is clear that they don't have any correlation SNR, and are tabulated in Table 1 with an inadequate level of significance.

Statistical density distributions and Kernel Density Estimation (KDE) for the set of parameters is given in As clear from the scatter plots, orbital frequencies relate to the SNR in a linear fashion. Also, cosine angles of orbital inclination expresses the expected bi-modal distribution, as the parameter was constrained between 0 and 2π and has sinusoidal behavior. Other parametric distributions are non–Gaussian and non–consequential. The heat map shows no multicollinear relation of substantial degree is observed amongst the parameters, except orbital frequency and normalized CO mass has a slight negative correlation.



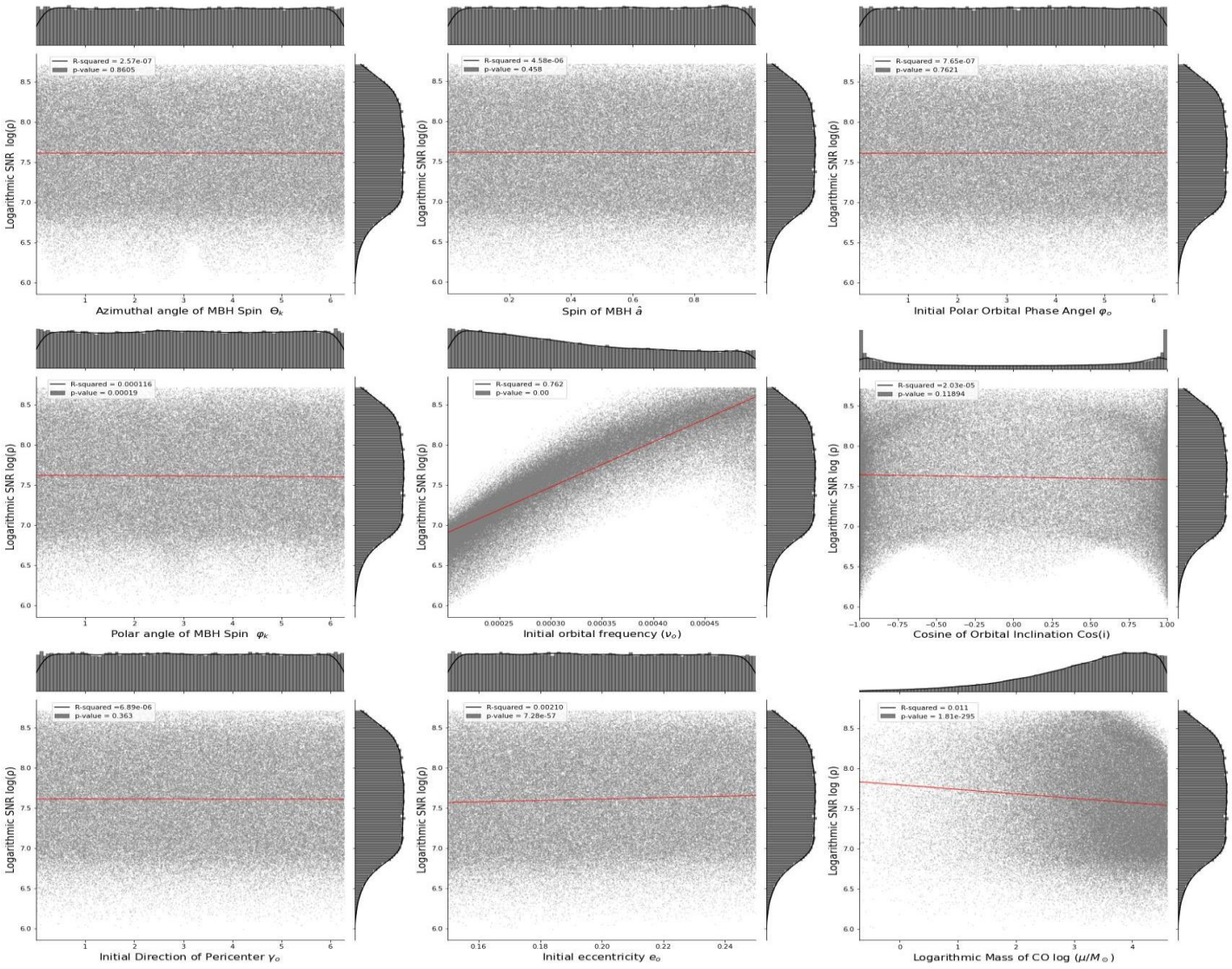


Fig 1: Scatter plots and marginal histograms of independent parameters with dependent SNR ρ. Red line is used for regression line establishing a correspondence between parameters and SNR. (continued from previous page)

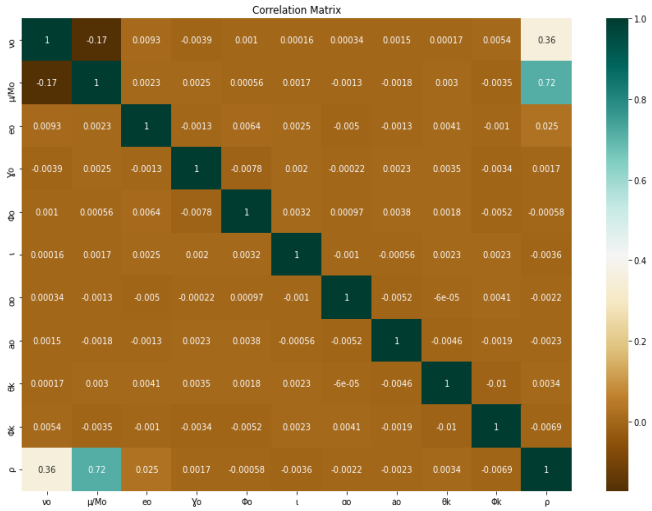


Fig 2: Heat-map and Correlation Coefficient Matrix, Negative correlation exists between μ/M and ν_o , Clearly, SNR ρ is highly sensitive to μ/M and ν_o

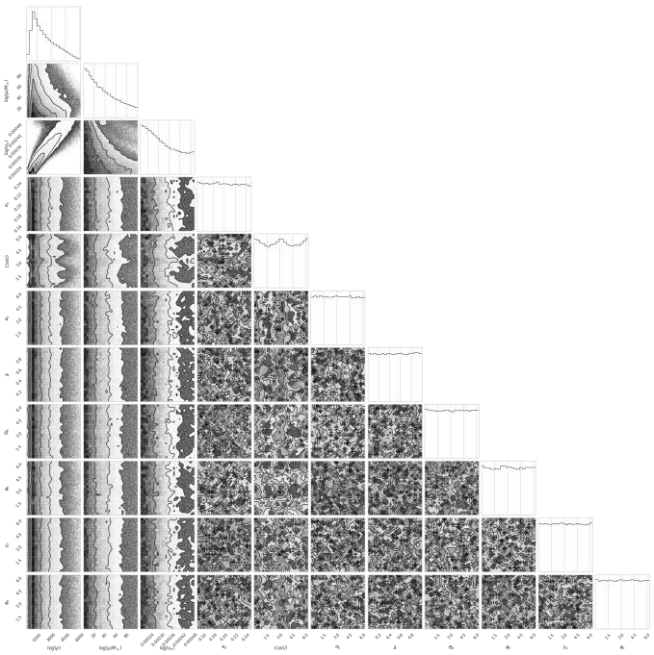


Fig 3: Corner Plot of EMRIs parameter and their mutual Correlogram: Statistical Density Contour Variation, diagonal represent 2-D posterior distribution.

TABLE I. STATISTICAL P ARAMETRIC CORRELATION ONTO THE SNR

Parameters	R-squared	p-values
ν_o	.762	0
ln μ	.011	1.81×10^{-295}
e_o	.0021	7.28×10^{-57}
γ_o	6.89×10^{-6}	.363
φ_o	7.65×10^{-7}	.7621
Cos(i)	2.03×10^{05}	.1189
α_o	8.95×10^{07}	.743
$S/M^2 = \hat{a}$	4.58×10^{-06}	.458
θ_k	2.57×10^{-07}	.8605
φ_k	.000116	.00019

If $p<<0.05$, indicates strongly significance, if $p \leq 0.05$ it is just significant.

B. *Back-of-Envelop Estimates of SNR*

At time of capture of CO, semi-major axis is calculated for for each EMRI simulation. To approximate the fiducial-fit, quantitatively, it is better to use a parameter of gravitational radius r_g to understand the the initial orbit dynamics in terms of influence radius of MBH. EMRIs event rate sweeps between the semi major axis range in terms of gravitational radius is $8.81r_g \leq a \leq 16.24r_g$. Semi-major axis a, mass of CO , initial orbital eccentricity e_o , cosine of orbital inclination cos and spin of MBH â contributes to our best fit model, and rest of the parameters are has no or very negligible contribution.

$$\log(\hat{\rho}) = -2.86\ (a / r_g) - 0.026\log(\mu/M_{\odot}) + .75\ e_o - .031\ \mathrm{Cos}(i) + .005\ \hat{a} + 14.5 \quad (5)$$

Power law was generated by using multiple linear regression method with (forward and back-ward) step-wise approach. The best fit line was drawn using a generalized linear model (glm–function) based on Gaussian error distribution. EMRI signal is sensitive to each parameter of the model.

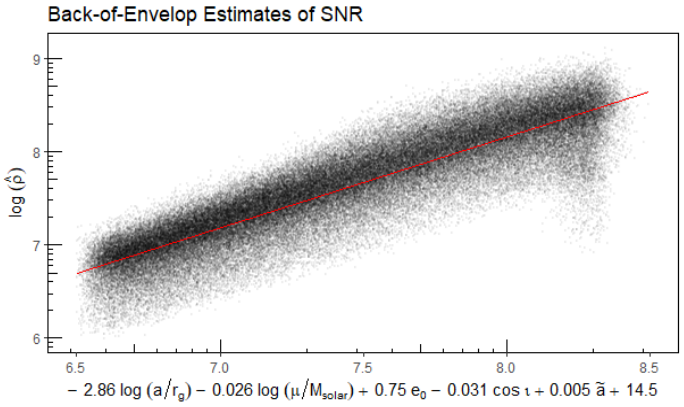


Fig 4: Mass–normalized SNR as a function of parameters obtained by GLM **a, cosi, μ, e_o** . Red line corresponds to the best–fit estimates $\log(\hat{\rho}) = -2.86\ (a / r_g) - 0.026\log(\mu/M_{\odot}) + .75\ e_o - .031\ \mathrm{Cos}(i) + .005\ \hat{a} + 14.5$ of SNR. Radial parameter ranges between $8.81r_g \leq a \leq 16.24r_g$

Most influential parameter is semi-major axis a be the to estimate SNR. It is anti correlated with SNR, closer initial orbits will result in louder EMRI event. Negative weak dependency exist between CO's mass and SNR even though our results are mass normalized. It indicates that mass normalized SNR of an EMRIs still, slightly, varies with CO's mass. Strong Mass Segregation (SMS) may or may not be the reason of this effect. e_o increasingly contributes to SNR with relatively stronger regression coefficient. Spin remains highly uncertain parameter proportionally relates with positive coefficient but for higher spin distributions the term will not significantly impact SNR. Likewise, bi modal distribution of inclination angle confines, typically, at maxima's will remain trivial to the best-fit.

C. *EMRI Events In LISA Mission Life Time*

In upper panel of Figure 6.5 express SNR distribution of probabilistic EMRIs for 10^5 mission realizations in LISA sensitivity band. $\rho = 20$, was set to be the threshold limit of detection, all EMRIs are louder then this limit and hence detectable. AS M32 is very near to earth so it is an expected trend to observe **D.** = .77Mpc. The expectation of high maximum SNR is observed at $\rho_{max} = 4.7 \times 10^6$ with median value at ρ median = 59829 for 10^5 realizations, simulated for set of 10 parameters. SNR remains loud even for a single detectable EMRI during mission lifetime.

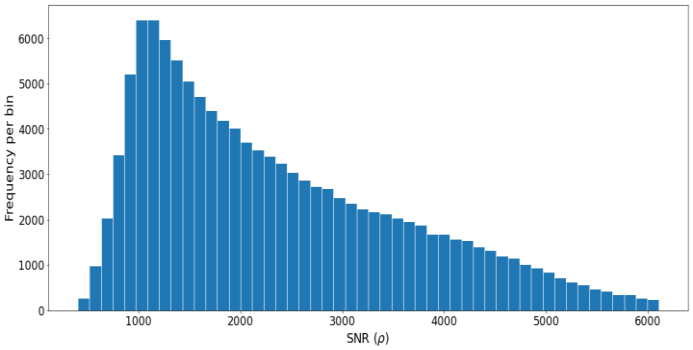


Fig 5: Histogram expressing SNR distribution of probabilistic EMRIs for 10^5 realizations with LISA sensitivity.

We calculated EMRI event rate for 2 years LISA mission life, and calculated $N_{EMRI} = 9.39$ per year. Decimal part of the result is unrealistic, event rate of 9.39 per year is averaged for 10^5 mission realizations. To observe the probability distribution of event rates, We increase the event rate by factor of 10000 and expressed in 6.5. The distribution is in agreement with the Poisson distribution.

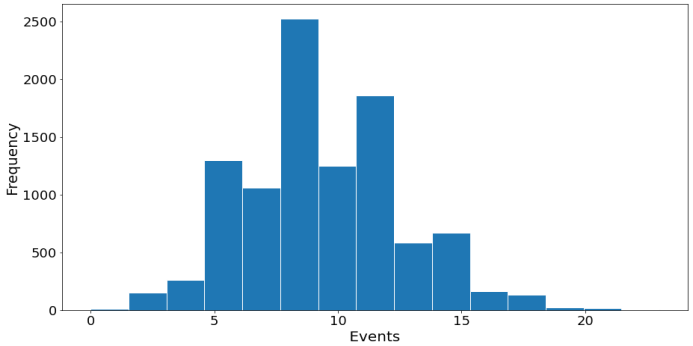


Fig 6: Poisson probability distribution normalized over 10^5realizations for number of EMRI events N EM RI = 9.39 per year be detectable in ISA frequency band form GC of M32 over mission duration of 2–years.

GR manifests the classical theory of gravity associated with the curvature of the manifold and provides precise

measurements in for testifying strong gravity. There exists no turntable parameters in GR besides Newton's Gravitational constant that gives definite predictions. Thus tests to GR have strong implications probing new physics. Since, GR might not be the ultimate theory of gravity, confronting such tests of GR in a strong gravity regime is therefore consequential. These tests correspond to the low energies and scales much shorter than Planck length. At present, there is no finalized theory of quantum gravity. Statistical considerations of EMRIs thus quantifies the modifications to general relativity. GWs studies are dependent on matched filtering techniques too, in available waveform models. Waveform models are very sensitive to slightest changes in orbital evolution of COs. These effects will be apparent by the mismatching of signal with theoretical models.

Having frequent occurrences of EMRIs at lower red shifts z, investigating the waveform templates will allow us to measure luminosity distance D L (z) within 10% precision and few square degrees of the sky localization. The distance of the source can be deduced from the amplitude of the signal, z, in turn, can be measured. The data can be used to compute cosmological parameters like Hubble constant H_o . Difficulty lies in the absence of EM counterparts of EMRIs. However, the analysis can be done by associating the independent red shifts measured by available EM data from the galactic catalog that makes use of a cluster of the galaxies correlating to the cosmic web, at particular z, to spot the MBH hosting EMRI.

ACKNOWLEDGMENT

This research was conducted under the supervision of Dr.Asad Ali. He provided the simulation source code based on his previous studies in the context of MLDC round 4. We acquired the knowledge of Galactic EMRIs and methodology to compute SNRs from Rafia Sarwar. Dr.Fazeel Mehmood Khan helped us sorting the queries and checking the consistency of scaling relations used.

References

[1] John Kormendy, and Luis C. Ho, "Coevolution (Or Not) of Supermassive Black Holes and Host Galaxies", Annual Review of Astronomy and Astrophysics, vol. 51, pp. 511–653, August 2013.

[2] Stanislav Babak et al., "Science with the space-based interferometer LISA. V. Extreme mass-ratio inspirals", Physical Review D, vol 95, pp. 103012, May 2017.

[3] Pau Amaro-Seoane, "Detecting Intermediate-Mass Ratio Inspirals From The Ground And Space". Phys. Rev. D, vol. 98, pp. 063018, September, 2018.

[4] C. P. L. Berry, and J. R. Gair, "Observing the Galaxy's massive blackhole with gravitational wave bursts", Monthly Notices of the Royal Astronomical Society, vol. 429, pp. 589–612, February 2013.

[5] L. Barack, and C. Cutler, "Lisa capture sources: Approximate waveforms, signal-to-noise ratios, and parameter estimation accuracy", Phys. Rev. D, vol. 69, pp. 082005, April 2004.

[6] Pau Amaro-Seoane, "Relativistic dynamics and extreme mass ratio inspirals". Living Reviews in Relativity, vol. 4, May 2018.

[7] David Merritt, "Dynamics of galaxy cores and supermassive black holes". Reports on Progress in Physics D, vol. 69, pp. 2513–2579, August 2016.

[8] J. R. Gair, Christopher Tang, and Marta Volonteri, "LISA extreme-mass-ratio inspiral events as probes of the black hole mass function", Phys. Rev. D, vol. 81, May, 2010.

[9] Clovis Hopman, "Extreme mass ratio inspiral rates: dependence on the massive black hole mass", Classical and Quantum Gravity, vol. 26, April 2009.

[10] J. R. Gair, "Probing black holes at low redshift using LISA EMRI observations", Classical and Quantum Gravity, vol. 26, April 2009.

[11] Curt Cutler, "Angular resolution of the LISA gravitational wave detector", Physical Review D, vol. 57, pp. 7089–7102, June 1998.

[12] S. Gillessen et al., "An Update on Monitoring Stellar Orbits in the Galactic Center", The Astrophysical Journal, vol. 837, February 2017.

[13] F. Yusef-Zadeh, D. Choate, and W. Cotton, "The Position of Sagittarius A $*$ at the Galactic Center", The Astrophysical Journal, vol. 518, pp. L33–L35, May 1999.

[14] Ali, A., Christensen, N., Meyer, R., and Rover, C., "Bayesian inference on EMRI signals using low frequency approximations", Classical and Quantum Gravity, vol. 29, pp. 145014, June 2012.

[15] A. Ali, "Bayesian Inference on EMRI Signals in LISA Data", PhD thesis, The University of Auckland, New Zealand, 2011.

[16] R. O. Hansen, "Multipole moments of stationary space-times. Journal of Mathematical Physics", vol. 15, pp. 46–52, 1994.

[17] Christopher P. L. Berry et al., "Astro2020 Science White Paper: The unique potential of extreme mass-ratio inspirals for gravitational-wave astronomy", White paper submitted to Astro2020 (2020 Decadal Survey on Astronomy and Astrophysics), March, 2019.

[18] Igor D. Karachentsev, Dmitry I. Makarov, and Elena I. Kaisina. Updated nearby galaxycatalog.The Astronomical Journal, 145(4):101, Mar 2013.10.1088/0004-6256/145/4/101.ISSN 1538-3881.doi:URL http://dx.doi.org/10.1088/0004-6256/145/4/101.

[19] Lee S. Finn, "Detection, measurement, and gravitational radiation" Phys. Rev. D, vol. 46, pp. 5236–5249, December 1992.

Strategizing Pakistan's Space Policy for Defensive Discourse: A Case Study of Pulwama-Balakot Crisis

Noor Ul Huda Atif
Centre for International Peace and Stability
National University of Science and Technology
Islamabad, Pakistan
nooratif96@gmail.com

Abstract— ***Outer space is a rapidly developing frontier that offers opportunities in all aspects of commercial and strategic domains. A well-established policy, which adheres to an appropriate strategy, proves to be helpful in realizing these opportunities. For a state such as Pakistan, that relatively has a small-scale space program with handful of satellites, which bear the burden of providing both commercial and strategic support to country, it requires a well-planned policy to exploit outer space technology emerging in international security domain. Pakistan should advance its space program for the strategic and defensive discourse as the hostile acts of the adversary in the region grows as evidently witnessed in the Pulwama-Balakot Crisis of 2019. The National Space Policy of Pakistan provides a framework for the development and launch of Lower Earth Orbit (LEO) and Geo-synchronous satellites, yet it lacks in various aspects of defensive strategy. It requires revision to reach technical advancement taking place in the field of space sciences leading to the development of Anti-Satellite (ASAT) weapons. While emerging technologies are making way into the international security, incidents like Balakot strike 2019 suggests that Pakistan should direct its space policy for its security and take a defensive discourse to devise a revised space policy. This paper resolves to explore the options for Pakistan to devise a defensive space policy that secures the space assets and the country.***

Keywords— Space Policy, Pakistan Space Policy, Defensive discourse, Discourse Analysis, Pulwama-Balakot, National Space Policy

I. INTRODUCTION

Outer space serves as an unknown, mysterious frontier for humans, yet to be completely explored, developed and exploited. In the short while of the space ventures, the exploitation of outer space ousted the exploration and development mainly due to the militarization, which gained momentum given the space race. The space policies of USSR and US revolved around the newly initiated space race rather than space security and sustainable use for a better future. Over the time lack of effective policy and strategies for the use of space led to placement of spy satellites and Anti-Satellites (ASAT) for offensive and defensive measures. A comprehensive space policy entails the elements of national security, defense, science and technology, research and development, academics and education and the law and advocacy. Like any other international affair, the astropolitics around the formulation of space policy during the Cold War era has had overwhelming influence on South Asian region.

South Asia has been a hot seat of geopoliticatl conflicts historically. Ever since the independence in 1947 following the separation of subcontinent, the two new states with grievances, grudges and completely different ideologies were born. This rivalry between two newly created states was due to a flash point in the form of unresolved territorial dispute of Jammu and Kashmir. Over the time, the states of Pakistan and India instead of resolving the disputes have only amplified enmity through the increased military prowess and stockpiles of conventional and unconventional arms that has led to increased strategic instability in the region. The near equal military expertise and built up has sustained deterrence in the past seven decades however, the imbalance of space capabilities between both countries account for an effective space policy directed to enrich the space program of Pakistan with strategic space assets capable of performing Intelligence, Surveillance and Reconnaissance (ISR) for the armed forces.

India and Pakistan share belligerent relations, which have the tendency to aggravate over the slightest event. Evidently, a large scale bombing at a military convoy in Pulwama, Illegally Indian Occupied Kashmir (IIOJK) led to military escalations on both sides of border initiated by the Indian Air Force, as they released payload at Balakot, an area in the Khyber PakhtunKha (KPK) province. The initial scanning of the area was conducted via the PRSS-1, the only strategic remote sensing satellite of Pakistan, which enabled Pakistan to effectively deny the false Indian allegation of destroying a Madrassa harboring 350 terrorist [1]. The incident emphasizes on the significance of strategic space assets and is used as a case study for the initiating a defensive discourse among the policy-makers in this paper.

II. PULWAMA-BALAKOT CRISIS-2019

India and Pakistan share confrontational relations since partition with Kashmir being the flash point. The seven decades of independence of both states have seen severed diplomatic, economic and military ties and 2019 only added to the fuel. As the Indian Prime Minister Narendra Modi prepared for elections in April 2019, Pakistan anticipated that the reflection of his anti-Pakistan rhetoric would manifest into a mishap that will help PM Modi gain the popular vote for a second regime in India as Prime Minister.

On 14 February 2019, a suicide bomber hit an Indian Army convoy at Lethpora in the Pulwama district of Illegally Indian Occupied Jammu and Kashmir (IIOJK). Immediately

after the attack, Indian media resorted to its usual banter against Pakistan. The venomous Indian media as always took the opportunity to accuse Pakistan of the Pulwama attack where 40 soldiers of Indian armed forces had died. Pakistan however, denied the Indian allegations and condemned the attack that was intentionally being blamed to aggravate the fire of belligerence between both states.

On 19 February, the Prime Minister of Pakistan Mr. Imran Khan attributed the Pulwama attack to Indian government's desire of conducting a false flag operation against Pakistan for the upcoming elections, as had been anticipated. Pakistan was prepared for a false flag operation by India given the deteriorating political and military morale on other side of border [2].

The Indian Air Force (IAF) in the early of 26 February 2019 intruded into the international borders of Pakistan and conducted a failed attempt at neutralizing an alleged terrorist training camp in Balakot, Khyber PakhtunKha, Pakistan. According to Pakistan, the Air force intercepted three Indian Air Force teams attempting to enter the Pakistan at various sectors. Pakistan Air Force apprehended two of the three teams at the border by the combat air patrol aircraft, where the third one was able to cross the Line of Control (LoC) from the Kiran Valley near Muzzafarabad. However, the other two intercepted teams propelled the third team to retreat, flee the scene releasing their payload, and dump their fuel in an open area missing their said target. The Indian Air Force, government and media claimed to damage a militant training camp in Balakot killing 350 militants under training. However, their claims were rendered catatonic by the international media, defence analysts and organizations. In this particular case, the satellite technology proved to be a valuable asset to silence the false prerogatives of India [3].

The 27 February 2019, Indian Air Force again attempted the same stunt of entering the borders of Pakistan challenging the country's sovereignty. This time they met with the JF-17 fighter aircraft formations rather than the patrolling aircrafts of Pakistan Air Force (PAF). The confidence from their previous attempt compelled them to conduct airstrikes in the broad daylight; however, they were apprehended and chased away by the PAF aircrafts. The aircrafts engaged in an air combat where the Pakistan shot down a Mig-21 and a Su-30MKI aircrafts of Indian Air Force and captured an Indian Air Force pilot.

A. Technical Component of Air-Combat

The Pulwama-Balakot crisis and the air combat that followed it were dependent on two main elements of the technology: the satellite imagery and remote sensing technology and secondly, the high-tech combat aircrafts. The air combat that was considered a conventional air combat hinted towards an electronic war where modern technology had a significant role to play. The high imagery from satellites essentially established that IAF had wrongfully entered Pakistan challenging its sovereignty and damaging cultivation in the early hours of 26 February 2019. The high-resolution satellite images from various satellites around the world confirmed that no infrastructural damage was adhered during the Indian intrusion. On 27 February 2019, the high-tech combat equipment employed in the aircrafts played a significant role in Operation Swift Retort.

1) Role of Satellite Technology in Crisis

Within a few hours of attack, Pakistan using its only strategic satellite employed with the Remote Sensing Capabilities, PRSS-1 was able to detect the region where the Indian Aircraft released its payload, damaging cultivation. The satellite images from PRSS-1 confirmed that there was no infrastructure damage on ground and area, which was repeatedly being claimed by the Indian media. Later the high-resolution images taken by the European Space Imaging on the next day of strikes also established that there were no signs of casualties and no infrastructural damage on the site. The Australian Strategic Policy Institute, while analyzing the satellite data from WorldView-2 satellite, rejected the Indian claim of the strike that killed 350 militant under training. Micheal Sheldon, a digital forensics analyst from Atlantic Council conducted an independent investigation on the issue and stressed that the target site showed no signs of any infrastructure damage and that the botch was mysterious in the light of the autonomous nature of the supposedly used missiles. A major comparison was drawn by the Reuters, which conducted an investigation based on high-resolution satellite images by "Planet Labs". It showed images of the said target site from April 2018, compared them to the images of February 2019 after the strike, and concluded that the landscape was unchanged. The remarks made by Reuters were that "there were no discernible holes in the roofs of buildings, no signs of scorching, blown-out walls, displaced trees around the madrasa or other signs of an aerial attack". Satellite imaging and remote sensing played an essential role in the manifesting Indian propaganda against Pakistan.

2) High-Tech Combat Aircrafts

Anticipating that IAF would return with more confidently, Pakistan had already set up a trap of communication jammed environment for it. When the IAF aircrafts entered the region, they lost contact with one another and were unable to communicate back at the ground station. The multi-role JF-17 and F-16 aircrafts employed with high-tech combat equipment were able to bring down the Indian Mig and Sukhoi Fighter jets. The communication jammers blocked the signals to the aircraft radars which practically blinding the aircrafts. PAF's JF-17 fighter aircrafts though used under the conventional capacity during the Operation Swift Retort in 2019, are being upgraded to the electronic Warfare suit, which will enable it to be a smart machine and assess its situation and react to it [4].

III. Outer Space Policy for Pakistan

Outer space is an essential entity in the international security and the advance technological world and requires legitimization for its utility. The global importance of the domain has become evident as defining the future. The frontier that requires the immediate humanly attention is exploited more than its development and exploration with the change in global security architecture. As a global common, the outer space is an entity that holds significant value in the international arena in modern times mainly due to its ability to provide various services both for commercial and military purposes. However, the utilization of outer space requires a comprehensive set of guidelines, which adhere to the international laws and treaties. In a fragile region of South Asia, a comprehensive space policy will have to entail the main elements of national security and strategic stability. The hostile relations of the two states of

India and Pakistan negatively affect the regional peace and stability. The similar scenario in future can lead to severe consequences as India now has the Anti-Satellite weapon. India has made clear of its adversarial ambitions over time and Pulwama-Balakot crisis evidently suggests that it will be willing to make such an attempt again in the future.

Space acts as a force multiplier for the armed forces for the intelligence and reconnaissance missions. Defensive measures embedded in the space policy provide the modernization that is essential for the forces fighting wars in a technically advanced era. Pakistan's policy-makers and academia is in dire need of opening a discourse for a defensive space policy. Although a comprehensive policy comprises of various components, however, in this case it is evidently essential for Pakistan to follow the defensive discourse and open to measures for securing strategic and spatial assets from the threats emerging from space activities of adversary. Pakistan's missile capabilities evidently manifest that the country is proficient enough to enrich its space program with strategic satellites employed with ISR capabilities.

A. Pakistan's Space Vision

Pakistan as a nascent space state is determined to broaden the horizon of its capabilities in the field of space technology. The increasing significance of outer space in technically advanced era specifies the growth of modern technology with the influence of command, control and communication. The dual-purpose satellites, including the commercial and strategic spatial assets and satellites evidently strengthen the national security.

Pakistan's Space Vision was developed in 2011 with the aim of utilizing space for socio-economic benefits. Pakistan has been geo-strategically a significant state in the international security events that accounts for high-tech military gains. The recent event of Balakot strike and the following Operation Swift Retort, where the adversary has used coercive measures to entice through its belligerent actions is compelling enough to incorporate the strategic and defensive measures into the vision plan. The 'space vision' functions by an operational framework of Pakistan's Space of Program -2040. Under this framework, Pakistan has set its ambitions of developing and launch of certain quantity of satellites. This framework will provide the institution with the roadmap for development of five Geo-stationary satellites that may include the multi-purpose and navigation satellites and six Low Earth Orbit (LEO) satellites which will include the remote sensing and optical remote sensing satellites and the communication satellites.

The space vision that was initially named the space vision 2040, was to ensure the research and development of said eleven satellites by the year 2040, which is a very minimal quantity. As a nascent space faring state, Pakistan is to engage in large number of space assets and satellites that can match the advance high-tech satellites in space by the adversary. The emerging space technology as an essential component of the international security manifests threats emerging from space for Pakistan from the adversary in the region [5].

The space vision that was initially named the space vision 2040, was to ensure the research and development of said eleven satellites by the year 2040, which is a very minimal quantity. As a nascent space faring state, Pakistan is to engage in large number of space assets and satellites that can match the advance high-tech satellites in space by the adversary. The emerging space technology as an essential component of the international security manifests threats emerging from space for Pakistan from the adversary in the region.

B. A Defensive and Strategic approach

For Pakistan, a strategic and defensive approach to the space policy entails the security to space assets, ground systems, control and command centre, strategic assets and their movements and the terrestrial humans. Spatial defense measures are enhanced through the thrust areas of intelligence, surveillance, reconnaissance and navigation. Exploitation of space for real-time military utilization has significant advantages. It gives an upper edge over the adversary in the communication aspect and the reconnaissance missions. Real-time spatial information used efficiently can be significantly employed for early-warning missile attacks, deliverance of precision guided munitions through satellite signals, or jamming enemy networks.

Space technology is specifically essential for the Air Force and acts as a force multiplier by allowing battlefield situational awareness through space communication and space sensors. The link established between the fighter aircrafts and electronic radar satellites allows communication with network centric systems across the country. The assistance in Ballistic Missile Defence system is a significant role of space technology. The imperative of space situation awareness is essential for gathering real-time intelligence on the adversary aircraft, missiles and space borne threats from the Anti-Satellites weapons. As in the case of Operation Swift Retort, PAF resorted to jamming the communication and radar systems of adversary aircrafts, similarly, the space assets can also be rendered inoperable by resorting to jamming that gives an upper edge.

C. Current R&D to modify the Defensive Measures

The direction of the space policy currently can be estimated through the budget of 2020-2021 and budget 2021-2022 for SUPARCO. Pakistan is determined to enhance its research and development in the field of space sciences and space technology. However, the lack of dedicated research centers and satellite development institutes are a hurdle in realization of the Pakistan Space Vision. In the year 2021, SUPARCO was authorized for the establishment of Space Application Research Center in Gilgit-Baltistan and Pakistan Space Center. These centers will be responsible to undertake the feasibility study and research for various satellite programs to be launched in future. These future projects under the research and development include the Pakistan Remote Sensing Synthetic Aperture Radar Satellite and Pakistan Satellite Navigation Program, Pakistan Multi-Mission Satellite (PAKsat-MM1), Pakistan Optical Remote Sensing Satellite (PRSS-02), advance system for PAKSat-1R Ground control segment and the development of Online Satellite Image Service. The Radar Satellite will develop Pakistan's reconnaissance and surveillance capabilities assisting the military in detection of friendly and adversary objects approaching. PRSS-1 is already employed as country's only strategic satellite and an Optical Remote Sensing Satellite PRSS-2 will enhance will strategic capabilities further [6].

IV. CONCLUSION

Pakistan's ISR capabilities lag in the space technology, which weakens the defence of state and the handful of spatial assets owned by the country. The incident of Pulwama-Balakot crisis evidently directs to the emergence of electronic warfare, where the victory will bselong to the technical sound side. In the incident, Pakistan mainly relied on the international media and analysts to decipher the satellite data and images in order to nullify the false Indian claims. If Pakistan had its own ISR capable satellite, the jet movements could have been intercepted in time and the incident could have been prevented from occurring. It is evident from the incident that ISR capable satellites play a vital role; they would have assisted in protection of state and land sovereignty. The policy-makers must incorporate the enhanced spatial defensive measures so to avoid such mishap in future as the adversary has progressed further since the incident with the development of Anti-Satellite weapon and various intelligence, surveillance and navigation satellite [7]. Along with that the Basic Exchange Cooperation Agreement (BECA) that will ensure the real-time geospatial information sharing between United States and India that will enable both the states to eye the naval and ground movements of Pakistan and China at Gwadar Port and the China-Pakistan Economic Corridor (CPEC) project. Pakistan Air Force is determined to upgrade the fighter aircrafts at par with the suit of electronic warfare where it will be able to configure its surroundings automatically, the additional linkage of space communication and information will enhance the interception and networking properties with the ground system. This combination will provide the intelligent combat property to the fighting aircraft. The satellites operating as the eyes in the sky will increase the functionality of the combat machines and provide amplified battlefield situational awareness.

Pakistan's strategic approach to the space assets requires a defensive path rather than the offensive one. India's offensive account as a space power threatens the strategic stability of the region and security of Pakistan. The current research and development requires a speedy process, which will enable the country to defend against offensive adversarial actions. The changing International security situation has once again increased Pakistan's geostrategic significance and hence the need of defensive spatial measures for the country.

V. REFERENCES

[1] SPD Official 1 (Militarization of Outer Space: threats to security of Pakistan and strategic stability of South Asia), interviewed by Noor Ul Huda Atif, SPD Head Quarter, Rawalpindi, 31 May 2019.

[2] "After Balakot, Pakistan Threatened to Respond to India's Six Missiles 'Three Times Over': Report", News 18, accessed April 4, 2019, https://www.news18.com/news/world/pakistan-threatened-to-respond-to-indias-six-missiles-three-times-over-report-2071289.html.

[3] "Indian aircraft violates LOC, scramble back after PAF's timely response: ISPR", *Dawn News*, Accessed 4 August 2021, https://www.dawn.com/news/1466038

[4] Pakistan Air Force Officer (Strategizing Pakistan's Space Policy for Defensive Discourse), interviewed by Noor Ul Huda Atif,, 21,August 2021

[5] Emerging Issues, 2012. "Regulation of Space Activities," no. September

[6]Khan, Javed Iqbal. "Federal Budget Publication." Federal Budget 2021. Finance Division , 2021.

[7] Express Web desk, "What is Mission Shakti-ASAT," *The Indian Express*, March 27,2019, accessed June 22,2019, https://indianexpress.com/article/what-is/mission-shakti-asat-missile-5645166/

Multi-GNSS Navigation Performance Assessment and Improvement Quantification

Arif Hussain
GNSS and Space Weather Lab
Sukkur IBA University,
Sukkur, Pakistan
arif.hussain@iba-suk.edu.pk

Syed Hadi Hussain Shah
Department of Electrical and Computer Engineering
Muhammad Ali Jinnah University,
Karachi, Pakistan
hadi.shah@jinnah.edu

Hina Magsi
GNSS and Space Weather Lab
Sukkur IBA University,
Sukkur, Pakistan
hina.phdees21@iba-suk.edu.pk

Arlsan Ahmed
GNSS and Space Weather Lab,
Sukkur IBA University,
Sukkur, Pakistan
arlsan-ahmed@iba-suk.edu.pk

Faheem Akhtar Chachar
Department of Electrical Engineering
Sukkur IBA University,
Sukkur, Pakistan
faheem.akhtar@iba-suk.edu.pk

***Abstract*— The Global Navigation Satellite Systems (GNSS) offer an easy, efficient, and cost-effective way to determine the location, time, and velocity anywhere around the globe. However, the existing systems have only been successful in outdoor or open-sky environments and often lack consistency in maintaining the required navigation performance (RNP) thresholds in urban contexts where availability and accuracy of GNSS are degraded due to signal blockage, multipath (MP) effects, and NLOS reception. In recent years, GNSS technology has undergone remarkable developments in terms of satellite constellations, signal quality and transmission, receiver technology and positioning estimation techniques. The completion of emerging navigation systems (i.e., BeiDou and Galileo) along with the modernization of existing constellations (i.e., GPS and GLONASS) promises significant improvements in satellite visibility, geometry, quality of navigation signals, and thus overall localization accuracy. The aim of this paper is to record, quantify and compare the performance of satellite-based navigation systems in single and multi-GNSS mode under different operating environments. For this purpose, a series of field experiments are carried out in multi-GNSS and GPS-only mode with total observation period of 24 hours and 864,000 data samples at standard open-sky and degraded site (i.e., surrounded by high-rise buildings). In the multi-GNSS mode, all four global constellations (i.e., GPS, GLONASS, Galileo and BeiDou) are utilized simultaneously for the first time over Pakistan. The performance assessment in this paper is carried out using fundamental quality indicators, e.g., satellite visibility or service availability, satellite geometry in terms of PDOP, and statistical accuracy measures (i.e., Circular Error Probable (CEP) and Distance Root Mean Square (DRMS)). The results of performance assessment indicate that combining multiple satellite constellations in multi-GNSS mode results in increased satellite visibility/availability, better geometry and thus significantly improved localization accuracy. It is then further analyzed that increased satellite availability in multi-GNSS mode may not result in consequential improvements in positioning accuracy at standard open-sky environment, however, significant improvements were observed at the degraded site. The statistical accuracy of reported positions was found to be improved by five times and outages were reduced by almost 50% of the observation period in the multi-GNSS mode at the degraded site.**

Keywords— GNSS, Performance Assessment, Positioning Accuracy, Environment Contexts.

I. INTRODUCTION

The positioning and navigation technologies have become more prevalent and pervasive in our modern and technology-driven society. The significance of accurate, reliable, and uninterrupted localization and navigation services is obvious for certain applications such as road, rail, aerial and marine transport, precision agriculture, surveying and multi-modal logistics [1]–[4] , but certain high-tech and safety-critical applications such as autonomous driving architectures (i.e., Unmanned Ariel vehicles, auto-bot), intelligent transportation systems, e-Health, Geo-fencing and other safety-critical applications majorly rely on accurate positioning and precise navigation to carry out essential operations [5]–[8]. Among the numerous technical solutions to precise positioning and navigation [9], [10],the Global Navigation Satellite System (GNSS) has established itself as an efficient and cost-effective technology for outdoor navigation.

The GNSS is long-established, prevalent and all-weather satellite-based navigation system that determines the location, time and velocity anywhere around the globe. The first satellite based navigation (Global Positioning System (GPS)) was declared fully operational system in 1995 with a constellation of 24 satellites in Medium Earth Orbit (MEO) [11], [12]. However, poor positioning performance i.e., limited availability and degraded accuracy was a major hurdle to the practical realization of GPS in several critical applications [13], [14]. In recent years, the landscape of satellite-based positioning has experienced dramatic changes and advancements in terms of satellite constellations, signal transmission, quality of signals, receiver technology and mitigation models [15]. As of 2020, the GNSS has grown from the U.S. GPS - only system to four independent global constellations including the Russian GLONASS, European Galileo, and Chinese BeiDou, leading to remarkable boost in satellites availability. Besides four global constellations, there are further regional i.e., QZSS (Japan), IRNSS (India) and Satellite Based Augmentation Systems (SBAS) substantially aiding the availability and accuracy. Compared to the early 2000s, when a single constellation receiver (GPS-only) relied on less than 10 satellites to estimate a positioning solution [16], [17], now a multi-constellation GNSS receiver (GPS+GLONASS+Galileo+BeiDou) can acquire more than 30 satellites on a given geo-location [18]. Furthermore, GNSS modernization has enabled signal transmission at multiple

frequencies, increasing capability in terms of signal acquisition, atmospheric correction, multi-path detection, resilience to interference and precise positioning. The modernized radio navigation signals are stronger, accurate and more resilient to natural or man-made interference [19]. These notable advancements in satellite-based navigation systems in terms of satellite constellations (i.e., Satellite visibility and geometry), signal transmission, quality of signals and receiver technology promise significant improvements in GNSS performance.

Keeping in view above fact, this experimental case study is intended to assess, quantify and compare the performance of a GNSS receiver in a single (GPS) and multi-GNSS mode in different signal reception conditions. For this purpose, a series of field experiments are carried out at pre-surveyed and carefully selected experimental sites i.e., standard open-sky and degraded environment. At first, the GNSS performance in both configuration modes is evaluated at nominal open sky and degraded environment (i.e., surrounded by high rise buildings) using fundamental quality indicators, e.g., satellite visibility or service availability, satellite geometry in terms of PDOP, and statistical accuracy measures (i.e., Circular Error Probable (CEP) and Distance Root Mean Square (DRMS)). Then, in order to compare the resilience of multi-constellation GNSS with single-constellation under degraded environmental conditions, the improvement in navigation performance due to combination of all four satellite constellations is computed and compared with reference to GPS-only mode.

II. GNSS PERFORMANCE ASSESSMENT METHODOLOGY AND FIELD EXPERIMENTATION

This section presents a detailed overview of the performance assessment framework adopted in this paper, fundamental quality indicators of GNSS and field experimentation which includes the details of the technical equipment and candidate sites on which experiments are performed.

A. Performance Assessment Framework

The availability and accuracy of GNSS-based localization and navigation is highly influenced by several systematic errors (e.g., clock biases, orbital errors and receiver noise), atmospheric effects (e.g., ionospheric scintillation, solar and geomagnetic storm) and environmental factors (blockage, fading, multi-path and/or NLOS reception), all of which can lead to serious inaccuracies or even outages in navigation services [20], [21]. The scope of this research is limited to investigation of environmental factors by analyzing fundamental quality indicators of GNSS i.e., satellite visibility, service availability, PDOP and statistical accuracy measures.

1) Satellite Visibility (N): Satellite visibility represents the number of satellites that can be acquired or tracked at a given geo-location and time of the day. It has direct and determinable effects on accurate positioning and precise navigation. With more satellites on hand, better positioning accuracy can be achieved by selecting a group of potentially strong satellites [18].

2) Service Availability: For proper operation and accurate positioning and navigation solution estimation, a GNSS receiver requires a minimum number of satellites and below these thresholds, the receiver experiences outages. Specifically, a minimum of 4 and 7 satellites are required for single and quad-constellation mode respectively to estimate the navigation solution [22]–[24]. The availability can be defined as percentage of time that the services of the system are available to user, which is an indication of the ability of the receiver to provide reliable positioning information. In this paper, the service availability is characterized and quantified by two events i.e., Tracking and outage.

- **Tracking :** $N \geq N_{TH}$
- **Outage :** $N < N_{TH}$

Where, N represents the number of tracked satellites and N_{TH} shows the satellite threshold or minimum number of satellites required for successful operation. For single-constellation $N_{TH} = 4$ and quad-constellation $N_{TH} = 7$.

3) Position Dilution of Precision (PDOP): The satellite geometry, which indicates the spatial distribution or actual geometric locations of the satellites in the sky as perceived by the GNSS receiver, contributes significantly to the overall accuracy of the navigation solution. For given number of satellites, the poor geometric distribution (i.e., satellite clustered together in the one part of sky) results in degraded positioning accuracy and the severity of this effect is usually estimated by Position Dilution of Precision (PDOP). The PDOP is geometrically determined factor that refers to positioning inaccuracies caused by degraded spatial distribution of satellites [25]. The better geometric distribution (i.e., satellites spread over sky) yields a lower PDOP value while higher PDOP values are the indication of degraded satellite geometry. From estimated/reported coordinates (i.e, x, y, z), the PDOP can be calculated as.

$$PDOP = \sqrt{{\sigma_x}^2 + {\sigma_y}^2 + {\sigma_z}^2}$$

where, σ^2 represents the variance.

4) Statistical Accuracy: The accuracy is the key parameter of the navigation performance that measures the deviation/dispersion in the reported position with reference to the true/mean positions. It is the statistical measure of performance that is associated with the probabilistic distribution of positioning error. In positioning and navigation systems, accuracy usually refers to the radius of circle around a mean/true position also referred as confidence region. The smaller the radius of region or circle, the higher the accuracy [26]. In this study, two most commonly used accuracy parameters i.e., Circular Error Probable (CEP) and Distance Root Mean Square (DRMS) are used for performance assessment.

a) Circular Error Probable (CEP): The CEP is a fundamental statistical accuracy measure and is defined as the radius of a circle, centered on the true position and expected to include 50% reported positions. For example, if a CEP of 3 m is mentioned and 2000 solutions are computed then it is highly expected that 1000 values will in a circle having radius of 3 m [18], [27]. Using the standard deviation (σ) of estimated coordinates, the Circular Error Probable can be estimated as

$$CEP = 0.62\sigma_x + 0.56\sigma_y$$

b) *Distance Root Mean Square (DRMS):* The DRMS is

a two-dimensional accuracy parameter that includes the 65% of reported positions within the confidence region [18], [27] It is estimated by taking the square root of the average of squared positioning errors.

$$DRMS = \sqrt{\sigma_x{}^2 + \sigma_y{}^2}$$

where, σ^2 represents the variances of reported coordinates. An example of statistical accuracy of reported positions can be seen in Fig. 1. The positioning solution estimated at every epoch is plotted as blue point while the red and green circle show the CEP and DRMS respectively also known as confidence region.

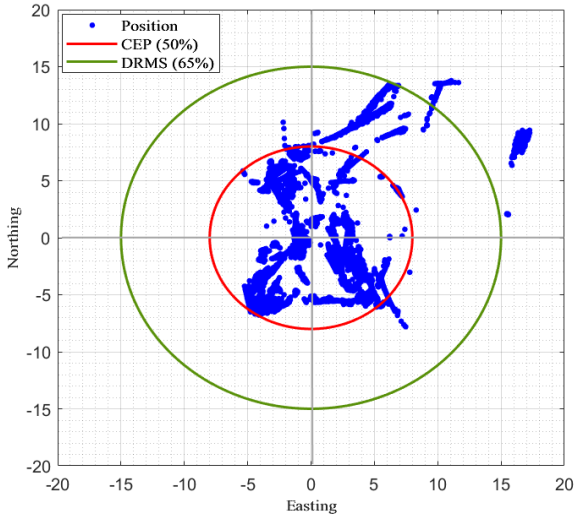


Fig. 1 Statistical Accuracy of reported position estimated in terms of CEP.

B. *Field Experimentation*

In this study, a total of four field experiments are conducted on two carefully selected experimental sites i.e., standard opensky and degraded environment. The first site i.e., open sky has excellent signal reception conditions with no blockage and mostly LOS reception as shown in Fig. 2(a). On the other hand, the second site (Fig. 2(b)) which is characterized as degraded environment has significant chances of signal obstruction and multipath/NLOS reception that can result in degraded navigation accuracy. These two experimental sites, namely Standard Open-Sky and Degraded Environment represent the two main operating environments for GNSS receiver. The details of each experiment performed are given in Table I.

The experimental setup used in this study is sown in Fig. 3, which consists of PolaRx5s GNSS receiver, high precision antenna and computing machines. In each experiment GNSS raw data was logged at the rate of 10 Hz for an observation period of six hours. The raw data is then processed and fundamental quality indicators are extracted for performance assessment.

TABLE I. FIELD EXPERIMENTATION

S. No.	Experimental site	Mode	Observation Period
1	Standard Open-Sky	GPS-Only	06 (Hours)
2	Degraded Environment	Multi-GNSS	06 (Hours)
3	Standard Open Sky	GPS-Only	06 (Hours)
4	Degraded Environment	Multi-GNSS	06 (Hours)

III. PERFORMANCE EVALUATION RESULTS

In this section, the navigation performance achieved by GPS-only and multi-GNSS receivers at two candidate sites is presented and discussed in detail.

A. *Performance Assessment in GPS-only mode*

The performance evaluation results of a GNSS receiver in GPS-only configuration and in terms of fundamental quality indicators such as satellite visibility or service availability, PDOP and standard accuracy measures (CEP and DRMS) over entire experimental period of 6 hours on both candidate sites are shown in Fig. 4. Fig. 4(a), (b) and (c) in the top half of figure shows the performance assessment results in standard open-sky environment which is characterized by the absence of reflective surfaces, and with optimal conditions for satellite tracking or acquisition (e.g., negligible obstructions) as shown in Fig 2. While, Fig. 4(d), (e) and (f) together represents the overall performance achieved by a GPS receiver on a degraded site having reduced satellite visibility and high probability of signal blockage and multipath effects due to presence of obstructions.

The satellite visibility along with service availability which is characterized by Tracking and Outage events are shown in Fig. 4(a) and Fig. 4(d) for Open-Sky and Degraded environments respectively. As expected, no outage at all was experienced by the receiver in an open sky environment during the entire observation period of 6 hours (00:00 – 06:00) due to optimal signal reception conditions. The average satellite visibility, N, was found to be 09 which is quite a good number as compared to required threshold for single-constellation receiver (i.e., N¿= 4). With adequate satellite visibility, there is a high probability of accurate estimation of positioning and navigation solution. On the other hand, the receiver experienced significant outages at the degraded site which can lead to disastrous consequences in safety-critical applications. As it can be clearly seen in Fig. 4(d), the receiver was only able to provide the positioning solution for less than 3 hours with the outage of almost 52% due to the presence of signal blocking scenarios as shown in Fig. 2. The average and maximum number of satellites dropped to 4 and 6 respectively and this limited satellite visibility may also result in poor



Fig. 2 The candidate sites used in the field experimentation; (a) Standard open-sky environment having excellent signal reception conditions (b) Degraded



Fig. 3 Experimental setup consisting of Septentrio's PolaRx5s Multi-constellation GNSS receiver used in the field experimentation to acquire GNSS data.

satellite geometry which ultimately contribute to more inaccuracies in positioning estimation.

The PDOP is a key index used for analyzing the effect of satellite geometry on the accuracy of positioning solutions. The obstructions present in between the satellite and receiver not only result in reduced satellite visibility but also affect the spatial distribution of satellites and yielding the poor satellite geometry which is indicated by a higher PDOP value. Fig. 4(b) and Fig. 4(e) show the reported PDOP value in open sky and degraded environment respectively for the observation period of 6 hours. In open-sky views, the PDOP value was found to be less 2 for more than 90% of observation time which is the indication of excellent geometric distribution of satellites and this was expected due to optimal environmental conditions with negligible blockage. However, at the degraded site, the extremely poor PDOP values were observed with average PDOP value greater than 10 which is normally considered as imperfect satellite geometry. The geometry of satellites in the sky and accuracy of positioning solution are highly inter-linked because the PDOP values determines the amplification factor of positioning errors. For the same number of satellites, poor geometric distribution can result in decreased positioning accuracy. Based on the PDOP values reported in both experiments in the single-constellation mode, it can be concluded that satellite geometry is significantly influenced by environmental conditions and it is more likely to be affected in urban or dense urban areas.

Once the satellite visibility and geometry are checked, the accuracy of the reported position is analyzed in open-sky and degraded environment cases. As expected, the adequate satellite visibility along with excellent geometry in open-sky case results in good accuracy of positioning solution. The accuracy of reported position in terms of CEP and DRMS is shown in Fig. 4(c) and Fig. 4(f). For the case of the open-sky environment, the values of CEP and DRMS were observed to be 1.15 m and 1.36 m respectively. In most navigation applications, the CEP of less than 1.5 m is usually considered as an acceptable level of accuracy. However, significant inaccuracies in positioning solution were reported at the degraded site due to severe signal obstruction, poor geometry and multipath signal reception. The value of CEP was around

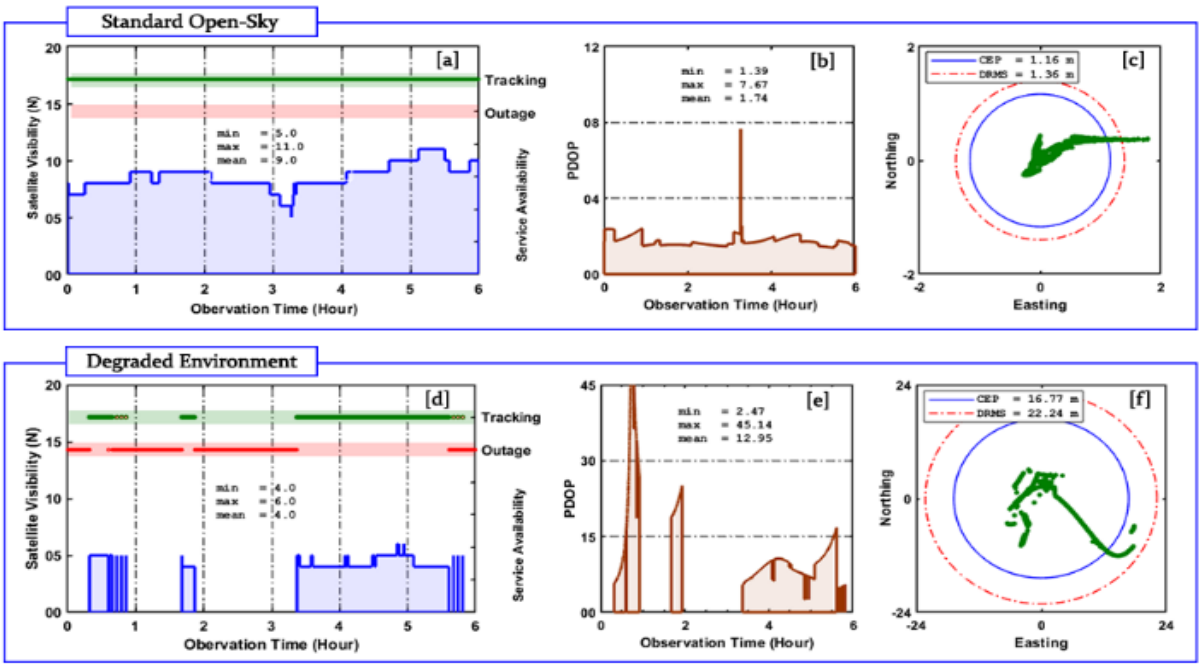


Fig. 2 The performance assessment of GNSS receiver in quad-constellation mode at standard open sky and degraded environment using fundamental quality.

16 m and DRMS was found to be 22.24 m at the degraded site which shows a quite large inaccuracy.

B. Performance Assessment in Multi-GNSS mode

The performance evaluation results of a GNSS receiver in multi-GNSS configuration and in terms of fundamental quality indicators such as satellite visibility or service availability, PDOP and statistical accuracy parameters (CEP and DRMS) over entire experimental period of 6 hours on both experimental sites are shown in Fig. 5. Fig. 5(a), (b) and (c) in the top half of figure shows the performance assessment results in standard open-sky environment while Fig. 5 (d), (e). and (f) represent the overall performance achieved by a GNSS receiver on a degraded site. The integration of all four satellite constellations such as GPS, GALILEO, BeiDou Russian GLONASS resulted in remarkable boost in satellite visibility and availability of direct Line-of-Sight (LOS) signals as shown in Fig. 5(a) and Fig. 5(d). As it can be clearly seen in Fig. 5, the increased satellite visibility results in reduced outages, better satellite geometry and thus improved positioning accuracy.

In both cases, the receiver was found to be in complete tracking mode without any interruption. The average satellite visibility, N, was observed to be 38 at open-sky and 24 at the degraded site which is a quite large number as compared to single-constellation where average satellite visibility was found to be less than 10 in both cases. Similarly, noticeable improvements were observed in satellite geometry; the PDOP value was found to be less than 1 for the whole observation period at open-sky site and less 2 for 90% of experimentation time at the degraded site as shown in Fig. 4(b) and Fig. 4(e) respectively. Interestingly, even at the open-sky site with almost same environmental conditions, the average PDOP value was reduced by around 54% due to increased number of tracked satellites. In the same way, at the degraded site, the average PDOP value was 1.77 which almost 7 times less than its counterpart in open-sky case. These are the very noteworthy improvements in satellite visibility and geometry which promise a significant accuracy enhancements even on the degraded sites.

The accuracy levels estimated for the reported position in multi-GNSS mode at open-sky and degraded site are shown in Fig. 5(c) and Fig. 5(f) respectively. As expected, the increased satellite visibility along with better geometric distribution resulted in significantly improved positioning accuracy. For the open-sky case, the accuracy parameters were found to be less than 1 during entire observation period of the experiment. In fact, almost 90% values of the estimated positioning solution were observed to be in confidence region having a radius of 0.4 m which is usually considered as highly accurate level of positioning accuracy in most of the navigation applications.

Compared to GPS-only mode at open-sky, the statistical accuracy was found to be improved by 1.7 times in multi-GNSS mode as CEP reduced to 0.80 m. Although, it is a very good improvement but GPS-only receiver also gives a sufficiently accurate positioning solution in open sky views. Compared to the GPS-only mode at open-sky, statistical accuracy was found to be improved by 1.7 times in multi-GNSS mode as CEP reduced to 0.80 m. Although, it is a very good improvement but GPS-only receiver also gives a sufficiently accurate positioning solution in open sky views. However, very noticeable accuracy improvements were observed at the degraded site in multi-GNSS in comparison with GPS-only receiver configuration. The availability of redundant range measurements due to combination of all four satellite constellations resulted in significantly improved accuracy of positioning solution. The CEP and DRMS were found to be 3.21 m and 4.40 m which are almost 5 times smaller than their counter parts in singleconstellation. Hence, it can be established that combination of multiple navigation

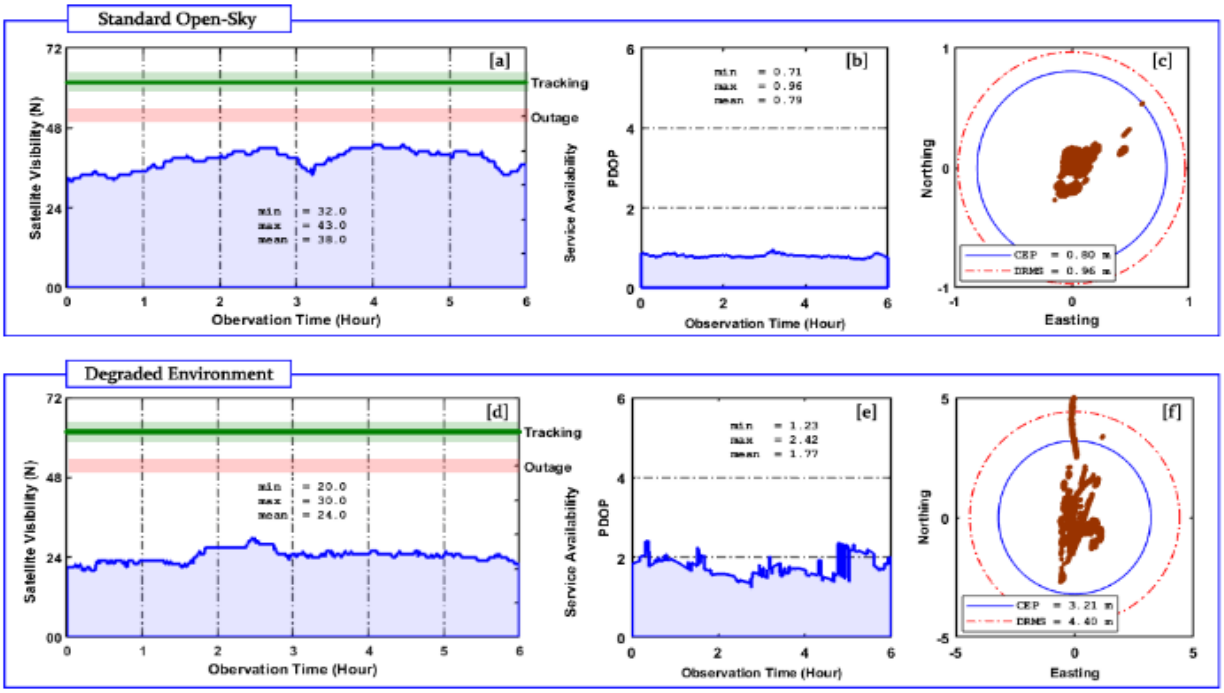


Fig. 5 The performance assessment of GNSS receiver in quad-constellation mode at standard open sky and degraded environment using fundamental quality indicators.

system can significantly mitigate the environmental effects by leveraging the redundancy of range measurements.

IV. Conclusion

In this paper, a comprehensive study on the GNSS performance in single and multi-constellation mode using fundamental quality indicators and under different signal reception conditions (i.e., environments) is presented. The navigation performance is evaluated by quantifying and analyzing the fundamental quality indicators of GNSS i.e., satellite visibility along with service availability, PDOP and statistical accuracy of reported position. Based on the detailed analysis of performance evaluation results on both candidate sites, it can be concluded that single-constellation (GPS) receiver can only provide a user with accurate, reliable and seamless positioning and navigation services in open-sky views. However, poor signal reception conditions (i.e., blockage or multipath) in degraded environments make it very hard for a GPS receiver to function properly without using any aiding devices. On the other hand, the integration of all four satellite constellations such as GPS, GALILEO, BeiDou Russian GLONASS resulted in remarkable boost in satellite visibility and availability of direct Line-ofSight (LOS) that resulted in reduced outages, better satellite geometry and thus improved positioning accuracy. In fact, the accuracy of reported positions was found to be improved by almost five times and the outages were reduced by almost 50% in the multi-GNSS mode at the degraded site.

Acknowledgement

This work was supported by the Higher Education Commission (HEC) of Pakistan through the National Research Program forUniversities (NRPU) under Grant 6250/Sindh/NRPU/R&D/HEC/2016.

References

[1] G. N. S. S. European, “GNSS Market Report,” doi: 10.2878/565013.

[2] I. Skog and P. Händel, “In-car positioning and navigation technologiesa survey,” *IEEE Trans. Intell. Transp. Syst.*, vol. 10, no. 1, pp. 4–21, 2009, doi: 10.1109/TITS.2008.2011712.

[3] C. Stallo *et al.*, “GNSS-based location determination system architecture for railway performance assessment in presence of local effects,” *2018 IEEE/ION Position, Locat. Navig. Symp. PLANS 2018 - Proc.*, pp. 374–381, Jun. 2018, doi: 10.1109/PLANS.2018.8373403.

[4] S. Lo, “Navigation for Aviation,” *Position, Navig. Timing Technol. 21st Century*, pp. 1871–1891, Dec. 2020, doi: 10.1002/9781119458555.CH61.

[5] G. B. Michael Dooley, Paolo Pirjanian, Nikolai Romanov, Lihu Chiu, Enrico Di Bernardo, Michael Stout, “Application of localization, positioning & navigation systems for robotic enabled mobile products.”

[6] A. F. G. Ferreira, D. M. A. Fernandes, A. P. Catarino, and J. L. Monteiro, “Localization and Positioning Systems for Emergency Responders: A Survey,” *IEEE Commun. Surv. Tutorials*, vol. 19, no. 4, pp. 2836–2870, Oct. 2017, doi: 10.1109/COMST.2017.2703620.

[7] C. B. Lin, R. W. Hung, C. Y. Hsu, and J. S. Chen, “A GNSS-Based Crowd-Sensing Strategy for Specific Geographical Areas,” *Sensors 2020, Vol. 20, Page 4171*, vol. 20, no. 15, p. 4171, Jul. 2020, doi: 10.3390/S20154171.

[8] S. Suryaatmadja and N. Maulani, “CONTRIBUTIONS OF SPACE TECHNOLOGY TO GLOBAL HEALTH IN THE CONTEXT OF COVID-19,” *J. Adm. Kesehat. Indones.*, vol. 8, no. 2, pp. 60–73, Jun. 2020, doi: 10.20473/JAKI.V8I2.2020.60-73.

[9] P. D. Groves, “Principles of GNSS, Inertial, and Multisensor Integrated Navigation Systems, Second Edition | Artech books | IEEE Xplore.” https://ieeexplore.ieee.org/document/9101092 (accessed Aug. 01, 2022).

[10] Nasir SaeedHaewoon NamTareq Y. Al-NaffouriTareq Y. Al-NaffouriMohamed-Slim Alouini, “A State-of-the-Art Survey on Multidimensional Scaling Based Localization Techniques.” https://www.researchgate.net/publication/333678948_A_State-of-the-Art_Survey_on_Multidimensional_Scaling_Based_Localization_Techniques (accessed Aug. 01, 2022).

[11] N. R. Council, “The Global Positioning System: A Shared National Asset,” May 1AD, doi: 10.17226/4920.

[12] B. W. PARKINSON, T. STANSELL, R. BEARD, and K. GROMOV, “A History of Satellite Navigation,” *Navigation*, vol. 42, no. 1, pp. 109–164, Mar. 1995, doi: 10.1002/J.2161-4296.1995.TB02333.X.

[13] P. Misra, B. P. Burke, and M. M. Pratt, “GPS performance in navigation,” *Proc. IEEE*, vol. 87, no. 1, pp. 65–85, 1999, doi: 10.1109/5.736342.

[14] W. Y. Ochieng and K. Sauer, “Urban road transport navigation: performance of the global positioning system after selective availability,” *Transp. Res. Part C Emerg. Technol.*, vol. 10, no. 3,

pp. 171–187, Jun. 2002, doi: 10.1016/S0968-090X(02)00008-6.

[15] N. Joubert, T. G. R. Reid, and F. Noble, "Developments in Modern GNSS and Its Impact on Autonomous Vehicle Architectures," *IEEE Intell. Veh. Symp. Proc.*, pp. 2029–2036, 2020, doi: 10.1109/IV47402.2020.9304840.

[16] "Global Positioning System Standard Positioning Service Performance Standard." https://rosap.ntl.bts.gov/view/dot/16930 (accessed Aug. 01, 2022).

[17] W. Lechner and S. Baumann, "Global navigation satellite systems," *Comput. Electron. Agric.*, vol. 25, no. 1–2, pp. 67–85, Jan. 2000, doi: 10.1016/S0168-1699(99)00056-3.

[18] A. Hussain, A. Ahmed, H. Magsi, and R. Tiwari, "Adaptive GNSS receiver design for highly dynamic multipath environments," *IEEE Access*, vol. 8, pp. 172481–172497, 2020, doi: 10.1109/ACCESS.2020.3024890.

[19] yu yasyukevich, A. yasyukevich, E. Astafyeva, Y. V Yasyukevich, A. Yasyukevich, and E. Astafyeva, "How modernized and strengthened GPS signals enhance the system performance during solar radio bursts How modernized and strengthened GPS signals enhance the system performance Lermontov str," doi: 10.1007/s10291-021-01091-5ï.

[20] M. Karaim, M. Elsheikh, and A. Noureldin, "GNSS Error Sources," *Multifunct. Oper. Appl. GPS*, May 2018, doi: 10.5772/INTECHOPEN.75493.

[21] A. Hussain, F. Akhtar, Z. H. Khand, A. Rajput, and Z. Shaukat, "Complexity and Limitations of GNSS Signal Reception in Highly Obstructed Enviroments," *Eng. Technol. Appl. Sci. Res.*, vol. 11, no. 2, pp. 6864–6868, Apr. 2021, doi: 10.48084/ETASR.3908.

[22] D. N. Aloi, M. Alsliety, and D. M. Akos, "A methodology for the evaluation of a GPS receiver performance in Telematics applications," *IEEE Trans. Instrum. Meas.*, vol. 56, no. 1, pp. 11–24, Feb. 2007, doi: 10.1109/TIM.2006.887190.

[23] A. Khodabandeh, S. Zaminpardaz, and N. Nadarajah, "A study on multi-GNSS phase-only positioning," *Meas. Sci. Technol.*, vol. 32, no. 9, p. 095005, May 2021, doi: 10.1088/1361-6501/ABECED.

[24] A. Hussain, A. Ahmed, H. Magsi, J. B. Soomro, S. S. H. Bukhari, and J. S. Ro, "Adaptive data length method for gps signal acquisition in weak to strong fading conditions," *Electron.*, vol. 10, no. 14, Jul. 2021, doi: 10.3390/ELECTRONICS10141735.

[25] R. Langley, "Dilution of Precision," *GPS Solutions*. https://www.semanticscholar.org/paper/Dilution-of-Precision-Langley/c04cd3dc971734ebe2ba1aa113e417e8b28b248c (accessed Aug. 01, 2022).

[26] C. Specht, P. S. Dabrowski, J. Pawelski, M. Specht, and T. Szot, "Comparative analysis of positioning accuracy of GNSS receivers of Samsung Galaxy smartphones in marine dynamic measurements," *Adv. Sp. Res.*, vol. 63, no. 9, pp. 3018–3028, May 2019, doi: 10.1016/J.ASR.2018.05.019.

[27] "Measures of Accuracy in the Navstar/GPS: 2drms Vs. CEP." https://www.ion.org/publications/abstract.cfm?articleID=12097 (accessed Aug. 01, 2022).

GNSS TEC BASED IONOSPHERIC ANOMALIES RELATED TO THE 2019 M_W 6.2 THAILAND EARTHQUAKE

Shireen Mushtaq
Institute of Space Technology
Islamabad, Pakistan
shireenbajwa2013@gmail.com

Rimsha Ashraf
Institute of Space Technology
Islamabad, Pakistan
mrimsha853@gmail.com

Dr. Munawar Shah
Institute of Space Technology
Islamabad, Pakistan
shahmunawar1@gmail.com

Punyawi Jamjareegulgarn
King Mongkut's Institute of Technology Ladkrabang,
Prince of Chumphon Campus, Thailand
jpunyawi@gmail.com

***Abstract*— Detecting seismic ionospheric perturbation by Global Navigation Satellite System (GNSS) is an inevitable approach and has proven to be a new field in the investigation of Earthquake (EQ) precursors. In this paper, the temporal Total Electron Content (TEC) anomalies are investigated from the International GNSS Service (IGS) stations around the epicenter of the November 20, 2019, Thailand EQ (M_w 6.2), that occurred on UTC=23:50:43 h. Seismo ionospheric perturbations are estimated with TEC during thirty-one days (twenty days prior and ten days followed by EQ). The solar and geomagnetic activity indices are checked in the context of EQ. Quiet geomagnetic activity is observed on the day of EQ. However, Kp is larger than 3 immediately after the EQ. Results depict the TEC perturbation measured at three GNSS stations. Furthermore, clear positive anomalies are detected within three days prior to EQ M_w 6.2, (-3, -2, and -1 days) during quiet geomagnetic activities. Since, Kp >3 after the EQ. Therefore, the ionospheric perturbation is related to geomagnetic storms.**

Keywords: Ionospheric perturbation; Thailand Earthquake; Total Electron Content.

I. INTRODUCTION

For several years, the seismic events have been studied their relationship with ionospheric anomalies from various satellites and a connection has also set up with the lithosphere during the main shock preparation period. [1] The ionospheric perturbations related to EQ inside the breeding zone have been accounted from GNSS TEC as pre- and post-seismic precursors. [2]

There are several studies about ionospheric anomalies induced by EQ. For example, the recent studies included the investigation of abnormal ionospheric signatures related to M_w greater than 6.5 EQs in New Zealand from TEC.[3] Moreover, the investigation of possible statistical relation among ionospheric TEC anomalies and the global inland EQs ($M_w \geq 6.0$) during 2003-2017 was also proposed.[4] Earliest ionospheric perturbation associated with EQ was monitored in 1964 after the Alaska EQ (M_w 9.2, March 28, 1964).[5] To evaluate the ionospheric disturbances, the pre- and post-seismic Taiwan EQ (M_w = 6.4) obtained from GNSS TEC during quiet geomagnetic storm conditions.[6] They reported the possible relationship between the EQ and the GNSS TEC. [7] To recognize the seismo-ionospheric perturbations, the TEC obtained from GNSS stations made a great contribution.[8] In the recent years, the GPS-based TEC anomalies before EQ have been revealed using TEC maps and TEC measurements over distinct stations.[9] Anomalous TEC variations were investigated for the Tohoku EQ 2011 over the epicenter beyond the upper confidence bound.

They found pre-seismic TEC anomalies in quiet geomagnetic periods. [10] Ionospheric TEC perturbation was examined between 2000- 2019 EQs of different magnitudes (M > 6.0). They distinguished that the positive anomalies are greater than the negative anomalies. Furthermore, these studies show that the daily variations in TEC anomalies can fund considerable precursors earlier to the worldwide EQs ($M \geq 6$). [11] TEC perturbation of twenty-four EQs was investigated in China of different magnitude between Mw (5-8). The TEC results show the positive and negative variations before EQ. Moreover, the perturbation was not steady and not corresponding to the EQ magnitudes.[12] The correlation between ionospheric TEC variations and three faults are examined of twenty eight EQ that have greater than 7 magnitudes.[13] The procedures and developments of ionospheric seismology for the 2008 Wenchuan EQ and 2011 Japan EQ are obtained from GPS TEC.[14] The global ionospheric map (GIM) is used to observe anomalies in the TECU related to thirty five EQs that their magnitudes greater than 6.0 happened in China between May 1998 - April 2008.[15]

In this paper, ionospheric disturbances are monitored in the form of variation over the Thailand EQ of M_w 6.2 using TEC to provide an exacting evidence about seismo ionospheric anomalies.

II. CASE STUDY

The EQ of November 20, 2019 in Thailand (M_w 6.2) happened on UTC = 23:50:43h at the geographical location of Latitude (19.45°N) and Longitude (101.36°E), and shallow hypo central depth 10 km according to United States Geological Survey (USGS). According to Global Disaster Alert and Coordination System or GDACS (https://gdacs.org/report.aspx?eventid= 1194401&episodeid=1279805&eventtype=EQ), there are



Fig. 1 The EQ Location (M_w 6.2) is denoted by red filled star. The black color filled circles denote the GNSS stations, while the red circle is the preparation zone estimated by Dobrovolsky equation, which is about 463.5 km.

no reports of casualties or damage. Some people near the epicenter and surrounding areas felt aftershocks throughout the morning period. Residents of Chiang Mai, Thailand have long felt the shakes but no major damage. Up to 8,000 people were exposed to strong shaking.

Table 1

The information for the selected EQ in Thailand.

No.	Date	Time (UTC)	Latitude (°N)	Longitude (°E)	M_w	Depth (km)
1	20/11/2019	23:50:43	19.45	101.36	6.2	10

III. DATA COLLECTION AND METHODOLOGY

In the present paper, the ionospheric disturbances related to M_w 6.2 EQ are studied from the GNSS TEC obtained from IGS stations working in the EQ breeding zone. The various morphological parameters (magnitude, depth, and location) of the EQ are attained from USGS https://earthquake.usgs.gov/earth /search/. Different geomagnetic indices (i.e., Dst, Kp, Ap and F10.7) are analyzed to verify the space weather conditions (SWC) and quiet days earlier and afterward the EQ. For this task, the source data during October 31-November 30, 2019 are regained from International Services of Geomagnetic Indices (ISGI) (http://isgi.unistra.fr/data _download.php) and OMNI web NASA https://omniweb.gsfc. nasa.gov/form/dx1.html.

To examine the temporal anomalies, the daily GNSS TEC data are retrieved from the IGS stations within EQ geographical position. Furthermore, the TEC data are obtained via this website http://www.ionolab.org/webtec/single.html?locale=en.
These IGS stations are in operation during the resultant EQ preparation zones. The EQ radius is calculated by Dobrovolsky equation as shown in Eq. (1). [16]

$$\acute{R} = 10^{0.43*M} \quad \textbf{(1)}$$

where the radius of seismic region is represented by Ŕ (unit: km) and M is the EQ magnitude. Here, the M is 6.2, hence, the EQ radius is about 463.5 km as depicted in Fig. 1.

Slant TEC (STEC) is monitored by the Global Positioning System (GPS) satellite. It is computed in expressions of TEC unit. The STEC is evaluated via following equations. [17]

$$STEC = \frac{f_1^2 f_2^2}{40.28(f_2^2 - f_1^2)} (l_1 - l_2 + \lambda_1(N_1 + b_1) - \lambda_2(N_2 + b_2) + \epsilon) \quad \textbf{(2)}$$

$$STEC = \frac{f_1^2 f_2^2}{40.28(f_2^2 - f_1^2)}(P_1 - P_2 - (d_1 - d_2) + \epsilon) \quad \textbf{(3)}$$

where f_1 and f_2 denotes carrier wave frequencies, λ_1 and λ_2 denotes wavelengths, l_1 and l_2 are the carrier phases, N_1 and N_2 depicts the uncertainties of the signal, b_1 and b_2 symbolizes the carrier phases of the signal, P_1 and P_2 denotes the pseudo-ranges, and ϵ is the random residuals of the signal. To transform STEC into VTEC, the below equation is used. [18]

$$VTEC = STEC \times \cos(\arcsin(R\sin Z/(R+H))), \quad \textbf{(4)}$$

where the Earth radius is denoted by R, H is the IPP ionospheric height, and Z represents the zenith angle of the satellite.

To recognize the anomalies, we analyze the TEC and DTEC for twenty days prior and ten days next to the main shock day. To recognize the TEC anomalies, the confidence bounds are computed by using the below equations.

$$\text{Upper bound (UB)} = m + 2\sigma \quad \textbf{(5)}$$

$$\text{Lower bound (UB)} = m - 2\sigma \quad \textbf{(6)}$$

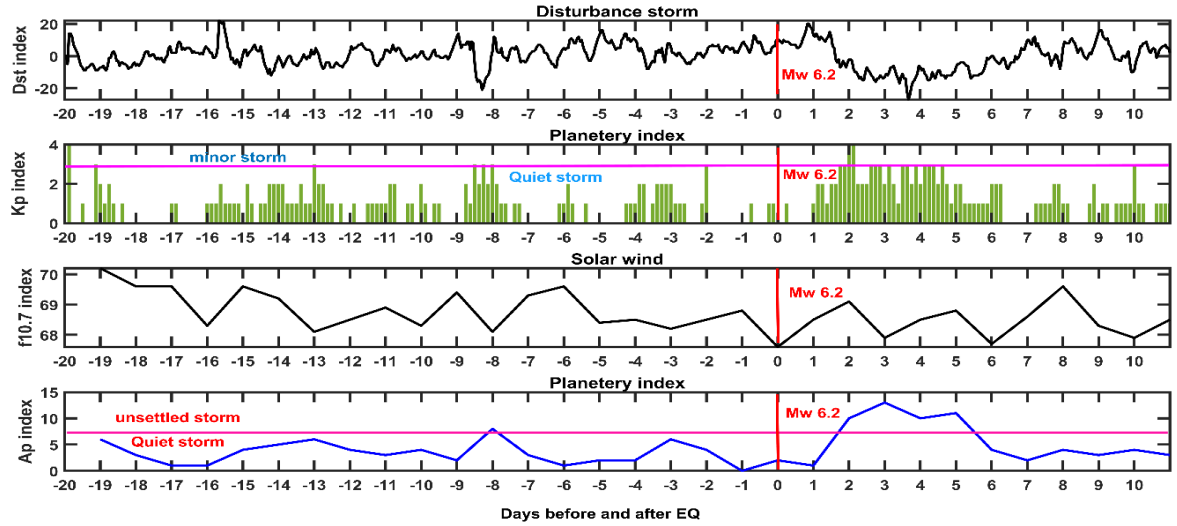


Fig. 2. The Geomagnetic indices afore and next to the Mw 6.2. Here, the Kp shows active geomagnetic storm after the EQ day.

where the standard deviation and the median of the TEC time series are denoted by σ and m, respectively. Moreover, the TEC deviation from the upper bound (DTEC) is computed by subtracting the original TEC from the respective UB.

TEC Deviation (DTEC) =TEC original – Upper Bound **(7)**

To differentiate either the ionospheric disturbances related to EQ or geomagnetic storm, this procedure has been used. All calculations were executed by MATLAB. All maps and graphs were also plotted with MATLAB functions.

IV. RESULTS AND DISCUSSION

In this paper, The GNSS TEC data were used to examine the seismo ionospheric anomalies preceding the Thailand EQ. The ionospheric parameters are affected by solar and geomagnetic storm conditions. The main purpose of including solar and geomagnetic storm conditions in this research work is to differentiate whether ionospheric anomalies are induced by the storm or seismic process. In Fig. 2, the solar conditions and geomagnetic storm show the EQ happened in the quiet geomagnetic activities (Kp < 3, Dst < −10 nT, Ap < 7 and F10.7 < 100). However, the Kp is greater than 3 immediately after the EQ day.

The lower and upper bounds are calculated at the same period as the geomagnetic storm data by using daily TEC variation data of the selected GNSS stations near to the EQ epicenter. Ionospheric anomalies are examined in the TEC values from three IGS stations named as CMUM (Chiang Mai University, Muang), CUUT (Chulalongkorn University, Thailand) and CPNM (Chumphon University, Muang). As seen in Fig. 3, the CMUM station showed the positive TEC anomalies on days -3, -2, -1 before the EQ day and on the EQ day. But, the storm became active after the EQ day; therefore, there are no EQ induced pre-seismic anomalies at the CMUM station. Likewise, the CUUT station showed the positive TEC anomalies on days -2, -1 before the EQ day and on the EQ day. The CPNM station also showed the positive TEC anomalies on day -1 before the EQ day and on the EQ day (Fig. 3). Because the storm is active after the EQ day,

we cannot say confidently about the pre-seismic ionospheric anomalies. The TEC deviations (DTEC) from upper bound are calculated for the selected GNSS stations to indicate anomalous ionospheric situations and also filtered out the anomalous days. The DTEC for three IGS stations before and after the EQ can be computed using Eq. (7) and shown in Figs. 4-5. We use the temporal and continuous wavelet transform method to find out the DTEC. The positive anomalies are observed from the results of DTEC. But these are storm induced TEC anomalies and no clear evidence of EQ induced ionospheric perturbations came out.

V. CONCLUSION

We investigated the ionospheric TEC anomalies for the Thailand EQ by analyzing the possible reasons for these anomalies based on solar and geomagnetic storm conditions. The Dst, F10.7, Kp and Ap indices were examined. The studied indices showed the EQ occurred during the quiet geomagnetic activities. Ionospheric TEC data were determined by using GNSS data. The TEC results show that EQ anomalies appeared three days earlier and on the EQ day during quiet geomagnetic storm conditions. But, the storm is active after the EQ day and these ionospheric anomalies are associated to the storm. As for the computed DTECs, the positive anomalies are more than the negative anomalies. The data showed the clear ionospheric anomalies over the three days before and on the EQ day.

ACKNOWLEDGEMENTS

The Author is obliged to the USGS,ISGI,OMNI web NASA and IONOLAB for providing data about the TEC data, respectively.

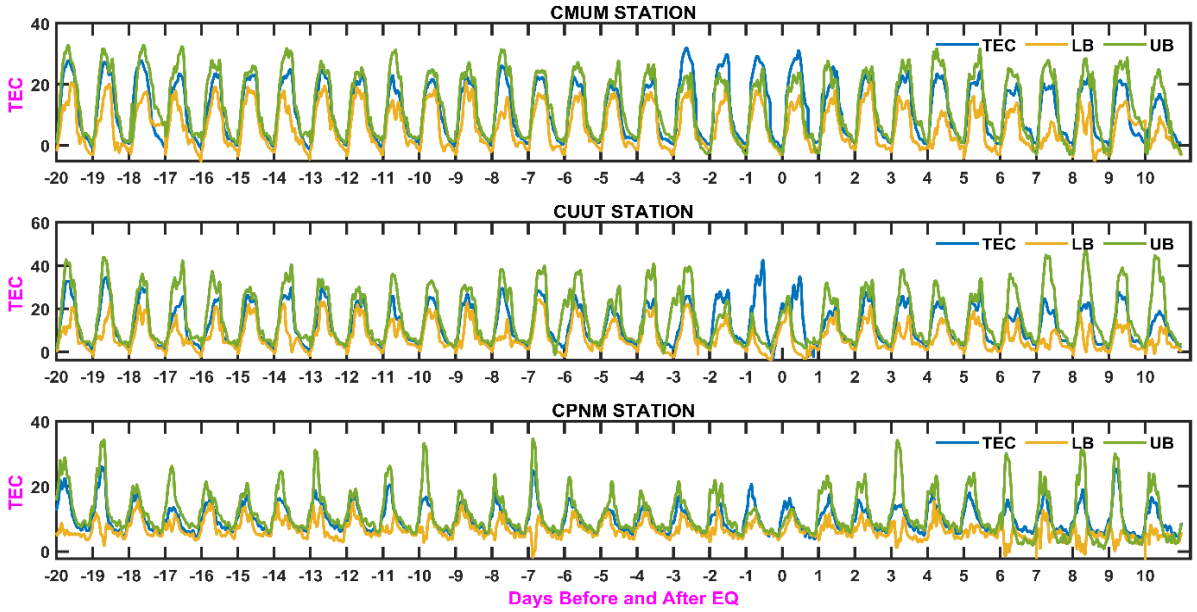


Fig. 3. The TEC measured at three GNSS stations (CMUM, CUUT, CPNM) along with confidence bounds for indicating the seismic ionospheric anomalies.

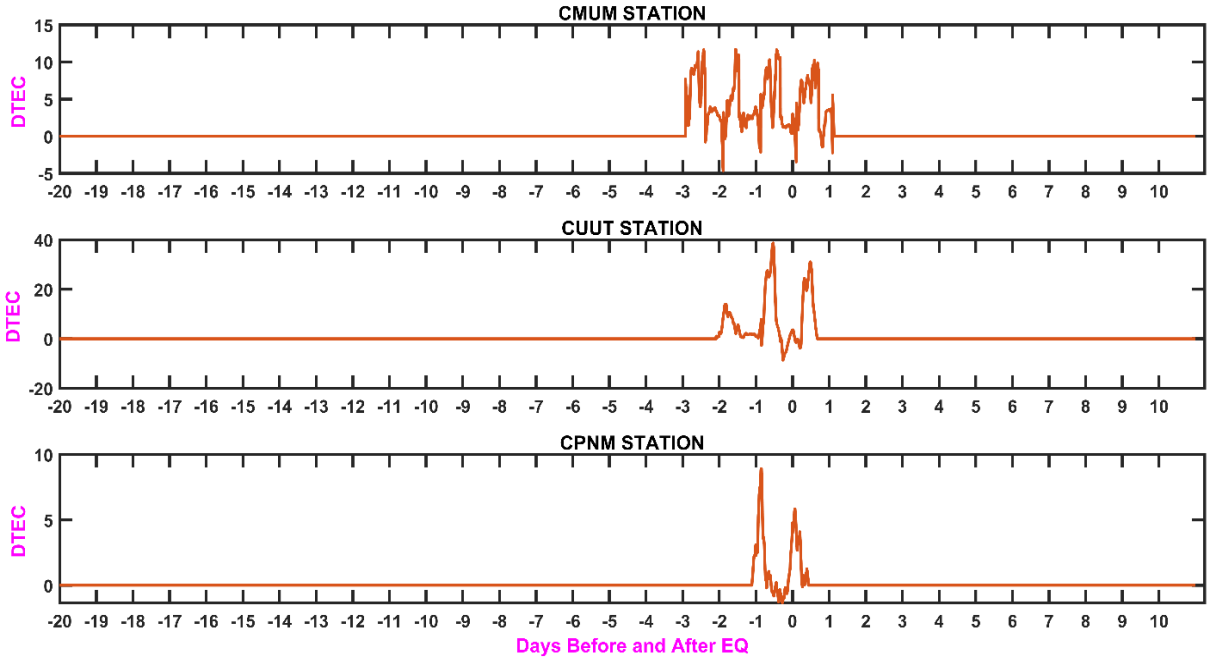


Fig. 4. The DTEC values beyond the upper bounds for all three GNSS stations.

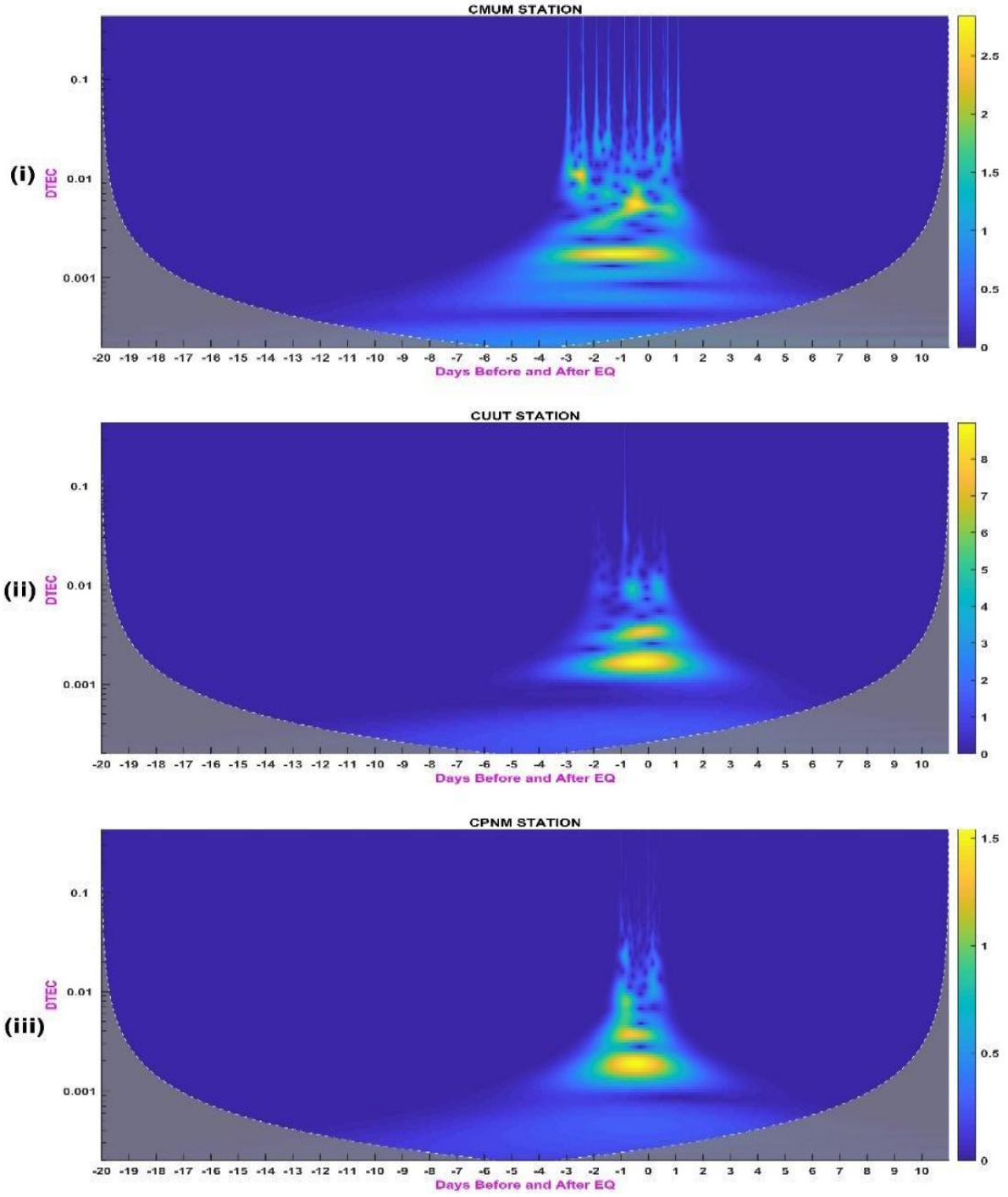


Fig. 5. Wavelet spectrums of DTEC values beyond the upper bounds depicting the TEC disturbances before and on the main shock day for all three Thailand stations (i) CMUM, (ii) CUUT and (iii) CPNM stations.

REFERENCES

[1] A. Kiyani *et al.*, "Seismo ionospheric anomalies possibly associated with the 2018 Mw 8.2 Fiji earthquake detected with GNSS TEC," *J. Geodyn.*, vol. 140, p. 101782, 2020, doi: 10.1016/j.jog.2020.101782.

[2] M. Shah and S. Jin, "Pre-seismic ionospheric anomalies of the 2013 Mw = 7.7 Pakistan earthquake from GPS and COSMIC observations," *Geod. Geodyn.*, vol. 9, no. 5, pp. 378–387, 2018, doi: 10.1016/j.geog.2017.11.008.

[3] M. A. Adil, A. Abbas, M. Ehsan, M. Shah, N. A. Naqvi, and A. Alie, "Investigation of ionospheric and atmospheric anomalies associated with three Mw >6.5 EQs in New Zealand," *J. Geodyn.*, vol. 145, no. April, p. 101841, 2021, doi: 10.1016/j.jog.2021.101841.

[4] F. Zhu and Y. Jiang, "Investigation of GIM-TEC disturbances before M ≥ 6.0 inland earthquakes during 2003–2017," *Sci. Rep.*, vol. 10, no. 1, pp. 1–7, 2020, doi: 10.1038/s41598-020-74995-w.

[5] K. Davies and D. M. Baker, "Ionospheric effects observed around the time of the Alaskan earthquake of March 28, 1964," *J. Geophys. Res.*, vol. 70, no. 9, pp. 2251–2253, 1965, doi: 10.1029/jz070i009p02251.

[6] A. R. Abbasi, M. Shah, A. Ahmed, and N. A. Naqvi, "Possible ionospheric anomalies associated with the 2009 Mw 6.4 Taiwan earthquake from DEMETER and GNSS TEC," *Acta Geod. Geophys.*, vol. 56, no. 1, pp. 77–91, 2021, doi: 10.1007/s40328-020-00325-1.

[7] S. Pulinets and D. Davidenko, "Ionospheric precursors of earthquakes and Global Electric Circuit," *Adv. Sp. Res.*, vol. 53, no. 5, pp. 709–723, 2014, doi: 10.1016/j.asr.2013.12.035.

[8] Y. Zou and T. Zhao, "Ionospheric anomalies detected by GPS TEC measurements during the 15 August 2007 Peru earthquake," *2010 Int. Conf. Microw. Millim. Wave Technol. ICMMT 2010*, no. August 2007, pp. 1216–1219, 2010, doi: 10.1109/ICMMT.2010.5525006.

[9] Y. Zou, "Ionospheric anomalies detected by GPS TEC measurements during two strong earthquakes in Indonesia," *2010 2nd Conf. Environ. Sci. Inf. Appl. Technol. ESIAT 2010*, vol. 2, pp. 199–202, 2010, doi: 10.1109/ESIAT.2010.5567309.

[10] M. Akhoondzadeh, "Anomalous TEC variations associated with the powerful Tohoku earthquake of 11 March 2011," *Nat. Hazards Earth Syst. Sci.*, vol. 12, no. 5, pp. 1453–1462, 2012, doi: 10.5194/nhess-12-1453-2012.

[11] M. Ulukavak, M. Yalçınkaya, E. T. Kayıkçı, S. Öztürk, R. Kandemir, and H. Karslı, "Analysis of ionospheric TEC anomalies for global earthquakes during 2000-2019 with respect to earthquake magnitude (Mw≥6.0)," *J. Geodyn.*, vol. 135, no. September 2019, 2020, doi: 10.1016/j.jog.2020.101721.

[12] F. Ke, Y. Wang, X. Wang, H. Qian, and C. Shi, "Statistical analysis of seismo-ionospheric anomalies related to Ms > 5.0 earthquakes in China by GPS TEC," *J. Seismol.*, vol. 20, no. 1, pp. 137–149, 2016, doi: 10.1007/s10950-015-9516-x.

[13] M. Ulukavak and M. Yalçlnkaya, "INVESTIGATION of the RELATIONSHIP between IONOSPHERIC TEC ANOMALY VARIATIONS and FAULT TYPES before the EARTHQUAKES," *ISPRS Ann. Photogramm. Remote Sens. Spat. Inf. Sci.*, vol. 4, no. 4W4, pp. 383–388, 2017, doi: 10.5194/isprs-annals-IV-4-W4-383-2017.

[14] S. Jin, G. Occhipinti, and R. Jin, "GNSS ionospheric seismology: Recent observation evidences and characteristics," *Earth-Science Rev.*, vol. 147, pp. 54–64, 2015, doi: 10.1016/j.earscirev.2015.05.003.

[15] J. Y. Liu *et al.*, "Seismoionospheric GPS total electron content anomalies observed. before the 12 May 2008 Mw7.9 Wenchuan earthquake," *J. Geophys. Res. Sp. Phys.*, vol. 114, no. 4, pp. 1–10, 2009, doi: 10.1029/2008JA013698.

[16] I. P. Dobrovolsky, S. I. Zubkov, and V. I. Miachkin, "Estimation of the size of earthquake preparation zones," *Pure Appl. Geophys. PAGEOPH*, vol. 117, no. 5, pp. 1025–1044, 1979, doi: 10.1007/BF00876083.

[17] S. Jin, R. Jin, and J. H. Li, "Pattern and evolution of seismo-ionospheric disturbances following the 2011 Tohoku earthquakes from GPS observations," *J. Geophys. Res. Sp. Phys.*, vol. 119, no. 9, pp. 7914–7927, 2014, doi: 10.1002/2014JA019825.

[18] J. A. Klobuchar, "Ionospheric Time-Delay Algorithm for Single-Frequency GPS Users," *IEEE Trans. Aerosp. Electron. Syst.*, vol. AES-23, no. 3, pp. 325–331, 1987, doi: 10.1109/TAES.1987.310829.

INVESTIGATION OF SEISMO IONOSPHERIC ANOMALIES ASSOCIATED WITH THE M_W 6.7 MONGOLIA EARTHQUAKE

Rimsha Ashraf
Institute of Space Technology
Islamabad, Pakistan
mrimsha853@gmail.com

Shireen Mushtaq
Institute of Space Technology
Islamabad, Pakistan
shireenbajwa2013@gmail.com

***Abstract*—The seismo-ionospheric anomalies associated with the M_w 6.7 Mongolia Earthquake (EQ) occurred on Jan 11 ,2021, are investigated from the Global Navigation Satellite System (GNSS) based Total Electron Content (TEC) acquired from the stations in seismic region. To observe the EQ anomalies, it is mandatory to take into account the variations in solar and geomagnetic storm activities, the present study has the worldwide geomagnetic storm level, particularly the Disturbance Storm Time (Dst), Kp, Ap, F 10.7 indices prior to EQ and after the EQ. It is clear that the EQ happened during the quiet geomagnetic conditions Kp < 3. But the storm was active five days before the EQ. The electromagnetic variations within the ionosphere related to EQ are statistically examined in TEC from IGS stations. Our results from TEC clearly show that the ionospheric anomalies are induced several days before the EQ near the epicenter and positive anomalies appear on -4th Day, -3rd Day, -2nd Day, - 1 Day and on main shock day. Based on the obtained results, anomalies in TEC are more likely related to the geomagnetic storm indices due to its abnormality during the EQ preparation period. Furthermore, enhancement and depletion in TEC prior to EQ supports the presence of storm anomalies over the seismic zone.**

***Keywords*—Earthquake; Global Navigation Satellite Systems; Total Electron Content; Geomagnetic Storm**

I. INTRODUCTION

The seismic activity that yields ionospheric effects have gained attention for many years, the GNSS TEC has been proved to be an efficient tool to monitor and estimate the ionospheric anomalies which are mainly associated with large magnitude and shallow hypo central EQs within the EQ preparation zone(EPZ). [1-3]. The partially ionized zone of Earth's upper atmosphere is the ionosphere, it is the portion of the atmosphere where ionized molecules and free electron density have an impact on the propagation of electromagnetic waves of radio frequency. Researches have been conducted during the last decade to monitor changes that took place in the ionosphere before or after the main shocks of large magnitude EQs. Therefore, the importance of examining the ionosphere layer as precursor in EQ prediction research has been revealed [4]. Geomagnetic storms, atmospheric circulations and magnetic activities are the main source for triggering ionospheric disturbances [5].Recently, GPS TEC assists in studying the relationship between EQ and ionospheric precursors [6]. The ionospheric disturbance was first reported above the EQ epicenter in 1964 after the Alaska EQ (M_w 9.2, March 28, 1964) [7].

Table 1
Detailed information about EQ

M_w	Date	Time (UT)	LAT (°)	LONG (°)	Depth (km)	EPZ (km)
6.7	11/01/2021	21:32:59	51.12	100.47	10	760.3

Furthermore, the anomalies in ionosphere happened due to EQs, and raised upward to the ionosphere in the form of vertical electric fields into the ionosphere. Similarly, the evolution of gases such as Radon from the epicenter produces some chemical modifications which prevail up to the ionosphere [8]. Additionally, some seismic ionospheric anomalies are also revealed as false indications and that are not considered as EQ precursors [9]. Moreover, the anomalies appearing in the ionosphere are also due to the strong solar storm. Therefore, it is mandatory to investigate the geomagnetic indices a few days prior and afterward the EQ in the course of the EQ zone. The basic aim of including geomagnetic indices is to investigate whether the ionospheric disturbance is due to geomagnetic storm or EQ. Many studies shows that geomagnetic storm is completely quiet during the three days prior to EQ [3],[10-12], In order to further clarify geomagnetic storm anomalies ,the main goal of this paper is to statistically analyzed and examined GPS TEC to monitor anomalies generated in ionosphere for twenty days before and ten days next to the main shock and additional idea of this study is to explore the variance among seismic and geomagnetic storm anomaly.

II. CASE STUDY

The M_w 6.7 occurred on January 11, 2021 at 33 Km SSW of Turt in Mongolia at UT =21:32:59 hours having geographical location of Latitude (51.21°N) and Longitude (100.47°E), as reported by United States Geological Survey (USGS) and it is presented in Table.1. This EQ has a shallow hypo central depth of 10 km, as shown in Fig. 1. There are about 19000 people living within 100 km of the epicenter. USGS PAGER estimates that up to 4000 people were exposed to strong shaking https://www.gdacs.org/report.aspx?eventid=1251188 &episodeid=1352410&eventtype=EQ.

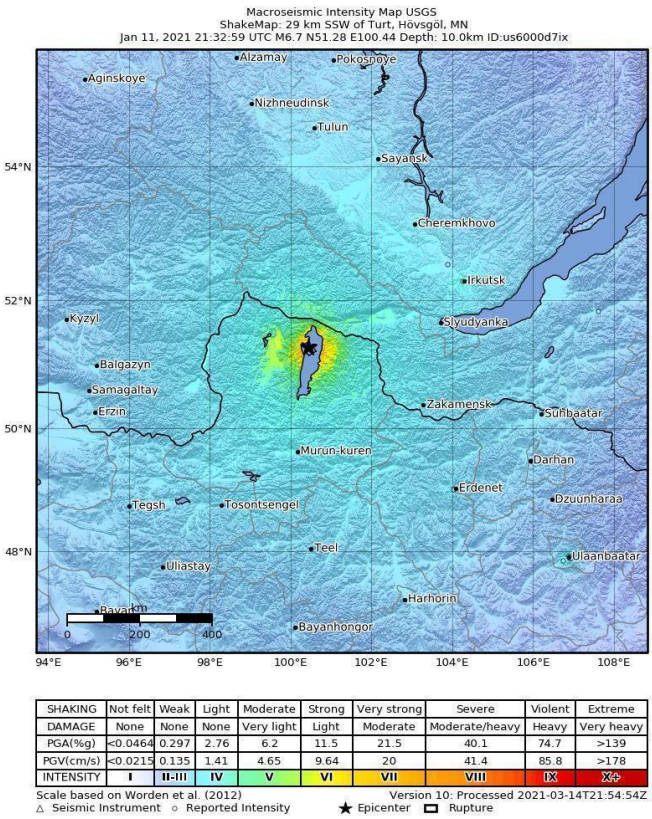


Fig.1 Geographical position of the EQ epicenter. Black star shows the coordinates of the epicenter and the colored portion depicts the intensity of EQ. The location map is taken from USGS.

DATA COLLECTION AND METHODOLOGY

In the study, we have investigated the ionosphere TEC variations from IGS stations related to the shallow hypo central Mw 6.7 Mongolia EQ.These IGS stations operating in the EPZ. Various morphological parameters of the EQ comprise the magnitude, depth, and location and information about the EQ are obtained from USGS website https://EQ.usgs.gov/EQs/search/.Moreover,To distinguish EQ and storm anomalies in the TEC, the examination of these indices has equivalent significance, the data of geomagnetic and solar indices (Kp, Dst, Ap and F10.7) are acquired from ISGI https://isgi.unistra.fr/datadow nload.php OMNI web NASA https://omniweb.gsfc. nasa.gov /form/dx1.html

The examination of TEC anomalies related to EQ, requires that IGS stations work inside the EPZ. EPZ, as estimated by Dobrovolsky et al.[14] in the form of $\rho = (10^{0.43M})$ km. Radius of the EPZ is represented by ρ, where M symbolizes the magnitude of EQ and its radius is computed by the Dobrovolsky equation and it is about 760.3 km, as shown in Figure 2.

TEC is estimated from IGS stations in the form of Slant TEC (STEC). It is computed with the ray path of the recorded signal in the unit of TEC, where 1 TEC is equivalent to 10^{16} e/ $m^{2.}$ [13].

$$STEC = \frac{f_2^2 f_1^2}{40.3(f_2^2 - f_1^2)} \left(L_1 - L_2 + \lambda_1(S_1 + b_1) - \lambda_2(S_2 + b_2) + \epsilon \right) \quad \textbf{(1)}$$

$$STEC = \frac{f_2^2 f_1^2}{40.3(f_2^2 - f_1^2)}(P_1 - P_2 - (d_1 - d_2) + \epsilon) \quad \textbf{(2)}$$

Where STEC denotes Slant Total Electron Content, f_1 (1575.42 MHz) is carrier phase frequency of GPS signals and f_2 (1227.60MHz) is frequency (f_2) at second end. P_1 and P_2 are the pseudo ranges measured in L_1 and L_2, respectively. S represents uncertainty of signal and b denotes the instrumental biases, differential code bias is represented by d. Moreover,
transformation from Slant TEC into Vertical TEC is done by the next equation.

$$VTEC = STEC \times cos\left(arcsine\left(\frac{RsinZ}{R+H}\right)\right) \quad \textbf{(3)}$$

Where, R denotes the Earth's radius and H indicates single layer height thickness. Furthermore, the elevation angle of the satellite is represented by Z.

To probe into the ionospheric abnormalities and its relationship with the EQ, the TEC data is acquired from permanent three IGS stations functioning in EPZ.The named as KSTU, ULAB, and IRKT was monitored to compute the upcoming EQ relation with ionosphere. The TEC from IGS stations are obtained from http://www.ionolab.org/indephp?p age=webtec&language=en.

To recognize any TEC anomalies trends, confidence bounds of TEC values are calculated [15]. TEC more than the upper bound (UB) is measured as a positive anomaly and TEC less than the lower bound (LB) as a negative anomaly. The limits are computed by the median (m) and standard deviation (σ) of twenty pre and ten post days after the EQ day by the following equation. Then bounds are computed by below equations [11].

$$\text{Upper Bound} = m + 2\sigma, \quad \textbf{(4)}$$

$$\text{Lower Bound} = m - 2\sigma. \quad \textbf{(5)}$$

Where, m denotes median and standard deviation is depicted by σ.

To confirm the anomalous ionospheric situations the Deviation TEC (DTEC) is calculated. Deviation TEC can be calculated for selected IGS stations by this formula:

$$TEC_{deviation} = TEC_{original} - \text{Upper Bound} \quad \textbf{(6)}$$

IV. RESULT

In this paper, The ionospheric anomalies from IGS stations within EPZ are considered within the twenty days earlier and ten days next the EQ of the M_w 6.7, Mongolia EQ. Fig. 2 show the geographical positions of EQ and IGS stations that lie in the EPZ.Our outcomes are to delineate the geomagnetic storm (Kp>4) or EQ induced perturbations within five days pre-and post-EQ the M_w 6.7 event over the epicentral regions. Geomagnetic storms are quiet on the day of EQ but there is a monotonous increase in geomagnetic storm analysis a few days before EQ and right after EQ, meaning the storm is active beyond 5 days pre-and right after main EQ day (Fig. 3). The confidence bounds are calculated by using daily TEC data from selected IGS stations within the EPZ. The TEC retrieved from IGS stations displays irregularities within five days before the EQ (e.g., -4, -3, -2, -1).Ionospheric anomalies are on the EQ day. The KSTU station showed positive TEC anomalies on days -2, -1 before, on the EQ day and one day after EQ.The ULAB station showed positive TEC anomalies on days -4,-3,-2,-1, on the EQ day and one day after EQ as shown in the

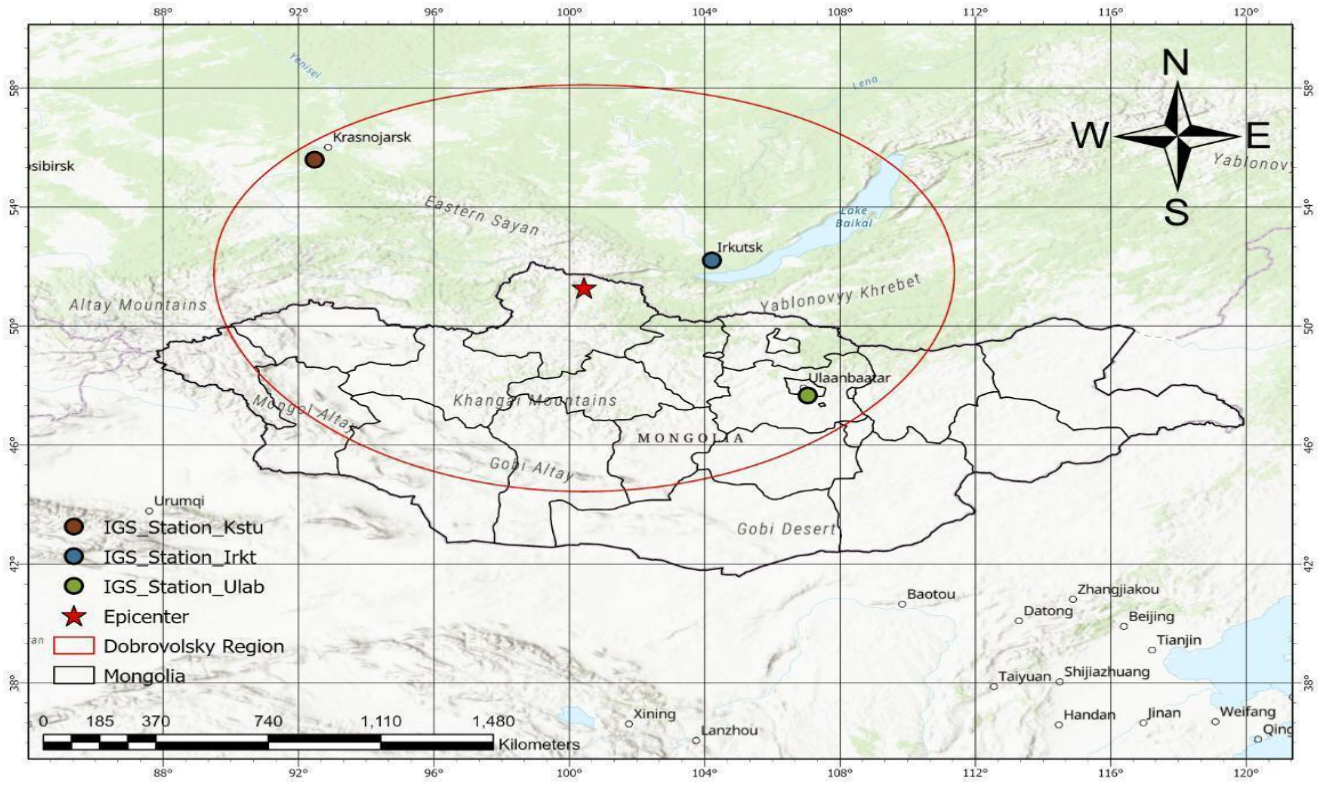


Fig. 2 Location of EQ epicenter and GNSS permanent stations functioning in the EPZ. The red star depicts the site of the epicenter where small colored circles represent IGS stations and the red line denotes the EPZ estimated by the Dobrovolsky equation.

Fig. 4. If an original TEC is more than either of the lower or upper boundary then we declare that an abnormal signal is detected. As per previous results positive ionospheric anomaly is TEC above upper confidence bound (Fig. 4)[10]. To provide further proof in the preparation period of M_w 6.7 EQ, TEC variances are examined from three IGS stations (i.e. IRKT,KSTU and ULAB stations).Temporal and spatial graphs show TEC anomalies on the EQ day and three days afore the EQ day (Fig. 4 and 5).The ionospheric anomalies are clearly observable in IGS stations.

Similarly, the deviations in TEC among the observed TEC and upper bound are discovered pre and post the EQ, as shown in Fig. 5. Enhancement in TEC prior to EQ supports that anomaly may be due to the Kp>3 storm over EPZ. Fig.5 depicts DTEC anomalies that are because of geomagnetic storms and no association of activating ionospheric disturbance has been observed. Fig. 6 showed the cross wavelet spectrum of TEC anomalies 20 days before and 10 days after main shock. It shows that an increase in TEC disturbances appeared on the 4th day before the main event. After the 4th day, the disturbances were prolonged and enlarged, and attained its maximum value at EQ day. Then, the TEC disturbances disappeared after 2 days of main shock. Our findings indicate that abnormal disturbances of ionospheric TEC lie between -4, -3, -2, -1 and day of EQ. [16-17] Further, storms are active 5 days before main shock and right after it, so anomalies is induced by storm.

V. CONCLUSION

In the present paper, seismo ionospheric perturbations of shallow hypo central EQ having M_w 6.7 monitored by IGS stations in Mongolia functioning nearby epicenter from GPS TEC, has been discussed. The geomagnetic storm is active beyond 5 days before EQ of M_w 6.7 (Kp>4) ; it shows no association with the epicenter. Investigation on TEC improves our results which depicts that enhancement and depletion in TEC prior to EQ supports the induction of storm anomalies over the seismogenic zone. Lastly, since present study EQ has been preceded by geomagnetic activity, so looking for genuine ionospheric perturbations instigated by seismic activity is the task. Finally, the comprehension to what extent EQs and geomagnetic conditions are related to one another is undeniable for the field of EQ prediction.

ACKNOWLEDGEMENT

The authors would like to thank the IGS community for the availability of TEC data. Additionally, we are also grateful to the USGS, ISGI and OMNI WEB for making data available for the EQ, solar indices, Geomagnetic indices, and TEC data.

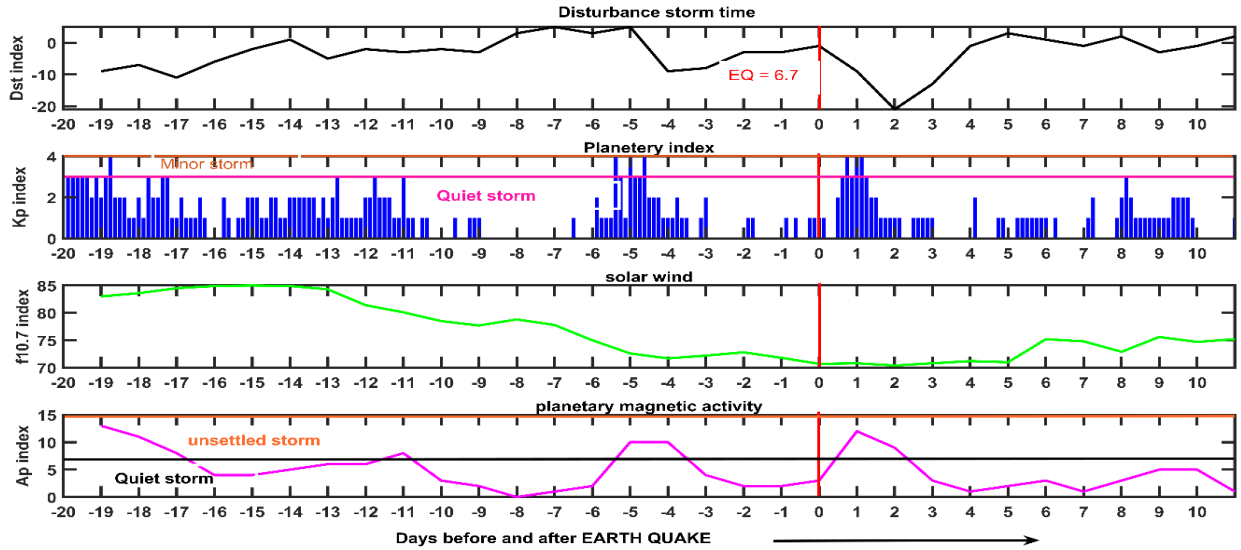


Fig. 3 Geomagnetic and solar storm conditions during observational period. (a) Dst values, (b) Kp index, (c) F10. 7, (d) Ap. Red lines depict EQ day.

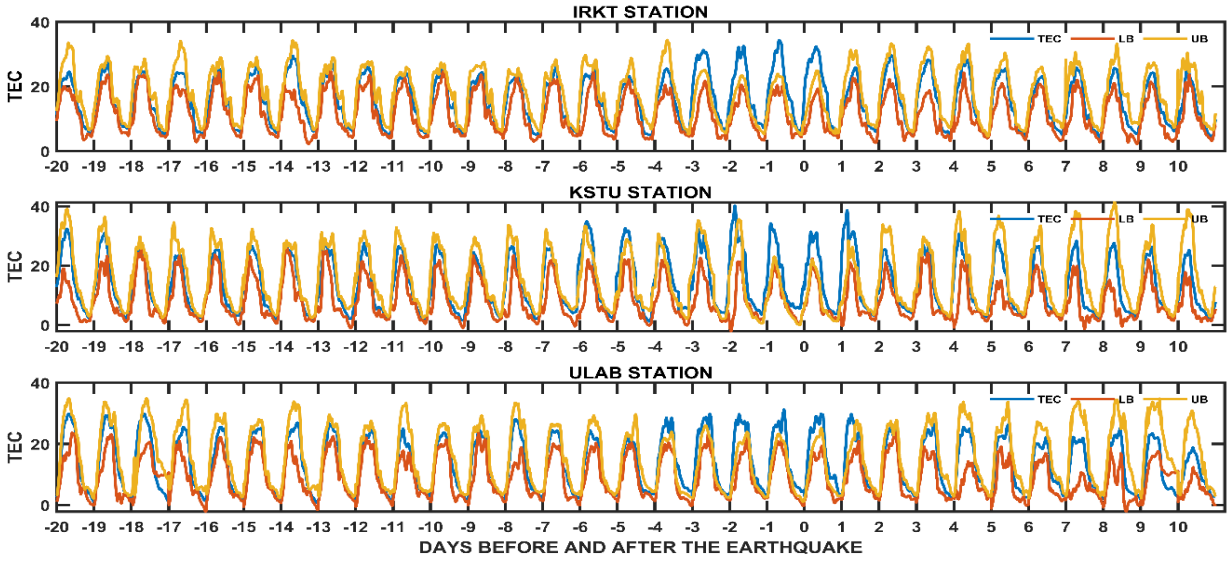


Fig. 4 TEC measurement recorded at three IGS stations (KSTU, ULAB, IRKT)for thirty days twenty days prior and ten days next to EQ.

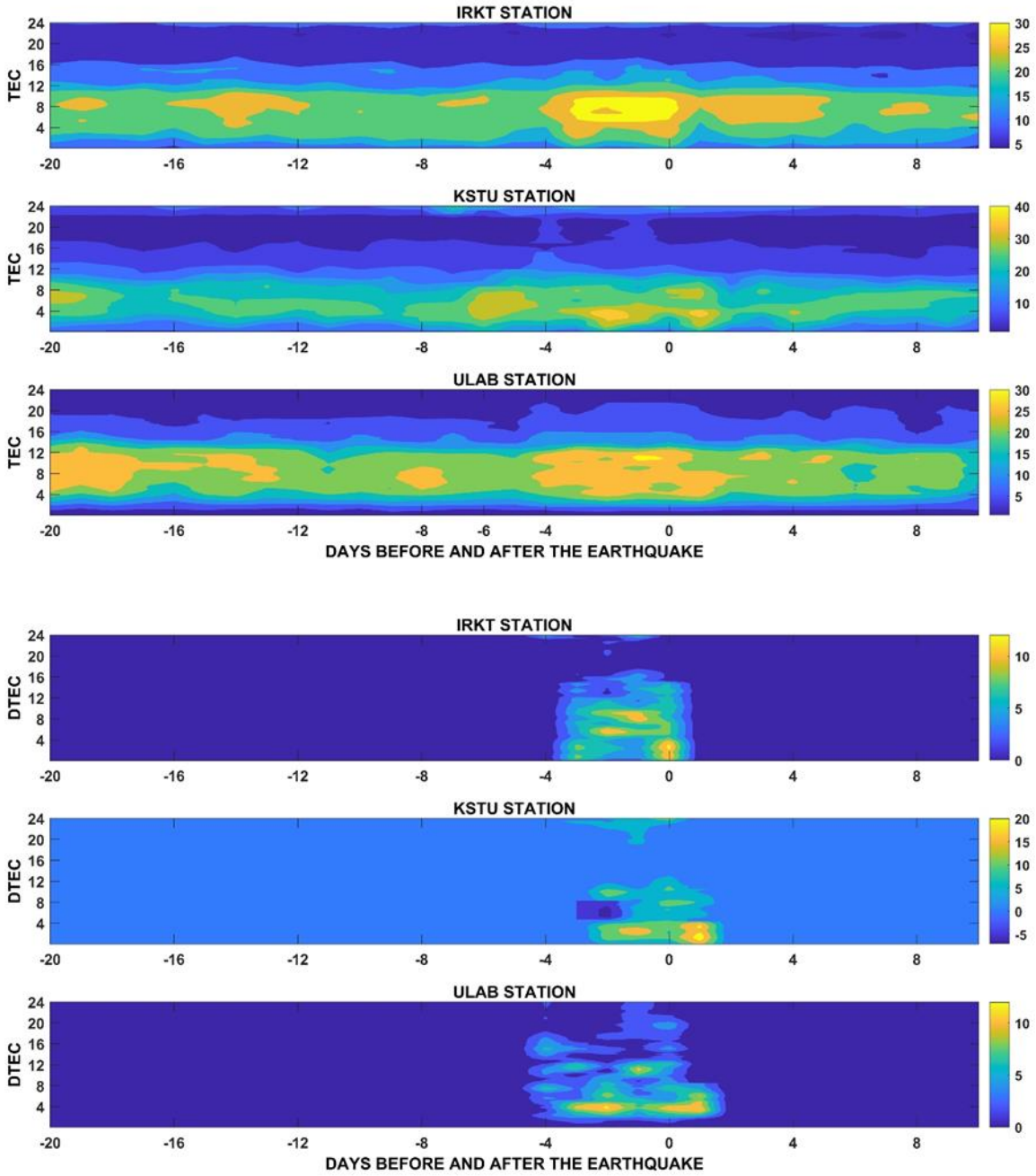


Fig. 5 Spatial TEC (upper) and DTEC (lower) recorded at three IGS stations (KSTU, ULAB, IRKT) shows variations due to geomagnetic storm twenty days before and ten days after EQ.

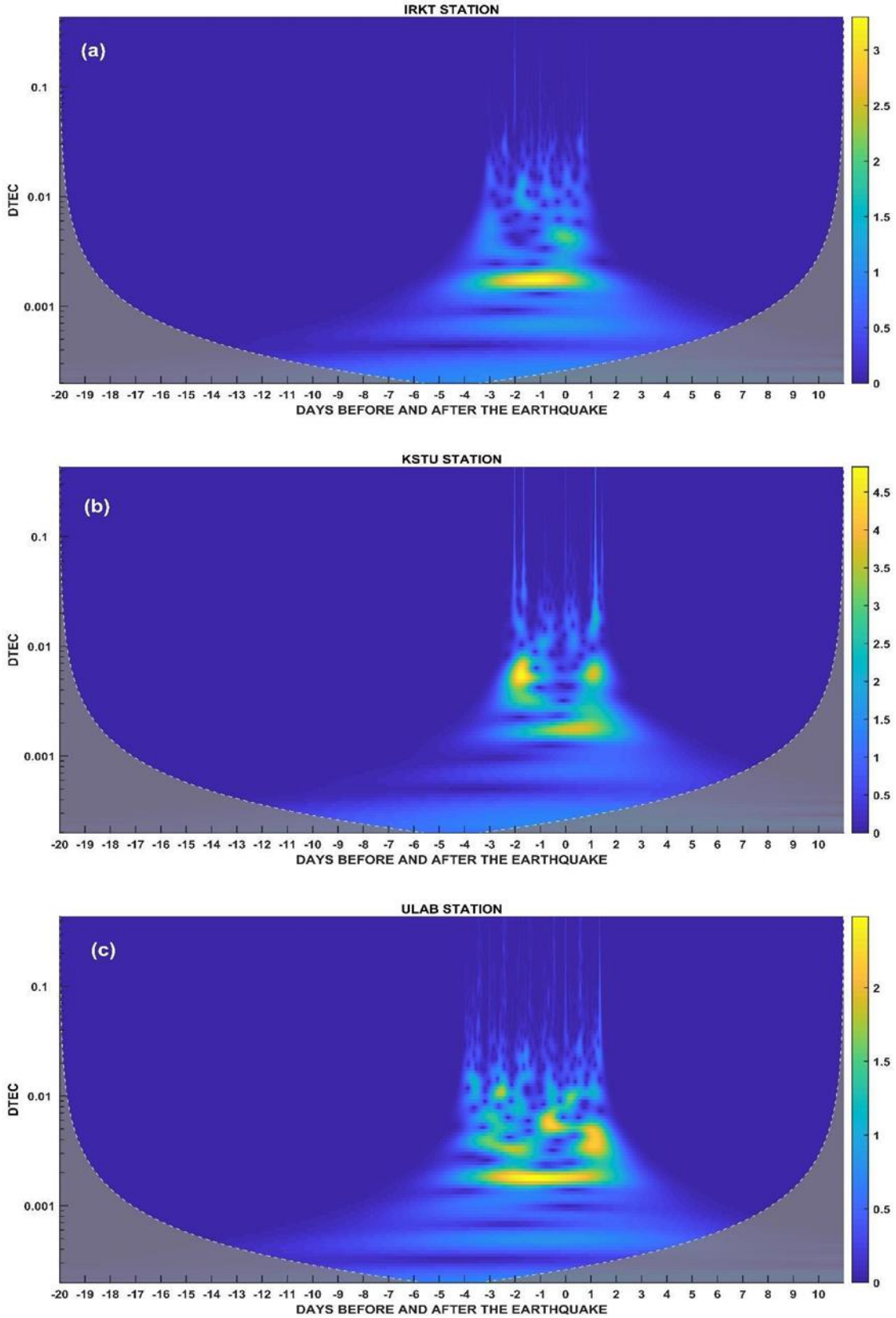


Fig. 6 Wavelet spectrum of DTEC retrieved from IGS station (a) IRKT (b) KSTU and (c) ULAB stations depicts TEC disturbances before the main event of EQ.

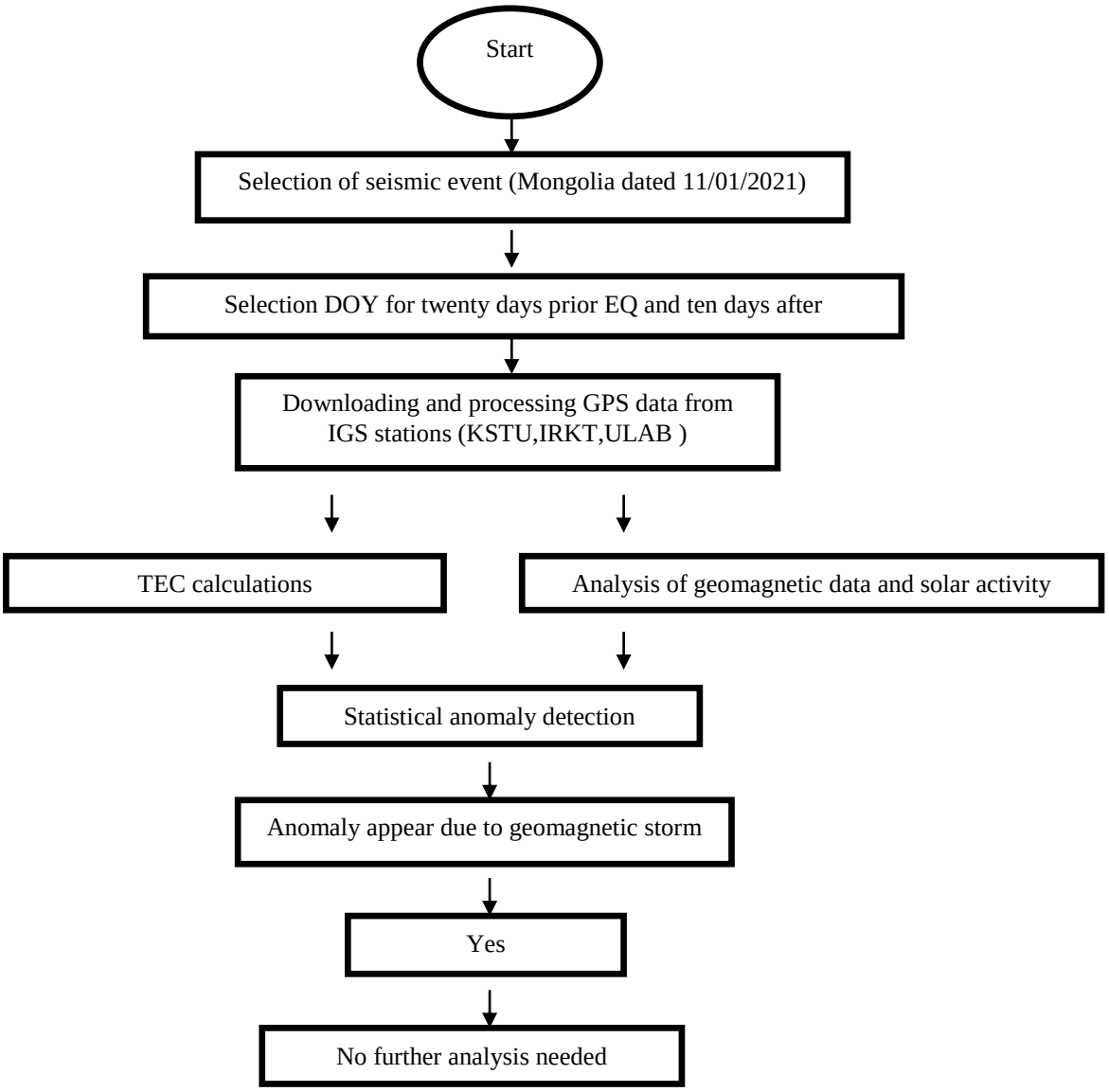


Fig. 7 Flowchart depicts methodology adopt in Proposed paper

REFERENCES

[1] K. Davies and G. K. Hartmann, “Studying the ionosphere with the global positioning system,” *Radio Sci.*, vol. 32, no. 4, pp. 1695–1703, 1997, doi: 10.1029/97RS00451.

[2] Z. Hong-ping and Z. H. U. Wen-yao, “Real - t i m e Monitoring and Prediction of Ionospheric Electron Content by Means of GPS t .,” vol. 45, no. 2, pp. 331–337, 2004, doi: 10.016/j.chinastron.2004.07.00.

[3] M. Shah *et al.*, “Total electron content anomalies associated with earthquakes occurred during 1998–2019,” *Acta Astronaut.*, vol. 175, no. May, pp. 268–276, 2020, doi: 10.1016/j.actaastro.2020.06.005.

[4] MUP lukavac, “Deep learning for ionospheric TEC forecasting at mid-latitude stations in Turkey,” *Acta Geophys.*, vol. 69, no. 2, pp. 589–606, 2021, doi: 10.1007/s11600-021-00568-8.

[5] E. Astafyeva, “Ionospheric Detection of Natural Hazards,” *Rev. Geophys.*, vol. 57, no. 4, pp. 1265–1288, 2019, doi: 10.1029/2019RG000668.

[6] A. Kiyani, M. Shah, A. Ahmed, H. Hussain, and S. Hameed, “Seismo ionospheric anomalies possibly associated with the 2018 M w 8 . 2 Fiji earthquake detected with GNSS TEC,” *J. Geodyn.*, vol. 140, no. July, p. 101782, 2020, doi: 10.1016/j.jog.2020.101782.

[7] K. Davies and D. M. Baker, “Ionospheric effects observed around the time of the Alaskan earthquake of March 28, 1964,” *J. Geophys. Res.*, vol. 70, no. 9, pp. 2251–2253, 1965, doi: 10.1029/jz070i009p02251.

[8] S. Pulinets, “Ionospheric precursors of earthquakes: Recent advances in theory and practical applications,” *Terr. Atmos. Ocean. Sci.*, vol. 15, no. 3, pp. 413–435, 2004, doi: 10.3319/TAO.2004.15.3.413(EP).

[9] S. Jin, G. Occhipinti, and R. Jin, “GNSS ionospheric seismology: Recent observation evidences and characteristics,” *Earth-Science Rev.*, vol. 147, pp. 54–64, 2015, doi: 10.1016/j.earscirev.2015.05.003.

[10] M. Freeshah *et al.*, “Analysis of atmospheric and ionospheric variations due to impacts of super typhoon mangkhut (1822) in the northwest Pacific Ocean,” *Remote Sens.*, vol. 13, no. 4, pp. 1–20, 2021, doi: 10.3390/rs13040661.

[11] A. R. Abbasi, M. Shah, A. Ahmed, and N. A. Naqvi, “Possible ionospheric anomalies associated with the 2009 Mw 6.4 Taiwan earthquake from DEMETER and GNSS TEC,” *Acta Geod. Geophys.*, vol. 56, no. 1, pp. 77–91, 2021, doi: 10.1007/s40328-020-00325-1.

[12] M. A. Adil, A. Abbas, M. Ehsan, M. Shah, N. A. Naqvi, and A. Alie, “Investigation of ionospheric and atmospheric anomalies associated with three Mw >6.5 EQs in New Zealand,” *J. Geodyn.*, vol. 145, no. March, p. 101841, 2021, doi: 10.1016/j.jog.2021.101841.

[13] H. Li, Y. Yuan, Z. Li, X. Huo, and W. Yan, “Ionospheric electron concentration imaging using combination of LEO satellite data with ground-based GPS observations over China,” *IEEE Trans. Geosci. Remote Sens.*, vol. 50, no. 5 PART 2, pp. 1728–1735, 2012, doi: 10.1109/TGRS.2011.2168964.

[14] I. P. Dobrovolsky, S. I. Zubkov, and I. Miachkin, “Estimation of the size of earthquake preparation zones,” *Pure Appl. Geophys. PAGEOPH*, vol. 117, no. 5, pp. 1025–1044, 1979, doi: 10.1007/BF00876083.

[15] M. Shah and S. Jin, “Pre-seismic ionospheric anomalies of the 2013 Mw = 7.7 Pakistan earthquake from GPS and COSMIC observations,” *Geod. Geodyn.*, vol. 9, no. 5, pp. 378–387, 2018, doi: 10.1016/j.geog.2017.11.008.

[16] L. M. He, L. X. Wu, A. De Santis, S. J. Liu, and Y. Yang, “Is there a one-to-one correspondence between ionospheric anomalies and large earthquakes along Longmenshan faults?,” *Ann. Geophys.*, vol. 32, no. 2, pp. 187–196, 2014, doi: 10.5194/angeo-32-187-2014.

[17] A. Ali, C. Sheng-Chang, and M. Shah, “Continuous wavelet transformation of seismic data for feature extraction,” *SN Appl. Sci.*, vol. 2, no. 11, pp. 1–12, 2020, doi: 10.1007/s42452-020-03618-w.

Estimation of Drag Reduction of a Cargo Tractor-trailer using CFD Analysis in Different Configurations

Muhammad Rashid Liaqat
Department of Avionics Engineering
and Aviation Technology
The Superior University
Lahore, Pakistan
rashid.liaqat@superior.edu.pk

Ahmad Hammad
Department of Avionics Engineering
and Aviation Technology
The Superior University
Lahore, Pakistan
ahmad.hammad@superior.edu.pk

Dr. Mohsin Khalil Ahmad
Department of Avionics Engineering
and Aviation Technology
The Superior University
Lahore, Pakistan
mohsin.khalil@superior.edu.pk

***Abstract*—Conventional cargo tractor trailer vehicles with blunt body have poor aerodynamic design, which results in high drag force and high fuel consumption at highway speeds (above 70 km/hr). In this study, improvement in aerodynamic design of cargo freighters is proposed for better fuel economy. Computational Fluid Dynamics (CFD) was employed to numerically investigate the flow characteristics at both rear and front of the vehicle. Flow physics in terms of velocity distribution, pressure distribution and turbulent kinetic energy around the vehicle is studied. The vehicle is modelled in different configurations for improved pressure distribution. This study presents the numerical simulation basis for the reduction in cargo trailers' drag for better fuel economy**

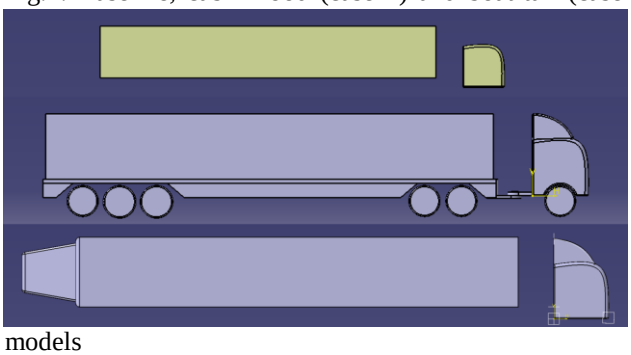
Keywords— CFD, Aerodynamics, Drag, Tractor-Trailer)

I. INTRODUCTION

Heavy commercial vehicles have the most poor aerodynamic performance compared to other ground vehicles due to the blunt frontal area which generates fluid flows with huge pressure gradients, hence, increasing the overall pressure drag[1, 2]. It is estimated that a 40-tonne articulated truck at 60 mph can consume four times more fuel than an average car[3].

Efforts for reducing the fuel consumption focus on modifying the flow field around the vehicle so that the pressure gradient between the front and the back of the vehicle is reduced[4]. Commonly used methods are employing flow deflectors, micro vortex generators, synthetic jets, boundary layer separation control or by external add-ons.

Fig.1. Baseline, cabin hood (case 1) and boat-tail (case 2) models



Studies have been carried out to improve the fuel economy of cargo vehicles [9,10]. Different strategies have been proposed in these studies to reduce drag, increase fuel economy and reduce the greenhouse emissions. several types of active and passive flow control mechanisms[11] have been investigated for the improvement in aerodynamics of road vehicles. On heavy ground vehicles, the pressure drag is the most dominant force, contributing more than 90% of the total drag produced[12]. Fuel consumption caused by aerodynamic drag on heavy vehicles can vary widely because it is affected by different factors such as truck type, terrain topography, and road conditions. Aerodynamic drag varies directly with square of velocity of the vehicle. At lower speed, rolling friction dominates whereas at highway speeds aerodynamic drag starts dominating and most of the vehicle's fuel is consumed overcoming aerodynamic drag. It is estimated that the tractor generates 45% of the total drag and the trailer 30%[13].

This study focuses on the design and evaluation of different add-ons for reduction in vehicle drag for better fuel economy. A comparative study of tractor-trailer cargo vehicles with various configurations was done. Two add-ons were designed: cabin hood and boat tail, and their performance were compared against a baseline model. The figure 1 shows the baseline, case 1 and case 2 models.

II. MODELING AND SIMULATION

3D modeling is crucial for any fluid flow simulation. CATIA V5 has been used for modeling because of its user friendliness. Originally a realistic model was made but it was later simplified to save computational resources while also reducing geometric errors. Models have been simplified by removing the wheels, axles, tractor trailer connecting rods and trailer side skirts. The wheel and shaft housing has been completely filled.

For CFD analysis, ANSYS Fluent was used to numerically simulate the flow with the given boundary and flow conditions with pressure based solver. The baseline configuration was simulated for the analysis of flow physics, inflation layers were introduced to capture flow separation at the top of both cabin and trailer surfaces. Velocity inlet at atmospheric pressure and pressure exit with 0 gage pressure were defined at inlet and outlet, respectively. "Wall" type boundary conditions were assigned to the vehicle geometry as well as the bottom of domain which is translated as a boundary through which no mass can penetrate and no slip condition was enforced as well. Along the top and side walls of domain "symmetry" condition was employed which is read as a boundary through which mass cannot pass but unlike wall boundary condition which enforces zero mass flux via zero-velocity condition, the symmetry condition enforces this with zero-shear condition. As there is no shear stress at the symmetry condition faces, it can be treated as far-field region for top and side walls of the control volume.

A. *Grid Generation and Discretization of Domain*

An unstructured grid is devised around the vehicle with refined mesh at the surfaces of vehicle. For better and refined mesh different surfaces were given different element sizing via faces selection option. Computational domain size was defined keeping in mind to simulate a continuous medium and unbounded flow field. Size of the domain was created to make sure that flow over truck geometry does not interact with walls of domain.

B. *Model*

For this problem, fluid flow was assumed to be steady, incompressible and fully turbulent as the Reynolds Number for the case was quite high. There are only two unknowns velocity v and pressure p for the Navier-Stokes equations which are not sufficient for the solution due to high turbulence. For simplicity, Realizable κ-ε turbulence model was incorporated which models turbulent kinetic energy k and turbulent dissipation ε [5].

The Realizable κ – ε turbulence model have shown better results than the standard κ – ε model for fluid flows that includes recirculation, boundary layers under strong adverse pressure gradients, and flow separation [6]. The SIMPLE segregated algorithm was used because the fluid was incompressible[7]. For turbulence parameters, the inlet and outlet were assigned a turbulent intensity of 5% and turbulent viscosity ratio of 10. Following boundary conditions were defined at the named selections of parts, to simulate the flow field in computational domain:

TABLE I. BOUNDARY CONDITIONS FOR BASE TRACTOR TRAILER VEHICLE

Boundary Condition Name	Boundary Condition type	Value
Inlet	Velocity inlet	20 m/s
Outlet	Pressure outlet	0 Pa
Symmetry	Symmetry	--
Bottom	Wall with no slip	--
Vehicle Surfaces (Cabin and Trailer)	Wall with no slip	--
Side Wall	Symmetry	--
Top	Symmetry	--

III. RESULTS AND ANALYSIS

All numerical simulations were carried out with similar assumptions, mesh size, boundary conditions, solution schemes and solver settings as discussed in the previous section. Fuel consumption and approximate savings' estimation were estimated for all vehicle configurations so that best design can be recommended to the local trucking and transport industry.

A. *Velocity Distribution*

For the baseline model it can be seen that maximum velocity occurs at the cabin top and minimum velocities occur at trailer top as well as rear of the trailer in terms of flow recirculation due to adverse pressure gradient. The recirculation zone at rear as well as flow separation at top is also visible in the velocity contours.

For the case 1, the flow stagnates at front of the cabin due to obstruction in flow, expands over the cabin hood where maximum flow velocity can be observed, separates from trailer top and attaches downstream with increase in energy, has recirculation zones between cabin and trailer and a huge wake region trailing behind the vehicle due to adverse pressure gradient formed by the blunt rear.

For case 2, it can be seen that velocity profile in the front is similar to case 1 but velocity profile at the back is different as there is a smaller wake region due to the boat-tail.

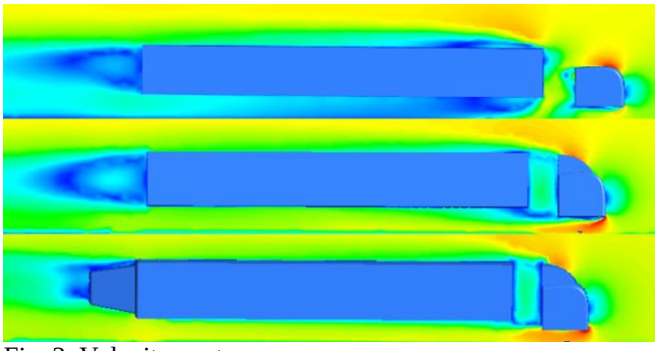


Fig. 2. Velocity contours

B. *Pressure Distribution*

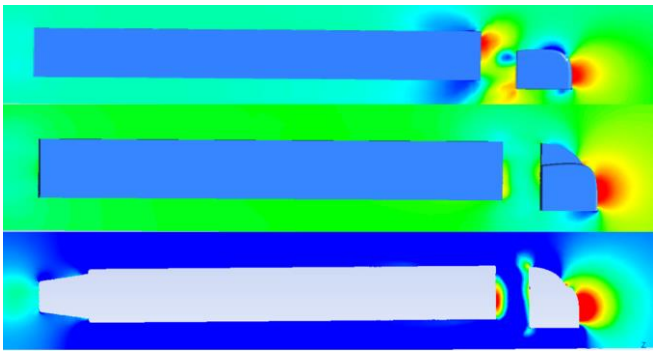


Fig. 3. Pressure contours

For baseline case it was noted that the flow stagnated with maximum pressure at front of the vehicle. Secondary flows were captured between the cabin-trailer gap, trailer top due to flow separation, trailer bottom due to ground effects and trailer rear due to adverse pressure gradient. Higher the difference of pressure at front and rear of the vehicle, higher will be its pressure drag. So in order to reduce the drag, one has to modify the geometry in such a way that this difference is reduced.

To improve the flow physics over vehicle's cabin, a hood was designed so that there is no stagnant air on trailer top and also to minimize flow separation over top of the trailer. It was observed that the flow over the cabin and trailer front has been improved significantly; however, it has not changed at the rear as there is no change in geometry at rear of vehicle.

In case 2, to reduce wake behind the vehicle, boat-tail geometry was created to reduce the region of adverse pressure gradient. As expected, the pressure distribution at the front is similar to case 1 but it is different at the back as there is a smaller under-pressure area.

C. *Qualitative Comparative Analysis*

Qualitatively we can see that flow at the front and top of the vehicle is improved in case 1 because the addition of a hood stops the flow from stagnating at the edge of the trailer, instead it transits smoothly from the front to the top of the trailer. This helps reduce the over-pressure area. However it does not change the flow field in the wake region. In case 2, the boat tail at the rear modifies the flow field at the back so that it returns to far-field conditions smoothly. This reduces the under-pressure area, which decreases the overall pressure gradient, and hence, the pressure drags.

D. *Quantitative comparative analysis*

By comparing the results obtained in previous sections, it was observed that Case-2 had the most efficient aerodynamic design with minimum drag force as compared to other configurations. Tabular description of differences in drag forces can be seen in the following table:

TABLE II. COMPARISON OF VARIATION IN DRAG FORCE W.R.T. CONFIGURATIONS

Case/Configuration	Drag Force at 20 m/s (N)	Drag Force at 30 m/s (N)	% Difference at 20 m/s	% Difference at 30 m/s
Base Tractor-Trailer	527.87	1172.46		
Case-1	286.68	619.87	45.69	47.13
Case-2	226.90	595.97	57.02	49.17

As drag force is function of square of velocity, drag forces at varying velocities were calculated and are as shown in the following table:

TABLE III. VARIATION OF DRAG FORCE (N) WITH VARYING VELOCITY

Case Name	60	65	70	75	80	85	90
Base	366.58	430.22	498.95	572.77	651.69	735.69	824.80
Case-1	199.08	233.65	270.97	311.07	353.93	399.55	447.94
Case-2	157.57	184.93	214.47	246.20	280.12	316.23	354.53

E. *Estimated fuel savings*

All ground vehicles, which move on roads, have to overcome rolling resistance and aerodynamic drag. At lesser speeds, rolling friction has more impact and most of the fuel is used on it whereas, at highway speeds aerodynamic drag starts dominating. In other words it can be said that at highway speeds, most of the fuel is consumed overcoming aerodynamic resistance of the vehicle. If the vehicle shape is aerodynamically designed, it will have lower aerodynamic drag; hence it will have better fuel economy. Fuel consumption per 100 km was estimated by an equation [8]:

$$L/100 = 0.008051 \times F_D \quad (1)$$

Where,

L/100 is the amount of fuel consumed per 100 kilometers

FD is the drag force faced by the vehicle

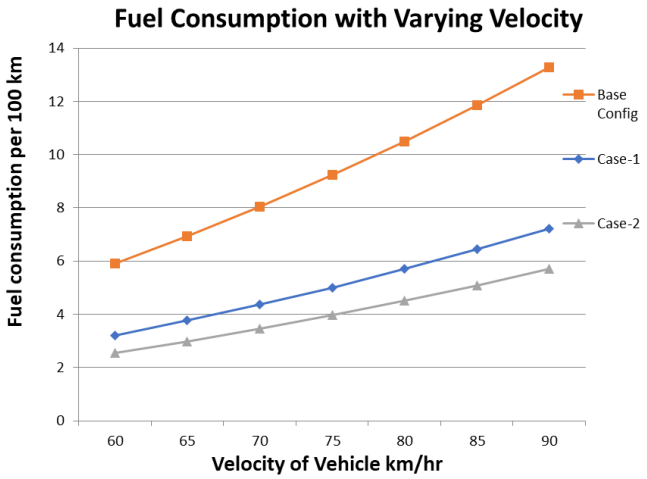


Fig. 4. Fuel consumption trend against velocity

It can be seen that Case-2 shows encouraging results in terms of minimum fuel consumption per 100 km. This decrease in fuel consumption is only due to the modification in design which led to better pressure distribution. Using the above mentioned empirical relation, it is estimated that Case-2 geometry, with lesser drag, will consume 57% lesser fuel at highway speeds i.e. above 70 km/h.

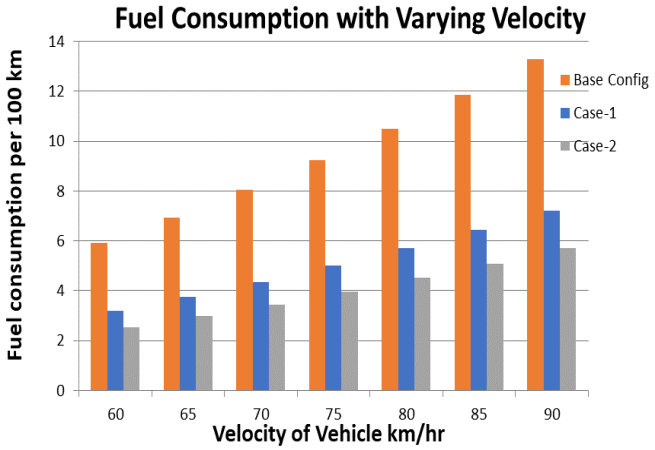


Fig.5. Fuel consumption vs velocity

IV. CONCLUSION & RECOMMENDATIONS

Following conclusions were drawn as a result of this study:

- Flow was simulated at different flow speeds for all the models, and it is concluded that the co-efficient of drag CD varies slightly against a variation in vehicle speed. However, drag force follows a second order variation with slight deviation as theoretically expected.
- In 3-D analysis, it is concluded that every modification leads to a significant variation in flow characteristics and overall drag of vehicle can be changed.

- It is estimated that with using the Case-2 modification, a vehicle may save up to 57% fuel at highway speeds, resulting in annual savings in millions of liters of fuel.
- Vehicles with low aerodynamic drag at highway speeds can travel at higher speeds thus increasing overall Heavy Traffic Vehicle HTV speeds on highways and decreasing time of delivery as well as shipment costs.
- Experimental studies can be done on different add-ons installed on vehicle in order to validate the current study
- Cabin and Trailer design can be modified to streamline the flow around the vehicle for better aerodynamic characteristics

REFERENCES

[1] Schoon, R.E., "On-road evaluation of devices to reduce heavy truck aerodynamic drag". 2007, SAE Technical Paper.

[2] Chowdhury, H., Moria, H., Ali, A., Khan, I., Alam, F. and Watkins, S., "A study on aerodynamic drag of a semi-trailer truck". Procedia Engineering, 2013. 56: p. 201-205.

[3] Mohamed-Kassim, Z. and A. Filippone, "Fuel savings on a heavy vehicle via aerodynamic drag reduction". Transportation Research Part D: Transport and Environment, 2010. 15(5): p. 275-284.

[4] Cooper, K.R., "Truck aerodynamics reborn-lessons from the past". 2003, SAE Technical Paper.

[5] ANSYS 16 User Manual. 2016.

[6] Shih, T.-H., Liou, W. W., Shabbir, A., Yang, Z., Zhu, J., "A new k-ϵ eddy viscosity model for high reynolds number turbulent flows". Computers & Fluids, 1995. 24(3): p. 227-238.

[7] Patankar, S.V. and D.B. Spalding, "A calculation procedure for heat, mass and momentum transfer in three-dimensional parabolic flows, in Numerical Prediction of Flow, Heat Transfer, Turbulence and Combustion". 1983, Elsevier. p. 54-73.

[8] Roy, S. and P. Srinivasan, "External flow analysis of a truck for drag reduction". SAE transactions, 2000: p. 808-812.

[9] R. Pankajakshan, B. Mitchell, and D. L. Whitfield, "Full-scale simulations of drag reduction devices for class 8 trucks," in The Aerodynamics of Heavy Vehicles II: Trucks, Buses, and Trains, ed: Springer, pp. 339-348, 2009.

[10] L. A. Raman and H. R. Hari, "Methods for Reducing Aerodynamic Drag in Vehicles and thus Acquiring Fuel Economy," Methods, vol. 3, pp. 26-32, 2016.

[11] M. N. Sudin, M. A. Abdullah, S. A. Shamsuddin, F. R. Ramli, and M. M. Tahir, "Review of research on vehicles aerodynamic drag reduction methods," International Journal of Mechanical and Mechatronics Engineering, vol. 14, pp. 37-47, 2014.

[12] R. M. Wood and S. X. Bauer, "Simple and low-cost aerodynamic drag reduction devices for tractor-trailer trucks," SAE Technical Paper, 2003

[13] D. G. Hyams, K. Sreenivas, R. Pankajakshan, D. S. Nichols, W. R. Briley, and D. L. Whitfield, "Computational simulation of model and full scale Class 8 trucks with drag reduction devices," Computers & Fluids, vol. 41, pp. 27-40, 2011.

SIMULATIONS OF THIN GRAY FLUID OVER A MOVING FLAT PLATE

Sadia Maryam
School of Interdisciplinary Engineering & Sciences,National University of Sciences and Technology
Islamabad, Pakistan
sadiamaryam.38@gmail.com

Mazhar Shehzad
School of Interdisciplinary Engineering & Sciences, National University of Sciences and Technology
Islamabad, Pakistan
mshehzad.mscse16@rcms.nust.edu.pk

Ammar Mushtaq
School of Interdisciplinary Engineering & Sciences , National University of Sciences and Technology
Islamabad, Pakistan
ammar.mushtaq@sines.nust.edu.pk

***Abstract*—The objective of this research is to present a generalized numerical solution valid for all temperature differences i.e. for both the cases when $\theta w = 1$ (Linear Radiations) and for $\theta w > 1$(Non-Linear Radiations) of a thin gray fluid. Firstly, on a moving flat plate, two dimensional boundary layer equations are presented for thin Gray fluid flow and heat transfer. Using similarity transformations, governing partial differential equations are transformed into highly non-linear ordinary differential equations.By using Runge-Kutta numerical integration, the governing ordinary differential equations are solved, and the effects of the related parameters of practical importance are studied. The results of the research conclude that the non-dimensional parameter temperature ratio parameter θw shows thinness in the boundary layer. The Radiational effects are strengthened as θw becomes greater than 1. Prandtl number Pr and Radiation Parameter Rd show the same effects when there is an increment in their values, thermal boundary layer thickness increases by 103.3 % and 336.6% in the case of Rd. The uniqueness of this research is that it gives numerical solution for all temperature differences.**

Keywords— Boundary layer, Gray fluid, Numerical solution

I. INTRODUCTION

Initially, the mechanics of fluids in motion was divided into two fields of study. The first one is called hydrodynamics, which describes the fluid across surfaces and bodies, assuming fluid is inviscid, incompressible, and irrotational, and secondly, the hydraulics sector, which was largely an area of the experimental field for fluid behavior in equipment such as pipelines, pumps, and ships. Hydrodynamics looked as if it would be a good theory for flows inside the region not close to solid boundaries however concepts like friction and drag were not explained by it. [1]. Ludwig Prandtl proposed a theory to connect these disciplines. In 1905, during the third Congress of Mathematicians in Heidelberg, He presented his physical phenomenon.Prandtl's [2] paper gave the primary description of the physical phenomenon concept. A physical fact is that the narrow zone of flow adjacent to a surface effects the flow by the friction between the solid surface and the fluid surface. In other words, he anticipated that a friction control would force the fluid near to the surface to stay on the surface. He assumed no-slip conditions on the surface, where the flow was inviscid, and frictional results were experienced only in a very physical phenomena.Continuity Equation and Navier Stoke's equation are the places to begin Prandtl's physical phenomenon theory.Prandtl's theory was applied by Blasius [3] to explain the steady two-dimensional laminar flow that forms on a semi-infinite plate parallel to a unidirectional flow. The physical phenomena of flow on a flat moving surface was explored during a quiet ambient fluid in 1961 by Sakiadis[4]. He discovered the same ordinary differential equation (ODE) as Blasius but with different boundary conditions. Falkner and Skan worked on Blasius' physical phenomenon to wedge flow i.e. flow in which the plate is not parallel to the flow. Crane [5] in 1970 investigated the physical phenomenon of flow over an eternal moving surface with a continuing temperature. The work of Crane was further extended by Mclead and Rajagopall [6] in 1987. In their study they examined flow in a very viscous fluid that arises as a result of stretching a boundary. Falkner and Skan [7] investigated streamline flow passing through a wedge. The physical phenomenon equation can be converted into an ordinary differential equation by using similarity equations, also called as the Falkner-Skan equation. Furthermore, Hartree [8] and Ste-Wartson [9] analyzed these equations.

The heat emitted by a substance above absolute zero is electromagnetic radiation. Rafael Cortell [10] implemented a numerical solution to Sakiadis flat plate flow in hydraulics with thermal radiation. The movement of an optically thin, incompressible and viscous fluid over a stretched plate is investigated by Raptis [11]. Elbashbeshy[12] studied the effect of radiation on the flow of a viscous fluid and how heat is transmitted over an isothermal wedge .[13] Biliana Bidin and Roslinda Nazar examined numerically steady two-dimensional flow of a viscous fluid over a stretching sheet in the presence of thermal radiation using an exponentially stretching sheet . An electrically conducting viscous incompressible micropolar fluid is applied to a shrinking sheet with radiation effects and its heat characteristics and hydromagnetic (MHD) axisymmetric stagnation point flow are investigated by Shahzad Ahmed, M. Ashraf and K.S. Syed [14]. There is an exponentially shrinking sheet and heat dissipation during thermal radiation which is taken into account by Asmat Ara , Najeeb Alam Khan, Hassam Khan ,Faqiha Sultan [15]. By applying a diffusion approximation to the Rosseland approximation. Impact of thermal radiation on temperature distribution in an absorbing and emitting material that flows over a wedge is studied by Viskanta and Grosh [16].
A characteristic convection-radiation interaction on a physical phenomenon with uniform suction along a vertical plate was explored by Hossain et al. [17]. The original convection flow of an optically dense viscous fluid over an isothermal frustum have been researched by Yin [18]. Extensive research on the consequences of radiation and fluid flow has been done. Ali et al.[19] studied the free convection flow during the existence of radiation. Murthy et al.[20] investigated during the existence of radiation the

flow through a permeable medium. Researchers Bestman and Adiepong [21] investigated the thermal properties of unsteady hydromagnetic free convection flows. A viscous Gray fluid enclosed by a stationary plate has been studied by England and Emery[22].Muthucumarawamy and Chandrakala [23] investigated mass transfer and influence of radiation on a thin Gray and viscous fluid. The radiational effects on flow through an impulsively started vertical plate of changing temperature and mass flow were examined by Muthucumarawamy and Vijayalakschmi[24]. Research has been conducted by Rajesh [25] near vertical plates the radiation effects of thin gray fluidson free convection. By varying the temperature of an impulsively started vertical plate, Rajput and Kumar[26] studied the effects of radiation and rotation on MHD flow of a thin gray fluid. An analysis of the radiation effects of flow past an impulsively started infinite , isothermal vertical plate is presented by Das et al [27]. Soundalgekar and Takhar [28] examined the free convective of a Gray gas, which is optically thin, past a semi-infinite vertical plate. An investigation of the radiation impact on blended convection and an isothermal vertical plate has been finished by Hossain and Thakar [29].

II. GOVERNING EQUATIONS

For an incompressible fluid flow the equations for conservation of mass, linear momentum, and energy are given as :

$$\nabla \cdot V = 0 \tag{1}$$

$$\rho \frac{\partial V}{\partial t} = \nabla . \tau \tag{2}$$

$$\rho c_p \frac{dT}{dt} = \tau . L - \nabla q \tag{3}$$

Where V is the velocity vector, ρ is the density, τ is the Cauchy stress tensor, T is the fluid temperature, c_p is the specific heat constant, q is the heat flux, L and $\frac{d}{dt}$ are the material derivatives. Cauchy stress tensor τ is defined as:

$$\tau = \begin{bmatrix} 2U_{xx} & U_{xx} + U_{yy} \\ U_{yy} + U_{xx} & 2U_{yy} \end{bmatrix} \tag{4}$$

If fluid characteristics are considered independent of temperature,then the time-averaged differential equation for energy is linear . The idea of a co-efficient of heat transfer is therefore determined by the rate of transmission from a wall is given by

$$q = \alpha(T_W - T_r) \tag{5}$$

Where α (Heat Transfer Co-efficient) is the only function of the flow field, T_W is the wall temperature and T_r is the recovery of adiabatic wall temperature.Similarly the physical phenomenon equation may also be a specific case for the final energy. Fluids approaching solid boundaries are at rest, whereas viscous effects retain a layer in the area near the wall .Because of the huge Reynolds number , these viscous layers are relatively thin in comparison to the current length. When the wall and fluid are at different temperatures, the temperature fluctuates. The velocity and thermal physical phenomenon layer is located in these regions. The work of Prandtl in 1905 showed that this thinn region of fluid flow can be examined independently of the majority fluid flow there and the pressure may be influenced by the free flow. Additionally, the velocity normal to the wall depends on the order and thickness of the physical phenomenon, the characteristic velocity being that of the free stream and the distance being from the front. Thus, the physical phenomenon equations for Blasius flat plate flow problem are often summarized by continuity, momentum and energy equations.

III. PROBLEM FORMULATION

Taking into consideration a moving flat plate with a two-dimensional incompressible flow in the presence of parallel free stream heat transfer. Plate placed at $y = 0$ is moving with the constant velocity U_w and U_∞ is the velocity of the fluid outside the boundary . In the vertical direction magnetic field of strength $B(x) = B_o/\sqrt{x}$ is applied and the induced magnetic field is ignored by taking a small magnetic Reynold number. Considering joined effects of Joule heating and viscous dissipation analysis of heat transfer based on non-linear thermal radiation is implemented. Constant temperature T_w of the plate is sustained while the ambient fluid temperature is T_∞. The boundary layer equations of the flow and heat transfer are

$$\frac{\partial u}{\partial x} + \frac{\partial v}{\partial y} = 0 \tag{6}$$

$$u\frac{\partial u}{\partial x} + v\frac{\partial u}{\partial y} = \vartheta \frac{\partial^2 u}{\partial y^2} + \frac{\sigma B^2}{\rho}(U_\infty - u) \tag{7}$$

$$u\frac{\partial T}{\partial x} + v\frac{\partial T}{\partial y} = \alpha \frac{\partial^2 T}{\partial y^2} - \frac{1}{\rho Cp}\left(\frac{\partial q_\gamma}{\partial y}\right) \tag{8}$$

Due to parallel free stream and nonlinear thermal radiation the following boundary conditions are produced.

$$\begin{aligned} u = U_w, \quad v = 0, \ T = T_w \text{ at } y = 0 \\ u \to U_\infty, \quad T \to T_\infty \text{as } y \to \infty \end{aligned} \tag{9}$$

Where along and normal to the plate are x- and $y-$ coordinates respectively, ν the kinematic viscosity, σ the electrical conductivity of the fluid, $B(x) = \frac{B_o}{\sqrt{x}}$ the magnetic field strength, u and v be the velocity components along the x- and y- directions respectively, α the thermal diffusivity, T the fluid's temperature, $\frac{\partial q_r}{\partial y}$ be the rate of radiative heat flux, c_p the specific heat constant. The rate of radiative heat flux $\frac{\partial q_r}{\partial y}$ is given by :

$$\frac{\partial q_r}{\partial y} = 4\sigma^* k^* (T^4 - T_\infty^4) \tag{10}$$

where $\sigma *$ is Stefan -Boltzmann constant and k^* is the mean absorption coefficient, respectively. Now (7) can be written as:

$$u\frac{\partial T}{\partial x}+v\frac{\partial T}{\partial y}=\ \alpha\frac{\partial^2 T}{\partial y^2}\ -\frac{1}{\rho C_p}[\ 4\sigma^* k^* T_\infty^4\{\ [1+(\theta_w-1)\theta]^4-1\}] \quad (11)$$

The dimensionless variables in this problem are :

$$\eta=y\sqrt{\frac{U}{2\vartheta x}}, u=Uf'(\eta), v=\sqrt{\frac{U\vartheta}{2x}}\ (\eta f'-f), \quad \theta(\eta)=\frac{T-T_\infty}{T_w-T_\infty} \quad (12)$$

Where $f(\eta)$ represent the dimensionless stream function and $\theta(\eta)$ represent the non-dimensional temperature. where $U=U_w+U_\infty$. Using (11), (5) is automatically satisfied and (6), (10) generate the following differential equations by implementing (8) :

$$f'''+ff''+M(\gamma-f')=0 \quad (13)$$

$$f\theta'+\frac{1}{Pr}\ \theta''-Rd\ \theta\ \left[1+\frac{3}{2}\ \theta\ (\theta_w-1)+\theta^2(\theta_w-1)^2+\frac{1}{4}\theta^3(\theta_w-1)^3\right]=0 \quad (14)$$

with boundary conditions:

$$f(0)=0, f'(0)=1-\gamma, \theta(0)=1, \quad f'(\infty)\to\gamma, \quad \theta(\infty)\to 0 \quad (15)$$

Where $\gamma=\frac{U_\infty}{U}$ is the velocity ratio parameter, $Rd=\frac{32x\sigma^* k^* T_\infty^3}{\rho C_p U}$ is the Weissenberg number, $Pr=\frac{\nu}{\alpha}$ is the Prandtl number, $M=\frac{\sigma B_o^2}{\rho U}$ are the radiation parameter and $\theta w=\frac{T_w}{T_\infty}$ is the temperature ratio parameter.

The analysis is non-dimensional and the values range therefore the values considered are chosen merely to check the stability of numerical solution. However dimensional quantities related to physical phenomenon can be verified as well.

IV. Numerical Solution

In order to solve the higher-order differential problems numerically. They are transformed into a system of 1st order equations using new variables. Therefore, let $y_1=f; y_2=f';\ y_3=f'';\ y_4=\theta$ and $y_5=\theta'$. The equivalent first-order equations are as follows:

$$y_1'=y_2; y_2'=y_3; \quad (16)$$

$$y_3'=-M(\gamma-\ y_2)-y_1\ y_3 \quad (17)$$

$$y_4'=y_5; \quad (18)$$

$$y_5'=-(y_1\ y_5\ Pr)+(PrRdy_4\ [1+\frac{3}{2}y_4\ (\theta_w\text{ -1})+y_4^2\ (\theta_w\ -1)^2+\frac{1}{4}\ y_4^3(\theta_w\ -1)^3\ ] \quad (19)$$

with boundary conditions

$$y_1(0)=0;\ y_2(0)=\ 1-\gamma; y_4(0)=1;\ y_2(\infty)=\ \gamma;\ \ y_4(\infty)=\ 0 \quad (20)$$

The solution of Eq. (15-19) is obtained using the fifth order Runge-Kutta integration technique with the following initial conditions

$$y_1(0)=\ 0;\ y_2(0)=\ 1-\gamma;\ y_3(0)=\ u_1\ \ y_4(0)=\ 1;\ \ y_5(0)=\ u_2 \quad (21)$$

This solution can agree with the original BV P for suitable values of u_1 and u_2.

V. Results and Discussion

Using Runge-Kutta integration, the boundary value problem given in Equations 12 and 13 with boundary condition's equation 14 is solved. To make sure that the accuracy of obtained computations and validation of the code we have reproduced the results of [30] in Table 1 and computational values of $\theta'(0)$ for different parametric values have been found out in Table 2 After code validation now we will examine the impact of various emerging parameters on velocity and temperature flow values.

Fig 1 indicates the influence of increment in the velocity ratio parameter γ on the horizontal velocity. A decreament in the boundary layer thickness and enhancement in velocity is observed by an increase in γ when $0\le\gamma<0.5$. An inverted boundary layer is formed and the plate velocity is more than the free flow velocity in range of γ. The velocity field f' is showing an increment for $\gamma>0.5$. The momentum boundary layer becomes thicker when γ increases as the velocity profiles come closer to the free stream velocity.

Velocity distribution on Hartman number M is discussed for two different values of γ in Fig 2. The results show that when $\gamma<0.5$, M increases with a decrease in velocity, and when $\gamma>0.5$, The power of the magnetic field is exactly proportional to velocity. The profiles approach free streams with lower values of η in both situations. If M is increasing, it demonstrates that the intensity of the magnetic field is boosted, the momentum boundary layer thickness is thin. This results from Lorentz force induced perpendicular to the flow by the applied magnetic field. In Fig 3 Prandtl number Pr on the temperature distribution is shown. Thermal diffusivity is dominant for lower values for Prandertl fluid number (such as air and the other gases), during the transfer of energy from the plate, convection dominates when large Prandtl numbers are present (such as water or oil from the machine). This rise in Pr means that thermal boundary layer thickness decreases and the amount of heat dissipation at the plate increases. Impact of Magnetic field on the temperature values is shown in Fig 4. There is an increase in boundary layer thickness by increase in Magnetic field. Consequentlly, the boundary layer thickens due to Lorentz's force acting on the fluid motion. Fig 5 displays the behavior of the temperature ratio parameter $\theta_w=\frac{T_w}{T_\infty}$. By increasing the values of temperature ratio parameter a decrease in boundary layer thickness is seen hence increasing $\theta_w$thins the boundary layer. Fig 6 shows an increment in the value

of velocity ratio γ , Which increases temperature θ thus increase's boundary layer thickness. Fig 7 displays the graph for different values of M . When $0 \leq \gamma < 0.5$, the wall velocity gradient is negative and continues to decrease as the value of γ increases. While on the other hand when $\gamma > 0.5$, the shear stress at the plate is positive and continues to increase as γ increases. Fig 8 Plots different values of Radiation parameter Rd for the wall temperature gradient vs θ_w graph. Increase in Radiation Parameter Rd values, thins boundary layer.

Table 1**:** Comparison of values of $f''(0)$ with those of Cortell

γ	M	*Cortell [18]*	*Present*
0	0	-0.627555	-0.627563
1	1.5	-1.359455	-1.35946

Table 3.2: Numerical values of $\theta'(0)$ for various parametric values velocity ratio γ, Hartman number M Temperature ratio θw, Prandtl number Pr, Rd Radiation parameter.

Pr	γ	M	θw	Rd	$\theta'(0)$
0.72	0.6	0.5	1.5	1	-1.1624
1					-1.36844
3					-2.36318
7	0	0.5	1.5	1	-3.84224
	0.7				-3.56439
	1				-3.44776
7	0.6	0	1.5	1	-3.59957
		1			-3.60676
		2			-3.61097
7	0.6	0.5	1.5	1	-3.60382
			2		-4.43135
			3		-6.47122
7	0.6	0.5	2	0	-1.40757
				1	-4.43135
				2	-6.14564

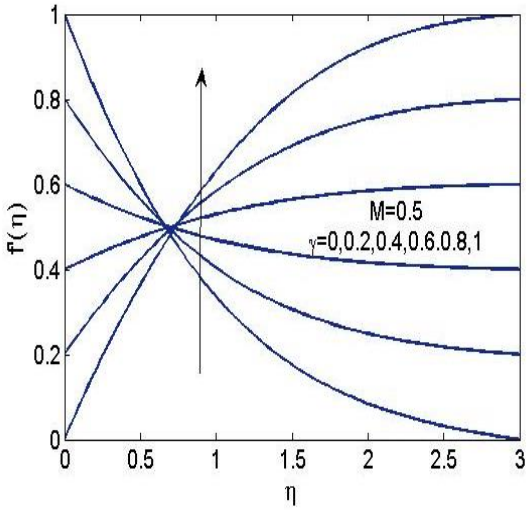


Figure 1:Impact of γ on velocity profile f '

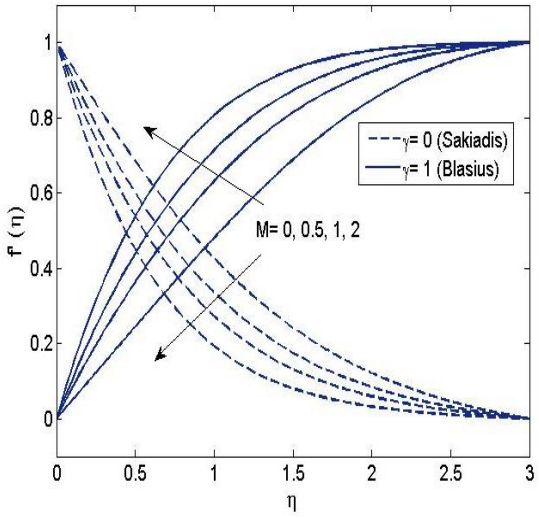


Figure 2:Impact of M on velocity profile f '

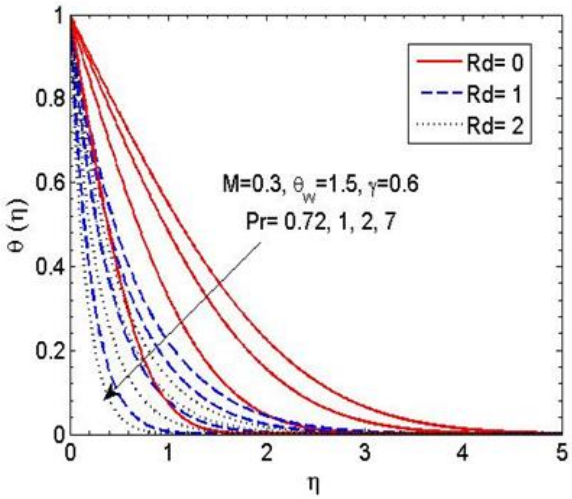


Figure 3:Impact of Pr on temperature profile θ

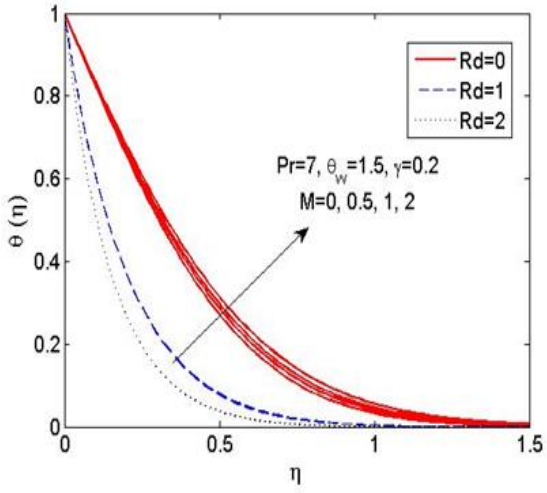


Figure 4:Impact of M on temperature profile θ

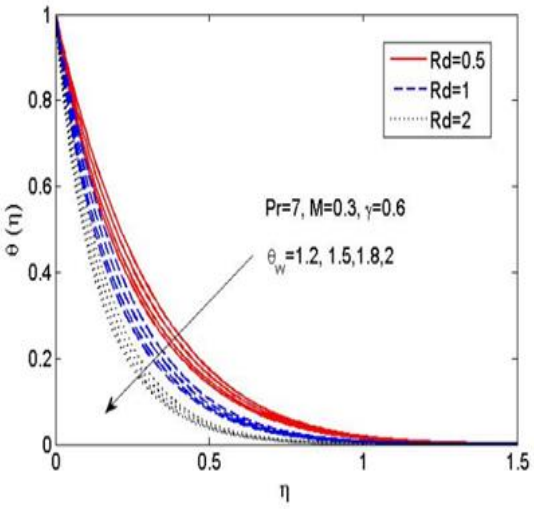


Figure 5:Impact of θw on temperature profile θ

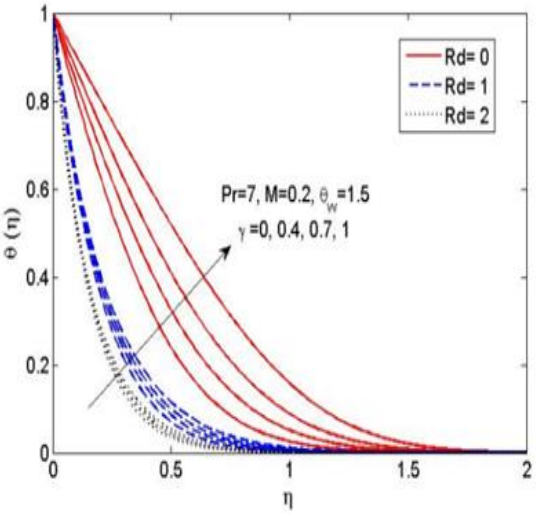


Figure 6:Impact of γ on temperature profile θ

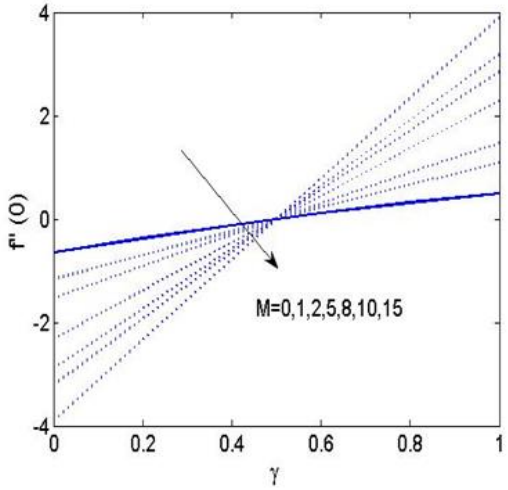


Figure 7:Impact of M on f''(0) against γ

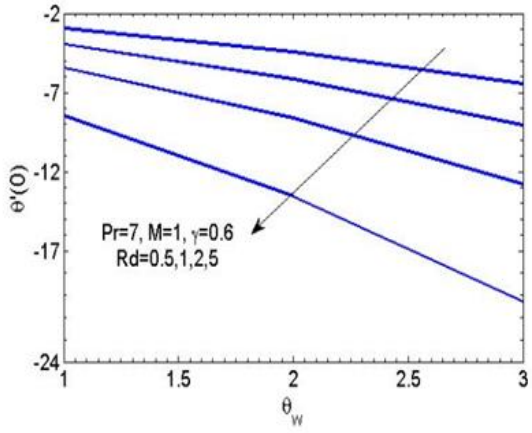


Figure 8:Impact of Rd on θ against θw

VI. Concluding Remarks

This research is pioneer work in the development of generalized numerical solution of boundary layer flow of thin Gray fluids. The presence of non-linear radiative effects in the energy equation led to the highly non-linear but interesting differential equation. Given partial differential equations of thin Gray fluid were simplified by applying appropriate similarity transformations and numerical solutions using the bvp4c scheme. The main results of this study may be summed up as:

- The current problem incorporates an extra parameter called the temperature ratio parameter, compared to the problem of linear heat transfer $\theta_w = \frac{T_w}{T_\infty}$. It shows the difference between the surface temperature and the ambient fluid temperature. This problem gives results for all temperature differences i.e. linear as well as non-linear radiations.
- Regardless of the value chosen for the velocity ratio γ, a higher temperature ratio θ_w and Prandtl numeral Pr ratio leads to thinner boundary layers and a higher temperature and heat transfer from the plate.
- With an increase in velocity ratio γ and Hartman number M both the temperature and boundary layer thickness show an increase.
- By increasing Radiation parameter Rd, thickness of thermal boundary layer decreases with the other parameters fixed.

Acknowledgment

I take this opportunity to record my sincere thanks to all the faculty and staff members of RCMS for providing valuable guidance always.

References

[1] P.P. Puttkammer, Boundary layer over a flat plate, Engineering Fluid Dynamics (2013)

[2] John Anderson, Ludwig Prandtl's Boundary layer, Cambridge U.press,New York (2005)

[3] Blasius, H. Grenzschichten in Flüssigkeiten mit Kleiner Reibung. Zeits Math. Physics,56, 1-37 (1908)

[4] Sakiadis, B. C. Boundary ‐ layer behaviour on continuous solid surfaces: I. Boundary ‐ layer equations for two ‐ dimensional and axisymmetric flow. AIChE J. 7, 26–28 (1961).

[5] Crane, L. J. Flow past a stretching plate. Zeitschrift für Angew. Math. und Phys. ZAMP 21, 645–647 (1970).

[6] Mclead, J.B. and Rajagopal, K.R, on the uniqueness of flow of a Navier-Stokes fluid due to a stretching boundary, Archive for Rational Mechanics and Analysis (1987).

[7] V.M. Falkner, S.W. Skan, Some approximate solutions of the boundary layer equations, Philos. Mag 12 (1931) 865-896.

[8] D.R. Hartee, On an equation occurring in Falkner and Skan's approximate treatment of the equations boundary layer, Proc,Camb.Philos.Soc.33 (1921) 223-239.

[9] K.Stewartson, Further Solutions of the Falkner-Skan equation, Proc.Camb.Philos.Soc.50 454-465.

[10] Rafael Cortell, A Numerical Tackling on Sakiadis Flow with Thermal Radiation, Department of Applied Physics, Polytechnic University of Valencia, 46022 (2007).

[11] Raptis, A, Perdikis C and Takhar H S, Applied Math. Computational. 153 645 (2004).

[12] E.M.A Elbashbeshy, MF. Dimian, Effect of Radiation on the flow and heat transfer over a wedge with variable viscosity, Applied Mathematics and Computation 132 445-454 (2002).

[13] Biliana Bidin, Roslinda Nazar, Numerical Solution of the boundary layer flow over an exponentially stretching sheet with thermal radiation, School of Mathematical Sciences University Kebangsaan Malaysia (2009).

[14] Shahzad Ahmed, M. Ashraf, K.S. Syed, Effects of Thermal Radiation on MHD Axisymmetric stagnation point flow and heat transfer of a Micropolar Fluid over a shrinking sheet, World Applied Sciences Journal 15(6):835-848, (2011).

[15] Asmat Ara, Najeeb Alam Khan, Hassam Khan, Faqiha Sultan, Radiation Effect on boundary layer flow of an Eyring-Powell fluid over an exponentially shrinking sheet , Ain Shams Engineering Journal (2014).

[16] R. Viskanta, R.J. Grash, Boundary Layer in Thermal Radiation absorbing and emitting media, Int. J. Heat Mass Transfer 5 (1962) 795-806.

[17] M.A. Hossain, M.A. Alim , D.A.S. Rees, The Effect of Radiation on free convection from a porous vertical plate, Int. J. Heat Mass Transfer 42 (1999) 181-191.

[18] K.A. Yih , Effect of Radiation on natural convection about a truncated cone, Int. J. Heat Mass Transfer 42 4299-4305 (1999).

[19] M.M.Ali , T.S. Chen and B.F Armaly, Natural Convection Radiation Interaction in Boundary Layer Flow over Horizontal Surfaces, AAIA Journal, Vol.22, No.12, pp.1797-1803 (1984).

[20] P.V.S.N. Murthy, S. Mukherjee, D. Srinivasacharya and P.V.S.S.S.R. Krishna, Combined Radiation and Mixed Convection from a Vertical Wall with suction in a Non-Darcy Porous Medium, Acta Mechanica, Vol.168, No. 3-4, pp.145-156 (2004).

[21] A.R. Bestman and S.K. Adjepong, Unsteady Hydro-Magnetic Free Convection Flow with Radiative Heat Transfer in a Rotating Fluid, Compressible, Optically thin Fluid, Astrophysics and space science, Vol.143,No.2. pp.217-224 (1988).

[22] W.G. England, and A.F. Emery, Thermal Radiation Effects on the Laminar free convection boundary layer of an absorbing gas, Journal of Heat Transfer 91,37-44 (1969).

[23] R. Muthucumarawamy and P. Chandrakala, Effects of Thermal Radiation on moving vertical plate in the presence of the optically thin Gray gas, Forsch Ingenieurwesen 69,205-208 (2005).

[24] R. Muthucumarawamy and A. Vijayalakshimi, Radiation Effects on ow past an impulsively started vertical plate with variable temperature and mass flux, Theoretical and Applied Mechanics, 32(3), 223-234, (2005).

[25] V. Rajesh, Radiation Effects on MHD free convective ow near a vertical plate with ramped wall temperature, International Journal of Applied Mathematics and Mechanics 6(21), 60-77 (2010).

[26] U.S. Rajput and S. Kumar, Rotation and Radiation Effects on MHD ow past an impulsively started vertical plate with variable temperature, International Journal of Mathematical Analysis 5(24),1155-1163, (2011).

[27] Das UN, Deka RK, Soundalgekar V M, Radiation Effects on flow past an impulsively started vertical infinite plate, J TheoMech 1:111-115(1996).

[28] Soundalgekar VM, Takhar HS, Radiation Effects on free convection flow past a semi-infinite vertical plate, Model Meas Control B 51:31-40 (1993).

[29] Hossain MA, Takhar HS, Radiation Effect on mixed convection along a vertical plate with uniform surface temperature, Heat Mass Transfer 31: 243-248 (1996).

[30] Cortell, R, Flow and heat Transfer in a moving fluid over a moving flat surface, Theoretical and Computational Fluid Dynamics, Vol.21 No.6, pp.435-446 (2007).

Author Index

Author	Page	Author	Page
Aamer Shahzad	66	Dr. Muhammad Adnan Shahid	163
Abdul Hanan	114	Dr. Muhammad Tahir	86
Abdul Hanan Hamid	156	Dr. Munawar Shah	71, 76, 260
Abdur Rafeh Abbasi	156	Dr. Najam Abbas Naqvi	48
Absar Ahmed Khan	56	Dr. Rehan Mahmood	79, 86, 91
Adnan Maqsood	106	Dr. Rizwan Mughal	91
Ahmad Hammad	197, 273	Dr. Salma Zainab Farooq	151
Ammar Mushtaq	213, 277	Dr. Shahid Mahmood	168
Areeba Azhar	124	Dr. Waqas A. Qazi	177,181,191
Arif Hussain	253	Ejaz Nazir	71
Arooj Shafique	91	Erman Senturk	156
Asifullah Khan	140	Faheem Akhtar Chachar	253
Asim Khan	71	Faisal F. Khan	232
Asim Mehmood	19	Gohar Majeed	19
Asim Shahzad	124	Hadia Batool	228
Asiya Khan	114	Hammad Munawar	146
Asra Imtiaz	52	Hamza Akbar Khan	220
Awais Munawar Qureshi	96	Hamza Bin Babar	71
Ayesha Hakim	114	Hamza Malik	146
Ayesha Malik	173	Hassan Sadiq	48, 187
Azeema Azhar	117	Hina Magsi	253
Beenish Batul	42	Hira Aftab	42
Daboor Sultana	76, 156	Hussna Zainab	52
Dr. Ali Sarosh	6	Ijaz Ali	202
Dr. Amir Rashid Chaudhry	206	Ilyas Mahmood Qureshi	197
Dr. Arslan Ahmed	253	Imaan Shahid Raja	206
Dr. Asad Ali	241	Imtiaz Nabi	151
Dr. Hayat Muhammad Khan	91	Irtiza Ali	15
Dr. Hossein Raza Hamdani	52	Javid Rashid Ch	206
Dr. Imran Tahir	206	Kashif Mehmood	19

Khalid Mahmood	114	Muneef U. Rehman	232
Khudeja Salim	232	Muzaffar Habib	26
Labeeqa Zaheer	181	Nabeel Uddin Sheikh	206
M. Naveed Tahir	124	Naeem Akhter	112
Mamoona Waheed	173	Nauman Latif	197
Maria Siddiqua	112	Noman Ahsan	202
Mazhar Shehzad	201, 277	Noor Ul Huda Atif	248
Moaz Rao	197	Obaid Ur Rehman	2
Mohamed Freeshah	71	Osama Ali Ahmed Awan	6
Mohammad Usman	48, 187	Oscar Lionel	104
Mohsin Javaid	96	Pawan Kumar	104
Moosa Bin Saif	168	Punyawi jamjareegulgarn	260
Muhammad Abubakar Arshad	86	Rafia Sarwar	241
Muhammad Adeel Khan	19	Raja Muhammad Sohail Khan	146
Muhammad Ahmad	202	Rehan Mahmood	83
Muhammad Anas	26	Rimsha Ashraf	260, 266
Muhammad Arif Arshad	126	Rizwana Kausar	96
Muhammad Arqim Adil	71, 156	Sabih Ahmad Khan	220
Muhammad Asfandyaar Arshad	91	Saddam Hussain Khan	140
Muhammad Ayaz Ahmad	220	Sadia	197
Muhammad Danish Majeed	163	Sadia Maryam	277
Muhammad Ibtisam Babar	117	Saif Ullah Khan	163
Muhammad Ihtisham Babar	117	Salem Mohammed Alohani	26
Muhammad Mubeen	168	Salman Amir	206
Muhammad Rashid Liaqat	273	Salman Qadri	114
Muhammad Saifullah	114	Saqib Mehdi	156
Muhammad Saqlain	163	Saqlain Abbas	194, 202
Muhammad Shaarif Younas	197	Shahzad Hameed	2
Muhammad Shoaib Ul Hassan	48, 187	Sheeza Khalid	177
Muhammad Umair Shahid	202	Shireen Mushtaq	260, 266
Muhammad Waleed Khan	140	Shujaat Hussain	96
Muhmmad Ahsan khan	132	Subhe Seeme	163
Muhmmad Waqas	241	Suleman Qamar	140

Sumaira Abbasi	228	Usama Rehman	19
Sunnyaha Saeed	151	Usama Saleem	15
Syed Hadi Hussain Shah	253	Usman Azeem	79
Syed Irtiza Ali Shah	220	Usman Imran	91
Syed Muhmmad Basit Ali	15	Zahid Mehmood	6
Taimur Ali Shams	220	Zohair Anjum	206
Tanveer Ahmad	114	Zuhaib Hassan	2
Tariq Abbas	191	Zukhruf Liaqat	66
Tayyaba Shafaq	206	Zulkarnain Abbas	202

PROCEEDINGS

Seventh International Conference on Aerospace Science and Engineering

December 14 – 16, 2021

Institute of Space Technology

Islamabad, Pakistan

Organized by

National Center of GIS and Space Applications (NCGSA)

NCGSA

NATIONAL CENTER OF GIS & SPACE APPLICATIONS

PARTNERS & SPONSORS

CONFERENCE SECRETARIAT

Institute of Space Technology, 1 Islamabad Expressway,
Islamabad 44000, Pakistan

+92-51-9075799, +92-333-2662857

icase@ncgsa.org.pk

www.ncgsa.org.pk | www.ist.edu.pk

/IST.islamabad | /ICASE.IST | /ncgsa.ist